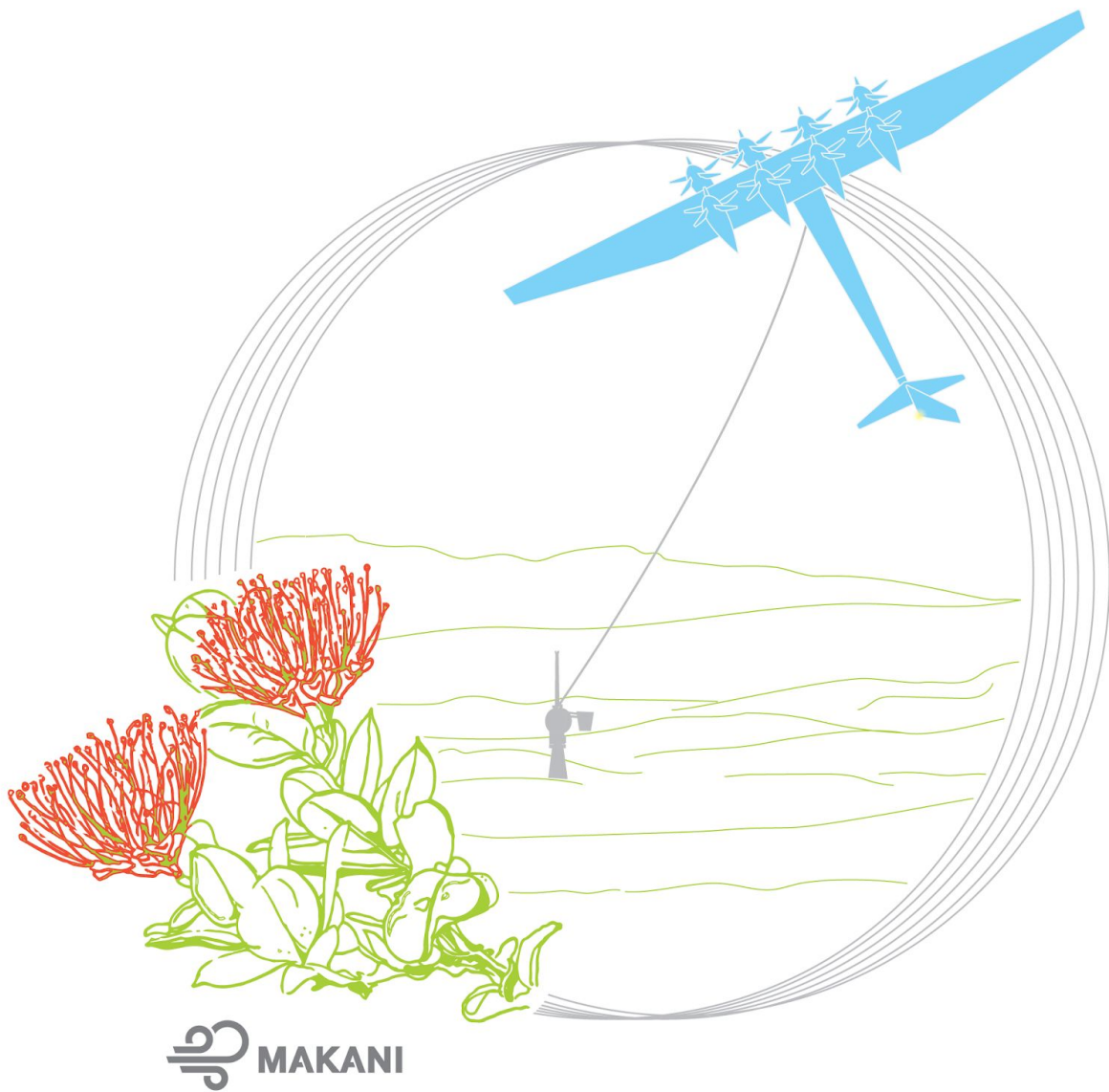


# The Energy Kite

Selected Results From the Design, Development and Testing of  
Makani's Airborne Wind Turbines

Part I



Paula Echeverri | Tobin Fricke  
Geo Homsy | Nicholas Tucker

# The Energy Kite:

Selected Results From the Design, Development and Testing of  
Makani's Airborne Wind Turbines



**A long-exposure photograph of the Makani M600, SN4 "Lanakila," in night flight over the northern slopes of Mauna Kea, May 2019.**



# The Energy Kite:

Selected Results from the Design, Development and Testing of  
Makani's Airborne Wind Turbines

Paula Echeverri, Tobin Fricke, Geo Homsy, Nicholas Tucker, on behalf of the Makani team



The Energy Kite: Selected Results from the Design, Development, and Testing of Makani's Airborne Wind Turbines, Part I of III / by Paula Echeverri, Tobin Fricke, Geo Homsy, Nicholas Tucker, on behalf of the Makani team.

Copyright © 2020 by Makani Technologies LLC

Distributed under the [Creative Commons CC BY 4.0 License](https://creativecommons.org/licenses/by/4.0/). You are free to copy and redistribute this material in any medium or format for any purpose, even commercially.



Intended for electronic publication and distribution. Copies of this volume may be found at <https://archive.org>

Additional information is at <https://x.company/projects/makani>

Corresponding author: Paula Echeverri, [paulae@alum.mit.edu](mailto:paulae@alum.mit.edu)

Published September 2020

Photos: Andrea Dunlap and archive team

Front cover illustration: Kate Stirr

Frontispiece photo: Betsy Pfeiffer

Editing and layout: Betsy Pfeiffer

Cover art: Hawaiian 'ōhi'a lehua flower and Makani's M600 energy kite flying crosswind on the big island of Hawai'i.



*For Corwin Hardham  
Energy kite pioneer, inspiring leader, loving friend, and stupendous badass  
1974–2012*

A dusty grammar school usher and a sub-sub-librarian take many pages to tell you everything known about whales before each steps aside (well, before each dies, actually) to permit you to hazard the extremely perilous, mind- and heart- and molecule-altering voyage that is *Moby Dick*, in the course of which voyage you realize that neither the usher nor the sub-sub, nor you, nor for that matter the crew of the Pequod nor their lunatic captain knows Thing One about what a whale is. When it's a damp, drizzly November in your soul, Ishmael tells us, plunge in without preparation! The sea awaits!

—Tony Kushner, from *Angels in America*

# Contents

<b>Acknowledgements</b>	<b>ix</b>
<b>Foreword</b>	<b>x</b>
<b>Introduction</b>	<b>1</b>
<b>Oktoberkite and the MX2: Best Practices in Energy Kite Design</b>	<b>7</b>
Geo Homsy <i>Overview of current best practices in energy kite design, with application to the design of our next generation "MX2" system. Gives MX2 technical details where known and suggests approaches to completing the design.</i>	
<b>Airborne Wind Turbine Performance: Key Lessons From More Than a Decade of Flying Kites</b>	<b>89</b>
Nicholas Tucker <i>A look at the performance limits and sensitivities of airborne wind turbines, building an analytical model to enumerate and quantify major loss factors and compare performance to HAWTs.</i>	
<b>M600 Energy Kite Description</b>	<b>225</b>
Paula Echeverri, Tobin Fricke, Geo Homsy, Nicholas Tucker <i>Description of the M600 system as-built and the M600 power curve as-flown.</i>	
<b>The Makani Autopilot: A Critical Retrospective</b>	<b>259</b>
Tobin Fricke <i>A complete overview of the Makani autopilot, estimator, and simulator; includes a discussion of lessons learned and open problems.</i>	
<b>Makani's Flight Testing Approach</b>	<b>339</b>
Paula Echeverri <i>Account of flight testing programs at Makani, with an emphasis on testing of the M600 system, and a discussion on selected learnings.</i>	

# Acknowledgements

Although this report carries only a few authors' names on the title page, the credit is truly due to the entire Makani design, engineering, build, testing, and operations teams. Over two hundred people have worked tirelessly on this project over a period of thirteen years, and they have produced thousands of work products along the way. Our work as authors has been to write the overview articles of Part I, reporting on their accomplishments, and to curate a limited but representative selection of the team's own documentation providing detailed background. Without the Makani team's technical acumen, dedication to the cause, and perseverance under challenging conditions, these volumes would not exist, and our accumulated knowledge and experience would be lost to the years. We, and the energy kite pioneers of the future, owe them a huge debt of gratitude.

# Foreword

The world needs enormous amounts of affordable clean energy to replace existing fossil fuel power plants, and to meet the growing demand for electricity in developing countries. Makani's expert team was motivated by this need, and worked hard for 13 years to develop a new airborne wind power technology that could make a difference. This report, and the accompanying videos, software, and test data, documents some of the most important accomplishments and lessons learned. We hope that this material will be helpful to future investigations.

The scale of the problem that Makani sought to address is immense. It's a huge task to bring a new energy technology to market—the development time for clean power technologies such as conventional wind and solar power was measured in decades, with the total development cost equal to billions of present-day dollars. After that, the scale of the deployment needed is also immense—a fleet of 10,000 mature 1-MW energy kites would be required to provide 1% of the electricity in the United States. These kite systems would need to be low in cost and extremely reliable.

These challenges of scale, both in terms of development time and cost and in terms of the deployments needed to make a difference, led Makani to make bold decisions. We increased the power capacity and size of the kites in huge steps, we rapidly pushed into difficult operational environments, and we took on new challenges without waiting for all the answers to our prior challenges. This approach was taken in an effort to reach commercial scale and maturity as quickly as possible—the need for clean power is urgent!

Significant progress was made. Many required new technologies were invented from scratch. More than 200 patents were awarded. New mathematical models, design frameworks and simulation tools were developed. The world's first large-scale energy kite system was manufactured and tested.

As a way to assess progress, the 2010 NREL presentation [Engineering Challenges of Airborne Wind Technology](#) provides a basic roadmap for the development of energy kite systems. Of the many challenges identified in that presentation, Makani was able to successfully:

- Bring a comprehensive reliability methodology to the development of critical subsystems
- Develop a realistic plan with an independent agency for the certification of Makani's energy kite system
- Establish an automated process for the calculation of design loads over the full operational environment
- Develop and validate a robust simulation capability
- Develop a fully autonomous control system including launch and landing

- Establish new models for the aeroelastic analysis of tethered flight vehicles and calculate flutter boundaries
- Complete dozens of test flights of large-scale highly-instrumented energy kite systems in a wide range of environments, including a flight from a floating offshore platform
- Develop a comprehensive systems engineering model for energy kite systems that can find optimum configurations using detailed component cost, weight and performance data

Despite this progress, enormous challenges remain. There are no examples of flight vehicles operating continuously without any maintenance for months at a time, yet continuous unattended operation is at the core of the mission specification for a wind power system. There are no examples of flight vehicles being manufactured in the large quantities and at the low cost required for the commercial success of a wind power system. It will be difficult to develop a robust fault-tolerant energy kite system—there are many failure modes that can prevent a successful landing of the kite. Many environmental challenges, such as icing and lightning strikes, still remain to be addressed.

In the end, the business case for the further development of Makani’s technology was not strong enough to secure additional investment. Many risks remain, and conventional wind power technology continues to improve, with reliability going steadily up and costs coming rapidly down.

We are grateful for the support provided over many years by ARPA-E, Google, X, Alphabet, and Shell. In particular, the enthusiastic engagement and support of Sergey Brin was instrumental in Makani’s progress. These supporters shared our passion for the mission, provided plenty of excellent advice, and encouraged Makani to be bold and move fast.

Finally, I’d like to acknowledge the Makani team. Perhaps 200 individuals worked on the project at one time or another over 13 years. Some worked for only a few months, while others contributed 10 years or more. The skill, creativity, commitment and determination shown by this team was extraordinary and inspiring. It has been a great privilege working with the Makani team, laughing with them, and sharing our failures and successes. Thank you all!

*—Fort Felker  
CEO, Makani*

# Introduction

Makani has spent the last 13 years designing and building kites to harness energy from the wind with the goal of creating a new way to bring wind power to more people around the globe. Founded by kitesurfers in 2006, the team started testing their airborne wind power concept with soft kites and iterated through eight models of rigid kite, culminating in the M600 energy kite, a prototype utility-scale system.

At 85 feet in span, the Makani M600 energy kite is designed to produce electricity from wind at utility scale in deep water offshore environments. It pushes technological boundaries in several areas, including high-maneuverability and high-lift aerodynamics, hover to wing-borne flight transition, high voltage electrical propulsion / generation systems, and tethered flight stability and control.

The M600 uses an on-board generation (“props-on-kite”) approach. This allows use of a high performance rigid wing, enabling easy launch and land operation by using the power system in propulsion mode to hover the kite. The propulsion / generation system uses a novel high voltage DC drive and transmission architecture and control scheme, enabling it to reliably transfer up to 1 MW of electrical power to and from the electrical grid through a tether less than 30 mm in diameter.

The wing is a bonded carbon fiber monocoque structure comprising two main spars enclosed between laminated, cored upper and lower wing surfaces. The fuselage, empennage, and the four powertrain pylons are similarly constructed. The tether comprises a mechanical load-bearing core of pultruded carbon fiber rods, surrounded by a bedding layer, a layer of spiral-wound insulated electrical conductors, and covered in an aerodynamically fluted jacketing material.

The M600 starts each flight as a VTOL tailsitter, “borrowing” power from the grid to hover. Its control software autonomously coordinates with the ground station to pay the tether out, as the craft ascends to full height. When the tether reaches full length, the craft accelerates rapidly, transitioning from a hover flight mode to a high-lift, high tension tethered flight mode, and transitioning from motoring to generation.

After extensive testing in Southern California and in Hawaii, the M600 completed its first offshore power-producing test flight in Norway in August, 2019.

The M600 flight program has been successful in demonstrating launch, land, and autonomous control of crosswind power generating flight. It is the largest and most powerful craft ever to successfully do so.

Regrettably, the absolute power performance of the M600 falls far short of the original design intent. The reasons for this underperformance are understood in retrospect, and possible solutions are discussed clearly in this volume.

As well, it is unclear whether such a system can be manufactured, installed, and operated to meet an LCOE competitive with conventional horizontal axis wind turbines using currently available materials and techniques—the technology, as it currently exists, is not “ripe” for today’s market.

Makani’s owners elected to discontinue funding for the project in early 2020. However, we have graciously been given permission to place our accumulated knowledge into the public domain, so that others may benefit from the knowledge and experience gained.

In 1948, Palmer Putnam published his monograph *Power from the Wind*,<sup>1</sup> detailing the design, operation, and lessons learned from the world's first megawatt-class wind turbine. It is in this same cooperative spirit that we have assembled this volume: hopefully, and as a helpful guide for the next wave of airborne wind pioneers. Herein we discuss the underlying theory, design guidelines, engineering best practices, and areas for further refinement and development as we currently see them.

This report is intended for technical audiences actively involved in research and development of airborne wind energy, for all those working on difficult problems in the fight against climate change, and, not least, for those inspired by novel and beautiful flying machines. Hopefully the knowledge assembled here will serve as a springboard for successful and economically competitive development in the future.

## Structure of the Report

This document is presented in four parts: three written volumes, plus an online resource library.

**Part I** comprises five technical articles describing the state at which Makani had arrived when we stopped our work.

- “Oktoberkite and the MX2: Toward Best Practices in Energy Kite Design” — Overview of current best practices in energy kite design, with application to the design of our next generation “MX2” system. Gives MX2 technical details where known and suggests approaches to completing the design.

---

<sup>1</sup> P. C. Putnam, *Power from the Wind*, New York, NY, USA: Van Nostrand Reinhold, 1974.

- “Airborne Wind Turbine Performance: Key Lessons From More Than a Decade of Flying Kites” – A look at the performance limits and sensitivities of airborne wind turbines, building an analytical model to enumerate and quantify major loss factors and compare performance to HAWTs.
- “M600 Energy Kite Description” – Description of the M600 system as-built and the M600 power curve as-flown.
- “The Makani Autopilot: A Critical Retrospective” – A complete overview of the Makani autopilot, estimator, and simulator; includes a discussion of lessons learned and open problems.
- “Makani’s Flight Testing Approach” – Account of flight testing programs at Makani, with an emphasis on testing of the M600 system, and a discussion on selected learnings.

**Part II** is a large collection of technical artifacts, in various styles and at various stages of maturity.

Note that these artifacts were produced as Makani internal work products and are presented here as they were written. They may contain references to other material that has not been released or that no longer exists.

The first group is comprised of detailed technical design documents specific to Makani. These files are not necessarily foundational to the problem of airborne wind energy, but they should be of significant interest to other practitioners nonetheless. These include:

- “Makani Systems Overview” – Comprehensive overview (slide deck) of the M600 system, including market opportunity, system components, design methods, and validation approach.
- “A Low Cost Fiber Optics Network for Energy Kites” – Describes how Makani has achieved commercial-aviation-like network integrity and reliability, using low cost consumer-grade COTS components.
- “Base Station Team Final Documentation” – Documentation of base station design considerations for the next generation system, as would have been developed for a commercial demonstration project beginning operations in 2023. Based on lessons learned operating the GS02 machine that was used in Hawaii and Norway flight testing.
- “Ozone Rev1 Design Document” – Explains the process for arriving at electrical specifications for the Makani motor controller, and notional electronic design that meets those specifications. Requires extensive Makani-specific context (motor out operation, etc) to understand 100%, but will be useful in general for high-power-density aviation designs
- “Control Telemetry User’s Guide” – Description of the telemetry data produced by the simulator and flight tests. Essential to understanding and making use of the online archive of flight test data.

The next group of papers presents Makani's attempts to understand the underlying physics of energy kite stability and control. These are presented in the hope that they may prove useful for further research on tethered flight:

- "Effect of Design Parameters on the M600 Stability in Crosswind" – An introduction to the problems introduced into flight stability by the tether.
- "Kite Stability in Crosswind Flight" – Gives a ground-up derivation of tethered crosswind flight stability.
- "Tether Attachment and Bridle Knot Trim Considerations for Energy Kites" – Makani's observations on placement of bridle attachment points for energy kites, to maximize controllability and power output.
- "Crosswind Kinematics" – Calculations of the motion required to follow a flight trajectory while also tracking angle of attack, angle of sideslip, and airspeed commands.

These are followed by a few papers on best practices for energy kite design:

- "The Spreadsheet Kite Structure Sizer" – Explains how we compute predicted airframe mass from performance requirements and input parameters.
- "Dimensionalizing and Sizing of Control Surfaces for Stability and Authority" – Gives best practices on how to size an empennage and associated control surfaces, for adequate stability and control authority. Includes an important observation specific to energy kites, in which the propulsion system *extracts* energy from the flow instead of adding. This has significant implications for surface sizing.
- "BigM600 Tail Sizing White Paper" – TLG (consultant) work product. A much more detailed approach to tail sizing than that used by Makani in the preliminary design.
- "Airfoil Design for the October Kite - Feasibility Studies" – TLG (consultant) work product. Gives a discussion of how to design from first principles a high-lift, two-element, actuated flap airfoil for energy kite use.

**Part III** comprises a sampling of reports analyzing flight test events, as well as several documents illustrating our progress toward long-term permitting and type certification for airborne wind turbines:

- "Selected Decks From RPX Lessons Learned Reviews" – Collection of presentations prepared after select Remote-Perch Crosswind (RPX) M600 flights in 2016–2018, in which the engineering teams reported on observations from flight data and test day events.
- "Selected Decks From All-Modes Lessons Learned Reviews" – Collection of presentations prepared after select M600 flights in 2018–2019, in which the engineering teams reported on observations from flight data and test day events.
- "Root Cause Analysis and Corrective Actions for FCW-01 Loss of Kite" – Report of the Root Cause and Corrective Actions investigation after loss-of-kite during the final approach of the first floating offshore crosswind (FCW-01) flight test.

- “FAA Determination of No Hazard to Air Navigation for Temporary Structure” – FAA notice of Determination of No Hazard to Air Navigation for Temporary Structures at the Parker Ranch test site in Hawaii (dated 12/14/2019) and at the Sherman Island test site in California (dated 8/18/2014). Should be of interest to, and serve as precedent for, those seeking to conduct similar long-term testing of large airborne wind energy systems.
- “Design-Accompanying Assessment for Certification: Letter Report and Overview of Standards and Evaluation Aspects” – Summarizes DNV-GL’s (consultant’s) review of the M600 design to identify which subsystems and/or components fall within existing wind turbine standards (e.g. IEC, ISO, UL), and which do not. Lays out a roadmap for a technology qualification process to be developed for type certification of energy kites.
- “Bird and Bat Conservation Plan: Makani Energy Kite Project, South Kohala District, Island of Hawai‘i, Hawai‘i” – A report prepared in consultation with Rana Biological and Akinaka & Associates, outlining potential impact to threatened species at the Makani test site on the island of Hawai‘i as well as specific measures to ensure flight testing operations would minimize and mitigate impact.

**We are also sharing an online resource library**, comprising a large body of material that does not fit into a printed format. These include:

- Makani’s entire avionics, flight controls, and simulation code repository
- Flight data logs for every crosswind flight of the M600
- A non-assertion pledge for the free use of Makani’s worldwide patent portfolio
- A feature-length documentary film
- Additional photo and video material including full flight test videos and quick interviews on assorted technical topics

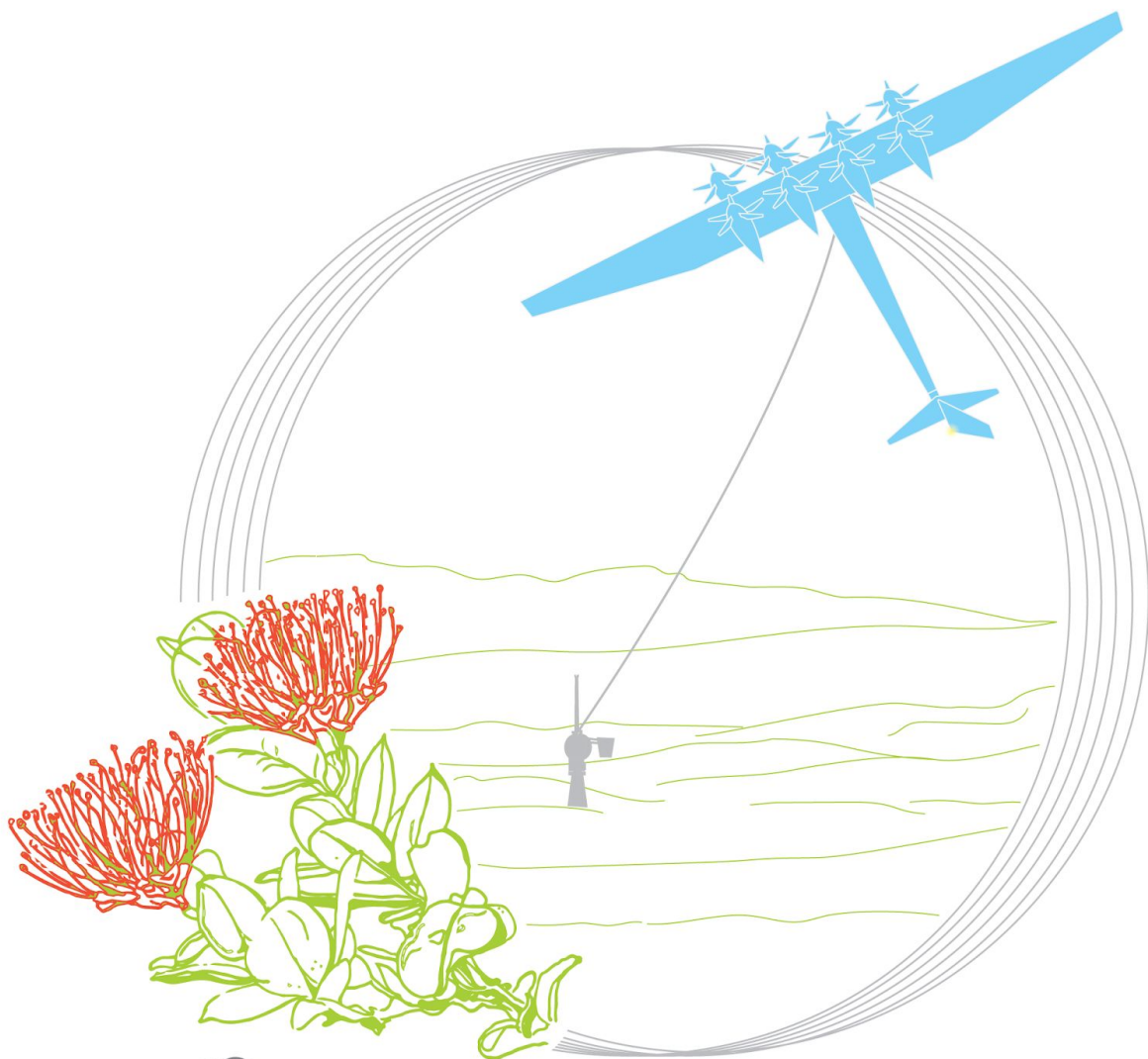
An index to these resources, with locations, access instructions, and instructions for use, is given at <http://x.company/projects/makani>.

Finally, Makani and NREL have cooperatively developed KiteFAST: an extension of NREL’s coupled dynamics wind turbine model, OpenFAST, for use in the simulation of energy kites. This aero-servo-elastic simulation tool is intended to be used for energy kite certification. NREL will publish the extension as part of the OpenFAST code repository at <https://github.com/openfast>.



# Oktoberkite and the MX2

Toward Best Practices in Energy Kite Design



Geo Homsy



Oktoberkite and the MX2: Toward Best Practices in Energy Kite Design  
Corresponding author: Geo Homsy, [geo.homsy@gmail.com](mailto:geo.homsy@gmail.com)

The Energy Kite: Selected Results from the Design, Development,  
and Testing of Makani's Airborne Wind Turbines, Part I of III  
by Paula Echeverri, Tobin Fricke, Geo Homsy, Nicholas Tucker,  
on behalf of the Makani team.

Copyright © 2020 by Makani Technologies LLC

Distributed under the [Creative Commons CC BY 4.0 License](https://creativecommons.org/licenses/by/4.0/). You are free to  
copy and redistribute this material in any medium or format for any purpose,  
even commercially.



Intended for electronic publication and distribution. Copies of this volume may be found at  
<https://archive.org>

Additional information is at: <https://x.company/projects/makani>

Published September 2020

<b>1 Introduction</b>	<b>11</b>
1.1 Energy kites are not airplanes	11
1.2 System architecture	12
1.3 Shortcomings of the M600	13
1.4 The basis of design (Oktoberkite)	13
1.5 What is missing	14
<b>2 System sizing and basis of design workflow</b>	<b>15</b>
2.1 Pencil Specs spreadsheet	15
2.2 Wing Structure Concepts and Sizing spreadsheet	15
2.3 ASWING	16
2.4 Force Balance Loop and Sensitivity Analysis	16
<b>3 Basis of design results</b>	<b>18</b>
3.1 A note on aerodynamic surface sizing for energy kites	18
3.1.1 Rotor effects on dynamic pressure	18
3.2 Wing sizing	18
3.2.1 Summary of sizing results	20
3.3 Stabilizer and control surface sizing	21
3.3.1 Distinction between geometric and aerodynamic tail volumes	21
3.3.2 A note on static lateral stability	22
3.3.3 Stabilizer and control surface sizing workflow	23
3.4 Bridle and tether attachment	26
3.5 Ground station docking	28
3.6 Mass estimation	31
3.6.1 Wing	31
3.6.2 Fuselage and empennage	31
3.6.3 Pylons and powertrains	32
3.6.4 Avionics and other masses	32
3.7 Determining the target mass: Hover thrust capability	32
3.7.1 Hover lift capability vs. moment capability	32
3.8 Roll control in hover	33
3.8.1 Interim solution for Oktoberkite	34
3.8.2 Notional long-term solutions for MX2	34
3.9 Rotor and powertrain sizing	36
3.10 Summary of basic specifications	36
3.11 Predicted performance	37
<b>4 Detailed aerodynamic design</b>	<b>39</b>
4.1 Progressing from preliminary to detailed specifications	39
4.1.1 Airfoil specifications	39

4.1.2 Planform and twist	41
4.1.3 Tail volumes	42
4.2 Preliminary airfoil design	42
4.2.1 Leading edge design	43
4.2.2 Accommodating the spar box and choosing a flap chord ratio	45
4.2.3 Selecting slot gap and overlap	46
4.2.4 Flap shape	47
4.2.5 Flap deflection study	47
4.3 MSES predicted results	51
4.4 Airfoil verification via CFD	53
4.5 Empennage redesign	54
4.5.1 Sizing for stability	54
4.5.2 Sizing for trim and maneuverability	56
4.5.3 Aerodynamic and structural sizing choices	58
4.6 Pylon design and rotor placement	59
4.6.1 Pylon structural considerations	59
4.6.2 Pylon design and placement for best hover performance	61
4.6.3 Pylon design and rotor placement for best crosswind performance	69
4.7 Rotor sizing and design	70
4.8 Bridle and CG placement	70
<b>5 Unfinished work</b>	<b>72</b>
5.1 Flight stability of tethered air vehicles	72
5.2 Tuning and evaluation in simulation	73
5.3 Rotor placement, sizing, design, and pitch selection	74
5.4 Flight controller	76
5.4.1 Pursue designs with passively stable orbits	76
5.4.2 "Soft" path control	77
5.4.3 Total energy approach to longitudinal control (TECS)	77
5.5 Detailed structural design	82
<b>6 Conclusions</b>	<b>84</b>
<b>7 References</b>	<b>86</b>

# 1 Introduction

This chapter summarizes Makani's approach to designing the MX2: the next-generation energy kite proposed to follow the M600. We hope this will be useful for other groups as a starting point, on the way to developing canonical best-practices for energy kite design.

A word of introduction on project terminology: The MX2 design consisted of two phases. In the first phase, we addressed the questions: "With all other subsystems held constant (tether, powertrains, avionics, ground station, ground power), can the M600 be given a new airframe rendering it capable of delivering 600 kW in 11 m/s of wind?<sup>1</sup> If so, what does such an airframe look like?" The resulting study laid out a basis of design for an airframe that should be able to meet the specification. We called this basis of design "Oktoberkite," since the deliverable date for the project was in October of 2019.

In the second phase we set out to complete a detailed aerostructural design, and to begin fabricating production flight articles for the intended Makani offshore pilot program. During this phase, the Makani project was discontinued. As a result, the detailed MX2 design is incomplete. However, much progress has been made, and this article describes that progress and the state of the design as it stands.

So, in this article, the term "Oktoberkite" refers to the basis of design, and the term "MX2" refers to the (incomplete) detailed design project.

We begin our review by observing that, while there are hundreds, if not thousands, of competent airplane designers in the world, adhering to a well established set of best practices, the same is not true of energy kites. And while energy kites of the configuration used by Makani (*i.e.* single main wing, standard fuselage and empennage, and onboard generation) appear to superficially resemble airplanes, it has become clear that standard airplane design flows are inadequate to address the requirements particular to energy kite operation.

These requirements are laid out in this article, along with suggested best practices for energy kite analysis and design.

## 1.1 Energy kites are not airplanes

Airplanes can be designed for different mission profiles to maximize range, speed, payload or other factors. Since energy kites are an emerging technology, it is not *a priori* clear for what parameter(s) a design should be optimized. What is clear is that an energy kite's operating environment, parameters, and behaviors are significantly different than those of an airplane, and that new design techniques and methods are needed to address these differences. For

---

<sup>1</sup> Approximately the original design intent of the M600.

instance, some of the most significant features of crosswind energy kites *not* present in airplanes are as follows:

1. A tether connection to the ground that:
  - a. Represents a significant dynamic stress hazard<sup>2</sup> not present in airplanes
  - b. Greatly impacts stability and trim, depending on attachment point<sup>3</sup>
  - c. Has a Center of Mass (COM) hundreds of meters away from the kite's COM
  - d. Has a Center of Drag (COD) tens of meters away from the kite's COD
  - e. Creates a significant amount of the system drag
  - f. Allows greatly increased wing loading: tether tension can easily exceed the weight of the kite by a factor of 10 to 15
2. A flight path that is never straight and level, but instead is constantly turning, rolling, climbing, and diving
3. Rotors that *extract* kinetic energy from the air, rather than adding to it, thereby reducing the dynamic pressure present at the control surfaces, and making aerodynamic stability and control significantly more challenging

Recognizing these differences has led to important realizations on the fundamentals of energy kite flight dynamics not previously described. These fundamentals are discussed in the Oktoberkite project's library of white papers developed during the fall of 2019, many of which are included in Part II of this report.

Another important realization is the connection between the Loyd parameter for energy kites and the endurance parameter for fixed-wing aircraft: The Loyd parameter,  $C_L^3/C_D^2$ , is exactly the square of the endurance parameter.<sup>4</sup> This has enabled a consultant skilled in aircraft design to optimize for a known performance parameter that is useful for both fixed-wing aircraft and for energy kites.

## 1.2 System architecture

The MX2 Energy Kite shares its basic architectural features with the M600:

- Single two-element lifting surface, with actuated flaps doubling as ailerons
- Single-boom fuselage, with standard "low tee" empennage or with "high vee" empennage
- Four pylons, each fitted with a top and a bottom powertrain

---

<sup>2</sup> As discussed in the article, "Makani's Flight Testing Approach" [6], in the flight "RPX-09," the tether went slack and then snapped tight, effortlessly tearing the airframe into three pieces.

<sup>3</sup> These effects are discussed in Part II, in the articles "Tether Attachment and Bridle Knot Trim Considerations for Energy Kites" [8], "Effect of Design Parameters on the M600 Stability in Crosswind" [7], and "Kite Stability in Crosswind Flight" [9].

<sup>4</sup> As it happens, the task of keeping an airplane in straight and level flight with constant speed while minimizing power expended is geometrically analogous to the problem of extracting the most power from an energy kite traveling crosswind at constant speed. It is no surprise, then, that the parameters to be optimized in each case, endurance parameter *resp.* Loyd parameter, are directly related and give the same design optimum.

- Two-point bridle (though the MX2 bridle is much smaller and may be a rigid bar linkage)
- 4-Series, 2-Parallel stacked power system architecture

### 1.3 Shortcomings of the M600

The M600 was shown to have several shortcomings. Among these were:

- The novel, untested airfoil design made rosy assumptions about the  $C_{L,max}$  that could be reliably achieved in flight, along with overly optimistic  $C_D$  targets.
- As a result, the system  $L/D$  (i.e. including parasitic tether drag) was insufficient to produce the assumed “glide speed”<sup>5</sup>
- The sizing of the wing, combined with lower than expected lift and higher than expected drag resulted in low power performance
- The roll-stiffening effect of a very tall bridle<sup>6</sup> rendered the ailerons unable to exert sufficient roll authority to fly small loops, which are important to power production<sup>7</sup>
- The potential energy swings resulting from large loops forced us into large speed variations. At low winds, we’re often flying much faster than optimum at the bottom of the path, and at high winds, we must fly much slower than optimum at the top of the path to prevent overspeeding at the bottom.
- The resulting large differences in airspeed disallowed the rotors from operating at peak extraction capability through much of the loop<sup>8</sup>

In addition:

- It was shown that there were flight stability issues associated with the choice of a tall bridle<sup>9</sup>
- Empennage sizing was planned for the M600 without taking dynamic pressure deficit due to generation into consideration (see section 3.1.1 Rotor effects on dynamic pressure below), hence the passive stability was inadequate
- The rudder and elevator were undersized, due to the same dynamic pressure deficit

### 1.4 The basis of design (Oktoberkite)

Informed by these deficiencies, the Oktoberkite design team developed an overall airframe basis of design for the MX2 to address the shortcomings. The main differences are:

<sup>5</sup> By “glide speed,” we mean here the equivalent of maximum forward speed of a glider at a given sink rate:  $V_k = (L/D) * V_{sink}$ . In the energy kite context,  $V_{sink}$  is replaced by  $V_{wind}$ . Hence, the glide speed is  $(L/D) * V_{wind}$ . Note that the Loyd optimum kite speed is  $\frac{2}{3}$  of the glide speed [2].

<sup>6</sup> The bridle of the M600 is about 4.5 meters tall (i.e. in the Z direction), or about 18% of the wingspan.

<sup>7</sup> See chapter on “Airborne Wind Turbine Performance” [4] for why small loops are important.

<sup>8</sup> Also, the M600 was fitted with identical rotors at all station positions, even though the apparent airspeed of the top rotors greatly exceeds that of the bottom rotors in crosswind. As well, the inboard rotors see significantly lower airspeed than the outboard rotors. These effects combined, dictated that not all rotors could be extracting maximum power at the same time.

<sup>9</sup> See “Effect of Design Parameters on the M600 Stability in Crosswind” [7].

- The  $C_L$  capability of the wing is more conservatively specified
- The wing area is about 60% larger
- The bridle is of much smaller height, and is placed more carefully, with an eye toward allowing sufficient maneuverability while maintaining adequate flight stability
- The empennage and control surfaces are much larger, for adequate stability and control even when the rotors are operating at maximum generation (hence maximum dynamic pressure deficit)

## 1.5 What is missing

Items remaining incomplete at the end of the Oktoberkite project include:

- Rotor sizes and pitches were never completely or carefully specified, though much work has subsequently been done
- The idea of different rotors at different station positions was not investigated, even though it is likely critical to high-wind performance
- Rotor placement (*i.e.* pylon spacing and Z positions of rotor axes) for best crosswind performance and best hover performance was not well understood, hence underspecified. We developed a much deeper understanding of ideal rotor placement during the detailed design phase. These insights are discussed below in Section 4, Detailed aerodynamic design
- Docking / perching was left unspecified
- Roll control during hover was quite problematic with the M600. This problem is still unresolved
- We had intended to verify and refine the required control authority via CSIM, but this was left incomplete
- A high wind control strategy, especially in light of the additional challenges imposed by imperfect control and turbulence, had yet to be developed and tested
- Finally, although we made significant progress in understanding the bridle's effects on stability and we attempted to develop best practices analytically,<sup>10</sup> we never quite verified the analysis numerically

Obviously, there is significant work left to be done, but it is my hope that this article gives a clear roadmap for how to approach the remaining design issues and practices that were, sadly, left unfinished.

---

<sup>10</sup> See "Kite Stability in Crosswind Flight" [9].

## 2 System sizing and basis of design workflow

Figure 1 below shows the toolchain used during initial development of the MX2:

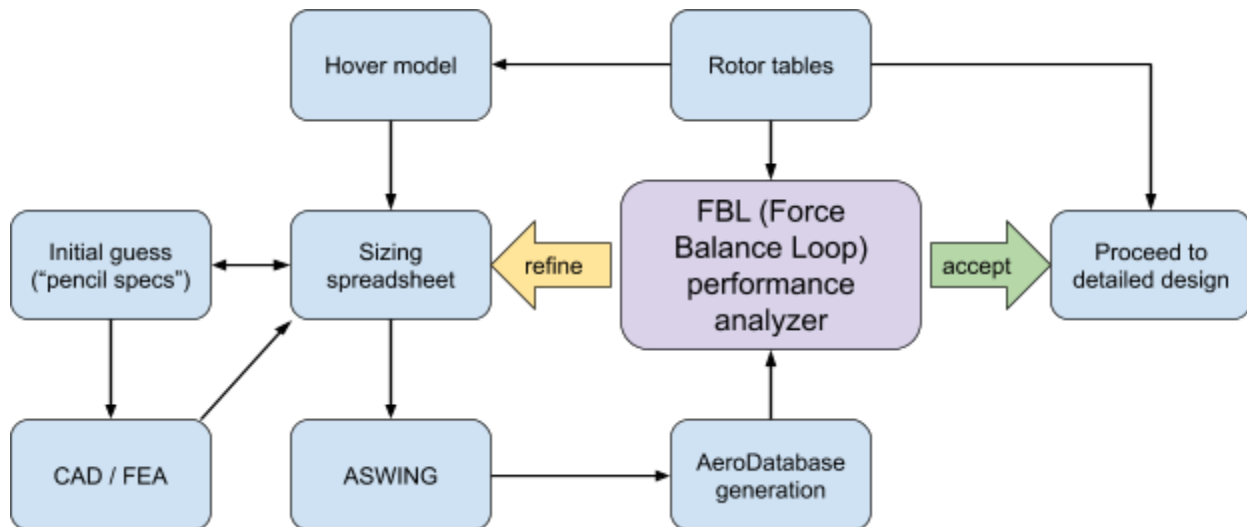


**Figure 1: Basis of design workflow used for initial sizing and preliminary design of the MX2. The preliminary design effort was called “Oktoberkite.”**

As indicated by the color scheme, the Force Balance Loop (FBL) tool, discussed below, is the heart of this preliminary design workflow. We develop best-guess inputs to the FBL, and the FBL results are used as a judge of whether the design should be further refined.

Details of the tool suite are as follows.

### 2.1 Pencil Specs spreadsheet

The “Pencil Specs” is a spreadsheet of initial guesses for specifications, based on early FBL runs and simple scaled M600 models. Over time, as the fidelity of the spreadsheet mass models and the quality of the FBL results increased, these specs were deprecated.

### 2.2 Wing Structure Concepts and Sizing spreadsheet

The Wing Structure Concepts and Sizing spreadsheet takes the nominal operating airspeed and the total lift as input parameters.<sup>11</sup> Its primary function is to size a wing structure based on the

<sup>11</sup> Generally, this is chosen by assuming an achievable L/D, choosing the wind speed at which we wish to reach a chosen tension, and assuming the Loyd optimum airspeed. For instance, for the Oktoberkite, we wished to reach a tension of 250 kN at 11 m/s wind speed, at an assumed L/D of about 8.8. This gives a Loyd optimum airspeed of  $\frac{2}{3} * 11 \text{ m/s} * 8.8 = 65 \text{ m/s}$ . We used the tension as a proxy for the total lift.

resulting aerodynamic and tether loads. It makes some assumptions about structural configuration (e.g. box beam spar, ribs, uncored bottom skin, cored top skin, etc.). The empennage and fuselage sizing is also included in this sheet to size the entire airframe.<sup>12</sup> Given the hand-calculation nature of this tool, it is only suitable for preliminary sizing—providing an estimate of the planform geometry that can be achieved with a specified mass budget. Final sizing and analysis is performed with more sophisticated techniques, as discussed in section 4, Detailed aerodynamic design, below. For a discussion of how the sizer works, see [13].

## 2.3 ASWING

ASWING is a program developed by Mark Drela’s group at MIT to perform aerodynamic and coupled aero-structural analysis of vehicles, from preliminary design phase through detailed structural modeling. We use it to produce the aerodynamic databases used in our simulation tools, and in conjunction with our CAD based FEA tools to check deflection and perform modal, aero-elastic, and flutter analyses. This allows us to confirm the structural design to a reasonable level of confidence before investing in more costly forms of analysis.

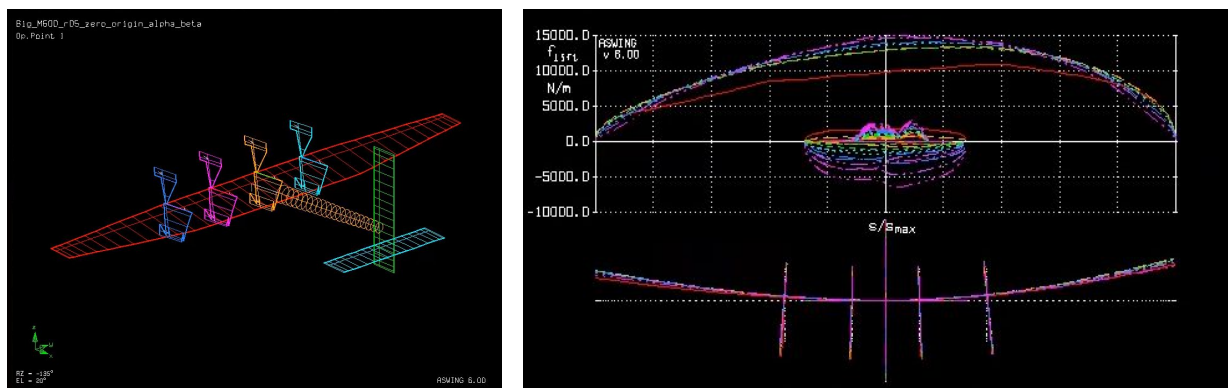


**Figure 2: We used ASWING to generate aerodynamics databases. Example output from ASWING is shown. On the left is a geometric representation of the aero-beam models used as input. On the right is a lift and drag distribution, and output from the beam-bending model.**

## 2.4 Force Balance Loop and Sensitivity Analysis

The Force Balance Loop (FBL) is a Python-based code that optimizes flight plans, or “loops,” for total power production. It works by parameterizing kite states (called “poses”) around a closed loop, solving for the state derivatives between those prescribed states, and determining the forces and moments required to achieve the required state derivative. An optimizer then varies the states to optimize for power and to constrain and minimize force and moment residuals.

Working directly with poses is a significant simplification: It allows the tool to determine the best flight strategies for a kite across the full wind range in minutes, and it obviates the need for

<sup>12</sup> A more detailed explanation is given in the article titled “The Spreadsheet Kite Structure Sizer” [13].

control system design and tuning necessary to run the full time-stepping simulator (discussed in “The Makani Autopilot” article [3]).

Iterating with slightly adjusted variables can reveal sensitivities of the system to changes in different properties or constraints, for instance, finding how a change in mass affects maximum power generated. This is tantamount to numerically computing the gradient of the objective function (power) with respect to the constraints and input parameters.

While a simplified tool is powerful during early design stages, we should be wary of its limitations. In particular, FBL assumes perfect control and a perfectly smooth wind field. Both result in optimistic results, both in terms of required control authority and also in overall performance, especially during highly constrained high wind operation. As such, more detailed simulation is required during later design to further refine concepts.

## 3 Basis of design results

This section goes through the workflow in more detail, discussing how decisions are made and how each tool is used. But first, a note on how reduced dynamic pressure due to generation affects surface sizing:

### 3.1 A note on aerodynamic surface sizing for energy kites

The Oktoberkite project uncovered a significant deficiency in the procedure by which the M600 main wing, stabilizers, and control surfaces were sized: The reduction in dynamic pressure due to rotor drag (generation drag) was handled improperly or ignored altogether. This condition is specific to energy kites, and we spent considerable effort developing a new sizing workflow that addresses this additional challenge. This section summarizes our approach to surface sizing, and represents what we believe to be best practice.

#### 3.1.1 Rotor effects on dynamic pressure

When generating power, the rotors extract momentum from the airflow, hence reducing the dynamic pressure on portions of the wing and at the vertical and horizontal tail. The dynamic pressure incident on the tail,  $q^*$ , is estimated from the airspeed dynamic pressure,  $q$ , using the method below:

$$q^* = q \cdot (1 + C_{Thrust})$$

Where the coefficient of thrust,  $C_{Thrust}$ , is defined as:

$$C_{Thrust} = \frac{2 \cdot Thrust}{\rho \cdot V^2 \cdot A_{rotors}} = \frac{Thrust}{q \cdot A_{rotors}}$$

In practical terms, this means the effectiveness of an aerodynamic surface will be *less* than what would be calculated using the overall airspeed of the vehicle—exactly the opposite of the case of an airplane, in which the propulsion system is *adding* energy to the airflow. It is important to compensate for this deficiency, as discussed in Section 3.3.

### 3.2 Wing sizing

To determine wing size, we begin with the targeted performance of 600 kW electricity delivered at 11 m/s of wind speed. Since  $P_{aero} \leq \frac{1}{3} v_w \cdot Thrust$  [2], and assuming  $P_{elec} \approx 0.65 P_{aero}$ , this means we will need 250 kN of tether tension at 11 m/s. Therefore, (using lift as a proxy for tension), we should arrange the wing  $C_L$  and  $S$  such that the wing produces 250 kN of lift at 11 m/s of wind.

What should the kite speed be? To answer this question, we should take a step back to fundamentals of crosswind power extraction. As discussed in Loyd's seminal paper [2] and further refined in the article "Airborne Wind Turbine Performance" [4], it is instructive to express the aerodynamic power available from a kite in terms of the wind power density  $P_w = \frac{1}{2}\rho v_w^3$  and the reference area of the kite,  $S$ , by introducing a proportionality constant  $\zeta$ :

$$P_{aero} = P_w S \zeta$$

To achieve the goal with the smallest wing possible, we desire that the kite is operating at its maximum achievable zeta in the target wind speed. From Loyd we know that  $\zeta_{max}$  is achieved at  $v_k = \frac{2}{3}v_w(\frac{L}{D})$ . So, if we know the achievable L/D, we can deduce the optimal kite speed.

We estimate the achievable L/D of the kite system (including the tether) to be about 8.8, based on experience with the M600. Hence, the target kite speed is about 65 m/s.

With the target lift of 250 kN and the target airspeed of 65 m/s in hand, we go through the preliminary wing sizing workflow, based on the Wing Structure Concepts and Sizing spreadsheet. The spreadsheet embodies an estimate of the achievable section  $C_l$  available with a dual-element airfoil, chosen conservatively as 2.0 for this preliminary sizing exercise. We manipulate the spreadsheet inputs to achieve the necessary lift while minimizing wing mass. This results in an initial size guess of 54 m<sup>2</sup> and a span of 26 m.

With a rough sizing in hand, we then construct a rough aerodynamic model<sup>13</sup> based on this sizing, and use ASWING to generate an aerodynamic database for the design. This aerodynamic database, along with the structural size and mass and inertia estimates from the spreadsheet, are imported into the FBL tool, and used as a model to estimate the design power curve that should be achievable with such a wing.

We iterated this procedure a few times to converge on an aerodynamic design and a structural design that allowed us to achieve the target power specified for the project. This sizing workflow is summarized in figure 3.

---

<sup>13</sup> By saying "rough" aerodynamic model, we mean we do *not* use any actual airfoil L/D polars. We use a "generic" airfoil proxy, with  $d_{C_l} / d_{\alpha} = 2\pi$ , and we assume a  $C_{l_{max}} = 2$ .

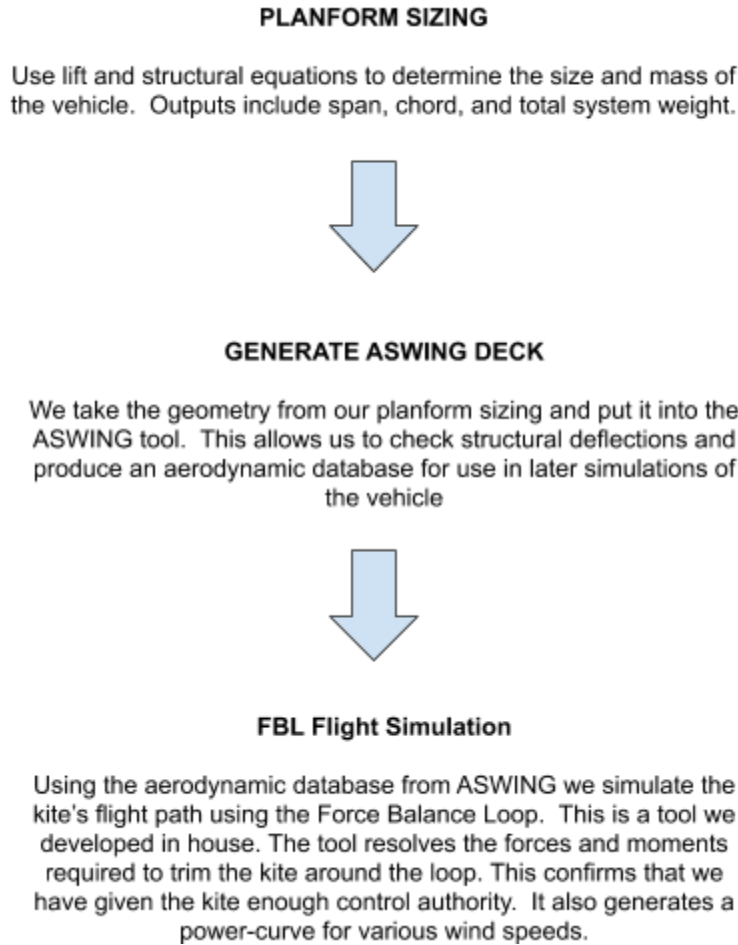


**Figure 3: The spreadsheet sizer / ASWING / FBL workflow is iterated until the notional design is optimized and meets the performance targets.**

### 3.2.1 Summary of sizing results

We arrived at a wing of area 54 m<sup>2</sup> and a span of 26 m, as shown in figure 4 below. This preliminary design has an increased chord, but roughly the same wingspan, as the M600. Obviously, this decreases its aspect ratio. In an airplane, a reduction of aspect ratio from around 20 to around 12 would make a large impact on drag and, hence, performance. In a kite, however, the tether contributes significantly to the “system” drag (drag other than rotor drag due to power generation). By reducing tether length—while simultaneously decreasing aspect ratio—the total system drag of the Oktoberkite increases only slightly, but its lift is increased by about 60%.<sup>14</sup>

Power produced per wing area is largely determined by the Loyd parameter,  $C_L^3/C_D^2$ . Note that the lift coefficient is cubed, while the drag coefficient is squared. The large gain in lift more than

<sup>14</sup> Also note, another way of thinking about this in dimensionless terms is that, by increasing wing area, the effect drag coefficient of the tether is actually *reduced*.

offsets the small increase in drag.<sup>15</sup> Adding this area via span rather than chord would indeed lower induced drag and increase the value of  $C_L^3/C_D^2$ , but would bring with it a thinner, less mass efficient wing structure<sup>16</sup> and reduce the maneuverability of the kite. As we will see later, high maneuverability is essential to support the small path radii necessary for optimal power production.

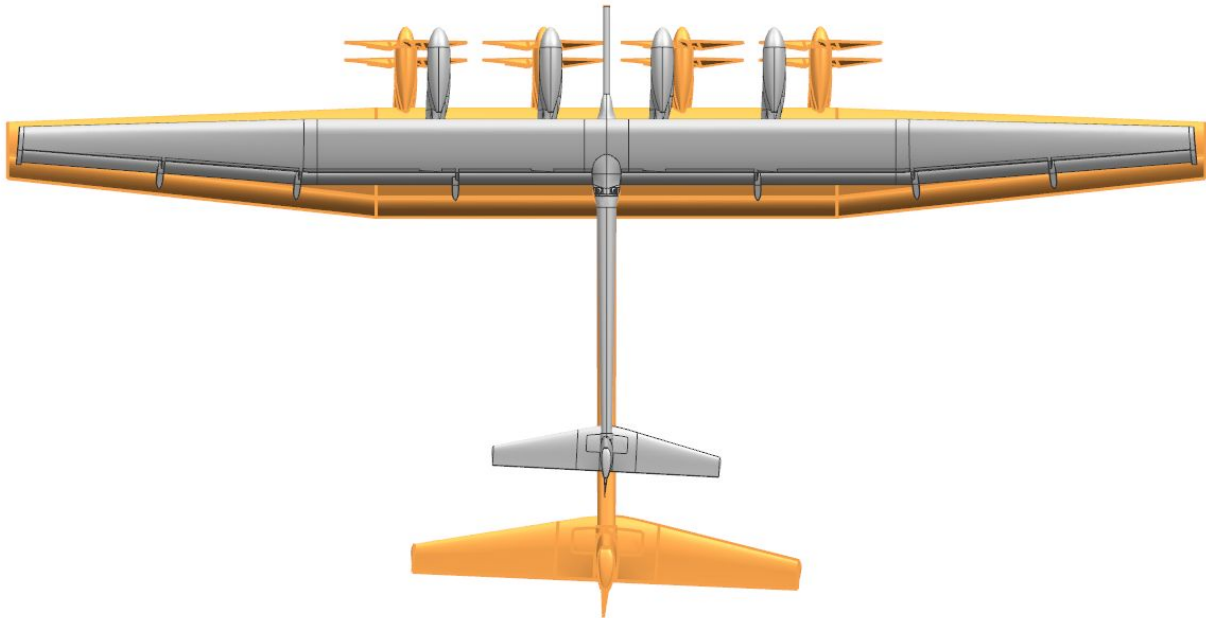


**Figure 4: Comparison of the Oktoberkite (orange) to the M600 (gray). The Oktoberkite has approximately the same span, but about 60% more chord, hence 60% more wing area, than the M600. This allows it to meet its performance target of 600kW at 11 m/s of wind.**

### 3.3 Stabilizer and control surface sizing

To correctly size the tail, empennage, and ailerons, we took care to compensate for the deficit in dynamic pressure due to generation (introduced above). To clarify our thinking, we developed a conceptual framework for dealing with this deficit, discussed below.

#### 3.3.1 Distinction between geometric and aerodynamic tail volumes

In order to clearly distinguish between the aerodynamic effectiveness of a surface and the actual geometry of a surface, we coined the terms “geometric tail volume” and “aerodynamic tail volume.” These terms allow us to easily understand if the surface in discussion has the loss in dynamic pressure effects imposed on it or not.

<sup>15</sup> This is a bit of an oversimplification, since there is an induced drag term that includes  $C_L^2$ . However, the general conclusion holds nonetheless.

<sup>16</sup> Especially important with the much reduced bridle size, which has the effect of increasing bending loads on the wing.

The geometric tail volume is the standard definition of tail volume: the total surface area multiplied by the distance from the reference point. The aerodynamic volume is smaller, by the ratio of  $q^*/q$ , because the dynamic pressure at the tail is *less* than that implied by the airspeed of the vehicle, as shown below (recall that  $q^*$  is the reduced dynamic pressure:  $q^* = q(1 - C_T)$ ).

$$\bar{V}_{geom} = \frac{\sum_i^N A_{VS_i} x_{VS_i}}{B_{ref} S_{ref}} \quad \bar{V}_{aero} = \frac{q^*}{q} \frac{\sum_i^N A_{VS_i} x_{VS_i}}{B_{ref} S_{ref}} = \frac{q^*}{q} \cdot \bar{V}_{geom}$$

The tail design flow is then as follows: using the FBL tool, we establish approximate control moment requirements in terms of aerodynamic tail volume. We then design the airframe to the corresponding geometric tail volume. For empennage sizing, we use an estimated  $q^*/q$  value of 0.69, corresponding to  $C_T$  of the rotors of -0.31. This  $C_T$  corresponds to a thrust in the stall region of the propeller operating envelope, where we do not operate, so this leads to a conservative estimate for  $q^*$ .

Note that, since the pylons are far forward of the wing and have significant vertical surface area, it is necessary to explicitly account for them by computing *the entire vertical surface volume*, instead of just the tail volume. In other words, in the surface volume equations above, the sum was taken over *all vertical surfaces*, including the pylons. This results in a larger tail volume than required for a standard fixed-wing aircraft, since additional tail volume is required to offset the pylon lateral forces forward of the CG.

A similar technique should be used to compensate for reduced dynamic pressure on the ailerons in the center section of the wing (the portion of the span where the rotors are located). However, since the sum above is now a moment integral over the half-span of the wing, and the rotors are mounted significantly inboard while the ailerons have significant area outboard (where the moment arm is greater), the resulting change in surface effectiveness can be considered negligible for a rough design.

### 3.3.2 A note on static lateral stability

A deficiency in the M600 tail surface sizing is that it is not designed for a significant static lateral stability margin. Although the tail volume would be sufficient for stability of a horizontal fixed-wing aircraft, when forward pylon area and reduced dynamic pressure at the tail due to generation are taken into account, the tail volume does not provide enough margin to guarantee stability in all flight conditions. This was found during the test program to be quite a significant issue, as the bridle's destabilizing effect in yaw can easily overpower the tail in certain scenarios, resulting in overall lateral instability.<sup>17</sup>

---

<sup>17</sup> The tail is typically sized to produce a sufficiently positive  $C_{n\beta}$  stability coefficient to ensure yaw stability. However, the tether attachment point, if chosen improperly, can produce large destabilizing yaw moments at certain combinations of tether pitch and yaw, easily overpowering the vertical stabilizer.

### 3.3.3 Stabilizer and control surface sizing workflow

This section summarizes our surface sizing workflow. It consists of two main stages: stability and control. These stages are discussed separately in the following subsections. The detailed derivation and application of these sizing methods can be found in the article, “Dimensionalizing and Sizing of Control Surfaces for Stability and Authority” [12].

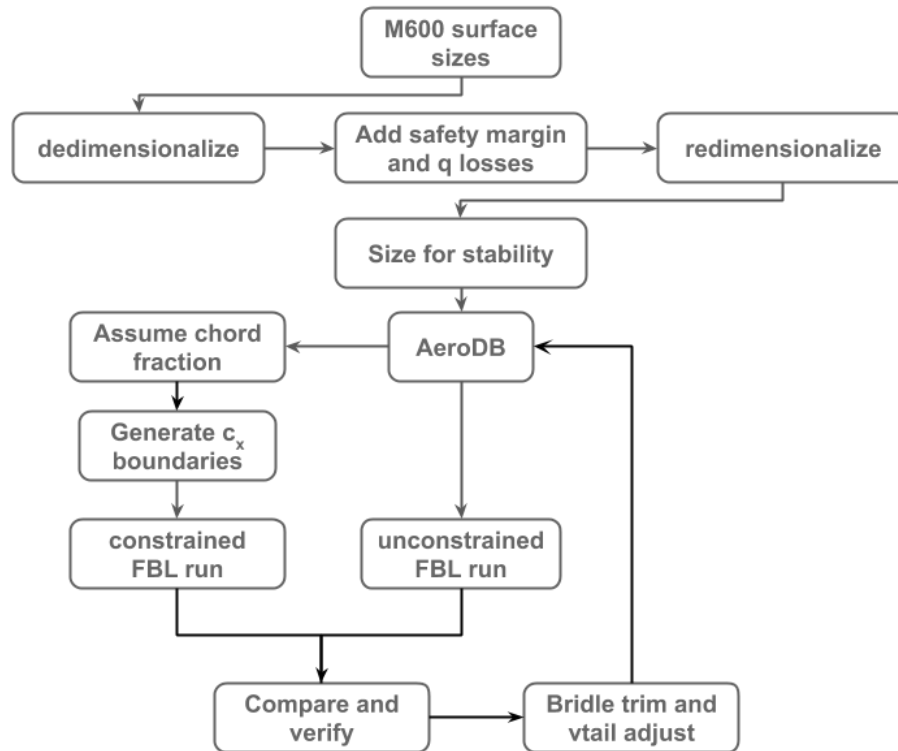


**Figure 5: Details of the tail sizing workflow. We take a guess based on the M600 tail volumes, while adding margin and q losses. This gives us a sizing for static stability. We then run the FBL with no moment constraints, to see if trim is correct, and to evaluate how much control surface area is required. We then constrain the control moments and rerun the FBL to check the control surfaces are sufficient.**

#### 3.3.3.1 Sizing for stability

The vehicle requires a minimum specified tail volume to be stable to first order in pitch and yaw. To determine the initial sizing for each tail surface, we follow a scaled approach from the M600, while at the same time compensating for known deficiencies, as shown in figure 5:

1. Calculate the non-dimensionalized tail volume coefficients of the M600
2. Adjust for forward pylon area

3. Apply a factor for margin
4. Adjust for reduced aerodynamic efficacy due to reduced dynamic pressure
5. Re-dimensionalize them for the new vehicle

Preliminary results are shown in figure 6. Note the dramatically increased tail area. This is due in part to the larger wing size, but also due to the compensation for reduced dynamic pressure.

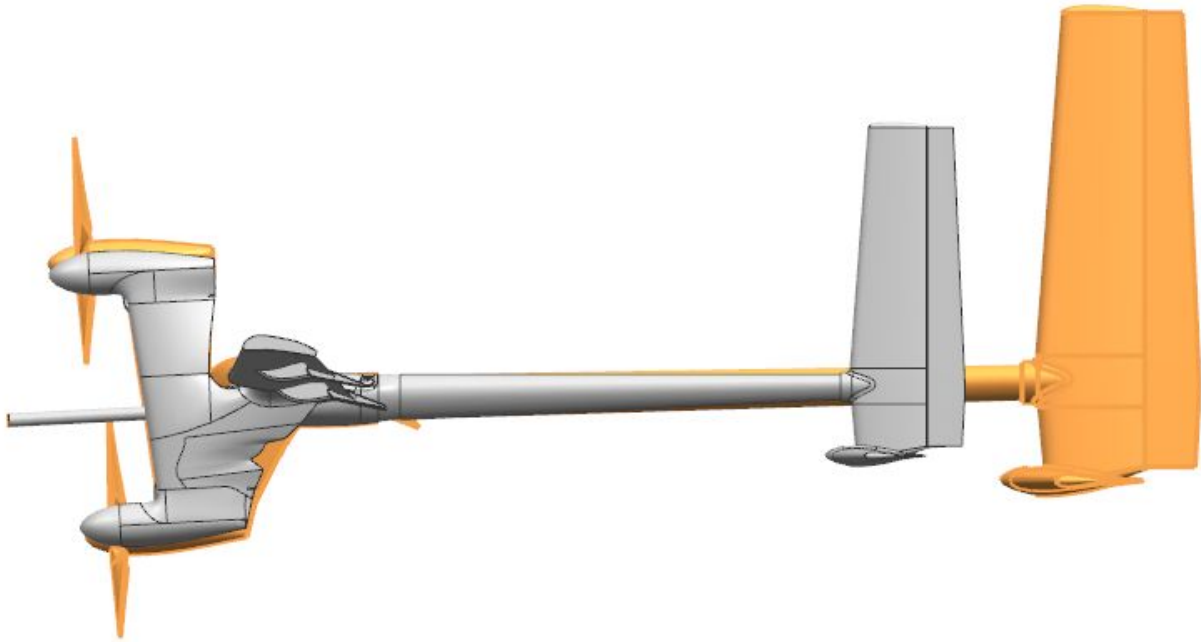


**Figure 6: Side view shows the increased tail size required due to (a) reduced dynamic pressure at the empennage while generating in crosswind flight, and (b) pylon area forward of the rotation reference point.**

### 3.3.3.2 Sizing for control

To size control surfaces we first determine the range of control moments required for maneuverability using the FBL tool, then size the aerodynamic control surfaces to satisfy that requirement.

To review, the unitless moment coefficients for roll, pitch, and yaw are defined in table 1:

Coefficient	Axis	Control surface	Equation
$c_l$	roll	ailerons	$c_l = \frac{M_x}{q \cdot S_{ref} \cdot b_{ref}}$
$c_m$	pitch	elevator	$c_m = \frac{M_y}{q \cdot S_{ref} \cdot c_{ref}}$
$c_n$	yaw	rudder	$c_n = \frac{M_z}{q \cdot S_{ref} \cdot b_{ref}}$

**Table 1: Dimensionless coefficient definitions for roll, pitch, and yaw moments.**

We begin the process by running the FBL without control moment constraints, but we apply a quadratic regularization term to the control moments, to encourage the optimizer to use less control if possible.<sup>18</sup> This allows us to form an initial “guess” as to how much control authority is necessary to achieve maximum power output.

In parallel, we calculate the maximum available range of moment coefficients  $c_m$  and  $c_n$  based on the horizontal and vertical tail sizing for stability, assuming a reasonable chord fraction for the control surface, and using the computed value of  $q^*$ . Similarly, the available  $c_l$  range is determined assuming an aileron span equivalent to the full wingspan.

Following these two steps, we have the required ranges of  $c_l$ ,  $c_m$ , and  $c_n$  (from FBL) and the available ranges of  $c_l$ ,  $c_m$ , and  $c_n$  (from surface sizing). If the range required from the regularized FBL runs is within the computed range available, we proceed to a verification step: We decrement the available control ranges by a safety factor (1.3 was used for the Oktoberkite design), and introduce these as limit constraints into the FBL.

Finally, rerunning the FBL with the conservative constraints allows us to verify that the control surfaces, as designed, are sufficient to achieve the predicted performance. The control surfaces for the Oktoberkite are shown visually in figure 7.

<sup>18</sup> In brief, we penalize use of control surfaces by subtracting quadratic moment terms from the score (*i.e.* from the power produced):  $P^* = P - k_x (c_x^2) - k_y (c_y^2) - k_z (c_z^2)$ . This is best understood as a kind of regularization technique—it forces the optimizer to try and minimize use of the control surfaces.

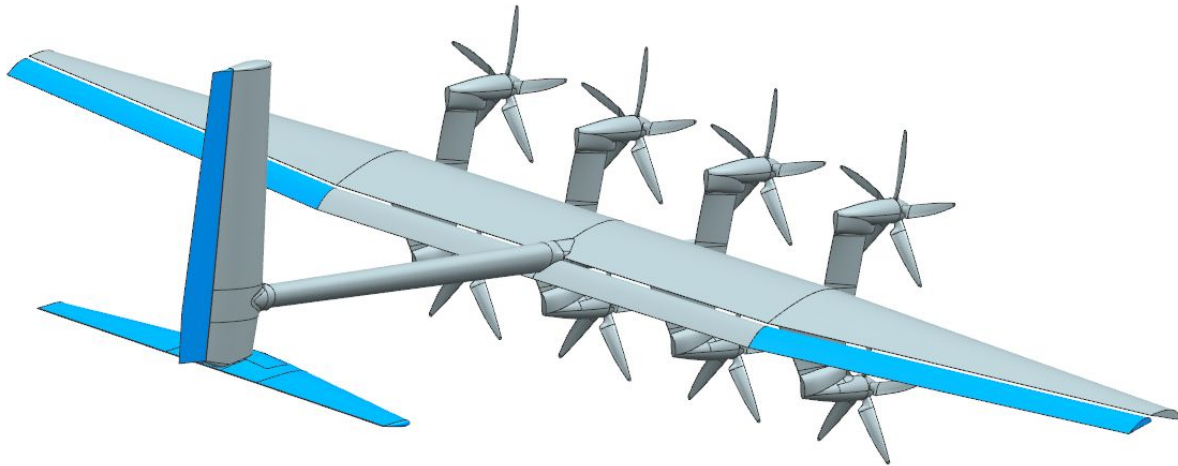


**Figure 7: Actuated control surfaces for the Oktoberkite, shown highlighted in blue, after the stabilizer and control surface sizing workflows were complete, and cross-checked against each other.**

### 3.4 Bridle and tether attachment

The M600 bridle geometry produces large and destabilizing yaw and roll moments on the kite, requiring constant control surface actuation<sup>19</sup>. “Fighting the tether” requires significant control authority and limits the operating envelope of the M600. This effect is a major contributing factor to the M600’s inability to generate rated power.

We used both analytical and numerical methods to determine a better bridle attachment scheme for Oktoberkite. Encouragingly, different analyses from an applied aerodynamics standpoint, a theoretical standpoint, and a numerical investigation standpoint all yielded similar results. The consensus result is that using a smaller bridle height is extremely important to maneuverability, to the ability to fly tight circles, and hence to the ability to generate power.

---

<sup>19</sup> It should be noted that the M600 became “mis-bridled” due to it ending up much more massive than originally planned. The heavy bridling would have remained detrimental to maneuverability, but it wouldn’t have been nearly so bad if we could have shifted the bridle point sufficiently laterally. We could not, though, for structural, pylon interference, and bridle collapse reasons.

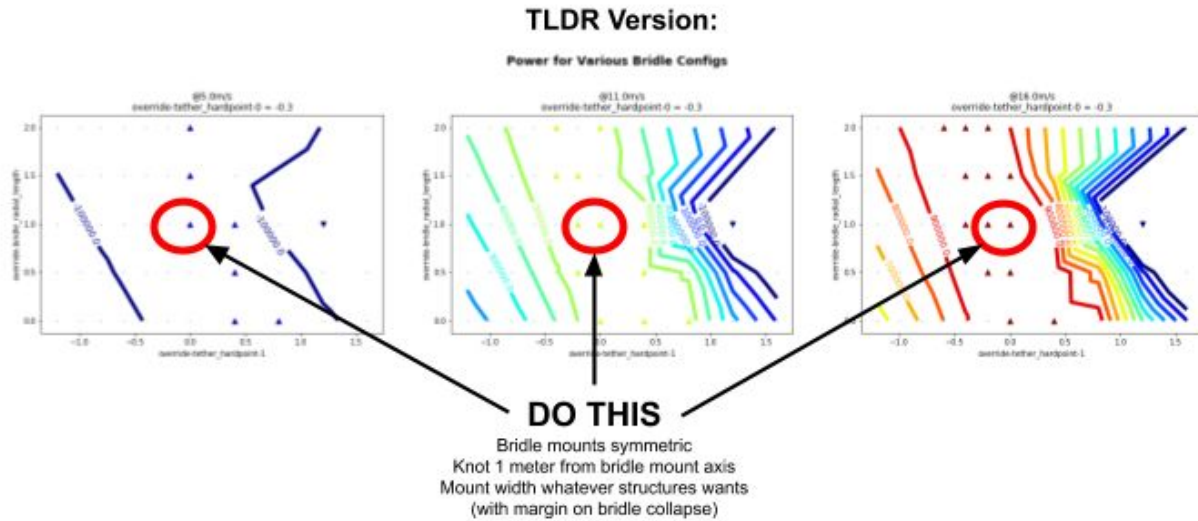


**Figure 8: Power generated at various wind speeds, contoured as a function of the (y,z) position of the bridle knot. The position of the plateau at z=0 indicates the best bridle positions have a “virtual” y offset, to counter the aerodynamic imbalance introduced by the body turn rates. The slope of the plateau is related to the average tether roll angle needed for balanced operation of the ailerons.**

A detailed discussion of how to select a bridle geometry can be found in the article "Tether Attachment and Bridle Knot Trim Considerations for Energy Kites" [8].

It is also worth noting that such a small bridle is more easily constructed using a solid bar linkage than with a combination of soft goods and anchoring materials. This also permits fairing a portion of the tether and integrates nicely into a notional perching design (see Section 3.5, Ground Station Docking, below). A notional CAD design of such a bridle, featuring a faired tether and all internal power conductors, is shown in figure 9.



**Figure 9: A CAD mockup of a rigid bridle design. The pitch pivots would be at the wing. The two lower images are close-up views of the roll pivot. Fairings provide (a) drag reduction, (b) protection for the high voltage tether conductors, and (c) an attachment point for a “slack bridle” for passive roll control during hover. The “wishbone” would mate with the ground station cradle for perching.**

### 3.5 Ground station docking

Use of a rigid “wishbone” bridle as described above affords a method for ground station docking that was not available with the M600’s soft bridle: We envision the ground station to feature a “receiver horn” with a “landing notch” that guides the wishbone into the correct location, and locks it in place. Large elastomeric “pitch bumpers” on the sides of the horn maintain the wing at a given pitch attitude when it is docked.

Figure 10 gives an exploded view of the notional docking system, showing the wishbone and how it fits into the receiver horn.

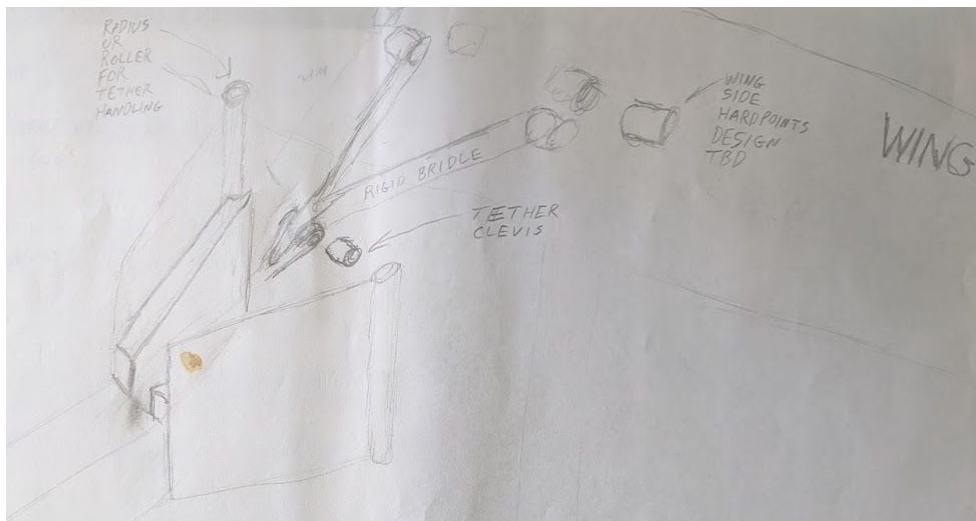


**Figure 10: An exploded view of the rigid “wishbone” bridle, showing how it fits into the receiver horn.**

The landing notch is taller than the bridle wishbone, so the exact elevation of the kite as it begins to engage the landing notch is unimportant—when the thrust is decreased, the wishbone “lands” on the bottom surface of the notch. See figure 11 for a kite’s eye view of the receiver.

Figure 12 and figure 13 give several more views of the entire assembly in the “mated” configuration: The wishbone is resting on the bottom of the landing notch, and the pitch bumpers are in contact with the bottom skin of the wing. The extent of the wing in contact with the pitch bumpers will, of course, have to be designed to handle the bumper loads. Figure 12 gives a notional outline of a reinforced area of bottom skin designed to mate with the pitch bumpers.

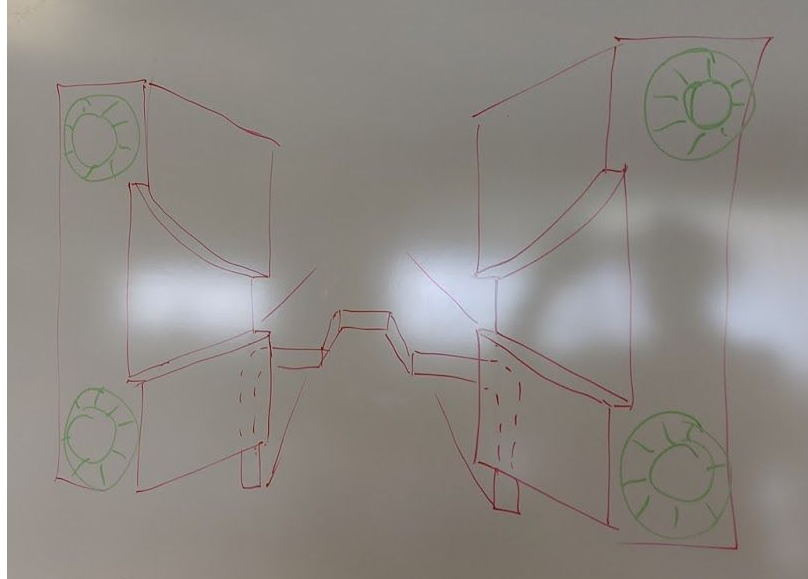


**Figure 11: A “kite’s eye” view of the receiver horn. The bridle wishbone slides into the red landing notch. The bottom surfaces of the landing notch support the kite weight when docked. The pitch bumpers, shown in green, stabilize the kite pitch angle as the wishbone is drawn into the notch.**

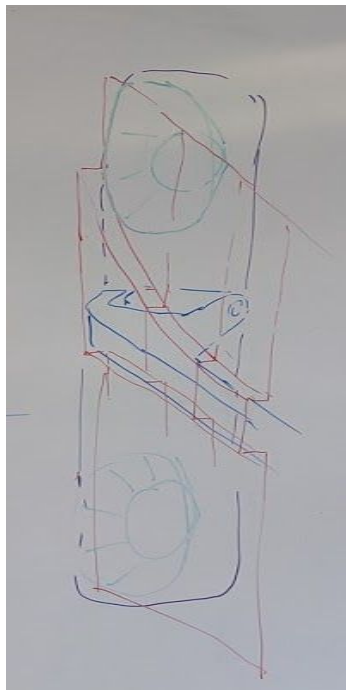


**Figure 12: An x-ray view of half of the wishbone (blue) in the landing notch (red), showing the pitch bumpers (green) pressing against a reinforced surface patch of the wing (black) intended for pitch stabilization**

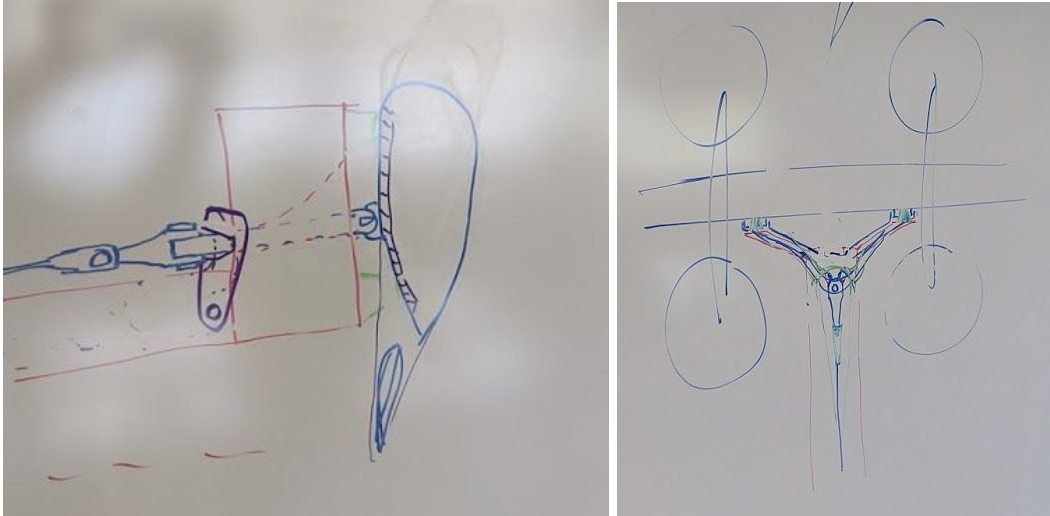


**Figure 13: A side view and a top view of the wing mated to the ground station receiver horn.**

## 3.6 Mass estimation

In addition to forming a rough aerodynamic design, the wing structure sizing spreadsheet provides a mass estimate as well, allowing the design parameters to be varied in order to optimize crosswind kite performance within an allowable mass budget. The mass estimate is tallied as is detailed below.

### 3.6.1 Wing

The spreadsheet assumes a particular assembly architecture for the wing: a box spar, ribs, and cored skin. The sheet first sizes the wing for aerodynamic performance, then sizes the spar and skin for the necessary strength and stiffness, and finally computes a mass estimate of the wing from mass estimates of the subcomponents.

### 3.6.2 Fuselage and empennage

The fuselage structure is sized for stiffness in order to prevent aero-elastic flutter problems. We make a first pass at sizing using a deflection limit for a given control authority load, determined from FBL. For simplicity, at the preliminary stage, we assume a circular tube with a constant taper along its length. This provides a mass estimate of the fuselage. The fuselage structural design will be revisited during more detailed analysis and design.

The tail surfaces are scaled based on the surface mass density from the M600: The tail surface area is multiplied by this density to determine an estimated mass for the empennage. We include mass for actuators in the estimate as well. The mass of these surfaces will be more accurately determined during detailed design.

### 3.6.3 Pylons and powertrains

Masses for the pylons and powertrains were taken directly from the M600, since these system components were judged to be perfectly suitable to apply to the new design.

### 3.6.4 Avionics and other masses

Masses for the avionics, wiring harnesses, and other equipment were taken directly from the M600, since these were also judged to be suitable.

## 3.7 Determining the target mass: Hover thrust capability

As discussed in the basis of design workflow, the airframe is sized for best available aerodynamic performance, *while meeting the assigned mass target*. The question remains as to how to assign a mass target. Early in the M600 project, it was thought that mass affected crosswind performance significantly. This is true at low wind speeds, when the tether tension is low, and the potential energy inflow and outflow of the kite around the flight path is much larger than the aerodynamic power generated. However, at higher wind speeds, as the tether approaches full tension and the kite approaches its rated power, mass contributes less significantly to power variation and reduction in overall output. The article “Airborne Wind Turbine Performance” [4] gives a lot more detail on this point.

The choice of target mass therefore depends on the “hover” flight mode: If the kite can hover stably and controllably in the range of expected wind conditions, the kite mass is acceptable.

### 3.7.1 Hover lift capability vs. moment capability

The kite operates as a Vertical Take Off and Landing (VTOL) vehicle. Its attitude is stabilized in pitch and yaw using differential rotor thrust. Consequently a Thrust to Weight Ratio (TWR) of at least 1 is necessary but not sufficient to ensure the kite can hover. To maintain attitude, the flight controller partitions the thrust to counter static moments (*i.e.* relatively constant moment applied to the kite due to tether tension and average aerodynamic moment) and dynamic moments (*i.e.* to cancel out disturbances introduced from gusts or tether dynamics).

The static moment requirement depends in large part on how well balanced the kite design is for hover. It is primarily affected by the choice of rotor positions and the tether hardpoint location, relative to the kite’s center of gravity.<sup>20</sup>

---

<sup>20</sup> Additionally, it was discovered, during detailed aerodynamic design of the MX2, that the *spanwise spacing* between pylons must be chosen to be sufficiently large to allow adequate inflow to the aft (top) rotors in hover orientation. Failure to do so results in “starvation” of the aft rotors, resulting in a strong pitch back moment. This is discussed in detail in Section 4.6.2, Pylon spacing and placement for best hover performance.

The dynamic moment requirement is related to what control authority is needed to counteract disturbances, so it depends on how large the disturbances are, how much control error the kite can tolerate, and what accelerations are required for perching and trans-in/out maneuvers.

To estimate the maximum allowable hover mass for the Oktoberkite, M600 hover flight test data was analyzed and scaled to form an estimate of thrust and moment requirements for the Oktoberkite design. Applying all the historic hover flight data from the M600 to the Oktoberkite allows us to estimate what portion of the time the new kite's (thrust, moment) capability envelope would be exceeded, if the scaled thrust and rotor moment commands were issued by the flight controller.

This approach doesn't consider ways in which we might reduce the static moment requirements for the Oktoberkite (such as better rotor z positions to balance the tether, gravitational, and aerodynamic moments), so in this sense it is conservative. However, it also neglects ways the requirements might get more stringent (e.g. more dynamic landing conditions offshore, higher wind speed and turbulence envelopes, possibility of requiring roll moments from the rotors, etc.).

The summary conclusion for the Oktoberkite project was that our initial target mass of 1850 kg from the Pencil Specs seems reasonable. We probably have enough margin to go to 1900 kg or so, depending on how willing we are to saturate a powertrain's capability during a HoverTransOut with a motor out (the most extreme and demanding case) and how much margin we want to leave to account for unknown changes to hover requirements in the MX2 design.

### 3.8 Roll control in hover

Makani has had plenty of difficulty with our design intent of using the bridle for passive roll control in hover. The article "The Makani Autopilot" [3] gives an excellent overview of the trials and tribulations we faced.

In brief, the original design intent was that in hover, the dynamic pressure of the wind on the wing, crossed with the moment arm of the aerodynamic center of the wing relative to the bridle "knot point" (i.e. the bridle "height"), would exert a roll-stabilizing moment on the airframe. However, there are many unforeseen and second-order effects that have made this difficult in practice, even to the point of loss of the entire craft. Below is a brief restatement of the problem along with some root causes. A more detailed discussion may be found in the technical appendix "Root Cause Analysis and Corrective Actions for FCW-01" [11].

Problem summary:

- Loss of roll-restorative roll moment after trans-out

A summary of the root cause analysis is roughly as follows:<sup>21</sup>

- Excessive hover altitude results in large tether pitch angles at the kite (*i.e.* the tether departure direction points down, along the tail)
- Because the bridle is a triangle between two hinge points aligned in the y direction, the large tether pitch angle results in significant (undesired) yaw stiffness due to the bridle
- To make matters even worse, the large tether pitch angle results in *decreased* roll stiffness due to the bridle
- The large yaw stiffness tends to result in large yaw moment commands
- The resulting difference in blown lift between port and starboard rotors causes the large yaw commands to couple into destabilizing roll moments
- Side-winds redirect the center of blown lift on the wing in the port or starboard direction, and this also results in destabilizing roll moments: If the wing rolls to port, the blown lift is advected to starboard by the apparent crosswind, and this results in a *larger* (destabilizing) roll moment to port

### 3.8.1 Interim solution for Oktoberkite

The Oktoberkite design team did not have sufficient time to design and thoroughly test a solution to the hover roll stability problem, choosing to concentrate first and foremost on crosswind performance for the preliminary design. We therefore provisioned space and mass for a stopgap design, consisting of a smaller, lighter weight actuated bridle that was “tall” like the M600 bridle, but that would be effective in hover only. Such a bridle was envisioned to “unlock” and run freely during crosswind; so, other than a small amount of increased drag, its effect on crosswind performance would be negligible.<sup>22</sup> Such a slack bridle would at least be no worse than the situation on the M600 and would be subject to revision and/or replacement as the design matured.

### 3.8.2 Notional long-term solutions for MX2

At the time Makani was shut down, we were actively pursuing three separate avenues to improve hover roll control: enhanced modeling, better control schemes, and active control.

The improved models we were working on include:

- Better modeling of roll moment due to blown lift in an off-axis wind environment
- Finer characterization of the area of roll instability vs. tether pitch, to allow better control schemes to stay away from the unstable areas

---

<sup>21</sup> Note: the x, y, and z directions, and the pitch, roll, and yaw angles are defined by the craft body in crosswind. These definitions are preserved in hover. In a nominal hover orientation, x points toward gravitational “up,” y points out the right wingtip, and z points toward the ground station. This is *not* the same standard as typically used for hover-only craft.

<sup>22</sup> Note that such a bridle need only withstand tether forces associated with *hover*, not with *crosswind*, so the bridle material can be substantially smaller and lighter weight. We had computed, for instance, that 6 mm diameter Spectra line would suffice for tether tensions up to 20 kN.

Areas for improvement of the trans-out and the hover controllers might include:

- Improve trans-out controller to stabilize the kite position and attitude at a lower elevation, hence a lower tether pitch angle
- Choose a better open-loop pitch command for the end of trans-out, to try and put the kite closer to its desired tether tension when the hover controller takes over
- Change the reference variables of the hover controller from (height, horizontal tension) to (elevation angle, tension along tether axis). This is intended to reduce cross-coupling between height and tension, thereby hopefully reducing low frequency oscillations in tension
- Use a blended controller between high hover and low hover. The low hover controller would weight azimuth angle more strongly when preparing to dock, while the high hover controller would deemphasize azimuth angle (leading to reduced yaw moment commands) and instead concentrate on roll stability

Finally, we were evaluating several schemes proposed for active roll control during hover. Ideas include, from order of least invasive to most invasive:

- **Canted rotors:** The axis of rotation of one or more rotors is canted in the pitch direction. This couples a portion of the rotor thrust into the z direction. This z component of thrust, combined with the y offset of the pylon, results in roll moment. The main disadvantage of this idea is that the effect is relatively small, and is likely to be insufficient.
- **Rotor coupling torques:** An additional degree of freedom is used in the motor speed controller, allowing pairs of counter-rotating motors to be controlled differentially, *without* introducing a net thrust, nor pitch moment, nor yaw moment. This differential torque couples into the airframe in the roll direction. Again, the effect is relatively small, and is likely to be insufficient.
- **Tip thrusters:** Thrusting rotor assemblies are built into two circular ducts perforated through the wingtips along the z axis. We did some work on sizing these, and it is probable that enough roll moment can be produced. However, the size, weight, and power requirements of such a system are significant. Also, the effect on the aerodynamics of the main wing during crosswind is obviously an area of much concern. We had decided to prototype such a system in order to actively stabilize the M600 in hover and collect data. However, the program was shut down before this could be executed.
- **Tilt rotors:** In this approach, we envision placing two of the main power generating rotors on rotating wingtips, such that their thrust vector may be pointed more along the z direction for hover stabilization. This obviously has the largest potential effect of all the schemes envisioned, and is certainly more than adequate. However, it is a significant structural challenge to place this amount of mass, power, and complexity at the

wingtips. It also represents a major teardown of the existing system architecture, hence was clearly out of scope for the amount of time and money we had available.

Some of these are also discussed in the article “The Makani Autopilot” [3].

Note that one of the greatest obstacles to choosing a path forward on hover roll control, is that it is not known what amount of roll moment control is sufficient. Clearly, understanding roll disturbances in hover and accurately modeling them is an essential first step in choosing an approach.

As can be seen, we have at least a preliminary understanding of the effects that conspire to make hover roll stability challenging, and a large quiver of possible engineering approaches to apply. This gives us some confidence that the problem is eventually solvable. But it cannot be overstated that *this is an existential problem* for any kite of the Makani configuration. For those wishing to use our experience to advise *de novo* airborne wind projects, we advise thinking this through anew, from the beginning—making sure you have a good understanding of the dynamics and a good plant model, and developing suitable simulations and control schemes, ideally *before* building prototypes.

### 3.9 Rotor and powertrain sizing

As mentioned above in Section 3.6.3, Pylons and powertrains, the rotors and powertrains for the Oktoberkite basis of design are identical to those of the M600. This is only a near-term stopgap solution, though. The intent was to study the tradeoffs in rotor design with an all-up system model in the C-sim. Section 5, Unfinished work, gives some more ideas for revisiting the rotor design.

### 3.10 Summary of basic specifications

Table 2 is a brief summary of the airframe basis of design developed for the Oktoberkite project. This served as a basis for initial development of the MX2 Draft Specification. We filled out the specification document more thoroughly as we dug more finely into detailed problems. These details will be covered in Section 4, Detailed aerodynamic design.

Parameter	Value	Units
Wing area	54	m <sup>2</sup>
Wing span	26	m
Aspect ratio	12.5	
Mean aerodynamic chord	2.07	m
Kite mass	1852	kg
Tether mass	275	kg
Tether length	300	m
Tether tension at rated power	250 - 300	kN
Nominal path loop radius	90	m
Cut in wind velocity (estimated)	6.5	m/s
Target power point 1	600	kW
Target $v_w$ point 1	11	m/s
Max electrical power	1000	kW
$v_w$ at max electrical power	16	m/s
Nominal air density	1.225	kg/m <sup>3</sup>

**Table 2: Basis of design specifications, at the end of the Oktoberkite project and the beginning of the MX2 detailed design phase.**

### 3.11 Predicted performance

Our preliminary basis of design describes an airframe capable of delivering 600 kW of electricity to the grid at 11 m/s wind speed at sea level, as shown by the blue curve in figure 14. This is accomplished by increasing the wing area, flying smaller circles and making other adjustments to the airframe, as described in this report.

These predictions, provided by the relatively simple FBL tool, are preliminary. Ultimately, power curves should be provided from test data and simulation that is well validated by flight test data. As such, we expect some degradation of performance in more detailed models, especially in the high wind regime near rated power. Historically, all simpler design tools have failed to capture the challenges there. See *The Energy Kite, Part I, "Airborne Wind Turbine Performance,"* [4, sec. 10], for a detailed discussion of these challenges.

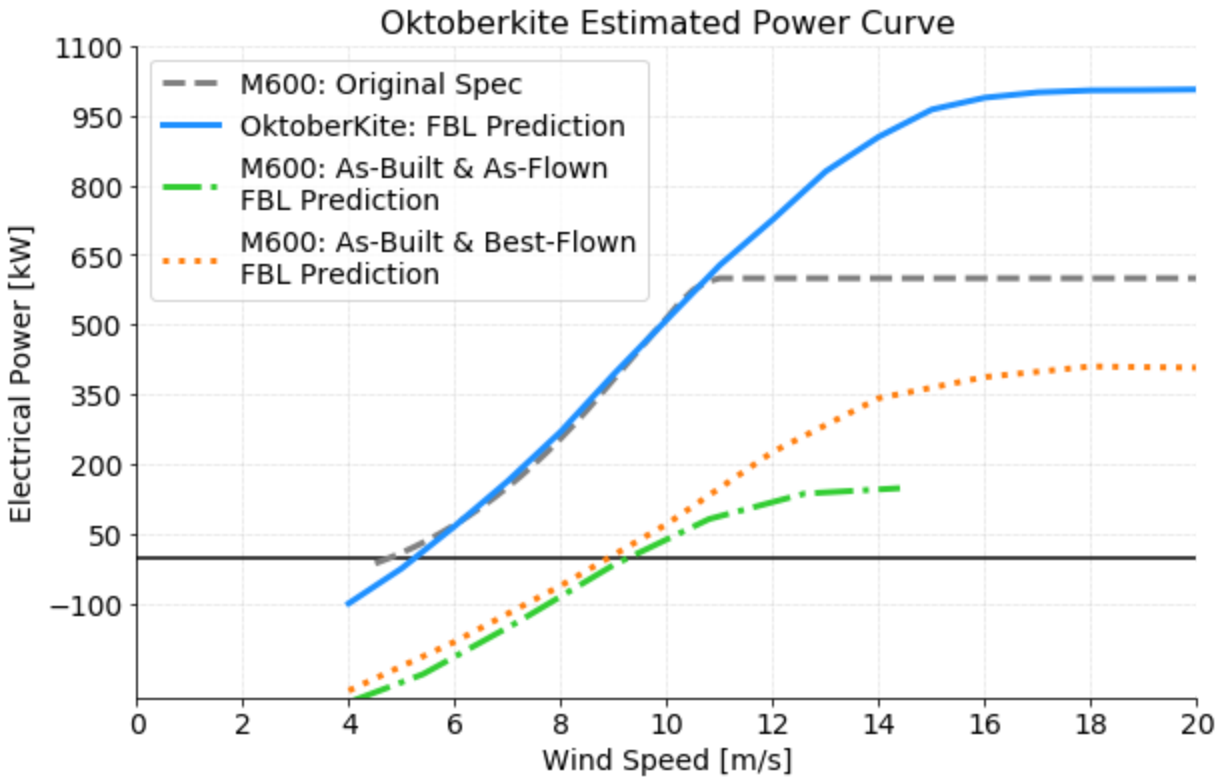


**Figure 14: FBL optimizer predictions for the power curve of the Oktoberkite (blue) as compared to the original M600 specification (dashed). Also shown are the FBL predictions for the M600 as built and flown (green), and of the best available performance from the M600 with higher-risk flight maneuvers (orange). Note that blue line and dashed line are at sea level, while the remainder are at 2600 ft MSL.**

## 4 Detailed aerodynamic design

At the conclusion of the Oktoberkite basis of design effort, Makani hired a professional aerodynamics design house, TLG, to cooperatively develop the detailed specification and system design for the MX2 with us. The work packages in this effort are four-fold:

1. Work together to flesh out a complete airframe design specification, and to use this specification to inform items 2-4
2. Develop a detailed design for a bespoke airfoil that meets the MX2 specification requirements, and redesign the wing planform with the new airfoil
3. Resize and redesign the fuselage, empennage, and tether attachment for stability and control
4. Do a detailed structural design of the entire craft, and produce build documents

The first and second work packages are mostly complete. Sadly, though, the Makani project was shut down prior to completion of work packages 3 and 4. Significant work has been done on stability and control, but the detailed structural design is barely started.

### 4.1 Progressing from preliminary to detailed specifications

#### 4.1.1 Airfoil specifications

Design of an airfoil suitable for energy kites is a difficult task *a priori*, because the requirements for such an airfoil are very, very different from those of a cruising airfoil for an airplane in straight and level flight. In brief, the significant differences include:

- **High wing loadings at low aerodynamic speed:** The kite's aerodynamic speed is limited by the wind speed and the L/D of the kite, so the aerodynamic speed is much lower than a typical aircraft. To make matters more difficult, the kite needs to develop very high wing loadings (on the order of ten to twenty times its weight) in order to generate useful power.
- **High  $C_L$ , all the time:** The above requirement dictates that the airfoil have a high lift coefficient. This requirement is in effect for the entirety of power generating flight—this is not a typical cruise airfoil with a high lift device that is deployed for take off and landing.
- **Two element airfoil is dictated:** The high lift requirement dictates at least a two element airfoil—a single element airfoil with the required lift would be extremely large, leading to high mass, low stiffness, or both. We have discovered no way to achieve design closure with a single airfoil.

- **Needs to maintain performance *without large laminar flow lengths*:** The airfoil will be in-use nearly 24/7,<sup>23</sup> for months at a time without inspection, cleaning, or service, unlike a typical aircraft. Hence there will be fouling and wear and tear on the leading edge. For this reason, exotic, super-clean, high precision designs are disallowed.
- **Thick section:** Recall the total lift is ten to twenty times the weight of the wing, hence the spar needs to be of very high stiffness and strength. On the other hand, low mass is a necessity for hovering. The resulting strength to weight requirement dictates that the spar is quite deep (especially with a much smaller bridle) resulting in the requirement of a thick section for the airfoil.
- **Aerobatic maneuverability requirements:** The kite is circling vertically in a gravitational field. To maintain closure of the flight loop requires re-orienting the lift vector periodically around the loop to compensate for gravity. The resulting roll moment requirements dictate the ailerons must introduce a difference in  $C_L$  of *circa* -0.45 to +0.45 from nominal. This is a rather prodigious acrobatic requirement not seen in typical airplane designs.
- **Dual purpose flaperon:** Normally for high  $C_L$ , one would use a two element, constant section airfoil, which is relatively easy to design and analyze. However, in the case of an energy kite, the maneuverability requirements dictate a dual-purpose second element: It needs to function as a high lift device, and simultaneously as an aileron.

It should be obvious from the above discussion that this airfoil is not typical in any sense. It is certainly not available from stock airfoil selections, hence needed to be designed from scratch.

To begin building a basis of design, we needed a notion of how large a  $C_L$  is achievable. We also needed to build in some angle of attack (AoA) margin, to allow for imperfect control and turbulence and shear in the wind environment, without stalling the wing.

To build in this AoA margin, we defined two specifications:  $C_{L,max,oper}$  is the coefficient of lift at the *maximum intended AoA during normal operation*. In other words, the flight controller should never command an AoA larger than this, and the design should assume this to be the highest  $C_L$  that can be reliably and safely achieved.

On the other hand,  $C_{L,max,stall}$  is the maximum coefficient of lift achieved by the airfoil *at stall*.

Our design spreadsheet used a sectional  $C_{L,max,oper}$  of 2.0. This was believed to be achievable with a two element airfoil, while allowing a comfortable AoA margin before stall.

For generating aerodynamic databases using ASWING for the Oktoberkite project, we chose a notional set of basic specifications, including section  $C_{l,min} = -0.5$ ,  $C_{l,max} = 2.5$ , and

---

<sup>23</sup> Typical sites and cut-in wind speeds mean most systems will be flying ~70% of the time!

$\partial C_l / \partial \alpha = 6.28$ , which we believed were achievable with a two-element airfoil, based on rules of thumb. It is understood that these are stall values, not a safe operating range.<sup>24</sup>

For the detailed aero design, we chose to specify the airfoil by its  $C_{l,min,oper} = -0.5$ ,  $C_{l,max,oper} = 2.0$ , and a stall margin (measured by AoA) of +/- 5 degrees. Terminology is as shown in figure 15, below. In retrospect, the  $C_{l,min,oper} = -0.5$  was probably a bit over-ambitious—our in-house CFD analysis indicated flow separation on the lower surface at very low AoA. In any case, we do not require a zeta parameter of less than zero, so a  $C_{l,min,oper}$  of zero should provide a sufficient zeta range for all crosswind flight conditions. This relaxation of the  $C_{l,min,oper}$  specification should allow it to be met.

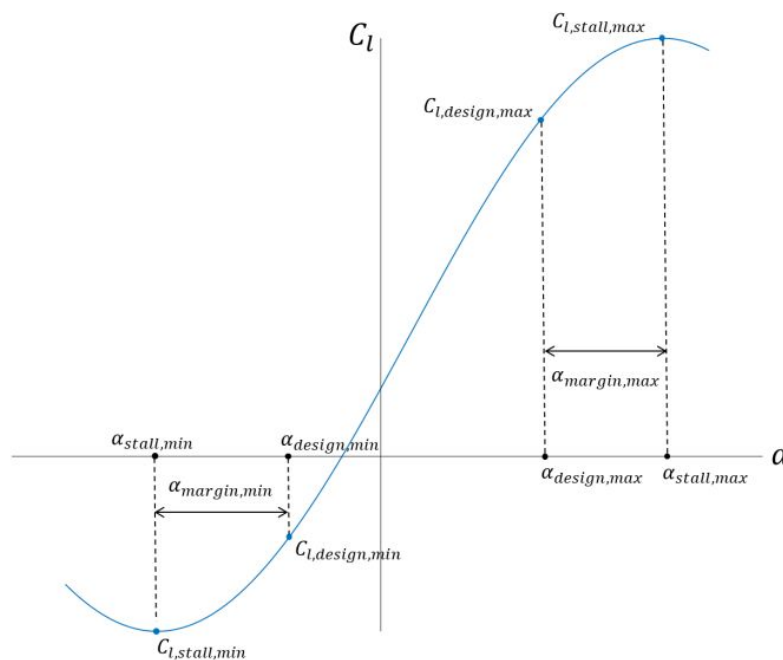


**Figure 15: Airfoil operating point definitions.**

#### 4.1.2 Planform and twist

As discussed above, the basis of design specified a planform and twist generated using the design spreadsheet, based on lifting-line theory.

To progress to a more sophisticated design, TLG took the planform we provided, but they discarded the twist and re-twisted the design to reoptimize the performance tradeoffs between incidence angle and camber.

<sup>24</sup> ASWING uses a “soft stall” model that blends the lift curve slope from its nominal value to a “stalled” value over a small range of  $C_l$  around the prescribed  $C_{l,min}$  and  $C_{l,max}$ .

To do this, they first ran a Vortex Lattice Method (VLM) code on the provided planform, then adjusted the wing incidence angle and sectional twist angles to match the desired elliptical lift distribution. They were able to accomplish this with an untwisted center section—something we had neglected to specify in the initial design, but which would allow simpler spar design, lower cost manufacturing, and simplicity of pylon to wing structural interfaces.

The  $C_l$  sectional lift coefficients from the retwisted design are shown below in figure 16, along with the  $C_l$ 's from the preliminary (Oktoberkite) design. They are in good agreement.

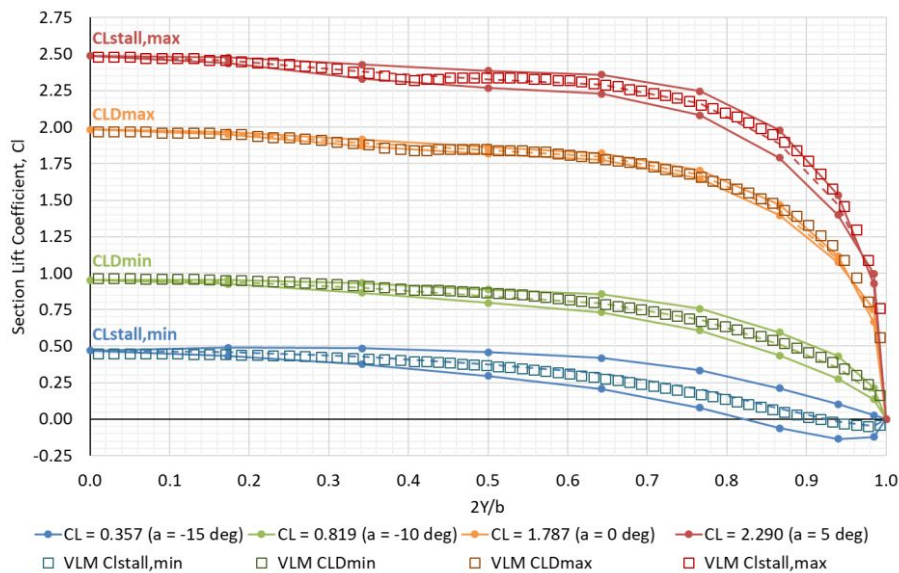


**Figure 16: Sectional lift coefficients from Makani’s Oktoberkite basis of design, compared with those from the VLM-based retwisted design produced by TLG during the first phase of detailed aerodynamic design.**

### 4.1.3 Tail volumes

The Oktoberkite provided notional tail volumes, but it made no effort to adjust the details of the empennage to optimize the flight stability coefficients.

## 4.2 Preliminary airfoil design

The first phase of the TLG work was a feasibility study, to do a preliminary airfoil design in order to see if the design specification was likely to be achievable. “Preliminary” means, in this context, that an airfoil was designed, and analyzed with MSES, but not analyzed via CFD, nor wind tunnel tested.

### 4.2.1 Leading edge design

To design the leading edge, TLG adopted the “inverse method” technique. In this technique, a starting, or “seed” airfoil is chosen that is close to the required performance, and a desired coefficient of pressure,  $C_p$ , profile is chosen as a design goal. The  $C_p$  profile of the seed is compared with the desired  $C_p$  profile, and local curvature changes are made to bring the seed closer to the desired. This process is iterated until the  $C_p$  profile is satisfactory, and the final product is evaluated for other performance metrics (*i.e.* in Makani’s case, the Loyd parameter  $C_l^3/C_d^2$ ).

Makani is also quite concerned with low cost and low maintenance. This, in turn, dictates that the airfoil performance must be reasonably immune to surface imperfections and surface fouling. To achieve this, TLG decided the best approach was to choose a  $C_p$  profile with a positive pressure gradient for as much of the upper forward surface as possible, up to the desired turbulent transition point. The tail end of the  $C_p$  profile, after transition, was tailored to be as close to a Stratford pressure recovery<sup>25</sup> as possible.

In summary, the leading edge workflow is as follows:

- Start with a single element, “seed” airfoil, with correct full chord
- Thicken to meet the structural spar depth requirements as given by Makani
- Given the  $C_l$  requirement and the turbulent transition requirement, develop a notional  $C_p$  profile around the leading edge that disfavors early transition, *at the nominal operating alpha*
- Compute the difference in  $C_p$  profiles
- Adjust the leading edge shape to converge to the  $C_p$  requirement

---

<sup>25</sup> A Stratford pressure recovery profile is a unique  $C_p$  profile specifically tailored to produce a boundary layer on the verge of separation *at all points* along the upper aft (recovery) surface of the airfoil. This can be thought of as eliminating “weak spots” that are prone to separation by equalizing the probability of separation at all points. It allows maximum pressure recovery with a minimum of chordal length.

The results are shown in figure 17 and figure 18:

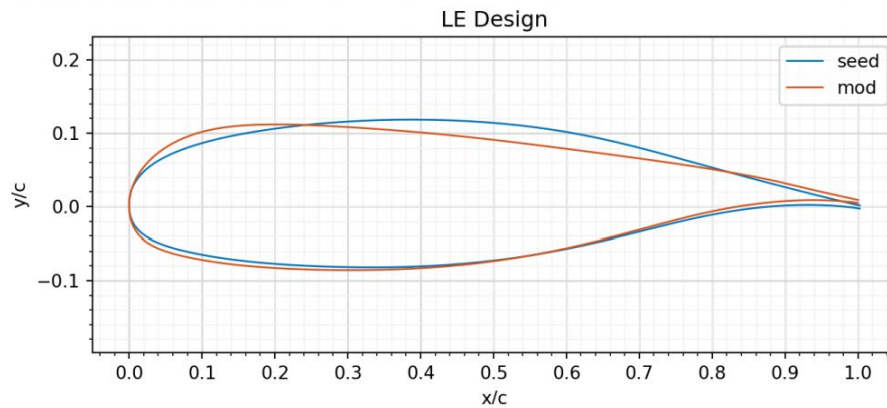


**Figure 17: Single element airfoil resulting from inverse method design technique. Seed airfoil is shown in blue, while final is shown in red.**

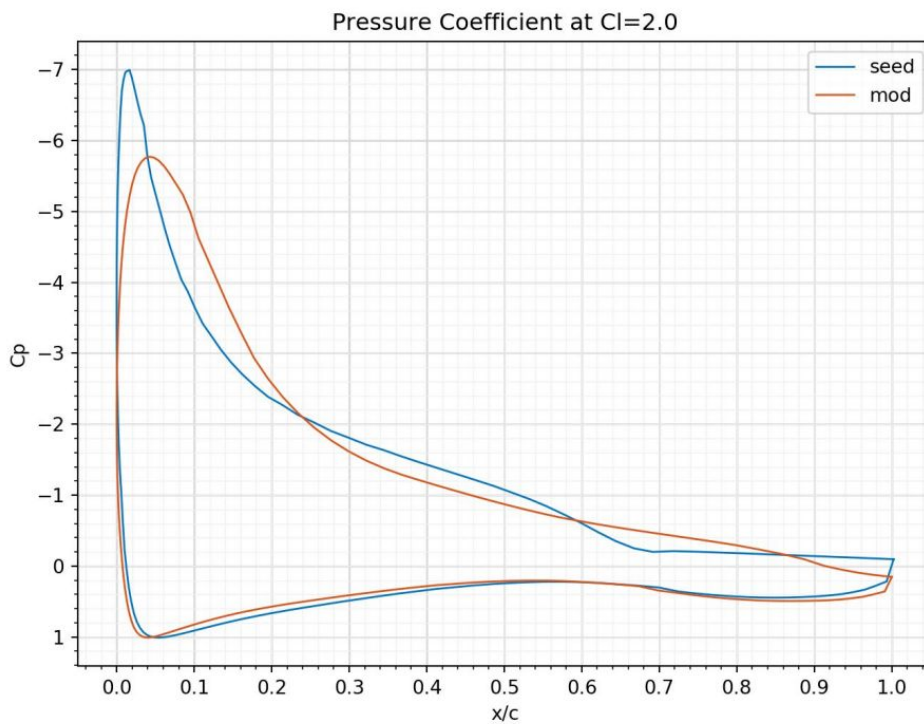


**Figure 18: The  $C_p$  profile of the single element airfoil, versus its seed airfoil. Note that the initial gradient is held positive for a longer (0.05)  $x/c$  run. This is to make the boundary layer around the leading edge more tolerant to fouling and contamination for the first 5% of the chord. The gradient after transition has been smoothed, to be closer to a Stratford pressure recovery. The Stratford profile attempts to equalize the probability of separation along the entire recovery portion of the chord.**

To confirm the robustness to flow separation, TLG checked that the skin friction coefficient as predicted from MSES did not become negative (which would indicate a flow separation bubble). The results are pictured below in figure 19.

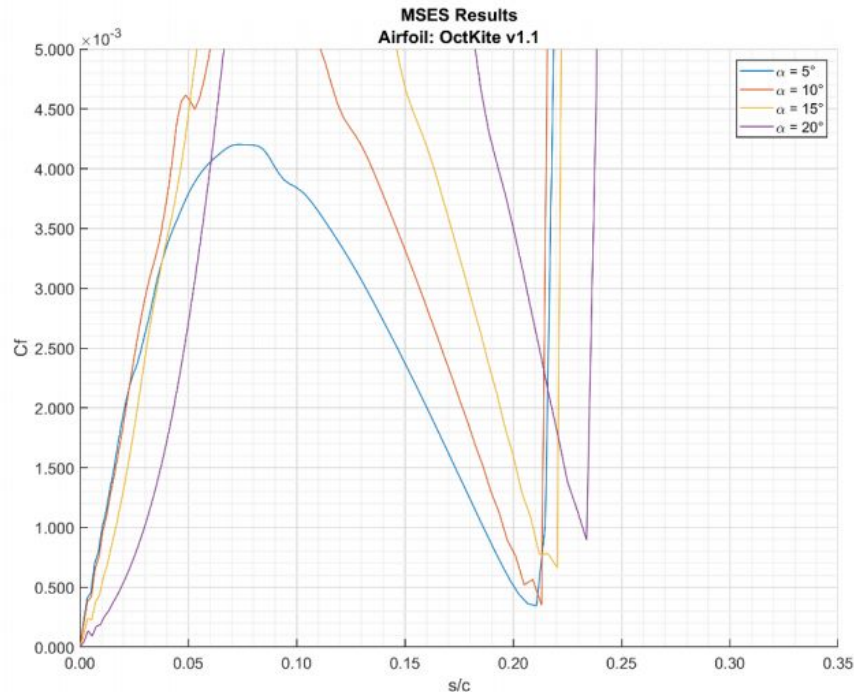


**Figure 19: The skin friction coefficient of the new airfoil, plotted vs. arc length over chord from the stagnation point. The minimum skin friction coefficient stays comfortably in the positive range, indicating robustness against flow separation bubbles.**

#### 4.2.2 Accommodating the spar box and choosing a flap chord ratio

TLG then modified the lower (pressure) surface slightly to accommodate the 19% minimum spar box height, and inserted a “generic” flap.

To decide on the flap chord ratio, they used data from Makani’s analysis of the M600 airfoil sections. Since the M600 has a fixed flap chord, but a variable main section chord, the M600 flap chord ratio actually varies, past the wing taper break, from 0.21 up to 0.38. Furthermore, Makani had done additional analysis of the idea of increasing the M600 flap chord in an attempt to increase flap roll authority. In all, Makani had 24 predicted data points for  $\partial C_l / \partial \delta$ , for six flap chord ratios, two angles of attack ( $0^\circ$  and  $15^\circ$ ), and two flap deflections ( $\pm 10^\circ$ ). These data are shown in figure 20. Based on these data, TLG chose a flap chord ratio of 0.25 as a starting point for detailed design.

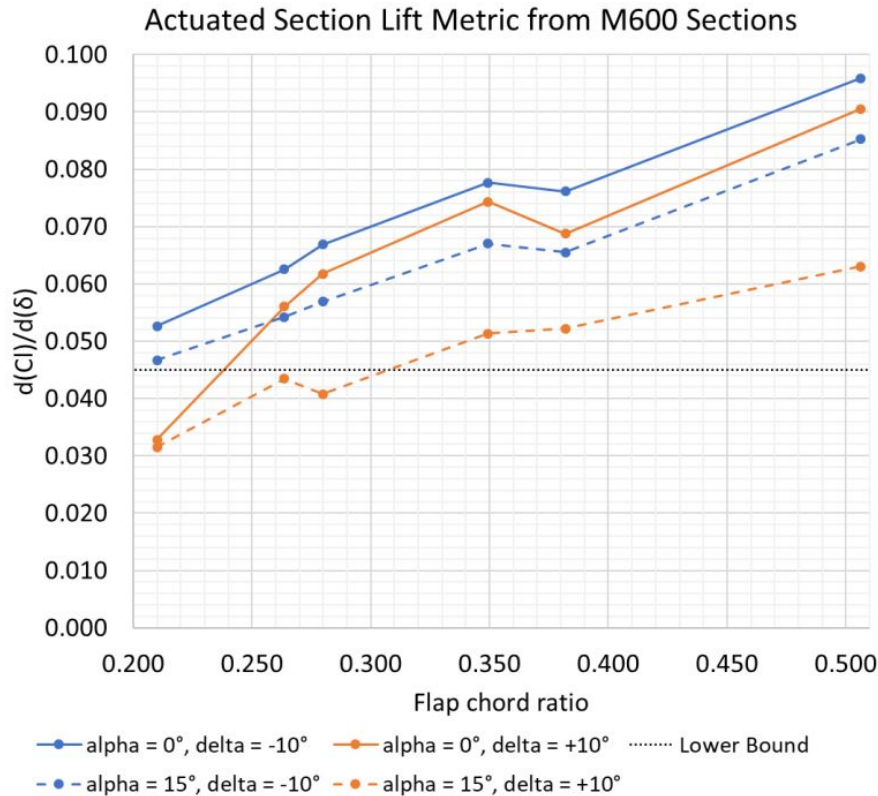


**Figure 20: Actuated section lift metric,  $\partial C_l / \partial \delta$ , from M600 analyses at different station points along the wingspan. The desired actuated section lift metric, 0.045 per degree, is shown as a dotted line. Based on these data, TLG chose an initial flap chord ratio of 0.25, to likely be able to satisfy the section lift metric.**

### 4.2.3 Selecting slot gap and overlap

The M600 airfoil suffered from slot “choking” at large positive flap deflections. To choose an initial guess for slot gap and overlap, TLG started with an M600 station closest to the selected flap chord ratio, and added some gap margin to reduce slot choking. Initial gap and overlap were set to 12% and +2%, respectively.

They next modified the trailing edge of the single element airfoil generated during leading edge design to insert a “generic flap” of the chosen flap chord ratio at the selected gap and overlap. The result is shown in figure 21.

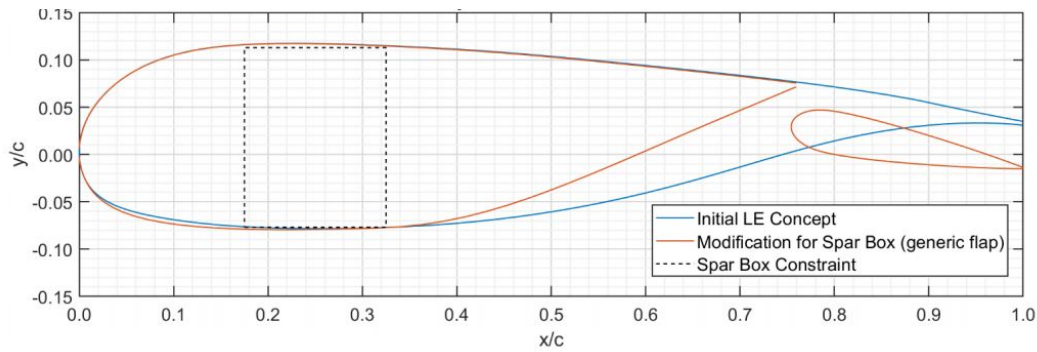


**Figure 21: The leading edge airfoil design, modified to accommodate a 25% generic flap, with 12% gap and 2% overlap.**

#### 4.2.4 Flap shape

Since the MX2 does not have a “flaps retracted” cruise configuration, there is no need for a flat bottom surface on the flap. This allows the choice of a symmetric airfoil for the flap, thereby reducing tooling costs. TLG chose, as a first candidate, a NACA0018, but with the point of maximum thickness moved forward to 20% chord, in order to make the curvature around the leading edge more uniform. This is to allow the flow to stay attached around the leading edge curvature over a wide range of local angles of attack (*i.e.* to be robust against detachment at extreme flap deflection angles).

#### 4.2.5 Flap deflection study

With a two-element airfoil with a movable flap, the nominal (undeflected) flap angle is analogous to camber. The amount of camber affects the wing incidence angle and the twist needed to match the desired spanwise lift profile.

To investigate the tradeoff between camber and incidence angle, TLG first produced airfoils with five different nominal flap positions, shown in figure 22, and then evaluated their endurance parameters as a function of  $C_l$ .

This was done both with the raw section  $C_l$  and  $C_d$ , and with a “trim corrected”  $C_l$  and  $C_d$ . The trim correction augments  $C_l$  with an estimate of the tail lift required to balance the pitching moment of the main wing, and augments  $C_d$  with the induced drag corresponding to the augmentation of tail lift.

A third set of runs was done using the raw  $C_l$ , but with  $C_d$  augmented by a fixed tether drag term.

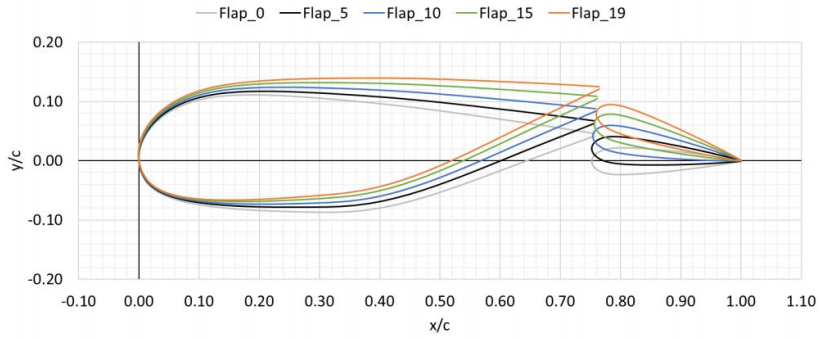


**Figure 22: The five candidates for nominal flap deflection angle. These were analyzed and, for each, the endurance parameter was plotted vs.  $C_l$ .**

The three cases were each run in MSES for each nominal flap deflection, with a 5% fixed transition, and with a free transition. As illustrative examples for comparison, the plots including tether drag, in both the fixed and free transition models, are reproduced in figure 23.

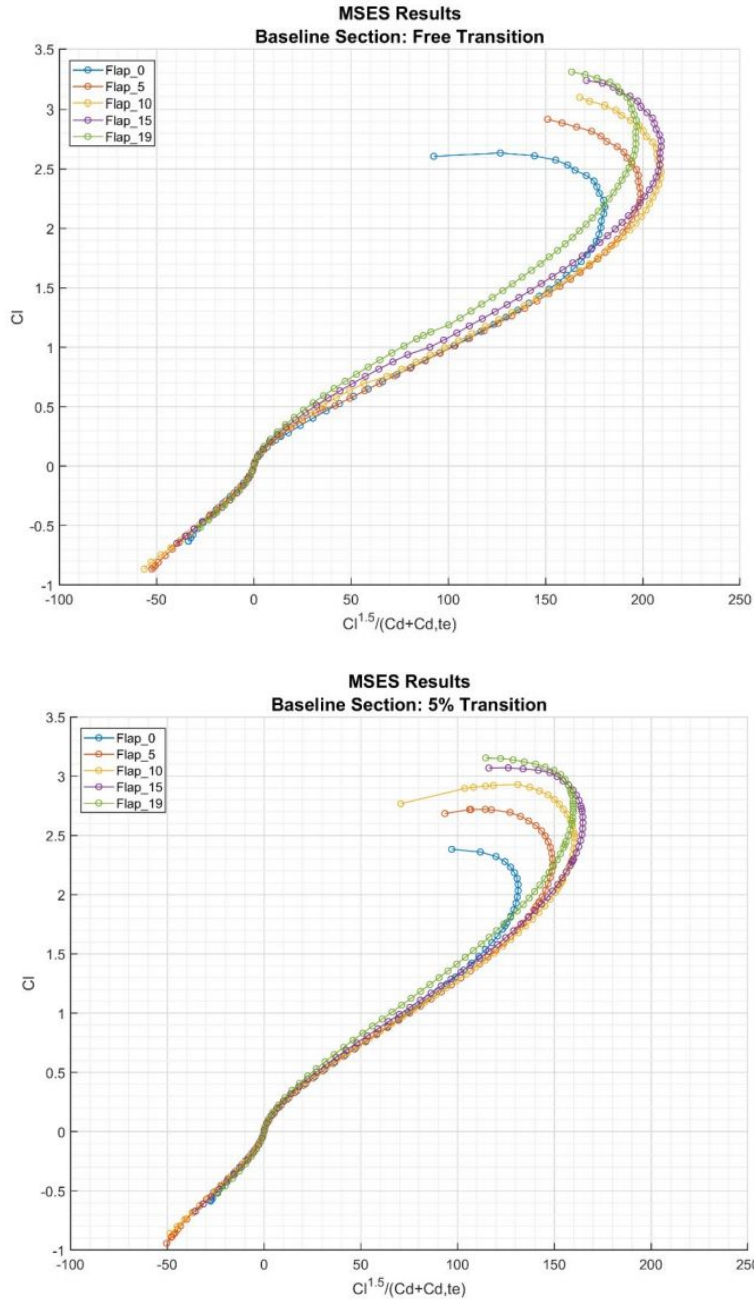


**Figure 23: 2D section endurance parameter vs.  $C_l$ , for various flap deflections. Tether drag term included. (Top) Free transition. (Bottom) Transition at 5% x/c. Note that introduction of the fixed transition nearly collapses the curves onto each other in the low  $C_l$  case. Flap<sub>10</sub> was chosen as the best compromise.**

The general observations are as follows:

- Either too much or too little nominal flap deflection reduces the peak endurance parameter
- The trim correction tends to favor lower nominal flap deflections
- Forcing the transition to 5% tends to reduce performance in all cases, but it reduces performance of the low nominal deflection cases *more* at intermediate values of  $C_l$ , so that the different flap deflections look almost identical in slope
- The smallest nominal deflection that achieves nearly the best peak endurance parameter in both the tripped and untripped cases is about ten degrees

In addition, since the force-tripped curves all nearly collapse onto the same curve, at least at low  $C_l$ , this allows us to choose the same nominal flap deflection of ten degrees, both for the center section and for the wingtips. In other words, the desired  $C_l$  profile to achieve an elliptical lift distribution is attained entirely by use of twist and incidence. The camber may be made constant across the entire span.

After the nominal flap deflection of ten degrees was chosen as a good compromise, a complete set of polars was computed in MSES. The nominal section, compared with the M600 section, is shown in figure 24, along with the pressure profiles for both. Note that the two sections are strikingly similar even though the design problem was approached *without a priori knowledge* of the M600 airfoil. Despite their superficial similarities, the new design is expected to be far more robust against early turbulent transition, as indicated by the sharper and more leading suction peak, and should also suffer from less slot choking at large flap deflections.

TLG also offers many possibilities for further improvement. For more details, see the conclusion of the TLG report, "Airfoil Design for the October Kite" [10].

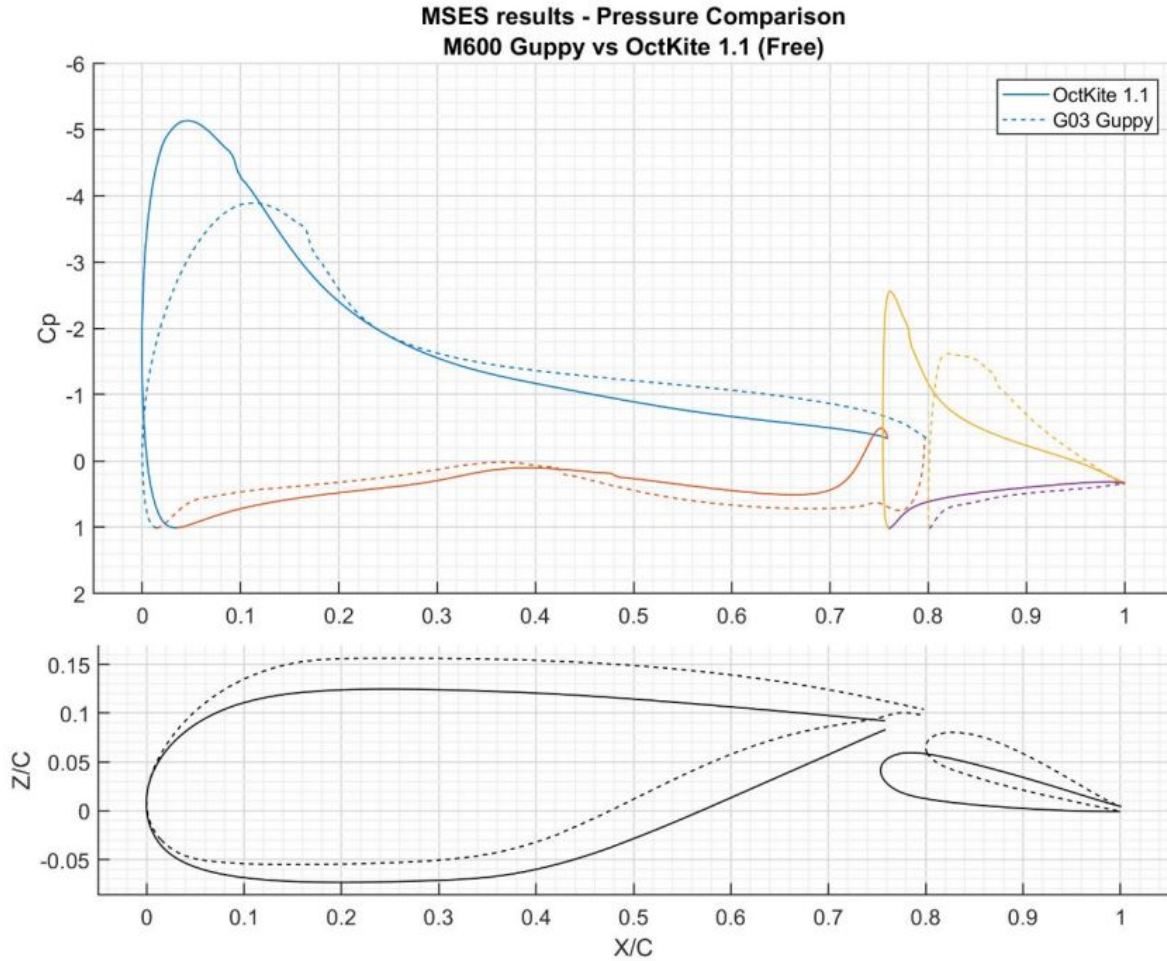


**Figure 24: (Top) A comparison of the pressure profiles of the two airfoils. Note the earlier, sharper suction peak, and the Stratford-like pressure recovery. (Bottom) A comparison of the geometry of the M600 “G03 Guppy” airfoil, with the TLG-designed “OctoberKite 1.1” airfoil.**

### 4.3 MSES predicted results

As noted above, a complete set of polars was produced with MSES. These can be found in the TLG article “Airfoil Design for the October Kite” [10]. As examples,  $C_l$  vs.  $\alpha$  and endurance parameter vs.  $C_l$  are reproduced in figure 25.

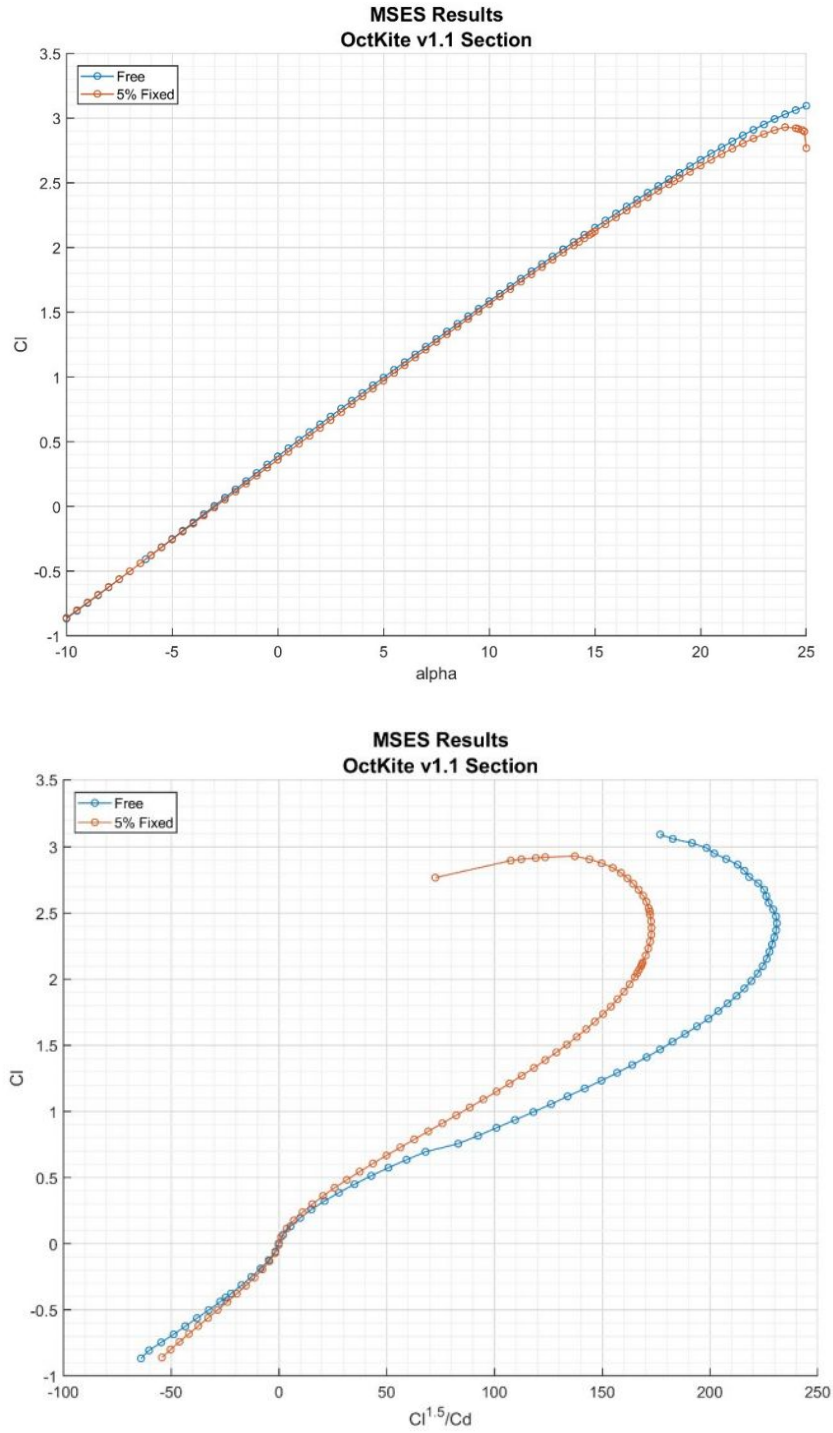


**Figure 25: Example MSES polars of the TLG-developed airfoil.  $C_l$  vs.  $\alpha$  and endurance parameter vs.  $C_l$**

Flap effectiveness was assessed by plotting  $C_l$  and  $\partial C_l / \partial \delta$  vs.  $\alpha$ . Figures for the forced transition case are reproduced below in figure 26. As this figure shows, the preliminary airfoil design is predicted to meet the required  $C_l$  range and the required minimum  $\partial C_l / \partial \alpha$ , from  $-10^\circ$

to  $+10^\circ$  of flap deflection. The  $\partial C_l / \partial \delta$  requirement is achieved considerably outside the range of nominal flap deflections (in fact, nearly up to  $+20^\circ$ ). The TLG report suggests that the design can likely be further improved in subsequent iterations, to achieve even larger ranges of flap effectiveness.

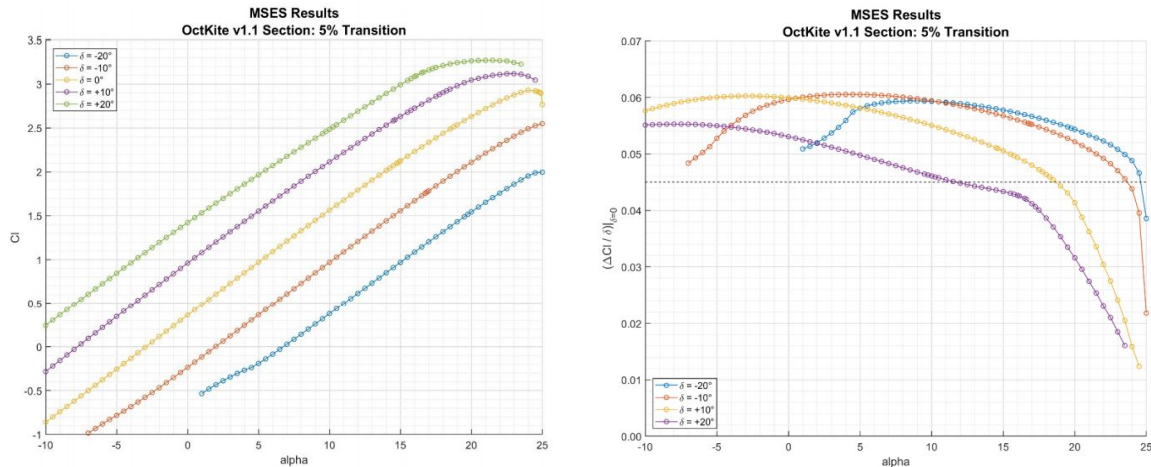


**Figure 26:  $C_l$  and  $\partial C_l / \partial \delta$  for the “Octoberkite 1.1” airfoil. Note the flap retains the specified marginal effectiveness of  $> 0.045$  well outside the required AoA range of  $-10^\circ$  to  $+10^\circ$ .**

## 4.4 Airfoil verification via CFD

At the conclusion of airfoil preliminary design, Makani undertook RANS CFD analysis of the airfoil performance. We concluded the performance meets the upper  $C_{l,oper,max} \geq 2.0$  and  $\alpha_{range,max} \geq 5^\circ$  margin criteria, but doesn't quite meet the lower  $C_{l,oper,min} \leq -0.5$  and  $\alpha_{range,min} \geq 5^\circ$  margin criteria. In retrospect, it was probably unreasonable to ask for such a wide  $C_l$  range from a two element airfoil, and it is unclear that  $C_{l,oper,min} \leq -0.5$  is a needed operating point, since the lowest we should ever wish to set our proxy for zeta,  $C_L^3 / C_D^2$ , should be zero. It seems reasonable, then, to modify the requirement to  $C_{l,oper,min} \leq 0$ , which should be achievable with the requisite 5 degrees of alpha margin.

Of more concern, the CFD analysis results in significantly larger  $C_d$  predictions than does the MSES analysis. The predictions are off by nearly a factor of two in places. As a result, the CFD predicts that the proposed airfoil sorely misses its design target of  $C_l / C_d \geq 75$  at  $C_{l,oper,max}$ .

This is clearly a problem that must be further investigated before proceeding to wind tunnel mockups and section testing.

## 4.5 Empennage redesign

After the initial airfoil design, TLG turned their attention to the tail and empennage design. This section is simply a summary of their work, which is included in whole in the technical appendix “Big M600 Tail Sizing White Paper” [18].

They first wrote out solutions for the lateral and angular displacement of a the fuselage boom (treated as a simple cantilevered beam) in terms of the lateral load. Equating the lateral beam load with the normal force coefficient on the tail surface yields an *effective* tail surface lift coefficient in terms of the normal force coefficient, taking the elastic relief of the tail boom into account. Other parameters taken into account are the static incidence angle (with an unbent boom), the control surface deflection, the area of the tail surface, and the modified dynamic pressure.

### 4.5.1 Sizing for stability

TLG then proceeded to sizing for stability. They used a classical approach based on the definition of static margin, so that we could then corroborate Makani’s results based on incremental changes to the M600 surface sizing.

They began with the  $C_L$ ,  $C_m$ ,  $C_{L\alpha}$ , and  $C_{m\alpha}$  for the main wing body, and augmented these with the appropriate terms based on the normal force at the tail surface, to arrive at the effective  $C_L$ ,  $C_m$ ,  $C_{L\alpha}$ , and  $C_{m\alpha}$  for the craft taken as a whole. These expressions were then substituted back into the definition of static margin. The resulting equation was solved iteratively to find a value of tail surface area (as a function of boom length) sufficient to guarantee the desired static margin.

Before taking values for the stability derivatives  $C_{L\alpha}$  and  $C_{m\alpha}$ , though, the effect of the propellers was added to arrive at effective values for the wing with propellers. The analysis considers the propellers as lifting bodies, and adds a propeller-related offset, based on edgewise propeller area, to the derivative terms  $C_{L\alpha}$  and  $C_{m\alpha}$ . A comparison of the results with and without propeller effects on the stability derivatives is show in figure 27. Clearly it is important to consider the lateral effective area of the props; their position forward of the CG causes a destabilizing effect that must be compensated by increased tail area.

The results of the iterative solutions for the horizontal stabilizer, including prop effects and boom elasticity effects, are shown in figure 28.

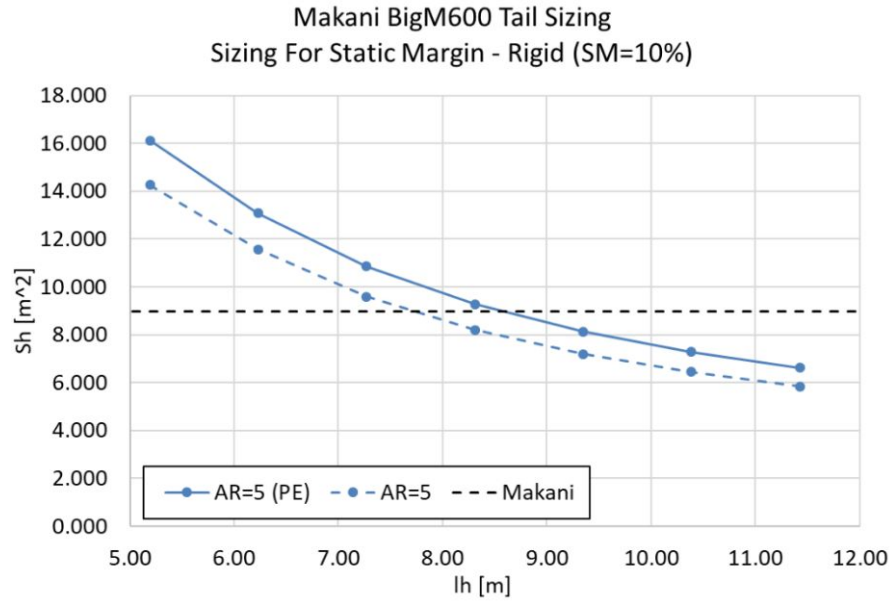


**Figure 27: Horizontal tail area as a function of boom length, sizing for stability. This is with a rigid tail boom—it does not include the boom flexure effects. The solid line includes propeller effects on  $C_{L\alpha}$ , while the dashed line does not. Clearly, consideration of propeller effects on longitudinal stability is important to achieve adequate stabilizer sizing.**

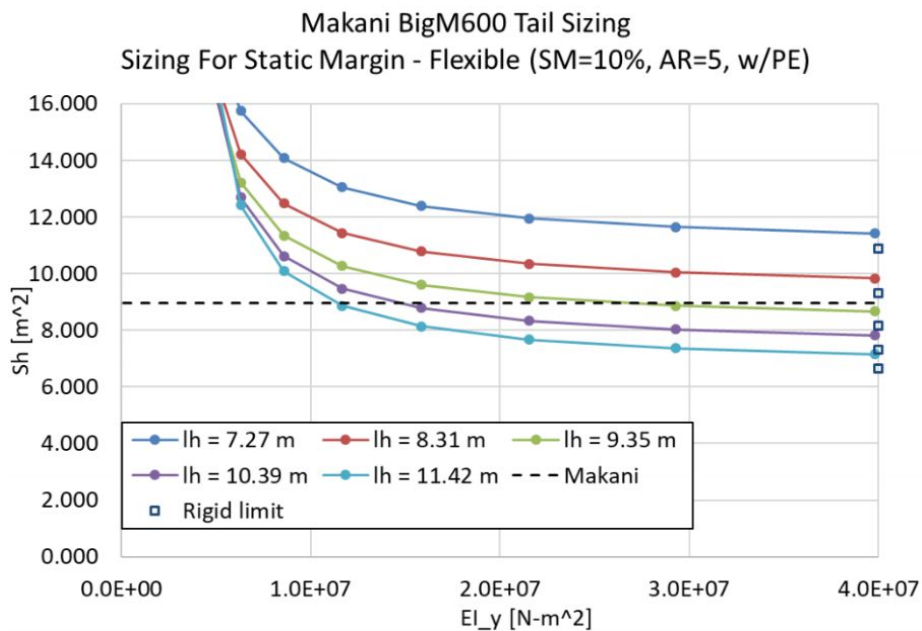


**Figure 28: Horizontal stabilizer area plotted against boom equivalent stiffness, for selected values of boom length. Clearly there are diminishing returns to making the boom too stiff. An  $EI$  value of  $1.0 \cdot 10^7 Nm^2$  to  $2.0 \cdot 10^7 Nm^2$  seems to be the sweet spot, where the curves start to level off. The M600 tail boom stiffness was estimated to be between  $0.96 \cdot 10^7 Nm^2$  and  $1.14 \cdot 10^7 Nm^2$ .**

### 4.5.2 Sizing for trim and maneuverability

To get an idea for trim values and maneuverability ranges for  $C_m$  and  $C_n$ , we ran the FBL tool with the tail off, to produce residual  $C_m$  and  $C_n$  functions around the loop. The mean value implies the surface trim, and the range implies the deflection range necessary to achieve adequate maneuvering to fly the loop as optimized.

Using the augmented values for  $C_{ma}$  from the discussion above, including the propeller effects and boom elasticity effects, and putting it to zero, yields a constraint equation on the tail surface area, the elevator (resp. rudder) deflection, and the elevator (resp. rudder) chord fraction. This constraint equation is iteratively solved, similar to the above, to find the minimum tail surface size as a function of boom length, for a particular chord fraction, to provide trim and maneuverability. Results for the horizontal tail and vertical tail are shown in figure 29 and figure 30.

Clearly the horizontal does not require very much elevator area: A chord fraction of 0.25 is way more than adequate, while the vertical tail requires a tremendous amount of rudder area to reach its maneuverability requirement. Results shown are for a rudder with 0.40 chord fraction, and one can see that essentially the entire rudder effectiveness is used to exert yaw moment.

This is related, among other things, to the large yaw rates of the kite—a large  $\hat{r}$  at the main wing results in a correspondingly large  $C_n$  requirement for the tail. Such a large  $C_n$  requirement also dictates a large vertical tail surface, because the normal force coefficient on the surface of a single element airfoil must be bounded to avoid flow separation. So, trying to offset this problem by changing the incidence angle of the tail, or by using an all-moving tail surface, is not a sufficient solution. The problem is fundamentally that *the varying  $C_n$  from the wing itself* must be offset, and that offset requires a certain minimum vertical tail volume.

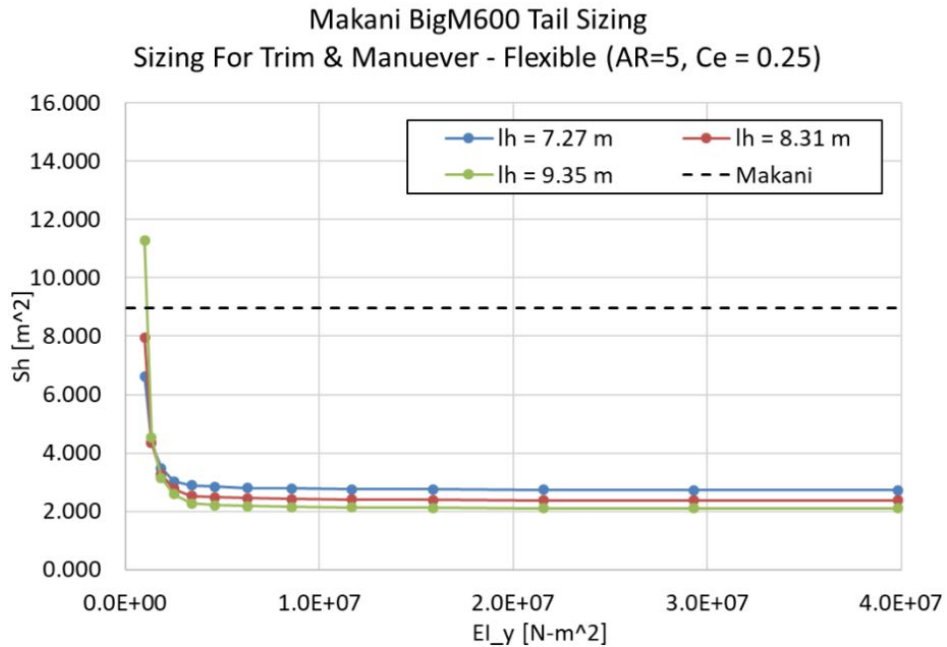


**Figure 29: Horizontal tail area necessary for trim and maneuverability as a function of boom stiffness, using an elevator chord fraction of 0.25. Clearly the pitch moments demanded by the flight path optimizer are easily handled by a reasonably sized rudder.**

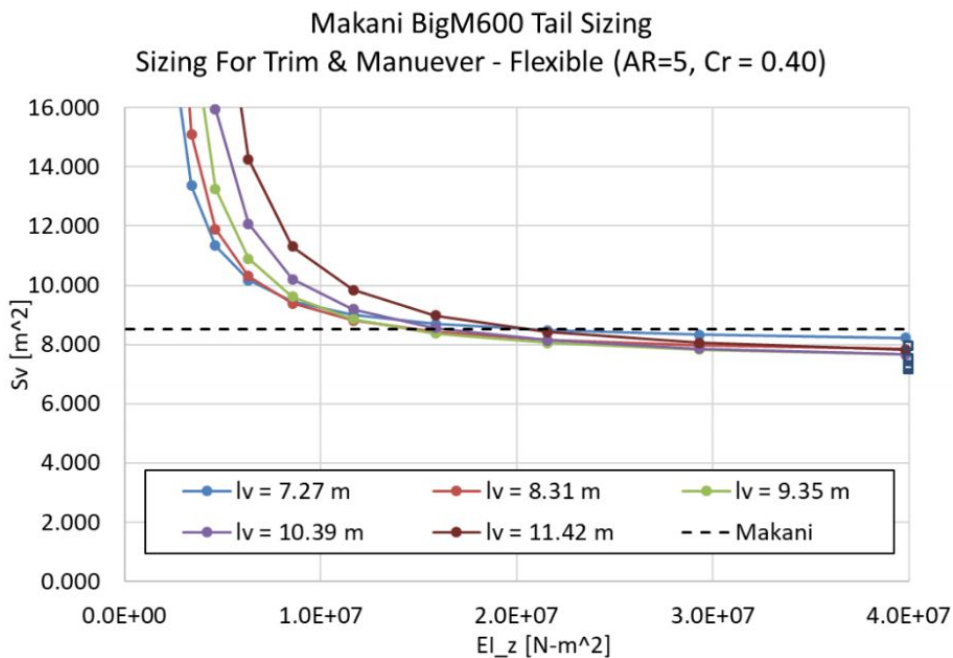


**Figure 30: Vertical tail area needed for trim and maneuverability, as a function of boom stiffness, for a rudder chord ratio of 0.4. The prodigious rudder size requirements are attributed to the aerodynamic yaw moment on the main wing due to the high yaw rate in flight. The problem is also constrained by the minimum surface size (not shown) necessary to prevent flow separation at the tail, for the large yaw moments required.**

### 4.5.3 Aerodynamic and structural sizing choices

Given the above data, TLG made their recommendations for the best-so-far aerostructural design choices for the tail. These are summarized in table 3.

	$C_{N,ih}, C_{N,iv}$	$S_i/S_w$	$l_h/C_{ref}$	$l_v/b_{ref}$	EI [N-m <sup>2</sup> ]	$i_h$ [deg]	$C_{L,\alpha}^h, C_{Y,\beta}^v$
<b>Horizontal</b>	0.078	0.185	4.574	N/A	2.0E+07	5.0	0.0145
<b>Vertical</b>	0.078	0.157	N/A	0.365	2.0E+07	N/A	-0.0123

**Table 3: Chosen aerostructural parameters for tail design, as recommended by TLG.**

They then proposed seven different configurations that would meet this set of requirements, and did more detailed aerodynamic analyses on all of them, using vortex lattice methods. The options were:

- Two flavors of low “T” tail (fin and stab variants)
- Dual-boom with “V” tail (up “V” and down “V”)
- Single boom with “V” tail (up “V” and down “V”)
- Cruciform tail

The VLM computations produced linear aerodynamics models around the trim point that were then run in FBL against the original configuration. This allowed us to validate that the sizing was approximately correct, and that there were no sign errors in the algebra, etc. The results were in good agreement if only one aerodynamic variable was allowed to vary at a time. The VLM databases showed cross-coupling of moment effects due to surface deflections, as could be expected. These cross-coupling effects can be taken into account in the next phase of more detailed design.

Finally, to evaluate lateral directional stability of the entire craft, they ran VLM models of the entire craft (with a subset of four of the seven configurations), and extracted the stability derivatives in order to evaluate anhedral and dihedral effects. The results are shown below in figure 31.

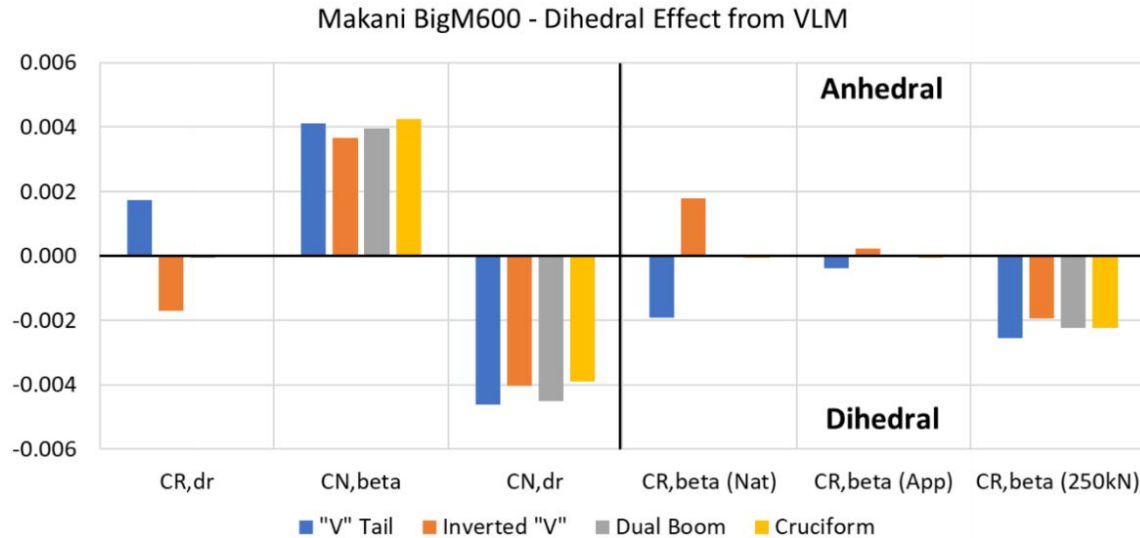


**Figure 31: Dihedral and anhedral effects from the VLM models of the four tail configurations evaluated.**

TLG left the analysis here, with the choice of the best architecture to be determined. It is worthwhile to note that the tether influences on stability were *not* explicitly treated, due largely to Makani’s failure to send complete white papers in time for consideration. But the tether effects are significant, as discussed in [7] and [9], and should certainly be taken into account in a more thorough treatment of the problem.

## 4.6 Pylon design and rotor placement

### 4.6.1 Pylon structural considerations

One of the main airspeed limits on the M600 was thought to be the need to avoid whirl-flutter modes.<sup>26</sup> And in turn, the (perceived) airspeed limit on the M600 was one driver (though far from the only) of its less-than-spectacular performance. To try and avoid this with the MX2 design, we tried to size the pylon stiffness to avoid such modes at the targeted airspeeds.

Sadly, analyzing whirl-flutter modes needs a coupled aero-structural numerical approach, with detailed 3D propeller force and moment tables. There is no simple method of complete analysis—the computational task is significant, making it difficult and expensive to iterate rapidly.

We did, however, settle on and use a couple of rules of thumb. Namely, that the structural modes be “fast” and “well separated.” To motivate this, consider:

<sup>26</sup> Oddly, during preparation for MX2 whirl-flutter analysis, we discovered a flaw in the setup for the original whirl-flutter analysis of the M600. Rerunning this analysis showed the M600 to be far less limited by whirl-flutter than was initially thought.

- Increasing *all* mode frequencies by a constant factor is tantamount to changing the time scale of the system; hence the whirl-flutter speed can be expected to increase by the same factor.
- Since whirl-flutter comes about in part by cross-coupling between the two off-axis rotational vibration modes of the nacelle, reducing the gain product of these two modes will improve matters. If we make the simplifying assumption that each mode is modeled by a simple harmonic oscillator, then increasing the *ratio* of the frequencies will lower the gain product.

For this reason, our design approach with the MX2 pylons was to separate the structural mode frequencies early in the game, and perform a detailed computational check later. We used the mode frequencies of the M600 pylons (attached to a rigid wing) as a reference, and made design changes to improve the situation from there. The first three modes of the M600 pylon are at 4.26, 7.61, and 8.32 Hz. In contrast, the first three structural modes of TLG's first proposed pylon design are 4.78, 8.23, and 11.18 Hz, as shown in figure 32.

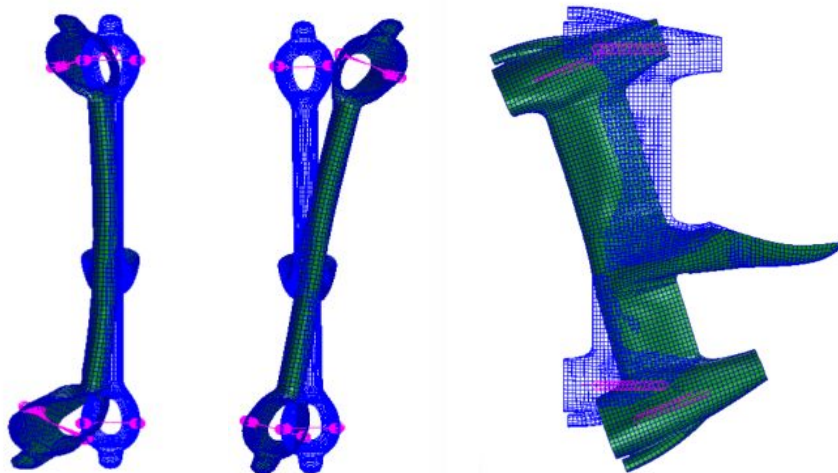


**Figure 32: The first three modes of the MX2 proposed pylon are at 4.78, 8.23, and 11.18 Hz. These are higher and further separated than those of the M600 pylon, which should result in a higher whirl-flutter airspeed limit.**

Note that the pylon modes when attached to an ideal rigid wing do not tell the whole story: It is the modes of the overall airframe structure that matter. Since the wing itself of the M600 had a high aspect ratio, it had fairly low bending and torsional stiffness. This gave rise to a proliferation of nacelle pitch and yaw modes of substantially lower frequencies than those of the pylon by itself—the wing bending and twisting between pylon attachment points was a significant contributor to nacelle motion. The MX2 wing, by virtue of its 60% increased chord and thickness, has about six times the bending stiffness, so is not expected to drop the pylon mode frequencies significantly.

## 4.6.2 Pylon design and placement for best hover performance

We now turn our attention to a problem that is only partially understood: The M600 exhibits a large “phantom pitch back” moment during hover. By “phantom,” we mean an effect not predicted by our simple hover model. As an example, if all eight rotors are running at the same speed, we observe a significant pitch back moment on the airframe. The hover controller senses this and compensates by increasing the speeds of the top rotors (*i.e.* the downwind rotors, in hover) to compensate. This is a problem because the top rotors reach their speed and power limits much earlier than the bottom rotors. This limits the total thrust available for hover and acceleration into crosswind, as well as limiting the control authority envelope available for pitching forward.

Much effort has gone into empirically modeling this effect over the years, by examination of flight data and improving our hover model, but this does not solve the underlying problem. And it is a problem: Any hover thrust deficit manifests as a limitation on the wing mass that can be carried into crosswind, hence a limitation on system energy production [4]. The current condition is a poor state of affairs.

We felt the phantom pitch moment likely resulted from some aspect of the airframe or rotor configuration. So we decided the design phase of the MX2 was the time to spend significant effort chasing a thorough understanding of the underlying cause. In this way, hopefully we would not be doomed to repeat the error and end up with a system that manifested the same problem as the M600.

We took on the problem in earnest after Oktoberkite, with a mind to understanding it well before finalizing MX2 design. What we found is interesting.

### 4.6.2.1 Single pylon not implicated

A 3D CFD analysis with a pair of rotors on a single pylon on a very long wing did NOT exhibit the effect. The rotor wake velocity field was roughly as expected. There were some very minor stagnation pressure effects on the wing, but not nearly enough to explain the pitch moment actually observed. Different rotor speeds produced different thrusts, and like rotor speeds produced like thrusts (and furthermore, in agreement with the thrust generated in the isolated rotor case).

### 4.6.2.2 An old result from two dimensions

We had a previous two dimensional CFD result, featuring two 1-D actuator “disks” (really line segment momentum sources) in a 2D domain. This model exhibited very strange behavior. A very large vorticity bubble was produced, almost completely upstream of the wing, and many times the chord in size. Basically all the downwash from *both* rotors ended up downstream of the wing. The situation is depicted in figure 33.

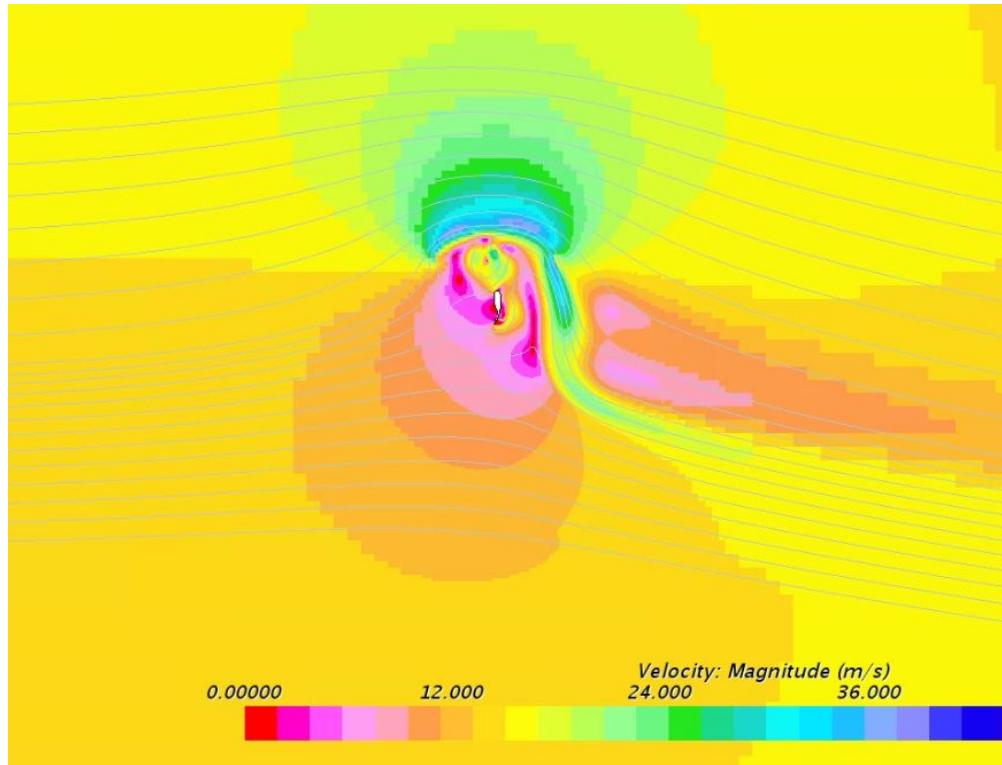


**Figure 33: Results from an earlier 2D CFD case, using actuator-disk model (i.e. momentum sources) in place of rotors. The wing is the very small white element. Note the strange behavior: A large vorticity bubble forms upstream of the wing, and nearly all rotor downwash ends up downstream of the wing.**

This led to the idea of constructing a narrow-domain 3D case, to see if a similar effect manifested.

#### 4.6.2.3 Problem reappears in narrow-domain case

A narrow CFD domain was constructed, of a width equivalent to the M600 pylon spacing, using slip walls as the side boundary conditions. A single pylon was centered in the domain. A moving reference frame (MRF) method was used, with a blade element model (BEM) of the rotors. Results are shown in figure 34.

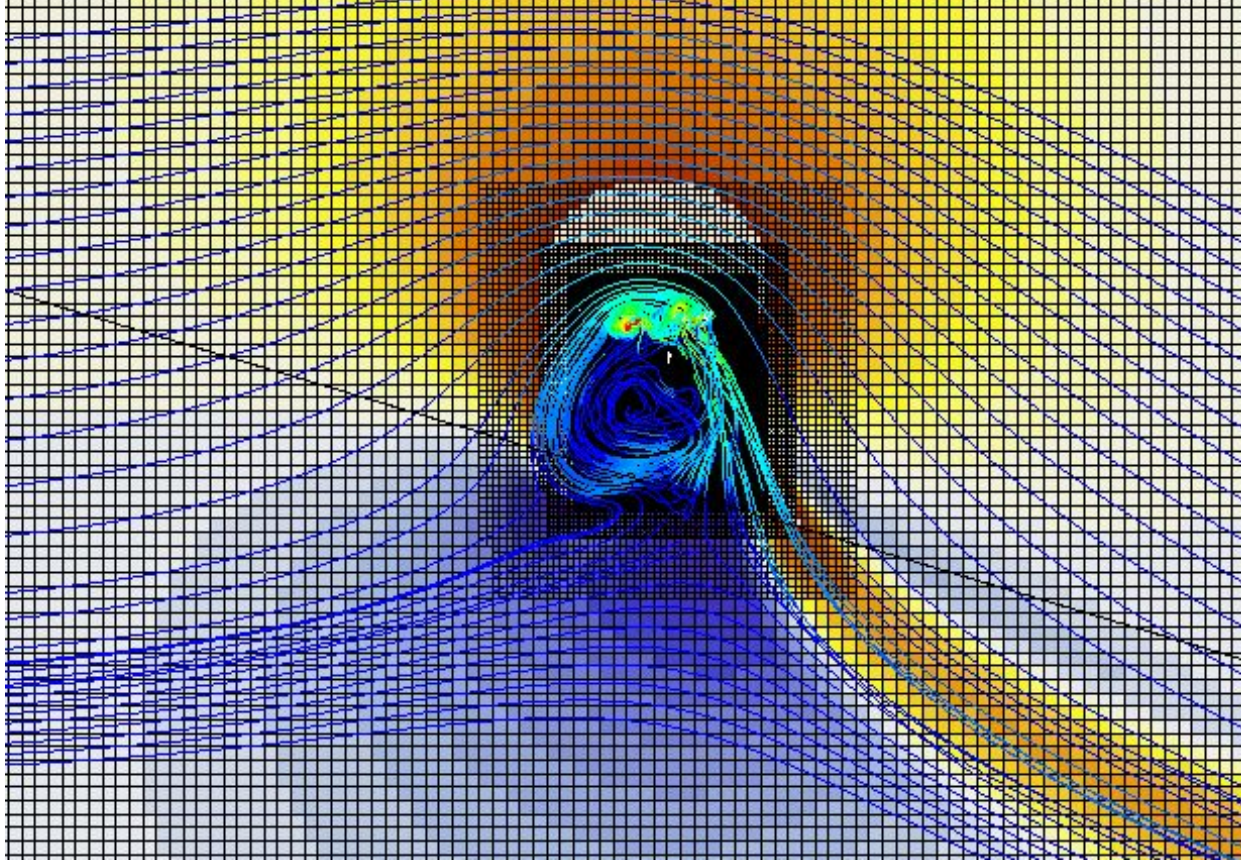


**Figure 34: CFD results from a 3D narrow domain case with a single pylon, bordered closely by slip-wall boundary conditions. Note the same emergent phenomena: a large upstream vorticity bubble, and essentially all of the downwash ending up downstream of the wing.**

The resulting flow field agrees closely with the 2D case: There is a large rotational “bubble” upstream of the wing, with marked upwash in front. Essentially all the propwash is behind the wing. There are radically different thrusts for the same rotor speed. Recall that this does *not* happen in the wide-domain case, so the presence of the wing itself is not implicated in this flow pattern—it is something about the width of the domain to which the problem is constrained.

We continued to the full unsteady aero case, to verify the results with better confidence. Indeed, the rotor thrusts are substantially different for the same rotor speed, with the bottom (upstream) rotor developing substantially more thrust. Figure 35 shows the thrust developed for each rotor as a function of time, showing the flow field developing and reaching steady-state over a period of about one second from the start of the experiment.

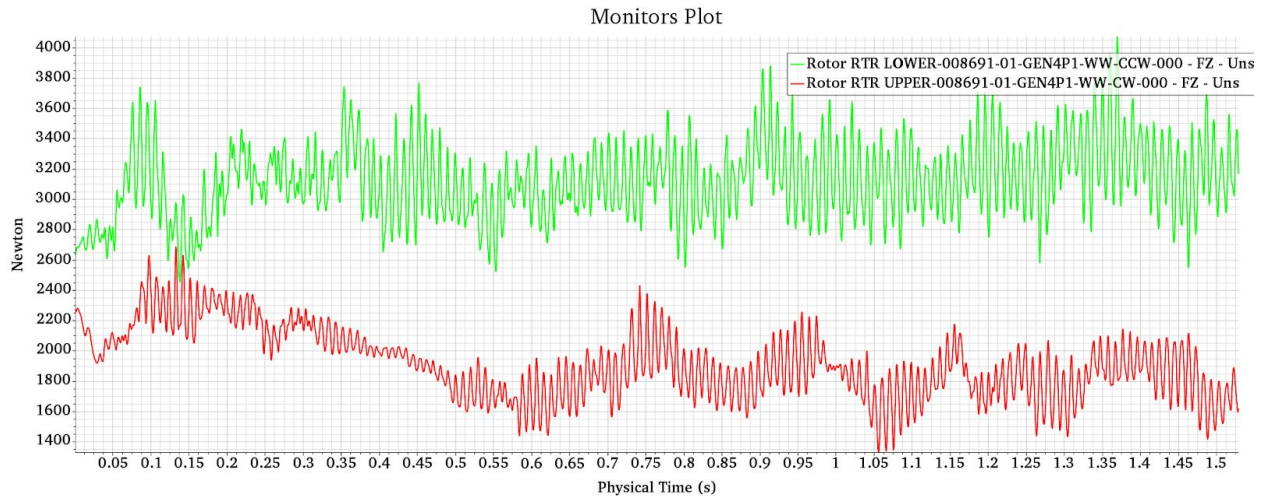


**Figure 35: Running two rotors at the same speed in the narrow domain case, with full unsteady aerodynamics, shows (a) the bottom (upstream) rotor thrust is much greater than the top (downstream) rotor thrust, and (b) the effect takes some time to develop, presumably as the rotation bubble becomes fully formed.**

#### 4.6.2.4 Investigating the difference between narrow and wide domains

The comparison of the wide and narrow domain cases indicates that something about the narrow domain is causing the difference in thrusts. A good first guess might be that due to the large upwash in front of the wing, and shielding from the bottom rotor, the top rotor might be “starved” for mass flow. To resolve this more clearly, we ran a single-sided domain case as well, to see if the problem manifested there. It did not.

To gain more understanding, we plotted streamlines for the single-sided case and the narrow case, to see whence the rear rotor was ingesting its mass flow. The streamlines are quite telling, as shown in figure 36.

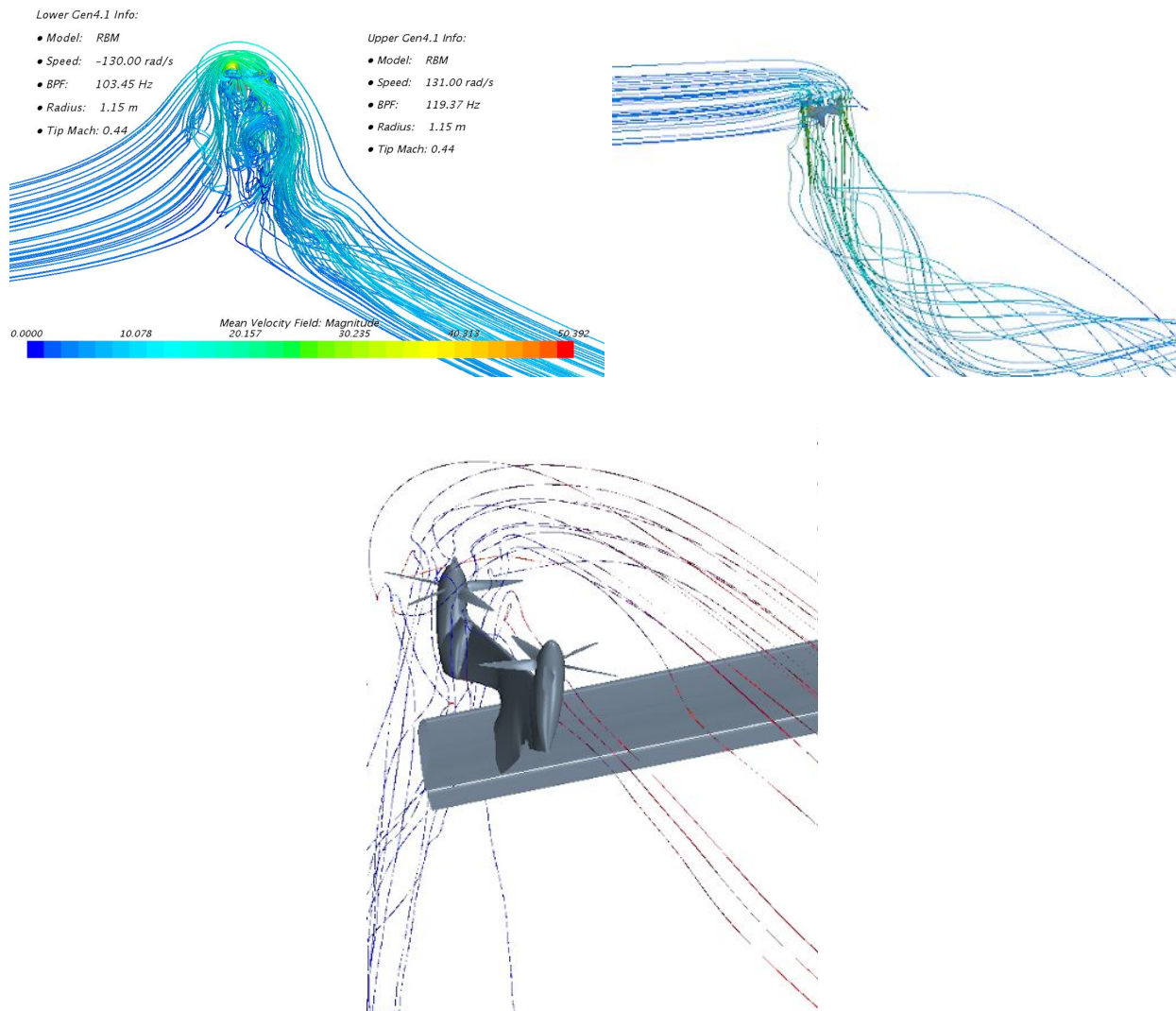


**Figure 36: Comparison of hover flow streamlines for a single pylon. (Top left) a narrow domain. (Top right) a one-sided domain. (Bottom) Axonometric view of top rotor streamlines in the one-sided domain case. Note the top rotor avoids the blockage of the bottom rotor by ingesting “fresh” upstream mass flow from the side.**

As shown in figure 36, in the single-sided case, the top (downstream) rotor is ingesting upstream mass flow by drawing it from the side. Another way of viewing the situation is to look at the average velocity magnitude field. Figure 37 compares a wide domain with a narrow domain. While the wide domain looks pretty much as expected, the narrow domain case is quite interesting. It seems to indicate that the top rotor is ingesting a good portion of the mass flow from the bottom rotor’s downwash. This would explain why: (a) the bottom rotor’s downwash seems to be missing in the side sectional view, (b) essentially all the resulting downwash is behind the wing, and (c) the top rotor is running much faster to develop the same thrust.

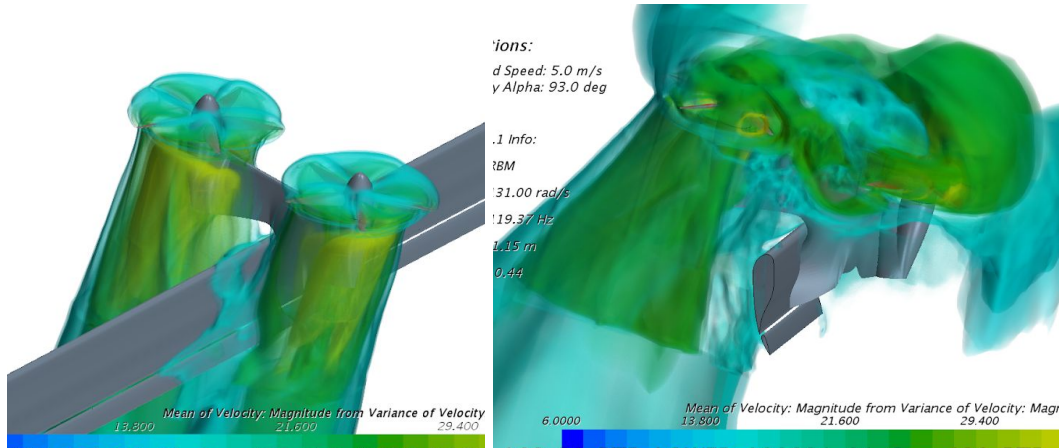


**Figure 37: Mean velocity magnitude fields for the wide domain (left) and the narrow domain (right). It appears that in the narrow domain case, the top (downstream) rotor is ingesting a significant amount of downwash from the bottom (upstream) rotor. This explains why the top rotor must spin faster to develop the same thrust: It is ingesting already-energetic flow.**

It is interesting to note that in figure 35, the top and bottom rotors start with approximately similar thrusts, but end up with dissimilar thrusts after some time. This is due to the time lag in development of the fully-formed, quasi-steady flow field: The vorticity bubble does not exist when the rotors first start spinning. The vorticity bubble may therefore be said to be *causative* of the difference in thrusts. This observation gives rise to the following mental model:

#### 4.6.2.5 A possible mental model

An instructive way of thinking about the difference in thrusts is by use of the Kutta-Joukowski theorem. For high Reynolds number inviscid flow, for lift to exist on a two-dimensional domain around which a crossflow is present, there must be circulation around the domain. In particular,

$$L' = \rho v_{\infty} \Gamma$$

In our case, the lift is given by the weight (per span) of the aircraft, and  $v_{\infty}$  is the wind speed. To rewrite:

$$W/b = \rho v_{wind} \Gamma$$

So it is simple to see that the circulation is inversely related to the wind speed. And obviously, in our static hover case, most of the circulation is captured in the vorticity bubble.

We can observe that the existence of positive circulation results in an *upwash* presented to the upstream rotor, and a *downwash* presented to the downstream rotor. So, obviously, from first

principles of propeller operation, the upstream rotor will develop higher thrust for a given rotational speed, resulting in the “phantom pitch back.”

We have observed empirically during flight testing that the phantom pitch back is quite large for low wind speeds, and then tapers off asymptotically as the wind speed increases. Interestingly, the form of our modified Kutta-Joukowski relation makes this quite obvious: If  $v_{wind}$  is nonzero but small,  $\Gamma$  is large, and the top and bottom rotors see very different effective inflow speeds. As  $v_{wind}$  increases,  $\Gamma$  decreases, and the top and bottom rotors start to perform closer to parity.

We have also noticed empirically from actual flight data that in an intermediate range of wind speeds (say, 5 to 8 m/s), the phantom pitch moment seems to “snap” on after a varying period of time, in a way that suggests metastable behavior. In this model the position and shape of the circulation bubble relative to the wing/rotor system eventually settles into a stable attractor state.

Note that there is ample classical precedent for this type of metastable flow behavior: A conventional airfoil, set in motion instantaneously, does not instantaneously generate lift—it manifests a flow separation bubble on the top aft surface, which is advected in the crossflow until it reaches the (sharp) trailing edge of the wing, at which point it is shed. At this time, the streamlines are oriented smoothly past the trailing edge and, absent stall conditions, remain so. This is, of course, the well known “Kutta condition.”

It is certainly plausible that there is some “Kutta-like” condition for hovering vehicles in a crossflow, probably having to do with the position and size of the circulation bubble, that is stable and is achieved only after some time.

#### 4.6.2.6 Possible solutions

If all the above supposition is correct, then *any* hovering device with two identical rotors placed similarly to the M600, restricted to a two-dimensional domain, will experience the pitch-back effect in a crosswind.

Possible ways around this are:

- Experiment with rotor placement: untried in our experience
- Experiment with different rotor characteristics: also untried, but might offer hope
- Escape the two-dimensional domain assumption by introducing 3D flow: As suggested by the shape of the streamlines in figure 36, widening the spacing between pylons might allow the top rotors to ingest more upstream mass flow.

#### 4.6.2.7 Effect of pylon spacing on pitch back moment

We reran the Moving Reference Frame, Blade Element Model analysis for narrow domains, sweeping the domain width and the wind speed. The results are summarized in Figure 38. As can be seen, the problem only really manifests at low wind speeds, with a very narrow pylon spacing. The problem is simple to fix by increasing the pylon spacing. Surprisingly, only a small increase is necessary – increasing the normalized pylon spacing (expressed as a multiple of rotor diameter) from 1.06 (as on the M600) to 1.29, reduces the magnitude of the pitch moment by nearly 2000 Nm, per pylon. Since we believe this affects mostly the inner two pylons, we could expect a pitch-back reduction of about 3800 Nm. There are diminishing returns, and further increasing the pylon spacing introduces other complications. For the MX2, we had tentatively settled on 1.293 times the rotor diameter.

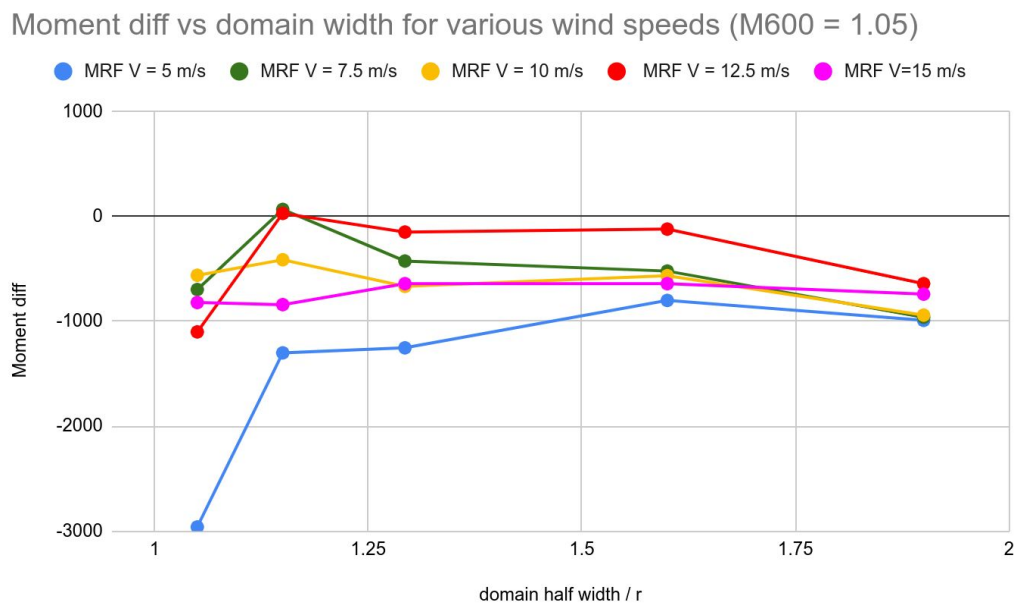


**Figure 38: “Phantom pitch back” moment, per pylon, as a function of wind speed and pylon spacing. Note the problem is most severe in the low wind, narrow spacing case; exactly where the M600 finds itself most of the time. Increasing the pylon spacing to 1.293 times the rotor diameter was tentatively chosen for MX2, to bound the magnitude of the problem. Other additional approaches are suggested in the text.**

As mentioned above, we had not fully investigated the effects of a steeper blade pitch on the top rotors, or placing the top rotors more forward in the body x direction (toward the nose). A more thorough investigation of these two ideas should be undertaken before finalizing a next generation design.

### 4.6.3 Pylon design and rotor placement for best crosswind performance

We now turn to a related problem of top and bottom rotors operating in different aerodynamic environments: the situation during maximum power generation.

Consider an energy kite with pylons of the M600 type (top and bottom rotors, nearly symmetrically disposed) in crosswind generation. Because of the circulation around the wing due to lift, the top and bottom rotors see different inflow velocities: The inflow on the top is faster than that on the bottom. This was a significant contributory factor to the inability of the M600 to deliver its nominal design power: Since all rotors had the same characteristics (diameter and pitch), they could not all operate along the Pareto frontier of maximum power under the same flight condition. That is, they could not all saturate the capability of their associated generators at once.

Adjusting the top and bottom rotors to different blade pitches might solve the power optimization portion of this problem (this is discussed below in section 5.3, below). But at the cost of introducing a new problem: spurious pitch moment.

To see this, let's assume for a moment that we have perfectly efficient rotors; *i.e.* they can develop shaft power equal to the thrust multiplied by the inflow velocity. Of course such a thing is not possible, but it yields a productive thought experiment nonetheless.

Let's set the power of the top and bottom power system to the same (maximum available) value, and see what the consequences are. The top rotor, of course, sees higher inflow velocity, thus requires less thrust to achieve the same power. Conversely for the bottom rotor. Accordingly, the pylon (hence the entire craft) experiences a net pitch forward to due generation.<sup>27</sup>

This effect will decrease as rotor  $z$  spacing increases (because circulation has units of length times velocity, so increasing characteristic length decreases characteristic velocity). Accordingly, we might try to moderate it by lengthening the pylons vertically. But this is a structural challenge, and promises to introduce a significant mass penalty (especially since the circulation velocity scales as  $1/r$ , so this approach will always yield diminishing marginal returns).

Another approach might appear to be adjusting the average  $z$  position of the two rotors, rather than their spacing. We produced a simple spreadsheet model to evaluate the feasibility of this approach. Sadly, moving in either direction has drawbacks. A summary of findings is as follows:

---

<sup>27</sup> This is perfectly analogous to the pitch back in hover: If we're delivering power, we feel a pitch back. If we're harvesting power, we feel a pitch forward. This is the case regardless of the particular aerodynamic state, as long as positive lift is being produced.

- Moving both rotors up to null the forward pitch moment results in an even larger velocity ratio, hence an even larger thrust ratio (about 2.0 in the spreadsheet model, with real M600 input parameters). This presents a significant rotor design problem if the rotor areas are to stay the same.
- Moving both rotors down reduces the thrust ratio for a small amount of movement, but the thrust ratio goes back up as the thrust decrease on the top rotor outpaces the thrust decrease on the bottom rotor.
- Moving the rotors down also results in more pitch down moment during generation

In summary, if the upper and lower powertrains have the same power rating, and if they are the same in number, then for a given vertical rotor spacing, there is a tradeoff between nulling pitch moments due to generation, and maintaining maximum thrust on all rotors. They are not both possible at the same time.

Note that I've said nothing about blade pitch—changing the pitch doesn't get around the fundamentals of momentum theory. I have also said nothing about rotor diameter—this thought experiment simply talks about thrust per power.

It seems perhaps the only solution to optimize rotor disc loading might be to make the bottom rotors larger in diameter, but this invites mismatches in the maximum torque capability of the generators, and the effect of such an approach on hover performance hasn't been thought through. The other option might be to place more, or higher rated, powertrains on top.

This is obviously a complex issue raising significant concerns. Much more understanding should be gained, perhaps through CFD studies, before trying to build more accurate flight simulation models and optimizing a design.

## 4.7 Rotor sizing and design

Detailed rotor sizing and design for the MX2 was not completed. There is a brief conversational discussion below in the Unfinished work section, that gives some motivation and ideas for how to approach the rotor optimization problem.

## 4.8 Bridle and CG placement

An airplane in flight is subjected to two main classes of forces: aerodynamic, and inertial.<sup>28</sup> This gives the craft at least two important "center" points: the center of gravity (CG), and the center of aerodynamic force (CAF).<sup>29</sup> These are the forcing functions in the equation of dynamics. For

---

<sup>28</sup> Here I lump propulsive force into the aerodynamic forces, and lump gravitation (weight) into the inertial forces (because the equivalence principle tells us that inertial mass and gravitational mass are equivalent).

<sup>29</sup> I will define the CAF as the point around which the aerodynamic moment is zero. I write "center of aerodynamic force" because the term "aerodynamic center" has a very specific (and distinct) definition.

the rotational degrees of freedom, the mass moment of inertia is typically taken with respect to the CG. This has the convenience that gravitation and acceleration produce no moment about the CG.

A kite also has significant tether tension acting on it. Since the tension is in general not aligned with the CG, the tether can produce large moments acting around the CG. In crosswind flight, the tether tension can exceed the weight of the craft by a large factor (for the M600, around 15x). So, assuming angular accelerations are small, maintaining attitude control requires that the tether moment be approximately balanced by the aerodynamic moment.

Therefore, there are *three* center points of interest, not just two: The CG, the CAF, and the center of tension CT (the point at which the tether tension may be said to act).<sup>30</sup> Since for small accelerations, tension and aerodynamic moments dominate inertial moments, it stands to reason that the position of CT relative to CAF affects the craft behavior more strongly than the relationship between CT and CG, or between CAF and CG. Since CAF to CG is the only relation to contemplate in stability analysis of free flight aircraft, it is evident that the stability analysis of a kite is not only more complex, but is more strongly related to the choice of CT.

This is not to say that the position from CG to CAF is unimportant—merely that there are larger moments in play, and they can affect stability significantly.

Intuitively, from a first glance, here are just a few of the moments *not present* in free flight, for an M600-like kite:

- If the flight path is curved (noninertial) and the CT is ahead of (resp. behind) the CG, there will be an in-turning (resp. out-turning) yaw moment
- If the flight path is curved and the CT is outboard of the CG, there will be unstable yaw modes (see above and think about the kinematics)
- If the CT is ahead of (resp. behind) the CAF, there will be a pitch-down (resp. pitch-up) moment
- If the CT is above the CAF, there will be unstable pitch modes
- If the CT is to either side of the CAF, there will be large roll moments (as well as large yaw moments during heavy generation and/or motoring)
- *Etc.*

Again, these are just a few of the most obvious effects. For some pictorial examples of these, with detailed numerical discussion, see “Effect of Design Parameters on M600 Stability in Crosswind” [7] and “Kite Stability in Crosswind Flight” [9].

---

<sup>30</sup> For a single-point tether attachment, CT is of course a single point. More generally, for a two-point bridle, the tether tension does not intersect a single point, but is tangent to some involute surface.

## 5 Unfinished work

### 5.1 Flight stability of tethered air vehicles

In traditional fixed-wing aircraft design, there exists a canonical set of linear inequalities which, when imposed on the aerodynamic stability derivatives, collectively ensure stable and controllable flight. They are derived by separating the flight dynamics into longitudinal and lateral subsystems, and then applying the Routh-Hurwitz stability criterion to each subsystem. Ensuring they are satisfied guarantees a subset of the normal modes of the flight dynamics, linearized around a straight-and-level-flight trim state, are stable.

There are two primary ways in which the presence of the tether renders the canonical inequalities inadequate (or incomplete) for a kite.

First, the forces and moments from the tether can easily exceed the inertial and gravitational forces by at least an order of magnitude. Clearly, any dynamic treatment that ignores the tether will be inadequate to evaluate stability.

Second, since the flight path is constrained by the tether, the assumption of straight and level flight is likewise inadequate as a starting point for stability analysis.

To address this significant shortcoming, we derived a formal statement of the system dynamics in crosswind tethered flight and linearized it in terms of the aerodynamic stability derivatives, the tether spring constant, and the bridle geometry. This allows us to evaluate the stability of the system's normal modes for any set of underlying design parameters. Details of the model derivation are given in the technical paper in part II titled "Kite Stability in Crosswind Flight" [9].

By using this model it is simple to see the M600 is unstable in the spiral mode.

By sweeping design parameters and producing root locus plots, we are able to investigate linearized system stability as a function of the underlying design parameters. Preliminary investigations indicate, unsurprisingly, that the attachment points and geometry of the tether and bridle are the variables that most affect stability.

This is an open area of investigation; we intended to have a bridle geometry optimized for stability and performance before finalizing the structural design of the new airframe, but the project was shut down before we had the chance to complete this analysis. Hopefully the material in [9] can serve as a useful basis for someone else to continue this important work. In particular, if it can be shown that a tethered system is somehow separable in a manner similar to a free-flying aircraft, we can then re-apply the Routh-Hurwitz criterion to the new dynamics to find a new set of canonical stability inequalities, specifically for kites.

## 5.2 Tuning and evaluation in simulation

The C-Sim is an energy kite flight simulator written in C. It is discussed in detail in “The Makani Autopilot” [3]. It has the following features required for tightly coupled, six-degree-of-freedom dynamic problems: a dynamic time-marching simulation, high and low incidence angle aerodynamic databases, 3DOF rotor aerodynamic models, large scale turbulence modeling, and a distributed tether model. The C-sim, coupled with the real-time flight controller used for real world flights, is Makani’s most comprehensive simulator of the M600. The Oktoberkite / MX2 design is currently implemented as an alternative configuration in the C-sim, which has never previously supported distinct kite platforms.

The MX2 is able to fly in the C-sim, but not reliably. If it does not lose control, it performs well and close to predicted power production. However, it frequently tends to lose control and crash, especially at higher wind speeds. There are many possible reasons, but we ran out of time and resources to investigate fully. Some of the possibilities are listed below in summary form:

- MX2 reaches the transition from the Loyd regime to the tension-limited regime much earlier than the M600: Given the larger wing area of the MX2, it reaches higher tether tension at much lower wind speeds than did the M600. Since we never implemented any plan to deal with closed loop tension limited operation (see “The Makani Autopilot” [3] and “Airborne Wind Turbine Performance” [4]), we have as yet no means to control the MX2 in this regime.
- There has never been any closed-loop plan to deal with power saturated flight in high wind with turbulence. The difficulties are clearly discussed in [4]. Since the MX2 has yet no such control scheme, it is not surprising that it doesn’t perform well in high winds.
- Controller gains are not well tuned: The LQR gain generation process has only been tested with the M600, so it is possible that there are specifics of the M600 embedded in the code that result in poor tuning.
- Feedforward controllers: There is a sinusoidal feedforward term fed into the crosstrack controller’s tether roll loop. This term is hand tuned, and it is possible we simply didn’t have enough time to tune it well.
- We did not have a lot of time to spend on optimizing rotor design for the MX2. Since rotor design is expected to make a much bigger difference in handling qualities for a power-limited, tension-limited kite (discussed in section 5.3), it is possible that the lack of deliberate and careful rotor design affects the MX2 more severely than it does the M600.

Given that the M600 controller evolved over many years of flight testing, but that it was never forced to venture into the regimes of tension limiting and constant full power around the loop, one might be left with the impression that the M600 controller is too “evolutionary” in nature, and given what we know now in retrospect, a new controller architecture might make more sense for the MX2. This has been discussed, but little action was taken due to the high complexity of the

problem and the lack of resources. Some rough ideas are hinted at below in section 5.4: Flight controller.

### 5.3 Rotor placement, sizing, design, and pitch selection

As discussed above, the FBL is the tool we used to evaluate and guide preliminary designs for the Oktoberkite / MX2. For simplicity and speed, the FBL has a “lumped rotor” model: That is, it scales the force from a single rotor, obtained from a lookup table, by the total rotor area available on the craft, and it applies the aggregated rotor force at a single point.

Of course, in the real world, there are multiple rotors, each in a substantially different aerodynamic environment, and this results in quite a large spread in the freestream velocity  $v_{app}$  at the various stations on the airframe. One can see when looking at C-sim data (or indeed flight data) for the M600 rotor speeds and torques, that rotors of single design applied at all stations cannot possibly all be operating at their maximum power at the same time. As well, if some rotor speeds exceed the range of high efficiency and start to produce significant additional drag, there can be large pitch and yaw moments applied to the airframe that can contribute to flight instability. These effects are not modeled in the FBL.

This begs the question of how to choose appropriate rotor designs for the new craft. Our intent was to use the C-sim to help in optimizing rotors for each station position. To see how this might work, consider the rotor performance map shown in figure 39. In this figure I have taken shaft power and freestream velocity as the independent variables, and the contours plotted are those of thrust. This is a useful projection in which to view the rotor maps, because it makes it painfully clear that a rotor can only extract maximum power in a very narrow range of airspeeds: Such a rotor would be operating way up in the upper right hand corner, just below the mach limit, and just above the maximum torque limit. As shown in the figure, this area covers a very narrow range of inflow speeds; about 58 to 78 m/s for this rotor.

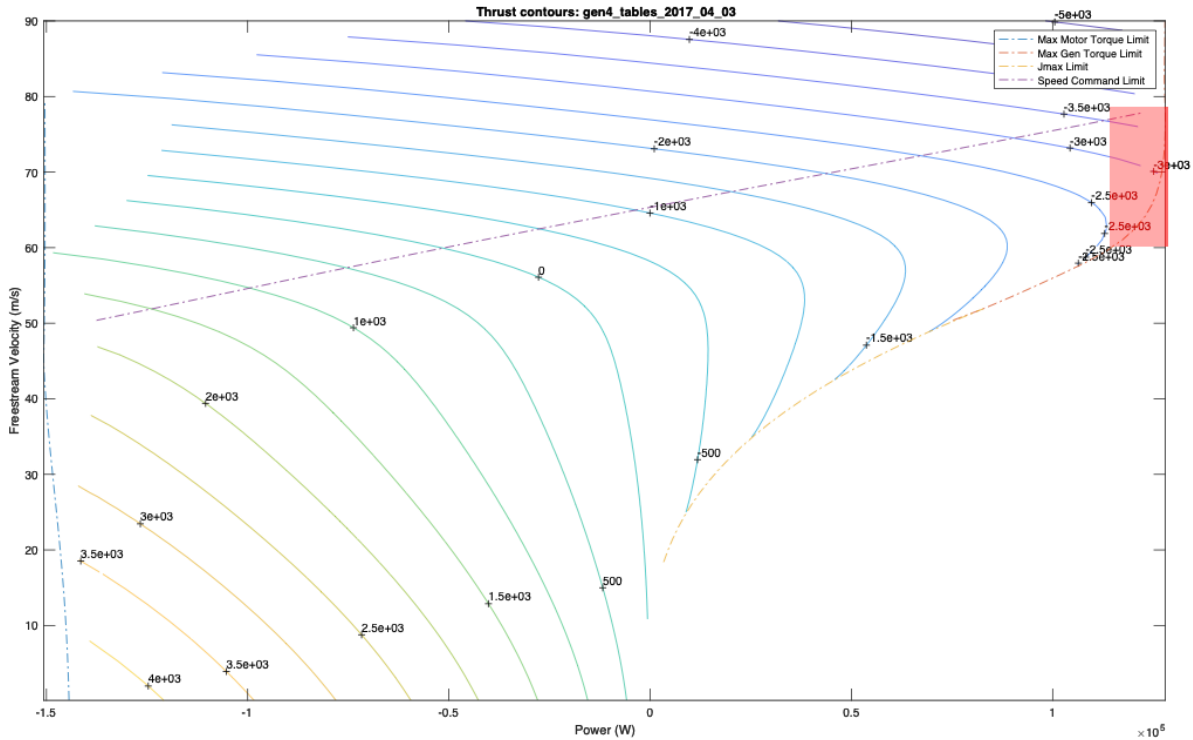


**Figure 39: A rotor map for a Makani Gen4 rotor, viewed in the  $(P_{shaft} \otimes v_{app})$  plane, showing the problem of tuning a fixed pitch rotor for maximum power. Clearly, to get anywhere close to maximum shaft power, the rotor must be operating in a very narrow range of inflow velocities. For example, the shaded box shows that to obtain at least 90% of rated power, the inflow velocity must be between 58 and 78 m/s.**

Consider now that distinct rotors in C-sim often see  $v_{app}$  inflow speeds, perhaps 50% different from each other, due mostly to wing circulation and body yaw rates. Obviously no single rotor will suffice for all eight stations. If we could run the C-sim and collect simulated  $(P_{shaft}, v_{app})$  data and plot it on such a chart, it should then be clear how we should change the rotor design to optimize performance at each station.<sup>31</sup> Changing the pitch of a rotor will displace the thrust contours, the stall line, and the motor torque limit, while changing diameter will displace the thrust contours and the mach limit.

Sadly, we never quite got the MX2 working very well in C-sim, largely due to unsolved flight control problems at higher wind speeds, so we were unable to optimize the rotor design choices within the time we had available. This would certainly be a fertile ground for further study using Makani’s released code-base [1].

Recall, we pointed out a few paragraphs above that the choice of rotors can have a marked effect on flight stability at high speed: The same pitch at all stations is very bad for yaw and pitch stability at high kite speeds, because the dropoff in rotor efficiency (*i.e.* the onset of

<sup>31</sup> One could, of course, also use an optimization code.

significant mach drag) occurs at a local airspeed dependent on the pitch. Intriguingly, it seems quite possible that such instabilities were one reason we could not run the MX2 in C-sim at high kite speeds—we had neither the time nor resources, nor indeed the optimization infrastructure, to choose distinct rotor pitches at each station.

As detailed in the article, “Airborne Wind Turbine Performance” [4], selecting rotors *specifically* for their increased drag at high airspeeds *may* offer a potential solution to the problem of overspeeding in high winds. If this avenue is to be pursued, then such rotors should be chosen so that their excess drag starts cutting in at a certain flight condition of the *entire craft*; and since they all have different  $v_{app}$  under this flight condition, this means all the rotors will be slightly different. Otherwise the craft will start to experience very large destabilizing pitch and yaw moments as some rotors reach their operating regions of excess drag, while others do not.

## 5.4 Flight controller

The article “The Makani Autopilot” [3] goes into significant detail on the design changes envisioned for the flight controller in the near- to mid-term.

For completeness’s sake, however, we would be remiss to not mention several novel approaches that were far-future ideas, well outside the scope of Makani’s core intent to develop a working prototype system. A note of warning: These ideas are at a very rudimentary stage of development, so none of this should be construed as a statement that they will work. I mention them only because they hint at the promise of greater simplicity and robustness.<sup>32</sup>

### 5.4.1 Pursue designs with passively stable orbits

Makani’s kites have always required aerodynamic control surfaces, and IMU and/or GPS, and a state estimator for operation. There is a growing body of literature (see, for example, [14, 15]) centered on designing the system so that the dynamics naturally converges to stable, periodic attractor orbits. And there is additional research on open-loop periodic control, in which a single periodic control input is applied “blindly” to the system, to excite it, and it converges to a stable orbit that depends on the structure of the control input. This is discussed, for example, in [16].

We had begun a project with Systems Technology Inc. to investigate the possibility of redesigning the stability derivatives of the Makani kite in such a way as to support this style of open-loop periodic control. We had some initial early successes: We achieved stable loop orbits with no control input, which were offset from ground level, but which still intersected the ground (*i.e.* would crash if the ground were present at  $z=0$ ). We also had a single-input, single-output controller that simply set the ailerons based on  $z$  height, and that was able to achieve stable orbits and remain aloft.

---

<sup>32</sup> These ideas and their discussion is my own; they do not carry the endorsements of any of Makani’s very excellent and experienced controls engineers.

Obviously neither of these is a complete solution by any stretch of the imagination. They are not provably robust to disturbances, the orbits are not high-quality for power generation, we were testing only at one wind speed, our system model was simplified from the entire CSIM model, etc., etc. However, this line of inquiry showed enough initial promise that I think it would be a grave mistake to start an energy kite project *de novo*, without first pursuing some understanding of what design features lead to passive stability.

#### 5.4.2 “Soft” path control

Another concept is what I would call “soft” path control. The existing controller is very much oriented toward precomputing what path and airspeed profile would be best for a nominal wind condition, and then trying to execute that path and airspeed profile as faithfully as possible. In Makani’s terminology, this is the “playbook.”

If unsteady aerodynamics are present, for example due to gusts and turbulence, the controller still tries to follow the path as faithfully as possible. This can lead to large control excursions with lots of high frequency content. It is not at all obvious that this is the best thing to do—in vernacular terms, trying to “ride through” gusts might be a better tactic than fighting them with all the control surfaces available. In the words of one of our excellent controls engineers, perhaps a “peaceful” flight path is better than a precise one. This could be advantageous from a loads standpoint, as well as perhaps for power generation.

Speaking of power generation, it is interesting to note that the power being generated *is not an input to the flight control*. This might seem a little strange, since the end-goal is power generation without crashing into the ground. Perhaps a control scheme that optimizes locally for power generation (for which only airspeed and aerodynamic angles are important), while having access to a limited amount of global state (such as gravity orientation and height above ground) might yield good results, while being considerably simpler. Again in vernacular terms, this might be described as flying mostly by “feel,” while taking care not to smack into the ground.

#### 5.4.3 Total energy approach to longitudinal control (TECS)

Longitudinal guidance of a powered, horizontal fixed wing aircraft requires simultaneous control of the elevator and throttle. In the early days of autopilots, there was typically an auto-throttle system and a separate auto-elevation hold system. A significant problem of these systems being separate was that the longitudinal flight dynamics include cross-coupling terms between the climb rate and acceleration, so neither the throttle nor the elevator is, by itself, a good regulator of longitudinal flight. A manual input to the elevator would cause a transient excursion in auto-throttle control, and vice versa.

A related drawback was that, while the elevator has a fast (and energetically efficient) response, the throttle has a slow response, and constant throttle up and throttle down autoregulation in

response to elevator excursions is wasteful, distracting, unintuitive, and caused more system wear than necessary.

To address these shortcomings and provide a unified longitudinal autopilot system, Lambregts [17] proposed a system nicknamed Total Energy Control System (TECS). The central idea is that the throttle affects the *total* energy of the system (the Hamiltonian), while the elevator does not. Conversely, the elevator controls the *flow* of energy between kinetic and potential (*i.e.* the time derivative of the Lagrangian), while not affecting the Hamiltonian. The TECS works by first computing the desired rate of change of the Hamiltonian and Lagrangian from primary guidance inputs (climb rate and acceleration along flight path), and then uses these commanded time derivatives as inputs to a conventional throttle controller and elevator controller, respectively.

This architecture allows the choice of a slow time response of the throttle system and a relatively fast response of the elevator system. Longitudinal dynamics are stabilized on a short time scale, while overall changes in desired guidance can be achieved with a slower throttle response. One could imagine that this approach might be similarly beneficial if applied to a kite.

#### 5.4.3.1 Longitudinal guidance of a crosswind energy kite

The case of an energy kite closely mirrors that of a fixed wing aircraft, with some notable exceptions:

1. The tether constrains the position of the kite relative to the earth frame. So, the derivative of the potential energy is no longer independent of position.
2. The wind (speed of the medium relative to the earth frame) is important to the analysis, since it is the wind, plus the tether constraint, that adds energy to the system.
3. Desired commands are not rate of climb and forward speed, but instead tether tension and forward speed. These can be scheduled from the average wind speed to optimize power performance of the system.

A notable *similarity* is that we wish to minimize throttling up and down too much, in the energy kite case, not only to minimize equipment wear, but more importantly to minimize “grid flicker” (voltage changes on the distribution grid due to rapidly changing power inputs).

We adapted the TECS principles to the kinematics and dynamics of a simple model of an energy kite: We call it the “kite on a cart” model. Our approach, in the Loyd (zeta limited) regime, is as follows: For a given long term average wind speed,  $\bar{v}_w$ , and the aerodynamic properties of the kite, it is simple to compute a Loyd optimum kite speed and the corresponding tension. These parameters are used to compute the desired potential energy,  $P_{cmd}$ , and the desired kinetic energy,  $K_{cmd}$ . These are used in sum and difference to compute the commanded Hamiltonian  $H_{cmd}$  and the commanded Lagrangian  $L_{cmd}$ . Finally, these are used as control inputs to a pair of PID controllers. The Hamiltonian controller controls the thrust (*i.e.* the power extraction via the rotors), and is designed to be slow, to minimize grid flicker. Conversely, the Lagrangian

controller controls the elevator, and is designed to be fast, and to regulate the tradeoff between tether tension and airspeed.

#### 5.4.3.2 The kite on a cart model

The simplified kite on a cart model is as follows: Everything is in the 2D  $xz$  plane. The base station is taken to be a massless, frictionless cart, riding freely along a line parallel to the  $x$  axis. The tether extends from the cart in the  $-z$  (up) direction to the kite. The cart is always directly below the kite. The tether is a massless, dragless spring of rest length  $L_0$ , acting at the kite's center of mass. The wind is in the  $-z$  (up) direction.

The kite has a throttle actuator that can apply thrust (positive) or power drag (negative) to the body in the  $x_b$  direction. It has an idealized main wing, with aerodynamic coefficients  $C_X(\alpha)$ ,  $C_Z(\alpha)$ , and  $C_M(\alpha)$ . And it has an elevator, with aerodynamic coefficient derivative  $C_{M\delta_e}$ .

#### 5.4.3.3 Energy of kite on a cart

We will use  $P$  for potential energy and  $K$  for kinetic energy (the standard physics terms are  $V$  and  $T$ , but these tend to get confused with velocity and thrust). The potential energy is the gravitational potential plus the spring energy. For simplicity, let us take the rest length of the tether to correspond with  $z = 0$ . Then:

$$P = -mgz + \frac{1}{2}kz^2$$

And of course,

$$K = \frac{1}{2}mv_k^2$$

Taking the sum and difference, we obtain:

$$\begin{aligned} H &= -mgz + \frac{1}{2}kz^2 + \frac{1}{2}mv_k^2 \\ L &= mgz - \frac{1}{2}kz^2 + \frac{1}{2}mv_k^2 \end{aligned}$$

It is convenient to rewrite these without the  $z$  coordinate, by writing  $z = -T/k$ :

$$\begin{aligned} H &= \frac{mg}{k}T + \frac{1}{2k}T^2 + \frac{1}{2}mv_k^2 \\ L &= -\frac{mg}{k}T - \frac{1}{2k}T^2 + \frac{1}{2}mv_k^2 \end{aligned}$$

And to rewrite them in terms of "specific" energy (per unit weight):

$$H_s = \frac{T}{k} + \frac{1}{2kW} T^2 + \frac{1}{2} v_k^2 / g$$

$$L_s = -\frac{T}{k} - \frac{1}{2kW} T^2 + \frac{1}{2} v_k^2 / g$$

Taking time derivatives:

$$\dot{H}_s = \dot{T}/k + \frac{1}{kW} T \dot{T} + v_k \dot{v}_k / g = v_k \left[ \left( \frac{T}{kW} + \frac{1}{k} \right) \frac{\dot{T}}{v_k} + \frac{\dot{v}_k}{g} \right]$$

$$\dot{L}_s = -\dot{T}/k - \frac{1}{kW} T \dot{T} + v_k \dot{v}_k / g = v_k \left[ - \left( \frac{T}{kW} + \frac{1}{k} \right) \frac{\dot{T}}{v_k} + \frac{\dot{v}_k}{g} \right]$$

$$\dot{H}_s = v_k \left[ \frac{T+W}{kW} \frac{\dot{T}}{v_k} + \frac{\dot{v}_k}{g} \right]$$

$$\dot{L}_s = v_k \left[ \frac{\dot{v}_k}{g} - \frac{T+W}{kW} \frac{\dot{T}}{v_k} \right]$$

#### 5.4.3.4 Controller Design

We've seen how, given the system's measured state, we can easily produce the Hamiltonian, the Lagrangian, and their respective time derivatives. The controller is easily constructed as a two stage system:

- A "guidance" stage consisting of a preprocessor that takes average wind speed and knowledge of the kite properties and produces a desired Hamiltonian and Lagrangian
- A "control" stage that manipulates the thrust to meet the Hamiltonian command, and the elevator to meet the Lagrangian command

These are constructed as follows:

##### 5.4.3.4.1 Guidance

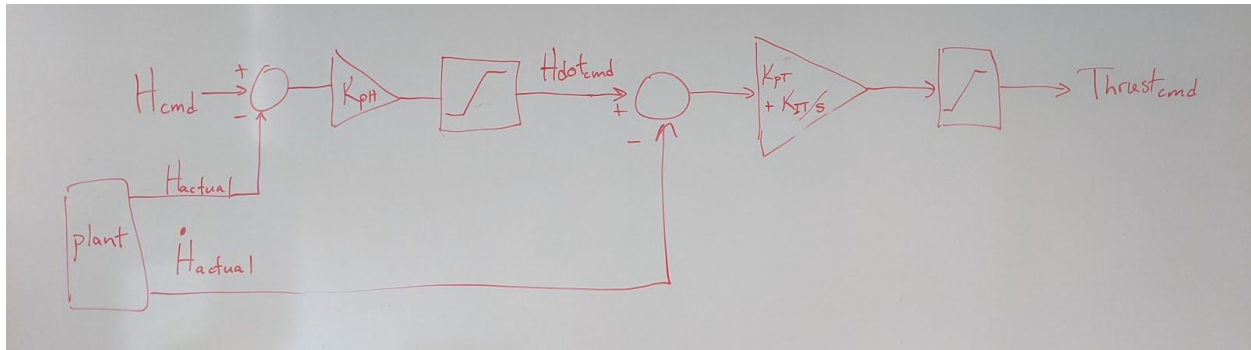
Recall, the central idea here was to produce smooth power performance in gusty wind conditions. To this end, we chose the following "guidance" scheme *in the Loyd regime*:<sup>33</sup>

- Given a smoothed, average wind speed  $\bar{v}_w$
- Given the kite aero parameter  $C_L/C_D$
- Given the tether spring constant  $k$
- Compute the Loyd optimal kite speed:  $v_k = \frac{2}{3} \frac{C_L}{C_D} \bar{v}_w$
- Compute the lift produced, as a proxy for the Loyd optimal tension:  $T \approx L = \frac{1}{2} \rho v_a^2 S C_L$
- Given the values for  $v_k$  and  $T$ , produce the kinetic energy  $K$  and the potential energy  $P$
- Finally, compute  $H_{cmd} = K + P$  and  $L_{cmd} = K - P$

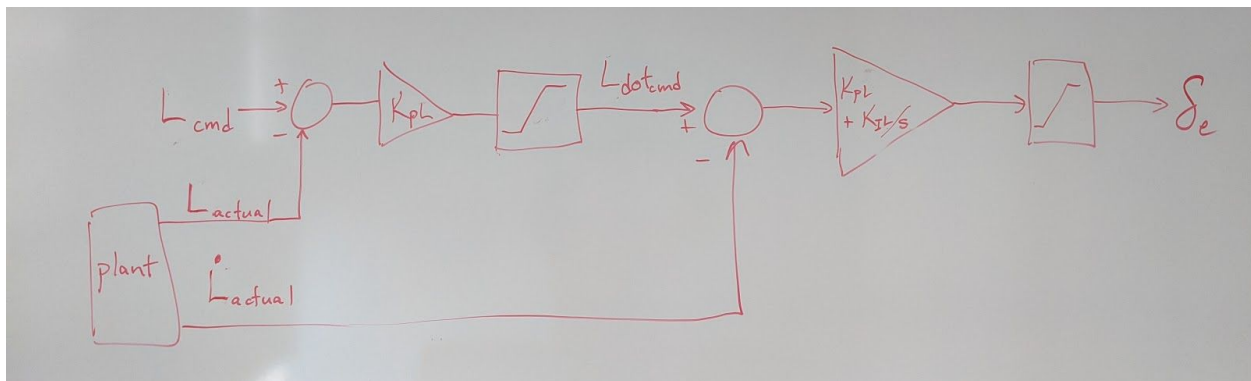
<sup>33</sup> A treatment for the tension limited regime has not yet been developed.

## 5.4.3.4.2 Control

A pair of side-by-side PID controllers is implemented, one for the thrust control and one for the elevator control. These are constructed as shown in figure 40:



**The Hamiltonian regulator (thrust controller)**



**The Lagrangian regulator (elevator controller)**

**Figure 40: Two PID controllers are constructed: one to control the thrust in order to regulate the Hamiltonian, and the other to control the elevator in order to regulate the Lagrangian.**

The gains  $K_{pH}$ ,  $K_{pT}$ ,  $K_{iT}$  are chosen to produce slow regulation of the Hamiltonian (say, on the order of 100 seconds). The gains  $K_{pL}$ ,  $K_{p\delta_e}$ ,  $K_{i\delta_e}$  are chosen to trade off tether tension with airspeed on a faster time scale. The effective bandwidth of the Lagrangian and elevator controller should probably be limited to below the first tether “plunge” mode (about 1Hz for the M600).

## 5.4.3.7 Performance

We implemented a prototype in Simulink. Although our first cut at numerical simulation used a pretty random guess at gains, performance was surprisingly good. We used an idealized M600, with the parameters given in table 4. We chose the controller gains (not carefully at all) for a very slow throttle response and fast elevator response.

Parameter	Value	Units
$m$	1500	kg
$C_L/C_D$	20	
$C_L$	3	
$S$	33	m <sup>2</sup>
$k$	50000	N/m
$v_w$	5	m/s

**Table 4: Kite parameters used for TECS control of the simple kite on a cart model.**

We ran the simulator for 200 seconds to establish a stable regulation state, and then turned on a Dryden turbulence model. The total energy of the kite remained quite stable, while the elevator started twitching around to adjust tether tension and regulate airspeed.

This approach appears to offer hope for smoother power control of an energy kite, with far simpler controller architecture. The hope is that we can smooth the power delivery, while improving the response of the airspeed to gusts. There are of course many problems to work out, not the least of which is generalizing the kite on a cart model to a full 3D model. It is also unclear how to deal with tension-limited operation. Consider, though, that tension limited operation is an unsolved problem anyway, so approaching longitudinal control using TECS might offer insight not easily available with Makani's "classical" approach. It remains to be seen.

## 5.5 Detailed structural design

Makani was wound down before we had a complete, detailed aerostructural design for the MX2. Briefly in outline form, the main issues to be considered in any complete design include, at minimum:

- Main wing:
  - The load cases should be defined as nominal, plus loop-cyclic variations
  - Significant loads include:
    - Tether tension and departure angle
    - Centripetal acceleration
    - Tail moments transferred to the wing through the fuselage attachment point

- Dynamic loads
- Pylons:
  - Centripetal loading introduces significant bending and (because the powertrains are forward of the aerostrut) twisting loads on the pylons
  - Stiffness should be so as to avoid whirl-flutter modes at expected flight speeds
  - The motor mounts and bearings experience *significant* structural loads not only from thrust, but also
    - Lateral due to centripetal acceleration
    - Lateral due to pylon vibration and twist
    - Lateral and overhung moment due to off-axis inflow
      - Requires a sophisticated higher dimensional propeller analysis that takes lateral inflow into account and produces not only thrust, but overhung moment as outputs
    - Overhung moment due to gyroscopic precession from body angular rates
    - Overhung moment due to gyroscopic precession from vibrational angular rates
- Fuselage
  - Must be stiffness-sized to avoid aeroelastic flutter
  - Must be strength-sized, along with its fuselage attachment points, to safely deliver sufficient pitch and yaw control moments to the wing
- Empennage
  - Since the craft is not restricted to land on a runway by means of landing gear, it is possible to consider “low tail” configurations
  - A “low tee” configuration may have a favorable influence on the dihedral derivative  $C_{l\beta}$ , so should not be ruled out
- Bridle
  - Sizing and placement is discussed in the part II article, “Tether Attachment and Bridle Knot Trim Considerations for Energy Kites” [8]
  - Structure may wish to employ a rigid wishbone design, for lower drag and lower mass
  - Bridle might also be useful for docking and perching, as described above

## 6 Conclusions

In this article, we have described Makani's best-so-far approach to designing an energy kite of the onboard generation class. We started with a summary of the basis-of-design procedure, centered around the Force Balance Loop (FBL) optimizer.

It cannot be overstressed how important this tool is to evaluating designs: It embodies *nearly* everything that is difficult and novel about energy kite design, as compared with airplane design. It models the additional tether forces and moments needing to be trimmed, the control effort associated with constant and repetitive aerobatic flight, and the extraction of aerodynamic power via the rotors. Working with this tool has given us a greater understanding of the fundamentals of energy kite design, and allowed us to define a detailed basis-of-design procedure that opens the door, at least in theory, to high performance designs of the future.

We then started to discuss the detailed design phase. This discussion is far from complete. We were in the process of developing deeper understanding of several existential problems (*not* modeled by the FBL tool) when the Makani project was shut down. Among these problems:

- The process for detailed design of rotor diameters and pitch profiles, including the possibility of employing different rotors at different station positions, was not yet thoroughly defined nor implemented.
- The physical insight and modeling capability necessary to make good choices for pylon and rotor placement was somewhat developed, at least for hover. But the crosswind generation case was not yet thoroughly understood.
- The problem of understanding and accurately modeling roll disturbances in hover was partially understood and developed. But the subsequent problem of how to manage such disturbances so as to guarantee control and stability, was not yet even close to being solved.
- A docking and perching strategy had not yet been finalized, nor simulated or validated in any detail.
- Our flight control software had not yet been well-tuned to start investigating the limits of the performance envelope of our emerging design.
- Although we had developed much more understanding of the dynamics and stability of tethered flight, we had not yet fully validated our analytic stability model. Nor had we yet been able to succinctly formulate conditions on the stability derivatives that would guarantee stable and controllable flight, while allowing for the aerobatic performance needed.

Lastly, we presented the state of our best-so-far understanding of these unresolved issues, hopefully with hints on how to move forward.

We began this article by observing that “energy kites are not airplanes.” Hopefully it is obvious by this point, in exactly how many ways this is true, and what complexities lie ahead.

It is our sincere wish that other brilliant and enthusiastic energy kite pioneers might find something of value in this report, and that its publication contributes in a significant way to the long term viability of the airborne wind energy field.

## **Acknowledgements**

*I cannot claim this article as my own; it is merely a summary and synthesis of the thinking of all those who actually did the hard work. Were it not for their skill and effort, this would not have been possible. I hope I have done them, and their work, some justice.*

*I would like to give personal thanks to everyone at Makani, especially the Oktoberkite / MX2 team, the Controls team, the Avionics and Power team, the Build and Validation team, and the Testing team. So many of you have taught me so many things during the past few years. It is truly an honor to have worked alongside you all. For that I am forever grateful.*

—Geo Homsy

## 7 References

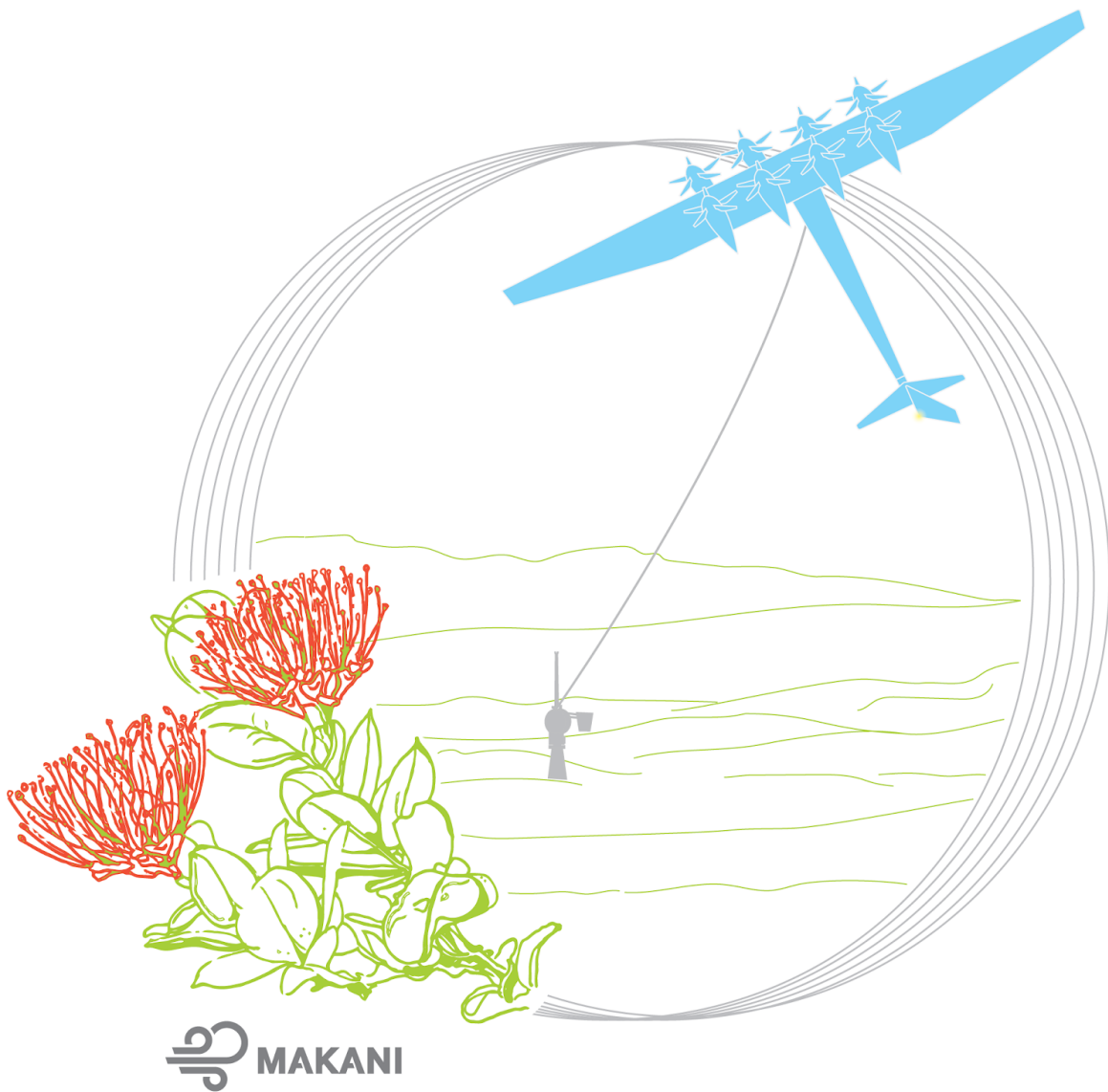
1. *Makani Code Release*, Makani Technologies LLC, 2020. [Online]. Available: <https://github.com/google/makani/>
2. M. L. Loyd, "Crosswind Kite Power," *J. of Energy*, vol. 4, no. 3, May-Jun 1980, Art. no. 80-4075, doi: <https://doi.org/10.2514/3.48021>
3. T. Fricke, "The Makani Autopilot," in *The Energy Kite: Selected Results From the Design, Development and Testing of Makani's Airborne Wind Turbines, Part I*, Makani Technologies, Alameda, CA, USA, 2020, [Online]. Available: <https://x.company/projects/makani>
4. N. Tucker, "Airborne Wind Turbine Performance," in *The Energy Kite: Selected Results From the Design, Development and Testing of Makani's Airborne Wind Turbines, Part I*, Makani Technologies, Alameda, CA, USA, 2020, [Online]. Available: <https://x.company/projects/makani>
5. P. Echeverri, T. Fricke, G. Homsy, and N. Tucker, "M600 Energy Kite Description," in *The Energy Kite: Selected Results From the Design, Development and Testing of Makani's Airborne Wind Turbines, Part I*, Makani Technologies, Alameda, CA, USA, 2020, [Online]. Available: <https://x.company/projects/makani>
6. P. Echeverri, "Makani's Flight Testing Approach," in *The Energy Kite: Selected Results From the Design, Development and Testing of Makani's Airborne Wind Turbines, Part I*, Makani Technologies, Alameda, CA, USA, 2020, [Online]. Available: <https://x.company/projects/makani>
7. J. Sicard, "Effect of Design Parameters on the M600 Stability in Crosswind," in *The Energy Kite: Selected Results From the Design, Development and Testing of Makani's Airborne Wind Turbines, Part II*, Makani Technologies, Alameda, CA, USA, 2020, [Online]. Available: <https://x.company/projects/makani>
8. G. Homsy, T. S. Orr, and N. Tucker, "Tether Attachment and Bridle Knot Trim Considerations for Energy Kites," 2019, in *The Energy Kite: Selected Results From the Design, Development and Testing of Makani's Airborne Wind Turbines, Part II*, Makani Technologies, Alameda, CA, USA, 2020, [Online]. Available: <https://x.company/projects/makani>
9. J. Sicard, G. Homsy, and M. Abraham, "Kite Stability in Crosswind Flight," in *The Energy Kite: Selected Results From the Design, Development and Testing of Makani's Airborne Wind Turbines, Part II*, Makani Technologies, Alameda, CA, USA, 2020, [Online]. Available: <https://x.company/projects/makani>
10. "Airfoil Design for the October Kite: Feasibility Studies," TLG, in *The Energy Kite: Selected Results From the Design, Development and Testing of Makani's Airborne Wind Turbines, Part II*, Makani Technologies, Alameda, CA, USA, 2020, [Online]. Available: <https://x.company/projects/makani>
11. K. Hallamasek, "Root Cause Analysis and Corrective Actions for FCW-01," in *The Energy Kite: Selected Results From the Design, Development and Testing of Makani's Airborne*

- Wind Turbines*, Part III, Makani Technologies, Alameda, CA, USA, 2020, [Online]. Available: <https://x.company/projects/makani>
12. Makani Oktoberkite Team, "Dimensionalizing and Sizing of Control Surfaces for Stability and Authority," 2019, in *The Energy Kite: Selected Results From the Design, Development and Testing of Makani's Airborne Wind Turbines*, Part II, Makani Technologies, Alameda, CA, USA, 2020, [Online]. Available: <https://x.company/projects/makani>
  13. F. Kapsenberg, "The Spreadsheet Kite Structure Sizer," in *The Energy Kite: Selected Results From the Design, Development and Testing of Makani's Airborne Wind Turbines*, Part II, Makani Technologies, Alameda, CA, USA, 2020, [Online]. Available: <https://x.company/projects/makani>
  14. A. P. Rodríguez, G. Sanchez-Arriaga, and M. S. Rivo, "Modeling and Stability Analysis of Tethered Kites at High Altitudes," *J. of Guid., Control, and Dyn.*, vol. 40, no. 8, 2017, doi: <https://doi.org/10.2514/1.G002550>
  15. L. S. Losantos and G. Sanchez-Arriaga, "Flight Dynamics and Stability of Kites in Steady and Unsteady Wind Conditions," *J. of Aircr.*, vol. 52, no. 2, 2015, doi: <https://doi.org/10.2514/1.C032825>
  16. G. Sanchez-Arriaga, A. P. Rodríguez, M. S. Rivo, and R. Schmehl, "A Lagrangian Flight Simulator for Airborne Wind Energy Systems," *Appl. Math. Model.*, vol. 69, 2019, doi: <https://doi.org/10.1016/j.apm.2018.12.016>
  17. A. A. Lambregts, "Functional Integration of Vertical Flight Path and Speed Control Using Energy Principles," presented at the First Annual NASA Aircraft Controls Workshop, NASA Langley Research Center, Hampton VA, USA, Oct. 25-27, 1983. Accessed: July 7, 2020. [Online]. Available: <https://ntrs.nasa.gov/archive/nasa/casi.ntrs.nasa.gov/19840012520.pdf>
  18. "Big M600 Tail Sizing White Paper," TLG, in *The Energy Kite: Selected Results From the Design, Development and Testing of Makani's Airborne Wind Turbines*, Part II, Makani Technologies, Alameda, CA, USA, 2020, [Online]. Available: <https://x.company/projects/makani>



# Airborne Wind Turbine Performance

Key Lessons From More Than a Decade of Flying Kites



Nicholas Tucker



Airborne Wind Performance: Key Lessons From More Than a Decade of Flying Kites  
Corresponding author: Nicholas Tucker, [nicholas.o.tucker@gmail.com](mailto:nicholas.o.tucker@gmail.com)

The Energy Kite: Selected Results from the Design, Development,  
and Testing of Makani's Airborne Wind Turbines, Part I of III  
by Paula Echeverri, Tobin Fricke, Geo Homsy, Nicholas Tucker,  
on behalf of the Makani team.

Copyright © 2020 by Makani Technologies LLC

Distributed under the [Creative Commons CC BY 4.0 License](https://creativecommons.org/licenses/by/4.0/). You are free to  
copy and redistribute this material in any medium or format for any purpose,  
even commercially.



Intended for electronic publication and distribution. Copies of this volume may be found at  
<https://archive.org>  
Additional information is at: <https://x.company/projects/makani>

Published September 2020

<b>1 Introduction</b>	<b>93</b>
1.1 Executive Summary	93
1.2 Example Systems	95
1.3 Numerical Model	95
<b>2 A Measure of Performance</b>	<b>97</b>
<b>3 Balance of System</b>	<b>99</b>
<b>4 Maintenance</b>	<b>107</b>
<b>5 System Cost</b>	<b>113</b>
<b>6 Kite Power</b>	<b>114</b>
6.1 Loyd Revisited	116
6.1.1 Tether Drag Losses	119
6.1.2 Path Offset Losses	121
6.1.3 Wind Shear Gains	123
6.1.4 Turning Losses	124
6.1.5 Efficiency Losses	130
6.1.6 Gravity Losses	131
6.1.7 Minimum Airspeed Losses	140
6.1.8 Tension Limiting Losses	140
6.1.9 Putting It Together	142
6.2 Lessons from Loyd Revisited	149
6.2.1 Minimum Turning Radius Constraints	149
6.2.2 The Push for Tighter Loops	154
6.2.3 Higher Power from Stronger Winds at Altitude?	156
6.2.4 Comparing AWT with HAWT Power Production	158
6.3 Conclusion	166
6.4 A Numerical Take on Path Shape	167
<b>7 Mass</b>	<b>171</b>
7.1 Hover	171
7.2 No Wind Upstroke	174
7.3 Mass in Crosswind	174
<b>8 Multi-kites</b>	<b>177</b>
<b>9 M600 Power Performance</b>	<b>182</b>
<b>10 High Winds Are Hard</b>	<b>185</b>
10.1 Overview	185

10.2 The Challenge	185
10.3 Strategies	188
10.3.1 Reducing lift	188
10.3.2 Non-optimal speed	190
10.3.3 Path	193
10.3.4 Excess Drag	199
10.3.5 Piecing Together a Strategy	201
10.3.5.1 Path Strategy	202
10.3.5.2 Lift and Speed Strategy	203
10.3.5.3 Rotor Strategy	207
10.3.6 Poking holes in our strategy	209
10.3.6.1 Turbulence	211
10.3.6.2 Control Variability	212
10.3.6.3 Tether Dynamics	213
10.3.6.4 All the Rotors	214
10.3.6.5 Kite Acrobatics	215
10.4 Power Saturation Summary	216
<b>11 References</b>	<b>220</b>
<b>12 Appendix</b>	<b>221</b>
12.1 Numerical Model Description	221
12.1.1 Overview	221
12.1.2 Sub-Models	222
12.1.2.1 Rotor Model	223
12.1.2.2 Aero Model	224
12.1.3 Known Shortcomings	224

# 1 Introduction

The goal of this document is to highlight several fundamental challenges for airborne wind energy that Makani has learned, in particular those that are perhaps under-represented in the field. The M600 (Makani's prototype that was tested from 2015-2019) was unable to meet its intended performance targets. While we will touch upon the specific issues of that design, the intent here is to discuss the challenges of energy kite performance more broadly, building up an understanding rather than a specific set of fixes. Where possible, we'll build an analytical foundation to frame the discussion, but building a complete mathematical toolset to design or evaluate an energy kite is not the explicit goal. As such, we presume the reader is somewhat familiar with the fundamentals of wind energy, and can pick up where the provided analytical tools stop short.

In the released design summary for the proposed next-generation system called MX2, Makani has sketched a system with some surprising characteristics: a short tether, a tall tower, and a comparatively low-performance-per-wing-area kite that's designed to fly tight paths as low as possible. Many, but not all, of the changes are driven by the general considerations we'll discuss here.

In addition, although Makani spent several of its early years designing, building, and testing several different types of energy kites, most of our collective experience is focused on onboard generation rigid wing kites. Many of the lessons here apply equally to soft fabric kites or systems with generation on the ground, but several do not. Rather than delve outside Makani's (and in particular this author's) area of expertise, we'll keep things centered on onboard generation designs.

Finally, this work is attempting to collect, condense, revise, and expand upon the efforts of dozens of individuals spanning many years. It's hoped that this author has represented their work appropriately.

## 1.1 Executive Summary

In order for any energy source to gain substantial market share, the cost of energy over the life of the system must be competitive. Renewables such as wind and solar have the added challenge that turning on your microwave doesn't tell the sun to shine brighter or the wind to blow harder, creating a mismatch between energy supply and demand. They then need to be even less costly in order to justify excess capacity that is only used when demand is highest, or potentially require additional infrastructure costs for energy storage. With the cost of energy as our guiding metric, we'll discuss the key challenges airborne wind energy faces.

These challenges can be summarized as follows:

1. Supporting infrastructure in a wind turbine plant is a large portion of the total cost of energy, especially offshore, and the primary way to reduce these costs is to increase the system size.
  - a. Airborne wind energy has some inherent infrastructure cost advantages compared to traditional wind turbines, particularly in deep water offshore applications, but required components and their share of the total cost of energy do not substantially differ.
2. Despite several similarities between airborne wind turbines and aircraft, maintenance costs need to be approximately an order of magnitude less than similarly priced aircraft in order for airborne wind turbines to remain viable.
  - a. It's not appropriate to directly apply the maintenance costs from traditional wind turbines to airborne wind turbines, as much of the improvement in the industry is the result of increased scale and reduced number of components for a given plant size, properties that airborne wind energy also needs to pursue.
  - b. Small systems will struggle to have maintenance costs per unit power as low as larger systems, regardless of their perceived simplicity, due to the additional number of components.
3. Reducing turbine costs cannot be the primary avenue for long term success, given that turbine costs form less than half of the total cost of energy for a plant, and about a quarter of total costs offshore. Turbine costs can lose the battle for a competitive cost of energy, but it's exceedingly difficult to win the battle on turbine costs alone.
  - a. It is more important for airborne wind energy to demonstrate a path to grow system scale than reduce turbine costs, as comparatively minor reductions in infrastructure and maintenance costs, as a result of larger scale, can easily outweigh aggressive turbine cost reductions.
4. Kites are largely free from the power limits imposed by the fixed swept area of the blades on a traditional wind turbine, but these gains are offset by the introduction of new loss mechanisms.
  - a. Path offset losses, tether drag, and powertrain efficiency/cycle-time are among the largest, typically reducing power to a third of the theoretical maximum of the kite alone.
  - b. A small minimum turning radius and reliable operation close to that limit is essential to reduce gravity pumping losses and path offset losses.
  - c. The specifics of path shape are relatively unimportant even in theory, and even less relevant in practice. Paths must generally be as low and as tight as practical, but otherwise, simpler is better.
  - d. Typical losses negate any gains from accessing stronger high altitude winds unless tether drag is exceptionally low and wind shear is very high.
  - e. Kite specific losses are on a similar scale as the induced flow losses for a typical 3 bladed traditional wind turbine, effectively trading one set of losses for another.
5. Mass is a key design constraint, especially for hovering systems featuring onboard generation.

- a. Power generation is strongly tied to wing area and weakly tied to mass, so the target for an optimal design is to get the largest wing possible into crosswind.
6. Multiple kites on a single ground station or a single shared tether have some clear benefits, but those benefits are only accessible after solving many novel control challenges, presenting a difficult development story.
  - a. Multi-kites begin to see induced losses similar to traditional wind turbines, somewhat degrading their benefits.
  - b. Simpler configurations of multi-kites may be worthwhile to pursue once a reliable single kite product is well developed and tested.
7. High winds pose a number of unsolved challenges, and these challenges only present themselves in the context of imperfect control and a turbulent wind field.
  - a. The main mechanism to limit power for traditional turbines, reducing lift, is difficult to implement for kites as they also use lift to turn.
  - b. Energy kites experience large swings in potential energy over their path, complicating other strategies as they must heavily reduce power for part of the path, and maximize it for the rest.
  - c. In order to ensure the system can maintain adequate margins, necessary because of the limitations mentioned above, it's likely that the power components cannot be fully saturated at high wind speeds.
  - d. The nature of the problem makes it difficult to evaluate outside the context of detailed flight simulation or physical flight tests.

Our hope is that by pointing out these potholes, others can then fill or avoid them. So, get ready for a bumpy ride, as we're aiming for a lot of potholes—there is much to discuss!

## 1.2 Example Systems

Throughout this text, we'll be pulling example values from several systems to demonstrate various effects. The key values for those systems are outlined in table 1.<sup>1</sup>

## 1.3 Numerical Model

Throughout this text we'll occasionally rely on results from a numerical model whose source code has been released [1]. This model is commonly referred to as the FBL at Makani. In most cases here, we lean on it to simply provide a numerical justification for a simplifying analytical assumption, but we'll also dive into a particular set of optimized results for a complete system in section 10, High Winds Are Hard. It's not the goal of this paper to describe that model in detail, but there is a brief description in the appendix of this section.

---

<sup>1</sup> All values are approximate. These systems all had various configurations that evolved over time.

Parameter	Units	Description	M600 Intent	M600 As-Built	MX2
-	-	-	Original design intent.	Prototype M600. Includes test equipment.	Oktoberkite next gen design.
$l_t$	m	tether length	400 <sup>2</sup>	440 <sup>2,3</sup>	300
$S$	m <sup>2</sup>	wing area	32.9	32.9	54
$b$	m	wing span	25.7	25.7	26
$C_L @ \zeta_L$	-	lift coefficient @ best performance	2.8	2.56	1.81
$C_{D_k} @ \zeta_L$	-	kite drag coefficient @ best power	0.207	0.244 <sup>3</sup>	0.123
$d_t$	m	tether diameter	0.025	0.0295 <sup>3</sup>	0.0295
$C_{D_t}$	-	tether drag coefficient	0.7	0.7 <sup>3</sup>	0.7
$C_D @ \zeta_L$	-	kite + tether drag coefficient @ best power	0.260	0.312 <sup>3</sup>	0.152
$\zeta_0$	-	performance metric, best, kite only	76	42	58
$\zeta_L$	-	performance metric, best, kite + tether	48	26	38
$A_{rotor}$	m <sup>2</sup>	rotor area	3.8	4.15 <sup>3</sup>	4.38
$N_{rotors}$	-	number of rotors	8	8	8
$r_{loop_{min}}$	m	minimum viable path radius	75	145 <sup>3</sup>	90
$h_{min}$	m	minimum kite altitude	85	110 <sup>3</sup>	70
$h_{tower}$	m	tether attachment height	15	5 <sup>3</sup>	15
$m_{kite}$	kg	kite mass	1310	1690 <sup>3</sup>	1850
$m_{tether}$	kg	tether mass	315	390	275
$\eta_{t2g}$	-	efficiency, thrust to grid	0.66	0.66	0.66
$v_{d_{min}}$	m/s	minimum viable airspeed	30	35	27
$F_{T_{max}}$	kN	maximum operating tension	280	240 <sup>3</sup>	250

**Table 1: Various approximate values for Makani systems we'll be using in analytical examples.**

<sup>2</sup> Includes bridle radial length.

<sup>3</sup> Varied for different tests, but the value represents the bulk of the flight test data.

## 2 A Measure of Performance

How do we best describe the performance of a source of energy? What are the key metrics? Ultimately, the goal of any source of energy, wind turbines included, is to provide energy that is needed at a competitive cost, and the metric of greatest importance here is the Levelized Cost of Energy, or LCOE.

Given that energy systems generally have high upfront costs and long lifetimes, the “levelized” portion of LCOE refers to assessing the lifetime impact of all costs and distilling it down to an average cost in today’s dollars. Included in this levelizing are items such as the cost of capital, the developer’s desired return on investment, taxes, and inflation.

LCOE is not the *only* metric that matters—a system that can better match demand by providing energy when needed, or one that can provide a consistent reliable base power, has more value than one that provides huge amounts of energy only when it’s windy—but for simplicity’s sake, let’s leave it as the main metric when comparing the performance of different energy systems. With renewables only providing ~6% of the world’s energy at the time of this writing,<sup>4</sup> this is especially true outside of a few markets where renewable penetration is large. In those increasingly saturated markets, the need for the energy system to match demand becomes of greater importance, and we see turbines value other metrics like capacity factor, which is a measure of the average power the turbine makes relative to its maximum rated power.

There are many ways to calculate lifetime costs, but as the focus here is on the energy system and not the underlying economics or financing, we utilize the simple method outlined by NREL in “Manual for the Economic Evaluation of Energy Efficiency and Renewable Energy Technologies” [3], which boils these factors down into a single factor called the Fixed Charge Rate, or  $k_{FCR}$ , which represents the yearly amortization rate of the total upfront costs.

From here, we can state that:

$$LCOE = \frac{C_{capex} k_{FCR} + C_{opex_l}}{AEP} \quad [1]$$

Where  $C_{capex}$  is the sum of the capital expenditures,  $k_{FCR}$  is the fixed charge rate,  $C_{opex_l}$  is the *levelized* annual operating expenses (note that the  $l$  subscript denotes this is a levelized value), and  $AEP$  is the Annual Energy Production of the power system.

The methodology in determining  $k_{FCR}$  will not be laid out here (see the reference) to avoid getting sidetracked by project economics that have little to do with turbine design, but we

---

<sup>4</sup> As of 2020. Not counting hydroelectric. IEA Global Energy Review 2020 [2].

should note that for risk levels associated with mature onshore systems in well developed markets and expected project life around 20 years, typical  $k_{FCR}$  values are around 0.1. Offshore markets, novel designs, or new markets will see higher rates as the projects carry more perceived risk, while publicly supported projects can see favorable financing and tax treatment and have very low  $k_{FCR}$  values.<sup>5</sup>

It is useful to break this apart further. Capital expenditures are commonly split between the cost of the turbine itself, which we'll call  $C_{sys}$ , and the cost of the roads, foundations, collection system, transformers and other systems that make up the rest of the plant. On a per system basis, these costs are called the Balance of System, or BoS, and on a plant basis they are called the Balance of Plant, or BoP. On the energy side of things,  $AEP$  can be broken down into the system rated power,  $P_{rated}$ , which is the maximum continuous power of the turbine system, typically in MW, capacity factor,  $k_{CF}$ , which is the average power normalized by the rated power, and  $t_{year}$ , which is a year in the units of choice, typically hours, so that the final result is in costs per MW·hr. We now have:

$$LCOE = \frac{(C_{sys} + C_{BoS}) k_{fcr} + C_{opexI}}{k_{CF} P_{rated} t_{year}} \quad [2]$$

LCOE is now written in such a way that we have the big drivers separated out, and each of these terms forms a key metric we will use to compare systems below. To reiterate, there's the cost of the system,  $C_{sys}$ , the cost of everything else,  $C_{BoS}$ , the cost to keep everything running,  $C_{opexI}$ , how effectively we're utilizing our maximum system performance,  $k_{CF}$ , and the final metric we can control: how large our system is,  $P_{rated}$ . Despite our best efforts, we're unable to control the length of a year.

In any comparison utilizing only one of these component metrics, one needs to keep in mind that it is just that: only one piece of the total picture. A comparison between components is only valid in the context of LCOE if the other components are similar. We should be wary of gaming these component metrics. As an example, downrating a power system with no change in costs results in a higher capacity factor, but this is offset by the lower system rating and corresponding loss in energy production for a net increase in LCOE.<sup>6</sup> With this in mind, we'll compare some of these inputs for AWTs with HAWTs. Let's begin our conversation on wind turbine performance by not talking about the turbine at all, and instead discuss all the other components.

<sup>5</sup> Financing and economics have a huge effect on LCOE. Favorable financing is often glossed over, or the benefits incorrectly attributed to energy system improvements. Much of the gains in wind turbine LCOE over the last few decades is from increased market confidence, which shows up as more favorable financing. The effect of financing also makes LCOE *market* specific in addition to *site* specific.

<sup>6</sup> A high capacity factor has value independent of LCOE, but can't be the singular goal. If this were the case, we'd see the large rotors from, for example, 2 MW HAWTs paired with small 500 kW power systems. Capacity factor would be high, but LCOE and total energy production would be poor, as the expensive rotors are underutilized. Heavily saturated markets where capacity factor is highly valued are trending this way, but this doesn't well represent new markets.

### 3 Balance of System

Of the many improvements made to traditional horizontal axis wind turbines (HAWTs) over decades, perhaps the most obvious is the ever increasing system size and power rating (illustrated in figure 1), which is expected to continue, especially offshore.

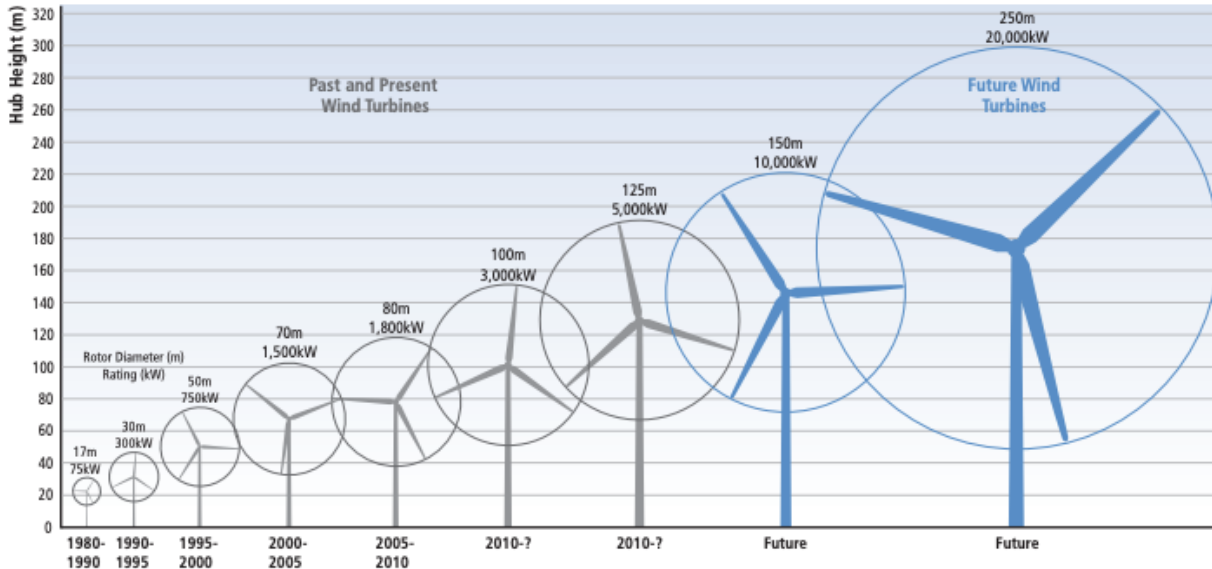


**Figure 1: HAWTs have grown dramatically over time, as shown in this 2011 diagram from the IPCC Special Report on Renewable Energy Sources and Climate Change Mitigation [4]. As of 2020, the largest HAWTs are ~15 MW, and are expected to continue to grow larger.**

With the additional constraint of needing the system to fly, airborne wind energy (AWE) systems face bigger difficulties increasing scale than HAWTs do. It's important to understand the pressures behind the growth of HAWTs and see how they may also apply to airborne wind turbines (AWTs). BoS is a surprisingly large portion of the total LCOE for wind energy systems and is indirectly responsible for much of this trend. What creates this trend? Why is one massive system better than several smaller systems if, when combined, they make the same total amount of power? To better understand, let's look at some examples of the importance of BoS costs, beginning with onshore HAWTs.

Numerous examples can be found in literature of breakdowns of these costs for HAWTs, such as the example in figure 2 from the NREL 2018 Cost of Wind Energy Review [5].

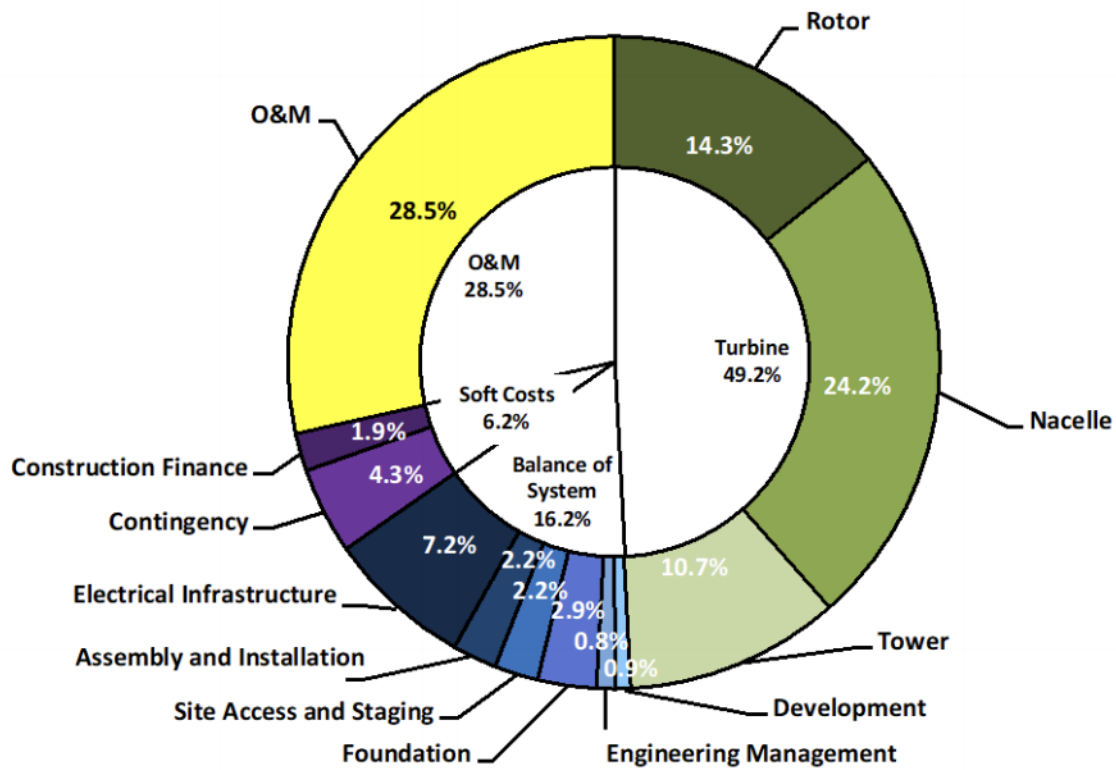


**Figure 2: Component-level LCOE contribution for the 2018 land-based wind reference project. Note: O&M represents operation and maintenance. Image is from NREL 2018 Cost of Wind Energy Review, [5, fig ES1].**

In this example, BoS and related soft costs (the purple and blue colors) are approximately 22% of the system LCOE for an onshore system.

Makani developed a bottom-up system cost, scaling, and performance model, and here we compare the total cost of energy breakdown in that model using a system similar to our MX2 next generation system under similar plant and site conditions as the NREL study.

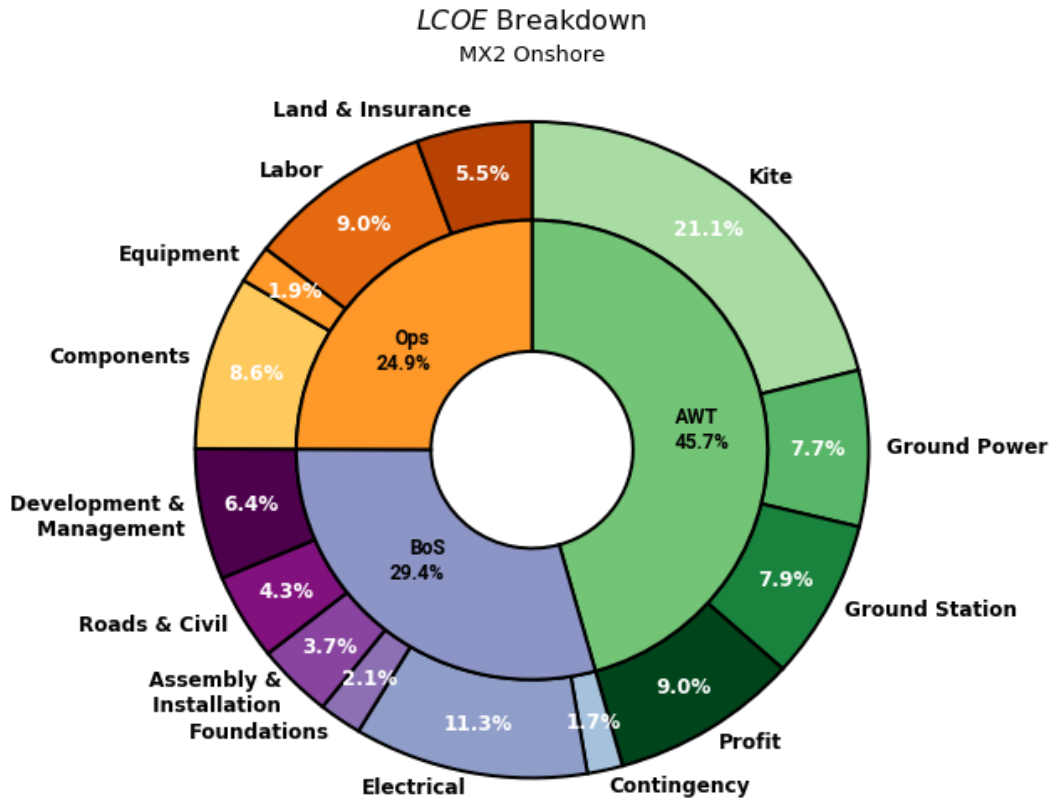


**Figure 3: LCOE breakdown for onshore, using a system similar to our MX2 system under similar plant and site conditions as the NREL study.**

Approximating the categories (and roughly the colors) from the NREL data, we find that AWTs have similar cost drivers. They aren't meaningfully different in components—collection systems still need to be placed, substations and connections still need to be made, and access routes to install and maintain systems must be in place. The commonality means BoS costs play a similarly large role for AWTs as they do for HAWTs.

How do BoS costs relate to system scale? NREL provides scaling models for BoS costs that reside in their System Advisor Model renewable energy cost tool [6], and we can compare the specific BoS cost-per-rated-watt from the NREL model with our internally developed BoS model.

Direct comparisons should be qualified—the models were developed independently and don't necessarily share identical underlying assumptions. However, best attempts were made to make similar inputs, and differences in output appear justified. Using these models, we can hold the total rated power of the plant constant and vary the system rated power, resulting in fewer systems in the plant as each individual system increases in size.

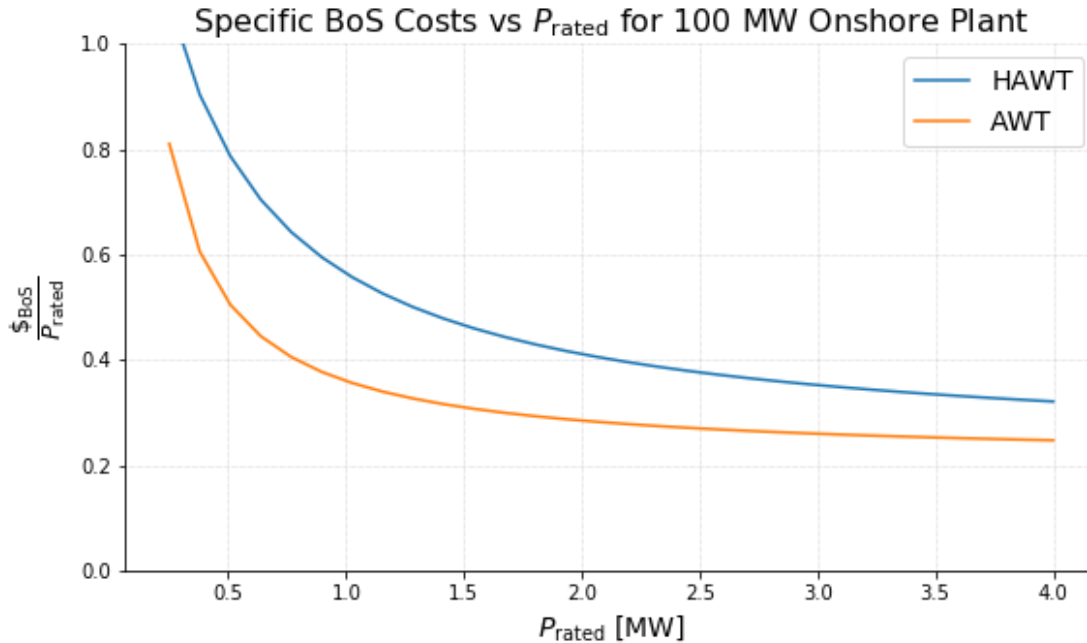


**Figure 4: Specific BoS Costs versus  $P_{rated}$  for 100 MW onshore plant.**

For a constant 100 MW onshore wind turbine project with typical siting, similar trends are present for both AWTs and HAWTs: BoS cost-per-rated-watt decreases with increasing system size. Larger systems are more cost effective than many small systems. Fewer systems mean fewer roads, fewer collection system trenches, fewer installations... In short, less of everything needed to install and support a wind turbine, which more than offsets the increased cost of the larger components and more involved installation process, driving the industry to larger and larger systems. We expect AWTs to have an advantage on specific BoS, requiring smaller access roads, foundations, towers, and crane pads on a per-rated-watt basis, and this appears to be the case.

Assuming that other system performance metrics are similar, AWTs appear to need to be at least  $> \sim 500$  kW to get down the steepest part of the curve and be competitive with the 2-4 MW onshore HAWT systems of today.

For offshore installations, we never created scaling models to fill out an entire curve, but we expect the shapes to be similar, just shifted substantially up and to the right, for both AWTs and HAWTs. This is easily explained by again pulling from the NREL case study, this time for offshore floating platforms:

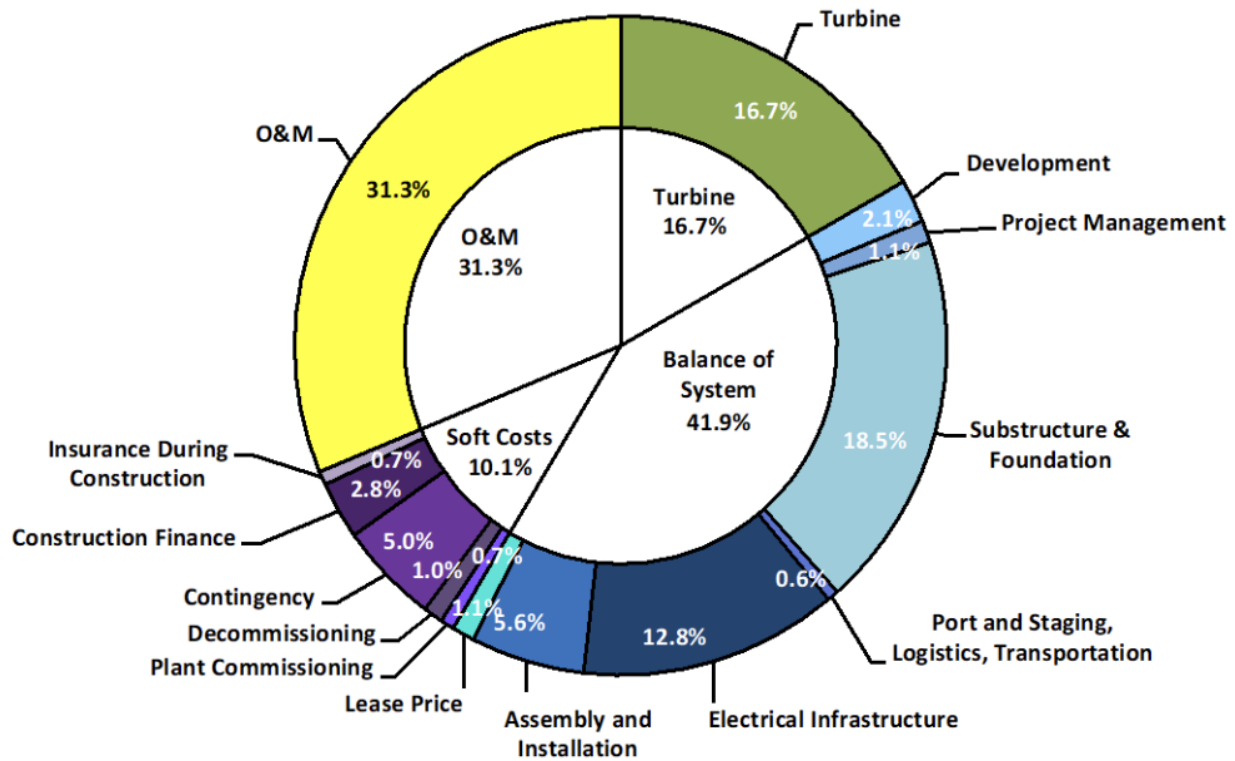


**Figure 5: Component-level LCOE contribution for the 2018 floating offshore wind reference project. Image is from NREL 2018 Cost of Wind Energy Review [5, fig ES3].**

The BoS and associated soft costs dominate the total cost of energy for offshore systems, at ~52% of the total. The turbine is just a small fraction of the cost of energy! Making electrical connections, running mooring lines, and making large floating platforms is expensive, quickly taking over and defining the problem. It becomes justifiable to spend more on the turbine on a cost-per-rated-watt basis to grow the system and push down relative BoS costs.

Again, it's important to highlight that for most costs here, AWTs do not substantially differ! For all categories except: Assembly and Installation, Port and Staging, Logistics, Transportation, and Substructure and Foundation, AWE expects to have similar (or higher) costs per rated power. These categories where AWE differs and can hope to see a benefit combine to just 20% of the total LCOE. AWE needs to claim a clear advantage in these areas to make a meaningful reduction in overall cost of energy.

Several rough case studies for offshore systems at Makani confirm similar cost breakdowns. Figure 6 shows the results for one such case study, again matching conditions to the NREL example as much as possible, using a system similar to the MX2:

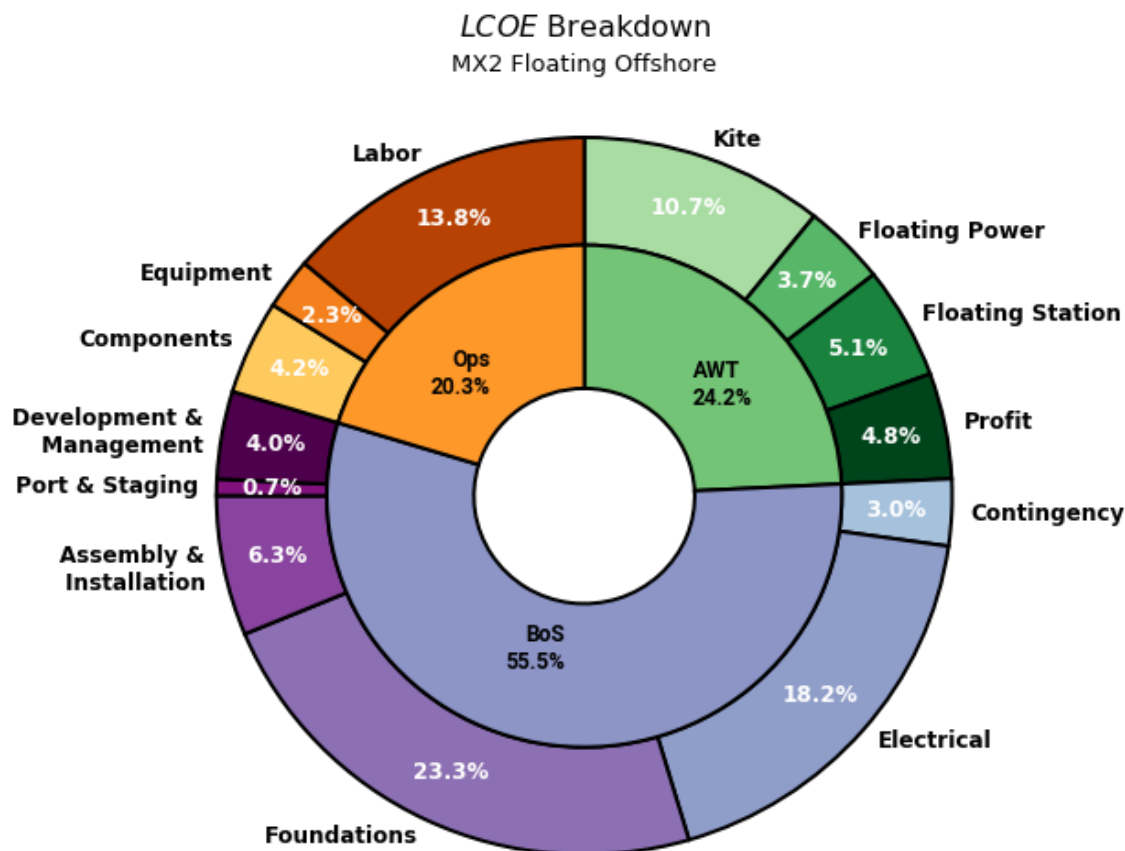


**Figure 6: LCOE breakdown for floating offshore, using a system similar to our MX2 system under similar plant and site conditions as the NREL study.<sup>7</sup>**

The turbine share of total costs for AWTs is smaller than for HAWTs—in this example, we’re using the same system as onshore. Larger offshore HAWTs generally pay a higher cost per rated power to reduce more BoS costs for an overall win. BoS is less dominant for onshore systems, so this tradeoff is less pronounced onshore—this is the main reason why offshore systems are larger than onshore systems today.<sup>8</sup> The optimum for offshore AWTs will follow the same trend—larger systems reduce dominating BoS costs—but using the same system in this comparison means we’re unable to capture this effect.

Maintenance for offshore AWTs was also modeled as a lower share of LCOE than HAWTs—there is certainly some benefit in being able to swap out a kite and perform turbine maintenance onshore—but confidence in matching the same conditions and assumptions, and in the predictive capabilities of the models, is lower. The key takeaway is simply that labor costs grow significantly offshore, taking up a larger portion of the operating costs. Maintenance costs

<sup>7</sup> “Floating Station” here refers to the equipment (winches, sensors, perch) on top of the floating foundation, not the foundation itself.

<sup>8</sup> Also, onshore systems typically have additional siting, transportation, and installation constraints, further pushing the trade-off to smaller systems than those offshore.

are rising (evident in the fact that operating costs offshore grow to be a similar component as the AWT, which is unchanged in cost), but the share of total LCOE is reduced as BoS becomes so dominant.

We expect AWTs to have an enduring advantage in platform cost-per-rated-watt over HAWTs in floating offshore applications, for three primary reasons:

1. AWTs have a lower overturning moment due to shorter towers.
2. AWTs have lower mass, centered at lower elevation above sea level.
3. AWTs can tolerate large platform motions.

The combined effect of these factors leads to smaller platforms that are less expensive to build and simpler to deploy.

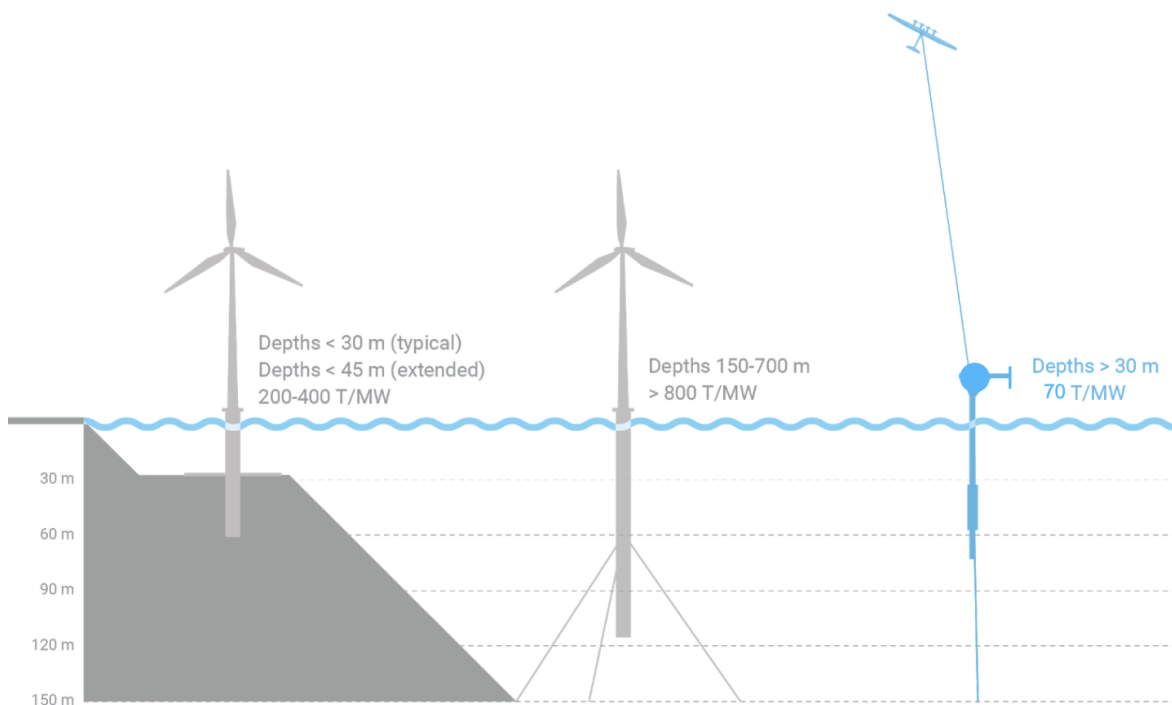


**Figure 7: Notional offshore platforms for fixed bottom (left) HAWTs, floating (center) HAWTs, and AWTs (right), with rough platform tonnage per rated watt.**

As shown in figure 7, Makani anticipated approximately an order of magnitude less foundation mass per unit power. This forms an enduring advantage for AWTs: even as system scale increases, the relative lack of an overturning moment will remain, keeping platforms small. Of course, this cost saving is primarily on the floating foundation itself. Installation costs per system go down as well, but, if systems are small, will need to be repeated for many systems. Electrical infrastructure follows this trend as well, but here AWTs have no initial advantage, requiring similar connections and installation processes.

Clearly, many touted AWE benefits are in danger of vanishing at smaller system sizes—AWT floating platforms and turbines may be able to reach a better cost-per-watt than HAWTs, but electrical infrastructure, installation, and maintenance costs grow with the increasing number of systems needed to meet a desired plant size, eating into those benefits.

In addition, many markets are increasingly space constrained—it doesn't appear in the LCOE metric, but when space to install turbines is limited, power per ground or sea area becomes important. As long as the LCOEs are competitive, a developer may choose a more power dense system to maximize total energy at the expense of a slighter higher cost of energy—the more power dense systems are typically also the higher rated systems.

AWTs can potentially meet renewable energy demand for small or semi-permanent installations in places where a large HAWT would be difficult to install, but in order to directly compete with HAWTs in the utility energy market and have a significant impact on overall renewable energy penetration, AWTs have significant incentive to be approximately 1 MW or larger.

## 4 Maintenance

Keeping the turbines operating via planned and unplanned maintenance is nearly the entirety of operating costs for turbines—land lease and insurance is typically a small component.

Cost of maintenance is difficult to model and predict—much of the existing literature on HAWTs relies on historical data and trends to predict performance of future systems. It's tempting to lean on this same HAWT historical data to form AWT predictions, but we need to at least understand the reasons for the trends for HAWTs and see how they can apply for AWE. We took two approaches—a broad, top-down comparison with the wind industry and aircraft, and a complex bottom-up approach, relying on extensive estimation of major component lifespans and repair or replacement costs. We'll describe some of the top-down comparisons here, and describe the key learnings from the bottom-up modeling we did.

We begin by setting an upper bound on maintenance costs with the naive assumption that maintenance is the only cost. If everything else was free, how much would maintenance need to cost to reach a desired LCOE target?

With  $C_{OM_n}$  as the cost in today's dollars in year  $n$ ,  $l_{sys}$  as the total system lifetime in years, and  $k_{WACC}$  as the real (inflation adjusted) weighted average cost of capital, the yearly levelized cost of operations and maintenance,  $C_{opex_l}$  is:

$$C_{opex_l} = \sum_{n=0}^{l_{sys}} \frac{C_{OM_n} (1 - k_{WACC})^n}{l_{sys}} \quad [3]$$

If we assume operations and maintenance costs per year to be constant in today's dollars, we can represent this as:

$$C_{opex_l} = C_{OM} k_{level} \quad [4]$$

where  $C_{OM}$  is the average annual operations and maintenance costs in today's dollars, and  $k_{level}$  is the levelizing factor, determined from the sum above to be:

$$k_{level} = \frac{k_{WACC}(1 - k_{WACC})^{l_{sys}} - (1 - k_{WACC})^{l_{sys}} + 1}{l_{sys} k_{WACC}} \quad [5]$$

We want to find some normalizing metric to compare with other vehicles, so let's define a new variable, the specific maintenance cost  $k_{OM}$ , which is the levelized cost to maintain a system per hour, scaled by system rating. If we define a specific system capital cost,  $k_{capex}$ , such that:

$$k_{capex} = \frac{C_{sys} + C_{BoS}}{P_{rated}} \quad [6]$$

we can then solve for the required system maintenance cost per hour in today's dollars,  $k_{OM}$ , in terms of LCOE and some system and economic characteristics:

$$k_{OM} = \frac{C_{OM}}{t_{year}} = \frac{P_{rated}}{k_{level}} \left( LCOE \cdot k_{CF} - \frac{k_{capex} \cdot k_{FCR}}{t_{year}} \right) \quad [7]$$

Now, for some examples. With a  $k_{WACC}$  of 6% and a 20 year project life,  $k_{level} = 0.61$ . Solving for  $k_{OM}$ , a 1 MW rated system with a 50% capacity factor at a competitive onshore LCOE of \$40/MWhr would require a maintenance cost of ~\$33/hr or less, even if the rest of the system were free!

Let's put these figures in context. In order to do so, we'll abandon any pretense of precision and pull out our biggest, broadest paintbrush.

We'll assume a  $k_{FCR}$  of 0.1 for this exercise, typical for projects with a 20 year life in well developed economies. AWTs, especially rigid wing onboard generation ones, share a lot in common with small aircraft, so to draw the comparison, we'll compare the cost of the system with the cost of maintenance for several types of flying vehicles. We'll draw lines to represent the required  $k_{capex}$  to meet a \$40/MWhr LCOE target.

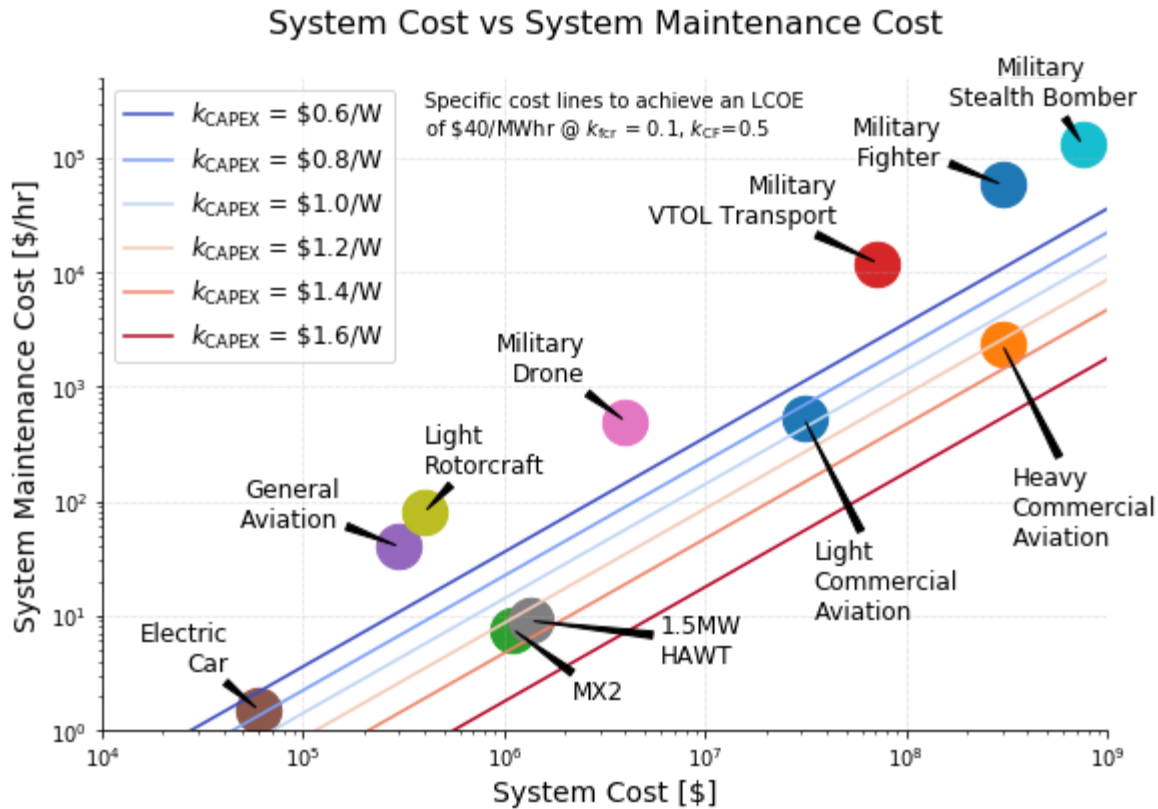


**Figure 8: System cost versus maintenance cost for various types of (mostly) flying vehicles.**

The resulting plot in figure 8 lays out the challenge clearly—wind turbines need maintenance cost per hour relative to system cost comparable to the absolute best aviation can muster with heavy commercial aviation passenger planes. As we move up and left and maintenance costs become a larger share, we need a lower cost-per-rated-watt (a lower  $k_{capex}$ ) to offset the increased maintenance costs.

Rather unsurprisingly, anything close to the relative maintenance costs of general aviation or military aircraft requires a specific system cost well below what the current wind industry is able to achieve, with current specific costs for the NREL onshore example system of ~1.4 \$/W (recall that we’ve lumped the cost of the turbine and the BoS in our definition—it’s not uncommon for *turbine only* specific costs to reach the required values).

Are maintenance costs an order of magnitude less than comparably priced aircraft a challenge? After all, the electric generators of AWTs are much simpler, and the reliability demands much lower, than the crewed gas turbine and piston powered aircraft we’re comparing them to. A simple bottom-up comparison was completed, pulling several sources of data to create a hodgepodge machine comparable to an AWT—the airframe-only maintenance expenses for a common general aviation aircraft, combined with estimated maintenance costs for two electric car powertrains.



**Figure 9: A conglomerate system resembling the complexity of an AWT—a simple airframe and several electric powertrain units.**

This rough estimate arrived at estimated hourly costs of ~\$14/hr, which, holding the rest of our assumptions from above, would require a  $k_{capex}$  of \$0.88/W to meet a competitive onshore LCOE target of \$40/MWhr. These rough approximations simply show that we need to pay attention, as unexpectedly high maintenance costs can quickly blow up the problem. Systems need to be as hands-off as possible!

With these considerations in mind, Makani also built a comprehensive bottom-up model, whose top level results are shared in the LCOE breakdowns from above. We won't be sharing this model, as it's complex, vaguely sourced, and highly specific to our designs, but it's worth distilling the results, which are more general in nature.

The model consists of infant mortality and mean time between failure (MTBF) estimates for each class of components, combined with estimated time to service and/or replace those components, and their scheduled maintenance frequency. Failures are classified by urgency—some will require an unscheduled trip to the turbine, while others can be addressed in the next scheduled maintenance. Technician time to get out to the system and access it for repairs is one of the largest sensitivities, and unfortunately, also carries one of the largest uncertainties. An example of some of the largest inputs to this general labor portion (ie, not the labor to replace a specific component) of the model for onshore systems is in table 2.

Despite relying on a large number of rough assumptions and estimates, the process of creating and using a maintenance model gave us several key lessons:

1. Larger systems reduce the total number of components in a given plant size, resulting in fewer trips, lower labor costs, and less kite downtime.
  - a. This is especially important for offshore systems, where time to access systems is large.
2. Offshore AWT systems should support easy kite swaps to enable heavy maintenance operations to occur onshore.
3. Maintenance costs are dominated by the power plants.
  - a. There are a large number of rotors, motors, motor controllers, and cooling systems to maintain.
  - b. Expected MTBFs for most powertrain components seem to necessitate ~6 month scheduled maintenance intervals, about twice that of HAWTs.

4. Onboard generation wind turbines will likely be more expensive to maintain than modern HAWTs on a cost per rated power basis.
  - a. Modeling uncertainty is large—it appears onboard generation wind turbines maintenance costs can be competitive, but a major cost reduction is unlikely.
  - b. Ground based power systems will have somewhat easier access, but face the same maintenance pressures to reduce the number of components and thus have the same incentive for increased scale.
5. Rotor life expectancy for onboard generation systems is an area of concern.
  - a. Inspection and replacement intervals will need to be several times longer than comparable rotors from general aviation, with costs a small fraction.
6. AWTs should be designed to facilitate quick powertrain swaps.
  - a. Smaller powertrain units than comparable power HAWTs enable easier maintenance, but the system needs to be designed to maximize this advantage.

Project Level General Maintenance Assumptions	Value	Unit
<b>Fault/troubleshooting</b> time multiple of unscheduled time	100	%
Average <b>kite wait time</b> before a tech response	8	hr
Average <b>travel time</b> for a tech to get a kite	0.5	hr
Average <b>time to get in a service position</b> once at the kite	0.5	hr
<b>General inspections</b> each time accessing the kite	0.25	hr
<b>% effectiveness</b> increase decrease in tech time year over year	1.0	%
<b>Burden rate</b> for handling spares	5	%
% of scheduled maintenance done <b>below cut-in</b>	20	%
<b># of carbon fiber repairs</b> per kite per year	2.0	
Cost per kite per year of <b>carbon fiber repairs</b>	1500	\$
Average # of hr down for a <b>carbon fiber repair</b>	24	hr
% of time that techs are working but <b>not fixing kites</b>	15	%

Table 2: **Some of the key inputs to Makani's labor model for onshore maintenance expenses.**

Anecdotal evidence supports the top takeaway, that larger systems reduce maintenance costs-per-rated-watt. Statements from several HAWT wind turbine farm operators agreed that the number of required technicians largely scales with the number of turbines (and therefore, number of total components), rather than the size of each turbine.

The model also decided several design trades for the next generation system—more rotors and variable pitch rotors were both rejected in large part due to the higher predicted maintenance

costs washing out the perceived benefits of those changes. A maintenance model is useful to gain some insight into difficult trades such as these, and reduce the temptation to add ever more complexity.

All of this is to say that maintenance costs are another compelling reason for energy systems to be as large as possible, and AWTs are not exempt, despite having comparatively easier to access and maintain power systems than HAWTs.

## 5 System Cost

Although the turbine itself draws all the attention, modern turbines are now so cost effective that wind energy costs have become primarily a siting, infrastructure, maintenance, and financing problem. As we saw above, the turbine itself is typically less than half the total cost of energy onshore, and a quarter or less offshore. Wind energy's ongoing challenge is to increase the denominator—lowering the cost of energy by increasing energy production—and to increase system rating to reduce balance of system and maintenance costs.

This isn't to say that system costs are irrelevant, or that the challenge of making a cost effective system is easy, but simply to point out that it's exceedingly difficult to substantially reduce the cost of energy through the cost of the turbine alone. In our offshore LCOE breakdowns from section 3, we see that even if the cost of the turbine is free,<sup>9</sup> we've only reduced the cost of energy by ~15-25%, placing an impossible 100% turbine cost reduction at parity with a relatively more realistic 15-20% capacity factor improvement or an increase in scale to reduce BoS and maintenance costs by 20-30%. A competitive cost of energy cannot be achieved by reducing the cost-per-rated-watt of the turbine alone, but a high turbine cost can certainly push it out of reach.

We should use this to reframe the priorities for a first generation AWT. The design needs to ensure that cost-per-rated-watt can be roughly competitive with traditional wind energy, at which point it becomes relatively unimportant, at least for a new technology entering the market. It's much more important to demonstrate that a large system with an acceptable level of performance (ie, a competitive  $k_{CF}$ ) is technically possible, as these are the key long term avenues towards success. As a fledgling industry, AWE needs to shorten development time,<sup>10</sup> and (in the opinion of this author) time spent incrementally lowering costs should be largely relegated to future optimizations, assuming work has been done to ensure costs can be roughly competitive and maintenance considerations have been designed in.

Makani developed cost models, estimates, and vendor quotes that show a path to a competitive cost-per-rated-watt, leaving the key challenge as needing to demonstrate reliable performance at scale.

---

<sup>9</sup> It's obviously *difficult* to build a business case around a free product, but it's also difficult to build one around a product with a lengthy development where the benefits are only realized at a rock bottom price.

<sup>10</sup> Despite several multi-year efforts from several companies, no AWT effort has publicly demonstrated hands-off operation of even a moderate sized (>500 kW) AWT for a reasonable length of time (>6 months of operation at a high level of availability) while achieving the necessary performance level. As Makani has clearly demonstrated, growing development costs and timelines can be hard to justify.

## 6 Kite Power

We finally arrive at the last piece of the LCOE puzzle, the energy production of the turbine. In this section, we'll introduce an analytical model to isolate the major sensitivities and losses for an AWT's power. To do so, we'll embody the mantra that "all models are wrong, but some are useful" by making extensive simplifying assumptions. Our goal is a relatively simple model that can be coded in an afternoon and teaches the big lessons on how to get power from a kite—the end result only needs to broadly capture the sensitivities to be useful.

Before we build a power model, we need a brief discussion of how we translate power into energy. Power is a function of wind speed,<sup>11</sup> so turbine performance is typically presented as power versus wind speed, called a power curve. A typical power curve will appear like the following, figure 10:

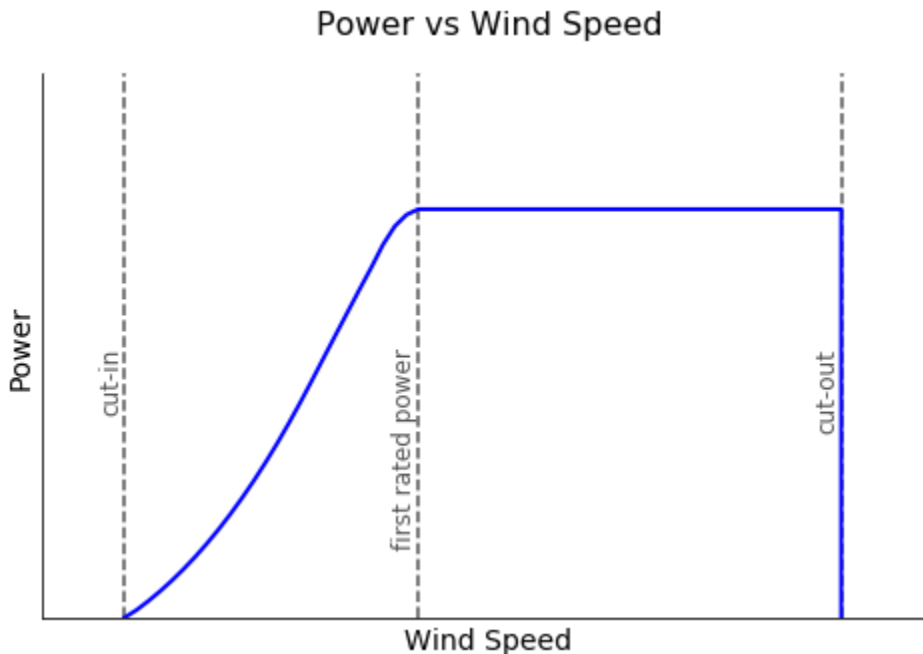


**Figure 10: A notional power curve for a wind turbine with key wind speeds denoting different regimes specified.**

A power curve has 2 major regimes, denoted with 3 wind speeds. The cut-in wind speed marks the first wind speed where the turbine makes power. The turbine makes more power as the wind grows stronger until it reaches its first rated power point, where the power system becomes saturated at  $P_{rated}$ , and is unable to accept any more power. The rated power continues until cut-out, where the turbine must shut down, typically to avoid excessive loads that could damage the system.

<sup>11</sup> And somewhat of turbulence, which we'll ignore here, as it's outside the scope of our simple model.

Power performance from cut-in to first rated power is dictated by the turbine's ability to extract power from the wind, while the rated power region is determined by the power system's maximum power. Here, we'll choose to focus on maximizing the ability of the turbine to make power from the wind, ie, the region from cut-in to first rated power. Power saturation, and the challenges associated with it, will be discussed in section 10.

A power curve does not directly give us the capacity factor,  $k_{CF}$ , needed to determine LCOE. Capacity factor is a function of both the power curve and the wind speed probability distribution. Wind speed probabilities are site specific, but are commonly described with "standard" distributions, taking the form of a Rayleigh curve. Sites can be classified by their average wind speed, with the International Electrotechnical Commission (IEC) specifying high (class I), to very low (class IV) categories. Rayleigh distributions for those average wind speeds is shown in figure 11 below:

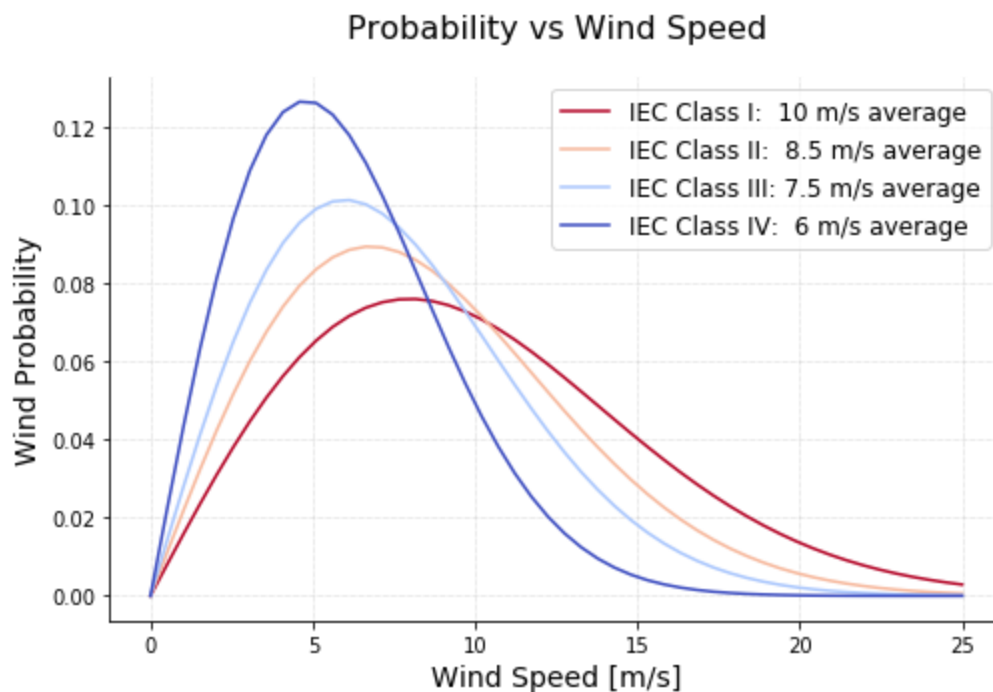


**Figure 11: Wind probability distributions for IEC Wind Classes, assuming a typical Rayleigh distribution.**

A wind speed distribution convolved with a power curve then provides a power probability distribution. Integrating the power probability distribution results in the average power for a given wind distribution. The average power is then adjusted for turbine availability (turbines may be down for maintenance, or for bird migrations, or to better match energy demand, or several other reasons) and any other plant level losses, and ratio of the net average power to the maximum power,  $P_{rated}$ , gives us the capacity factor,  $k_{CF}$ .

We'll leave this exercise to the reader. The goal here is to describe what we can do to influence the capacity factor rather than to arrive at a particular LCOE estimate. It's sufficient to draw a quick, obvious conclusion: moving the power curve between cut-in to first rated power to the left, via increasing turbine performance, increases capacity factor and lowers LCOE.

## 6.1 Loyd Revisited

All wind turbines generate power by converting the kinetic energy of the wind into useful motion. Power available in the wind for a given area perpendicular to the wind direction is given by:

$$P_{wind} = \frac{1}{2} \rho A_{swept} v_w^3 \quad [8]$$

Where  $\rho$  is the air density,  $A_{swept}$  is the area of wind, and  $v_w$  is the wind speed. For a HAWT,  $A_{swept}$  is clearly defined, as the blades sweep out a fixed area, setting an absolute maximum power that the turbine can reach for a given wind speed and air density. However, no turbine is able to extract all the power from the wind, due to both system inefficiencies and the physics of slowing down the wind to extract power.<sup>12</sup> HAWTs are able to get close to the fundamental limits, so it remains useful to reference their power to the power available in the wind, and to bundle these losses into a power coefficient, such that:

$$P_{HAWT} = \frac{1}{2} C_{HAWT} \rho A_{swept} v_w^3 \quad [9]$$

Translating this to AWTs, we see an immediate disconnect: AWTs can sweep out a variable area with respect to the wind. Without a fixed  $A_{swept}$ , AWTs can be largely unburdened by the amount of power available in a given area of wind, as they can easily sweep out a large area relative to the limits of the kite and its power system. It's instead useful to define a performance metric,  $\zeta$ , in terms of the kite's wing area,  $S$ , rather than the swept area, such that:

$$P_{AWT} = \frac{1}{2} \zeta \rho S v_w^3 \quad [10]$$

Unlike the HAWT case, there is no clear limit on power. We need a different base to build our reference for AWT power. To find it, we look to the foundational paper from Loyd [7], recontextualized for use here, with some strong influence from Vander Lind [8].

We begin by assuming a kite is flying perpendicular to the wind at speed  $v_k$ , with wing area  $S$ , operating at lift and drag coefficients  $C_L$  and  $C_D$ , creating lift and drag forces  $F_L$  and  $F_D$ , while located directly downwind from the tether attachment, at tension  $F_T$ . For an onboard

---

<sup>12</sup> Chiefly the Betz limit, as a result of induced flow losses, which we'll discuss later.

generation kite, we extract power from the force on the rotors,  $F_r$ , at the airspeed of the kite (the apparent wind),  $v_a$ , such that  $F_r = \frac{P}{v_a}$ . We can then set up the following force balance.

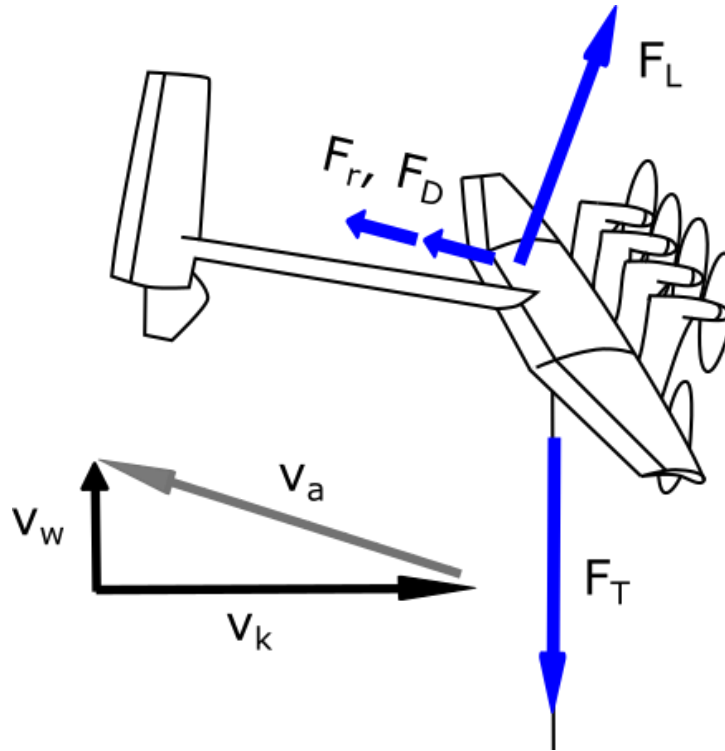


**Figure 12: Force balance for an onboard generation kite. The wind and kite speeds (black), create a “kiting triangle” that tilts the lift and drag forces (all forces in blue) forwards such that there is a component of lift pushing the kite along.**

From figure 12, we can utilize the similar triangles of the speeds and the forces to find the following relationship for the balance of forces along the  $v_a$  axis:

$$\frac{P}{v_a} + \frac{1}{2}\rho C_D S v_a^2 = \frac{1}{2}\rho C_L S v_a^2 \left(\frac{v_w}{v_k}\right) \quad [11]$$

If we assume that  $v_k \gg v_w$ , we can apply the small angle approximation that  $v_a \approx v_k$  and solve for power, simplifying this to:

$$P = \frac{1}{2}\rho S v_k^3 \left(C_L \frac{v_w}{v_k} - C_D\right) \quad [12]$$

Tension is an important measure for AWT design, so let's also find a relationship for it.

Again applying the small angle approximation we did above, we can simply assume that tension is approximately equal to lift:

$$F_T \approx F_L = \frac{1}{2} \rho C_L S v_k^2 \quad [13]$$

Equation 12 shows a sensitivity to kite speed, so to find the optimal speed we take the derivative of power with respect to  $v_k$ , set the derivative to zero, and solve to find the optimal kite speed, which we'll denote by adding the subscript  $L$  to indicate this as the Loyd optimum operating point:

$$v_{k_L} = \frac{2}{3} \frac{C_L}{C_D} v_w \quad [14]$$

We'll see later that the wind speed used to determine the best kite speed needs to be adjusted to accommodate various effects, but we'll leave it as a generic  $v_w$  for now. We can then substitute this back into equation 12 to find:

$$P = \frac{4}{27} \frac{C_L^3}{C_D^2} \frac{1}{2} \rho S v_w^3 \quad [15]$$

Comparing equations 10 and 15, we see that we've found a theoretical limit for  $\zeta$  at a given  $C_L$  and  $C_D$ . We'll call this maximum  $\zeta_L$  the Loyd limit:

$$\zeta_L = \frac{4}{27} \frac{C_L^3}{C_D^2} \quad [16]$$

This limit only assumes optimum kite speed, but a given kite design will also have an optimum  $C_L$ , usually at or near the highest achievable lift coefficient. We'll need to specify operating point for the kite, accounting for any aerodynamic margins required to ensure the target  $C_L$  is feasible.

Let's also introduce a baseline  $\zeta$  for a wing operating optimally,  $\zeta_0$ , where the subscript 0 indicates the  $\zeta$  for a kite without the tether,<sup>13</sup> operating at the optimal speed and target  $C_L$ , where the drag coefficient is only for the kite, denoted with  $C_{D_k}$ . We then use this to define a baseline power,  $P_0$ , for an AWT operating optimally without any of the losses we'll soon be adding in, at some reference wind speed,  $v_{w_{ref}}$ , measured at a specified height,  $h_{ref}$ , far upstream of the turbine. We need to be careful with what we're solving for here—this  $P_0$

<sup>13</sup> For very low drag, high lift designs, the optimum zeta may be at a lower lift coefficient for the kite alone than for the full system when including the tether drag, due to the greater influence of induced drag.

represents excess thrust power, not an electrical power. This thrust power can then go to the power system if we wish—for an onboard generation system, via rotor drag power that is then converted to electrical power—or into accelerating the kite.

$$P_0 = \frac{1}{2} \rho S \zeta_0 v_{w_{ref}}^3 \quad [17]$$

We'll be using this baseline power as the foundation to build our model on. Before moving on, let's look at how the tension of an optimally operated AWT compares with the theoretical minimum force for a given power at a given speed, in this case simply defined as  $F_{T_{min}} = \frac{P}{v_w}$ . Taking our optimal kite speed  $v_{k_L}$  from equation 14 and plugging it into equation 13 to find the tension at the optimal kite speed,  $F_{T_L}$ , we find that the tension ratio at the Loyd limit,  $\tau_L$ , is:

$$\tau_L = \frac{F_{T_L}}{F_{T_{min}}} = \frac{F_{T_L} v_w}{P} = 3 \quad [18]$$

The loading efficiency of an AWT at maximum performance is independent of the system itself! We'll compare this to the analogous tower loading efficiency of a HAWT in a later section.

### 6.1.1 Tether Drag Losses

Defining a  $\zeta_0$  is only useful to provide a comparison point to come back to. For AWTs, the  $C_D$  must include the drag of the tether, not just the wing. By again assuming  $v_k \gg v_w$  and modeling the tether as a rigid bar with constant drag properties, we can find an effective tether drag  $C_{D_{t,eff}}$  as a drag coefficient referenced to the kite wing area,  $S$ , and kite airspeed to be:

$$C_{D_{t,eff}} = \frac{1}{4} \frac{C_{D_t} l_t d_t}{S} \quad [19]$$

where  $C_{D_t}$  is the drag coefficient of the tether,  $l_t$  is the tether length, and  $d_t$  is the tether diameter (or reference length for  $C_{D_t}$ , if non-circular).

Given that the tether is a significant component of the overall drag, we need to include the impact of the tether length on the system performance via reduced  $\zeta$ . There are other detrimental effects of increasing tether length (such as increased mass, and, for an onboard generation system, reduced efficiency), but these will be ignored here.

We begin by breaking apart the total drag term into tether and non-tether components. It's useful to normalize this parameter to enable us to compare different kites and operating points.

By normalizing the tether drag per unit length relative to the airframe drag, we have a new metric, the tether drag ratio,  $k_{TDR}$ :

$$k_{TDR} = \frac{C_{D_t} d_t}{C_{D_k} S} \quad [20]$$

We should highlight that this ratio is not purely a function of the system, but also a function of how we choose to operate it— $C_{D_k}$  is not fixed, as it is a function of  $C_L$ , so  $k_{TDR}$  must be specified at some target  $C_L$  and its associated  $C_{D_k}$  that represents how we will fly our kite. Some approximate example  $k_{TDR}$  values are in table 3 below, including some fictional systems:

Kite	$C_{D_k}$	S [m <sup>2</sup> ]	$C_{D_t}$	$d_t$ [m]	$k_{TDR}$
M600 As-Built: Fluted Tether	0.244	32.9	0.7	0.0295	0.0026
M600 As-Built: Smooth Tether	0.244	32.9	1.0	0.027	0.0034
M600-ish: Thick Tether	0.244	32.9	0.7	0.045	0.0039
MX2: Fluted Tether	0.123	54.0	0.7	0.0295	0.0031
MX2-ish: High Drag Kite	0.2	54.0	0.7	0.0295	0.0019
Soft kite-ish	0.16	30	1.0	0.010	0.0021
MX2: Fully Faired Tether	0.123	54	0.1	0.035	0.0005

**Table 3: Tether drag ratios,  $k_{TDR}$ , for several example kites. Typical values appear to range from 0.002 - 0.004. Faired tethers are a dramatic improvement.**

The total drag coefficient for the system can then be shown to be:

$$C_D = C_{D_k} \left( 1 + \frac{1}{4} k_{TDR} l_t \right) \quad [21]$$

We can then define a power coefficient for tether drag,  $C_{TD}$ , as the ratio of  $\zeta_L/\zeta_0$ . For a constant  $C_L$  and  $C_{D_k}$ , this becomes only a function of  $k_{TDR}$  and  $l_t$ :

$$C_{TD} = \frac{\zeta_L}{\zeta_0} = \frac{1}{(1 + \frac{1}{4}k_{TDR}l_t)^2} \quad [22]$$

### 6.1.2 Path Offset Losses

It's important to consider the mechanism by which both HAWTs and AWTs generate their power from wind. All wind turbines work by redirecting and slowing down the incoming wind to generate a propulsive lift, in the process extracting the kinetic energy available in the wind. By definition, tethers of AWTs only support a tensile load, which means that for a kite in crosswind flight, the total aerodynamic forces on average must be in line with the tether, and the wing can only create forces to extract energy from the portion of wind aligned with the tether.

For AWTs with low tower heights, simply avoiding the ground requires an average elevation of the tether angle,  $\theta_e$ , above horizontal, which attenuates the effective wind. Since power scales with  $v_w^3$ , we can then define a power coefficient to represent the elevation losses for a kite operating at  $v_{k_L}$ :

$$C_{\theta_e} = \cos^3 \theta_e \quad [23]$$

This important relationship is worth confirming with the numerical model. A kite in pure crosswind flight (ie,  $\vec{v}_k \perp \vec{v}_w$ ) under zero shear conditions, in the absence of gravity and with rotors of constant efficiency, is optimized for airspeed while all other flight conditions are held constant. It should be noted that  $v_{k_L}$  is not a constant, as the wind speed used to determine  $v_{k_L}$  is also attenuated by  $\cos \theta_e$ .

The power attenuation shown in figure 13 is independent of system performance. We've only shown the effect of path elevation here, but the same power attenuation occurs for any angular offset from the wind. We'll revisit this effect in the context of azimuth offsets later.

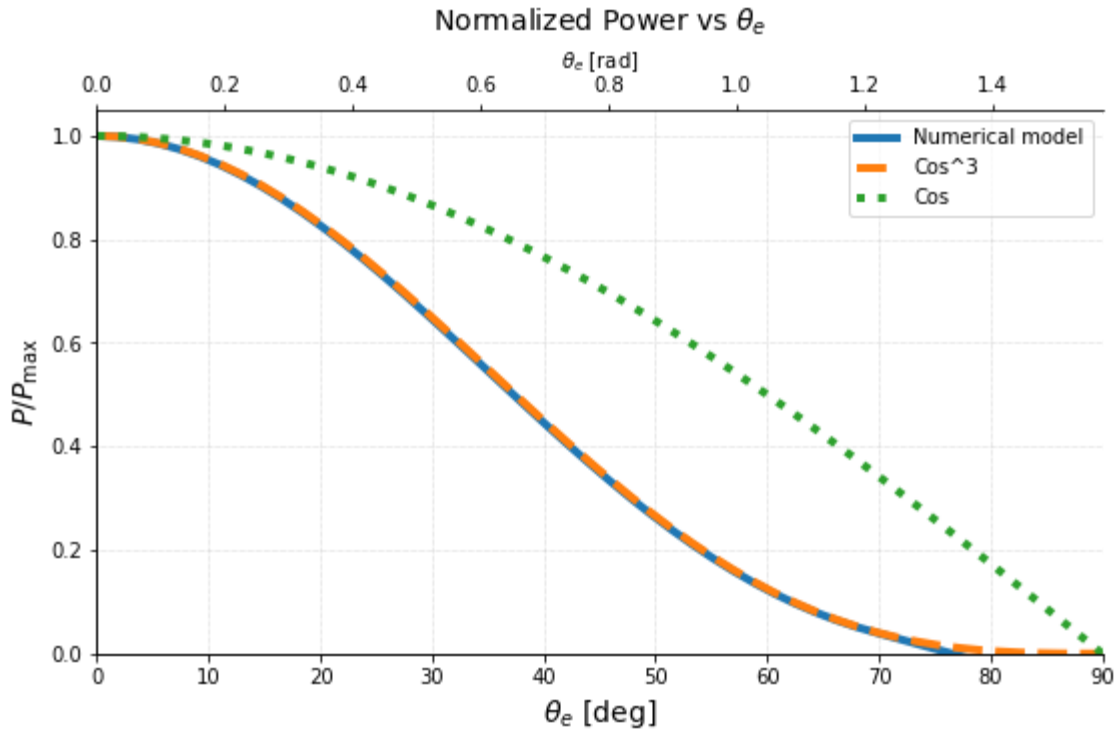


**Figure 13: Numerical model verification of the critical  $\cos^3$  angular offset losses.**

This wind speed attenuation is something we'll come back to again and again, so let's define our attenuated wind. The effective wind,  $v_{w_{eff}}$ , is the wind perpendicular to the approximate "flight plane," at the mean height of the path, which for AWTs we'll call the virtual hub height. Wind speed can vary with altitude, so we'll denote wind speed at this height as  $v_{w_{vh}}$ . For circular paths and a rigid tether, the flight path is indeed planar, but for all other paths, the flight plane is roughly found as the plane normal to the vector drawn from the path centroid to the tether attachment. We lose some nuances around the path with this single simplification for effective wind, but it captures most of the effect. The angle of this plane forms the mean elevation offset, or  $\theta_e$ , as discussed above. The effective wind can then be stated as:

$$v_{w_{eff}} = v_{w_{vh}} \cos \theta_e \quad [24]$$

For an AWT, minimum average tether elevation for a circular path is dictated by mean path radius  $r_{loop}$ , tower height  $h_{tower}$ , and desired ground clearance (ie, minimum altitude)  $h_{min}$ :

$$\theta_{e_{min}} = \sin^{-1} \left( \frac{r_{loop}}{l_t} \right) + \sin^{-1} \left( \frac{h_{min} - h_{tower}}{l_t} \right) \quad [25]$$

Using approximate values from the Makani M600 with a wingspan of 25 m, a tether of 440 m, and a short tower of 5 m, then choosing a relatively tight turning radius of 5 wingspans (125 m

radius) with a ground clearance at the bottom of the loop of  $\sim 3.5$  wingspans (90 m), we have a minimum elevation angle of 0.48 rad ( $\sim 28$  deg), and  $\cos^3$  of this angle is 0.7. The minimum elevation loss in this example is nearly one third of the power!

### 6.1.3 Wind Shear Gains

Wind in our altitudes of interest ( $\sim 50$  m to 300 m) typically follows a simple shear model, such that:

$$v_{w_{vh}} = v_{w_{ref}} \left( \frac{h_{vh}}{h_{ref}} \right)^{\alpha_w} \quad [26]$$

Where  $v_{w_{vh}}$  is wind speed at the virtual hub height (the mean path height),  $h_{vh}$ , while  $v_{w_{ref}}$  is the wind speed measured at some reference height,  $h_{ref}$ , and  $\alpha_w$  is the wind shear exponent.

Power in wind increases with  $v_w^3$ , so even relatively small increases in wind speed with altitude can provide meaningful increases in system performance. We can find the average virtual hub height,  $h_{vh}$ , of the kite with the following:

$$h_{vh} = l_t \sin \theta_e + h_{tower} \quad [27]$$

Using this virtual hub height in our equation 26 for wind speed allows us to define another power coefficient for the effect of wind shear,  $C_{\alpha_w}$ :

$$C_{\alpha_w} = \left( \frac{l_t \sin \theta_e + h_{tower}}{h_{ref}} \right)^{3\alpha_w} \quad [28]$$

Before we move on, it's useful to compare the power benefits of higher shear with the elevation losses needed to access those benefits. If we assume that  $h_{tower} \ll l_t \sin \theta_e$  and drop it, then we can combine our power coefficients  $C_{\theta_e}$  and  $C_{\alpha_w}$  and drop geometric constants to show that:

$$P \propto \cos^3 \theta_e \sin^{3\alpha_w} \theta_e \quad [29]$$

The first part is the cost of higher elevations, while the second is the benefit of accessing higher winds.

Setting the derivative of this to zero and solving to find the  $\theta_e$  for maximum performance gives us:

$$\theta_{e_{ideal}} = \tan^{-1} \sqrt{\alpha_w} \quad [30]$$

The ideal mean tether elevation accounting for the effects of elevation losses and wind shear benefits appears to be independent of tether length, system performance, or anything other than wind shear! For typical onshore shears of  $\alpha_w = 1/7 \approx 0.143$ , this evaluates to 0.36 rad (21 deg), and for typical offshore wind shears of  $\alpha_w = 0.1$ , ideal elevation is 0.31 rad (18 deg). Both are lower than the minimum elevation we derived above! Best operation of an AWT is typically as low as feasible, even in normal wind shear conditions.



**Figure 14: Makani employee and world champion kitesurf racer Johnny Heineken (white kite) keeping his kite low to reduce elevation losses.**

While AWTs are indeed accessing higher winds (typical tether lengths place the virtual hub height higher than most HAWT hub heights), it is generally advantageous to fly as low as possible, which means tighter turning radii and less ground clearance.

#### 6.1.4 Turning Losses

Not all lift produced by the kite can go towards power production. In practice, some portion of lift is used to make the turn and keep the kite and tether airborne. Here we'll look specifically at the turning losses.

A free body diagram in the frame of a kite turning a circular path directly downwind in the absence of gravity is shown in figure 15, using the assumption  $v_k \gg v_w$  to flatten the lift into the

plane spanned by the centrifugal and tension forces, making all forces planar. This frame is non-inertial, so we add a centrifugal force,  $F_c$ , that must also be balanced.

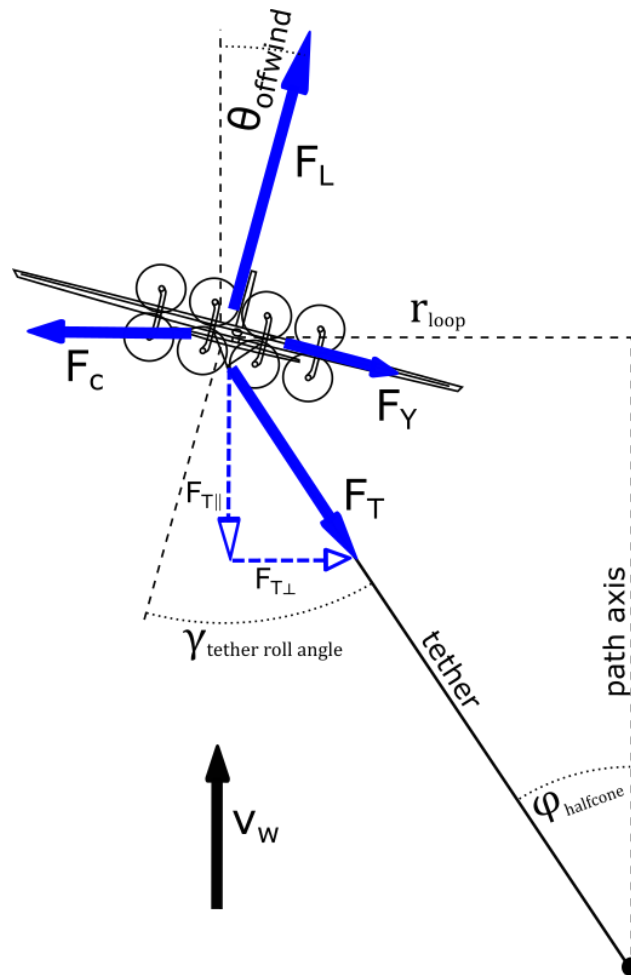


**Figure 15: Forces on the kite in the approximate lift and tension plane. Here, the path center is directly downwind, and the kite is flying towards the viewer.**

We propose that only the lift in the  $Span(\vec{v}_k, \vec{v}_w)$  plane contributes to power production. With our small angle approximations we can restate the  $\cos^3$  sensitivity as being in relation to the  $\theta_{offwind}$  angle of the lift instead of simply the tether elevation angle,  $\theta_e$ . In the absence of  $F_c$  in straight and level flight, they are identical. This proposed behavior is worth confirming via the numerical model. In this case, we place the path loop axis directly downwind in the absence of gravity, and vary  $r_{loop}$  to achieve differing  $\theta_{offwind}$ . Again, we optimize for airspeed under each condition.

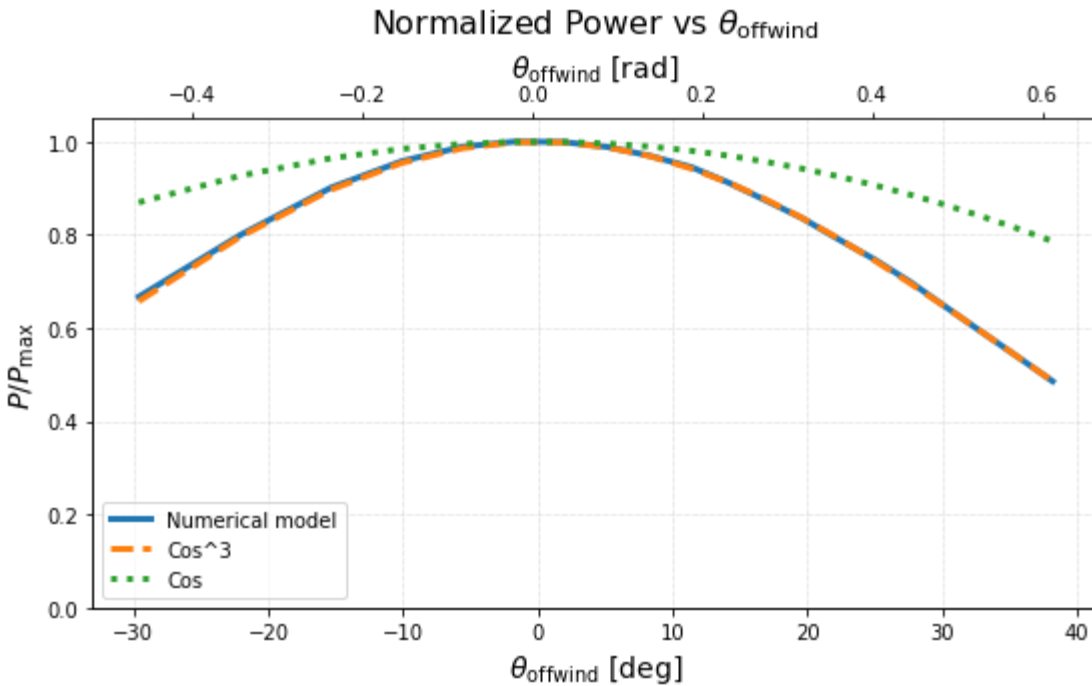


**Figure 16: Numerical model confirmation of the proposed  $\cos^3\theta_{\text{offwind}}$  losses**

Our example confirms the proposed  $\cos^3$  sensitivity to the  $\theta_{\text{offwind}}$  angle. Clearly, turning effort can have a large impact on the net power production, but it's not all bad. Turning the *right* amount can be used to help point the lift in the best power production direction (ie, as close as possible to downwind), despite the tether having some angle offset relative to the wind. Effectively, the  $\cos^3$  power loss implied by the instantaneous azimuth present at the sides of a flight path can be negated by choosing a turning radius that realigns the lift back downwind.

This benefit doesn't come for free, as it results in higher system loads. Tensions are typically higher for the same power from the required centripetal forces. To quantify the increase in tension, we revisit the tension factor  $\tau_L$  from section 6.1. Ideal operation<sup>14</sup> of a crosswind kite in straight and level flight occurs when  $\tau = 3$ , but looking at tension factor versus normalized power for the numerical example plotted in figure 16 shows this non-generalized result in figure 17.

<sup>14</sup> Assuming operation at optimum speed for a system operating far from the Betz limit.

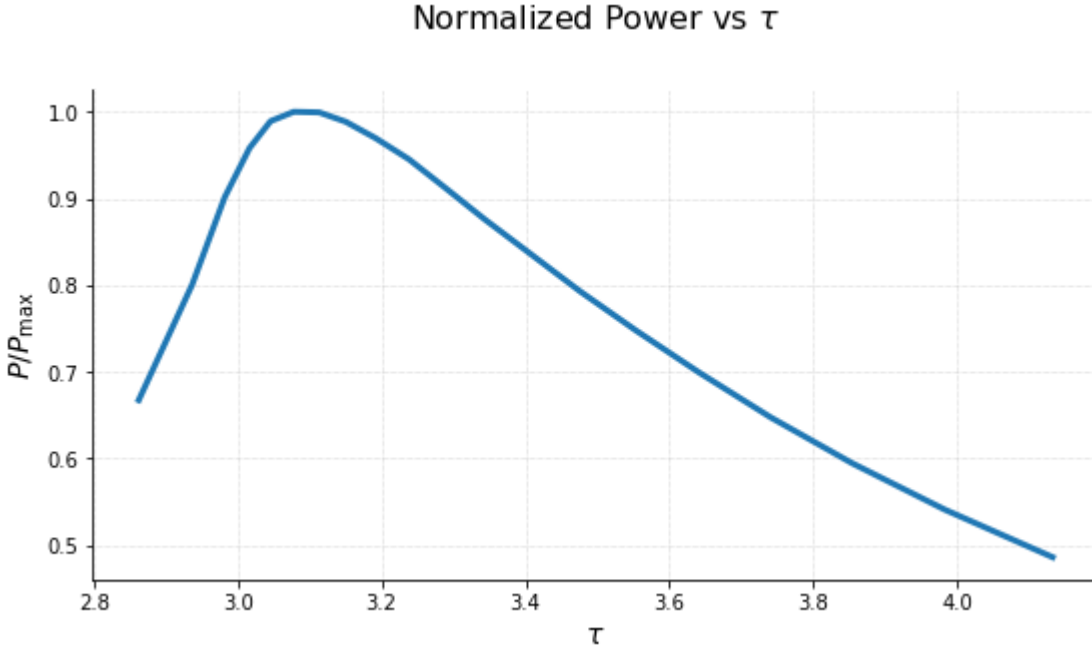


**Figure 17: Tension factor,  $\tau$ , changes as we vary  $r_{loop}$  and the tether carries different amounts of the required centripetal force.**

The penalty for this design and operating condition is small, with the peak power only shifted to  $\tau \approx 3.1$ , but it's something to be aware of.

Revisiting figure 15, we can solve for the ideal loop size for a circular path accounting for turning losses alone.

The kite's aerodynamic forces are expressed below:

$$F_L = \frac{1}{2} \rho C_L S v_a^2 \quad [31]$$

$$F_Y = \frac{1}{2} \rho C_Y S v_a^2 \quad [32]$$

Given that typically  $C_L \gg C_Y$ , then  $F_L \gg F_Y$ , and we make the assumption that  $F_Y \sin \theta_{offwind}$  will have a negligible effect on tension. With  $r_{curv}$  as the instantaneous radius of curvature (for a circular flight path,  $r_{curv} \equiv r_{loop}$ ), we can define the remaining forces:

$$\varphi_{halfcone} = \sin^{-1} \left( \frac{r_{loop}}{l_t} \right) \quad [33]$$

$$F_{T_{\parallel}} = \frac{F_L \cos \theta_{offwind}}{\cos \varphi_{halfcone}} \quad [34]$$

$$F_{T_{\perp}} = F_T \frac{r_{loop}}{l_t} \quad [35]$$

$$F_c = \frac{m_{eff,a} v_k^2}{r_{curv}} \quad [36]$$

We introduce here the effective mass for acceleration,  $m_{eff,a}$ . Derived from a rigid tether assumption, we can find that the effective inertia at the kite is the mass of the kite plus 1/3rd the mass of the tether. Assuming  $F_Y$  is small, then all the lift is from  $F_L$ , and the optimum will occur when  $F_L$  is in the  $Span(\vec{v}_k, \vec{v}_w)$  plane, and therefore when  $\theta_{offwind}$  is equal to zero.

By combining the equations above, adding the approximations that  $F_T \approx F_L$ , that  $F_Y$  is small, that  $v_a \approx v_k$ , and assuming a circular path so that  $r_{curv} = r_{loop}$ , we can then set  $\theta_{offwind}$  to its optimum of zero and solve for  $r_{loop}$  to find the following relationship for the ideal circular path size to minimize turning losses,  $r_{loop_{ideal}}$ :

$$r_{loop_{ideal}} = \sqrt{\frac{2l_t m_{eff,a}}{\rho C_L S}} \quad [37]$$

This is an interesting result. As both the tension and centrifugal force approximately scale together with  $v_k^2$ , they drop out, and the ideal radius of curvature becomes only a function of a few kite parameters, largely independent of any kite speed strategy or wind.

The above gives the ideal path radius in isolation, ignoring effects other than how path curvature changes the power produced by lift. In order to combine this effect with others, it's desirable to instead put it in terms of a power coefficient.

It was stated above that  $P \propto \cos^3 \theta_{offwind}$ , allowing us to define  $\cos^3 \theta_{offwind}$  as a power coefficient,  $C_{turn}$ . Again making the simplifying assumption that  $F_T \approx F_L$  and also assuming that  $\cos \theta_{offwind} \approx 1$  (ie, we are flying close to our ideal loop size as determined above), we can solve for  $\theta_{offwind}$  for a directly downwind circular path:

$$\begin{aligned} \theta_{offwind} &= \sin^{-1} \left( \frac{F_c - F_{T_{\perp}} - F_{Y_{\perp}}}{F_L} \right) \\ &\approx \sin^{-1} \left( \frac{2m_{eff,a}}{\rho C_L S r_{loop}} - \frac{r_{loop}}{l_t} - \frac{C_Y}{C_L} \right) \end{aligned} \quad [38]$$

By utilizing the identity  $\cos(\sin^{-1}x) = \sqrt{1 - x^2}$ , we then find our power coefficient for turning losses for a circular path:

$$C_{turn} = \left( 1 - \left( \frac{2m_{eff,a}}{\rho C_L S r_{loop}} - \frac{r_{loop}}{l_t} - \frac{C_Y}{C_L} \right)^2 \right)^{\frac{3}{2}} \quad [39]$$

We can check the accuracy of all these approximations by again using the same example from the numerical model as we used to show the  $\theta_{offwind}$  losses, and comparing results with the analytical model for  $C_{turn}$  in figure 18:

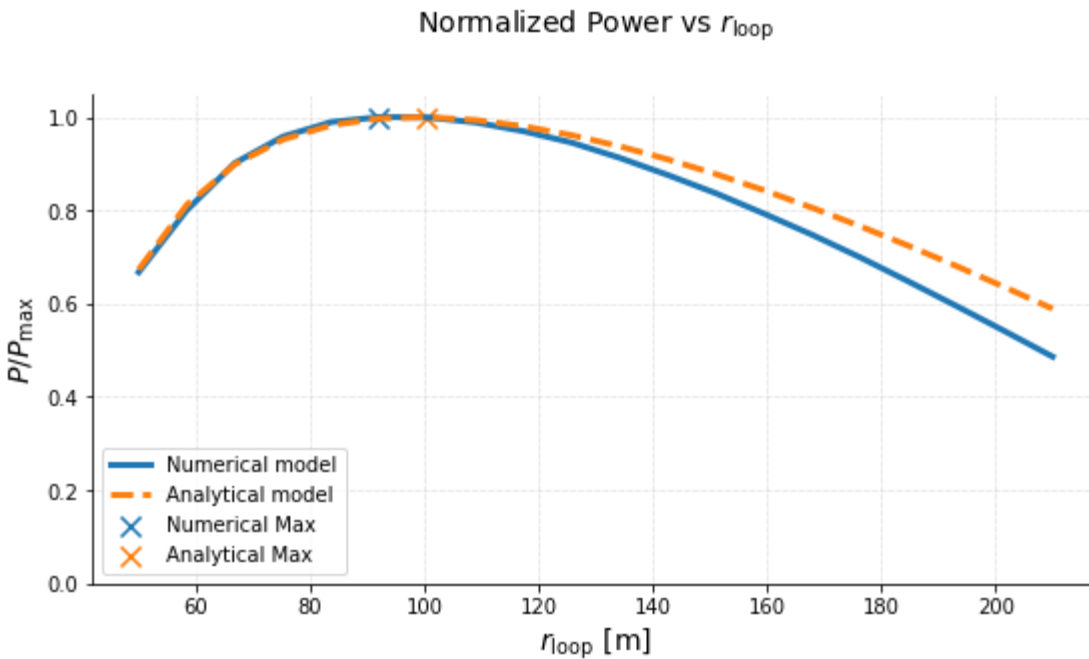


**Figure 18: Numerical confirmation of our analytical turning losses for a directly downwind circular path. The analytical model, despite much simplification, is a good fit.**

The coefficient  $C_{turn}$ , despite extensive simplification in its derivation, performs well, only showing meaningful differences at large loop sizes where the actual  $\theta_{offwind}$  is far from the assumed ideal, as one of the assumptions relies on being close to the ideal. Since we're targeting optimum operation, and path offset losses will also apply pressure for smaller path sizes, increasing errors at larger path sizes is acceptable.

For a path not directly downwind,  $\theta_{offwind}$  from turning is combined with  $\theta_e$  from path elevation, positively at the top of the path, negatively at the bottom. At the sides of the path,  $\theta_{offwind}$  only

comes from turning,<sup>15</sup> but we now have the kite moving into and out of the wind. Despite these nuances, numerical models have shown this  $\cos^3\theta_{offwind}$  factor derived from a path directly downwind to be a decent approximation for turning losses at typical path offsets.

### 6.1.5 Efficiency Losses

Thus far we've been working with thrust power, a force on the rotors at an airspeed. The power system's job is to convert that thrust power from the wind into a useful electrical power.

In this simple analytical approach, we'll stick with idealized constant efficiencies. For an onboard generation power system the total efficiency from thrust to grid,  $\eta_{t2g}$  consists of:

$$\eta_{t2g} = \eta_{rotors} + \eta_{motors} + \eta_{ctrls} + \eta_{tether} + \eta_{padtrans} + \eta_{collection} \quad [40]$$

Typical values are shown in table 4 below.

Variable	Value	Description
$\eta_{rotors}$	0.8	Rotor efficiency from thrust power to shaft power.
$\eta_{motors}$	0.94	Motor efficiency from shaft power to electrical power.
$\eta_{ctrls}$	0.96	Motor controller electrical efficiency.
$\eta_{tether}$	0.97	Tether electrical efficiency.
$\eta_{padtrans}$	0.975	Padmount transformer efficiency.
$\eta_{collection}$	0.97	Electrical efficiency of the collection system.
$\eta_{t2g}$	~0.66	Net efficiency from thrust to grid.

**Table 4: Typical component efficiencies for an onboard generation AWT.**

For positive power generation, this  $\eta_{t2g}$  simply forms our  $C_\eta$  power coefficient:

$$C_\eta = \eta_{t2g} \quad [41]$$

<sup>15</sup> For a path offset in elevation only. Azimuth offsets have a similar effect.

Pumping kites with ground based power generation will result in similar values, replacing the  $\eta_{rotors}$  with pumping cycle losses and removing the  $\eta_{tether}$  losses.

### 6.1.6 Gravity Losses

Equation 17 for  $P_0$  assumes the kite is operating at its ideal kite speed, which is roughly constant around the path (approximately:  $v_{k_L} \propto \cos(\theta_{offwind} + \theta_e)$ ). In order to do this, the kite must hold a constant kite speed while experiencing large changes in potential energy due to the changes in path height. This strategy causes large swings in power as the potential energy is effectively pushed into the grid on the downstroke, and pulled back out on the upstroke. A constant kite speed strategy creates fluctuations in power with changes in altitude.

When the fluctuation in power is larger than the power from the wind, we're effectively using the grid as a battery for a portion of the potential energy exchange. Using the grid as a battery means paying the difference between the amount of energy we can store and how much we then need to put back into the kite. As the kite begins making power from the wind, it utilizes the grid battery less and less, until the power from the wind is larger than the fluctuations.

With the effective mass at the kite from gravity as  $m_{eff,g}$ , equal to the mass of the kite plus half the mass of the tether, the potential energy exchange over a circular path is equal to:

$$\Delta E_p = 2r_{loop} m_{eff,g} g \cos \theta_e \quad [42]$$

Defining  $\eta_{pump_0}$  as the losses of our "grid battery" relative to the potential energy exchange,  $\Delta E_p$ , under conditions of no wind, we find:

$$\eta_{pump_0} = \frac{\eta_{t2g} \Delta E_p - \frac{\Delta E_p}{\eta_{t2g}}}{\Delta E_p} = \eta_{t2g} - \frac{1}{\eta_{t2g}} \quad [43]$$

Using the value of  $\eta_{t2g}$  from above of 0.66 results in a  $\eta_{pump_0}$  of approximately -85%! The kite only puts 2/3 of the potential energy into the grid, then needs to pull 3/2 the potential energy from the grid to put it back into the kite, resulting in a loss of most of the potential energy delta. Even ignoring grid implications of wild power swings, this is a bad deal.

Is this loss a significant amount of power? Let's take the MX2 kite as an example. With  $m_{eff,g}$  of 1988 kg and a circular path radius of 90 m at an average elevation angle of 0.45 rad, the potential energy exchange from top to bottom is ~3.2 MJ. As we just saw above, most of this energy is lost with a constant speed strategy under no wind conditions. With a total system  $C_L/C_D$  of ~12, a minimum kite speed of 30 m/s gives a path time of ~7.8 s, turning this energy loss into an average power loss of ~170 kW.

This is indeed significant for low wind speeds! Both the time and energy scale linearly with path radius, so this result is surprisingly independent of path vertical range (we'll derive this relationship in a moment). Paths stretched in the horizontal direction (such as ovals, racetracks, or horizontal figure eights) can spread this energy loss over greater time, but it's difficult to do enough to substantially change this problem, especially for larger and relatively heavier systems with a fairly short tether that operate close to their minimum radius, something we'll also investigate later. We need to adjust this equation to account for the reduced pumping losses as the kite begins to make power, but first let's describe an alternative solution.

The alternative to a constant kite speed strategy is to store the potential energy in kite speed. There are several consequences of a varying kite speed strategy, but here let's focus on one—the effect on power. Operation at  $\zeta_L$  requires the kite to fly at its optimal speed  $v_{K_L}$ . As we vary the speed, we'll move off this peak.

To determine these losses, we need to extract the optimal kite speed assumption from the Loyd limit for  $\zeta$ . Inspecting equation 12, it can be shown that we can put  $\zeta$  in terms of kite speed and aerodynamic properties. We'll denote this kite speed dependent version of  $\zeta$  by  $\zeta_v$ :

$$\zeta_v = C_L \left( \frac{v_k}{v_{w_{eff}}} \right)^2 - C_D \left( \frac{v_k}{v_{w_{eff}}} \right)^3 \quad [44]$$

It's important to note that we've baked in the tether losses here by using  $C_D$  rather than  $C_{D_k}$ . We also must use  $v_{w_{eff}}$  rather than  $v_{w_{ref}}$  here. This is because the optimum speed is based on the *effective* wind and total system drag. We've effectively captured the  $C_{TD}$  inside this definition of  $\zeta_v$ , but as  $\zeta_0$  is referenced to  $v_{w_{ref}}$  in our  $P_0$  definition, we have not captured the  $C_{\theta_e}$  or the  $C_{\alpha_w}$ —the wind speed attenuation is only used here to accurately represent the effect of the speed strategy.

It's worth taking a look at this term to describe the losses we anticipate. Taking the MX2 kite at an elevation angle of 0.45 rad (26 deg), in figure 19 we plot this  $\zeta_v$  as we change kite inertial speed at different wind speeds.

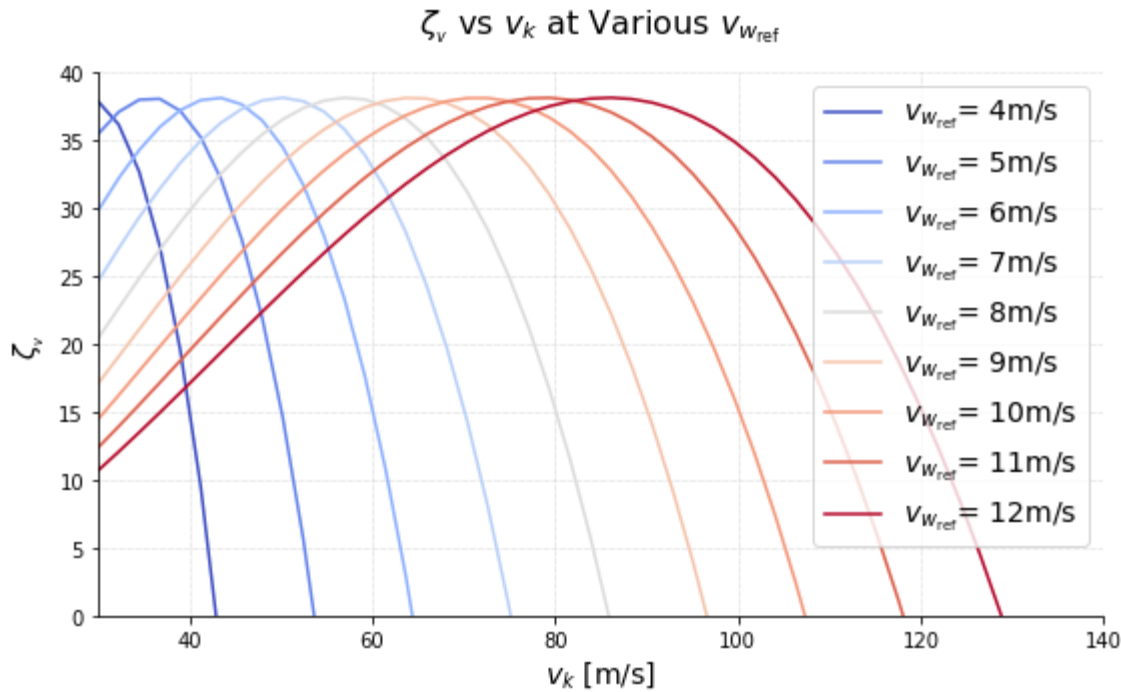


**Figure 19: Kite performance metric  $\zeta_v$  versus kite inertial speed at various wind speeds. For a fixed  $C_L$  and  $C_D$ , optimum speed increases linearly with wind speed.**

Each wind speed has an optimum at  $v_{kL}$ . As we fluctuate around the optimum speed, we expect to see the mean  $\zeta_v$  drop, with decreasing sensitivity as wind speed increases as the peak gets broader. This  $\zeta_v$  is applicable for a constant, non-optimal speed strategy, but we wish to know the net effect of a varying speed strategy.

Since the potential energy exchange is the main reason kite speed varies around the loop, we define the speed strategy in terms of a gravity factor,  $k_{grav}$ , defined such that a  $k_{grav}$  of zero is a constant kite speed strategy, and a value of 1 means the sum of potential and kinetic energy is a constant around the path.<sup>16</sup> In other words, it's a measure of how much of the potential energy we're storing in kite inertial speed. Comparing the change in kinetic energy over the change in potential energy, this can be written as:

$$k_{grav} = \frac{v_{kmax}^2 - v_{kmin}^2}{4 r_{loop} g \cos \theta_e} \tag{45}$$

If we chose a strategy such that the average kite speed,  $\bar{v}_k$ , is the optimum speed at the geometric middle of the path (not necessarily an optimum strategy, simply chosen for

<sup>16</sup> It should be noted that values greater than 1 are possible strategies, but they break some of our other definitions and have limited applicability that we'll discuss later, so we'll keep values here < 1.

convenience), and update our optimum speed  $v_{k_L}$  to include the effective wind speed, we have equation 46:

$$\bar{v}_k = v_{k_L} = \frac{2}{3} \frac{C_L}{C_D} v_{w_{eff}} \quad [46]^{17}$$

To capture the speed change around a circular path, we define a loop angle,  $\psi$ , to start at zero at the top of the path and increase moving in the direction of kite motion—this is clockwise for Makani systems when viewed looking downwind.<sup>18</sup> Making the simplification that an average kite speed,  $\bar{v}_k$ , is the average with respect to loop angle rather than to time, we can alternatively define  $\bar{v}_k$  as:

$$\bar{v}_k = \frac{1}{2} \left( v_{k_{max}} + v_{k_{min}} \right) \quad [47]$$

And we can define:

$$\Delta v_k = v_{k_{max}} - v_{k_{min}} \quad [48]$$

Combining these equations and solving for  $\Delta v_k$ , we then have:

$$\Delta v_k = \frac{2r_{loop} g k_{grav} \cos \theta_e}{\bar{v}_k} \quad [49]$$

The relationship between loop angle and kite speed for a constant  $k_{grav}$  fraction is nearly sinusoidal in shape. We'll make the simplifying approximation that it is, giving us:

$$v_{k_\psi} \approx \bar{v}_k - \frac{1}{2} \Delta v_k \cos \psi \quad [50]$$

We are now set up to find the average  $\zeta_v$  around the loop,  $\bar{\zeta}_v$  by using  $v_{k_\psi}$ . For simplicity, we'll also assume that all loop angles are evenly weighted,<sup>19</sup> making our solution for  $\bar{\zeta}_v$  for a strategy that varies around the loop with  $k_{grav}$ :

$$\bar{\zeta}_v \approx \frac{1}{2\pi} \int_0^{2\pi} \zeta_v \partial \psi = C_L \left( \frac{\bar{v}_k}{v_{w_{eff}}} \right)^2 \left( \frac{\Delta v_k^2}{8\bar{v}_k^2} + 1 \right) - C_D \left( \frac{\bar{v}_k}{v_{w_{eff}}} \right)^3 \left( \frac{\pi \Delta v_k^2}{8\bar{v}_k^2} + 1 \right) \quad [51]$$

<sup>17</sup> Note that the first equal sign in here simply represents a possible *strategy*, rather than a true equality. Later, we'll evaluate different average kite speed strategies under specific conditions, breaking this relationship.

<sup>18</sup> This loop angle definition differs from that in the crosswind controller.

<sup>19</sup> Ignoring that more time is spent in the slower portions of the loop than the faster ones.

This  $\bar{\zeta}_v$  is an approximation of the average  $\zeta_v$  for a given path size and elevation angle, accounting only for the effects of a varying speed strategy and tether drag.

It's useful to put this in terms of a power coefficient to isolate the effect of the kite speed strategy, so we do so by defining a power coefficient,  $C_{v_k}$ , as:

$$C_{v_k} = \frac{\bar{\zeta}_v}{\zeta_0 C_{TD}} \tag{52}$$

This definition is somewhat duplicative, requiring us to pull out  $C_{TD}$  after baking it in, but accomplishes the goal of isolating our power coefficients. Before attempting to combine the effect of pumping losses and a varying speed strategy, let's investigate this new term. Unlike other power coefficients derived above, this one has a sensitivity to wind speed. In figure 20, plotting  $C_{v_k}$  for different wind speeds and  $k_{grav}$  fractions for a kite with a loop radius of 80 m and elevation angle of 0.45 rad results in:

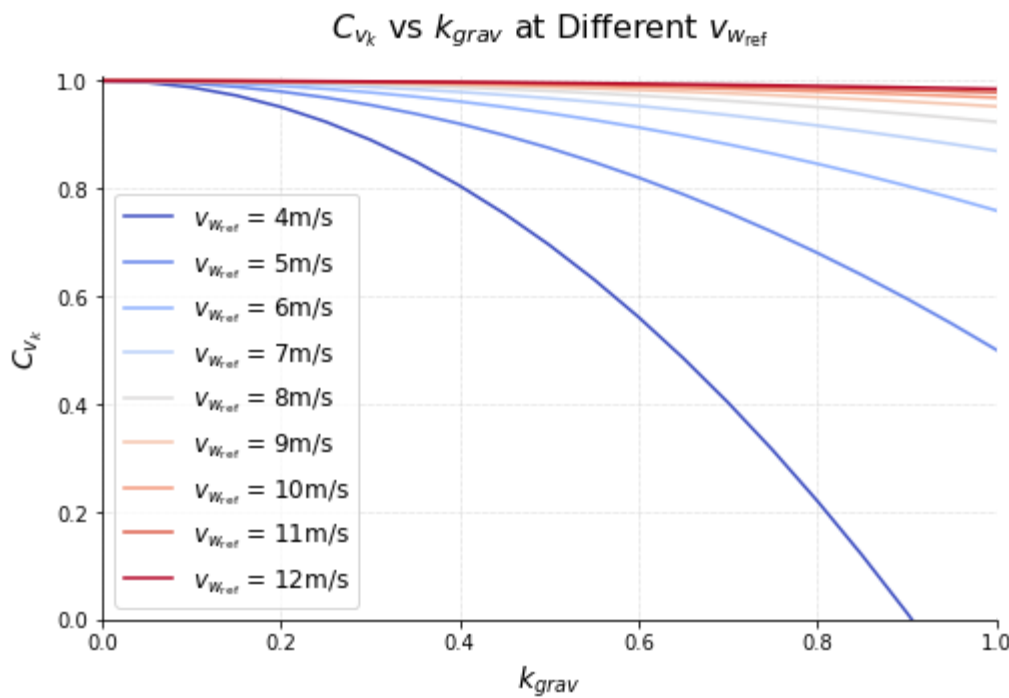


**Figure 20: Change in power coefficient  $C_{v_k}$  as a function of speed strategy  $k_{grav}$ . Low winds are highly sensitive to speed, and a varying strategy pays a large performance penalty.**

The effect of varying kite speed is particularly devastating at low wind speeds, even for these small loop sizes—the optimum kite speed forms a sharp peak, and the  $\Delta v_k$  for a given  $k_{grav}$  grows larger as  $\bar{v}_k$  gets slower at low wind speeds. In fact, higher  $k_{grav}$  fractions at low winds

are often impossible—inspecting the results will show that at some point large  $k_{grav}$  implies negative kite speeds. At low wind speeds, these effects push us towards a constant kite speed strategy, but we must also consider the pumping losses, so now is the time to incorporate those losses.

The rotor drag power (ie, thrust power before powertrain losses) fluctuation around the loop as a result of a given  $k_{grav}$  strategy can be approximated by taking the weight resisted by the rotor drag, assuming the rotors extract power along the inertial speed axis rather than the airspeed axis, and for simplicity, at  $\bar{v}_k$  rather than  $v_{k\psi}$  as a function of loop angle.<sup>20</sup>

$$P_{grav,\psi} = m_{eff,g} g (1 - k_{grav}) \bar{v}_k \sin \psi \cos \theta_e \quad [53]$$

For the no wind case, this is the only power. Let's plot it below for the MX2 kite at a  $\bar{v}_k$  of 40 m/s, an elevation angle of 0.45 rad (26 deg), and a  $k_{grav}$  of 0.5. We'll also plot the electrical power this results in. Since power changes sign, the definition of efficiency flips and we must multiply by  $\eta_{t2g}$  for positive power (generating) and divide by  $\eta_{t2g}$  for negative (consuming) power, resulting in:

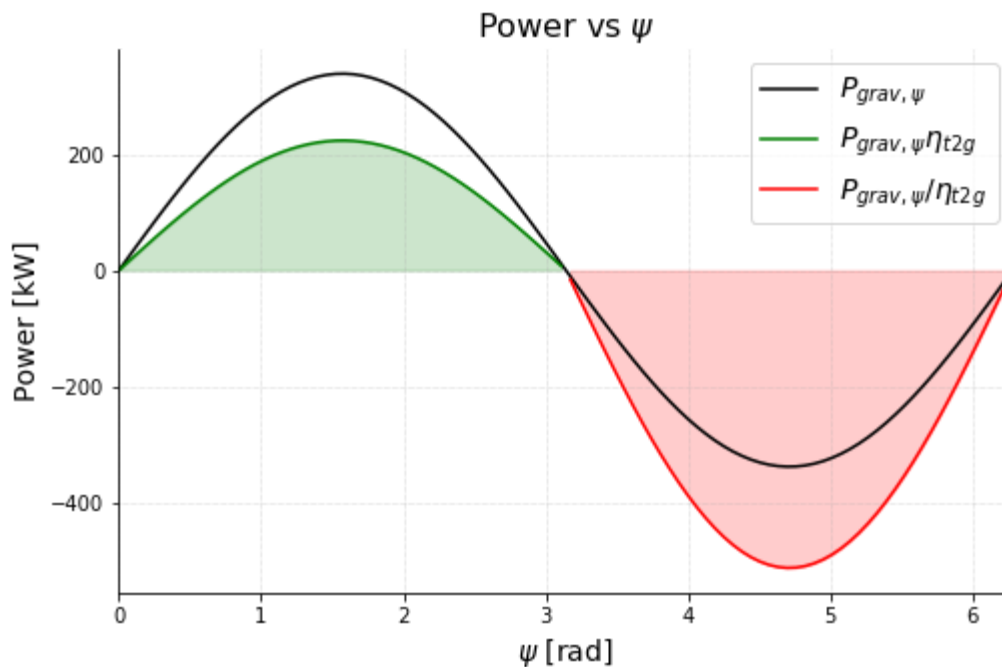


**Figure 21: Power vs loop angle, demonstrating the large swings in power resulting from the potential energy exchange at a  $k_{grav}$  of 0.5. Efficiency losses then mean the stored energy (green) is less than the consumed energy (red).**

<sup>20</sup> These assumptions have an impact of <1% for most kites and strategies, as verified from a numerical model. They distort the shape more than they distort the final result.

In figure 21, the shaded regions represent the energy stored (in green) and consumed (in red). Taking the difference between these two and normalizing by  $\Delta E_p$  gives us  $\eta_{pump_0}$  as in equation 43.

As the kite begins to make power from the wind, the power is offset, such that:

$$P = (P_{thrust} + P_{grav,\psi}) \eta \quad [54]$$

where  $\eta$  represents  $\eta_{t2g}$  inverted appropriately as the sum of the power flips sign (we don't bother naming this more specifically as we'll soon throw it out), and  $P_{thrust}$  is the power from the wind before any powertrain losses. We'll be defining this  $P_{thrust}$  more explicitly in section 6.2.4, in equation 80.

We can then approximate the pumping efficiency, again assuming all loop angles are weighted evenly (ie, ignoring that we spend more time at the slower top of the loop than the bottom), with  $P_{grav_{max}}$  representing the maximum power variation, found as  $P_{grav,\psi}$  with a loop angle  $\psi = \frac{\pi}{2}$ :

$$\eta_{pump} = \frac{\int_0^{2\pi} P - \int_0^{2\pi} P_{thrust}}{\Delta E_p}, \quad P_{thrust} < P_{grav_{max}} \quad [55]$$

When the condition is not met, where  $P_{thrust}$  is larger than the power variation, there is no pumping loss, and  $\eta_{pump} = 0$ . There's an exact analytical solution to be found here, but let's jump to a simpler approximate solution that can be shown to be close to numerical results.<sup>21</sup>

$$\eta_{pump} = \eta_{pump_0} \left( 1 - \sin \left( \frac{P_{thrust} \pi}{2 P_{grav_{max}}} \right) \right), \quad P_{thrust} < P_{grav_{max}} \quad [56]$$

As  $P_{thrust}/P_{grav_{max}}$  approaches 1,  $\eta_{pump}$  goes to zero. We're now ready to put our pumping losses into a new term. We begin by finding the average pumping power,  $P_{pump}^-$ , as the total energy lost around a path over the time around the path:

$$P_{pump}^- = \frac{\Delta E_p \eta_{pump} \bar{v}_k (1 - k_{grav})}{2\pi r_{loop}} = \frac{m_{eff,g} g \bar{v}_k (1 - k_{grav}) \eta_{pump} \cos \theta_e}{\pi} \quad [57]$$

The relationship is simple, and somewhat surprisingly independent of path radius, as increased energy losses of larger paths are then spread over more time.

<sup>21</sup> Absolute error of this simplification is typically  $\ll 0.05$ .

If it isn't yet readily apparent, our goal is put everything in terms of a geometric power coefficient to easily compare loss (and gain) factors, such that:

$$P = C_1 C_2 \cdots P_0 \quad [58]$$

Where  $C_1 C_2 \cdots$  are the various power factors. We can directly do this with other power coefficients as they all either attenuate the effective wind or our ability to make power from that wind. Pumping power does not attenuate effective wind, and instead is an additive term. As a result, we're looking for something to fulfill:

$$P = C_1 C_2 \cdots C_{pump} P_0 = C_1 C_2 \cdots P_0 + P_{pump} \quad [59]$$

Solving this for  $C_{pump}$  results in the following awkwardly roundabout definition, where  $C_{other}$  is all other geometric power factors:

$$C_{pump} = \left( 1 + \frac{m_{eff,g} g \eta_{pump} \bar{v}_k (1 - k_{grav}) \cos \theta_e}{\pi C_{other} P_0} \right) \quad [60]$$

As other losses build and  $C_{other}$  gets smaller,  $P_{pump}$  forms a larger part of the geometric power factors and  $C_{pump}$  gets smaller.

Let's investigate the product of these two power coefficients in isolation (ie,  $C_{other}$  is just  $C_{v_k}$ ) for various  $k_{grav}$  fractions and wind speeds. For the MX2 kite flying with an 80 m path radius at an elevation angle of 0.45 rad with an  $\eta_{pump_0}$  of -0.85 under no wind shear, we have figure 22.

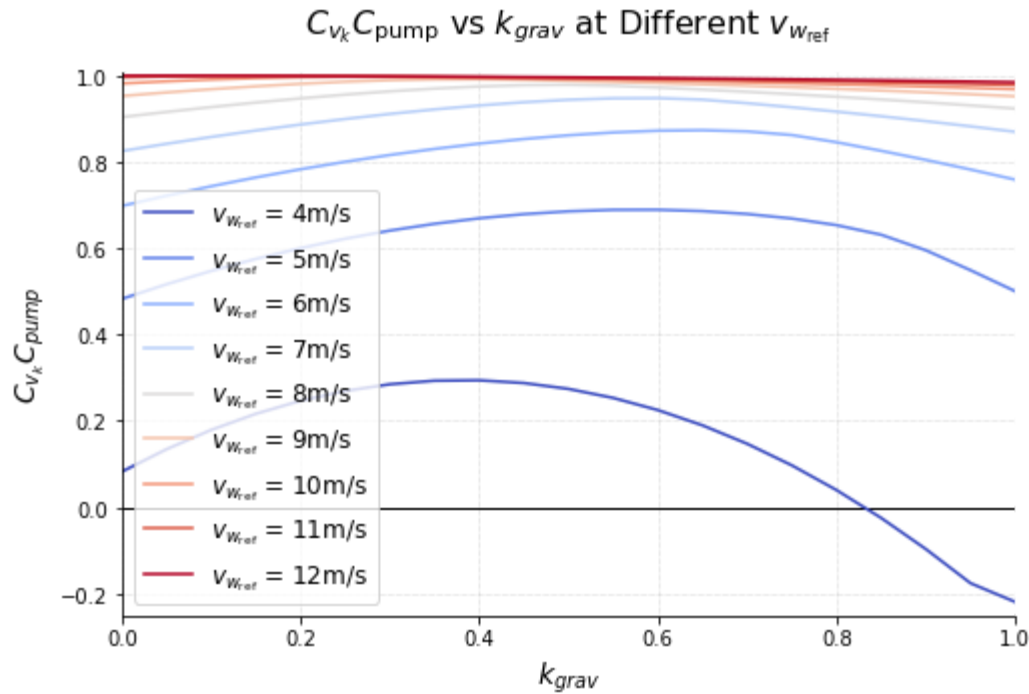


**Figure 22: The combined effect of speed and turning losses on power versus kite speed strategy  $k_{grav}$ . At low winds, performance suffers even with an optimum strategy balancing these losses.**

The end result is heavily detrimental to low wind speeds, and there is now no escaping it via low  $k_{grav}$  fractions. Kinks visible in the solution are where  $C_{pump}$  saturates at 1 as  $P_{thrust} > P_{pump, max}$  and pumping losses go to zero. Adding in additional losses ignored here increases the sensitivity to pumping losses, as  $C_{pump}$  becomes more dominant when total power is lower. This can shift the optimum to higher  $k_{grav}$  fractions.

Wind speeds  $> \sim 8$  m/s show a low sensitivity to kite speed strategy, and the ultimate  $k_{grav}$  strategy at moderate to high winds in real usage ends up being driven by other effects we've ignored here, such as power, airspeed, and tension constraints, the fact that the ideal kite speed is not constant for all path positions (path azimuth and elevation offset combine with wind speed and turning effort to make different effective wind speeds around the path), and that the rotor efficiency is not constant for all conditions. This simple model suggests that at high winds, a constant kite speed strategy is (slightly) better, but in more detailed models, optimized  $k_{grav}$  doesn't approach zero as winds increase, but instead climbs to 1 to address those constraints. We'll look into this strategy more in section 10.3.5.2.

The simplifications here still allow us to highlight the important lessons: moderate to high wind speeds are largely insensitive to kite speed strategy (as long as it's roughly centered on the optimum), while low winds require a tight compromise between pumping losses and off optimal speed losses. All strategies expect to see major losses at low winds, and the primary way to

improve performance is to turn *very* tight paths to reduce  $\Delta v_k$  in order to reduce non-optimal speed losses with higher  $k_{grav}$  fractions that reduce pumping losses.

### 6.1.7 Minimum Airspeed Losses

There is a minimum airspeed requirement for AWTs—the kite must at least be able to lift the mass of the kite and tether. This is often overshadowed by a minimum *controllable* airspeed, dependent on the desired control authority and size of the control surfaces.

As optimum mean kite speed increases linearly with wind speed, this minimum airspeed requirement hurts power production until the optimum airspeed is larger than the minimum. The mean effect of this airspeed constraint is easily investigated by revisiting our speed dependent  $\zeta_v$ , replacing the kite inertial speed with our minimum kite airspeed,  $v_{a_{min}}$ , approximating airspeed as kite inertial speed.

However, we already have a speed-dependent term in our power coefficient in the  $C_{v_k}$  term. It's possible for any speed-dependent term to go negative (ie, the system is now consuming rather than generating power), making combining them inappropriate—we need to incorporate this as a limit into the existing speed-based power coefficient. We desire the kite speed to be above the minimum speed, again approximating the airspeed limit as a kite inertial speed limit, such that:

$$\bar{v}_k - \frac{1}{2}\Delta v_k > v_{a_{min}} \quad [61]$$

If  $\bar{v}_k$  and  $\Delta v_k$  is such that this constraint is not met, we can solve for the  $\bar{v}_k$  that would meet the prescribed  $k_{grav}$  and speed limit:

$$\bar{v}_k = \frac{1}{2} \left( \sqrt{v_{a_{min}}^2 + 4 r_{loop} g k_{grav} \cos \theta_e} + v_{a_{min}} \right), \quad \bar{v}_k - \frac{1}{2}\Delta v_k < v_{a_{min}} \quad [62]$$

This  $\bar{v}_k$  is then substituted in place of  $v_{k_L}$  where the condition is met.

### 6.1.8 Tension Limiting Losses

Structural loads and therefore mass of both the kite and tether scale strongly with tension, so a small drop in  $\zeta$  may be justified if it carries a large drop in tension, enabling a larger kite such that the product  $\zeta S$  is larger.

If we again make the approximations that  $F_T \approx F_L$ , that  $v_a \approx v_k$ , that the kite is operating at the optimum speed  $v_{k_L}$ , and ignore the speed variations we just introduced around the path with our

$k_{grav}$  fraction,<sup>22</sup> then we can plug our expression for  $v_{k_L}$  into the equation for  $F_T$  in equation 13 and solve for the wind speed to find the tension limiting effective wind speed at the kite,  $v_{w_{eff},Tmax}$  :

$$v_{w_{eff},Tmax} = \sqrt{\frac{2F_{Tmax}}{3\rho S\zeta_L}} \quad [63]$$

Once a kite reaches its tension limit, it can maintain this tension by either lowering its  $C_L$  as kite speed increases, or by limiting increases in kite speed. From the Loyd fundamentals, we can find that the thrust power at the tension limit is equal to:

$$P_{Tmax} = F_{Tmax}v_{w_{eff}} - \frac{1}{2}\rho C_D S v_k^3, \quad v_{w_{eff},Tmax} < v_{w_{eff}} \quad [64]$$

From this relationship, it becomes apparent that maintaining tension by reducing lift and capturing the resultant drop in drag would be the better option, but in practice doing this extensively is difficult. Normal optimal operation for most systems has the kite operating at or close to its maximum lift coefficient, making peak tension loads more a function of kite speed than of lift coefficient. Flying faster and limiting loads via control of  $C_L$  becomes increasingly risky—as loads increase with  $v_a^2$ , the kite may need to maintain excess control margin in order to prevent an overload, so the simpler solution is to limit speed. Since any tension limiting represents a loss of power, we likely want the tension limiting point to be shortly before the power limited point anyways, so the simpler solution won't be too penalizing since we won't progress far enough into tension limiting to make large drag reductions.

Assuming kite speed,  $C_L$ , and  $C_D$  are held constant past the first point of tension limiting (ie, tension is controlled with kite speed), we can find the following simple relationship for power in the tension limited regime:

$$P_{Tmax} = F_{Tmax} \left( v_{w_{eff}} - \frac{2}{3}v_{w_{eff},Tmax} \right), \quad v_{w_{eff},Tmax} < v_{w_{eff}} \quad [65]$$

From this equation, the effect of a tension limit is clear—once the limit is reached, power ceases to increase with  $v_w^3$  and instead simply increases linearly.

For a constant lift coefficient, the above is functionally a maximum kite speed constraint, and it's tempting to incorporate it similarly to how we did for the minimum airspeed constraint, rolling it into the kite speed strategy term,  $C_{v_k}$ . However, this can become very constraining and difficult to incorporate analytically—large  $k_{grav}$  fractions and path sizes can hit both the minimum and

<sup>22</sup> The inclusion of varying speed around the loop makes an analytical approach to power difficult—constraints like this are more readily captured via numerical models.

maximum kite speeds and aren't viable strategies, creating analytical potholes that are annoying to fill. In recognition of the fact that a kite can tolerate some speeds higher than the first tension limited kite speed via reduced lift coefficient, we instead make a new term, and as an approximation attenuate power simply based on the mean kite speed. A new speed dependent term is acceptable as we shouldn't be concerned about sign flips this late into the power curve.

To do so we normalize by our baseline power,  $P_0$ . Again, we need to back out any duplicated terms accounted for in this definition—in this case, the elevation, wind shear, and tether drag power coefficients. Our new power coefficient becomes less than 1 once  $v_{w_{eff},Tmax} < v_{w_{eff}}$ , so rather than needing to define the start of this regime in terms of a wind speed, we can define it as:

$$C_{Tmax} = \min \left( \frac{F_{Tmax}(v_{w_{eff}} - \frac{2}{3}v_{w_{eff},Tmax})}{P_0 C_{\theta_e} C_{\alpha_w} C_{TD}}, 1 \right) \quad [66]$$

### 6.1.9 Putting It Together

At last we can piece together our power coefficients to define a total mean power for an AWT with all losses, referenced to  $P_0$ :

$$P_{AWT} = C_{TD} C_{\theta_e} C_{\alpha_w} C_{turn} C_{\eta} C_{v_k} C_{pump} C_{Tmax} P_0 \quad [67]$$

We'll also define a coefficient that captures all the factors together, for easy reference:

$$C_{all} = C_{TD} C_{\theta_e} C_{\alpha_w} C_{turn} C_{\eta} C_{v_k} C_{pump} C_{Tmax} \quad [68]$$

This power equation has several terms that are poorly defined when  $C_{all}$  becomes negative (ie, rather than generating power, the system is *consuming* power), so we'll truncate all results to positive regions only. This is fine, as an energy system that consumes power is a novel, but generally uninteresting, idea.

We're left with a lot of variables to potentially optimize over, so let's limit ourselves mostly to variables that describe *how to fly* a given kite. We'll lock in our kite as the simplified MX2 system described above, flying at its target lift coefficient with zero side lift, only varying the tether length.

This leaves us with a pleasantly short list:  $\theta_e$ ,  $k_{grav}$ ,  $r_{loop}$ , and  $l_t$ . This list can be made shorter by recognizing how strong of an effect  $\theta_e$  has on  $C_{\theta_e}$  and  $C_{\alpha_w}$  and how weak of an effect it

has on everything else. This allows us to use the  $\theta_{e_{ideal}}$  derived above in equation 30 as long as it is above the minimum height specified in equation 25. The kite should be operating at the ideal elevation angle for the current wind shear, as long as it's not constrained by the minimum altitude. This means that the best achievable elevation angle,  $\theta_{e_{best}}$ , should be:

$$\theta_{e_{best}} = \max(\theta_{e_{min}}, \theta_{e_{ideal}}) \tag{69}$$

As a brief aside, we need to address that the solution for  $\theta_{e_{ideal}}$  assumes zero tower height. If we revisit the derivation and include terms for tower height, an algebraically messy solution for best  $\theta_{e_{ideal}}$  can be found (not shown here, as things are already messy enough). The difference between the more accurate solution and the simplified form above is most pronounced at short tether lengths, high shear, and tall towers, so we compare the solutions at a short tether length of 300 m and relatively high shear of 0.2 to find:

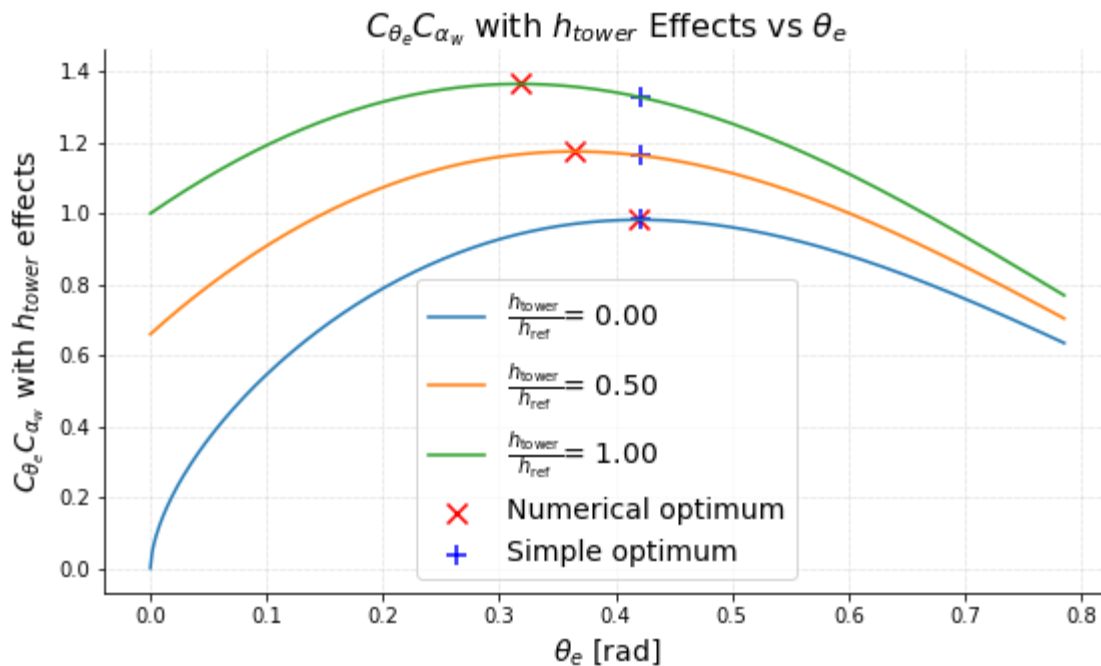


**Figure 23: Comparing the simple analytical solution for  $\theta_{e_{best}}$  in the context of maximum elevation and shear power coefficients. The simpler solution, even perturbed far from the zero tower height case it was derived, performs well enough.**

Even under these pessimistic conditions, the difference between the simplistic solution and the full solution is an elevation angle difference of  $\sim 0.1$  rad, and more importantly, a  $C_{\theta_e} C_{\alpha_w}$  difference of just under 3% if we use the naive solution for  $\theta_{e_{ideal}}$  with very high tower heights equal to the reference height. Less shear, shorter towers, or longer tethers will increase accuracy. With this in mind, we'll continue with the simpler form moving forward.

We now optimize  $k_{grav}$  and  $r_{loop}$  for various tether lengths<sup>23</sup> under zero wind shear conditions and a standard sea level air density of  $1.225 \text{ kg/m}^3$ , and for reasons that will soon be clear, begin the discussion by showing  $r_{loop}$  for the resulting optimized solutions:

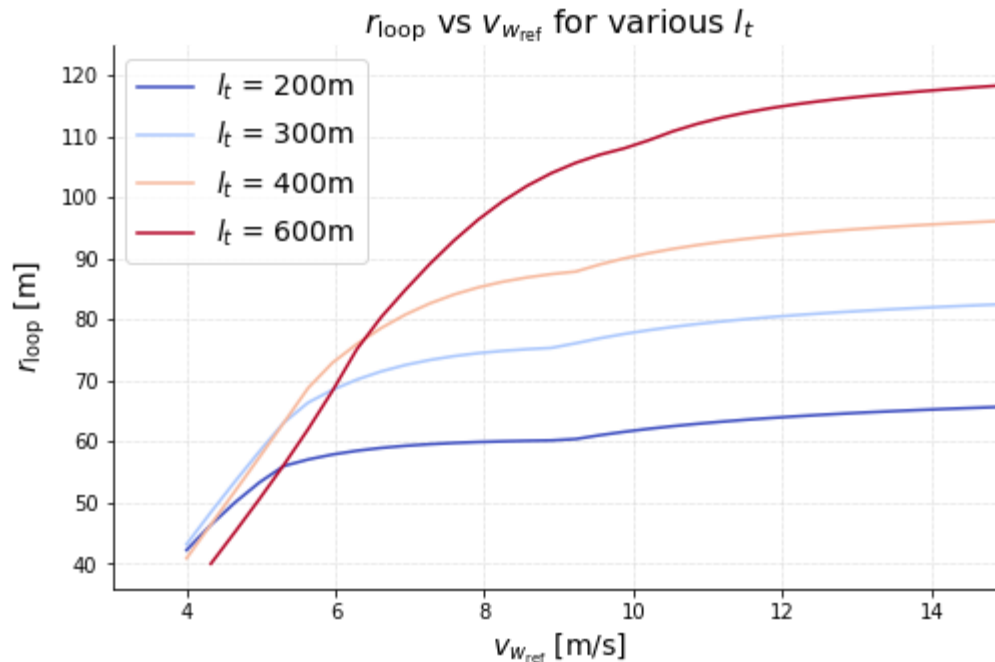


**Figure 24: Numerical optimization results for  $r_{loop}$  versus wind speed for the MX2 system using our analytical model.**

There are three regions of the optimum—a steep initial portion at low winds, and a flatter portion divided by a kink. In the steep initial portion, the kite seeks a very tight loop with large turning losses to support a high  $k_{grav}$  in order to eliminate even larger pumping losses. The small path size is effective at reducing speed variations, as  $k_{grav}$  for all solutions at low wind speeds are essentially equal to 1 in order to entirely eliminate pumping losses.

As the threat of pumping losses diminishes,  $k_{grav}$  decreases, and we enter the flat region, where we simply find the best trade between speed losses, elevation losses, and turning losses. As the sensitivity to speed variations diminishes at higher winds, the optimum path radius slowly increases to reduce turning losses. The kink is caused by the onset of tension limiting losses, which then changes that trade-off. As other losses diminish, the lines slowly trend towards the  $r_{loop_{ideal}}$  derived above in equation 37 in the context of turning losses alone, but generally stay well below that idealization in order to further reduce other losses.

<sup>23</sup> In an attempt to be perhaps too kind to longer tethers and keep things simple, we only change the tether length. Tether mass and  $\eta_{t2g}$  remain constant at their values shown in table 1 in all examples to follow. It makes no meaningful difference in our conclusions, as we'll soon see that tether drag alone makes long tethers unappealing, even in favorable situations.

However, the important thing to note is how *staggeringly* tight these paths are. With a minimum path radius of  $\sim 50$  m, and given that this denotes the center of a kite with a  $\sim 25$  m wingspan, the inner wingtip is a scant 1.5 wingspans from the path center!

A path radius this tight is simply not particularly feasible, at least not for heavier rigid wing onboard power generation systems. We'll investigate this further in section 6.2.1, Minimum Turning Radius Constraints. Even if a turning radius that tight is possible, the swept area will be so small that induced losses, which we'll soon discuss, will be meaningful. In addition, tight paths require high angular rate maneuvering that generates large aerodynamic moments, requiring large control surfaces and precise control that pose additional challenges.

For now, we'll simply constrain our path radius<sup>24</sup> for the MX2 system to a more reasonable but still tight minimum  $r_{loop}$  of 80 m and repeat the exercise (resulting in most cases riding this minimum turning limit), this time plotting in figure 25 what we're really interested in, the power curves:

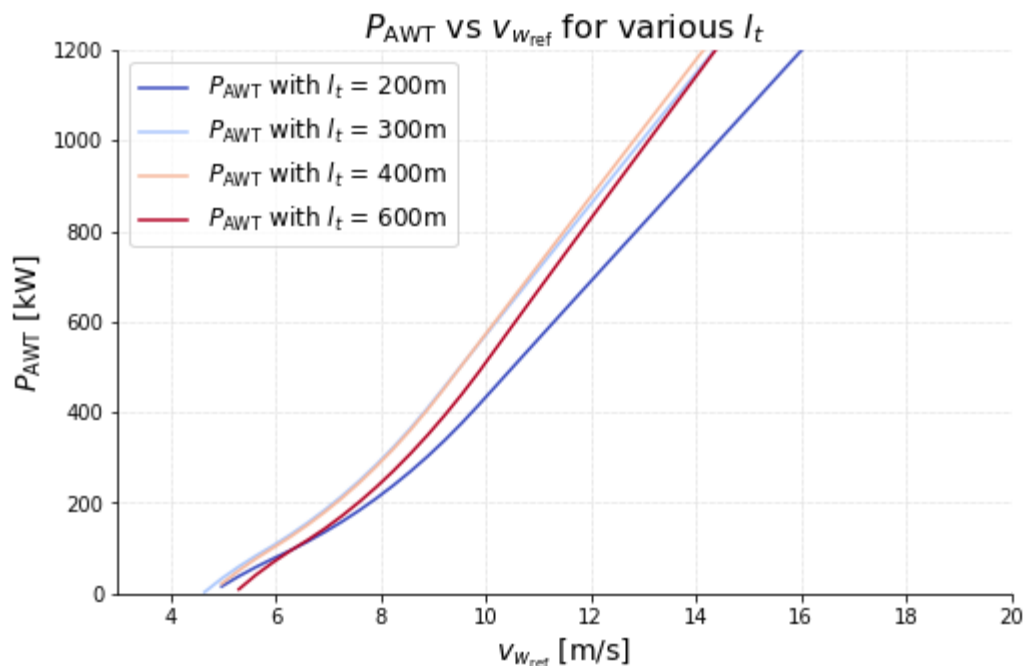


**Figure 25: Power curves from the analytical model, numerically optimized over  $r_{loop}$  (with a minimum of 80 m) and  $k_{grav}$  for the MX2 system. Curves are not yet clipped at rated power.**

Keep in mind we haven't yet clipped the power at the power system's max capabilities to create a rated power region. For most systems and sites, this should be occurring at 9-12 m/s of wind. From figure 25, an optimum tether length becomes apparent—too short, and the elevation

<sup>24</sup> These are some reasons we have an  $r_{loop, min}$  for our example systems in table 1. The M600 has additional reasons for its minimum turning constraint, namely bridling and stability concerns, discussed in the M600 Energy Kite article [11].

losses from meeting the minimum altitude constraint dominate. Too long, and the tether drag reduces performance.

We can also see, in figure 26, how the total power coefficient changes with wind speed:

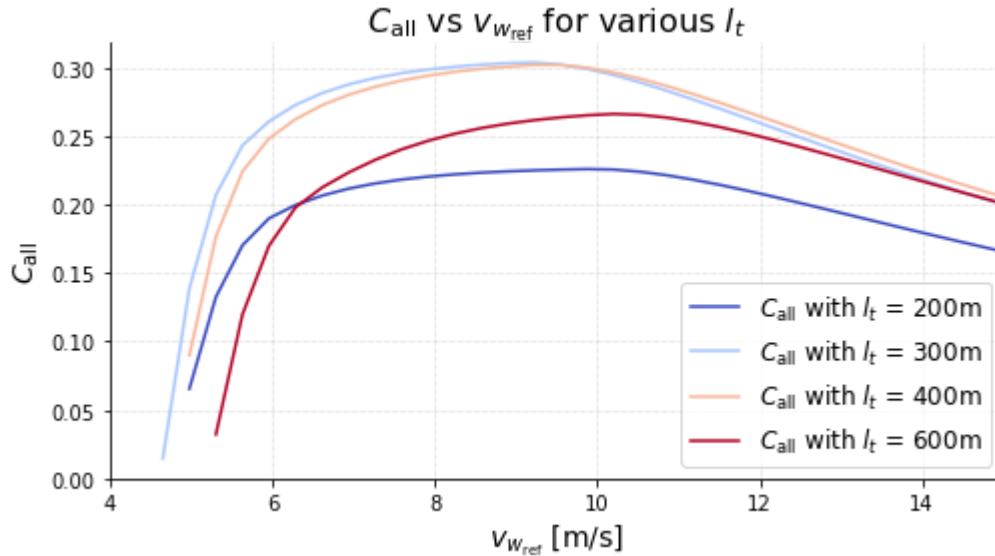


**Figure 26: Product of all power coefficients, referenced to  $P_0$ , for our optimized analytical model for the MX2 under zero wind shear.**

At best, our AWT is able to capture ~30% of the idealized  $P_0$  power. The  $C_{v_k}$  (which includes the effect of our minimum airspeed constraint) and  $C_{pump}$  terms act to create a virtual wall at low wind speeds. When there is little power available in the wind, the minimum airspeed requirement dominates the problem, and the airborne wind turbine simply becomes an airborne aircraft, consuming rather than generating power. It's difficult to imagine an AWT with an earlier cut-in than a HAWT in the absence of strong wind shear, due to the power offset imposed by a minimum kite speed.

Inspecting the breakdown of the various coefficients for our optimal 300 m tether case finds the following in figure 27.

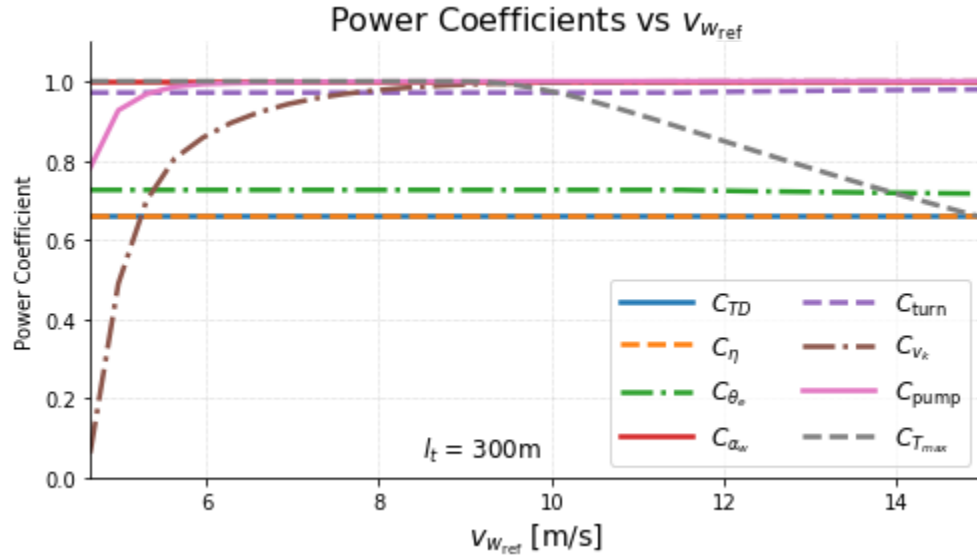


**Figure 27: Individual power coefficients referenced to  $P_0$  for our optimized analytical model for the MX2.**

The majority of the losses are captured with three constant and comparable losses: the tether drag, powertrain efficiency, and elevation angle losses, while the kite speed and tension losses round out the low and high wind speed losses, respectively (with a little bit of pumping losses at low winds as well). At this tether length and path radius constraint we see little in the way of turning losses, but longer tethers have optimal  $C_{turn}$  at much larger path radii, making the compromise between turning losses and other losses more pronounced.

What about higher wind shears? Repeating the exercise again, but for a “standard” wind shear of  $1/7 \approx 0.143$  and a reference wind height of 80 m results in figure 28.

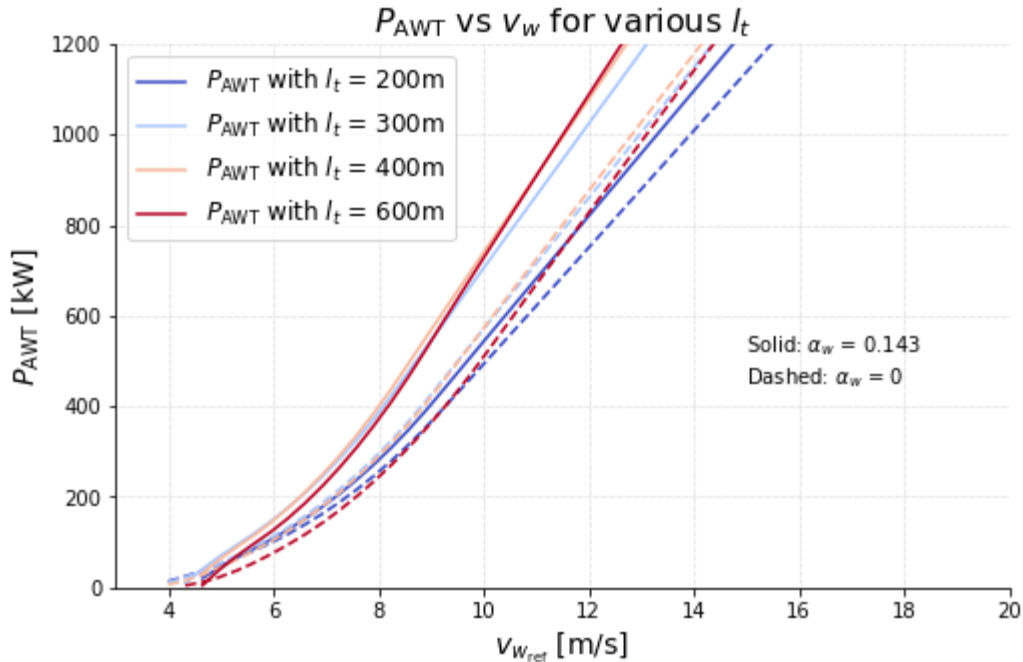


**Figure 28: Optimized analytical model power estimates for the MX2, comparing “normal” wind shear of 1/7 (solid lines) vs no wind shear (dashed lines) at various tether lengths.**

As AWTs have higher virtual hub heights than typical HAWT hub heights, they see a large sensitivity to higher wind shears. Interestingly, longer tethers and the stronger, higher altitude winds they access don't seem to translate into additional power, even with our simplistic tether loss factor that only models the increased drag. Considering those additional losses, shorter tethers around 300 m seem likely to be the best for all conditions. We'll investigate the reasons behind this in a later section.

Finally, we'll compare these results with the results from the more detailed numerical model. A deeper dive into the numerical model results is shown in the power saturation section and in the provided code tools, but here we'll just jump straight to the result. Updating the analytical model to a 90 m path radius to match the increased conservatism applied in the numerical model and using a  $k_{grav}$  of 0.7 to roughly match the speed strategy from the other model results in the comparison in figure 29 under zero wind shear at sea level conditions.

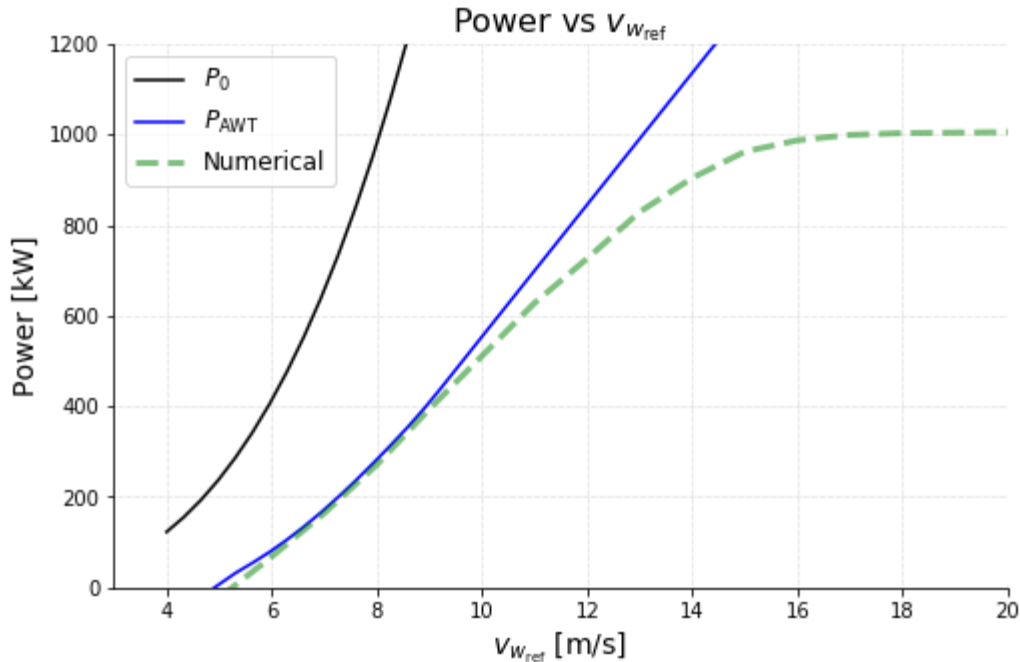


**Figure 29: Comparison of optimized analytical model result for the MX2 versus optimized numerical model. The analytical model fares well until power and tension constraints become significant.**

The analytical model has done well at capturing the major loss factors and the trades between them. We see a slow roll-off in performance as the kite begins to blend in power saturation strategies in the numerical model, rather than a sharp cutoff—again, we’ll investigate power saturation further in section 10a later section.

There’s much to glean from the models we’ve just created. Let’s see what we can learn, and how those lessons can apply to different kite designs.

## 6.2 Lessons from Loyd Revisited

### 6.2.1 Minimum Turning Radius Constraints

Our analytical model shows a strong preference for small path sizes, but there are both hard and practical constraints on minimum path size.

The hard constraint occurs when the kite simply cannot generate enough lift to make the desired turn, regardless of roll angle. This is the traditional minimum turning radius limit for un-tethered aircraft that are unconstrained in roll.

The practical constraint unique to AWEs is one of tether roll angle,  $\gamma$ , defined as the angle between the tether and the kite's pitch axis—at some limiting tether roll angle, the tether will hit parts of the kite for most designs.

Revisiting figure 15, we can find an approximation for this tether roll angle. This differs from the actual kite to tether roll angle due to the small angle approximation inherent in flattening the problem to a plane, the effects of the aerodynamic alpha and beta angles of the kite, and the effect of tether catenary from tether acceleration, weight, and drag. Fortunately, all these angles are typically small, making these decent approximations.

When we solved for  $\theta_{offwind}$  before, we were just looking for the mean effect. For roll limits it's desirable to keep some complexity and add a few more terms to capture major effects that cause roll angle to vary around the loop, to determine if limits are hit anywhere. Those major effects are the difference between  $v_a$  and  $v_k$ , and the component of gravity that can either help or hurt the required turning effort at the top and bottom of the loop.

Solving for the force balance in the crosswind plane, perpendicular to the flight path axis, we have:

$$\sum F_{\perp} = F_{L_{\perp}} + F_{T_{\perp}} + F_{c_{\perp}} + F_{w_{\perp}} + F_{Y_{\perp}} = 0 \quad [70]$$

Where the side lift and weight perpendicular to the path axis are given by:

$$F_{Y_{\perp}} = F_Y \cos(\varphi_{halfcone} - \gamma) \quad [71]$$

$$F_{w_{\perp}} = -m_{eff,g} g \cos \theta_e \cos \psi \quad [72]$$

Assuming the path is directly downwind in azimuth and only offset by some elevation angle, we can solve for  $v_a$  as a function of wind speed at the kite virtual hub height, kite speed, and loop angle by solving the side-angle-side triangle that results:

$$v_a = \sqrt{v_k^2 + v_{w_{vh}}^2 - 2v_{w_{vh}}v_k \cos\left(\frac{\pi}{2} - \sin(\psi\theta_e)\right)} \quad [73]$$

This allows us to avoid using the  $v_a \approx v_k$  assumption we've used extensively until now, and  $v_a$  can be used for the aerodynamic forces  $F_L$  and  $F_Y$  above rather than the  $v_k$  approximation.

Expanding equation 70 above results in equation 74.

$$\sum F_{\perp} = 0 = \frac{m_{eff,a} v_k^2}{r_{curv}} - \frac{r_{loop}}{l_t} F_L \frac{\cos(\varphi - \gamma)}{\cos \varphi} + F_L \sin(\varphi - \gamma) + F_Y \cos(\varphi - \gamma) - m_{eff,g} g \cos \theta_e \cos \psi \quad [74]$$

We can break out the reading glasses to see how this lengthy, shrunken equation can be numerically solved for tether roll angle if we wish, but it's desirable to have a simpler, shorter analytical solution, so some substitutions are in order. Assuming the kite is operating close to the ideal turning radius derived above,  $\cos(\varphi - \gamma) \approx 1$  and  $\sin(\varphi - \gamma) \approx (\varphi - \gamma)$ . These changes allow us to directly solve for tether roll angle  $\gamma$ .<sup>25</sup>

$$\gamma = \frac{m_{eff,a} v_k^2}{F_L r_{curv}} - \frac{r_{loop}}{l_t \cos \varphi} + \varphi + \frac{F_Y}{F_L} - \frac{m_{eff,g} g \cos \theta_e \cos \psi}{F_L} \quad [75]$$

Now that we have a model, let's investigate. We begin with a constant kite speed strategy with  $k_{grav}$  of zero to isolate the effects of gravity and the difference between kite inertial speed and airspeed. We take our MX2 system operating at its best achievable zeta lift ( $C_L = 1.81$ ,  $C_Y = 0$ ), with a path radius of 80 m at an elevation angle of 0.45 rad at a reference wind speed of 8 m/s and no shear, and in order to isolate effects, model the tether roll angle both with and without gravity. Here, we assume the instantaneous radius of curvature,  $r_{curv}$  is equal to the mean path radius,  $r_{loop}$ , and use a simple constant kite speed strategy with a  $k_{grav}$  of zero:

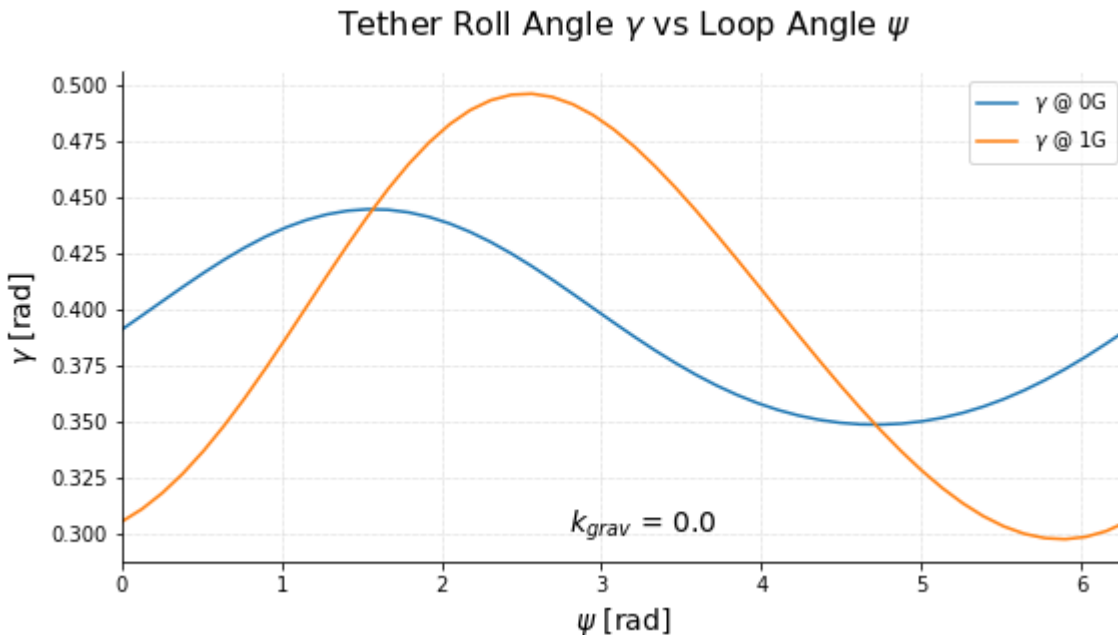


**Figure 30: Tether roll angle versus loop angle at 8 m/s of wind at a path radius of 80 m and elevation angle of 0.45 rad, both with and without gravity to isolate its effect.**

<sup>25</sup> This is functionally the same method used in the controller to convert a desired path curvature into a tether roll angle command. The only difference is that the controller has additional corrections to account for total path offset (elevation and azimuth).

The curve without gravity is purely a result of the elevation angle that causes the up and down strokes of the path to move the kite into and out of the wind, respectively. Gravity assists the required turn at the top of the path, and adds to the required turning effort at the bottom, so gravity adds to the required tether roll range and shifts the peak roll effort towards the bottom of the path. The maximum turning effort is generally in this overlap region where the kite is moving downwind near the bottom of the loop, simultaneously reducing the airspeed needed to make lift while gravity increases the lift needed to make the turn. This is problematic. The maximum turning constraint occurs with the kite pointed at the ground!

Let's look, in figure 31, at the limits of the tether roll angle versus wind speed for various  $k_{grav}$  speed strategies, using the model from equation 50 for speed as a function of loop angle,  $v_{k_{\psi}}$ , assuming  $\bar{v}_k$  is the optimal speed  $v_{k_L}$  and again using our example MX2 kite and path setup as above:

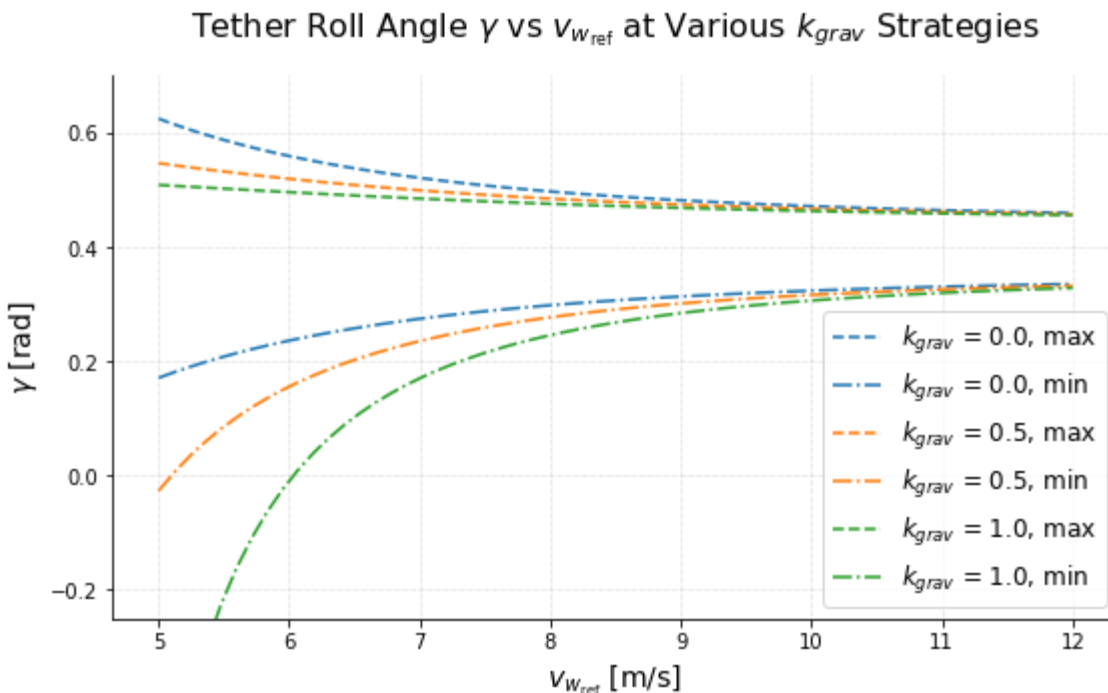


**Figure 31: Tether roll angle versus wind speed for various  $k_{grav}$  strategies. We've assumed the kite is operating centered around its optimal kite speed, effectively showing that as the kite speeds increase with wind speed, the required tether roll range decreases.**

As the wind speed increases and the optimum kite speed strategy linearly increases with it, the aerodynamic forces take over, scaling with  $v_w^2$  while gravity remains constant, causing the curves to asymptotically approach the no-gravity case. Counterintuitively, going faster *reduces* the maximum tether roll angle, and is comparatively easier.

We can now explore the limits of this kite. The MX2 hits physical limits at roll angles of approximately 55 deg. Leaving a 10 deg margin places our limit at 45 deg, or 0.785 rad. We want to find the worst case instantaneous turning radius,  $r_{curv}$ , around the path. In other words, for a kite that is following the prescribed circular path  $r_{loop}$ , how much turning margin does it have to correct control errors? What is the tightest it could turn at the maximum roll angle?

To find this, we return to the sum of the forces perpendicular to the path axis and solve for instantaneous curvature,  $r_{curv}$  at the tether roll limit, again taking our path setup from above. We find a weak sensitivity to the  $k_{grav}$  strategy, but a strong one to both wind speed (largely because in our kite speed is a linear function of wind speed) and lift coefficient, so varying those while  $k_{grav}$  is fixed at 0.75 and finding the worst case turning radius around the loop at our maximum roll results in figure 32:

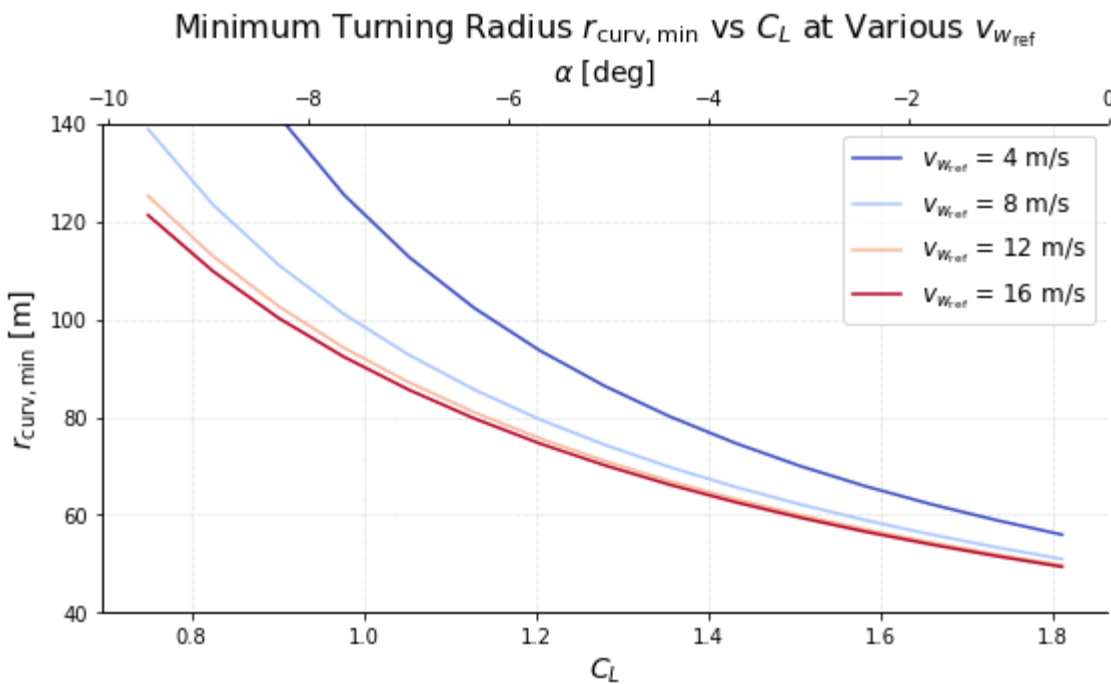


**Figure 32: Minimum instantaneous turning radius versus coefficient of lift at a constant path radius of 80 m. The difference between the path radius and the minimum instantaneous radius is the turning margin.**

We find that the MX2 flying prescribed 80 m radius circular paths at the target  $C_L$  of 1.81 is surprisingly close to its minimum turning radius at the worst part of the path, pointed nearly directly at the ground. An alpha control error of just a few degrees can leave the kite with little excess turning capability for path correction.

In this context, being able to make this turn while operating optimally appears possible with sufficient margin, but highlights the need for precise control, particularly in the portion of the

path where the kite is moving both downwind and at the ground. The limits shown here will be revisited when we look at power saturation, as they pose a larger problem as the need to also limit power via reduced lift arises at high wind speeds.

Before moving on, there are several assumptions we've baked in that should be reviewed. We've thus far assumed circular or close to circular paths. Horizontally oriented figure eight paths with downstrokes on the cross can alleviate at least the combination of simultaneously moving downwind and pointed steeply at the ground. Moving the sides of the path further out by either ovalizing the path or flying horizontal figure eights can get additional turning assistance from the tension, but wider paths also increase the required tether roll angle, so the net effect is typically a small increase in turning margin for increased power losses. With shorter tether systems, these minimum turning radius constraints require figure eight paths to cover a wide span of azimuth, and these power losses can be substantial. A system designed to fly these paths needs to be designed around a longer tether.

### 6.2.2 The Push for Tighter Loops

Small path radii are clearly beneficial in reducing gravity losses, but for this section we'll remove those losses and just look at losses directly dependent on  $r_{loop}$  that are independent of wind speed.

Taking the values for our MX2 system as defined in table 4, we use our model to create this non-generalized result for  $C_{\theta_e} C_{turn} C_{\alpha_w}$  as a function of path radius and tether length, in figure 33.

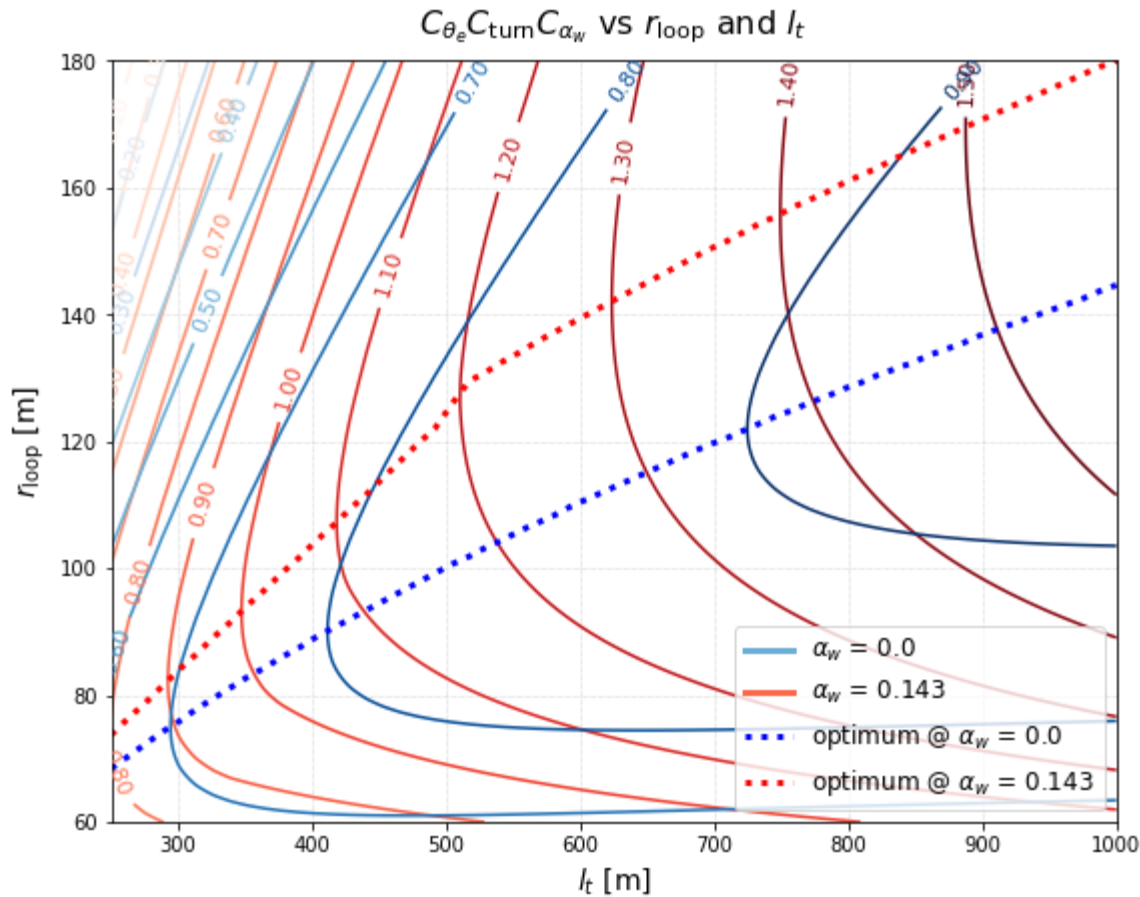


**Figure 33: Contours of combined power coefficients representing the effects of elevation losses, turning losses, and wind shear gains for different path radii and tether lengths, under conditions of both no shear (blue lines) and shear of 1/7th (red lines). Optimal path radii curves are highlighted.**

There’s a relatively sharp optimum in the path radius for a given system and tether length, especially at zero shear or shorter tether lengths. Following the line of best path radius, we see a kink in the positive wind shear case as the optimum switches from being constrained by minimum altitude to being allowed to track the best mean elevation for this shear, at which point the power becomes less sensitive to larger loop sizes. Under zero shear, this switch never occurs, so optimums shift to smaller path radii in an attempt to lower the mean elevation as much as possible.

Gravity losses ( $C_{pump}$  and  $C_{v_k}$ ) push the optimum tighter than that suggested here, but optimal radii remain small even without those effects. A much lighter kite, enabled perhaps by using a ground-based power system rather than an onboard power system, would see optimums shift to even tighter path radii, as the turning loss is diminished—a lighter kite needs less roll angle to make the same turn and  $r_{loop_{ideal}}$  will occur at smaller path sizes.

At a shear of 1/7, a combined coefficient  $> 1$  is still possible, meaning that despite the elevation angle and turning losses, it's still possible for the system to achieve more power by accessing higher winds than the same system directly downwind with no turning losses at the reference wind height. The increased drag of the tether is responsible for flattening this effect, something we'll dig into more in the next section.

An alternative approach to ever tighter loops is to increase the tower height. This should be approached carefully, given that AWEs have half the tension efficiency per unit power as HAWTs,<sup>26</sup> and the relative lack of overturning moments from short towers is the key offshore advantage of AWTs—enabling smaller, simpler platforms. However, cost models indicate that tower costs for a permanent installation are a tiny fraction of total LCOE ( $\sim 2\text{-}3\%$ ), so some additional expense here is warranted.

There's a similar sensitivity to changing tower height or minimum altitude.<sup>27</sup> We find that the change in power is approximately linear for changes of approximately  $\pm 30$  m in the above example, so pulling out the mean sensitivity for different tether lengths for a system with a minimum altitude of 80 m, a higher than normal tower height of 30 m, and a path radius of 80 m under conditions of zero wind shear gives us figure 34.

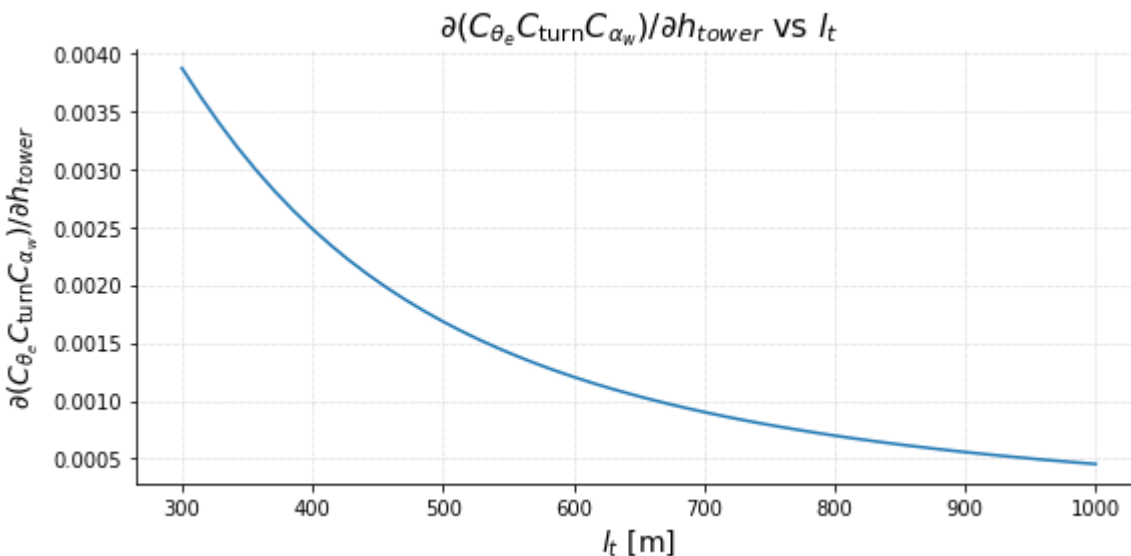


**Figure 34: Sensitivity of a subset of power coefficients to changing tower height (or minimum altitude) versus tether length.**

This system sees  $\sim 0.28\%$  change per meter of tower, making an 11 m increase in tower height or (reduction in minimum altitude) a relatively easy  $\sim 3\%$  gain in power.

<sup>26</sup> Discussed in section 6.2.4.

<sup>27</sup> Identical for zero shear conditions.

### 6.2.3 Higher Power from Stronger Winds at Altitude?

The increased performance by accessing higher, stronger winds at higher altitudes makes a seemingly strong case for AWTs, and this is amplified when looking at a  $C_{\theta_e} C_{turn} C_{\alpha_w}$  subset of power coefficients we plotted above in figure 33—despite elevation and turning losses, long tethers in moderate shear can give power up to 1.5 times  $P_0$ !

This effect wasn't present in the initial summary, where longer tethers at high wind shear were a wash. We pointed to the tether drag as the culprit, so let's repeat the exercise from the tighter loops section, again looking only at subset of power coefficients that are independent of wind speed (just for simplicity), but this time adding in the  $C_{TD}$ .

With this model, we revisit the sweep from before, but this time rather than showing all  $r_{loop}$ , we'll solve for the optimum for each tether length, resulting in the best total coefficient for a given tether length, in figure 35.

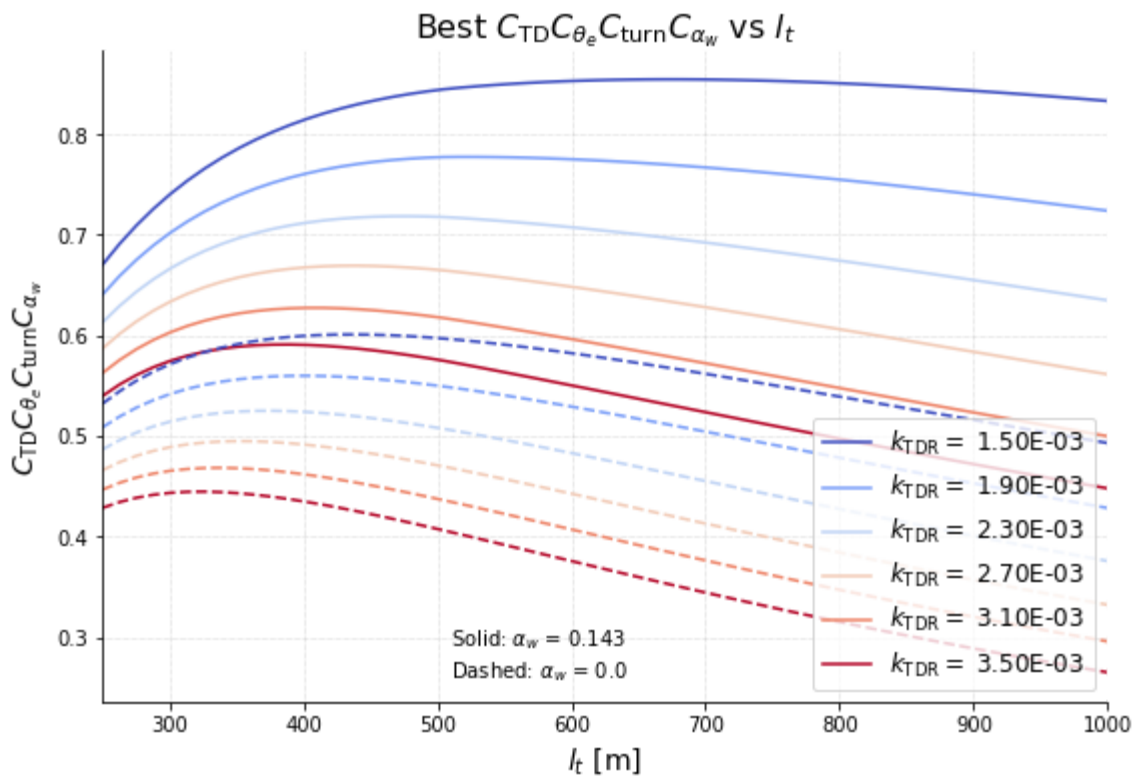


**Figure 35: Best possible (via optimized  $r_{loop}$ ) power coefficients representing tether drag, elevation, and turning losses with shear gains versus tether length. Various tether drag ratios,  $k_{TDR}$ , are shown, under conditions of shear (solid lines) and no shear (dashed lines).**

There are some key takeaways from this plot:

- All values are less than one.
  - The elevation, turning, and tether drag losses offset gains from accessing higher winds via longer tethers for all design points shown here.
- Power factor and ideal tether length are heavily impacted by wind shear and tether drag.
  - Low wind shears and low tether drag ratios prefer shorter tethers.
  - High wind shear and high tether drag ratios prefer longer tethers.

Figure 35 also effectively states that *the tether is almost always unsuccessful as a tool for a wing to create more power from stronger, higher winds*, especially given that this simple analysis has also ignored the other downsides of increasing tether length, such as increased resistive losses, increased mass to address those losses, and the opportunity cost of devoting mass to the tether rather than the wing. This isn't to say that kites aren't making additional power from stronger, high altitude winds—it's just that the losses required to access those winds more than offset the gains.

This conclusion is fairly robust, requiring either very low  $k_{TDR}$  or very low minimum altitudes and high shear to see this combination of power coefficients become greater than 1 at reasonable tether lengths. Using a high wind shear with an  $\alpha_w$  of 0.2, cutting our  $h_{min}$  to 40 m, and keeping our  $h_{lower}$  of 15 m sees this combination of coefficients become greater than 1 for tether lengths greater than 500 m. This is indeed aggressive—the minimum altitude places our kite < 2 wingspans from the ground at the lowest point! Alternatively, using the original values for shear and minimum height requires a  $k_{TDR}$  of approximately 0.0075, half the minimum value in the prior plot and less than half the low end values for unfaired tethers in table 3, to achieve a similar effect. A  $k_{TDR}$  so low likely requires either a faired tether, or a large draggy low performance per wing area kite, which means our high power coefficient is based on a low base of power. Tether drag dictates optimal tether length, which itself dictates a lot of design parameters.

#### 6.2.4 Comparing AWT with HAWT Power Production

What if we compare the same wing, but affixed to a hub on a tower instead of freely flying around on a tether? We've effectively described a traditional wind turbine, as the blades of a HAWT create power from the wind in the same manner as the wing of our kite. This wing-mounted-to-a-tower will represent our comparison HAWT.

Thus far, we've been ignoring an effect that becomes important for this comparison. As a turbine extracts energy from the wind, it slows it down, resulting in a lower wind speed at the turbine. We'll call this effect "induced flow," as operating the turbine has changed the flow of wind through the wind area it sweeps out. AWTs typically sweep out a large wind area relative to their power, resulting in a net induced flow that is small, allowing us to safely ignore it. In ignoring it, we've been assuming that the wind at the kite is the same as the incoming far field wind speed at the kite's virtual hub height,  $v_{w_{vh}}$ .

For our example tetherless kite, ie, a HAWT with a single blade, the distance from the hub that we can mount our wing (the “path” radius for our wing) is heavily constrained by the tower height. As a result, swept area drops dramatically and induced flow becomes significant.

We apply actuator disc theory to the swept area to account for the induced flow losses. The actuator disc model finds that the wind speed at the disc (where we sweep out the wind area) is the average of the upstream,  $v_{w_{vh}}$ , and downstream,  $v_{w_d}$ , velocities. We'll use  $v_{w_{vh,i}}$  to denote the wind speed at the kite after accounting for induced flow.

$$v_{w_{vh,i}} = \frac{1}{2} (v_{w_{vh}} + v_{w_d}) \quad [76]$$

The continuity equation for the actuator disc gives us an alternative equation for power extracted from the wind:

$$P = \frac{1}{2} \rho A_{swept} v_{w_{vh,i}} (v_{w_{vh}}^2 - v_{w_d}^2) \quad [77]$$

Combining equation 76 with equation 77 gives us an alternative form for power:

$$P = 2 \rho A_{swept} v_{w_{vh,i}}^2 (v_{w_{vh}} - v_{w_{vh,i}}) \quad [78]$$

The swept area perpendicular to the wind,  $A_{swept}$ , of our kite is given by the area of the annulus swept out by the wingspan,  $b$ , and projected by the elevation angle:

$$A_{swept} = 2\pi b r_{loop} \cos \theta_e \quad [79]$$

The alternate power equation above is solving for a thrust power extracted from the wind, before any powertrain losses. The power from this equation must be equal to the thrust power using the methods above as well. We'll lump together terms that define a thrust power, such that:

$$P_{thrust} = \frac{1}{2} \rho S \zeta_0 C_{thrust} v_{w_{ref}}^3 \quad [80]$$

Here, we've lumped all the coefficients that attenuate thrust power together into  $C_{thrust}$ , leaving out ones that are a function of the power system losses, defining it as:

$$C_{thrust} = C_{TD} C_{\theta_e} C_{\alpha_w} C_{turn} C_{v_k} C_{Tmax} \quad [81]$$

To include the effect of the induced flow, we need to substitute  $v_{w_{ref,i}}$  for  $v_{w_{ref}}$  in equation 80 for  $P_{thrust}$ , noting that the induced flow may not actually be changing the wind speed at the reference height—we're simply accounting for the fact that the reference point differs from virtual hub height. This additional complexity is simply to maintain our reference to  $P_0$ .

To put the first power equation in terms of  $v_{w_{ref}}$  rather than  $v_{w_{vh}}$ , we combine it with the following, substituting the induced flow versions where appropriate:

$$v_{w_{ref}}^3 = \frac{v_{w_{vh}}^3}{C_{\alpha_w}} \quad [82]$$

We can then equate these power equations 78 and 80 and solve for  $v_{w_{ref,i}}$ , and then use this value to define a new power coefficient for induced losses, by referencing it to the uncorrected wind speed. This results in:

$$C_i = \left( \frac{v_{w_{ref,i}}}{v_{w_{ref}}} \right)^3 = \left( \frac{4A_{swept} C_{\alpha_w}}{4A_{swept} C_{\alpha_w} + S \zeta_0 C_{thrust}} \right)^3 \quad [83]$$

Inspecting equation 83,<sup>28</sup> we see that the higher performance we make our wing, the greater the induced losses. A higher performance wing is accomplished by either increasing wing performance per wing area,  $\zeta_0$ , growing the wing area,  $S$ , or reducing losses to increase  $C_{thrust}$ .

We begin using this equation by checking the validity of neglecting the induced flow for most kites. The actuator disc model is most poorly suited to large and variable swept areas with very low solidity, but can still be used to place an upper bound on induced losses as the swept area gets very small.<sup>29</sup> These induced losses will be at their maximum with a high performance kite turning tight loops—ie, extracting a lot of wind power from a small swept area. As our MX2

<sup>28</sup> The reduced wind speed at the kite has the effect of lowering optimum kite speed and changing coefficients that are dependent on kite speed. We ignore this secondary effect, as including it would greatly complicate the solution. Since kite speed only linearly changes with effective wind speed, this secondary effect is small.

<sup>29</sup> Why is this a poor model? The shear implied by the streamtubes in the actuator disc model are in reality supported by vortices shed by the wing. While the net effect is indeed to slow down the wind in the swept area, areas just outside the swept region see increased wind speed—a benefit analogous to birds in formation making use of wingtip upwash. Actuator disc theory assumes an even and instantaneous pressure drop, but the discreteness of a kite (due to the low ratio of the wing area to the swept area, called solidity) means the specifics of where the vortices are and how they are convected away become important—the pressure drop is not even, and path errors, wind direction shifts, or intentional path movement can all move a kite out of the “streamtube” of actuator disc model validity.

system meets those criteria, we again use our simplified representation of it as our example kite. With a wind speed of 9 m/s and a constant  $k_{grav}$  fraction of 1 (at this high of a wind speed and small path radius,  $k_{grav}$  makes little difference), we find the following:

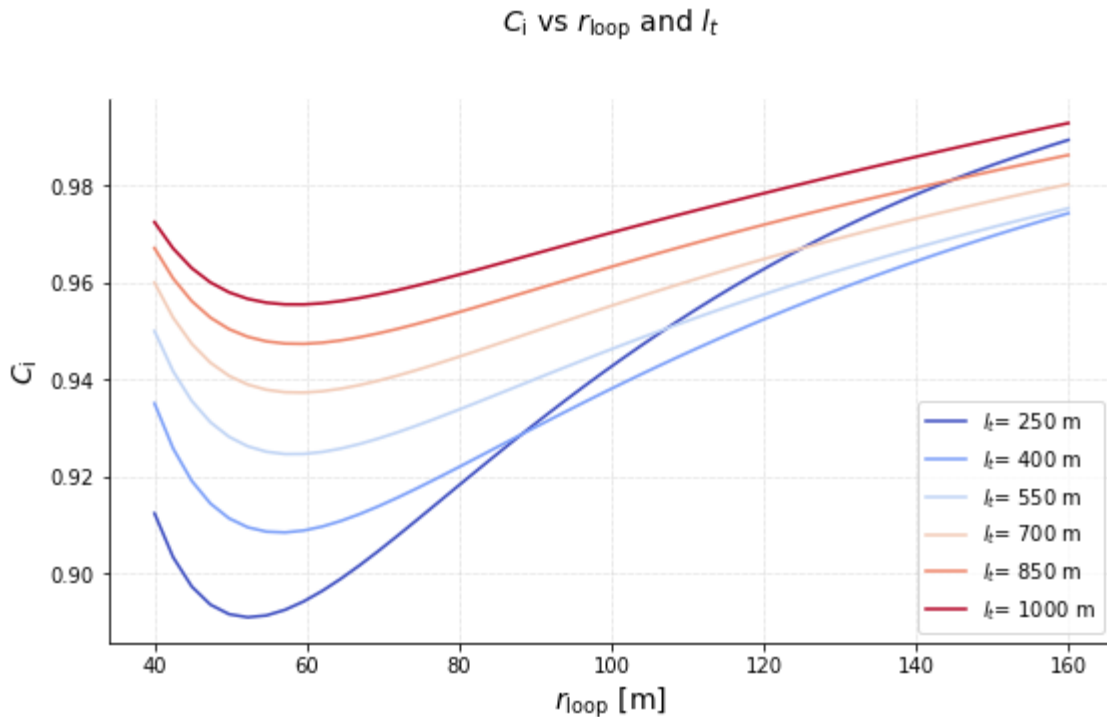


**Figure 36: Power coefficient representing the effect of induced losses on our MX2 versus path radius for various tether lengths. These losses are generally small for AWTs, even with the pessimistic (for AWTs) actuator disc model.**

For the selected system and tether lengths, induced flow losses max out at  $\sim 11\%$  and are  $\sim 8\%$  for a 300 m tether with 80 m radius paths. Overly tight loop sizes result in the kite's lift being used to make the turn rather than extract energy from the incoming wind, and induced losses top out and then diminish. There is now some motivation to turn larger loops than suggested above in section 6.1.9, before induced flow losses are added, but at such a low solidity, this should just be considered an upper bound on induced losses. Even if directly applicable, this is assuming circular paths. AWTs can increase  $A_{swept}$  with minimal offwind or turning costs by stretching the path horizontally into an oval, and/or by varying the path slightly from one loop to the next. For a kite, given that these losses are low even in the absence of these strategies, and given that the actuator disc model likely overpredicts AWT losses, we can state that induced flow losses for AWTs, even large high power kites turning small circles, is mostly irrelevant.

We're now prepared to compare our wing affixed to a tower—our kite turned into a HAWT—to an AWT. Doing so requires some additional assumptions, namely that our wing performance and

ideal speed isn't grossly affected by the higher rotational rate and growing airspeed delta from tip to tip.<sup>30</sup>

This comparison is easily accomplished by inspecting our various power coefficients. A HAWT has no elevation, turning, pumping, off ideal speed,<sup>31</sup> or minimum airspeed losses. With much less sensitivity to mass, there's less motivation to reduce loads before rated power, so we're unlikely to choose to carry anything resembling tension losses either. This leaves us with:

$$P_{HAWT} = C_i C_{\alpha_w} C_{\eta} P_0 = C_i C_{\alpha_w} C_{\eta} \frac{1}{2} \rho S \zeta_0 v_{w_{ref}}^3 \quad [84]$$

For simplicity in this example, we choose to place our HAWTs hub height at the reference height of 80 m, which sets  $C_{\alpha_w}$  to 1. Revisiting  $C_{\eta}$ , the only terms a HAWT is able to drop are the  $\eta_{rotors}$  and  $\eta_{tether}$ , leaving us with a  $C_{\eta}$  of 0.85. We know induced losses will be at their lowest at the largest loop size possible (and our above assumption most valid), so we'll choose  $r_{loop}$  accordingly. Minimum height is less of a concern for a mounted wing, so for this example we only allow a half span of clearance from tip to ground, setting  $r_{loop}$  to 54 m. We'll assume the structure supporting our wing from the inner tip to the hub has negligible drag or lift, and we'll leave this area out of our swept area as well, only looking at the swept annulus.

Let's begin by looking at just the induced losses. Most HAWTs have more than one blade, and blades don't typically have the same performance as wings, so to make the comparison complete, we'll vary the product of  $\zeta S$ , which can represent different numbers and sizes of blades of various performance, and reference it to our nominal values,  $\zeta_0 S_0$ . We assume the  $L/D$  remains constant so kite speed strategies as we change  $\zeta S$  remain constant as well. For HAWTs, if we hold  $\zeta$  constant, the ratio  $\zeta S / (\zeta_0 S_0)$  can be thought of as a multiplier on blade area or the number of blades—without turning losses, the discretization of the total blade area is unimportant.

Induced losses impose a limit on the maximum power a system can extract from a given wind flow, and this limit is called the Betz limit. With increasing  $\zeta S$ , induced losses cause the system to approach and hit this limit, so we also compare the power with the Betz limit power, which can be derived (not shown here) from actuator disc theory to be:

$$P_{Betz} = C_{Betz} \frac{1}{2} \rho A_{swept} C_{\alpha_w} v_{w_{ref}}^3 \quad [85]$$

Where:

<sup>30</sup> This is a surprisingly decent assumption at the chosen loop size. Correcting for this does not *significantly* change the blade performance or the overall conclusion. We should note that the aero database used is generated at a path radius of 100 m, and so is already accounting for much of the rate effects in the nominal case.

<sup>31</sup> For a balanced rotor, there is no potential energy exchange and no motivation to vary the speed from the optimum.

$$C_{Betz} = \frac{16}{27} \tag{86}$$

We can then define how close we are to the Betz limit with the ratio:

$$\frac{P}{P_{Betz}} = \frac{C \dots \zeta S}{A_{swept} C_{Betz} C_{\alpha w}} \tag{87}$$

Where  $C \dots$  represents whatever power coefficients you wish to represent. In figure 37, we'll just use  $C_i C_{\alpha w}$ . The wind shear terms cancel,<sup>32</sup> leaving only the effect of induced flow. The Betz limit is a direct result of induced flow—since that's all we're considering,  $P/P_{Betz}$  should be able to reach the limit, taking on a value of 1, as shown in figure 37.

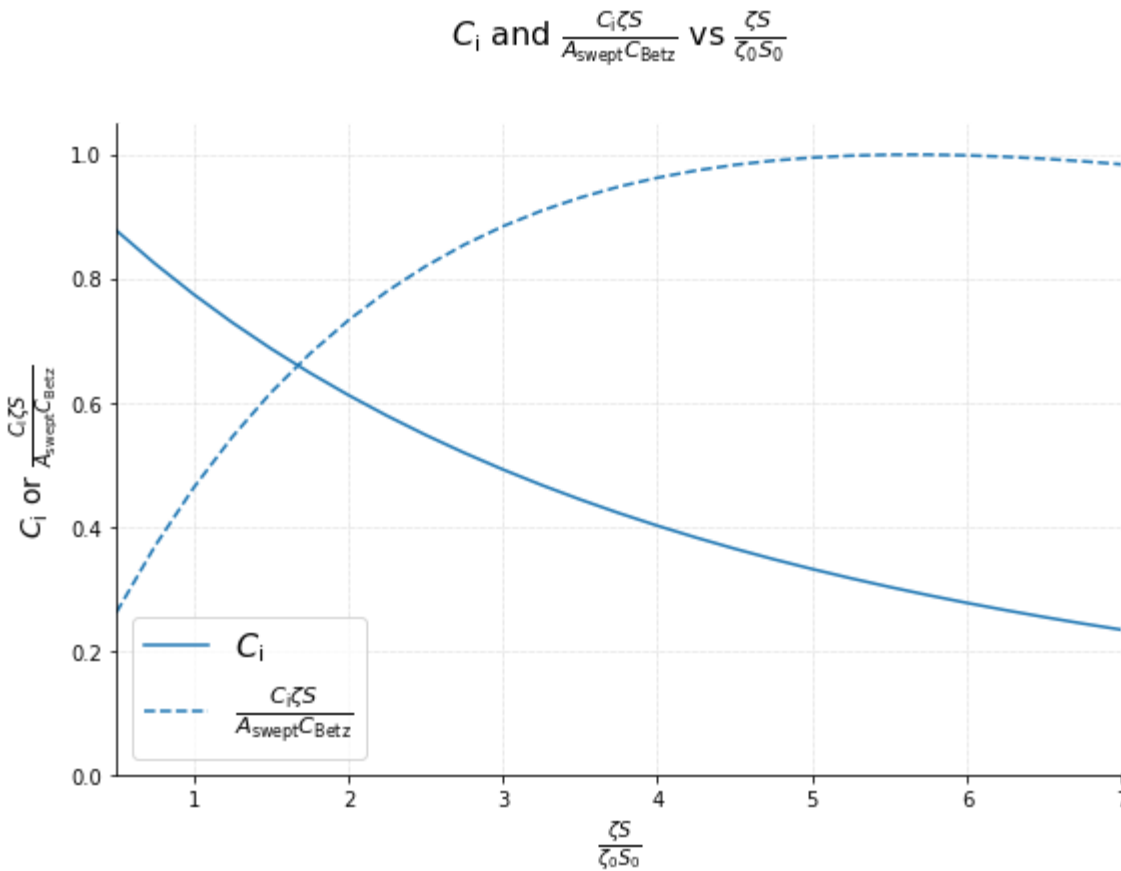


**Figure 37: Power coefficient representing induced flow losses and total power relative to the Betz limit versus normalized performance metric  $\zeta S/\zeta_0 S_0$ . Maximum power, as dictated by the Betz limit, is quickly reached with growing performance.**

From this plot we see:

<sup>32</sup> This example is also at the reference height, causing shear to have no effect anyways.

- Induced flow losses for a HAWT are significant.
- The Betz limit is rapidly approached with increasing  $\zeta S$ , with induced losses taking over such that further increasing  $\zeta S/(\zeta_0 S_0)$  over a value of 4 results in essentially no additional power.

Let's take a moment to discuss what else this means for HAWTs. Unlike AWTs, HAWTs are heavily influenced by induced losses. We showed, in equation 18, that the tension ratio,  $\tau_L$ , for an AWT operating optimally is equal to 3. If we assume that optimal operation for a HAWT means operating at the Betz limit, what is the  $\tau$  for a HAWT, where we replace tension with drag on the tower,  $F_{tower}$ ? To find the drag on the tower we first back our way through the Betz derivation a bit, equating  $P_{Betz}$  from equation 85 with equation 78 to find the wind speed at the disc,  $v_{w_{vh,i}}$ , as  $(2/3)v_{w_{vh}}$ . We can then find  $\tau$  for a wind turbine operating at the Betz limit as shown in equation 88.

$$\tau_{Betz} = \frac{F_{tower}}{F_{T_{min}}} = \frac{(\dot{m}v_{w_{vh,i}})v_{w_{vh,i}}}{P_{Betz}} = \frac{\rho A_{swept} v_{w_{vh,i}}^3}{P_{Betz}} = 1.5 \quad [88]$$

The tension ratio for a wind turbine operating near the Betz limit, as HAWTs typically do, is half that of an AWT operating optimally at a  $\tau_L$  of 3. In other words, for the same power, the loads on the tower from an AWT are approximately twice that of a HAWT, which cuts in half the perceived benefit of reduced bending moments from a lower tower height typical of HAWTs.

Now, let's pull together a power comparison. For simplicity, we'll lock all the wind dependent terms for our MX2 AWT, fixing path radius at a somewhat conservative 80 m as we did above, with a  $k_{grav}$  of 1. We'll grab coefficients from the best portion of  $P_{AWT}$ , at a wind speed of 9 m/s, where tension limiting has not really begun, and where  $C_{v_k}$  is close to 1.

We'll do the same combined performance metric sweep of  $\zeta S/(\zeta_0 S_0)$  for the AWT as well, with some adjustments. For an AWT, the discretization of the total wing area matters for turning losses, so unlike HAWTs, a constant  $\zeta$  with a growing  $\zeta S$  only represents increasing wing area, not increasing the number of wings.<sup>33</sup> HAWTs have no power sensitivity to blade mass, but AWTs do. In order to simplify the comparison, we hold mass constant as we vary  $\zeta S$ . As  $\zeta S$  increases, we need to increase the tension limit to avoid reaching it too early. Assuming we have a similar  $C_L/C_D$ , tension increases roughly linearly with  $\zeta S$ . As the tension increases, we adjust the tether thickness, scaling it simply as  $d_t \propto \sqrt{F_{T,max}/F_{T,max_0}} \propto \sqrt{\zeta S/(\zeta_0 S_0)}$ . The net effect is that depending on how we increase  $\zeta S$ , we have different effects on  $k_{TDR}$ . Growing wing area reduces  $k_{TDR}$  proportional to changes in  $\sqrt{S}/S$ , while growing  $\zeta$  at a constant  $C_L/C_D$  raises  $k_{TDR}$  proportional to changes in  $\sqrt{\zeta}$ . We'll favorably assume  $k_{TDR}$  is reducing by modeling

<sup>33</sup> As in multiple kites on a single tether, discussed in section 8.

increasing  $\zeta S$  via increased wing area alone in our models. We'll ignore the effect of increased tether mass.

We see from our plots above that as  $k_{TDR}$  decreases, the optimal tether length also increases, especially at higher shear. So, we evaluate both a no wind shear case with a 300 m tether, and a normal wind shear case with a 450 m tether.<sup>34</sup> We can now compare total performance—for the AWT, we'll compare both cases with and without induced losses as an upper and lower bound, and always include induced losses for the HAWT. Keep in mind that we expect reality for an optimized solution to be closer to the more favorable non-induced losses case.

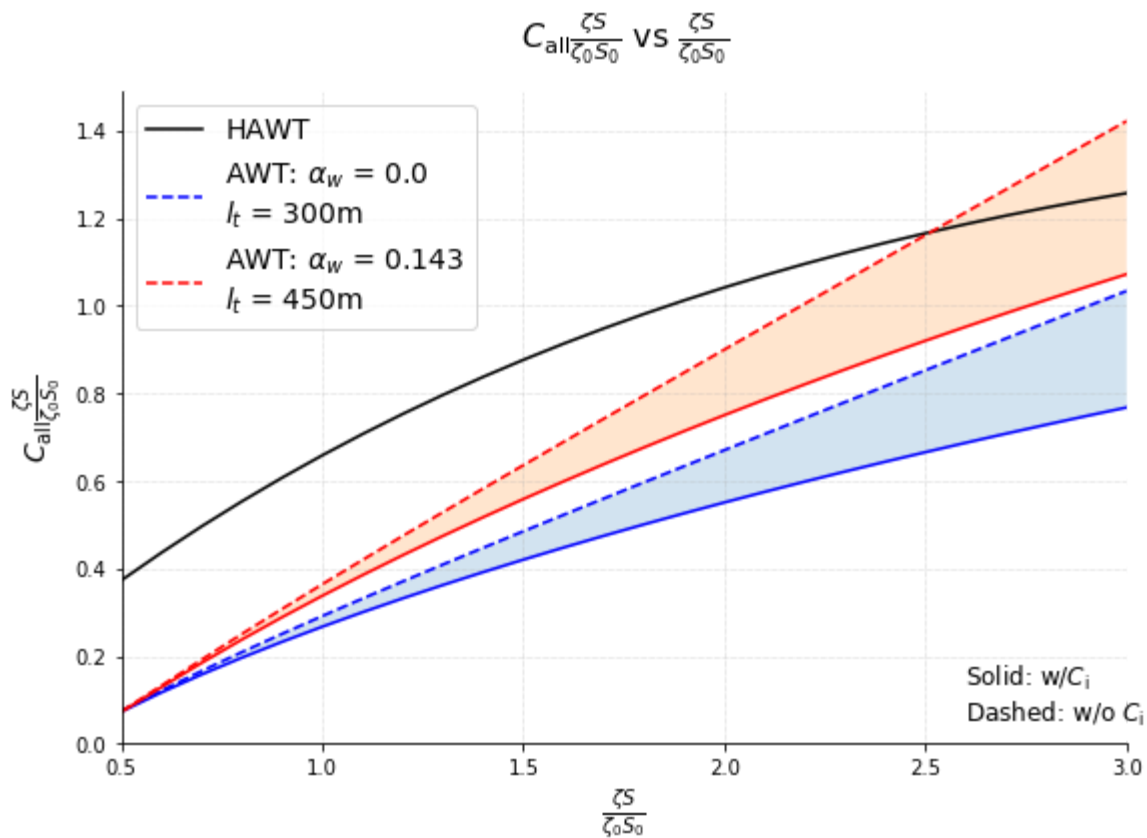


**Figure 38: HAWT vs AWT total power normalized by  $P_0$  versus normalized system performance metric,  $\zeta S/\zeta_0 S_0$ . AWTs are shown both with and without induced losses.**

There are some big takeaways from figure 38:

- The baseline single wing HAWT ( $\zeta S/(\zeta_0 S_0) = 1$ ) at the reference height outperforms the baseline AWT by a factor of 2-3x.
- HAWTs are quickly up against the Betz limit and see less overall power gain per increased blade performance, while AWTs can realize most of the benefit of increased wing performance.

<sup>34</sup> Hand-tuned to be approximately optimal.

- Three tower affixed wings ( $\zeta_S/(\zeta_0 S_0) = 3$ ), also known as a traditional HAWT, are competitive in power with an AWT of 3x the performance at normal wind shears

HAWTs have a strong motivation to have at least 3 blades for balancing reasons, and here we see why they don't have more: they can already approach the Betz limit with 3 normal sized wings. Of course, this wing isn't optimized for use on a tower—the value of higher  $\zeta_L$  is also diminished as the Betz limit is approached, and this is why we don't see HAWTs also chase high  $\zeta$  with high lift airfoils like AWTs do—a single element airfoil has significant simplicity and cost benefits that outweigh the heavily reduced gains of the multi-element airfoil due to the increased induced flow that a high performance multi-element airfoil creates. This means that in the 3 wing comparison case above, a HAWT would likely simplify its “wings” to a single element with lower  $\zeta$  for little performance loss, perhaps making up for some of it with increased blade area—adding blade area is often cheaper than adding an equivalent amount of  $\zeta$  through multi-element blades.

### 6.3 Conclusion

In this light, let's take a step back and critically examine the perceived power benefits of AWTs. A number of unique losses, in particular tether drag and elevation losses (from the combination of a minimum required altitude, turning losses, and a minimum turning radius) all act to reduce performance of an AWT relative to a HAWT with similar blades. Under these conditions, it's inaccurate to state that AWTs access higher power from higher winds, since the net effect is to create less power than the same wing mounted to a tower at the reference height!

This isn't to say that AWTs don't present any performance advantages compared to HAWTs:

- AWTs sweep out much more wind area, dramatically lowering induced flow losses.
  - AWTs can achieve higher performance per wing area than a 3 blade HAWT, especially in high wind shear or with very low  $k_{TDR}$  ratios, possibly making them more cost effective.
  - HAWTs remove so much energy from the wind area they sweep out that in a plant consisting of many wind turbines, downwind turbines see reduced performance (referred to in the industry as wake losses, and can be on the order of 10-15%). AWTs sweep out much more wind area relative to their power, and wake losses will be negligible.
- Lower bending moments from shorter towers support much smaller and cheaper foundations, which is a significant cost driver for offshore installations.

“These conditions” clearly include the system drag, path, and mass assumptions we've made. The biggest way to change this conclusion is with a very low  $k_{TDR}$  in moderate to high wind shears. When the cost of reaching higher winds is low, the tether can better pay for itself to access them. Ratios low enough to do so seem achievable only with significant tether fairing, something that Makani was not able to practically achieve.

It's also important to reiterate the detrimental effects of longer tethers we ignored in the above analysis—onboard generation AWTs must either pay additional resistive losses or increase mass. All AWTs must support the additional mass, and they should consider the opportunity cost of adding tether mass—increased tether mass generally directly takes away from mass that can be added to the wing (either to increase  $\zeta S$  or reduce costs), especially for onboard power generation systems. We'll explore this effect more in section 7, Mass.

Path changes can also be important. We've so far assumed a circular path and a minimum altitude of  $\sim 3$  wingspans at 80 m and  $h_{tower}$  of 15 m. A kite with a very tight minimum turning radius could instead make much flatter shapes, lowering the mean elevation to significantly reduce  $\theta_e$  at the cost of minor off-wind losses for the crosswind portion and accepting bigger losses for the brief tight turns.

One version of this could be horizontally oriented figure eights, with the additional benefit of eliminating the need to de-twist the tether. For the systems presented here, this isn't an optimal solution—the minimum turning radius constraint combined with shorter tethers simply pushes the sides of the path to large azimuth offsets, which hurts performance. A system that can turn more tightly can alleviate those losses, but unless the kite is substantially lighter, it will see large losses in the turns. Longer tethers can also ease the azimuth offsets, allowing us to stretch the path horizontally and spend less time turning, but longer tethers are less optimal, and they increase the turning losses for the same path radius. A very light kite with a low  $k_{TDR}$  could find a suitable compromise here.

Mass has a surprisingly small impact on crosswind performance, predominantly only affecting the low wind performance. A lighter kite can pull tighter turns and experience less elevation losses at shorter tether lengths, but changes large enough to be significant will likely only be possible with a different architecture, namely a ground-based power system, as the examples used here already represent very light construction methods for onboard power generation rigid kites.

In summary, AWTs nearly completely eliminate the shackle of induced flow losses, only to trade it for the shackle of tether, elevation, turning, gravity, and speed losses. Stronger high altitude winds provide a benefit that can recoup some of the difference, but not enough for the systems explored here to see a net benefit.

## 6.4 A Numerical Take on Path Shape

Thus far, we've limited the data to circular paths only, leaving non-circular paths to discussion alone.

Codes that can optimize path shapes certainly give non-circular results, outputting more organic shapes, typically compressed in the vertical dimension. What's unclear is how critical this shape is to the final result. The numerical model provided as part of the Makani software distribution has the capability to evaluate non-circular paths. A brute force investigation was taken for the Makani M600 using an earlier version of this tool. Different variations of simple closed curve paths<sup>35</sup>—shapes best described as eggs, beans, ovals, and racetracks—were evaluated at different scales, orientations, and azimuth and elevation offsets, resulting in ~25k different path shapes, each evaluated at a range of wind speeds.

The top percentile of mean power for the given paths at a variety of wind speeds with zero shear is shown in figure 39, looking downwind such that all paths are flown clockwise.

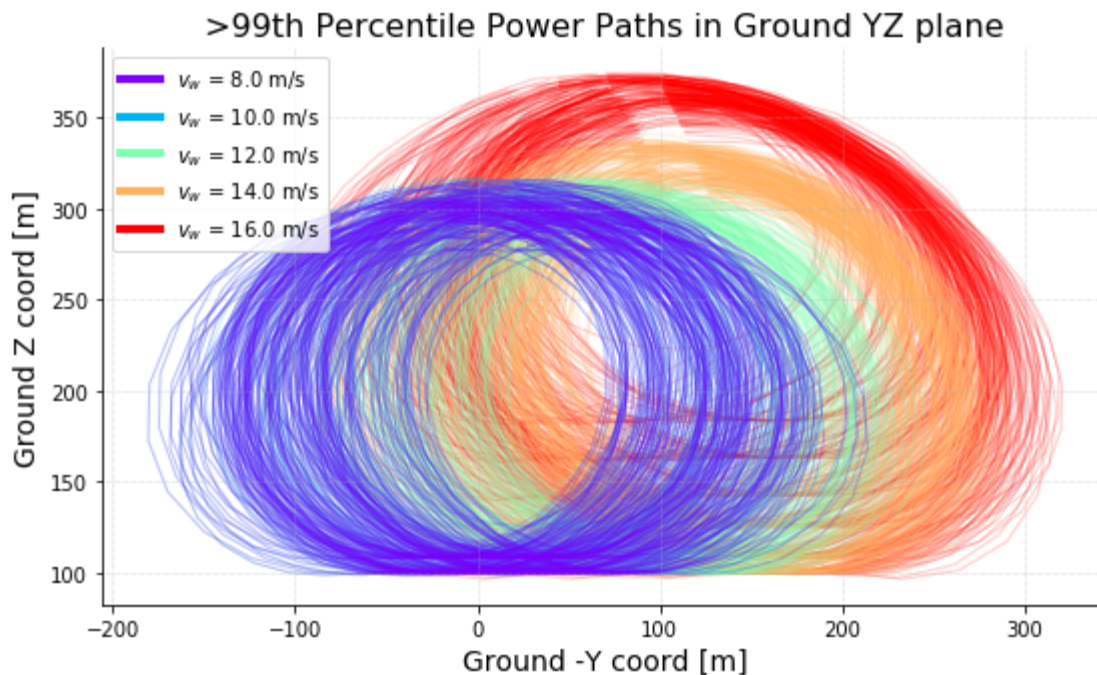


**Figure 39: Paths with the top percentile of power for ~25k brute force path evaluation of various closed path shapes, orientations, and locations for various wind speeds. There are two regimes visible—moderate winds where the kite flies tight<sup>36</sup> and low paths to make maximal power, and large offset paths at high winds to manage excess power.**

We see very similar optimal paths for 8 and 10 m/s of wind, as the 10 m/s solutions are nearly entirely obscured by the lower wind speed solutions. As expected, all these paths are as low as possible, and stretched only in the horizontal dimension. The M600 has more constraints limiting its ability to turn small path radii as a result of its heavy bridling and lack of strong tail

<sup>35</sup> Horizontally oriented figure eights weren't considered in this study, see comments in section 6.3.

<sup>36</sup> Well, tight for the M600, which struggled to turn paths of ~120 m radii in flight tests and was eventually limited to a minimum path radius of ~140 m. These are large relative to ideal operation of an AWT.

authority, so viable paths were limited in how vertically compressed they could be—easing this constraint was one of the strongest motivations for the MX2 design.

At high winds, the kite sees significant changes, increasing azimuth and elevation offset while increasing path sizes. We haven't discussed it yet, but this is occurring as part of the power saturation strategy, as the kite is reaching its power limit. Some paths enable the kite to saturate power more effectively, for a greater portion of the time.

Now, let's look, in figure 40, at the effect on power these variations on path can have.

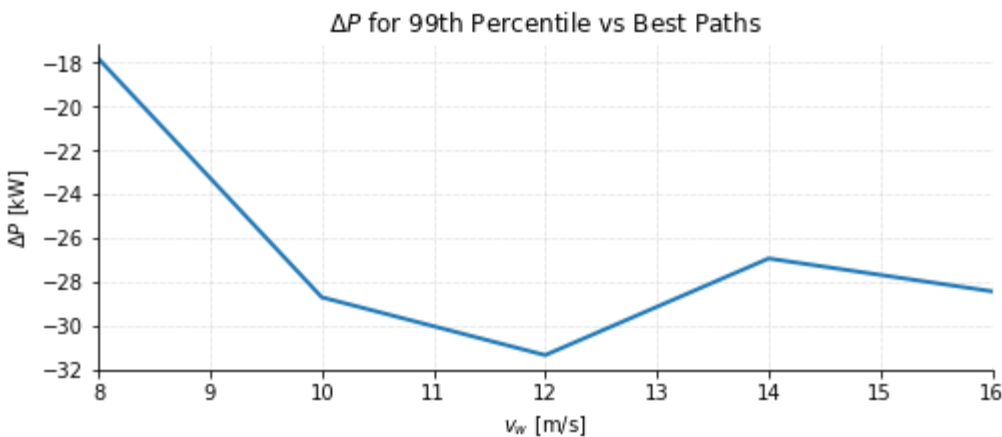


**Figure 40: Difference in power from the 99th percentile power to the best power for the paths shown in figure 39.**

The difference between the best and the worst of the paths shown in the plot above is surprisingly small. Meaningful, but small. For a kite with a tighter minimum turning radius such as the MX2, we expect these losses to become much smaller.

The overall conclusion is that we shouldn't over-index on the specifics of path shape. Chasing performance via path results in control and planning complexity, possibly resulting in increased control errors that can easily wash out the perceived gains. In the context of an unpredictable, turbulent wind field, a particular path may no longer result in the minor gains we fought so hard for.

This isn't to say that all paths should be neat, crisp circles or perfect horizontally oriented figure eights—there are still some important conclusions:

- For wind speeds where the kite is not becoming power limited, we want to:
  - Squash our paths vertically as much as possible, echoing the conclusion from above regarding gravity losses.

- For high wind speeds:
  - Path location and shape become a key part of the power saturation strategy, which we'll discuss more later.
- For all wind speeds:
  - It's beneficial to ease the path curvature where most constrained at the 4-5 o'clock position, where gravity is adding to the turning effort while the kite has reduced airspeed since it's moving downwind.<sup>37</sup>
    - This is best accomplished by tightening the curvature at the start of the downstroke, which still keeps the path vertically compressed.

Path variations such as these should be incorporated into final products, and Makani had planned controller development toward that goal. However, during development, simple paths are easier to implement, and during system analysis, easier to compare. Optimizers have very soft gradients for the large number of variables that control path shape, so minor changes in system, seed, and optimizer performance can result in larger path variations. The resulting difficulty in isolating the effect of a change is why we'll limit ourselves to simple circles for comparison purposes. Path changes beyond simple shapes should be considered a secondary improvement, and kite and controller design should not over-index on the specifics of the path shape.

---

<sup>37</sup> This conclusion is gleaned from the dataset, as it isn't apparent from Figure 39 above, especially with the visual distortion from flattening paths with significant azimuth and elevation offset into the YZ plane, which gives the appearance of sharper turns in the 4-5 o'clock region.

## 7 Mass

As a flying vehicle, we expect mass to play a large role in the performance of AWTs. Surprisingly, the relationship is found to be weaker than one might expect purely from a power generation perspective—once a system is in crosswind and generating power, changes in mass have a relatively small impact. Where mass matters a ton, at least for an onboard generation system that hovers to enter crosswind, is the weight limit it imposes on the total system for a given power system. The sensitivity to mass ends up being driven by the opportunity cost, as all optimal designs in Makani’s models ended with the same conclusion: get the biggest, highest performing kite your power system can muster into crosswind.

Here, we’ll investigate some of the relationships and limits imposed by system mass for a hovering onboard generation system.

### 7.1 Hover

It’s useful to begin system design with a target power level in mind, and then determine the mass limit. We’ll do an example exercise for the MX2, but the actual design process used a statistical approach with flight test data from the M600. That process is outlined in the MX2 design document [12].

Taking the hover thrust power equation and rearranging it to solve for system mass gives the following, where  $m_{total}$  is the total airborne mass of the system,  $P_{hover}$  is the limiting hover power available to the system,  $\eta_{hover}$  is the efficiency of the powertrain from the power limited component to thrust power,  $\rho_{min}$  is the desired minimum operating air density,  $k_{RF}$  is the rotor fraction available,  $N_{rotors}$  is the number of rotors,  $A_{rotor}$  is the swept area of a rotor,  $k_{TWR}$  is the desired thrust to weight ratio, and  $g$  is the acceleration of gravity:

$$m_{total} = \frac{\sqrt[3]{2(P_{hover}\eta_{hover})^2\rho_{min}k_{RF}N_{rotors}A_{rotor}}}{k_{TWR}g} \quad [89]$$

In order to choose a  $P_{hover}$ , we need to select the power parity point for generation and hover power in the system. To demonstrate what this means, imagine a system with an  $\eta_{12g}$  of 0.6, with the power parity point at the grid connection. In order to make 1 MW at the grid connection, the system must generate  $1 \text{ MW}/0.6 \approx 1.7 \text{ MW}$  of power at the kite. However, this 1 MW at the grid only translates to 600 kW of hover power at the kite!

Given that the ground side power equipment is a small portion of total capital costs that form part of the numerator in our equation for LCOE, and the size and mass of power generating components like the wing and power system are responsible for the power production that

forms the entirety of the denominator, it makes sense to place the power parity point as far up the generation chain as possible. In other words, the additional cost of ground based power components to support a higher hover power is usually more than offset by the additional power production of a larger and heavier kite.

A full system model optimization effort found the same, with the optimizer settling on hover to generation motor shaft power ratios close to 1. This means that we pick motor shaft power as the parity point, choosing  $P_{hover} = P_{shaft,max} k_{RF}$ , and  $\eta_{hover}$  becomes only the efficiency of the rotors. As a result of this choice, the downstream power train must support higher hover power levels than they receive in generation, due to reversals of the efficiency chain. For the MX2 system,  $P_{shaft,max} \approx 1.2$  MW, and  $\eta_{hover} = \eta_{rotors,hover} \approx 0.71$ . This efficiency is at maximum thrust with zero freestream velocity.

The rotor fraction allows us to set some safety margin for a powertrain failure. Makani systems utilize what we call a stacked powertrain architecture, which means that motors are chained in parallel connected pairs. This allows the system to support high tether voltages, resulting in a lighter, more efficient tether, while still having reasonable power system voltages, eliminating the need for onboard step down converters or exotic high voltage motor controllers. It does, however, also mean that loss of a single motor/rotor takes out its paired motor/rotor as well, and as such, the maximum  $k_{RF}$  for Makani systems is  $6/8 = 0.75$ . We can then use this value to find  $P_{hover} = P_{shaft,max} k_{RF} \approx 900$  kW.

Selection of number and area of rotors deserves its own topic, but we'll be brief here. A target first rated power point combined with expected system L/D gives expected kite airspeed from the Loyd fundamentals. We can then use this to choose a desired bound on rotor efficiency from inflow on the rotors as a function of the total rotor area. Once this exercise is completed, it's a matter of dividing up that area among several rotors, balancing the trade-offs of tether voltages and stacking, additional maintenance needs for each added power system, motor out margins, and overall mass. Motor mass largely scales linearly with required torque (for a gearbox-less system, much desired for the reduced complexity), pushing for a greater number of smaller rotors, but more rotors require additional structure and other fixed mass costs, pushing the other direction. Having completed this complex series of design trade-offs, Makani settled on 8 rotors, with a total rotor area of  $\sim 33$  m<sup>2</sup> for both the M600 and MX2 systems.<sup>38</sup>

Somewhat surprisingly, the desired thrust to weight ratio also deserves a longer section than we'll give it here. The obvious limit for a thrust to weight ratio is the acceleration phase during the transition into and out of crosswind flight, but transition into crosswind thrust requirements

---

<sup>38</sup> If rotor area sizing is a function of power and airspeed, then why do these two different kites have similar rotor areas? The MX2 made a conscious decision to utilize the M600 power system, but the reason these match the MX2 well is that the M600 did not hit original performance targets—it performed worse than expected, in large part due to not being able to turn the desired tight paths due to substantially missing the mass target. To address the weight growth, shaft power and rotor area grew, and ultimately the M600 power system became poorly matched to the airframe performance. The MX2 is expected to perform close to the M600 intent.

didn't provide many surprises. Despite (or perhaps as a result of) much concern during development, transition to crosswind flight was easier than expected.

The surprising part is that the "simple" hover condition proved to be difficult to define precisely, and at high winds may be just as limiting as the acceleration to crosswind. A hovering tilt kite operates in a complex environment—the wing is partially blown by the rotors and the wind, rotor wakes interact with the wing and tail differently at different wind speeds, and rotor inflow and wakes can block downwind rotors from operating as efficiently. Balancing the resulting moments from drops in downwind rotor thrust, tether tension, and airframe aerodynamic moments lower the net available thrust, requiring a higher peak thrust to weight ratio in our simple equation. No simple model confidently explained the flight test data, and verification of more complex models via system identification flight tests wasn't completed, so knowledge here is somewhat incomplete. The topic is covered in more detail in section 4.6.2 of the "Oktoberkite and MX2" article [12], but for brevity, here we'll simply state that  $k_{TWR}$  should be  $\sim 1.25$  to meet hover and transition into and out of crosswind needs.

A reasonable value for  $\rho_{min}$  is  $0.95 \text{ kg/m}^3$ , roughly equivalent to the standard atmosphere at 2500 m altitude.

At last, we can solve for mass. Using the values above, we arrive at a value of  $\sim 2180 \text{ kg}$ . This total mass has to be shared between the kite and the tether. Low tower heights do not support a great deal of catenary hanging below the tower. For the M600, typical operation had the tether leaving the tower with a slight positive elevation, meaning the tension created a downward load at the kite slightly greater than the tether weight. Without significant catenary hanging below the attachment point at the tower, the kite must support at least the full weight of the tether. With a mass of  $\sim 275 \text{ kg}$  for the 300 m MX2 tether, this leaves  $\sim 1905 \text{ kg}$  for the kite. The same values with an offshore focused system with a  $\rho_{min}$  of  $1.1 \text{ kg/m}^3$  gives approximately another 100 kg of mass.

It's difficult to add anything of note to the well-trodden ground that is the topic of hovering vehicles. Typical power density and rotor areas require that  $\sim 1/3$  to  $1/2$  the total mass of the kite will be the power system. The section on system scaling argued that the rated power should be as high as possible, but it's the hover challenge that places a practical limit here. A system around 1 MW isn't the largest possible, but it strikes what we felt is a good balance between capturing system scaling benefits while easing development of a first generation AWT.

In addition, the hover requirement creates a strong tie between the system rated power and its  $\zeta S$  performance. HAWTs are able to apply system rated power as a somewhat secondary optimization. For HAWTs, low wind sites or markets with heavy renewable penetration that value higher capacity factors can favor the cost savings of a smaller power system paired with a larger and higher performance rotor to increase capacity factor. The same trade isn't available for hovering onboard generation AWTs, as we're unable to reduce the size of the power system

relative to the performance of the kite—shrinking the power system results in a kite that is unable to hover. As such, AWTs in renewable saturated markets may be reliant on intentional curtailment or downrating rather than resizing of their powertrain to seek higher capacity factors.

## 7.2 No Wind Upstroke

Our kite needs to be able to remain flying even when the wind cuts out. This can impose a hefty climb requirement. If we assume circular flight paths, a complete drop in wind, and climb at the lowest controllable airspeed, we can state this power requirement roughly as:

$$P_{climb} = k_{TWR} \left( \frac{m_{total} g v_{a_{min}} \cos \theta_e}{\eta_{hover}} + P_{drag} \right) \quad [90]$$

If the limiting power in the system is shaft power as above, then  $\eta_{hover}$  is again just the rotor efficiency, which at the power limit and airspeed is higher at 0.85. A  $k_{TWR}$  over 1 is still needed to maintain a safety margin, but we can perhaps go lower—here let's choose 1.1. Operating at peak  $\zeta_L$ , the  $C_D$  of the MX2 system (including effective tether drag) is 0.123, giving a  $P_{drag}$  of  $\sim 110$  kW.

Solving equation 90 above for a path elevation of 0.45 rad and a minimum controllable airspeed  $v_{a_{min}}$  of 30 m/s results in a climb shaft power requirement of  $\sim 870$  kW. If we desire the kite to maintain a minimum airspeed climb in a motor out scenario (in order to survive a loop until a safe return to hover can be completed), this is perhaps uncomfortably close to our motor out shaft power limit of 900 kW.

In practice, this constraint is less limiting than our simplistic model has indicated. We find that optimal strategies store a large amount of potential energy in kite speed, and as a result, minimum airspeeds are only seen near the top of the path. It does need to be accounted for though—low wind strategies need to be adjusted in the event of a sudden loss in wind to ensure there's enough airspeed to maintain control of the kite at top of the path. Some of this can be done in response to a loss of wind, such as lowering alphas and adding power earlier, but there may need to be adjustment of the overall strategy to become more tolerant of a loss in wind, such as storing more energy in kite speed at the bottom of the path than is optimal for power production.

## 7.3 Mass in Crosswind

Finally, let's discuss the effect of mass on crosswind power generation. We'll use the analytical model for  $P_{AWT}$  described in section 6, and perturb the mass to find sensitivities. Inspecting equation 75, we find that the tether roll angle is approximately linear with changes in mass. If we assume the limit on turning radius is driven by the tether roll angle, and that we want to maintain

a similar amount of roll margin as mass changes, then we scale the minimum turning radius constraint of 80 m we applied in section 6.1.9 proportionally with the change in mass, where the nominal mass is the MX2 kite target of 1850 kg, limiting the minimum size to 60 m to keep things reasonable. Doing so, and once again optimizing the  $k_{grav}$  strategy and loop radius, under conditions of no wind shear, we find the following:

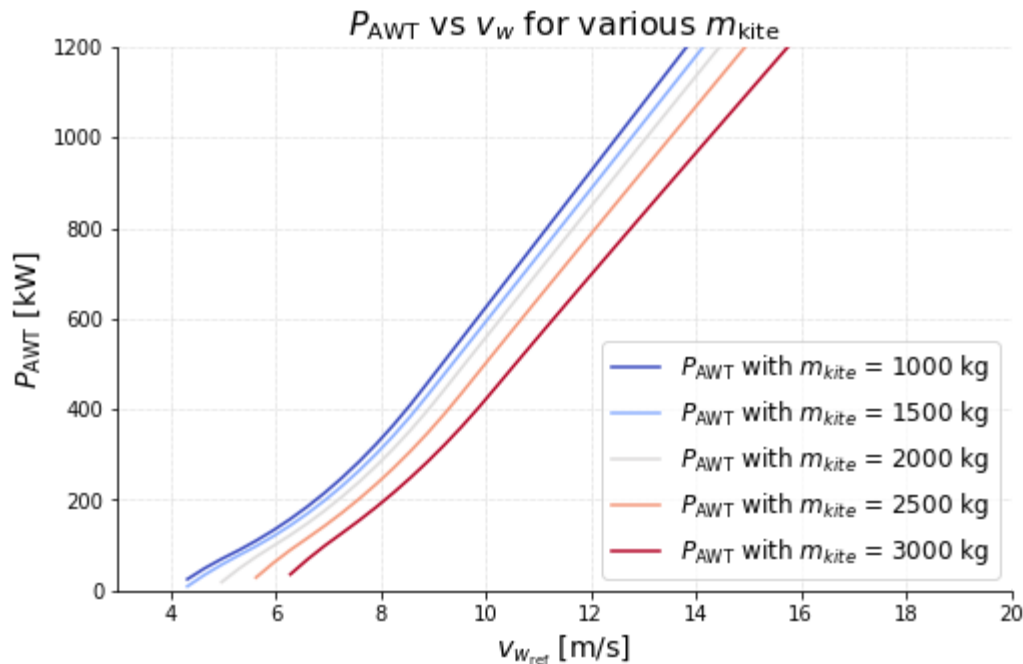


**Figure 41: Numerically optimized power predictions from our analytical model with the MX2 system for various kite masses, scaling minimum path radius linearly with increases in mass. Dramatically lighter kites only bring comparatively minor improvements.**

It requires a large mass growth to have a pronounced effect on the power, driven predominantly by the growing minimum radius constraint and its effect on the  $C_{\theta_e}$  losses as the minimum altitude constraint pushes the paths to higher elevations, with growing sensitivity as we drive off the  $\cos^3\theta_e$  cliff. Going the other direction, heavy mass reductions have a small impact.

Under positive wind shear, the effect in both directions shrinks, as the ideal path elevation gets closer to the minimum elevation limit and the  $\cos^3$  losses are offset by the shear gains. If the minimum turning constraint is held constant (ie, the heavier kites can turn just as tightly as the lighter ones), the sensitivity to mass shrinks even further. The combined effect is shown in figure 42.

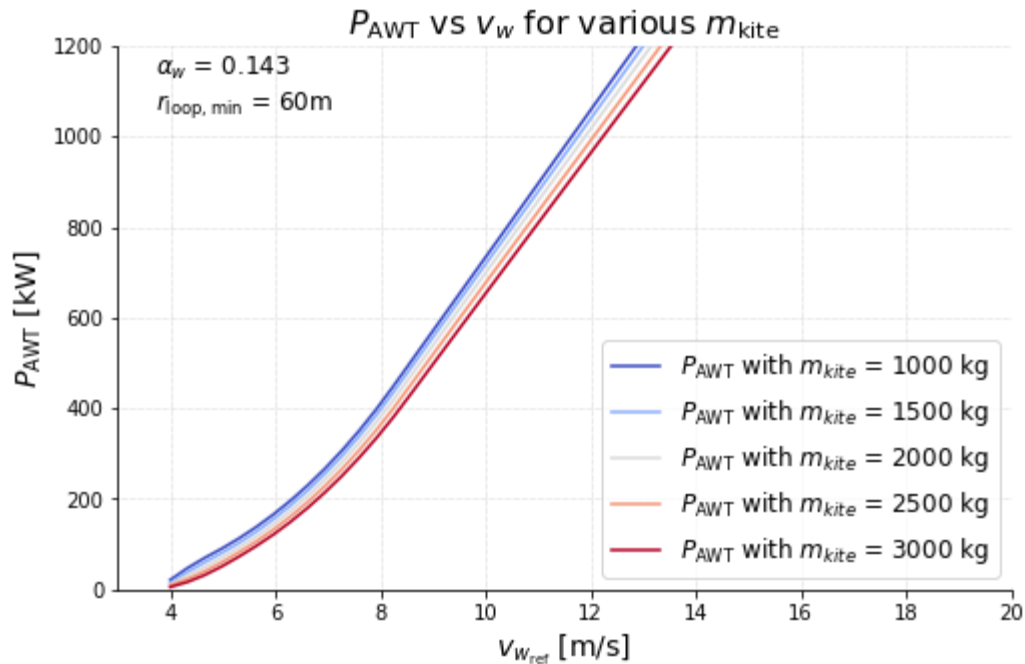


**Figure 42: Numerically optimized power predictions from our analytical model with the MX2 system for various kite masses, this time with positive wind shear and assuming a fixed constraint on path radius. Isolated this way, mass has negligible effect.**

The conclusions from these simple analytical results are consistent with those from more detailed models and simulation. Once in crosswind, changes in mass for a given kite design are relatively small and unimportant, with the biggest impact being a gradual degradation of the kite's minimum turning radius. Oddly, this *amplifies* the need for an accurate mass estimate during design. We have strong motivation in the design phase to maximize the  $\zeta S$  of the kite to maximize power production, which generally means lifting the biggest wing you can into crosswind, riding the limit of a given powertrain's capabilities in the hover and transition modes. If the mass grows even a little over the mass target, then the kite can't fly! Meanwhile, a kite that is lighter than expected has missed out on the opportunity to grow the kite's size, and sees little benefit of that reduced mass in crosswind.

## 8 Multi-kites

The significant effect of tether drag and the BoS cost benefits makes the idea of multiple kites (multi-kites) on a single tether appealing. One possible concept of multi-kites is a “Y” configuration, shown in figure 43, where the kites lift a shared stationary tether that then splits into several short tethers, enabling the kite to access stronger winds at higher altitudes without paying the drag penalty of a fully moving tether.

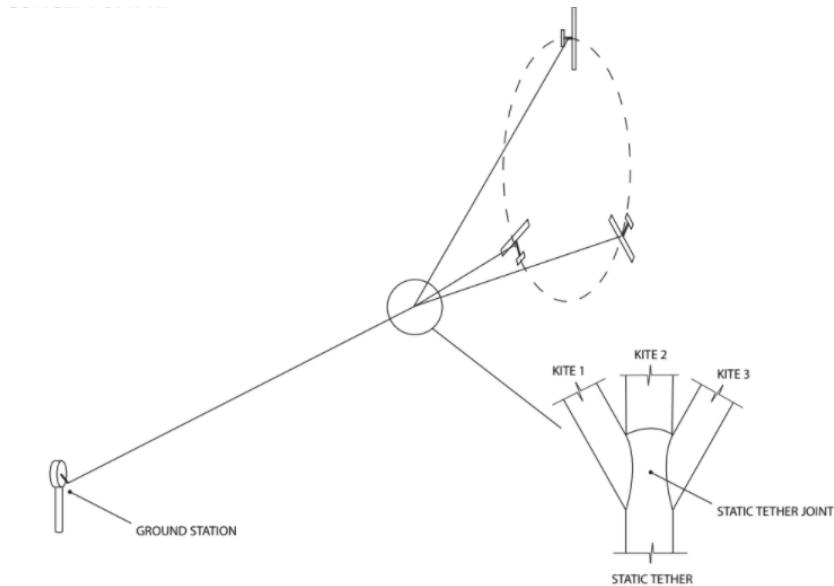


**Figure 43: Conceptual sketch of a “Y” multi-kite configuration, with a static tether section.**

This is a topic worthy of more discussion than we’ll give it, but let’s briefly explore the idea using our existing model with a few minor changes and notes:

- Tether drag is adjusted by the ratio of the moving tether length to the total tether length, effectively reducing the  $k_{tdr}$  by this amount.
- More kites in the same swept area means induced losses become important, so we must include it, diminishing one of the few clear advantages of AWTs.
  - We multiply the  $S_{\zeta_0} C_{thrust}$  in equation 81 for  $C_i$  by the number of kites to represent the increasing induced losses.
  - With an increasing number of kites, the actuator disc model will be increasingly accurate. We’ll again show results both with and without induced flow, but as we add kites we expect the induced flow result to be increasingly close to the truth.
- We optimistically neglect the mass of our static tether and the reduced efficiency from a longer total tether length.
  - As a result of these assumptions, longer static tethers in positive wind shear are always an improvement, as they access higher winds with no change in other losses, but in reality there will be some unmodeled losses that grow with length.

- We place a practical limit of 1000 m as the combined length in the example below.
- There's no practical way to transfer power from kites on the downstroke to the upstroke without paying most of the losses present in the powertrain, so there is little change in the  $\eta_{pump}$  and associated pumping losses.

We wish to vary the number of kites, but can't use the combined  $\zeta S$  metric to do so as we did to represent varying either the size or the number of blades for HAWTs in section 6.2.4, since the turning losses are dependent on the individual wing area for AWTs. As a result, we'll hold  $\zeta S$  constant and only vary the number of kites. We'll define a ratio of the static tether length over the total tether length as  $k_{static}$ . With some rough manual optimization of path size and  $k_{static}$  static tether length, we find the following, again using the MX2 system as our kite with a constant  $k_{grav}$  of 1 at 9 m/s of wind, as we did in section 6.2.4. We compare this with our representative HAWT made from the same wing, also from section 6.2.4, where the number of wings represents the number of blades, and with our nominal 300 m fully moving tether AWT design from that section as well, indicated with a  $k_{static}$  of 0. We limit ourselves to a positive shear case, as multi-kites have much smaller advantages in no wind shear conditions, as illustrated in figure 44.

The benefits of a Y configuration multi-kite are large, out performing the same system without a static tether and now outperforming the HAWT example at 3 wings/blades. This is largely enabled by the longer static tether allowing the kite to access the stronger high altitude winds without paying a price in terms of increased tether drag, with a secondary benefit that they can reduce elevation losses.

However, we have a few caveats:

- The static tether multi-kite sees a relatively small performance increase compared with several independent kites.
  - The multi-kite will be strongly influenced by induced flow and close to the bottom of their performance band, the  $k_{static} = 0.7$  example.
  - Separate systems will see little induced losses and will be close to the top of the performance band for  $k_{static} = 0$  example.
  - As a result, multi-kites provide a performance improvement of ~30% over the same kites operating as separate systems in this example.
    - This is meaningful, but less than perhaps hoped. The BoS cost saving effect will likely be more significant.
- Several effects we've ignored will reduce performance for multi-kites.
  - Tether electrical losses or mass (to add conductor area to address losses) will increase with longer tether lengths.
  - Mass of the lengthy static tether is significant, and will reduce the size of the system we get into crosswind.

- Even ignoring any additional tether mass growth to address tether efficiency and holding the tether linear density constant, the 1000 m total tether length of our example system will result in a  $m_{tethers}/m_{kites}$  of approximately 50%!
- As a result, minimum tension and airspeed will need to increase, hurting low wind performance.
- Mass of the static tether will add catenary sag, tilting the cone of the moving tethers upwards and effectively adding elevation angle losses.
- A typical  $k_{grav}$  strategy will result in faster speeds and higher tensions at the bottom of the loop, further tilting the moving tether cone upwards and increasing effective elevation angle losses.
- Multi-kites will have greater difficulty modifying path shapes, therefore missing out on secondary optimizations we haven't considered.

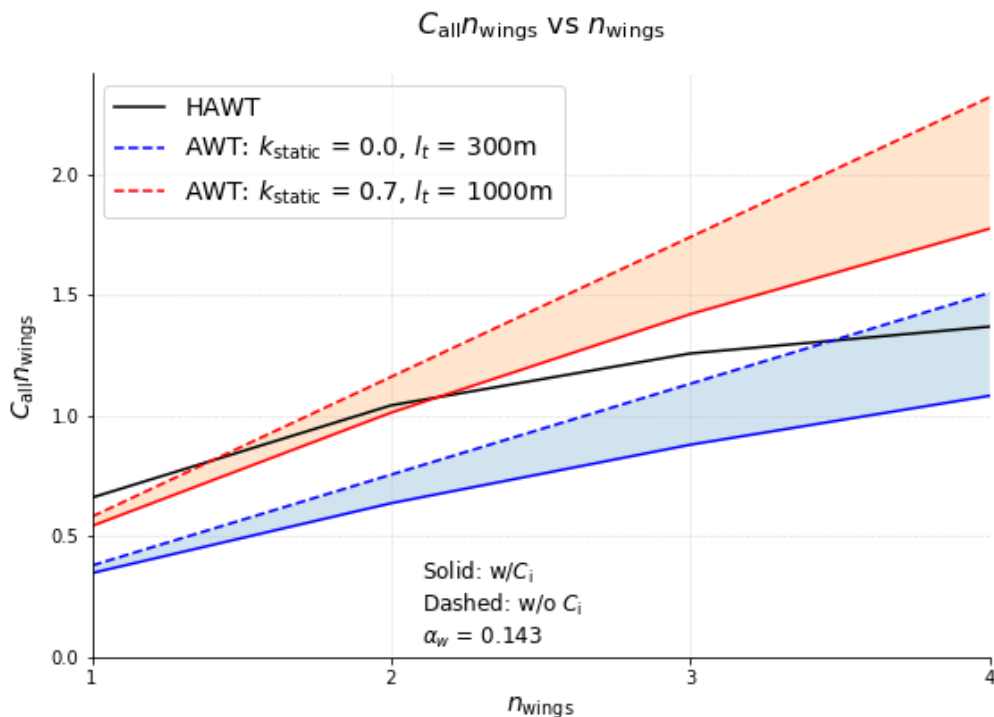


**Figure 44: AWT and HAWT normalized performance relative to  $P_0$  versus number of wings/kites/blades under wind shear of 1/7. Multi-kite Y configurations are represented with a  $k_{static}$  of 0.7, while multi-kite clockface<sup>39</sup> configurations are represented with a  $k_{static}$  of 0.<sup>40</sup>**

These points all perhaps miss the greater, non-quantifiable challenges of multi-kites. “Y” configuration multi-kites greatly increase the launch and land operational difficulties, add substantial complexity to crosswind control, and introduce a whole new set of single points of failure that could bring down the entire system. The main benefit is only unlocked with very long

<sup>39</sup> Described shortly below.

<sup>40</sup> Included in the plot is the nonsensical 1 kite solution with a non-zero static tether length, simply for completeness.

tethers, which raises regulatory issues. Even if these can be addressed, they will increase development and testing time dramatically, something the fledgling AWE industry has already struggled with.

There are some alternate configurations that can address some of these problems. A “clockface” design, where each kite is effectively separate, only sharing a ground station, foregoes the static tether benefits to ease launch and land (kites only need to synchronize crosswind and transition into and out of crosswind) and make it easier control, as kites don’t directly tug on each other as in a Y design. The clockface design isn’t particularly appealing purely from a power perspective, but when one considers the BoS scaling pressures discussed in section 3, it becomes much more compelling.

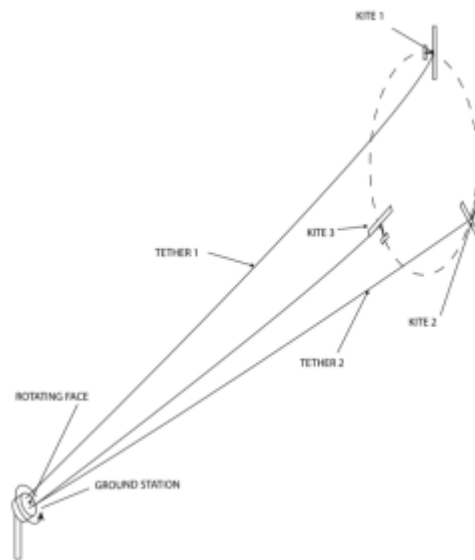


**Figure 45: Conceptual sketch of a “clockface” configuration for multi-kites.**

There are also hybrid solutions—a traveling crawler can enable the easier launch and land of a clockface configuration with the benefits of a Y configuration, but adds additional complexity.

These alternatives do little to change the bigger picture: multi-kites, while initially appealing, appear to offer less performance benefits than anticipated due to the introduction of substantial induced flow losses and the costs of carrying a tether that is a large portion of total airborne mass, especially in light of the opportunity cost of devoting that mass to the tether rather than the wing. The development challenges further push this idea, in this author’s opinion, firmly into the realm of the distant future. If AWE can create a successful, reliable product and gain years of real world experience with a single kite, then perhaps later designs can chase the potential gains of multi-kites, beginning with simpler clockface configurations to get the BoS advantages. An AWT design dependent on multi-kites as an initial product faces a daunting development challenge.

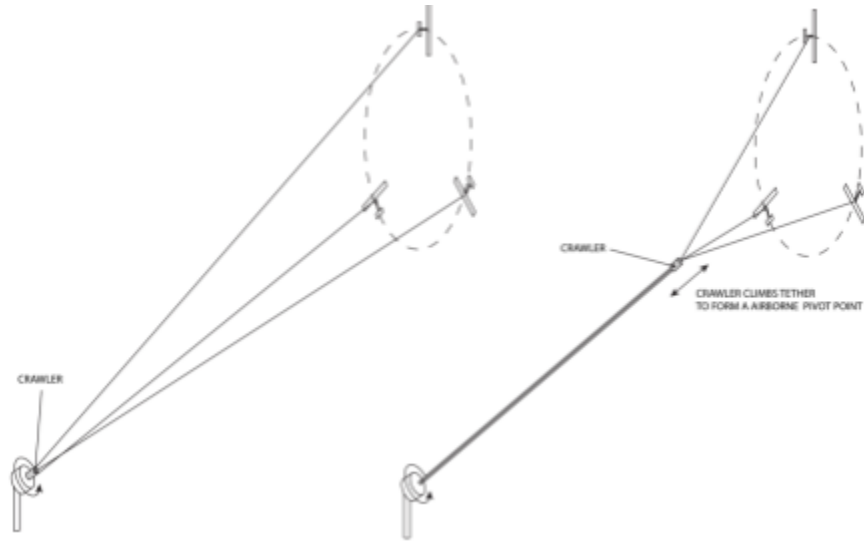


**Figure 46: Conceptual sketch of a traveling crawler design for multi-kites.**

## 9 M600 Power Performance

In “M600 Energy Kite Description” [11], we present the predicted and tested performance of the M600, Makani’s prototype energy kite, in comparison with the original design intent.

Here, let’s apply the simple analytical model we’ve developed here to take a more fundamental look at the reasons for the performance gap shown there.

Taking values for the M600 Intent and the M600 As-Built from table 1, we evaluate them in our analytical model. Before doing so, we need to make one additional change. The M600 As-Built has a hard  $v_{amax}$  speed constraint of 70 m/s based on a predicted whirl flutter mode of the props. We can add this to our  $C_{v_k}$  term in the same manner as our  $v_{dmin}$  constraint. We also need to select an  $r_{loop}$ , choosing the minimum values of 75 m and 145 m for each system, respectively, and choose a  $k_{grav}$  of 0.7 for the M600 intent and 0.5 for the M600 As-Built, broadly representative of how the kites were typically flown. We also repeat our MX2 example from figure 28.

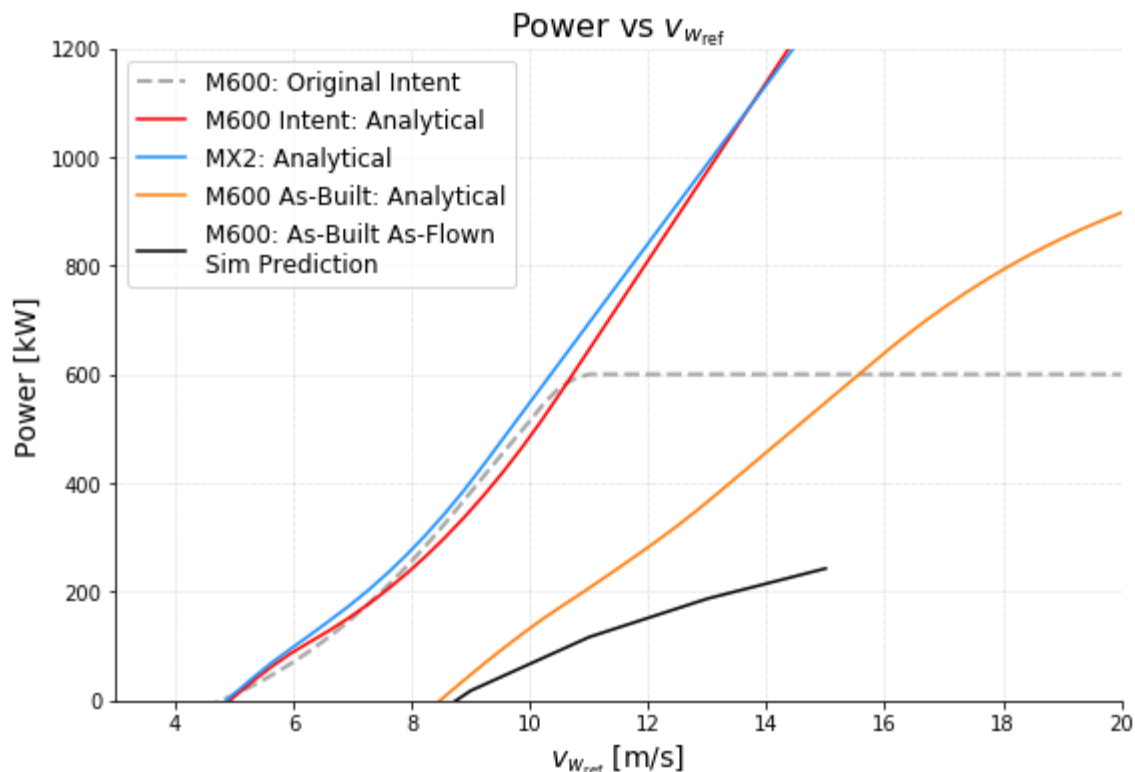


**Figure 47: M600 design intent power curve from more detailed models and our analytical model, along with analytical model results for the MX2 and the M600 As-Built. Also shown is the M600 As-Built and As-Flown simulation prediction, all under zero wind shear conditions.**

Our simple analytical model matches the M600 Original Intent power curve, which was created from an optimal control problem (OCP) optimizer at the time. The analytical model also captures the poor cut-in performance of the M600 As-Built, agreeing well with the simulation there.

As we noted in “M600 Energy Kite Description” [11], the large minimum path radius and worse aerodynamic qualities are responsible for most of the reduced performance,<sup>41</sup> and we’ve captured those effects well in our analytical model. What our analytical model doesn’t explain is the growing gap between the simulation prediction and the analytical model as winds continue to increase.

To understand this, we need to look at what “as-flown” signifies. For wind speeds greater than 10 m/s, we were forced to deliberately degrade the kite’s performance, for reasons we’ll examine shortly. Let’s take a look at some commanded flight parameters for the presented simulation prediction in figure 48.

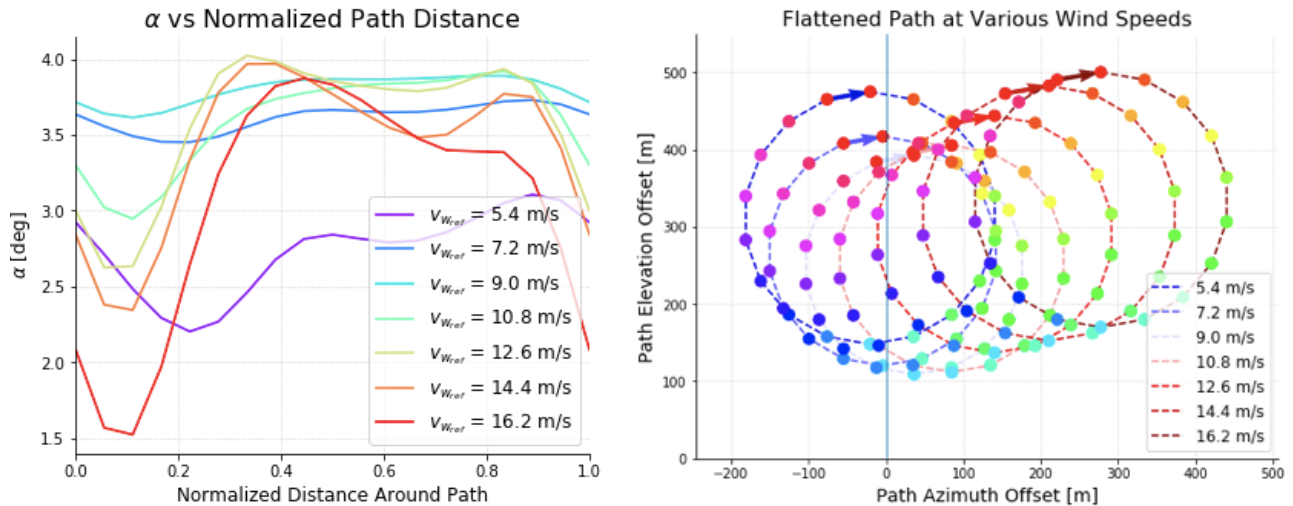


**Figure 48: Alpha and path commands for the M600 As-Built and As-Flown simulation prediction. The kite is only operating optimally at ~9 m/s of wind. Paths are shown flattened into the downwind viewing plane, with offsets shown relative to downwind.**

Optimum operation of this kite at a maximum alpha of 4 deg at the minimum path radius of ~145 m is only commanded at approximately  $v_{w_{ref}}$  of 9 m/s. This is where the analytical model, also operating optimally, agrees well. As wind speed increases, the commanded alphas begin to drop, path sizes grow larger, azimuth offset shifts sharply to the right, and the as-flown performance relative to the optimum continues to drop.

<sup>41</sup> We won’t get into *why* we had worse aero performance and large minimum path sizes for the M600 As-Built here. See the referenced article, “M600 Energy Kite Description” [11], for a more complete description of predicted and flight test performance, as well as the discussion of how we got there.

This begs the question: why are we commanding the kite in such a way to drastically reduce performance? The answer lies in some unique challenges for AWTs in high speed, turbulent winds, and those challenges are greatly exacerbated by large path sizes. The M600 was forced to degrade performance to avoid some of those challenges, and ultimately, high wind speeds remained an unsolved problem for the M600, with simulation indicating a maximum safe wind speed of  $\sim 15$  m/s.

# 10 High Winds Are Hard

## 10.1 Overview

Much of the focus in AWT literature and HAWT design has been on making as much power as possible, and indeed, this should be the focus to have a competitive power curve, with a comparatively early cut in and first rated power point.

However, the challenges of what happens *beyond* that point, as wind speed continues to increase with a saturated power system that is unable to accept any additional power, cannot be overlooked. High wind operation and power saturation remained an unsolved problem at Makani. Even in the history of HAWT development, it took some time to learn how to safely saturate power, with most HAWTs now using variable blade pitch to lower the angle of attack as the main power limiting mechanism.

This tool is available to AWTs as well, but with much stricter limits, and as a result this method is unable to fully address the problem. We'll begin by investigating the fundamentals behind the high wind problem, then look at the various strategies available to AWTs to handle power saturation, as well as the limitations of each strategy.

## 10.2 The Challenge

In order for a wind energy system to be competitive, it's desirable to saturate power at approximately 10 m/s, depending on the specifics of the site, power system, and local energy market.<sup>42</sup> All wind energy systems also have a cut-out point, where the cost of building the system to produce power at high winds and high loads isn't justified due to the rarity of high winds and their reduced value since all other wind based power is also at maximum production. Cut-out also depends on the specifics of the site and power system, but is typically around 20-25 m/s for lower wind sites and 25-30 m/s for high wind sites, especially offshore. A system designed for a particular cut-out needs to be able to survive gusts of several additional m/s, so for the examples to follow we'll use a wind speed of 24 m/s to represent the maximum wind speed for a 20 m/s design cut-out system, making our challenge as easy as possible.

---

<sup>42</sup> Again, it's *not* necessarily desirable to reach rated power as soon as possible—while attractive from a capacity factor and grid perspective, an excessively early rated power point implies throwing away a lot of available energy in the wind simply due to an undersizing of the power system relative to the rest of the system's power capabilities. Those capabilities have costs, achieved by things like larger and higher performance wings/blades, so this mismatch results in a higher total cost of energy as the costs of higher performance aren't accompanied with additional energy. On the opposite end, reaching rated power is too late maximizes use of the system's performance, but at the cost of an oversized power system that sees little use except at rare high winds, when other wind based power systems also make a lot of power and the grid has little need for more of it. As with all things, there's a compromise to be made.

From the basic  $P_0$  power equation, the core issue is readily apparent—power increases with  $v_w^3$ , and the maximum wind speed we desire to operate at is 2 to 2.5 times the desired first saturation point, meaning the system needs a way to reject somewhere around an order of magnitude more wind power than the power system is capable of. Excess unmanaged power shows up as overspeeding. With maximum wind power  $\gg$  rated power, high winds will approach the no power generation case, where the kite speed will equal  $(C_L/C_D)v_w$ . A kite with an L/D of 10 and mean elevation angle of 0.45 rad will reach approximately 180 m/s in 20 m/s winds, a speed that will cause numerous loads challenges. AWTs probably shouldn't have their speeds best measured in mach number.

Just as clearly, the wind energy industry has already solved this problem—the only question is if the solutions found there can be applied to AWTs. Before we dive into specific solutions, there is one additional challenge that AWTs must face.

We touched on it above when we described the potential energy pumping issue and the  $k_{grav}$  factor. The path described by an energy kite exchanges a large amount of potential energy from the top to the bottom, and  $k_{grav}$  encapsulates the largest decision to be made here—you can either pump that energy into and out of the grid, or store it as kite speed. Pumping energy into the grid creates large fluctuations in power that bring power saturation issues on the downstroke well before the mean power gets close to saturating.

In the analytical model above, we found that  $k_{grav}$  fractions for optimal power operation have a weak sensitivity at high winds, trending slowly towards 0 at higher winds, but more complex models show the true optimum  $k_{grav}$  in the absence of power system constraints is typically in the range of 0.6-0.8. For now, we'll assume a value of 0.7 in our examples below, but we'll expand upon this further in a moment.

From here, we can make an overly simple model for power generated around the loop, accounting for the “gravity power” that our selection of  $k_{grav}$  adds to the kite's power system. If we naively distill our prior work into a constant fixed power coefficient (and ignore the efficiency definition changing through the power sign flip, as it's not relevant here), we can find the electrical power around the loop to approximately be:

$$P_\psi = \frac{P_{AWT}}{P_0} P_0 + P_{grav, \psi} \eta_{t2g} \quad [91]$$

Assuming a  $P_{AWT}/P_0$  of 0.25 (approximately the best for wind speeds near the desired rated power point, from figure 26) with a  $k_{grav}$  of 0.7, we have figure 49.

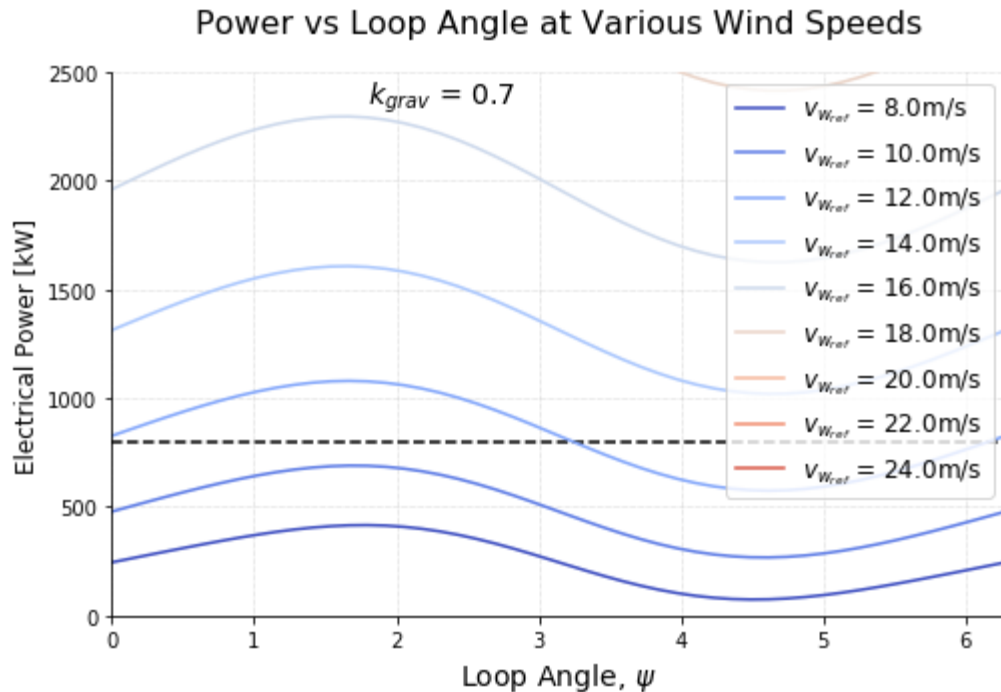


**Figure 49: Simple power versus loop angle model for the MX2, demonstrating rapid growth in power with wind speed, and more importantly, the presence of large variations in power despite a relatively high  $k_{grav}$ . Systems more constrained in airspeed, like the M600 As-Built, are unable to utilize such large  $k_{grav}$  and see even larger power swings.**

Higher wind speeds are intentionally cut off here, as they blow up the scale. Despite the small loop sizes and a strategy that stores most of the potential energy in kite speed, there is still approximately +/- 250 kW of power pumping in and out of the kite's power system.

The dashed line indicates the approximate electrical power limit of the MX2 system (as measured at the collection system), showing that the kite will need to start deploying power saturation strategies on the downstroke at ~10 m/s of wind, and will need to heavily reduce power to make it to 24 m/s, which is well off the scale in the above plot.

We've now set the stage for the problem: AWTs, just like HAWTs, need to develop a strategy to manage the rapidly rising power from the  $v_w^3$  relationship to survive to the target cut out wind speed, with the added challenge of a fluctuation of nearly a third the rated power caused by the potential energy exchange. This fluctuation creates a transitional zone that spans several m/s of wind speed, where the kite needs to make as much power as possible everywhere in the path except on the downstroke.

## 10.3 Strategies

### 10.3.1 Reducing lift

The most obvious strategy is to implement the now common HAWT solution—reduce the power by reducing the lift generated by the blades/wing. There are two limiting factors for this on AWEs:

1. A kite optimized for  $\zeta$  will generally have high lift multi-element airfoils that perform poorly with a risk of separation at low alphas.
2. Lift is used to make the turn. Reducing lift also reduces the ability of the kite to follow the desired path.

Let's begin by briefly examining the first item. In order to leave enough margin for control errors and gusts, the MX2 kite is limited to -10 deg to prevent separation. Below, in figure 50 we plot  $\zeta_L$  as a function of aerodynamic angle  $\alpha$  for the MX2 kite:

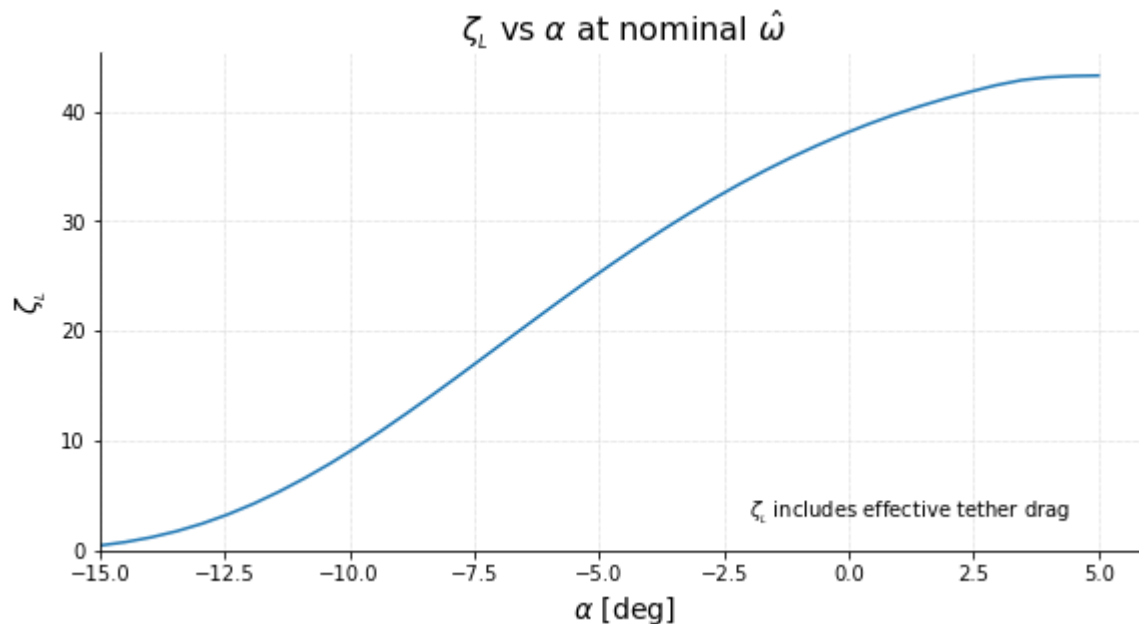


**Figure 50:  $\zeta_L$  performance metric for the MX2 kite at different alphas, at the nominal normalized angular rates.**

A minimum  $\alpha$  of -10 deg makes for a minimum  $\zeta_L$  of ~10, in the absence of any other restrictions.

The second issue, of making the required turn, is more troublesome. A quick inspection of the minimum turning plot in figure 32 makes this clear—the worst case minimum turning radius

limits us to  $\alpha \geq -7$  deg for a path radius of 80 m, which is a  $\zeta_L$  of 20, double the minimum possible from flow separation constraints. Lower than optimal, but is it low enough? It is possible to increase the target path radius to buy some additional margin between the commanded path radius and the minimum path radius,<sup>43</sup> but at the expense of increasing the potential energy exchange, which either expands the  $\Delta v_k$  (at some additional cost of increasingly off-optimal airspeeds), or requires reducing the  $k_{grav}$ , which throws more energy swings into the power system, which is exactly what we're trying to avoid.

The issue is compounded by how sharp this turning limit is. Close to the turning limit, it takes large changes in tether roll angle to tighten the turn. Revisiting the minimum turning radius plot, but this time holding wind speed constant (and at a higher, more relevant wind speed here of 14 m/s) and plotting the minimum turning radius as a function of maximum tether roll angle  $\gamma$ , we find:

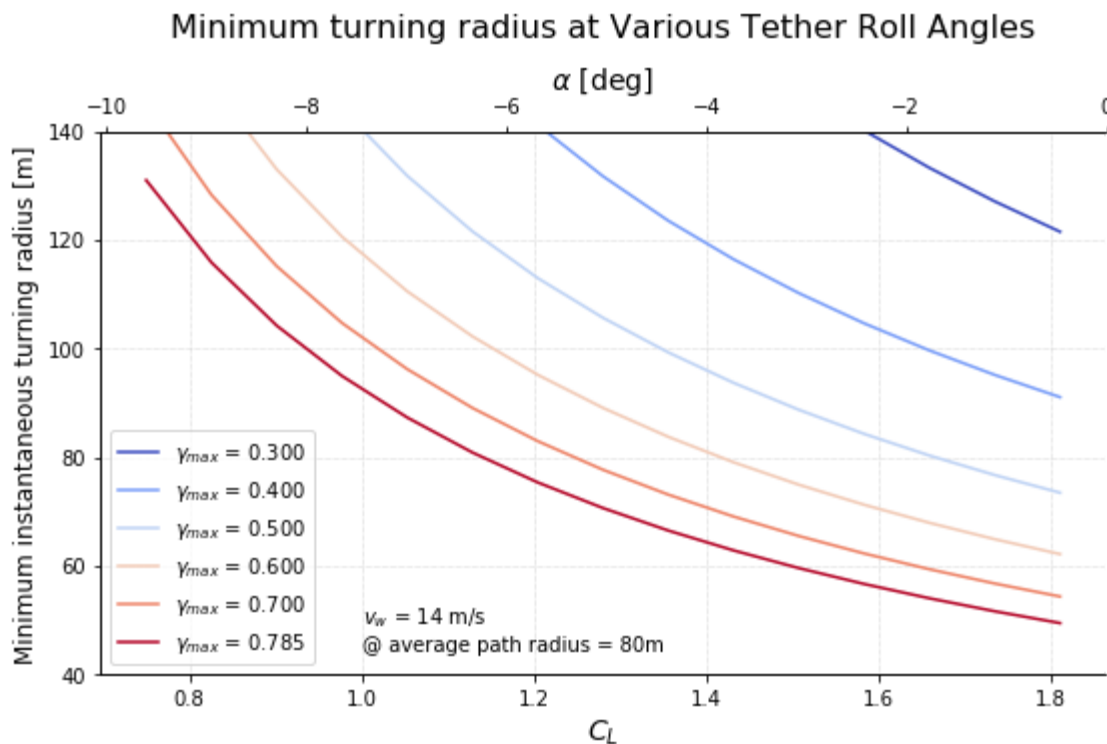


**Figure 51: Minimum instantaneous turning radius for the MX2 versus lift coefficient and alpha at various tether roll angles.**

In figure 51, we see that near the limit, each additional amount of roll gains less turning effort. Implementing a strategy of reducing lift only during the downstroke for the transitional wind speeds then implies a high roll rate in order to reach the maximum power reduction via reduced lift.

<sup>43</sup> Increasing the path radius only weakly affects the instantaneous minimum radius.

Based on the minimum turning limits shown, and the difficulty in increasing them, we'll choose a lower limit on  $\alpha$  of -7 deg, which reduces  $\zeta_L$  by a factor of about 2, and repeat the plot, in figure 52, with the simple power model created above:

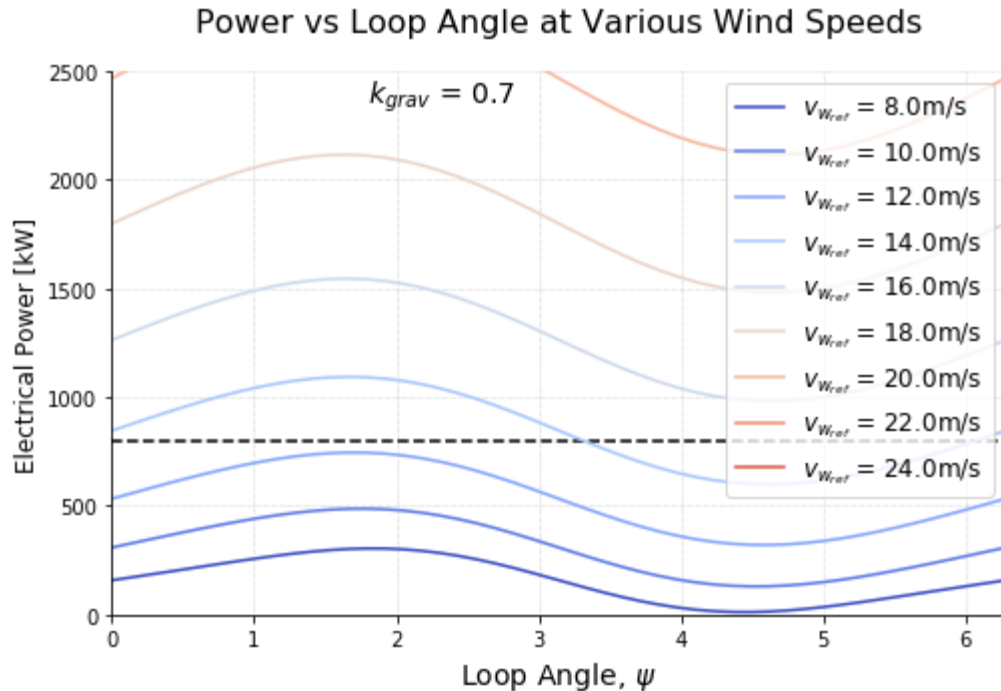


**Figure 52: Simple power versus loop angle model for the MX2, but at the minimum alpha while maintaining sufficient turning margin, -7 deg. This only delays the onset of power saturation by a few m/s of wind speed.**

Reducing  $\zeta$  by a factor of 2 only staves off the first power saturation point to  $\sim 12$  m/s! Other strategies will need to be used to shave the downstroke peak beyond this point, as well as shift the entire power production down to reach 24 m/s of wind.

This model is intentionally simplistic—path changes can alleviate some of this turning constraint, which, if we recall from above, is at its worst at the bottom of the downstroke. In addition, the  $k_{grav}$  factor represents a simple speed strategy—we can vary this factor around the loop to more selectively control power. Regardless of modeling simplifications, the conclusion remains: AWTs can only partially utilize lower lift as a means of power reduction, because they also use lift to stay in the air and have a tether roll angle constraint!

### 10.3.2 Non-optimal speed

Thus far, we've been assuming the kite is operating with a speed strategy centered around its optimal speed,  $v_{k_L}$ . What if our speed strategy is centered around a non-optimal kite speed?

Let's explore this by revisiting the plot of  $\zeta_v$  vs kite speed for the MX2 system, this time also plotting solutions at the lower  $\alpha$  and expanding the wind speeds shown. Again, we have chosen  $\theta_e = 0.45$  rad and zero shear:

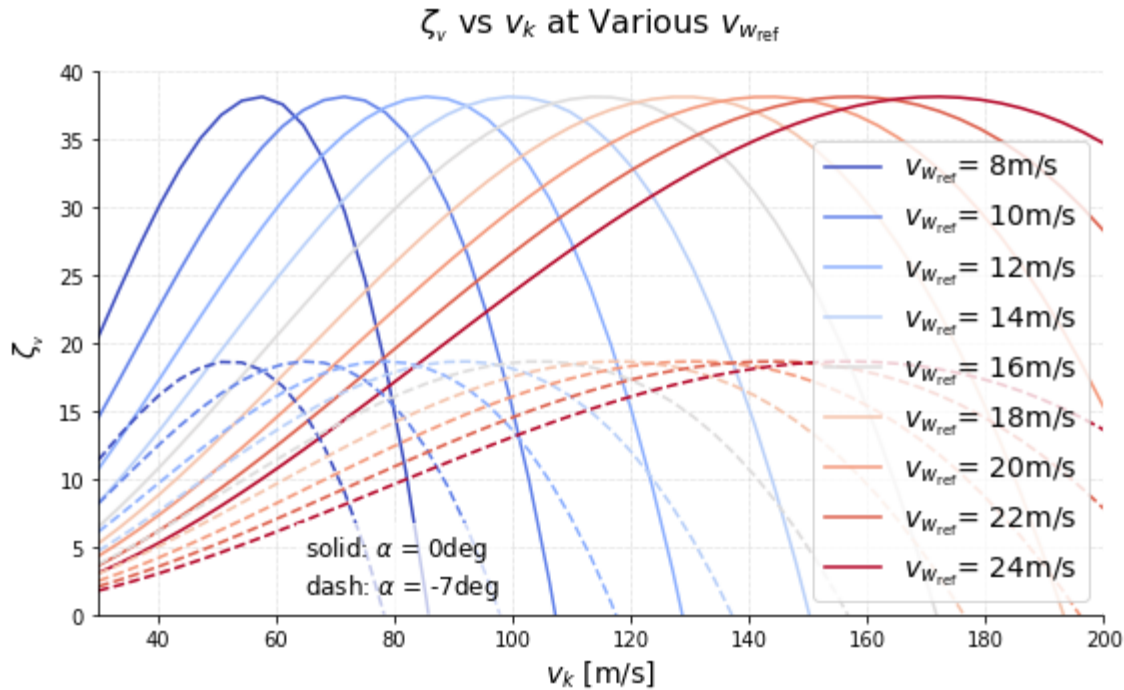


**Figure 53: Performance metric  $\zeta_v$  for the MX2 system versus kite speed for a variety of wind speeds and shears.**

The location of the peaks in figure 53 occur at  $v_{k_L}$ , and this kite sees little movement in its optimum speeds as a function of  $\alpha$ , since the ratio of L/D remains similar throughout the operating range. It appears there is some room to trim a significant amount of power while maintaining a reasonable kite speed range, especially at higher wind speeds.

Let's explore this further. To maximize this benefit, we need the kite to fly as slow as possible. Getting on the other side of this peak at high winds appears to simply require excessively high airspeeds and the very high tensions, structural loads, and rotor design challenges that go along with them.

So we'll target the low end, attempting to manage power by going slower than optimum. Let's assume our kite has a minimum controllable airspeed,  $v_{a_{min}}$ , of 30 m/s, and that  $v_a \approx v_k$ . We can then define the speed range in terms of  $k_{grav}$ . We plot the same data as above, but this time show power rather than  $\zeta_v$ , where we simplify power to  $(\zeta_v/\zeta_L)(P_{AWT}/P_0) P_0$  (again assuming  $P_{AWT}/P_0$  is a constant 0.25, and taking care to note that  $\zeta_v$  is at the reduced  $\alpha$  of -7 deg, while  $\zeta_L$  is at the best achievable  $\alpha$  of zero), and we focus on higher wind speeds and lower  $\alpha$ , since we're interested in kite speed mostly as a power limiting strategy here.

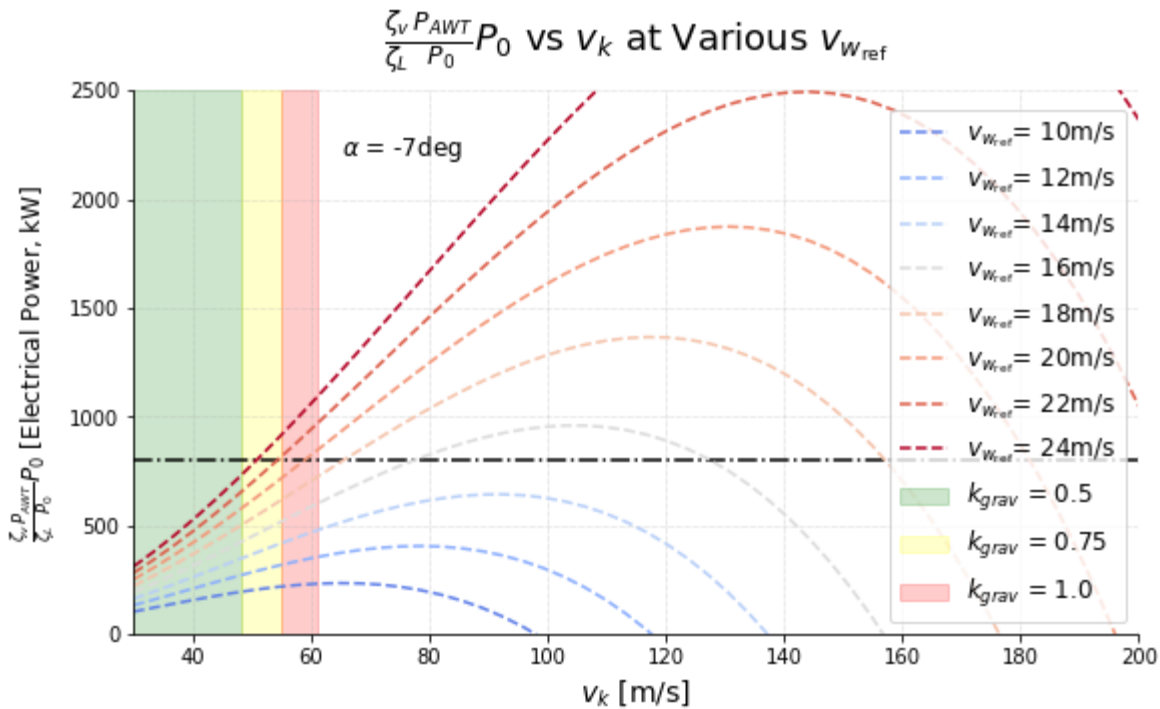


**Figure 54: Power versus kite speed for the MX2 system, with regions denoting various kite speed ranges for a given  $k_{grav}$  fraction, assuming minimum possible speeds and at our minimum viable alpha.**

Colored bands in figure 54 indicate the speed range dictated by a given  $k_{grav}$  strategy that touches the minimum airspeed—ie, as slow as possible. The higher bands are inclusive of the lower ones, and our approximate power limit is denoted with the black line.

The big conclusion is immediately obvious. Even in combination with the lowest possible lift needed to make the turn, the slowest possible speed strategy isn't able to keep power below the limit at high  $k_{grav}$  factors.

Attempting to manage excess power with a slow kite also leaves the strategy open to runaway, with a positive feedback loop as excess power shows up as additional kite speed, which then creates additional excess power, which then speeds up the kite, and on and on.

Lower  $k_{grav}$  factors from those shown can keep the power from wind within limits, but at the cost of the several hundred kW power swings from the energy extracted from the Hamiltonian required to meet that strategy, which then promptly puts the kite over the limit again. Larger path sizes will grow the speed range required for a given  $k_{grav}$  strategy, while smaller path sizes, if possible, will further limit the effectiveness of decreased lift as a strategy.

In short, there's plenty of merit in this strategy, but even combining it with the minimum lift strategy appears insufficient to fully manage excess power.

### 10.3.3 Path

What about the path location? In section 6.1.2, we discussed the  $\cos^3$  losses with increasing path elevation angle. Can it be effectively utilized to manage excess power at high wind speeds? Path location was previously investigated only in the context of elevation offset, but what about azimuth offset? Can both be utilized to shift power peaks around and address the transition zone?

Let's begin with the transition zone. Here, we desire a kite path that flattens the power peaks caused by the  $k_{grav}$  strategy and the potential energy exchange—ie, we want to remove power from the downstroke and add it to the upstroke. For a kite moving clockwise around a path viewed looking downwind, one could imagine an azimuth shift to the right would move the upstroke more downwind, and the downstroke increasingly offwind, as shown in figure 55:

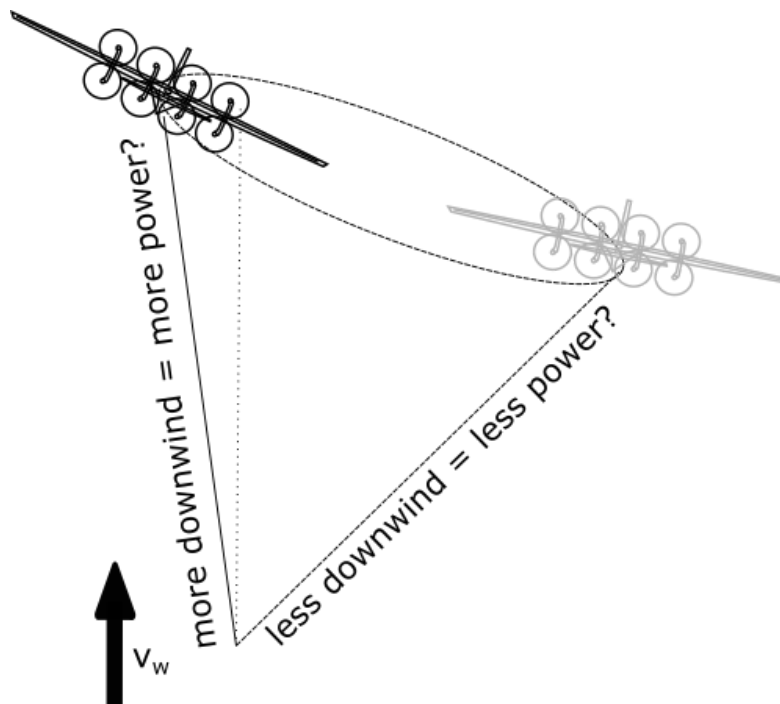


**Figure 55: Desired effect of azimuth offsets is to shift power from where it's unneeded to where it's needed.**

However, recall from above that power is really attenuated by  $\cos^3 \theta_{offwind}$ , ie, roughly by how much the *lift* is rolled offwind, not by the instantaneous path azimuth or elevation offset. For any path where the mean turning radius is close to the ideal size to minimize turning losses derived above, that model implies that this  $\theta_{offwind}$  angle approximately follows that of the path center

offset, and power attenuation is similar on both sides—if this is indeed the case, it is not a good way to accomplish our goal.

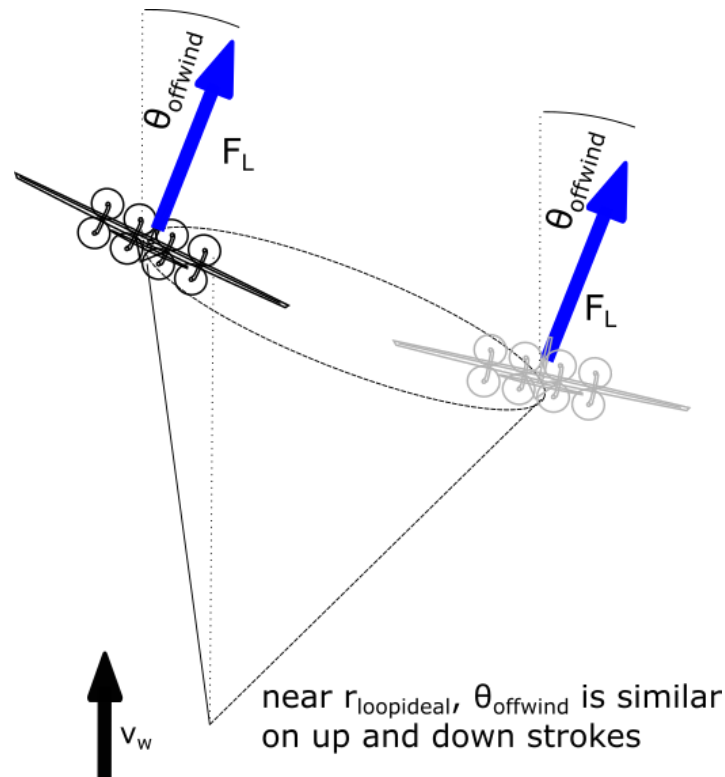


**Figure 56: Typical effect of azimuth offsets, assuming operation close to  $r_{\text{loop,ideal}}$ . In this condition, azimuth alone is ineffective at moving power around as power scales with  $\cos^3\theta_{\text{offwind}}$ , which is similar on both sides of the path.**

However, this effect is compounded by the fact that path offset from the wind introduces path components that are into and out of the wind. Non-circular paths create those components as well, but for optimal paths it's typically not significant, while the components from azimuth and elevation can be quite large. Until now, we've been ignoring the effect this movement into and out of the wind has on power. Does this expected relationship hold true with this effect?

It's possible to piece together an analytical model that captures the key trade-offs here, but this model would be lengthy to derive and cumbersome to use, so we'll instead jump straight to our numerical model.

For this numerical model, we utilize a simplified version of our MX2 kite, with all constraints removed or raised such that they will not be hit, and create a constant 80% efficient rotor and a constant 80% efficient power system from the shaft to the padmount. This is to better isolate the effect of azimuth offsets.

Aerodynamic angles, wind speed, path elevation, and path shape are held fixed as azimuth is swept. To test the hypothesis that power attenuation is a function of  $\theta_{offwind}$  and that for paths close to the ideal this matches the path center offset, we use equation 37 from above to calculate an  $r_{loop, ideal}$ . This gives an ideal path radius of 98 m when operating with a  $C_L$  of 1.81. In the example below, we use this value for path radius for a circular path and keep our path elevation of  $0.45 \text{ rad}^{44}$  from prior examples.

We begin a constant speed strategy at the Loyd optimum  $v_{k_L}$ , to attempt to isolate the effect azimuth has on power, which leaves no free variables to optimize over. To reiterate, the goal in the transition region is to shift power from the peak to the valley.

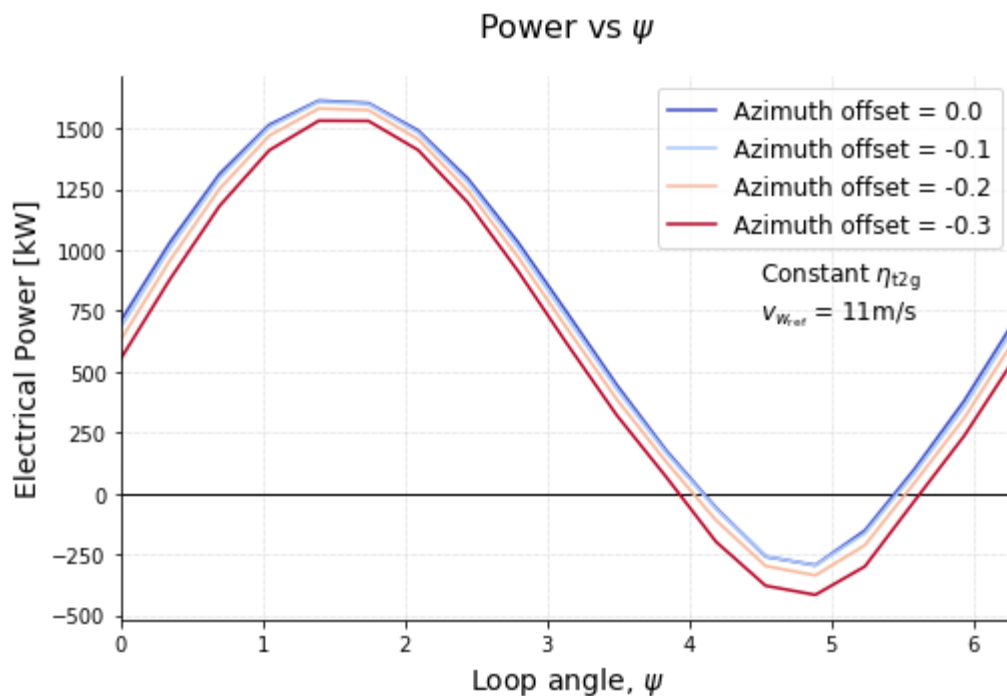


**Figure 57: Power versus loop angle at various azimuth offsets, providing numerical confirmation that turning near  $r_{loop, ideal}$  negates the ability of azimuth offsets to shift power.**

Clearly, the hypothesis is correct in this context—azimuth slews are wholly unable to shift power from the peak for a path at the ideal turning radius. The power looks very nearly sinusoidal with loop angle at all azimuths, demonstrating that the potential energy exchange is indeed the dominant effect for the power fluctuations. The phase shift in airspeed versus kite inertial speed that occurs with increasing azimuth offset doesn't appear to shift the power around much at all. There is an overall drop in power with increasing azimuth that is in line with  $\cos^3$  losses. While those losses can be useful for very high winds, they are not useful for shifting power around in the transition zone.

<sup>44</sup> Yes, this will slightly violate the minimum height constraint, which isn't relevant to this exercise.

We need to be careful that we're drawing the correct conclusions though, as the constant inertial speed strategy used here is naive. Strategies with a high  $k_{grav}$  will see substantial changes in kite inertial speed, which will in turn affect the airspeed, and the required roll angles and  $\theta_{offwind}$  losses. The kite will also move off the peak of the power versus kite speed relationship. Let's investigate a more complex case, with an optimized kite speed strategy.

For this iteration, we go back to our 80 m path radius, slightly tighter than the pure turning losses optimum, and open up kite speed strategy to an optimizer. Everything else is kept the same. We're trying to show just the effect of path location on power, so the optimizer is set up to seek best power in the absence of a power limit—there may be additional speed strategies that can better shift power around in the presence of a power limit. Before we dig into the effect on power, let's see some ways that a numerically optimized speed strategy differs from our  $k_{grav}$  approximations above.

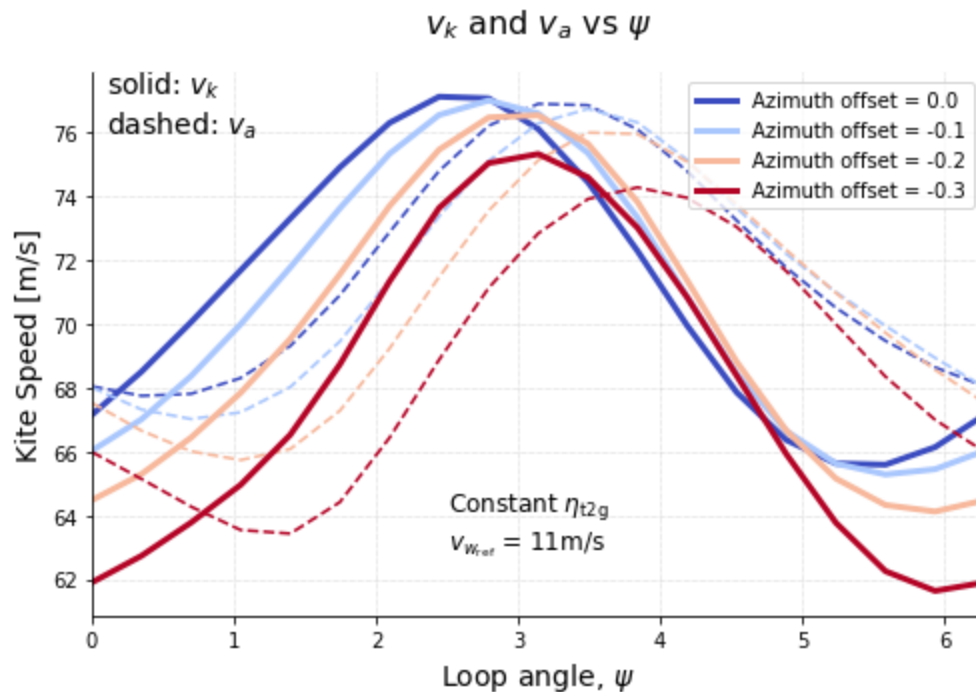


**Figure 58: Kite inertial and airspeed strategies versus loop angle at various azimuth offsets.**

Speed strategies are indeed fairly sinusoidal in shape, and generally centered such that the maximum inertial speed is at the bottom of the loop. What does this look like in terms of  $k_{grav}$  factor? The strategies in figure 58 do not exactly correspond to a simple  $k_{grav}$ , so we define an instantaneous  $k_{grav}$ . We define  $k_{grav,i}$  as the component of the kite's acceleration vector tangent to the path (ie, acceleration that changes the kite's kinetic energy, rather than turns the kite) measured in Gs. With this definition, there's a sign change for the upstroke. A  $k_{grav}$  strategy of 0.5 would result in a  $k_{grav,i}$  versus loop angle  $\psi$  that looks like a sine wave for a circular path,

reaching a peak value of 0.5 for the downstroke and a minimum value of -0.5 for the upstroke. Let's see what this new parameter looks like.

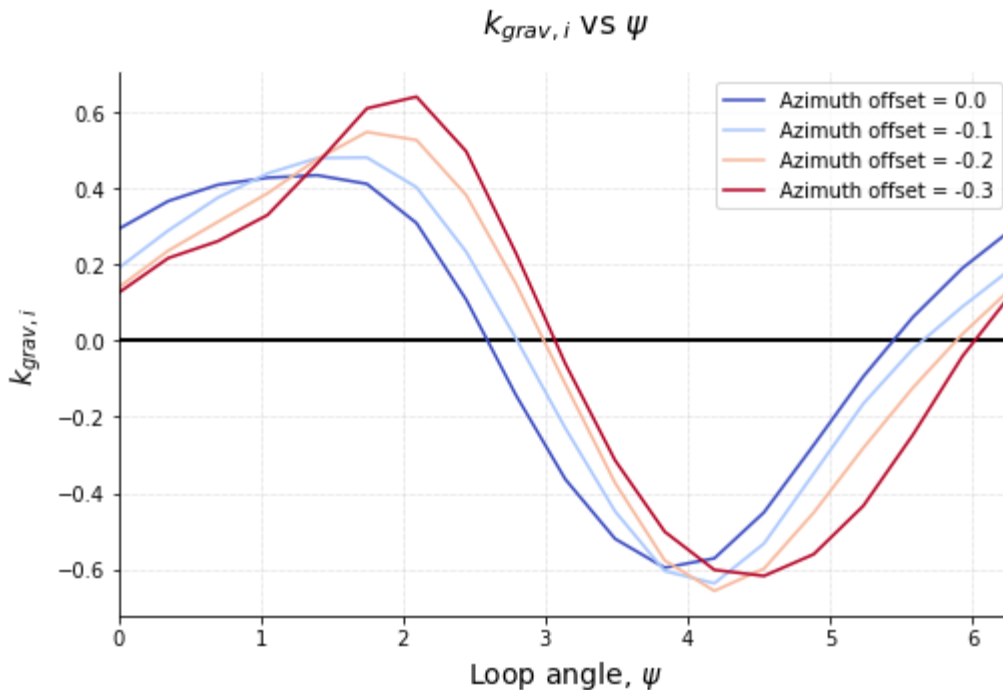


**Figure 59: Instantaneous  $k_{grav,i}$  factors versus loop angle. Real strategies can be more nuanced than a simple  $k_{grav}$  strategy, and can be utilized to shift some power around.**

Although potential energy still forms the main reason we vary speed around the loop, we should simply think of  $k_{grav,i}$  as the rate we're storing energy in the form of kite speed, as it does not necessarily align with moving through the gravity field. This is demonstrated by the phase shift in figure 59. The *peak* value of  $k_{grav,i}$  can usually be used as a decent proxy for a  $k_{grav}$  that represents the effect of the  $\Delta v_k$  in our simpler analytical model, but strictly speaking, the terms represent different things. Effects of a real speed strategy can only be well represented with a  $k_{grav}$  if the strategy is very nearly sinusoidal, which is usually the case.

The first thing to note is that the peak values of  $k_{grav,i}$  appears to be lower than our example above. Potential energy is not the only reason we vary kite speed, and in more detailed models we typically see higher  $k_{grav,i}$  at higher wind speeds as an attempt to minimize power swings from pumping potential energy. Without a constraint applied in figure 59, there is less motivation to maximize this effect. Applying a maximum power constraint will drive the optimized solutions to higher  $k_{grav}$  to minimum power fluctuations.

Now, we can show the effect on power.

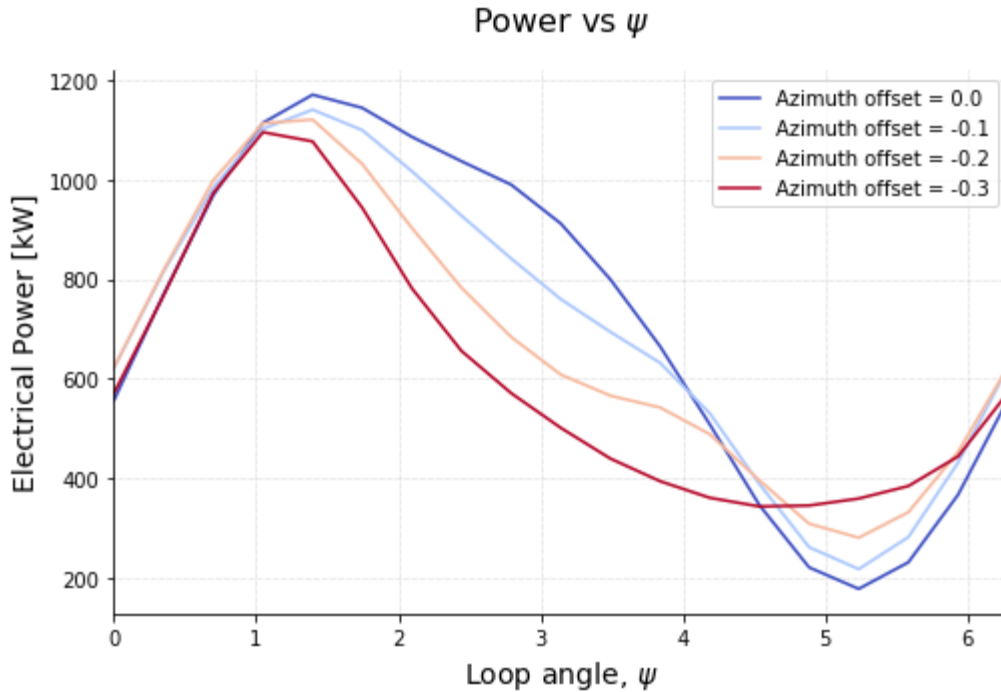


**Figure 60: Power versus loop angle at various azimuth offsets, demonstrating the complex relationship with power once combined with various speed strategies.**

In figure 60, there's now some movement of power near the peak to the valley in an optimal power strategy, but the key takeaway seems to be that speed strategies alone at constant aerodynamic angles can make a complex relationship with power around the loop. It becomes difficult to apply simple analytical trades here, even outside the context of power saturation constraints, as all the various strategies strongly interact with each other.

We can still draw some conclusions though. Overall, path shifts are generally ineffective at shifting power around the loop to offset potential energy induced power fluctuations, but they are effective at overall power reductions. The path elevation and azimuth offset from directly downwind needs to be an integral part of any high wind strategy.

High path offsets create substantial path components into and out of the wind that have second order effects with any speed strategy that can cause some shifts, but we should note that in the context of a turbulent wind field, it can be difficult to reliably make use of any of those effects.

Variable winds create another issue—path changes are slow, acting on time scales of tens of seconds, leaving the kite unable to utilize path change strategies solely for brief increases in wind speed. If the kite is chasing best performance at wind speeds below power saturation, it is unable to leverage path changes to respond to momentary increases in wind speed that require mitigation. A kite on a path that enables it to handle higher winds is then sacrificing performance in order to be prepared to survive the higher winds. The result is that any strategy

has to compromise between these opposing goals, resulting in a soft “knee” in the power curve near rated power.

Another beneficial aspect of large path offsets, aside from lowering the overall power level, is that the lower  $v_{w,eff}$  can continue to shift the  $\zeta_v$  versus  $v_k$  curves to the left, with the peak occurring at lower kite speeds. At very high offsets, it may even be possible to get kite speeds on the other side of the peak and reach a stable scenario where increasing kite speed results in less power production.

Combining all the power saturation strategies described thus far is typically enough for optimization codes with assumptions of perfect control and smooth wind fields to find fully saturated power solutions for most kites to the cut-out wind speeds of 20-25 m/s, with some roll-off in performance as we blend in power saturation strategies. However, these fail in more realistic scenarios, so let’s investigate a few more power management tricks before looking into some overall strategies those codes suggest.

### 10.3.4 Excess Drag

Our final strategy is to deliberately degrade the kite’s performance. The simplest implementation is to utilize existing aerodynamic surfaces at deflections large enough to cause separation.

Makani did some experimentation with this by deflecting the inboard most ailerons to their maximum “up” position, similar to an airbrake on a glider, causing airflow separation and a dramatic increase in drag for that section. However, this strategy is flawed—while presented primarily as a drag device, deflections like this have a similar relative impact on lift. As we noted above, lift is also used to make the turn, so sharp reductions in lift carry with them sharp changes in tether roll angle in order to follow the target path, and the lift reduction directly takes away from how far lift can be reduced by alpha. The spoiler solution is draggier than a similar drop in lift achieved by alpha, but the control challenges associated with the nonlinear behavior of an aileron spoiler made this solution less appealing.

One can of course envision a more pure drag device. Separating power management from the turning forces would greatly simplify the controller effort. The problem is one of complexity. Let’s sketch out what such a device would need to do. Assume there’s a strategy for the path, kite speeds, and alpha such that the kite is able to fully saturate the power system at a wind speed of 10 m/s. The ideal drag device would be able to completely manage the excess power of a wind increase until such time that a new strategy can be implemented, where the limiting factor is the path location operating on the timescale of tens of seconds.

If power saturation occurs at a thrust power of  $\sim 1200$  kW, and we desire the drag device to handle a change in wind speed of 2 m/s, then the power the drag device needs to dissipate is given simply by  $1200 \text{ kW} \left( \frac{12 \text{ m/s}}{10 \text{ m/s}} \right)^3 - 1200 \text{ kW}$ , which is approximately 875 kW. Assuming our drag device has a  $C_D$  of 1, is operating at sea level, and the kite average speed

$\bar{v}_k$  is 70 m/s, the required area of our drag device is  $\sim 3 \text{ m}^2$ . This is fairly large, but not entirely impractical. It's difficult to consider devoting mass, cost, and complexity to a system that reduces performance everywhere to only be helpful in such a narrow context, but the real threat to the idea is that an onboard generation kite already has a much larger set of variable drag devices—the rotors!

The fact that we're dealing with a power saturation issue clearly indicates the rotors should already be working hard, so for this use case, what we desire is for the rotor efficiency to dramatically drop. Let's begin by taking a look at a map of our MX2 rotor efficiency, truncating the color scale to positive efficiency only for clarity:

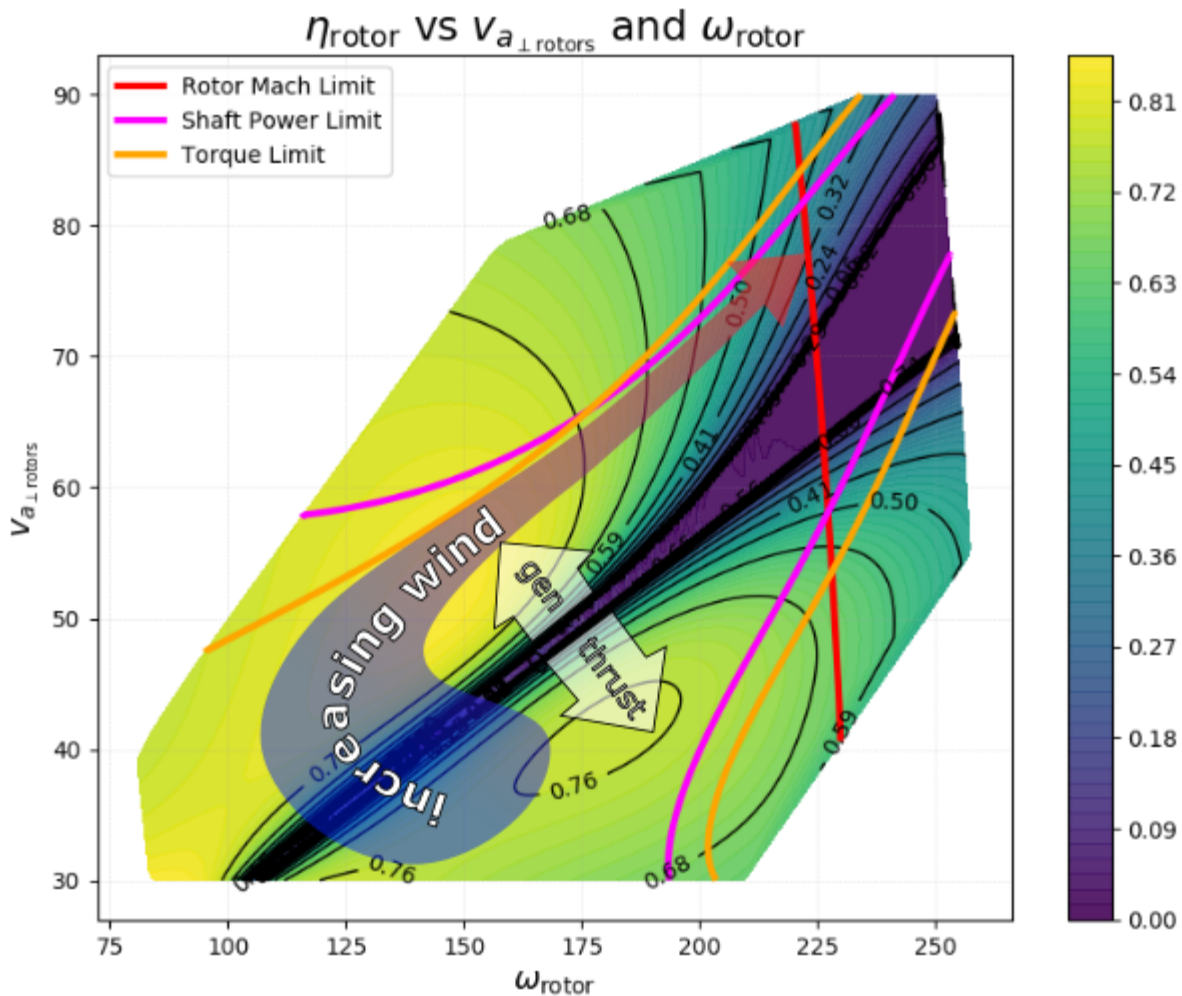


**Figure 61: Rotor efficiency as a function of rotor speed and airspeed for the 4th generation Makani rotors. The lower right represents forward thrust, consuming power, while the upper left represents rotor drag, generating power.**

Various fixed pitch rotor maps will look different, but the general form will be approximately the same. The blue arrow follows the approximate path a strategy takes through the map with

increasing wind speeds. We begin at the bottom on the lower side of the efficiency valley, where we're consuming power, then quickly moving to pass through the generation efficiency peak at moderate winds. As we reach the upper shaft power saturation line marked in magenta, we see that efficiency takes a nosedive as we follow this limit into higher airspeeds. At the uppermost corner, where the rotor is hitting its mach limit (in this case, a tip speed limit of  $\sim$  mach 0.8), efficiency is at just 40%. Given that first saturated power is reached at  $\sim$ 75% efficiency, and this occurs at a thrust power of  $\sim$ 1.2 MW, the excess thrust power this consumes is a massive 1.4 MW, making this drop in rotor efficiency several times more more effective than a large deployed drag device, and even better, we don't need to spend any additional mass, cost, or (hopefully) maintenance on it.

What are the potential downsides of this? First is noise—rotor noise is strongly coupled with rotor tip mach speed, and utilizing this strategy requires intentionally reaching these high tip speeds, likely limiting heavy use of such a strategy to offshore or other remote locations. The second is rotor life, as high speed rotors, especially those operating close to mach 1, result in increased wear.

### 10.3.5 Piecing Together a Strategy

We've identified many pieces of a power saturation strategy—can they be assembled into a robust solution?

Here, we'll lean entirely on our numerical model to balance these trades, adding in the numerous constraints we've been ignoring until now—constraints like limits on power, torque, rotor stall, tension, airspeed, and others. The solution is not general—perturbations of starting conditions, changes in the kite model, changes in the optimization parameters and penalties, and more can result in different strategies, but they all share some common traits. With that in mind, let's investigate a particular result.

Before we do so, it should be reiterated that several different codes, models, and optimization tools have been able to identify strategies that work under the simple conditions in each model, but Makani was unable to find successful strategies in simulation with imperfect control, imperfect sensors, and more importantly, realistic turbulent wind fields. As a result, these high wind strategies were never tested in flight—the risk was deemed too high, and we restricted ourselves to lower wind speeds during test flights. We'll talk more about the modeling work and the simulation needed to highlight these issues in a moment.

We're not going to dig into all the modeling details and settings here, as the code and model these results are based on is provided, but the high level view is that this model assumes perfect control and no wind turbulence. Taking the MX2 model and optimizing it for power across all wind speeds with a circular path shape and no wind shear for simplicity results in the power curve shown below, with the maximum and minimum power around the path also shown in figure 62.

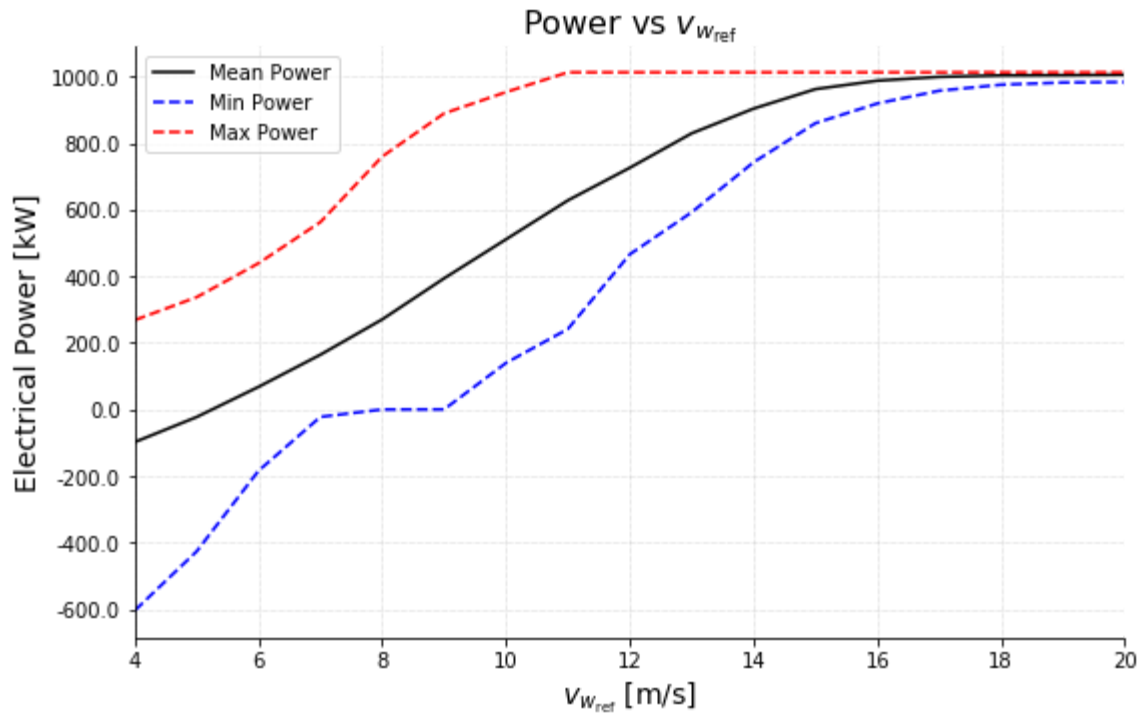


**Figure 62: Minimum, mean, and maximum power around a loop for different wind speeds. Note the kink in minimum power around zero, as the optimizer strives to minimize pumping losses by eliminating power consumption as soon as possible.**

This kite begins saturating power at  $\sim 11$  m/s of wind, and is mostly saturated at 15 m/s. We'll look for strategy changes across what we'll call the "transition zone" from 10-15 m/s, and in what we'll call the "survival zone" from 15-20 m/s.

#### 10.3.5.1 Path Strategy

In figure 62, we view the paths looking downwind, located by their centroids, rotated to be flattened into the viewing plane for clarity, and colored by position to denote model evaluation points—we'll reuse these colors to mark these positions in some later plots. The flattening undercuts how much azimuth slew is going on here—with a tether length of just 300 m and path radii around 100 m, an offset of  $\sim 280$  m is entirely perpendicular to the viewing plane we've squashed the paths onto. The arrows indicate the direction of travel—clockwise in this case. In later plots, we'll present data versus normalized path distance. In all those examples, we begin our path at the top, and proceed clockwise.

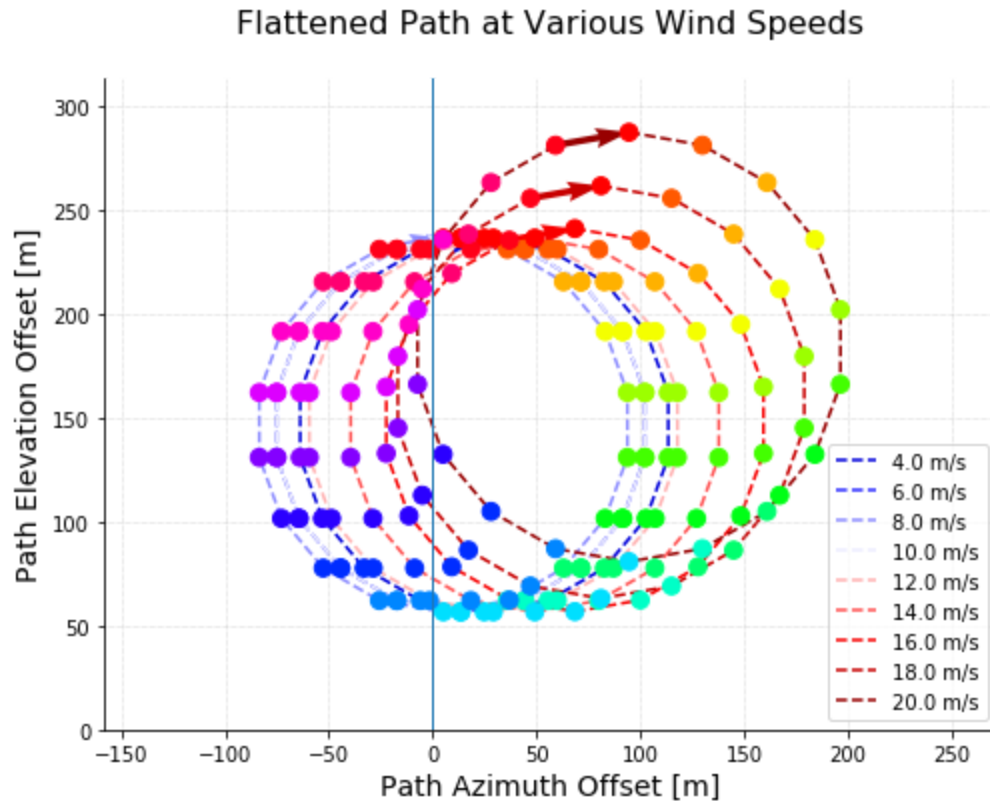


**Figure 63: Visualization of the path strategy at different wind speeds. Paths are flattened to the viewing direction, which is directly downwind.**

The path strategy in figure 63 has some small azimuth shifts that move the downstroke further off-wind in the transition wind speeds, but there isn't much of a strategy change until winds approach the survival zone at  $> 15$  m/s. At this point we begin to see substantial azimuth and elevation offsets, with slightly larger path radius as well.

#### 10.3.5.2 Lift and Speed Strategy

Before picking apart the lift strategy, it should be noted that this kite is an actively tension-limited kite. Tension limiting was discussed in section 6.1.8, and here the start of tension limiting intentionally coincides with the start of power limiting, also about 10 m/s of wind. The highest tension portions of the loop also roughly correspond to the highest power portions of the loop, and there's substantial overlap in the response to each—lower alpha and airspeed.

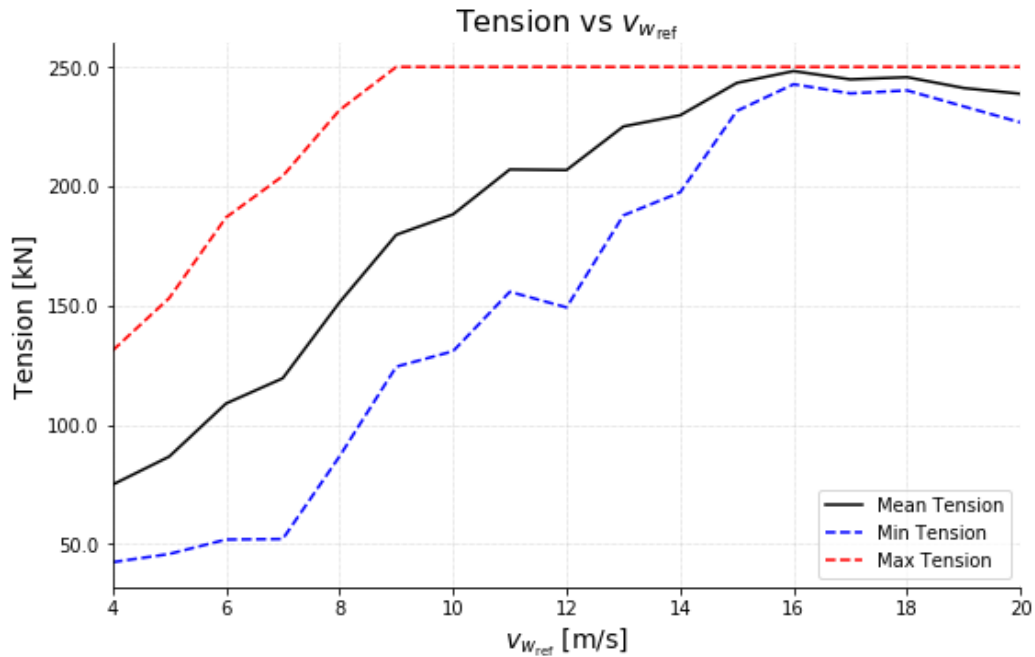


**Figure 64: Minimum, mean, and maximum tension versus wind speed. Tension limiting begins at around 9 m/s of wind, and the entire loop is nearly operating at the tension limit for wind speeds >15 m/s. Jaggedness is from optimizer solution variations.**

Airspeed strategies look fairly sinusoidal, and increase nearly linearly with wind speed until we reach the survival regime, at which point speeds no longer increase, utilizing the lower airspeed as a power and tension management strategy.

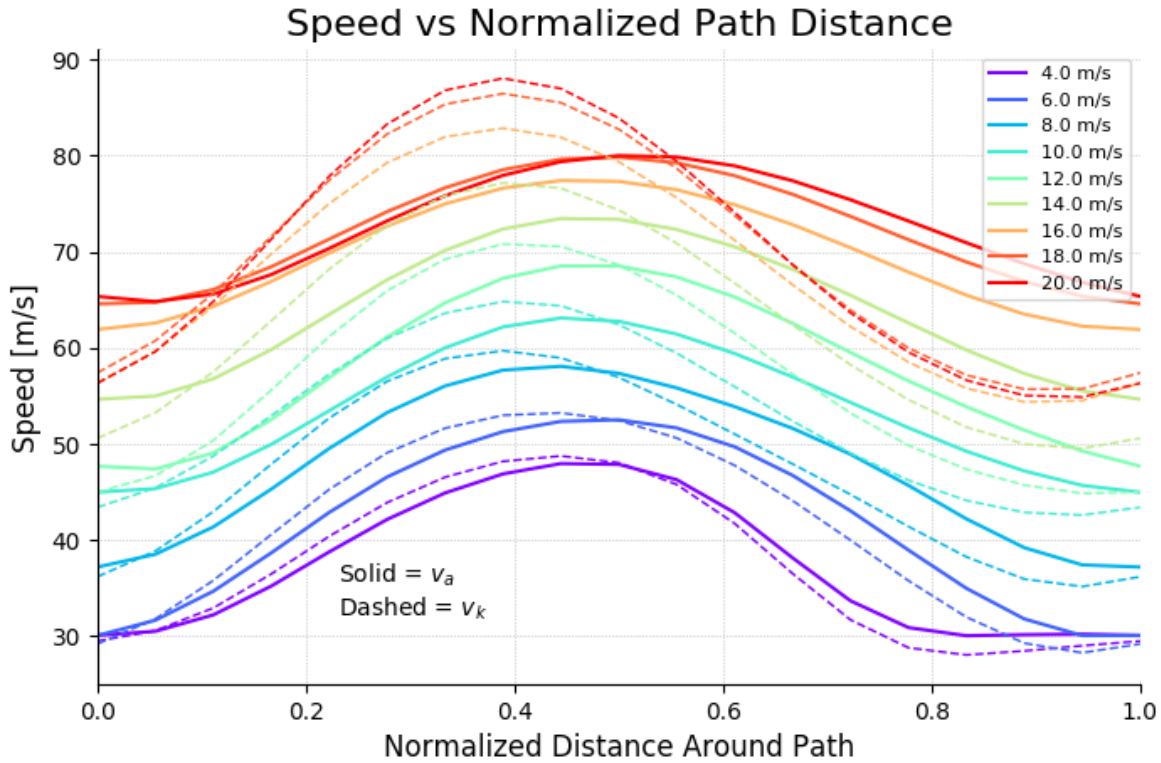


**Figure 65: Inertial speed and airspeed versus distance around the path at various wind speeds. The difference between them grows at higher wind speeds due to the increasingly offset azimuth and elevation strategies.**

How much is this model able to reduce alpha? In figure 51, we showed an analytical model that indicated a limit of  $\sim -7$  deg of alpha for this kite to continue being able to make the turn. Here, we see the limit here is slightly below the estimated limit. This alpha reduction begins primarily as tension management, looking like the inverse of the airspeeds in the transition zone from 10-15 m/s of wind with dips in alpha at the bottom of the path, but broadens that lower alpha region to be more on the downstroke as we move into the survival wind speeds  $> 15$  m/s, where it's now also working to manage power.

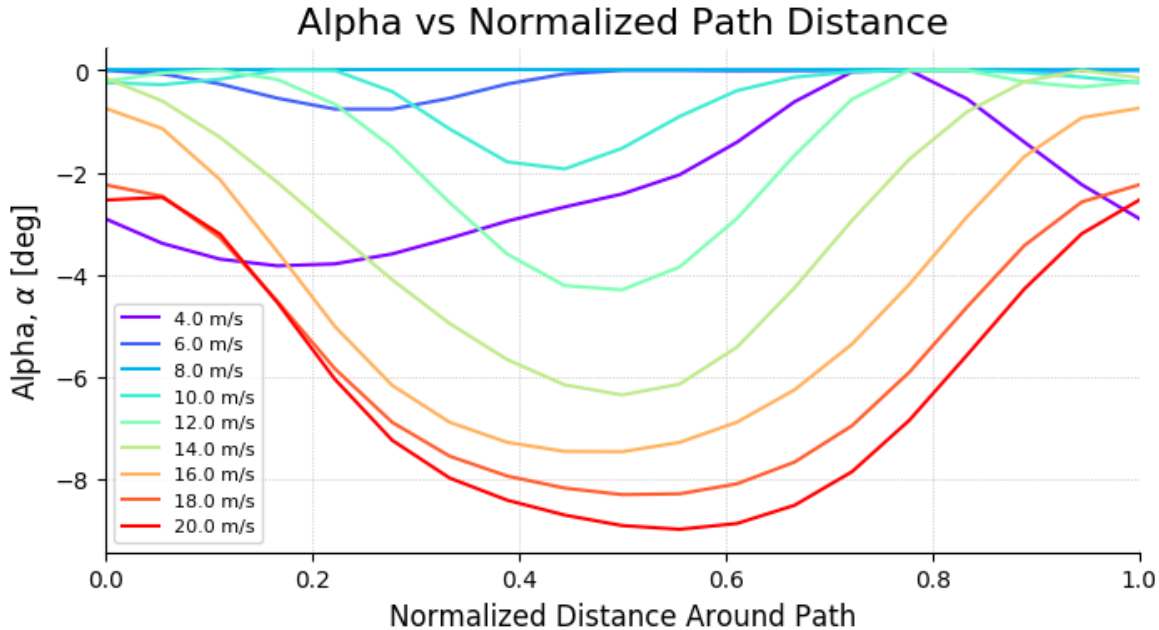


**Figure 66: Alpha versus distance around the path at various wind speeds. Low winds see alpha drops to minimize losses, medium winds see nearly constant operation at the optimum, while high winds see substantial reductions in alpha to manage excess power.**

We haven't discussed strategies at the lowest wind speeds, but there's also a drop in alpha for 4-6 m/s of wind. At these wind speeds, the downstroke, where the kite is moving downwind, sees very low effective wind speeds. With little power to be had from low winds, the kite instead shifts to reducing losses and lowers alpha in pursuit of a higher  $C_L/C_D$  to reduce drag. The minimum sink criteria,  $C_L^{1.5}/C_D$ , shares its peak with  $\zeta_L$ , but is only relevant if the aircraft can fly as slow as possible. Here, our speed strategy approaches the minimum airspeed, but the  $k_{grav}$  strategy dictates some higher airspeeds, making  $C_L/C_D$  more representative of losses.

Speaking of  $k_{grav}$  strategy, let's take a look at it.

A  $k_{grav,i}$  over one means we're accelerating the kite faster than 1 G, basically storing some of the wind energy in kite speed in addition to potential energy. We see this happening in a fairly concentrated region on the downstroke and upstroke, and these values only appear when the kite enters the transition zone as a strategy to shift power from the peak.

At moderate wind speeds of 8-10 m/s, the optimizer is just finding the balance between off-optimal speed losses and grid pumping losses, as we did in our analytical model before, with similar average absolute values of around 0.4-0.5 at these wind speeds.

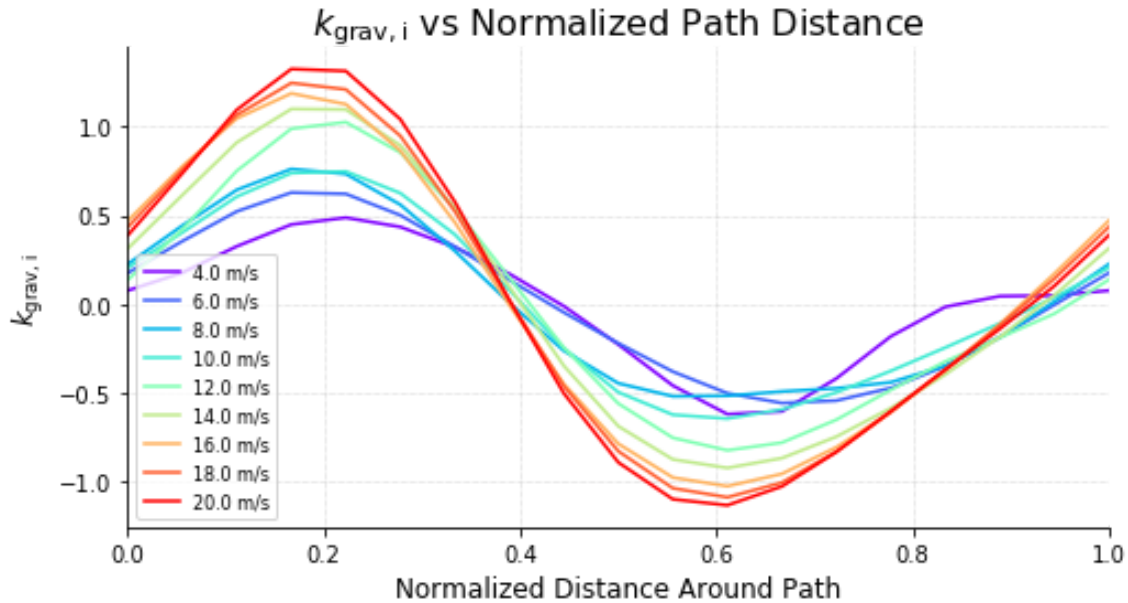


**Figure 67: Instantaneous  $k_{grav,i}$  fractions versus distance around the path at various wind speeds. At high wind speeds, the system stores a lot of wind energy in kite speed on the downstroke, as shown by the  $k_{grav,i}$  factors reaching well over 1.**

Interestingly, at the very low wind speeds  $\leq 6$  m/s, the trend is reversed from our analytical model, which was trending towards a  $k_{grav}$  of 1. The analytical model simply falls apart here. Minimum kite speeds combined with typical elevation angles result in the kite moving upwind or downwind faster than the effective wind speed on the upstrokes and downstrokes! This largely invalidates our model for  $\zeta_v$  at these very low wind speeds. The power penalty of going fast is higher and the balance shifts towards a slower, more constant speed strategy with lower  $k_{grav}$  values. Despite these inaccuracies, the analytical model still works well for predicting cut-in, and captures the sensitivities at medium and high winds well.

### 10.3.5.3 Rotor Strategy

Barring the nosedives to negative efficiencies as the rotor flops through a no power zone between generation and power consumption at the lowest wind speeds, the bulk of the “make as much power as possible” regime from 6-10 m/s of wind is at a fairly constant rotor efficiency, around 80%.

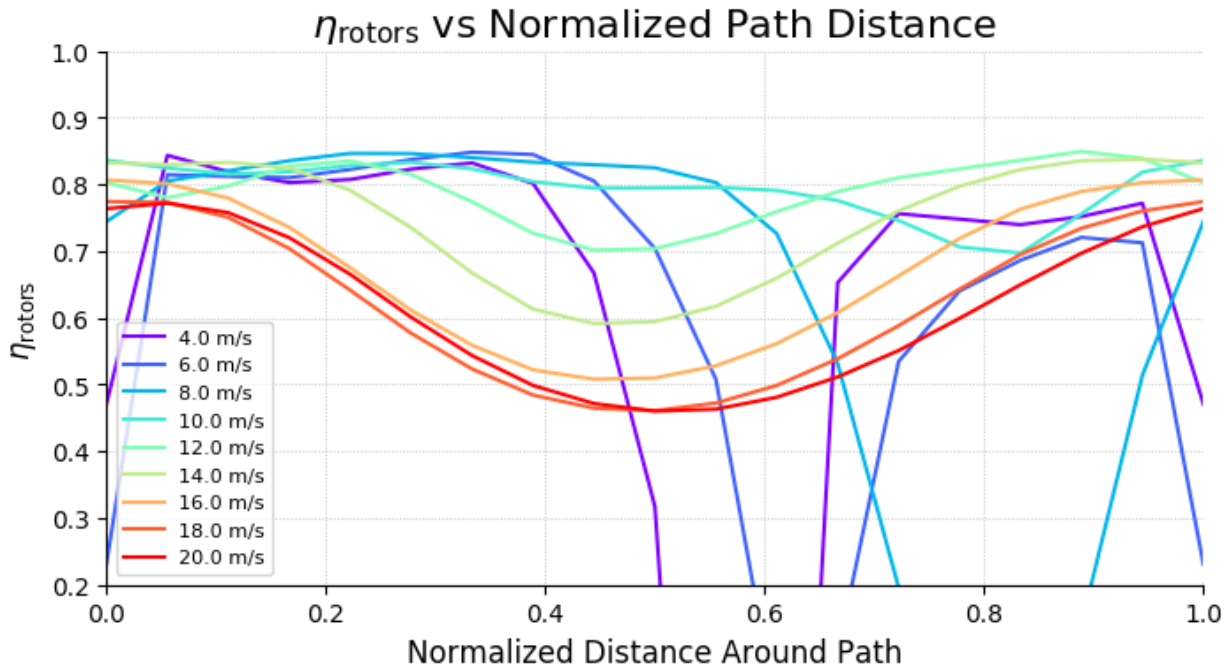


**Figure 68: Rotor efficiency from thrust/drag power to shaft power versus distance around the path at various wind speeds. Transitions between thrusting and generation at low winds aside, the system typically operates at a nearly constant efficiency until high winds and high kite speeds are reached.**

Throughout the transition zone the kite utilizes increasingly inefficient rotors, and is heavily reliant on draggy rotors to manage excess power at the highest wind speeds, shedding almost  $\sim 1.5$  MW of excess wind power from the drop in efficiency. Perhaps equally important is that the rotors are still fairly efficient at the top of the path in order to saturate power. In fact, if we look at what else the kite is doing at this point, nearly everything is working to maximize power. Alpha is only lowered by  $\sim 2$  deg, and kite speeds are near the ideal for the effective wind speed. Saturating power requires the kite to work fairly hard to make power for part of the loop, and then work equally hard to dump excess power for the rest, even at the highest wind speeds.

Alternatively, we can plot these solutions onto our rotor map. Using the same coloring for the paths and different positions for each wind speed as above, we find what is shown in figure 69.

In figure 69, we can easily visualize how well the rotor is matched to the airframe. At low winds, the strategy traverses the highest efficiency regions of the generation and consumption contours. The low efficiency valley in the middle corresponds with essentially no power or thrust, and has little effect. Power saturation is entered while still near the efficiency peak, and following the power limit sends us quickly off this peak, which is what we're looking for.

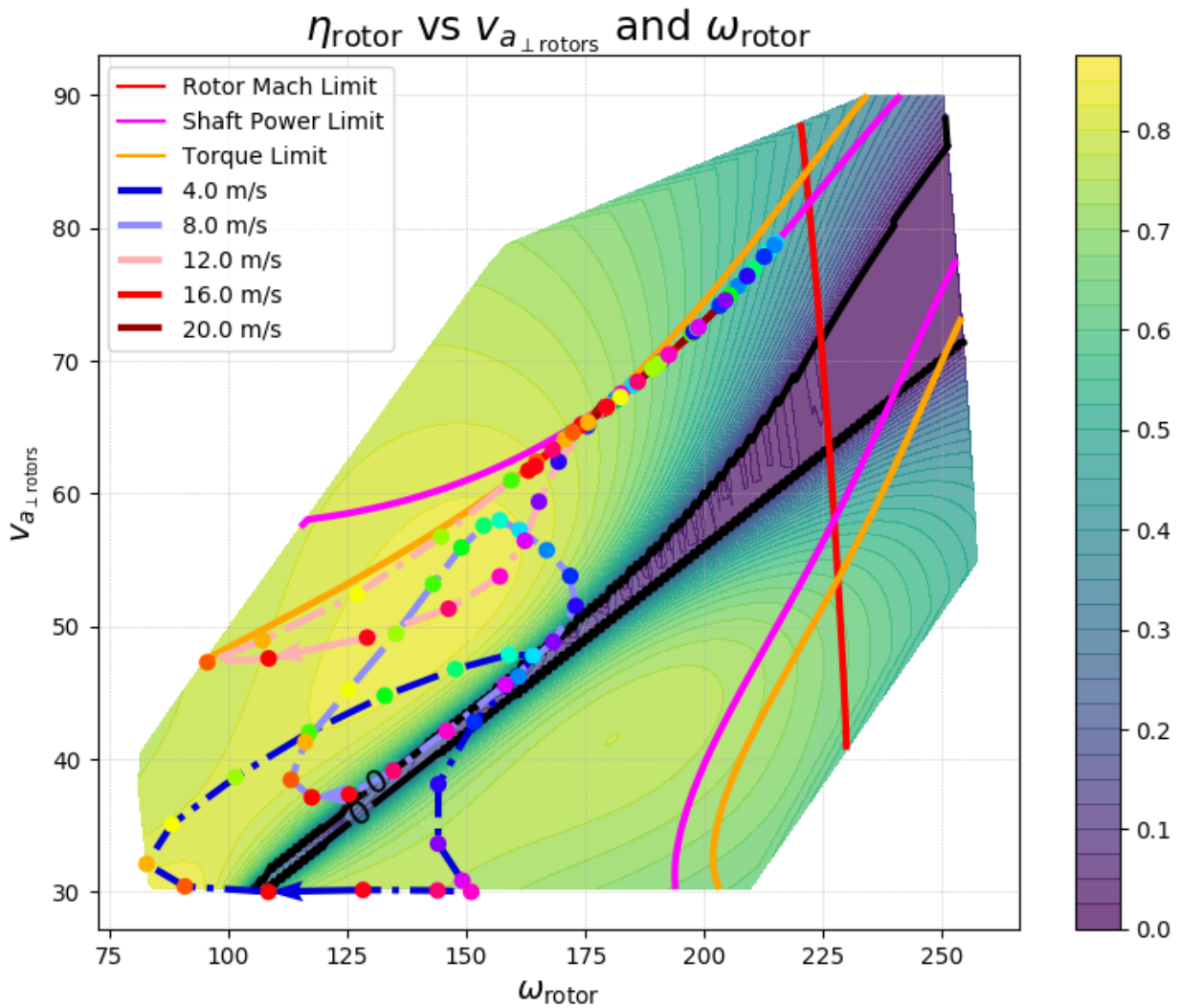


**Figure 69: Rotor map for the MX2 overlaid with loop solutions at various wind speeds. Path locations are colored the same way as in figure 63. High wind speeds ( $\geq 16$  m/s) loops are obscured, as solutions follow the power limit line.**

Now that we’ve identified a possible representative strategy, let’s pick it apart.

### 10.3.6 Poking holes in our strategy

As mentioned in the section introduction, power saturation remained an unsolved problem at Makani. Several optimization efforts in a variety of tools have been able to find solutions similar to that shown above, so perhaps the easiest way to highlight issues with these strategies is to pull out the key differences between the models where strategies like this work, and the model where it doesn’t.

Makani had 3 main efforts where we were able to find viable strategies to survive to a cut-out wind speed of  $\sim 20$  m/s. Those efforts included an older Optimal Control Problem (OCP) code

for the M600, the numerical model provided and used for the solution above, and a black box optimization on the outer loop control strategy implemented in the simulator.

The context where the strategies developed by these tools don't work is the full simulator, the source code of which has been released, with realistic turbulence provided by NREL's statistically derived TurbSim models [9], and imperfect knowledge of the system and sensors. At high winds, all these strategies fail in similar ways. Excess power leads to overspeeding, resulting in excessive loads and poor kite control.

All optimization models provide very similar results for wind speeds below the transition zone—tight low loops with a sinusoidal speed strategy at best  $\zeta_L$  alphas—and broadly similar strategies at the transition zone and beyond—larger path sizes at higher elevation and azimuth offsets, with reduced alphas.

Perhaps the most interesting of these models is the optimization using the simulator. It's the most complete model with the closest representation of reality. Why didn't this approach work? The simulation strategy optimization was only completed for the M600 simply due to a lack of time. A single simulation requires minutes of compute time, and optimization using this model requires hundreds of thousands of simulations. As a result, optimizing under a single set of conditions requires a large amount of compute resources, and the MX2 model wasn't yet mature enough in the simulator to devote those resources.

In the interest of not introducing yet another model only to arrive at a similar set of incomplete results, I'll only briefly summarize this attempt. The simulation optimization effort utilized a gentler turbulence model<sup>45</sup> and a fixed nominal configuration with perfect sensors. Both changes were attempting to address the lengthy compute—the ideal optimization process would use a wide range of wind fields and a monte-carlo variance of the physical system to ensure robustness, but computational requirements grow quickly. The brief summary of results is as follows:

- Moderate wind speed strategies are not particularly constrained or sensitive—the introduction of even a small amount of noise from control errors and turbulence during optimization results in widely varying strategies with relatively small power differences. Simpler tools combined with hand tuning can find similarly effective strategies that are smoother and much easier to design and implement.
- The introduction of turbulence and control errors smear out the transition zone we see in the simpler models—power mitigation efforts must begin earlier so that the kite is prepared to handle a wind increase or control error, with a detrimental effect on the power curve.
- Safe strategies could be found to survive to a cut-out wind speed of 20 m/s.

---

<sup>45</sup> The Dryden turbulence model, commonly used for aircraft flying at higher altitudes and faster speeds, but not particularly appropriate for ground level turbulence for wind turbines.

- No strategies could be found to saturate power for the M600. Any optimizations that were able to find survivable solutions up to 20 m/s of wind did so at a much lower average power level by flying large paths with significant azimuth and elevation offset, reducing power around the entire path.

Getting back to the presented solution, let’s discuss the effects included in simulation that cause it to fall apart.

### 10.3.6.1 Turbulence

The fact that simply removing or reducing turbulence from simulation is enough to find survivable (but not power saturated) solutions for the M600 is a strong indicator that turbulence drives the failure to translate solutions from simpler models.

Let’s dig into this using our simpler numerical model. Using the solution above and perturbing the wind, we can get thrust power sensitivity to wind gusts around the path for different wind speeds.

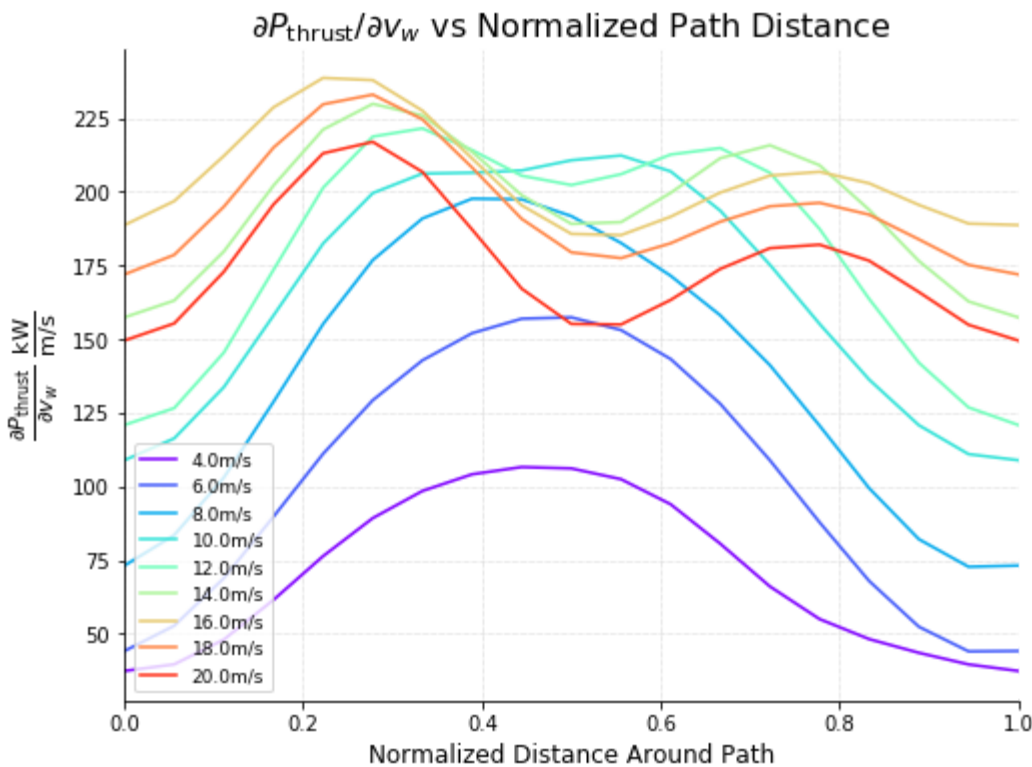


**Figure 70: Change in thrust power for a change in wind speed versus distance around the path at various wind speeds. High winds bring increased power sensitivity to gusts—unsurprising given the  $v_w^3$  relationship with power.**

The sensitivity in thrust power to wind gusts is huge. A small gust of just 3 m/s at moderate to high winds can create an additional 600 kW of excess thrust power! Here, the low mass of an AWT (compared to HAWT rotor inertia) works against itself, leaving little time to manage this excess power before accelerating into excessive speeds. For our MX2 kite, 600 kW of excess thrust power at an inertial speed of 75 m/s accelerates the kite at about  $4 \text{ m/s}^2$ , or nearly half a G—this is much too fast for path changes to have a meaningful effect, leaving immediate management of this to other strategies.

The shape of these curves is also interesting, and is mostly driven by path location as a result of the  $\cos^3$  sensitivity to wind combined with movement in and out of the wind on the upstroke and downstroke. Unfortunately, moving these curves around by changing the path shape and offsets also affects the mean power production—a path that is less sensitive to wind gusts is also a path that generates less power. There's still room for improvement here though. Penalizing high sensitivity to wind results in higher azimuth and elevation offsets from the wind direction, and there's a small region where this can be done with small impact on power. In other words, there's a tradeoff between reducing the average saturated power level and robustness of the saturated power solution to wind gusts.

#### 10.3.6.2 Control Variability

Imperfect control is another significant contributor to the issue. We see a similarly large sensitivity in power to most control parameters. Errors in alpha are an obvious example—we expect changes in lift to have a strong relationship with power. Repeating the exercise from above but for alpha results in figure 71.

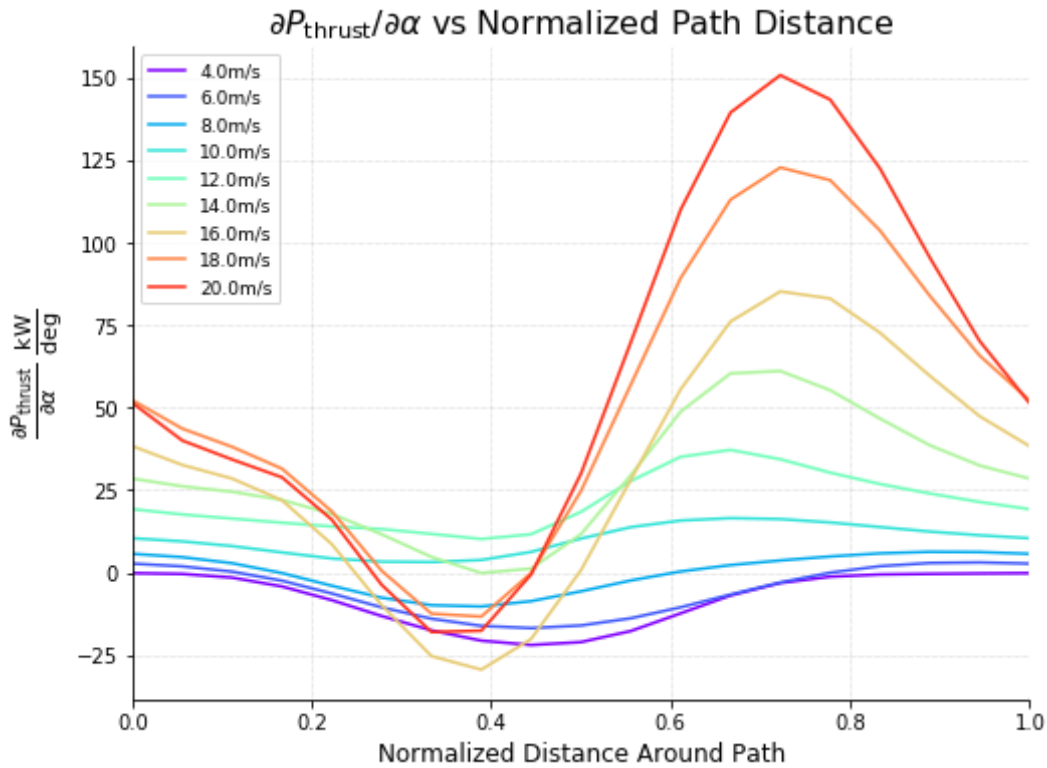


**Figure 71: Change in thrust power for a change in alpha versus distance around the path at various wind speeds. This sensitivity is highly dependent on path strategy and loop angle.**

In figure 71, the sensitivity is concentrated on the upstroke at high winds, where the kite is flying into the wind, but we find that a degree or two of error can result in a hundreds of kW change in thrust power. Again, with a relatively lightweight kite, these errors can build to become an overspeed problem quickly.

### 10.3.6.3 Tether Dynamics

Thus far, we’ve neglected to discuss any tether dynamics, and our models have all assumed a rigid, straight-line tether. There are two areas where a more realistic tether model makes things more difficult.

The first challenge is the energy stored in the tether. Energy stored in the spring of the tether can be given by the equation below, where  $E_t A_t$  is the net elastic modulus and cross-sectional area of the tether,  $E_{tether}$  is the energy stored in it, and  $k_{tether}$  is the spring constant of the tether. Here we’ll ignore the effect of catenary on the spring constant, as the total energy stored in the catenary is typically rather small:

$$E_{tether} = \frac{1}{2} k_{tether} \left( \frac{F_T l_t}{E_t A_t} \right)^2 = \frac{1}{2} \frac{F_T^2 l_t}{E_t A_t} \quad [92]$$

The MX2 and M600 share similar tether properties, with an  $E_t A_t$  of 18 MN, resulting in a  $k_{tether}$  for a 300 m tether on the MX2 of ~60 kN/m. The energy stored and released in the tether (again, neglecting the effect of catenary) as a result of a large normal tension variation from a low of 120 kN to the peak of 250 kN is ~400 kJ. Compared to the potential energy exchange of ~2.7 MJ, or the ~tens of MJ of thrust energy generated per loop, this is small, and it's fairly appropriate to have ignored it thus far.<sup>46</sup>

At high winds, ideal operation sees little change in tension around the path, so this should be even less impactful. However, gusts and control errors can create sudden swings in tension. Sudden reductions in lift come with sudden dumps of this stored energy into the system, making the control problem more difficult.

The second challenge is the tether plunge mode. Neglecting the mass of the tether and again ignoring catenary effects, we can find the natural frequency of this plunge mode below:

$$f_{plunge} = \frac{1}{2\pi} \sqrt{\frac{k_{tether}}{m_{kite}}} \quad [93]$$

With this simple model, the natural frequency of the plunge mode for the MX2 kite is approximately 0.9 Hz, and about 0.8 Hz for the M600. The tether plunge mode is omnipresent—the M600 sees this mode (closer to 0.75 Hz for the real system, as catenary and tether mass slightly slows this down) present in much of our flight test data. Bouncing the kite on the end of the tether creates additional controls challenges—shedding and gaining lift from gusts or control actions can excite this mode and begin to jerk the kite around. Actively controlling tension or power is challenging as the controller is bandwidth constrained.

#### 10.3.6.4 All the Rotors

In order to saturate power at high winds, the kite by definition needs to follow the power limit line on our rotor map. While effective at dissipating large amounts of excess power, this is highly constraining and difficult to achieve in practice. The model used here has a single representative rotor—the real system with 8 rotors has differing local airspeeds as a result of circulation created by the wing lift combined with body rates. The result is a fairly wide spread in operating conditions for each rotor. Future plans for the MX2 design were to incorporate location-specific rotor designs, changing pitch to match typical crosswind conditions at each station.

In addition, the rotors need to balance meeting thrust commands with moment commands. Optimums shift throughout the range of wind speeds. At low wind speeds and slow kite speeds, control surfaces lack effectiveness and undesirable rotor moments can overwhelm them, so

---

<sup>46</sup> It can become significant for offshore floating systems, or much longer tether lengths.

rotor moments should be kept low or used to actively steer the kite. Moderate wind speeds and kite speeds should have the rotors prioritizing best power as the control surfaces are more easily able to reject undesired moments.

It's unlikely that all rotors will be able to be simultaneously saturated for the breadth of conditions for the entire saturated power regime shown, like this simpler model with a single representative rotor is able to. Some derating of the system will be required to account for this effect, likely reducing the rated power by an anticipated 10-20% from that shown in the power curve plots above. This derating due to imbalanced rotor limits is at least partially responsible for the blackbox simulation optimization for the M600 resulting in less than fully saturated power. The net effect for the MX2 system remains unquantified—because this is inextricably tied to the overall power saturation strategy, it too remained unsolved for Makani.

### 10.3.6.5 Kite Acrobatics

An AWT under normal operation needs to be a fairly acrobatic aircraft. Optimal operation will have the kite turning tight paths at low elevation under consistently high alphas. This isn't unexpected, but the power saturated regime poses additional challenges here as well.

Reducing lift to manage power raises body rates that are already high, as the kite must quickly change its roll angle to compensate for the loss of lift and continue to make the turn. High performance AWTs, with wings more akin to gliders than stunt planes, can struggle here. In figure 72, we look at the body rates for our solution.

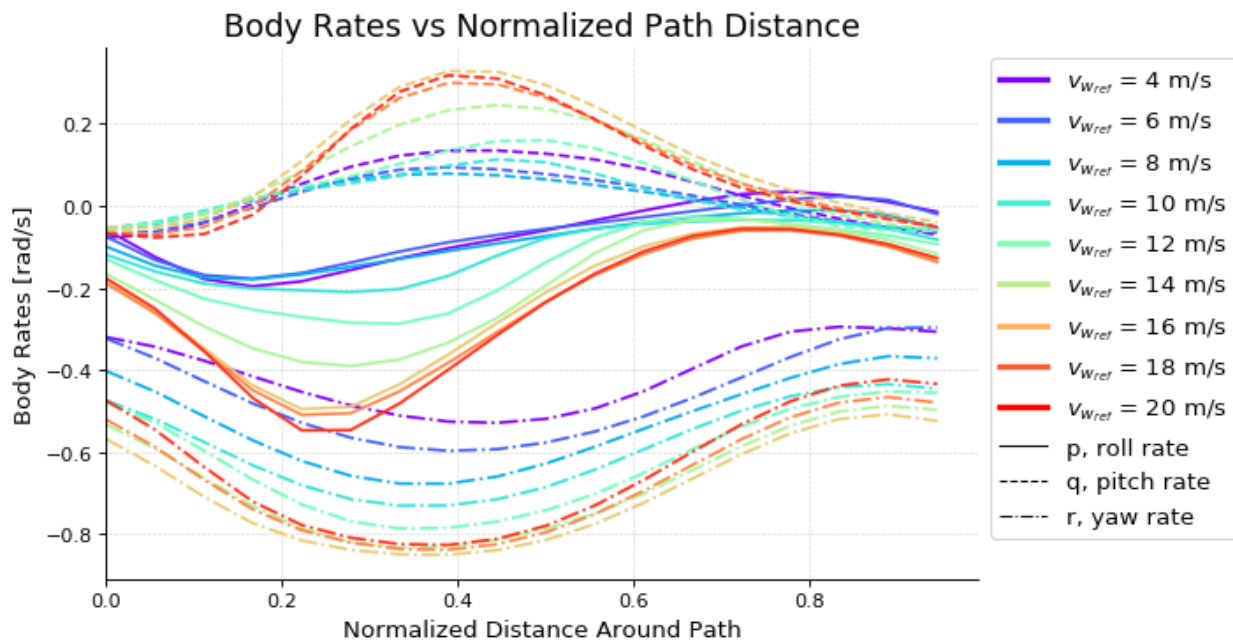


**Figure 72: Angular body rates about each axis versus normalized path distance at various wind speeds. High wind speeds bring with them higher body rates. Of particular importance are the large roll and yaw rates.**

The body rates shown here are assuming nominal operation, with perfect control and no gusts. Real rates can fluctuate by 10 deg (0.17 rad) per second or more. These high body rates bring with them large aerodynamic moments that then require large control surfaces to counteract. These considerations drove much of the MX2 tail design, and gave us additional motivation to avoid increases in span, despite the induced drag benefits of doing so.

## 10.4 Power Saturation Summary

In the end, it all comes down to addressing turbulence and shifts in wind speed. If a solution is to exist here, it would be helpful to contain a few key elements.

1. The kite should operate at the peak shaft power as a function of kite speed in the saturated power regime, such that the *combination* of changes in rotor efficiency and thrust power as the kite overspeeds leaves the system within the power system capabilities.
2. The path must be tight, at least in the vertical dimension, in order to reduce power and speed fluctuations from the potential energy exchange.
3. The kite design needs to be able to support large tether roll angles and high steady state body rates, and quickly stabilize under excursions.
4. It's desirable to fly a path such that the kite is operating at the peak propulsive power as a function of kite speed, such that overspeeds are passively stable.

The first criteria is met by our solution, which we can see in figure 73.

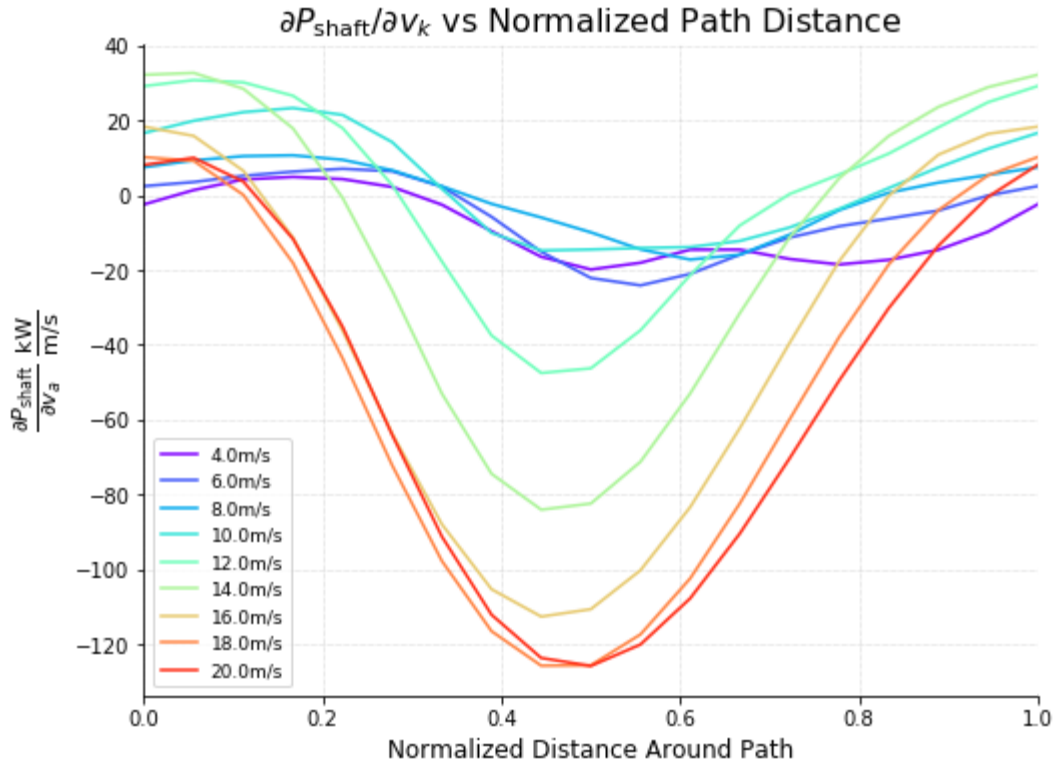


**Figure 73: Change in shaft power for a change in kite speed versus normalized distance around the path at various wind speeds. Thanks to plummeting rotor efficiency, increasing kite speeds at high winds can reduce shaft power, creating some room to generate additional drag.**

As kite speed increases, high winds generally see a decrease in shaft power, meaning that we come off the power limit line on our rotor maps and gain some drag thrust margin on our rotors, thanks to the plummeting efficiency of our rotors. The system is then able to add drag to correct an overspeed where the value in the above plot is negative (at lower wind speeds this isn't necessary, as we're not at maximum power). This derivative does not meaningfully change for changes in airspeed of 5-10 m/s.

The fourth criteria is not met here though. In figure 74, we plot the change in thrust power for a change in kite speed.

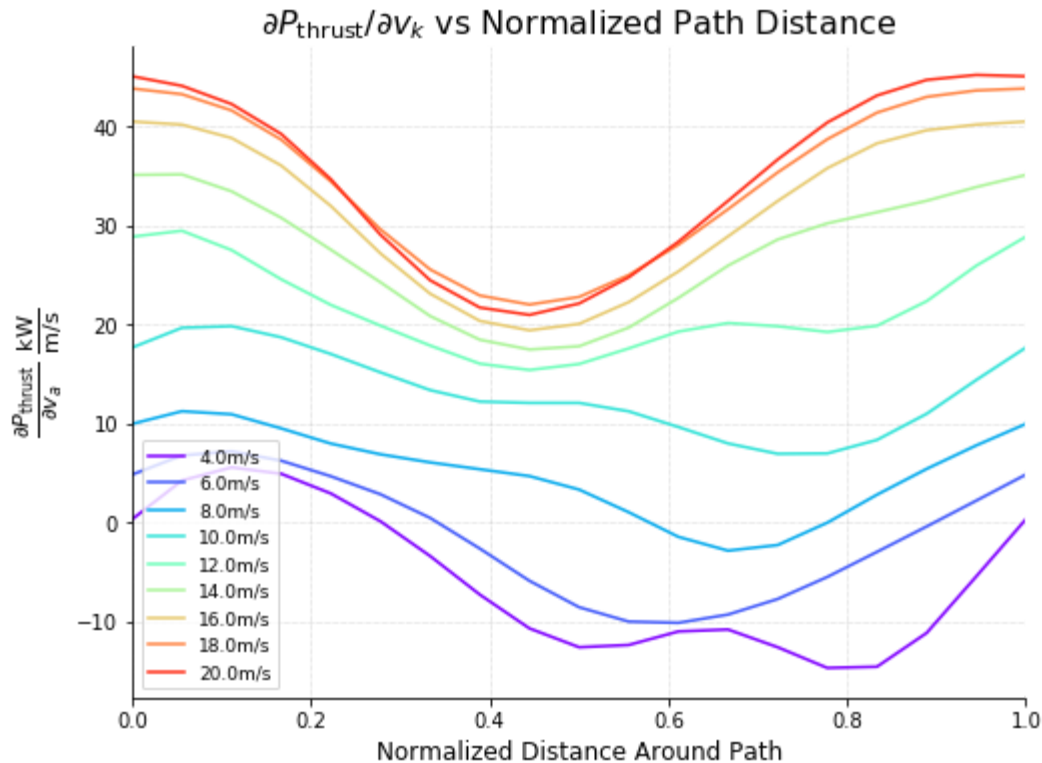


**Figure 74: Change in thrust power for a change in kite speed versus normalized path distance at various wind speeds. Comparing this with figure 73 shows the effect of dropping rotor efficiency—shaft power is decreasing even as thrust power is increasing.**

The kite continues to produce more thrust power as it overspeeds. In the absence of active control or in the presence of a power system failure, the kite will overspeed by tens of m/s. Larger path offsets can address this, lowering  $\partial P_{thrust}/\partial v_k$  at the cost of lowering the average power. Maximum continuous power will be limited not by the actual hardware, but by the system's lack of ability to safely maximize use of its hardware.

The net sensitivity to wind is perhaps best highlighted by comparing the relative sensitivities of the change in *shaft* power with kite speed (figure 73) to the change in *thrust* power with wind speed (figure 71)—we can use a shaft power margin created by a wind-induced overspeed to combat that overspeed. The peak drop in shaft power at high winds occurs at the bottom half of the path, where the kite is moving fast and rotor efficiency is ~50%, which means we have ~2x the shaft power drop available in the form of additional rotor drag power.

Making this comparison, at high wind speeds we see shaft power sensitivity to kite speed in the range of negative 0-120 kW/(m/s), and thrust power sensitivity to wind speed in the range of 150-225 kW/(m/s). Accounting for the factor of 2 increase in rotor drag power relative to shaft power, the peaks are a similar magnitude: ie, a wind increase of 1 m/s will cause an overspeed of about 1-2 m/s, at which point the rotor drag power limit raises enough that we can resist further overspeeding by re-saturating shaft power.

This is promising, but it doesn't take much wind before we need more overspeeding runway than we have to enable us to reel things back in. In this example, the runway is essentially already used up—figure 68 already has the rotors just about hitting their mach limit at high winds, and unable to tolerate any additional airspeed. There are still more tools to expand that runway that we haven't discussed here—variable pitch rotors, for example, or intentional de-rating of the system by making nominal operation further from our power limits so there's always margin to slow down, but each comes with substantial costs: literal costs in the case of the former, and reduced performance for the latter.

In the meantime, all models that lack turbulence and control errors should have their power saturated regime solutions called into question, including any results we've provided. It's very likely the real MX2 system would require path strategies that result in a rated power haircut of ~100-200 kW. The M600 was so restricted in minimum path radius, creating so many challenges that this author is unsure it would ever be able to safely fly at high winds regardless of power level and controller improvements.

Ultimately, the challenge is driven by shifts in wind and turbulence, and as such is stochastic in nature. It becomes a question of how large of a gust or wind shift can the system survive, and for how long. Only extensive simulation and flight testing can tell.

## 11 References

1. *Makani Code Release*, Makani Technologies LLC, 2020. [Online]. Available: <https://github.com/google/makani/>
2. IEA, "Global Energy Review 2020," Paris, France, 2020. [Online]. Available: <https://www.iea.org/reports/global-energy-review-2020>
3. W. Short, D. J. Packey, and T. Holt, "Manual for the Economic Evaluation of Energy Efficiency and Renewable Energy Technologies," NREL, Golden, CO, USA, 1995. [Online]. Available: <https://www.nrel.gov/docs/legosti/old/5173.pdf><sup>47</sup>
4. R. Wiser, Z. Yang, M. Hand, O. Hohmeyer, D. Infield, P. H. Jensen, V. Nikolaev, M. O'Malley, G. Sinden, and A. Zervos, "Wind Energy," in *IPCC Special Report on Renewable Energy Sources and Climate Change Mitigation*, O. Edenhofer, R. Pichs-Madruga, Y. Sokona, K. Seyboth, P. Matschoss, S. Kadner, T. Zwickel, P. Eickemeier, G. Hansen, S. Schlömer, C. von Stechow, Eds., Cambridge, United Kingdom and New York, NY, USA: Cambridge University Press, 2011. [Online]. Available: [https://www.ipcc-wg3.de/report/IPCC\\_SRREN\\_Ch07.pdf](https://www.ipcc-wg3.de/report/IPCC_SRREN_Ch07.pdf)
5. T. Stehly and P. Beiter, "2018 Cost of Wind Energy Review," [fig ES3], NREL, Golden, CO, USA, 2020. [Online]. Available: <https://www.nrel.gov/docs/fy20osti/74598.pdf>
6. *System Advisor Model*. (2020), National Renewable Energy Laboratory. Accessed: July 7, 2020. [Online]. Available: <https://sam.nrel.gov/>
7. M. L. Loyd, "Crosswind Kite Power," *J. of Energy*, vol. 4, no. 3, May-Jun 1980, Art. no. 80-4075, doi: <https://doi.org/10.2514/3.48021>
8. D. Vander Lind, "Analysis and Flight Test Validation of High Performance Airborne Wind Turbines," in *Airborne Wind Energy*, (Green Energy and Technology) U. Ahrens, M. Diehl, R. Schmehl, Eds., Berlin and Heidelberg, Germany: Springer, 2013, pp. 473-490, doi: [https://doi.org/10.1007/978-3-642-39965-7\\_28](https://doi.org/10.1007/978-3-642-39965-7_28)
9. B.J. Jonkman, "TurbSim User's Guide," NREL, Golden, CO, USA, Version 1.50, Aug. 26, 2009. [Online]. Available: <https://www.nrel.gov/docs/fy09osti/46198.pdf>
10. T. Van Alsenoy, "Sensitivity Analysis of Airborne Wind Turbine Design Variables: Using trajectory optimization," M.S. thesis, Dept. Wind Energy, Aero. Eng., TU Delft, Delft, Netherlands, 2014.
11. P. Echeverri, T. Fricke, G. Homsy, and N. Tucker, "M600 Energy Kite Description," in *The Energy Kite: Selected Results From the Design, Development and Testing of Makani's Airborne Wind Turbines*, Part I, Makani Technologies, Alameda, CA, USA, 2020, [Online]. Available: <https://x.company/projects/makani>
12. G. Homsy, "Oktoberkite and the MX2," in *The Energy Kite: Selected Results From the Design, Development and Testing of Makani's Airborne Wind Turbines*, Part I, Makani Technologies, Alameda, CA, USA, 2020, [Online]. Available: <https://x.company/projects/makani>

---

<sup>47</sup> A much-condensed version is provided in NREL's excellent System Advisor Model (SAM) help documentation [6].

## 12 Appendix

### 12.1 Numerical Model Description

#### 12.1.1 Overview

This model began as a small component of an overall system design model that estimated all costs and energy production for an entire plant of systems over the plant's life, with this sub-model responsible for evaluating the power performance of a given design. In its initial form, speed and simplicity were of paramount importance, so it leaned heavily on several of the analytical approaches we'll outline below.

The overall system model led us to identify much of the desired characteristics of a future onboard power generation system. However, flight tests and simulation efforts began to highlight the edges of the problem. AWTs operate in a highly dynamic manner, turning tight paths close to the ground in a turbulent environment, requiring a high amount of performance and precision. It should be no surprise that AWTs, when operated to chase best power performance, are highly constrained, maxing out power components, riding along tension limits, reaching airspeed and rotor speed limits, and saturating control surfaces.

As a result, we desired a model that captured more of these limits and the physics behind them, but still ran quickly enough to evaluate the numerous design tradeoffs ahead of us in a reasonable amount of time. The simple performance model was broken out of the larger system model and expanded in complexity and scope. The result, while somewhat clunky in its implementation as it has grown organically over time, has been very useful as a design tool. With run times on the order of minutes to evaluate performance across the full range of desired wind speeds, it's now too slow to tie into an overall system model, but fast enough for a single high performance desktop machine to perturb all the system inputs and complete a full sensitivity analysis in a matter of hours.

So how does this model work? At its most basic level, a kite state (called a pose within the model) is created from inputs consisting of the wind vector, the kite's position (assuming a rigid tether, with some methods from Van Alsenoy [10] to capture catenary effects on tension direction), the kite's velocity vector, and the kite's attitude, but parameterized in terms of aerodynamic angles between the kite's body frame and the apparent wind resulting from the wind speed and the kite's motion. One will find that an additional term is needed to fully define the orientation of the kite, as the rotation about the apparent wind is undefined—we call this additional term the lift-roll-angle, as it signifies how much the lift is rolled about the apparent wind, with a zero such that the wings of the kite are tangent to the flight sphere when the aero angles are zero. Finally, the kite's translational and rotational accelerations are also an

input—we're solving for force and moment residuals as a result of the state and its derivative. Most inputs do not result in a valid state, as the resulting forces and moments do not result in the desired accelerations. This is addressed with an optimizer at the next level.

Importantly, we make several simplifying assumptions to reduce the number of inputs. The rotors are modeled with a single representative rotor, and rotor drag (or thrust) is simply the inverse sum of other forces<sup>48</sup> along the rotor axis. The control surfaces are assumed to provide pure moments, and control saturations are managed via constraints, allowing us to avoid specifying all the control surface deflections. If control surfaces are largely separable (ie, they generate moments about predominantly one axis), we can approximate the control surface deflections surprisingly well.

Moving one level up in the model, we create closed paths that we call loops, and discretize it into poses. Orientation angles (two aero, one lift-roll-angle) and speed strategies are parameterized over the path, and from here we can compute the required accelerations for each pose. An optimizer functions at this level, adjusting path, speed, and orientation (via aero angles and lift-roll-angle) to both balance the forces, keep all constraints within limits, and optimize for power. This process gives rise to the name you'll see elsewhere, the Force Balance Looped (FBL) model. We have the ability to add in penalties, typically penalizing the required control effort (via penalizing the residual moment in terms of required control deflection). When power becomes increasingly saturated at high wind speeds and the signal to the optimizer goes away, we blend in a tension penalty.

Finally, there's a top level that varies the wind speed to create a power curve. It does so by creating and optimizing loops for each wind speed, feeding the optimized result of a lower wind speed as the seed of the next higher wind speed. This is an important step, as high wind speed operation is highly constrained, and finding a good solution is dependent on a good initial seed.

## 12.1.2 Sub-Models

The following sub-models are optional, and can easily be replaced with a user provided function. In several examples in this text we have done so, for example, to replace the rotor model with a rotor of constant efficiency.

### 12.1.2.1 Rotor Model

Rotor maps are typically dimensionalized in terms of rotor rotational speed and the freestream velocity as the lookup for thrust and torque. For our model, we instead have required thrust and freestream velocity. We could search the table to find the required thrust—an earlier version tried this approach and found it slow, and without additional steps to smooth the output, full of kinks that gave the optimizer difficulties. In addition, we'd like to non-dimensionalize the model to enable us to evaluate a similar rotor design, but at a different scale.

---

<sup>48</sup> Working in a non-inertial reference frame, including the pseudo-forces from the acceleration.

In order to do so, we non-dimensionalize the rotor table output in terms of a coefficient of power,  $C_p$ , and coefficient of thrust,  $C_t$ .<sup>49</sup> The relationship between  $C_t$  and  $C_p$  defines the performance of the rotor by describing how much thrust (or in the case of generation, negative thrust, ie, drag) translates into power. We find a polynomial fit for this relationship across different freestream velocities and for different rotor pitches. There is a similar relationship for  $C_t$  to rotor angular speeds at different freestreams, and we fit that as well, in order to apply torque and mach limit constraints. A stall constraint can be applied by enforcing a minimum  $C_t$ . The resulting model runs quickly, and returns the desired  $\eta_{thrust2shaft}$  necessary for the model, along with relevant constraints. We assume energy stored in the rotors is negligible.

### 12.1.2.2 Aero Model

Within the model, we simply need a function that accepts aerodynamic angles (alpha and beta) and non-dimensionalized body rates (omega hat,  $\hat{\omega}$ ), and outputs aerodynamic force and moment coefficients. Force coefficients can either be in reference to the kite body frame axes (represented with  $C_x, C_y, C_z$ ), or the aerodynamic frame (represented with  $C_D, C_Y, C_L$ ), while moment coefficients must be in the body frame (represented with  $C_l, C_m, C_n$ ). Since we don't specify flap deflections and instead just model the effect of flaps as optional constraints and penalties, an aero model can be as simple as a one line polynomial function, enabling easy evaluation of conceptual designs early in the process.

Eventually, we desired additional fidelity and to accept the input that is used in the simulator, which is a lookup table generated from some other model, with rate terms linearized about some nominal operating point. To ensure smoothness, we create a piecewise polynomial curve fit of the lookup tables, and this fitted model forms our required function.

### 12.1.3 Known Shortcomings

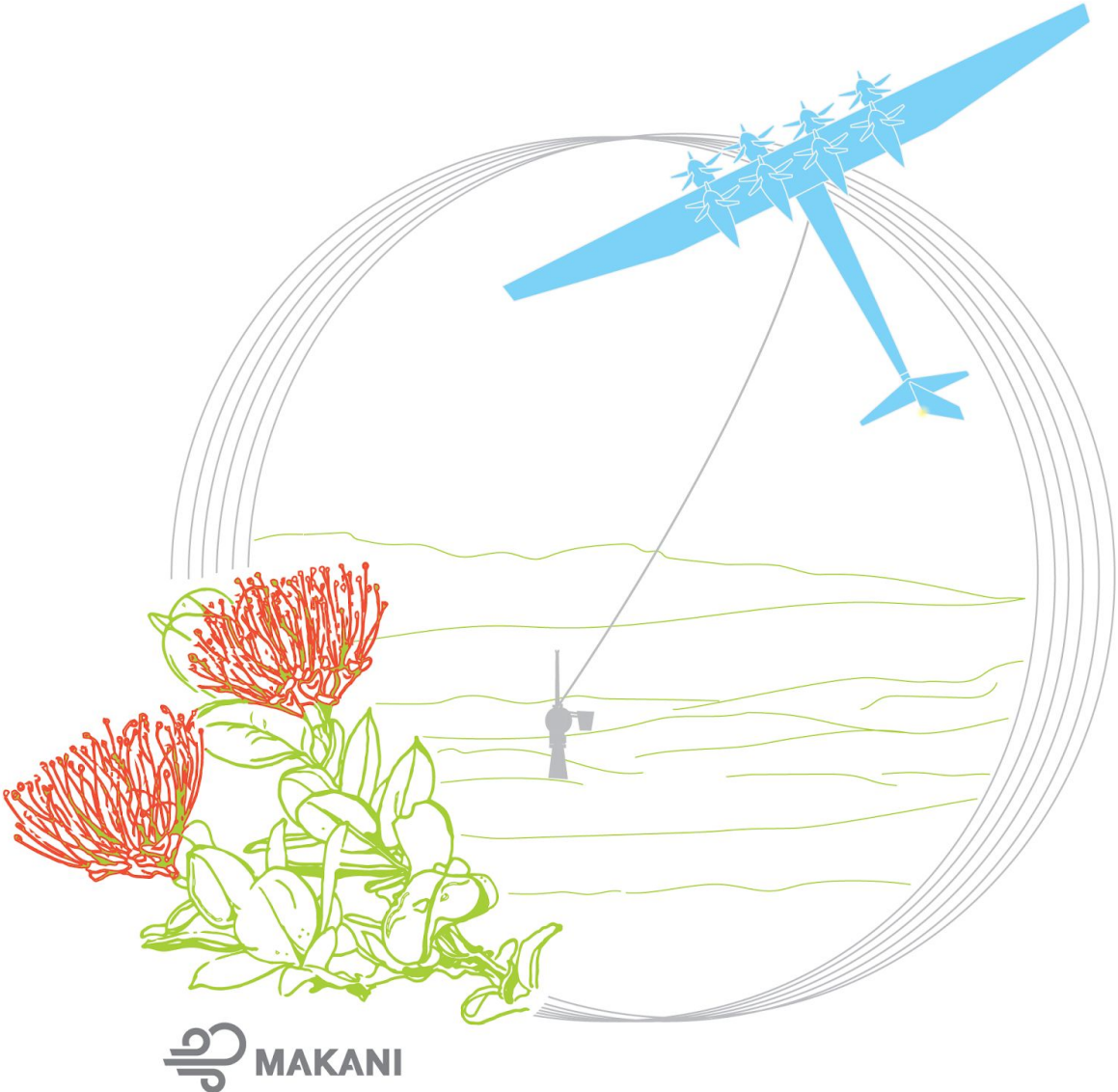
- Optimistic results.
  - In addition to any performance benefits resulting from simplified models, the results assume perfect control and no turbulence.
  - Due to perfect control and lack of variability, if it's beneficial to ride a limit, the optimizer will do so. In practice, this isn't possible, and sufficient margin needs to be built into the kite's operational targets.
  - As such, the results should be considered as an approximate upper bound on overall performance.
- No kite wake.
  - The influence of the kite's shed vortices on the incoming wind is ignored.

---

<sup>49</sup> As an aside, the aerospace and wind turbine industry have different ways of defining these coefficients. As long as things are consistent, the math works out the same. As the operating point of interest for our rotors is generation, we've chosen to use wind turbine notation for our coefficients in the code.

- For large, high performance kites turning tight paths, this effect can be significant.
- Rigid tether assumption.
  - For onshore systems, the energy storage in the tether is small, and can be justifiably ignored.
  - For floating offshore systems, the kite can store a large amount of energy in the floating platform and mooring lines, and simulation has shown that this can have a big effect on the results.
- Specific to onboard generation kites.
  - In its current form, it assumes a fixed tether length and onboard generation.
  - Creating path parameterizations in terms of curvature and payout speed, while possible with this method, is not implemented.
- Suggested future work:
  - A similarly simplified optimal control problem (OCP) setup would likely retain usefulness as a design tool, but has the added benefit of possibly aiding and supporting creation of a model predictive control (MPC) implementation, where the kite's controls are optimized in situ, in the controller itself, making the kite much more tolerant of control errors and gusts while subject to a litany of constraints.
    - To maximize usefulness as a design tool, it needs to be as fast and as simple as possible, with runtimes of minutes rather than hours.
    - To build an MPC implementation, it needs to be simplified to run in milliseconds.
  - Additional states to support offshore by representing the platform movement.

# M600 Energy Kite Description



Paula Echeverri | Tobin Fricke  
Geo Homsy | Nicholas Tucker



M600 Energy Kite Description

Corresponding author: Paula Echeverri, [paulae@alum.mit.edu](mailto:paulae@alum.mit.edu)

The Energy Kite: Selected Results from the Design, Development, and Testing of Makani's Airborne Wind Turbines, Part I of III  
by Paula Echeverri, Tobin Fricke, Geo Homsy, Nicholas Tucker,  
on behalf of the Makani team.

Copyright © 2020 by Makani Technologies LLC

Distributed under the [Creative Commons CC BY 4.0 License](https://creativecommons.org/licenses/by/4.0/). You are free to copy and redistribute this material in any medium or format for any purpose, even commercially.



Intended for electronic publication and distribution. Copies of this volume may be found at <https://archive.org>

Additional information is at: <https://x.company/projects/makani>

Published September 2020

<b>1 Description of System</b>	<b>228</b>
1.1 As-Built Properties	230
1.2 Power Curve	231
1.3 Hardware Subsystems	233
1.3.1 Airframe	233
1.3.2 Power System	235
1.3.3 Avionics	237
1.3.4 Tether	240
1.3.5 Ground Station	243
1.3.6 Ground Power	244
1.3.7 Spar Buoy	245
<b>2 Kite Fleet</b>	<b>249</b>
<b>3 Open Problems</b>	<b>253</b>
3.1 Power Curve	253
3.2 Roll Stability in Hover	255
3.3 Availability	255
<b>4 References</b>	<b>257</b>

# 1 Description of System

Makani's M600 energy kites are airborne wind turbines consisting of a fixed-wing carbon fiber kite with onboard generation, a tether, and a ground station. The kite, shown in figure 1, resembles a high aspect ratio glider, with the addition of eight electric motors/generators and eight rotors. Seven of these kites were built and integrated at Makani between 2014 and 2019, and five of them flew as part of Makani's testing program. These are referred to throughout the Makani Technical Report as SN1 through SN7.

The kite autonomously launches from a ground station in a vertical take-off and landing (VTOL) configuration and hovers as the tether is payed out; electrical power is supplied from the ground through the tether to support hover. Once the full tether is payed out, the system transitions into power-generating crosswind flight, flying circular loops. Figure 2 shows the kite in crosswind flight, climbing towards the top of the loop, during the offshore flight campaign in August 2019. When commanded to do so, the kite transitions out of crosswind, hovers as the tether is reeled in, and lands on a perch on the base station.

The tether contains electrical conductors allowing power transmission in both directions as medium voltage DC. In the offshore configuration, the ground station is mounted to a spar buoy. Associated with the ground station is a bank of electrical inverters forming a bidirectional interface with the electrical grid.

The M600 is a scaled-up version of the earlier Wing 7 prototype.<sup>1</sup> Wing 7 demonstrated all flight modes and demonstrated performance within error bounds of its design power curve in the mid-range of its wind speed envelope. The M600 system was unable to achieve its design power curve due to factors described in section 3.1 of this document. Given the learnings from the M600 project, Makani embarked on a redesign; we believe the resulting machine, termed MX2 and described in "Oktoberkite and the MX2" [5], would achieve its design power curve.

Makani still accomplished important milestones with the M600 system. At 600 kW rated power, this was the first airborne wind turbine on the 1 MW scale. We learned from building and integrating seven working kites, and operating in environments as diverse as the California desert and the North Sea. The M600 flight test program culminated in a spectacular demonstration of a utility-scale offshore, airborne wind turbine operating autonomously from a floating platform. Videos of this flight, which illustrate all flight modes and all the elements of the M600 system in its ultimate intended operating environment, can be found in [1, 12].

This article provides a high level description of the M600 systems as-built and as-flown by Makani. Section 1 describes the main hardware subsystems, and it is complemented by the detailed description of the controls system and the simulation that were used to develop and

---

<sup>1</sup> Wing 7 is described in Vander Lind [2].

test M600 systems given in “The Makani Autopilot” [4]. Section 2 describes each of the M600 kites that were built at Makani. Section 3 is a summary of the shortcomings of the M600 system. An overview of the M600 flight test program, highlighting some of our proudest achievements, is provided in “Makani’s Flight Testing Approach” [6].

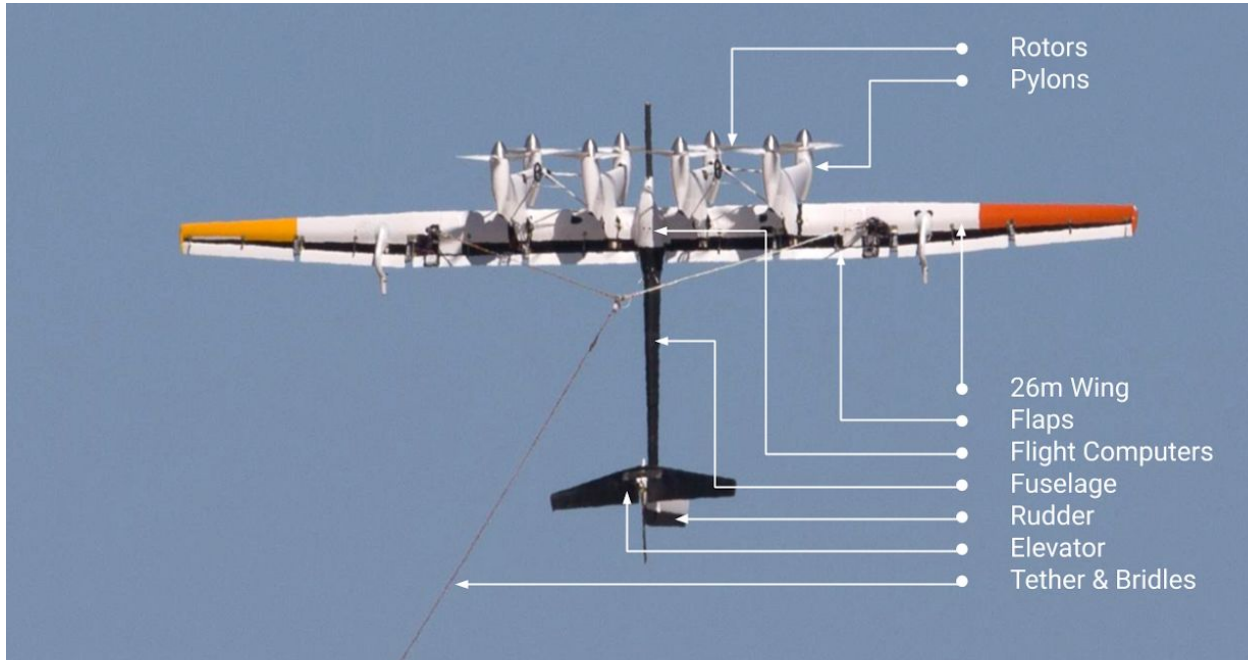


**Figure 1: Airborne components of an M600 Energy Kite.**

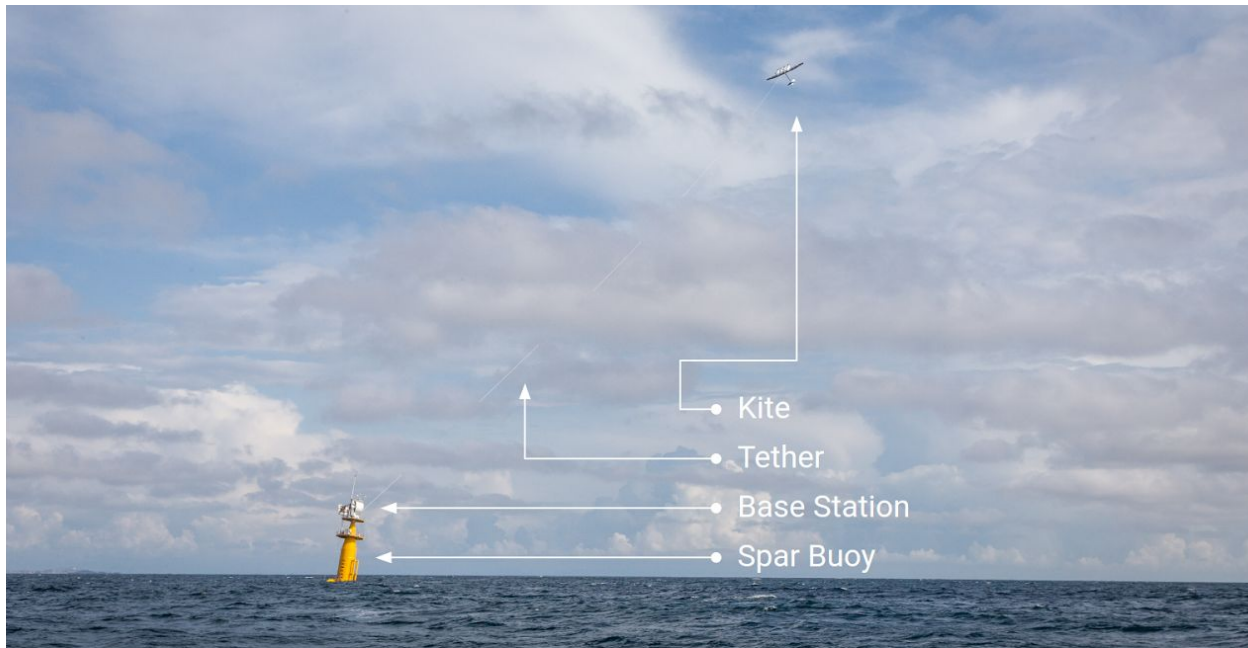


**Figure 2: M600 Energy Kite flying crosswind loops offshore.**

## 1.1 As-Built Properties

Table 1 and table 2 list principal properties of the last kite and tether slated for flight at the Hawaii test site. The full list of parameters describing the physical plant can be found in the configuration files of the autopilot and simulator codebase, which is available publicly at [github.com/google/makani](https://github.com/google/makani) in the `config/m600` directory [3].

Parameter	Value (as-built)	Units									
wing area	32.9	m <sup>2</sup>									
wing span	25.66	m									
mean aerodynamic chord	1.28	m									
mass <sup>2</sup>	1730.8	kg									
inertia tensor	<table border="1"> <tbody> <tr> <td>32730.0</td> <td>23.1</td> <td>36.7</td> </tr> <tr> <td>23.1</td> <td>9961.8</td> <td>17.9</td> </tr> <tr> <td>36.7</td> <td>17.9</td> <td>39609.1</td> </tr> </tbody> </table>	32730.0	23.1	36.7	23.1	9961.8	17.9	36.7	17.9	39609.1	kg m <sup>2</sup>
32730.0	23.1	36.7									
23.1	9961.8	17.9									
36.7	17.9	39609.1									
coefficient of lift	2.5	#									
coefficient of drag (including tether)	0.3	#									
number of rotors	8	#									
rotor diameter	2.3	m									

**Table 1: M600 SN6 as-built properties.**

<sup>2</sup> The original design intent specified a full system mass of 919 kg.

Parameter	Value (as-built)	Units
length	425.8	m
linear density	0.917	kg/m
outer diameter	0.0294	m
tensile stiffness	18e6	N
coefficient of drag	0.7	#
bridle point radius	4.79	m
bridle point y-offset	-0.50	m

**Table 2: Tether properties.**

## 1.2 Power Curve

Figure 3 shows the demonstrated power curve of the M600 compared to the original specification, and as predicted by two of our modeling tools. The M600 fell far short of its originally specified power curve (as described in more detail in section 3.1); however, the discrepancy is largely explained by our models when using as-built parameters.

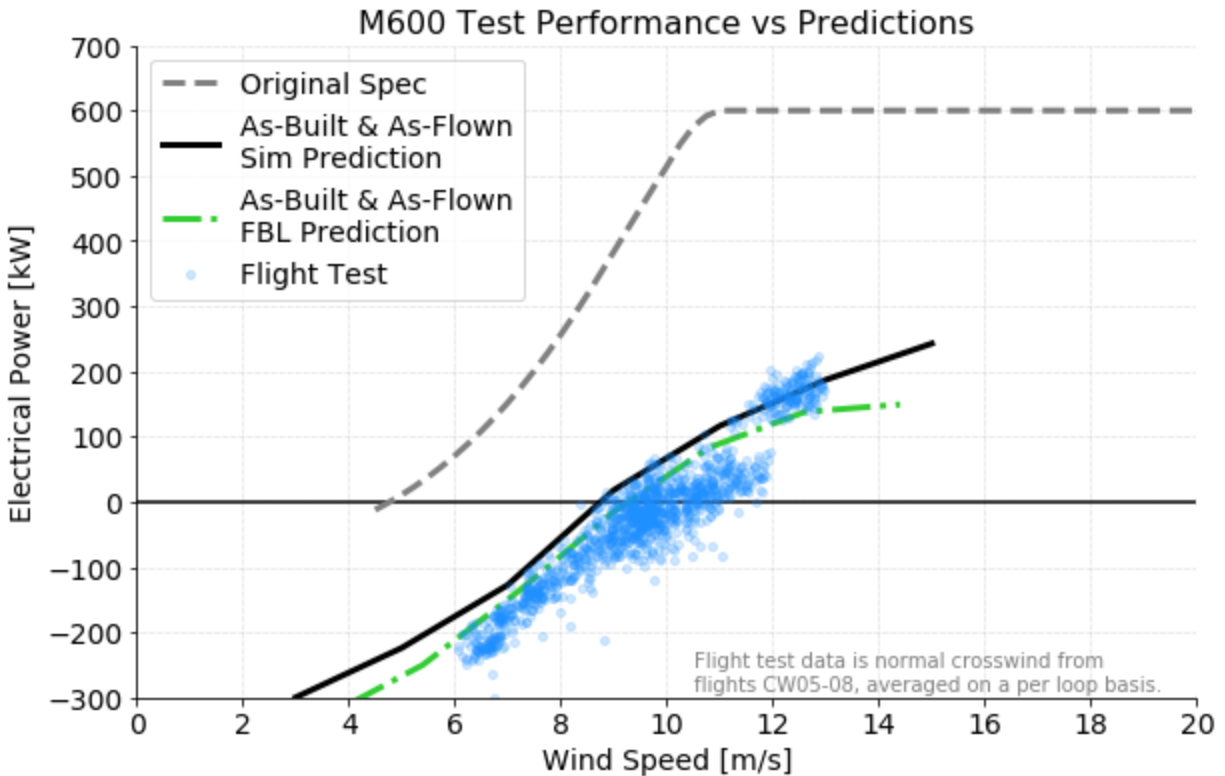


**Figure 3: Power curves for the M600, showing the large gap between original design intent and the realized system. Data shown is a subset of flight test data to isolate a single configuration. Note that our modeling tools accurately predict the performance deficiency of the M600.**

The force balance loop (FBL) prediction refers to the power curve derived using an analytical tool that solves the force and moment balance at each stance around the loop, described in “Airborne Wind Turbine Performance” [7]. The simulator prediction refers to the power curve derived from batch simulations run with the full physics simulation described in “The Makani Autopilot” [4]. Both tools are available in the Makani codebase repository [3]. The flight test data points shown here were collected during four flights in April and May of 2019 in the Hawaii test site, described in more detail in “Makani’s Flight Testing Approach” [6].

Predictions can easily be made to capture the as-built and as-flown conditions, but real world winds provide more variety than we typically captured in our simulations. Much, but not all, of the discrepancy between predictions and this test data can be attributed to a detrimental wind veer on several of our flight tests.

The broadest wind envelope established for an M600 crosswind flight was 5 - 12 m/s. A representative environmental launch criteria was set in preparation for crosswind flight CW-09 in Hawaii (described in more detail in [6]): wind speeds were required to be in the range of 5 - 11 m/s at 20 m to 400 m above-ground-level, and turbulence intensity was to be below Class C as per IEC-61400 standard definitions [16]. This envelope was established by interpreting the

change in flight quality scores from batches of simulated flights run in different wind conditions. The envelope was set just shy of conditions where flight quality scores (in this case, the likelihood of reaching excessive airspeeds) started to degrade quickly. This related to flying large path sizes in order to stay in conservative regimes of lateral dynamics, since the kite demonstrated poor lateral stability. Some of the discussion in section 3.1 also explains the tradeoffs between efforts to ensure robust flight and optimal strategies for power performance.

The 5 - 12 m/s wind envelope constitutes a narrow range of operating conditions compared to offshore wind turbines that publish power curves with cut-in wind speeds at 5 m/s and cut-out wind speeds at 25 m/s. This would have to be greatly expanded to achieve the annual energy production required of a commercial system. As with other challenges described below, some means of improvement are discussed in “Oktoberkite and the MX2” [5].

## 1.3 Hardware Subsystems

### 1.3.1 Airframe

Figure 4 is a rendering of SN5 as-built, highlighting the principal structural and aerodynamic surfaces of the airframe. The M600 is a modular carbon fiber composite structure comprising a single-piece wing backbone with hardpoints to support two attachment points for the tether bridle, four pylons, and the fuselage. Eight 5-blade rotors, each attached to an electrical motor/generator, are mounted at the top and bottom of each pylon. The cross section of the wing structure, comprising sandwich panel skins and bonded internal spars, is shown in figure 5. Eight ailerons are attached to the trailing edge of the wing and actuated with strain wave gearing servos. The vertical tail supports a rudder and a fully moving elevator. Winglets are attached at each end of the wing span, and various cowlings and fairings cover avionics components and condition the airflow around surface junctions for drag reduction. A more detailed description of the airframe architecture, including each of these structural elements, major interfaces, driving load cases, and fabrication techniques can be found in the “Makani Systems Overview” presentation included in Part II of this report [8].

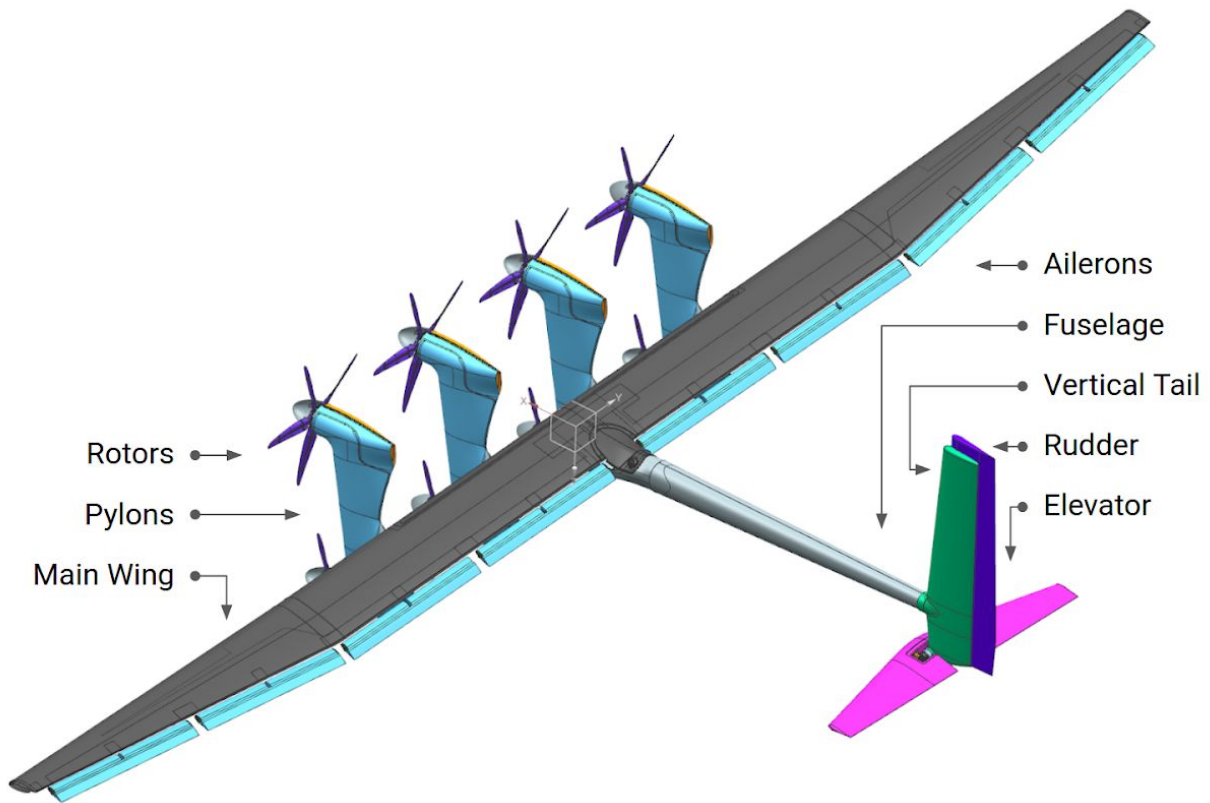


**Figure 4: Rendering of the M600 SN5 airframe highlighting the principal structural and aerodynamic surfaces.**

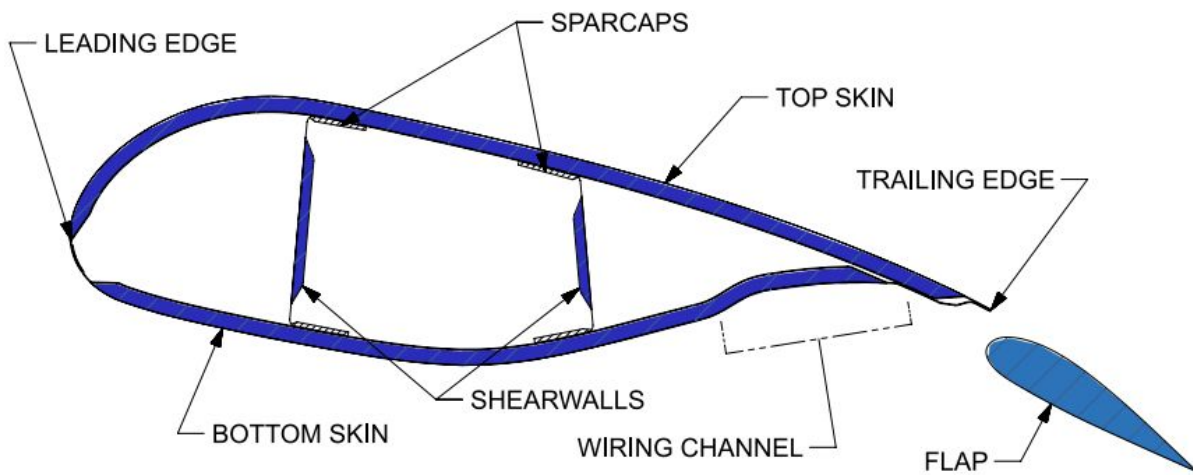


**Figure 5: Cross section of the M600 main wing structure.**

### 1.3.2 Power System

Eight powertrains are mounted to the M600 by way of pylons; each pylon holds two powertrains. Physically the eight powertrains are arranged in two rows of four powertrains each. The individual powertrains are named STO, STI, PTI, PTO, PBO, PBI, SBI, and STO, with the letters designating their placement: {starboard, port} × {top, bottom} × {inner, outer}.

The eight powertrains are arranged electrically in a "stacked" configuration, grouped into four pairs, where the two powertrains in a pair are connected in parallel, and the four pairs are then wired in series, as depicted in figure 6. Thus the voltage seen by each powertrain is only a quarter of the full tether voltage. This allows for a higher transmission voltage on the tether, reducing resistive losses, but necessitates a complex motor control system to keep motor currents appropriately balanced. Each electrical pair consists of two powertrains diagonally opposed on the airframe. In case of failure of one powertrain, that powertrain and its (diagonally opposed) partner are electrically shorted via a "short stack" module to maintain operation of the remaining six powertrains.

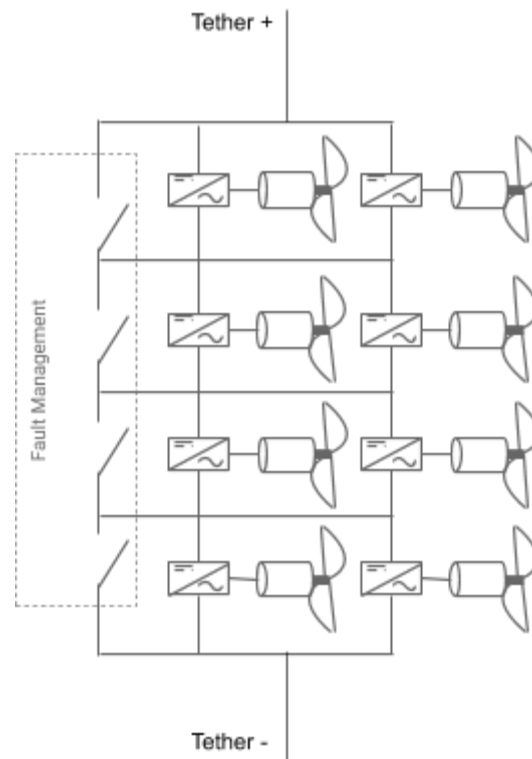


**Figure 6: The powertrains are electrically arranged in a 2-parallel, 4-series "stacked" arrangement. This allows each powertrain to operate on only  $\frac{1}{4}$  of the tether voltage. This comes at the cost of precisely balancing the currents through each stack level. If any stack level fails or misbehaves, the fault management system (shown at left) shunts it out of the stack, thus allowing the other six powertrains to continue operation.**

Each powertrain comprises:

- A 130 kW custom-made, liquid-cooled, axial-flux “outrunner”<sup>3</sup> motor.
- A motor controller designed in-house, comprising a main board with a microcontroller and network I/O, three gate driver boards, three half-bridge SiC MOSFET switching modules, and a bypass capacitor bank, in a liquid cooled enclosure [11].
- An external capacitor bank that provides bulk energy storage for electrical stack stabilization.
- A sealed liquid cooling loop consisting of a gear pump magnetically coupled to the motor shaft, a filter/accumulator, a radiator mounted in an aero duct, and hoses connecting the pump, the radiator, the motor, and the motor controller cooling plate.
- A 1400V MV power harness, allowing bidirectional electrical power transfer to and from the electrical grid, by way of the tether and the base station.
- Dual avionics harnesses, each comprising a 75 V avionics power bus and optical fiber network link.

See figure 7 for a look at the layout of a powertrain within a nacelle.

---

<sup>3</sup> By “outrunner” we mean the rotor is geometrically arranged *outside* the stator, as opposed to the more common configuration of motors in which the rotor rotates *inside* the stator.

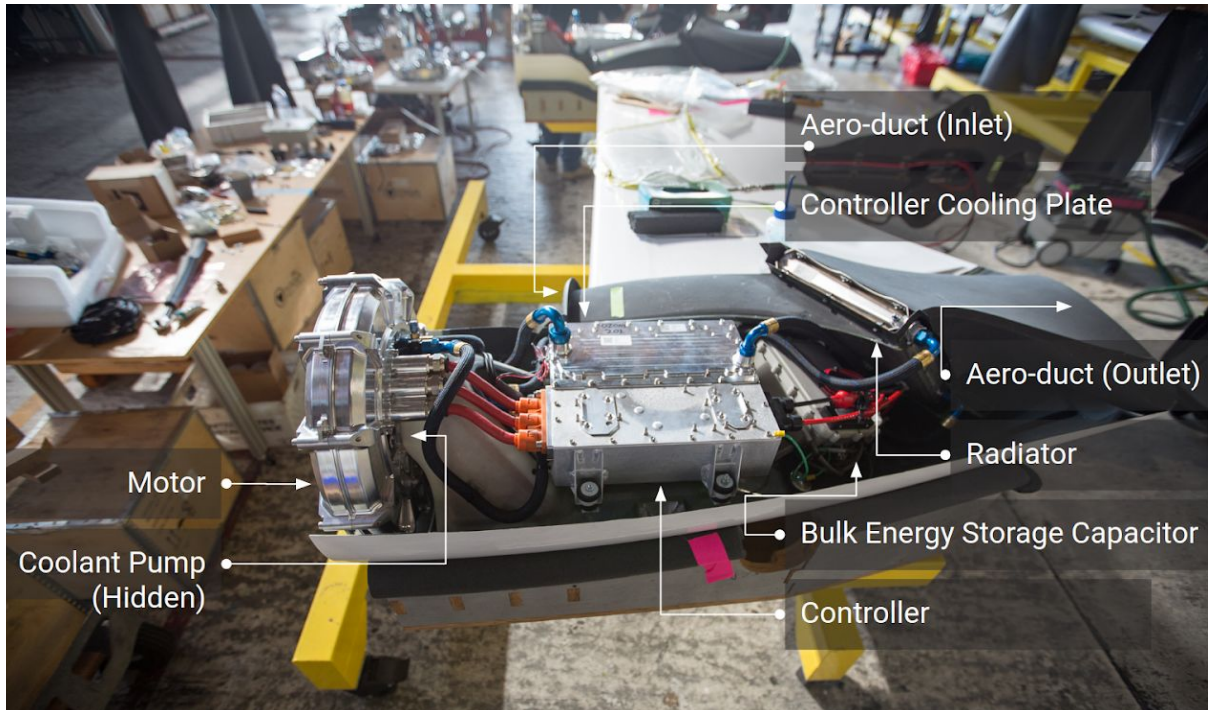


**Figure 7: A powertrain assembly mounted in a nacelle. The coolant pump is coaxial to, and magnetically coupled with, the main motor. It is not visible, as it is tucked away inside the motor mount. The radiator is sandwiched at a skew angle between the two halves of the aero-duct, which has a duct ratio of approximately 5:1.**

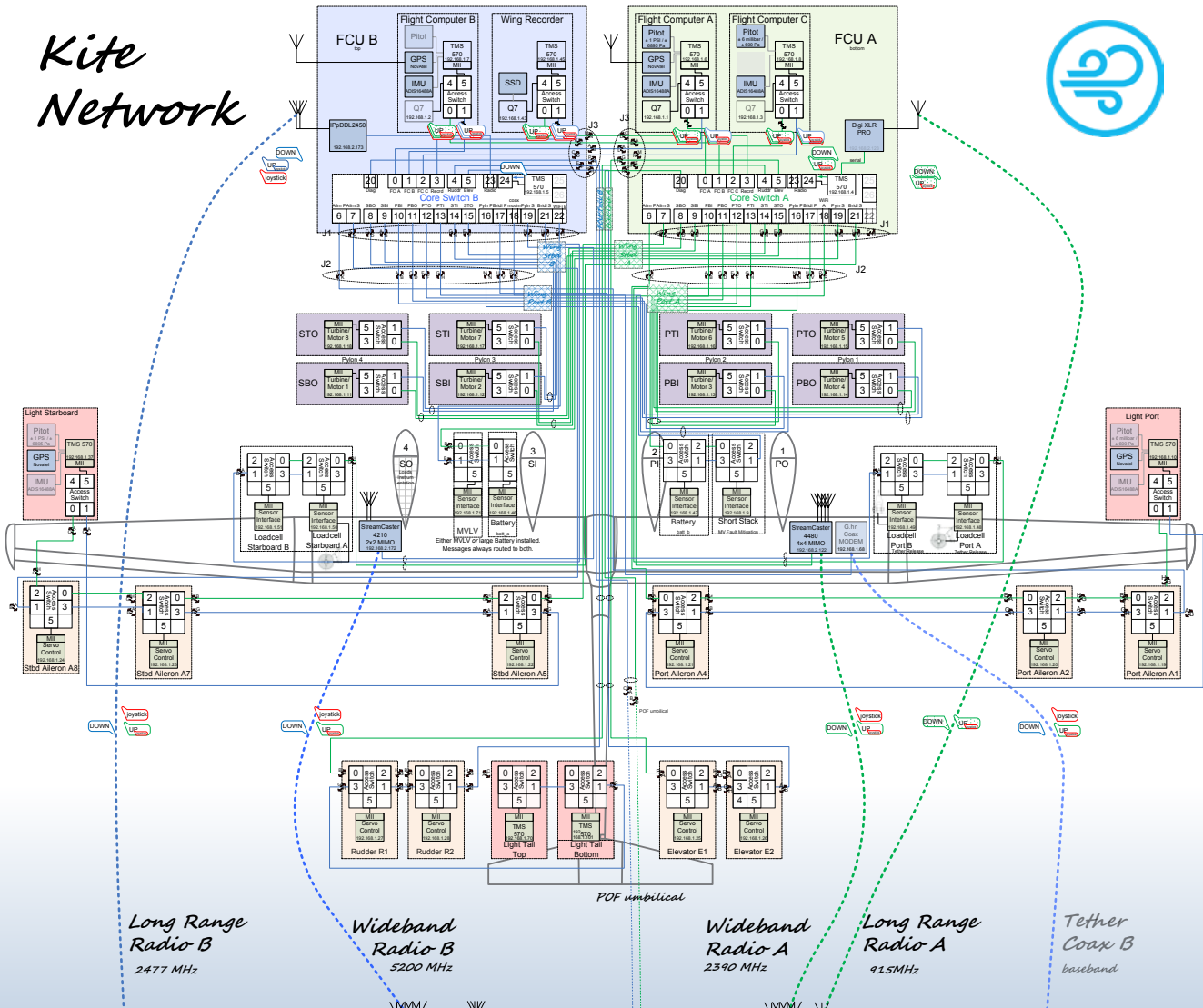
### 1.3.3 Avionics

The sensors, actuators, and flight computers are arranged as a collection of avionics nodes, each running custom firmware and connected to the others using ethernet over plastic optical fiber and using IP multicast to pass messages between nodes. The avionics network design is described in more detail in “A Low-Cost Fiber Optic Avionics Network for Energy Kites” [9], and the topology of the network at the Hawaii test site is depicted in figure 8 below. The full description of the avionics network as implemented, including the entire list of nodes, the messages sent on the network, the switches on the network, and the network topology, can be found at [github.com/google/makani](https://github.com/google/makani) under `avionics/network/network.yaml` [3].

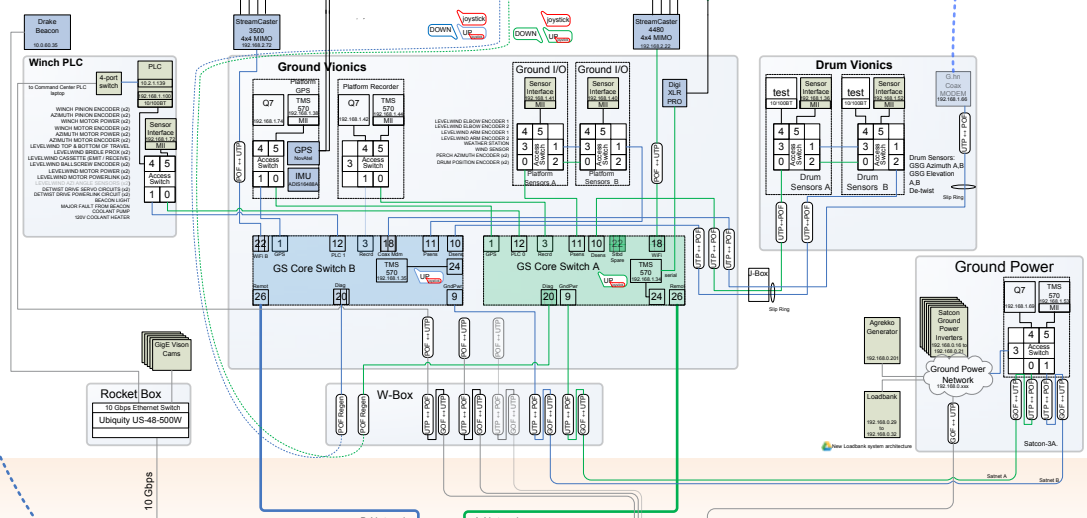
The autopilot software runs on one of the avionics nodes. For the purpose of fault tolerance, three redundant flight computers were provisioned and it was envisioned that each would simultaneously run its own copy of the autopilot software. This fault mitigation system was never implemented; all M600 flights flew using a single instance of the autopilot software. However, the three flight computers did provide triple-redundant inertial measurement units (IMUs), dual-redundant GPS, and dual-redundant dynamic pressure units. The estimator applies different voting schemes to determine which value to use.

Messages are passed between the base station and the kite via high bandwidth radio links. This being a prototype system, a large amount of telemetry data was sent down to the ground and logged for post-flight analysis. To eventually remove dependence on radio links it was envisioned to either integrate a fiber-optic or coaxial cable RF communication link into the tether, or to use ethernet-over-power (EoP) to send data over the electrical power conductors. EoP was prototyped but not implemented. The RF-over-coax data link was also prototyped, and integrated into the tether construction, but it was never actually commissioned in the field.

# Kite Network



# Ground Station



# Command Center

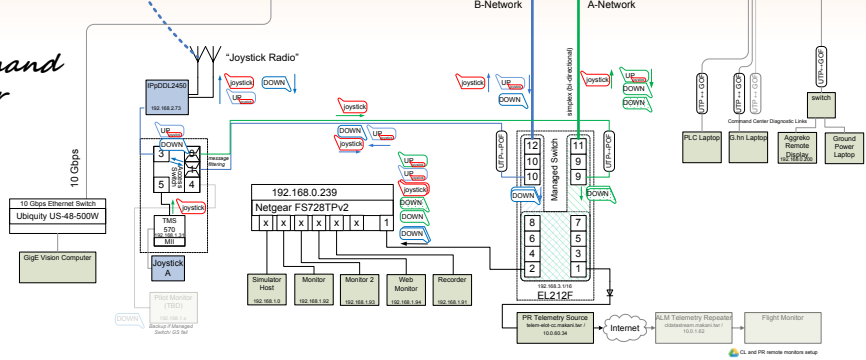


**Figure 8: (previous page) Avionics network diagram as implemented in the Hawaii test site, showing communications links between nodes on the kite, ground station, and command center.**

### 1.3.4 Tether

The tether connecting the kite to the ground station must satisfy a uniquely challenging combination of technical requirements:

- Must withstand tremendous tension (250 kN)
- Must withstand tens of millions of repetitive strain cycles, of a significant fraction of the total tension
- Must carry significant electrical power (1 MW)
- Should enable communication of flight data between the kite and the ground station
- Must be small, lightweight, and have low aerodynamic drag
- Must be able to withstand winding and unwinding from the tether drum thousands of times

This was achieved by way of a coaxial construction, shown in figure 9. The gauge section comprises a strength core of bundled, pultruded carbon fiber rods, surrounded by an elastomeric “bedding layer,” surrounded by a single layer of individually insulated conductors, wound with a short helical pitch. Finally, an outer protective jacket with specially designed aero-flutes for drag reduction completed the design.

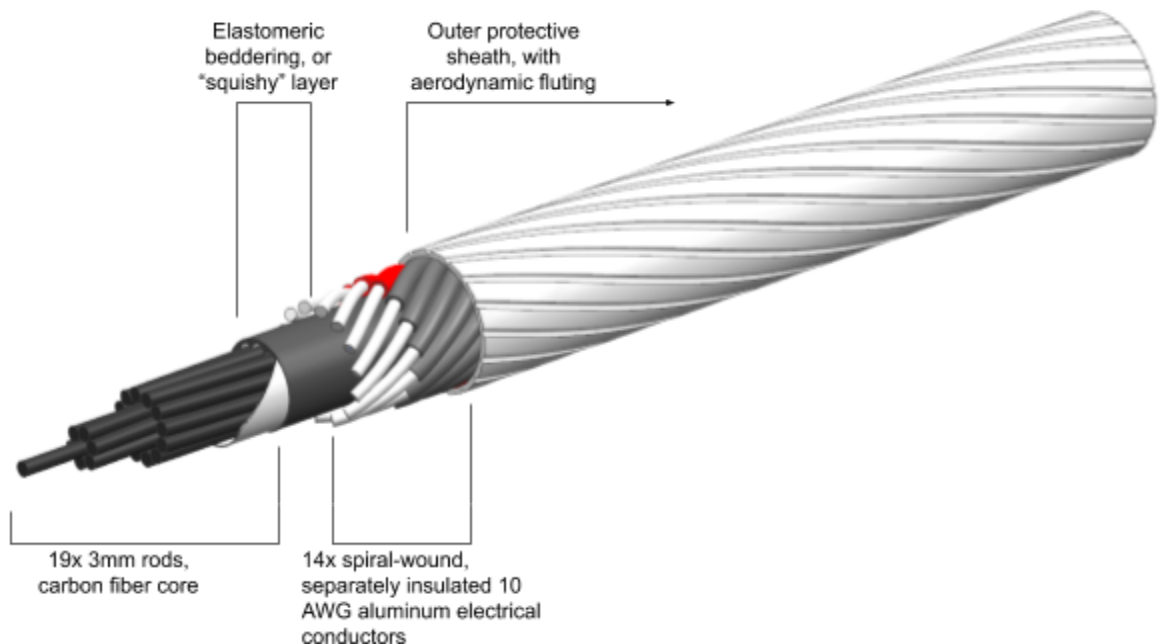


**Figure 9: The conductor gauge section, in a peel-away view. The strength core is a 1x19 bundle of 3 mm pultruded carbon fiber rods. The squishy bedding layer is shown in dark gray. There are fourteen helically wound aluminum conductors of alloy EC 1350, individually insulated with Tefzel. The outer jacket is fluted for lower aerodynamic drag.**

It was desirable to use aluminum electrical conductors for low mass. A long winding pitch for the aluminum conductors would have minimized electrical resistance (by decreasing overall conductor length), but would have exposed the conductors to the same repetitive strain of the carbon fiber core. Since aluminum would embrittle and crack under such conditions, we conceived the idea of winding the conductors at a smaller helical pitch length, and putting a “squishy” elastomeric layer between the strength core and the conductors. The design intent is that, when the core stretches, the conductors simply rearrange themselves into a slightly tighter (smaller diameter) helix, by compressing the bedding layer. This worked out remarkably well: for cyclical strain of the strength core of 1.4%, we were able to keep the conductor strain down to 0.1%.

The helicity of the strength core is opposite that of the conductors, and it is much much steeper. It is chosen to keep the gauge section of the tether torsionally balanced: the strength core torque-per-strain is equal and opposite to the conductor torque-per-strain. This ensures torsional waves do not reflect up and down the tether during dynamic stress conditions, and it minimizes creep and fretting.

The tether terminations at the lower and upper ends are identical and also embody significant technical complexity. The core termination is of the potted-cone type, in a titanium strength housing. Since the strength termination undergoes several millimeters of elongation during

cyclical strain, it would be unwise to bond the electrical termination rigidly to the core termination. For this reason, the electrical termination is bonded locally to the core, and the electrical termination is allowed to “float” axially with respect to the strength termination (see figure 10). However, if the electrical termination were allowed to float *rotationally* as well, then the tether would no longer be torsionally balanced at the terminus. For this reason, the electrical termination was fitted with an external torsional restraining device consisting of an external carbon fiber anti-rotation shell (not shown in the figure).

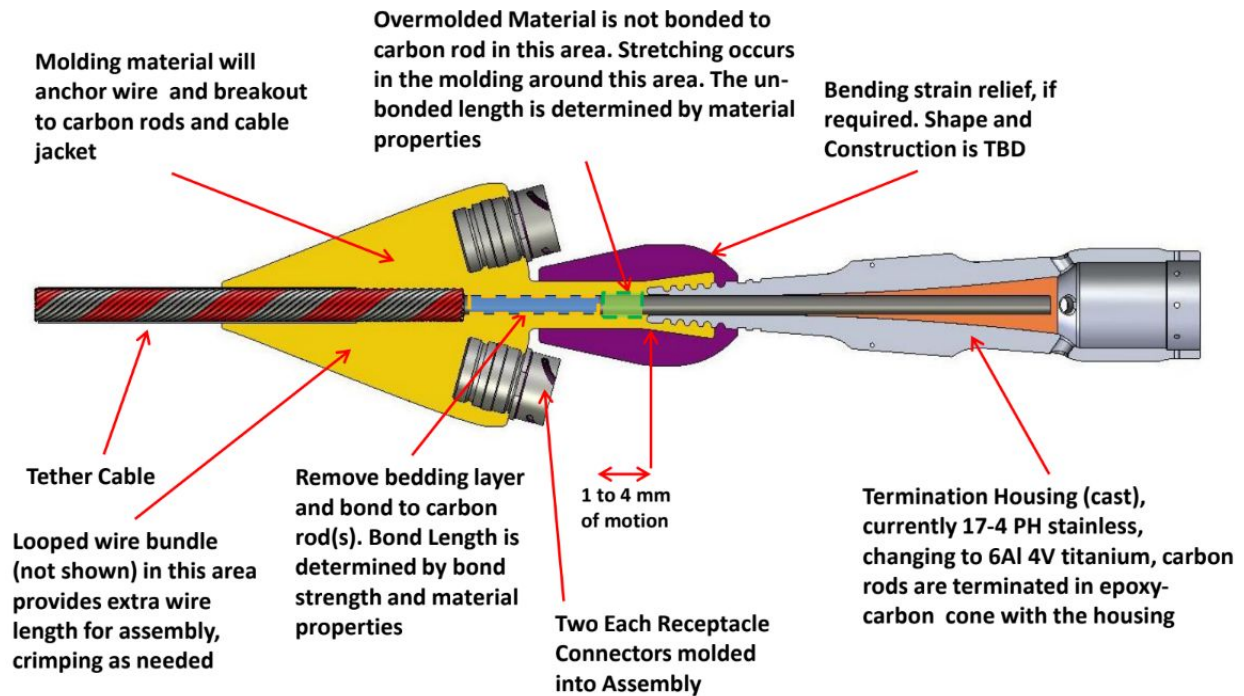


**Figure 10: The tether termination also embodies significant technical complexity. Internal bonding of the overmold structure is designed in such a way to allow the electrical termination to float axially, but not rotationally. This isolates the electrical conductors from the significant cyclical strain experienced by the strength termination.**

Because the kite flies in loops, always turning the same direction, the tether must be able to rotate axially at the ground station. This was accomplished by means of a slip ring and an active “detwist” drive. A two-axis gimbal, called the ground-side-gimbal (GSG), allowed the tether departure angle from the ground station to rotate freely in the other two degrees of freedom. The gimbal axes of the GSG were instrumented with encoders to be used as a means of estimating the kite's location from the tether departure direction at the ground. This information was also needed to actively “detwist” the tether.

On the kite side, the termination section facilitated the separation of the force-carrying and current-carrying members of the tether. The force-carrying member was attached to a bridle connected to two bridle hardpoints on the kite. The electrical conductors were connected to

silicone insulated copper conductors, wound around the port bridle. An emergency release mechanism allowed release of the tether from the hardpoints for glide landings.

### 1.3.5 Ground Station

The ground station is described in detail in "Base Station Team Final Documentation" [10] and depicted here in figure 11. The ground station features a platform able to rotate in azimuth, supporting the kite's perch and the drum to wind the tether, which is guided by a levelwind during pay-out and reel-in. At the end of pay-out, a "transform" maneuver is conducted such that the tether force is supported by the ground-side-gimbal (GSG) rather than by the skin of the drum. The transform motions of the ground station can be observed in videos (see "20190311 CW-03 - TransformUp Base Station View of Tether," "20190311 CW-03 - TransformDown Makani M600 Base Station Maneuver," and "20190607 CW-09 - TransformDown of Makani M600 GS02 Base Station" [1]. The ground station azimuth is measured via encoders and via a GPS compass. A mast supports an ultrasonic anemometer, which is the system's primary measurement of the wind speed and direction before the kite is launched, and a strobe light for visibility.

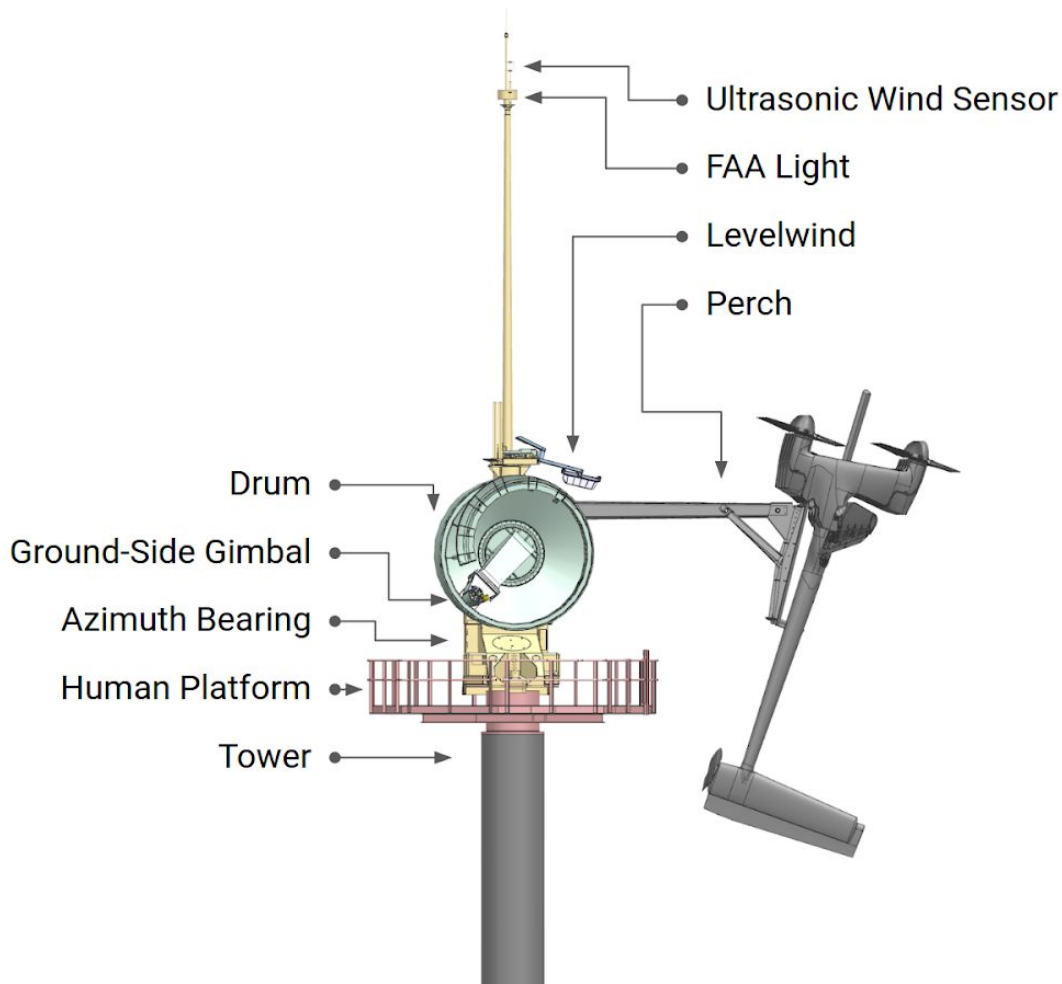


**Figure 11: M600 Perched on the ground station.**

### 1.3.6 Ground Power

The ground power system comprises six solar photovoltaic inverters, specially modified for isolated, two quadrant operation. Each inverter is a 250 kW, 480 VAC unit, supporting 600-900 VDC at its DC input bus. The inverters are programmed with a constant DC voltage, two quadrant control mode: they operate as transparent source or sink power bridges between the AC and DC buses, while maintaining a constant DC voltage.

On their AC side, they are linked in parallel through a switchgear, to support 480 VAC at 300 A each, for a total of 1800 A. On their DC side, however, they are linked in *series* to support the high DC voltage required at the tether. Peak power is 4800 VDC at  $\pm 600$  A, for a peak power capability of  $\pm 2.8$  MW, with  $\pm 1.5$  MW rated sustained power.

The kite flight controller limits the peak tether power to  $\pm 1.1$  MW, so the inverter DC link (and in fact the tether) is never asked to carry more than about  $\pm 230$  A.

For the purpose of flight testing without a connection to the commercial electrical grid, the system was supported by a 1.5 MW diesel generator. To dissipate generated power, and to provide a consistent and smoothly varying load to the diesel generator, a 1500 kW resistive load bank was employed, with real-time power monitoring and bespoke software to adaptively control the load steps.

### 1.3.7 Spar Buoy

In the offshore configuration, the ground station is mounted to a spar buoy: a steel tubular structure that mates with the ground station by means of a bolted flange and is anchored to the seabed by three wire-and-chain mooring lines. The spar buoy mass properties are tuned to achieve a pitch and roll response that resonates with the kite looping frequency. The spar has a heave damping plate and three yaw damping plates. There are four internal watertight decks for damage stability. A hawse pipe runs vertically from main deck to just below the lowest watertight deck, to facilitate ballasting operations. There is no internal access for personnel below the main deck. An external boarding ladder provides access to the secondary platform, where electrical and communications equipment are located. The principal particulars<sup>4</sup> are listed in table 3. Figure 12 and figure 13 show a general arrangement drawing and a photograph of the deployed spar buoy.

---

<sup>4</sup> The expression “principal particular” is commonly used in naval architecture to refer to a set of properties that characterise the scale of a vessel as-built.

Parameter	Value (As-Built)	Units
Platform length (baseline to interface)	62.05	m
Spar diameter (molded)	4.5	m
Spar thickness	25 (lower and upper spar) 30 (mid spar)	mm
Harbor draft	42.7	m
Installed draft	44.5	m
Height of access platform (above baseline)	57.25	m
Yaw plate length x width (each of three)	10 x 2	m x m
Heave plate diameter	8.5	m
Displacement (as-installed)	762.4	metric tons
Vertical center of gravity (as-installed, above baseline)	15.57	m
Vertical center of buoyancy (installed condition, above baseline)	22.75	m

**Table 3: Principal particulars of the spar-buoy.**

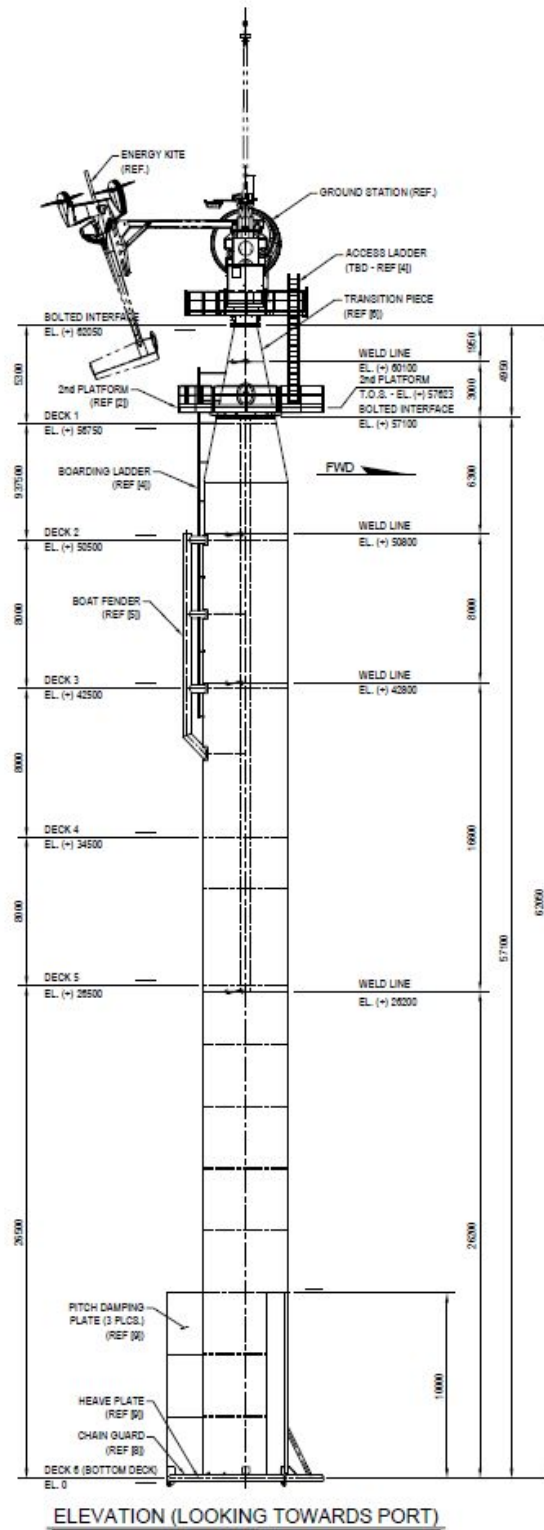


**Figure 12: Spar buoy general arrangement drawings provided by EPCI contractor Technip / Genesis.**



**Figure 13: Photograph of the installed M600 system in the North Sea at the Marine Energy Test Centre in August 2019.**

## 2 Kite Fleet

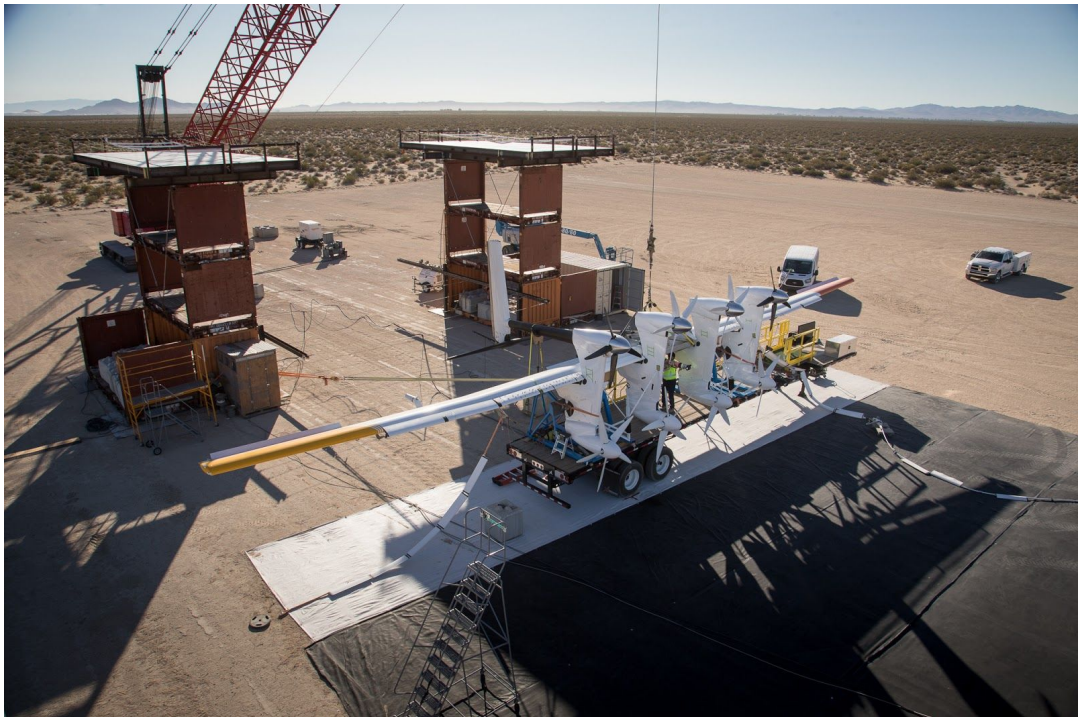
Eight M600 main wings were built, all pictured in table 4. One (SN1) was designated for hover flights only. Four kites flew crosswind flight, and all four were ultimately destroyed in crashes. Three unflown wings remained in Makani's inventory at the time of Makani's shutdown. The M600 flight test program conducted twenty crosswind flights, which are described in "Makani's Flight Testing Approach" [6] including accounts of how each of the airframes was lost.



<sup>5</sup>The Hawaiian kite blessing ceremony where Huapala (SN1) and Lanakila (SN4) were named is discussed in "Makani's Flight Testing Approach" [6] and footage of the naming ceremony is included in the Makani documentary *Pulling Power from the Sky* [13].

**SN2**

SN2 was the first crosswind-capable airframe and was flown in the test site at China Lake, California. SN2 was lost during hover at the end of flight RPX-06.

**SN3**

SN3 incorporated major hardware iterations, including the leading-edge slats visible in this photograph at the test site in China Lake. SN3 was lost to a mid-air breakup in flight RPX-09.

**SN4**



“Lanakila” flew every crosswind flight at the Hawaii test site. It was lost to a hard glide-landing in flight CW-12.

**SN5**



“Sleipnir,” named after the mythical eight-legged horse of nordic god Thor, flew the offshore campaign in Norway. All subcomponents underwent waterproofing upgrades. The kite was lost during final hover in FCW-01.

<p><b>SN6</b></p>	 <p>SN6 was ready for integration in Hawaii when Makani was shut-down.</p>
<p><b>SN7</b></p>	 <p>SN7 was brought up in Alameda when Makani was shut-down.</p>
<p><b>SN8</b></p>	<p>The main wing for SN8 was fabricated, but the full kite was never assembled.</p>

**Table 4: M600 Kites Built**

## 3 Open Problems

Makani was still working to address significant open problems with the M600 at the time that the project was shut down. Some of these would be addressed mainly through a major design iteration of the airframe via the MX2 project: our inability to meet the M600 design power curve, and the poor roll stability in hover. Other were unfinished goals that we would have continued to advance through the M600 flight test program, such as demonstrating system availability comparable, if not yet competitive, to commercial offshore wind technologies.

### 3.1 Power Curve

Many factors contributed to the M600's inability to generate the targeted electric power. These can be categorized into two broader issues that then have many downstream effects. The issues were:

1. The kite was unable to operate at its target lift coefficient, making the aerodynamic performance less than intended.
  - a. The wing was designed with a novel and unproven laminar flow airfoil. Imperfect control and turbulence left the kite unable to reliably fly as close to stall as desired.
  - b. Kite drag was higher than expected, further reducing performance.
2. The kite was unable to turn paths as tightly as desired.
  - a. The bridle exerted too much roll-stabilizing moment to be able to roll the kite far enough to achieve sufficient centripetal force.
    - i. The kite was ~40% heavier than even mid-design revised targets, and ~70% heavier than early conceptual design targets.
    - ii. Kite mass growth created a mismatch between the bridling and target path sizes that could not be fixed without large design changes.
  - b. Lateral stability was poor.
    - i. The pylons were intended to assist with turning. However, the forward lateral area of the pylons had a destabilizing effect, and the resulting poor yaw control meant they were never effectively utilized.
    - ii. Large yaw rates caused flight instability for several reasons,<sup>6</sup> and this resulted in a practical limitation on the achievable yaw rate.

And the resulting effects were:

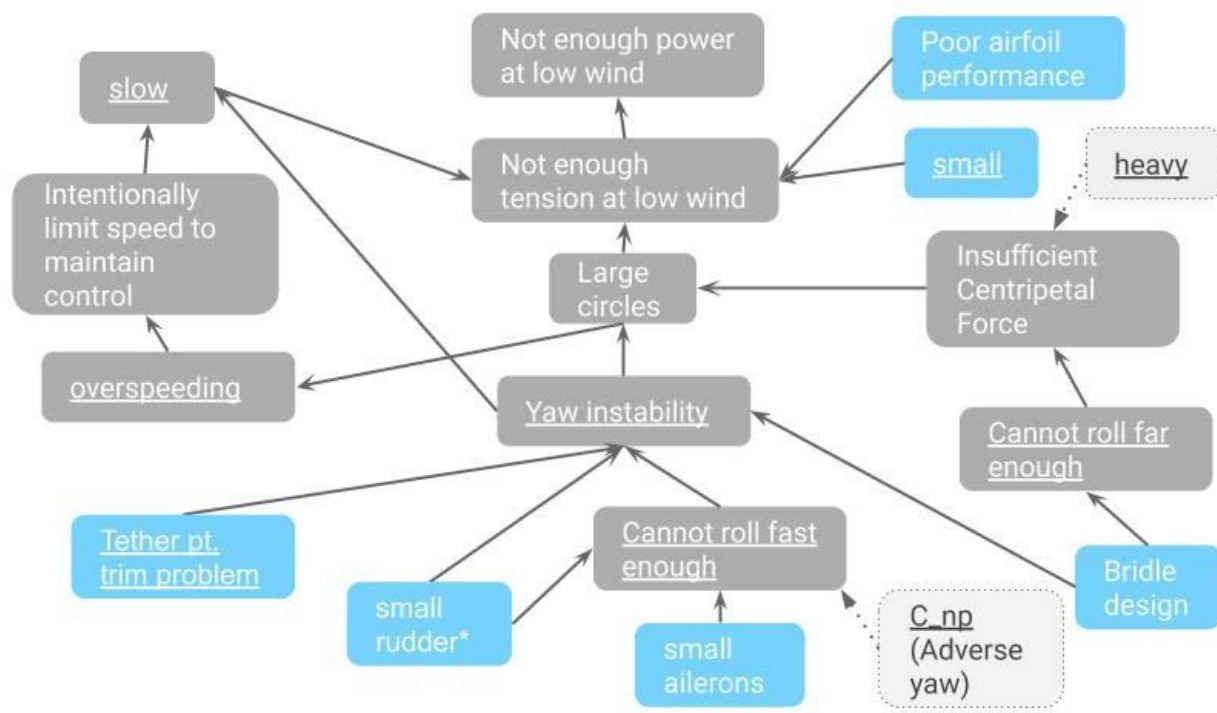
1. Lower lift and higher drag directly reduced performance.

---

<sup>6</sup> Most notably, large yaw excursions with a large bridle become unstable at certain pitches, leading to unstable flight modes.

- 2. Larger path sizes:
  - a. Increased the minimum mean elevation angle, reducing the effective wind and directly reducing performance.
    - i. The lower effective wind speed and higher drag shifted optimum kite speeds lower, causing the minimum controllable airspeed constraint to further reduce low wind performance.
  - b. Created a large potential energy exchange around the path, which:
    - i. Dictated much of the kite’s speed strategy, forcing it off optimal speeds.
    - ii. Created large swings in power.
      - 1. At low winds, these translated to large pumping losses.
      - 2. At high winds, these swings exceeded the power system’s capabilities, creating an overspeed hazard that required intentional performance degradation to keep in check.

These effects are discussed in more detail in “Airborne Wind Turbine Performance” [7].



\* small rudder does not cause instability, but it certainly doesn't help overcome it

Blue Boxes Denote Changes for Oktoberkite  
Dashed Grey boxes are not addressed

**Figure 14: A rough diagram of the factors adversely affecting the M600’s performance. Blue and dotted gray boxes are design aspects, and dark gray boxes are effects. Arrows indicate causality. The blue boxes are design aspects that the Oktoberkite / MX2 project sought to address, to enable the MX2 meet its design intent. The dotted gray boxes are design aspects the Oktoberkite / MX2 project did not address.**

One conclusion of all this is that the M600 airframe is fundamentally unable to generate 600 kW at 11 m/s. To achieve this performance, the airframe requires significant changes, which was the goal of the Oktoberkite / MX2 redesign project, discussed in detail in “Oktoberkite and the MX2,” included in this volume [5].

## 3.2 Roll Stability in Hover

The M600 system relied on the restoring action of a roll-bridle to maintain the kite's attitude around the vertical axis during hover. For this to work, adequate horizontal tension and tether geometry had to be maintained. Lack of roll stability was a significant contributing factor or primary cause of at least two crashes and several near misses [6, 14], yet roll stability remains a significant unsolved challenge of M600-type designs. Two avenues of attack are (1) to gain significantly greater control authority over the kite's position in hover (for the M600 we regulated tension rather than radial position); or (2) to add some additional actuator providing authority around the roll axis in hover. Some discussion of the proposed solutions is included in “Oktoberkite and the MX2” [5].

## 3.3 Availability

The M600 did not achieve significant “availability,” which, by its most general definition, means the amount of time in which the system is either operating or ready-to-operate out of a specified period, typically one year [15]. Although we did not yet even tally this metric, we can illustrate it: the M600 was flying for about 0.2% of the 8760 hours of 2019, and we can safely estimate that we were either flying or in a ready-to-fly configuration less than 1% of the time in that year. By comparison, commercial wind turbines often have availability values above 98%. Had Makani continued technology development in 2020, we intended to start tallying the availability of the M600 system and to see that metric improve.

Specifically, the areas of development for the engineering team that should affect our system availability comprised dispatchability, component reliability, automation, and robust flight controls. The first three areas can be described in general terms. By dispatchability, we understood the ability to get a new system quickly commissioned or an existing system re-commissioned after a fault, an upgrade or new release, or a maintenance procedure. Our strategy included priming a pipeline of complete kites, stocking test sites with rational supplies of spare parts, and continuously streamlining procedures to assemble, prepare, and check systems before flight. Our component reliability efforts were focused around formalizing, comprehensively implementing, and tracking end-of-line qualification testing for avionics and structural subcomponents. Our more direct automation efforts targeted the state machine by piping out-of-envelope calculations or fault detection algorithms to trigger the autopilot to end the flight. Some automation work was also being done to streamline preflight checks in order to support dispatchability efforts.

Robust flight controls can be singled out as a major and ongoing area of engineering effort at Makani. This work affected availability directly because three out of four major crashes can be attributed to our inability to retain control of the kite and, at the scale Makani operated, the times that we lost a kite in flight led to the longest periods of downtime. In part, this was compounded with pipeline challenges because we usually had only a single fully-commissioned kite on site at a given time. Mostly, however, the downtime after a crash was set to allow due time for the ensuing investigation of root causes and the implementation of corrective actions. Some of these crashes are discussed in detail in [6]. We intended to change the aircraft itself and to continue to improve flight controls, thus improving the plant's robustness to disturbances and increasing the locus of stability of the closed-loop plant, as discussed in [4] and [5].

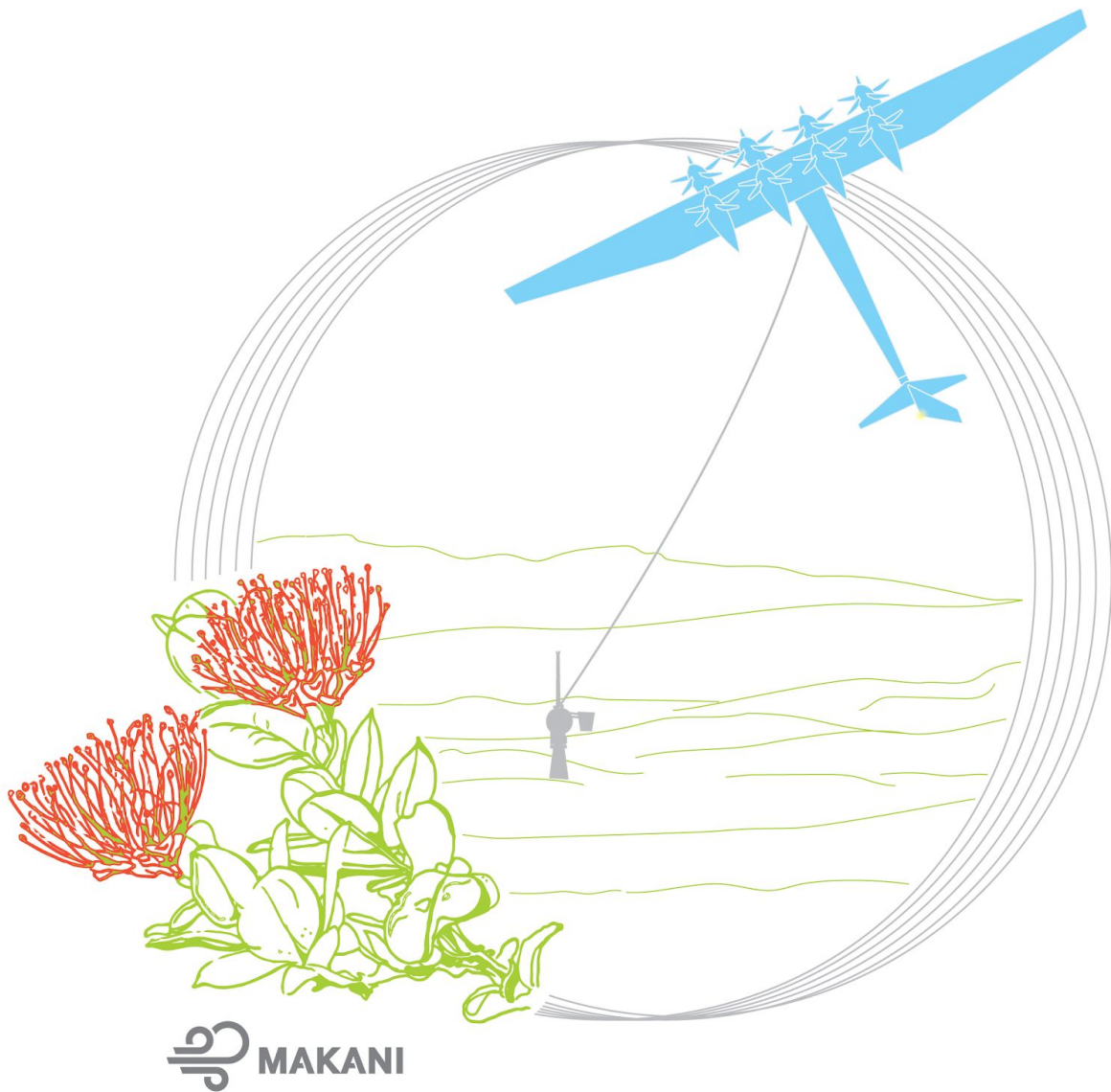
## 4 References

1. Makani Technologies, Alameda, CA, USA. *Makani - Energy Kite Technical Videos*. (Aug. 3, 2020). [Online Video]. Available: [https://www.youtube.com/playlist?list=PL7og\\_3Jqea4VRCZmMNK4LDH64sYgkLZzv](https://www.youtube.com/playlist?list=PL7og_3Jqea4VRCZmMNK4LDH64sYgkLZzv)
2. D. Vander Lind, "Analysis and Flight Test Validation of High Performance Airborne Wind Turbines," in *Airborne Wind Energy*, (Green Energy and Technology) U. Ahrens, M. Diehl, R. Schmehl, Eds., Berlin and Heidelberg, Germany: Springer, 2013, pp. 473-490, doi: [https://doi.org/10.1007/978-3-642-39965-7\\_28](https://doi.org/10.1007/978-3-642-39965-7_28)
3. *Makani Code Release*, Makani Technologies LLC, 2020. [Online]. Available: <https://github.com/google/makani/>
4. T. Fricke, "The Makani Autopilot," in *The Energy Kite: Selected Results From the Design, Development and Testing of Makani's Airborne Wind Turbines, Part I*, Makani Technologies, Alameda, CA, USA, 2020, [Online]. Available: <https://x.company/projects/makani>
5. G. Homsy, "Oktoberkite and the MX2," in *The Energy Kite: Selected Results From the Design, Development and Testing of Makani's Airborne Wind Turbines, Part I*, Makani Technologies, Alameda, CA, USA, 2020, [Online]. Available: <https://x.company/projects/makani>
6. P. Echeverri, "Makani's Flight Testing Approach," in *The Energy Kite: Selected Results From the Design, Development and Testing of Makani's Airborne Wind Turbines, Part I*, Makani Technologies, Alameda, CA, USA, 2020, [Online]. Available: <https://x.company/projects/makani>
7. N. Tucker, "Airborne Wind Turbine Performance," in *The Energy Kite: Selected Results From the Design, Development and Testing of Makani's Airborne Wind Turbines, Part I*, Makani Technologies, Alameda, CA, USA, 2020, [Online]. Available: <https://x.company/projects/makani>
8. "Makani Systems Overview," 2019, in *The Energy Kite: Selected Results From the Design, Development and Testing of Makani's Airborne Wind Turbines, Part II*, Makani Technologies, Alameda, CA, USA, 2020, [Online]. Available: <https://x.company/projects/makani>
9. K. Hallamesk, E. Chin, P. Miller, M. Mu, M. Scarito, E. Uhrhane, "A Low-Cost Fiber Optic Avionics Network for Energy Kites," 2017, in *The Energy Kite: Selected Results From the Design, Development and Testing of Makani's Airborne Wind Turbines, Part II*, Makani Technologies, Alameda, CA, USA, 2020, [Online]. Available: <https://x.company/projects/makani>
10. S. Nolet, D. Levy, and S. Chou, "Base Station Team Final Documentation," in *The Energy Kite: Selected Results From the Design, Development and Testing of Makani's Airborne Wind Turbines, Part II*, Makani Technologies, Alameda, CA, USA, 2020, [Online]. Available: <https://x.company/projects/makani>
11. A. Goessling, "Ozone Rev1 Design Document," 2015, in *The Energy Kite: Selected Results From the Design, Development and Testing of Makani's Airborne Wind Turbines, Part II*,

- Makani Technologies, Alameda, CA, USA, 2020, [Online]. Available: <https://x.company/projects/makani>
12. Makani Technologies, Alameda, CA, USA. *Makani*. (Aug., 2020). [Online Video]. Available: [https://www.youtube.com/playlist?list=PL7og\\_3Jqea4UFajQX-wwc702tUJcBMFMU](https://www.youtube.com/playlist?list=PL7og_3Jqea4UFajQX-wwc702tUJcBMFMU)
  13. A. Dunlap (Dir. of Photography, Ed., Narrator) and K. Stirr (Writer, Director), *Pulling Power from the Sky: The Story of Makani*, Makani Technologies, Alameda, CA, USA, 2020, included in *Makani*. (Aug., 2020). [Online Video]. Available: [https://www.youtube.com/playlist?list=PL7og\\_3Jqea4UFajQX-wwc702tUJcBMFMU](https://www.youtube.com/playlist?list=PL7og_3Jqea4UFajQX-wwc702tUJcBMFMU)
  14. K. Hallamasek, "Root Cause Analysis and Corrective Actions for FCW-01," in *The Energy Kite: Selected Results From the Design, Development and Testing of Makani's Airborne Wind Turbines*, Part II, Makani Technologies, Alameda, CA, USA, 2020, [Online]. Available: <https://x.company/projects/makani>
  15. "Definitions of Availability Terms for the Wind Industry," DNV GL, Høvik, Norway, white paper, 2017. [Online]. Available: <https://www.ourenergypolicy.org/wp-content/uploads/2017/08/Definitions-of-availability-terms-for-the-wind-industry-white-paper-09-08-2017.pdf>
  16. *Wind turbines – Part 1: Design Requirements*, International Standard IEC 64100-1 International Electrotechnical Commission, Geneva, Switzerland, 2005, [Online]. Available: [https://webstore.iec.ch/preview/info\\_iec61400-1%7Bed3.0%7Den.pdf](https://webstore.iec.ch/preview/info_iec61400-1%7Bed3.0%7Den.pdf)

# The Makani Autopilot

A Critical Retrospective



Tobin Fricke



The Makani Autopilot: A Critical Retrospective  
Corresponding author: Tobin Fricke, [fricke@gmail.com](mailto:fricke@gmail.com)

The Energy Kite: Selected Results from the Design, Development,  
and Testing of Makani's Airborne Wind Turbines, Part I of III  
by Paula Echeverri, Tobin Fricke, Geo Homsy, Nicholas Tucker,  
on behalf of the Makani team.

Copyright © 2020 by Makani Technologies LLC

Distributed under the [Creative Commons CC BY 4.0 License](https://creativecommons.org/licenses/by/4.0/). You are free to  
copy and redistribute this material in any medium or format for any purpose,  
even commercially.



Intended for electronic publication and distribution. Copies of this volume may be found at  
<https://archive.org>  
Additional information is at: <https://x.company/projects/makani>

Published September 2020

<b>1 Foreword</b>	<b>264</b>
<b>2 Introduction</b>	<b>266</b>
<b>3 A Very Brief Introduction To Crosswind Kite Power</b>	<b>267</b>
<b>4 Crosswind Flight Controller</b>	<b>268</b>
4.1 Top Level Control	268
4.1.1 Playbook	268
4.1.2 Path Shape Considerations	269
4.2 Path controller	270
4.3 Kinematics: The Required Motion	274
4.4 Inner loops	276
4.4.1 Trim and Linearization	276
4.4.2 The Linearized Plant	278
4.4.3 Linear Model to Gain Matrices	282
4.4.4 Validation	283
4.4.5 Discussion	284
4.4.6 Airspeed Controller	285
4.4.6.1 Discussion	287
4.4.7 Handling Actuator Saturation	288
4.4.8 Handling Periodic Errors	288
4.4.9 Tension Control	291
4.5 Conclusion	292
<b>5 Hover</b>	<b>293</b>
5.1 Hover Flight Modes	293
5.2 Hover Tension	294
5.2.1 Tension Command	295
5.2.2 Tension Plant	295
5.2.3 Tension Controller	295
5.3 Hover Path	295
5.3.1 Cat Facts	296
5.3.2 Tether Elevation Control	297
5.3.3 The Catenary Spring	297
5.4 PID in Practice	299
5.5 Hover Position	300
5.6 Hover Altitude	300
5.7 Hover Attitude	301
5.8 The Roll Control Problem and the Bridle	301
5.8.1 Other Mechanisms for Roll Stabilization	302

5.8.2 Where It Stands	302
5.9 Blown Lift and Phantom Moments	302
5.10 Future Improvements and Other Notes	304
<b>6 Actuation Allocation: The Motor Mixer</b>	<b>306</b>
6.1 Stacking	307
6.2 Roll Actuation	307
6.3 Combining Flaps and Rotors	307
6.4 Simplified Rotor Model	309
<b>7 Other Flight Modes</b>	<b>311</b>
7.1 Transition-In	311
7.3 Transition-Out	312
7.4 Off-Tether	314
7.4.1 Pilot Inputs	314
7.4.2 Wing Save	314
<b>8 Estimator</b>	<b>316</b>
8.1 Kite Rigid Body State	316
8.1.1 GPS woes	318
8.1.1.1 GPS Alternatives	319
Ground Line-Angle Sensing (GLAS)	319
Ultrawideband Ranging (UWB)	319
Light Sequence Decoding (LSD)	320
<b>8.2 Other Estimated Quantities</b>	<b>320</b>
8.2.1 Apparent Wind	320
8.2.1.1 Five-Port Pitot Probe	320
Alternatives to the Five-Port Pitot Probe	320
8.2.1.2 Complementary Filter	321
8.2.1.3 Angle of Attack and Angle of Sideslip	322
8.2.2 Wind Aloft	322
8.3 Validation	323
8.4 Discussion	323
<b>9 Simulator</b>	<b>324</b>
9.1 Simulator models	325
9.1.1 Kite	325
9.1.2 Rotors	325
9.1.3 Environment	325
9.1.4 Tether	325
9.1.5 Power System and Motors	326

9.1.6 Base Station	326
9.1.7 Buoy	326
9.1.8 Sensors	327
9.2 Simulator Modes	327
9.2.1 Desktop Simulation	327
9.2.2 Monte Carlo Batch Simulation	327
9.2.3 Hardware-in-the-Loop (HITL)	327
9.2.4 Dynamics Replay	328
9.3 What Wasn't Simulated?	329
9.3.1 Structural Modes of the Kite	329
9.3.1.1 Flight Testing Lesson: Flexible Body Modes	329
9.3.2 Propwash/Airframe Interaction	330
9.4 Potential Future Improvements	330
9.4.1 Automatic Model Tuning	330
9.4.2 Differentiability	330
9.4.3 Better Modularity and Linearization	330
<b>10 Visualizer</b>	<b>332</b>
<b>11 Software Development Methodology</b>	<b>333</b>
11.1 The Memorable Bugs	334
<b>12 Epilogue</b>	<b>336</b>
<b>13 References</b>	<b>337</b>

# 1 Foreword

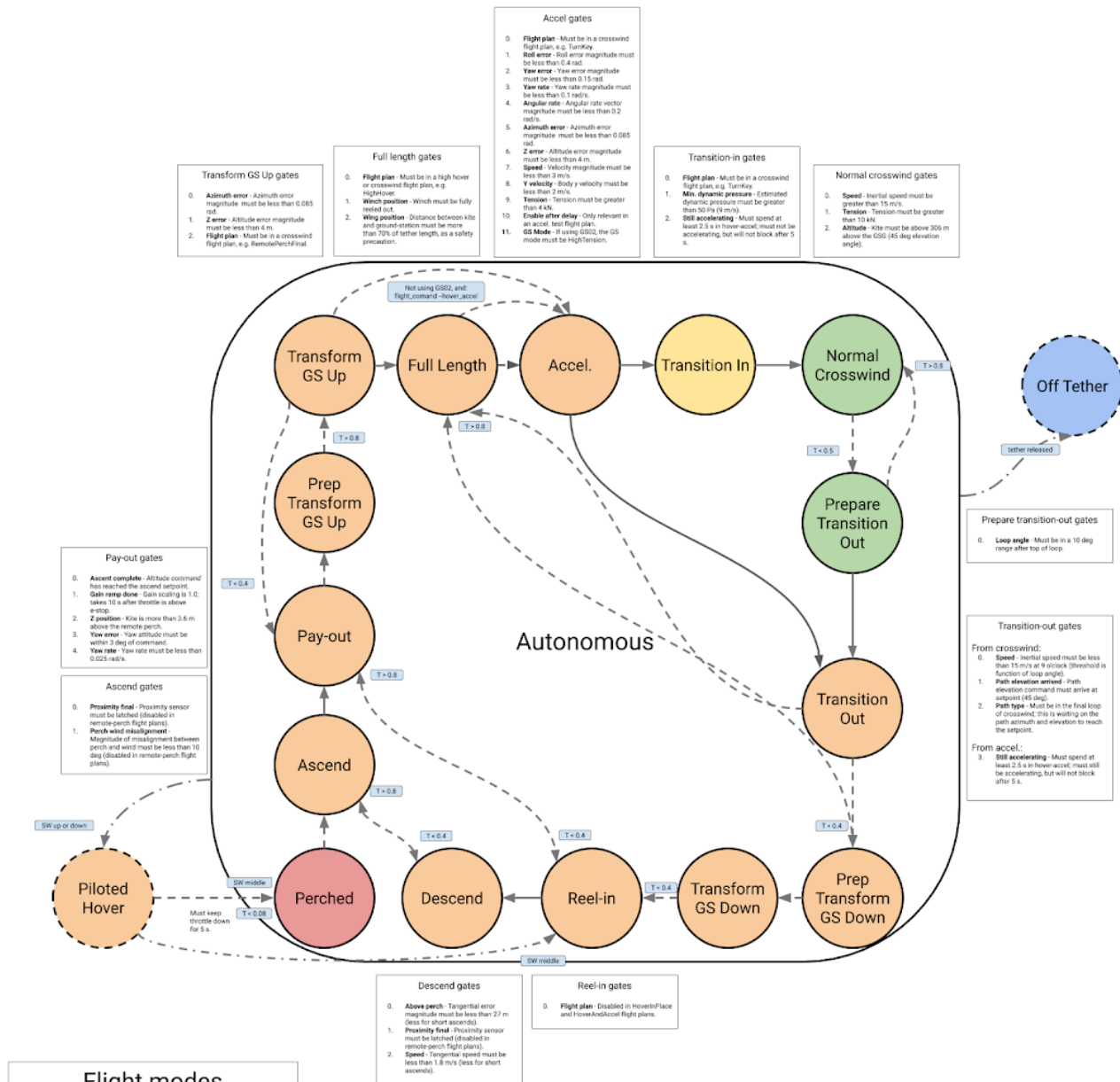
The Makani project has now been shut down. This document describes the flight control system as it was implemented. As a retrospective, this report is biased towards describing the particular challenges that remained outstanding and the ideas still on the whiteboards that we planned to implement—of course with no guarantee that those ideas would work as foreseen. Although many individuals contributed over the timespan of more than a decade to the Makani flight control system, this retrospective is being written by one of those engineers and is therefore also biased by his experience in particular. The control system described here is the result of more than a decade of experimentation and design, most of which occurred before the author's involvement; thus it is likely that many of the aspects which were sorted out during that earlier time may not be described here. It is hoped that this retrospective is of interest not just to the airborne wind energy community, but anyone building autonomous flying machines or robots of other kinds.

**Figure 1: (next page) An overview of flight modes and inputs governed by the Makani flight controllers. Of the seventeen flight modes, thirteen are sub-modes of the hover control (one hover mode is a manual mode), one is a transition-in sub-mode, two are crosswind sub-modes, and one is an additional manual mode. The numbered list (0-14) does not include prep-transform-up or prep-transform-down.**

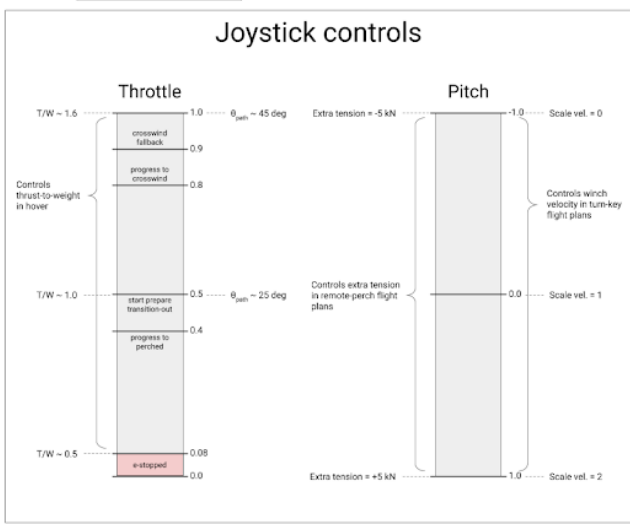


# Flight Mode State Machine

M10010



- ### Flight modes
0. **Piloted Hover** - Minimal sensor (i.e. no GPS) piloted hover mode where the pilot directly commands thrust and attitude with the joystick.
  1. **Perched** - Kite is stationary on the perch and motors are idling. In the remote-perch flight plans, the position of the kite is saved so the kite can return there.
  2. **Ascend** - Kite takes off from the perch or remote-perch and ascends until it reaches an altitude setpoint. Careful attention is paid to constrained degrees of freedom.
  3. **Pay-out** - Winch pays-out until the tether is completely unspooled and the GSG is in the crosswind position. Kite aims for the "accel-start" position. Pilot can scale winch speed with the pitch stick.
  4. **Full Length** - Kite is at full tether length and is neither paying-out or reeling-in.
  5. **TransformGSUp** - GS02 transform from reel to high tension mode.
  6. **Accel.** - Using the hover controller, the kite accelerates upward without pitching forward.
  7. **Transition In** - Kite pitches forward, comes off the tether sphere, and flies at a fixed aerodynamic climb angle to maximize altitude gain.
  8. **Normal Crosswind** - Kite flies circles and attempts to generate power.
  9. **Prepare Transition Out** - Kite is still flying circles, but the path center will move a little off downwind and the kite will eventually attempt to slow down to transition-out.
  10. **Transition Out** - Hovering mode following accel. or crosswind. Intentionally stalls elevator; doesn't tightly maintain position.
  11. **TransformGSDown** - GS02 transform from high tension to reel.
  12. **Reel-in** - Winch reels-in until the kite has contacted the perch and the proximity sensor is activated. Pilot can scale winch speed with the pitch stick.
  13. **Descend** - Kite descends onto the perch or remote-perch. Careful attention is paid to constrained degrees of freedom.
  14. **Off Tether** - The tether is released and the kite is pilot controls flaps with the joystick. Stability augmentation is activated with the momentary switch.



- ### Legend
- Hover controller
  - Transition-in controller
  - Crosswind controller
  - Manual controller
  - Autonomous controller
  - Piloted controller
  - Autonomous transition
  - Throttle transition
  - Switch transition

## 2 Introduction

The Makani M600 is a kite: a tethered fixed-wing aircraft powered by the wind. Like a traditional airplane, its flight is controlled using ailerons, an elevator, a rudder, and rotors. Unlike a traditional airplane, the motors and rotors can be used in not just the usual way to provide thrust but also in reverse, to create drag and produce electricity. The wind acts on the wing, propelling it forward; the rotors and generators extract energy from the relative wind. The software autopilot, the subject of this article, is responsible for flying the kite in such a way as to maintain stable flight and optimize power production. The autopilot's mission statement: Make power, don't crash.

The Makani system is divided into two main flight regimes: hover and crosswind. These are divided into seventeen flight modes, governed by the state machine depicted in figure 1. Of these flight modes, all but four are sub-modes of the hover controller, handling rising from or landing on the perch, pay out and reel-in of the tether, transform of the base station, and so forth. The crosswind controller governs two sub-modes. A dedicated "transition-in" controller handles the transition from hover to crosswind with one mode. Finally, an "off tether" flight mode allows free flight as a manually-piloted glider, and a "pilot hover" mode allows manual control of thrust and attitude, both for use as needed during testing.

For testing purposes, the progression of the flight mode state machine is governed through a joystick in the hands of a pilot, who may command the system to go forward towards crosswind flight, or to leave crosswind and return to the perch. For an installed system it was envisioned that this would be fully automated with the system automatically deciding when to launch and land. In this document we first describe the crosswind controller, followed by the hover controller, estimator, and other details of the software autopilot.

Where relevant, we follow the conventions of Stevens and Lewis [13] and Etkin [3].

### 3 A Very Brief Introduction To Crosswind Kite Power

Before delving into the details of the flight controller, it may help to briefly introduce the application of crosswind kite power.

The purpose of crosswind kite power is to generate electrical power using a kite. Consider a kite consisting of an airfoil mounted to an infinite railroad track, such that it can slide without friction along the axis perpendicular to the wind, and suppose that this airfoil is configured somehow to maintain a constant angle of attack (with constant coefficients of lift  $C_L$  and drag  $C_D$ ) with respect to the relative wind.

With the kite initially at rest, the relative wind is entirely composed of *the* wind, and the force of lift accelerates the airfoil directly along the railroad track. We call this *propulsive lift*. Now, with the airfoil having some velocity of its own, it experiences as relative wind the combination of the environmental wind and the wind from its motion along the track.

Drag acts in parallel to the relative wind, and lift perpendicular to it. As the airfoil accelerates, the forces of lift and drag rotate and stretch until the components of each along the axis of the track are equal and opposite. The kite reaches a steady-state velocity. The railroad track resists the force perpendicular to it, in the downwind direction. The situation is similar to a sailboat, where the downwind force is resisted by the keel, or a real kite, where the downwind force is resisted by its tether.

Suppose now that the drag consists of a fixed part  $C_D^{wing}$ , but also a variable part  $C_D^{rotors}$  that we can control. The dot product of force and velocity gives power. Power put into  $C_D^{wing}$  is simply lost to turbulence and heat, but power put into  $C_D^{rotors}$  is captured (with some imperfect efficiency) and converted into electricity for delivery to the power grid.

To get a feel for this scenario, it is useful to work out some small calculations as an exercise:

1. Given this scenario, with a wind speed  $v_w$ , a coefficient of lift  $C_L$ , and a coefficient of drag  $C_D$ , what is the kite's terminal velocity? (The forces of lift and drag are proportional in magnitude to  $C_L v_a^2$  and  $C_D v_a^2$ , respectively, where  $v_a$  is the airspeed.)
2. How much additional drag should be exerted to maximize power production (assuming that 100% of the additional drag is converted into useful power)?
3. What is the kite's terminal velocity with this additional drag? We call this the "optimal Loyd [9] speed."

For a practical system, the kite is tethered to a base station, and it must fly some flight path approximately perpendicular to the wind, such as a circle or an ellipse or a figure-eight.

## 4 Crosswind Flight Controller

The crosswind flight controller is built up in layers: a top level that chooses high-level parameters for the flight, a path controller, and inner loops that track rate, angle, and speed commands. Here we discuss these layers from top to bottom.

### 4.1 Top Level Control

At the top level, the crosswind controller chooses a path to fly based on the estimated wind speed and direction. The path is characterized by its shape, and by the schedules of airspeed, angle of attack, and angle of sideslip around the loop. We chose to always fly circular paths—simulations showed that there was not much to be gained by other shapes. Power production is relatively insensitive to the details of the path shape.<sup>1</sup>

#### 4.1.1 Playbook

The schedules of path center and path radius with environmental wind speed, airspeed, angle of attack, and angle of sideslip along the flight trajectory were developed using a combination of analytical tools and numerical optimization,<sup>2</sup> producing a lookup table termed the "playbook," which governs the top level of the flight controller.

Given a circular loop, "loop angle" is a convenient parametrization for airspeed, angle of attack, and angle of sideslip commands. This parametrization works for circular loops and works well when that circular loop is flown well<sup>3</sup> but for more general shapes—or even for circular loops in the presence of deviations from the intended flight path—the concept would need to be generalized.

We do not directly control for power generation.<sup>4</sup> Instead, we fly the prescribed trajectory at the prescribed airspeeds (etc) and power generation comes out "in the wash." In the idealized scenario discussed above, we could simply command the Loyd optimal airspeed and we would achieve maximum generation.<sup>5</sup> This approach is fairly typical of applications that must operate at a quadratic maximum of some quantity, rather than at the zero-crossing of a linear error signal. A drawback of this approach is that it relies on model correctness (knowing the wind

---

<sup>1</sup> These sensitivities are discussed in detail in the article titled "Airborne Wind Turbine Performance" [16].

<sup>2</sup> The optimization is done in part using an in-house tool called "force balance loop" (FBL), coupled with numerical optimization over an ensemble of simulator runs, and some hand tuning. It's also important that the playbook parameters be smooth with respect to wind speed to avoid erratic variation as the wind changes.

<sup>3</sup> Loop angle can be determined instantaneously by considering either the kite's position or heading. Care should be taken such that the loop angle estimate does not jump around discontinuously in the presence of an erratic position or velocity measurement.

<sup>4</sup> Many people seem to find this surprising at first.

<sup>5</sup> The sensitivity around this optimum airspeed also turns out to be fairly weak. Details in the "Performance" article [16].

aloft and  $C_L$ , for example) in order to get it right; the operating point is chosen in an "open-loop" manner and does not benefit from the model independence we typically gain from closed-loop control.

Eventually some feedback mechanism should be incorporated at this top level, transitioning the "playbook" from a purely open-loop mechanism to a closed-loop power controller that dynamically adjusts the flight parameters to optimize power production. Presumably this would take the form of a slow correction to the precomputed playbook.

#### 4.1.2 Path Shape Considerations

The exact "optimal" flight path tends to get a great deal of attention in the airborne wind energy community. Although the exact flight path is actually not that important from the perspective of power generation, it is subject to many trade-offs and is therefore a good candidate for numerical optimization. The flight strategy changes significantly with the wind speed; at lower wind speeds we want to capture as much power as possible from the wind, but at higher wind speeds we must avoid capturing too much power and exceeding system limits. In addition to changing the azimuth, elevation, and center of the loop, we can choose to store energy as kinetic energy (subject to increased loss due to drag) or exchange it with the electrical grid (subject to conversion losses). These many considerations are treated in greater detail in "Airborne Wind Turbine Performance" [16].

Achievable flight paths are also limited by the control authority available from the motors and control surfaces. An open question is whether a more general path shape—beyond circles—would provide enough additional freedom to substantially expand the flight envelope or increase robustness. One weakness of the current system is that the circular assumption is baked in at many points, and it has little ability to plan ahead or cope in an intelligent way with actuator saturations. We rely on the Playbook containing feasible flight strategies that can in fact be flown.

One is also tempted to consider figure-eight or lemniscate ( $\infty$ ) shaped paths that cross themselves as an alternative to simple closed paths that always turn in the same direction. Systems considerations come into play here: On one hand, it might be advantageous to not have to actively "detwist" the tether (as we must with a kite flying circles); on the other, there might be advantages to be realized from a kite that only turns in one direction<sup>6</sup> and disadvantages to a path so stretched in azimuth.

---

<sup>6</sup> The pylons of the M600 are themselves airfoils intended to generate side-lift to help provide centripetal acceleration.

## CROSSWIND OVERVIEW

- **Playbook** commands loop size and position as a function of wind speed, and airspeed and angle-of-attack commands as functions of loop angle.
- **Path loop** commands a curvature to follow a (generally circular) path.
- **Kinematics mixer** converts curvature commands to the inner loop control variables: [tether roll angle](#), [incidence angles](#), and [angular rates](#).
- **Lateral loop** controls tether roll angle, sideslip, roll, and yaw rates using ailerons, rudder, and yaw moment.
- **Longitudinal loop** controls angle-of-attack with the elevator.
- **Airspeed loop** controls airspeed with thrust or drag. Could be integrated with the longitudinal loop in the future.
- **Motor solver** converts thrust and moment commands to motor speeds.

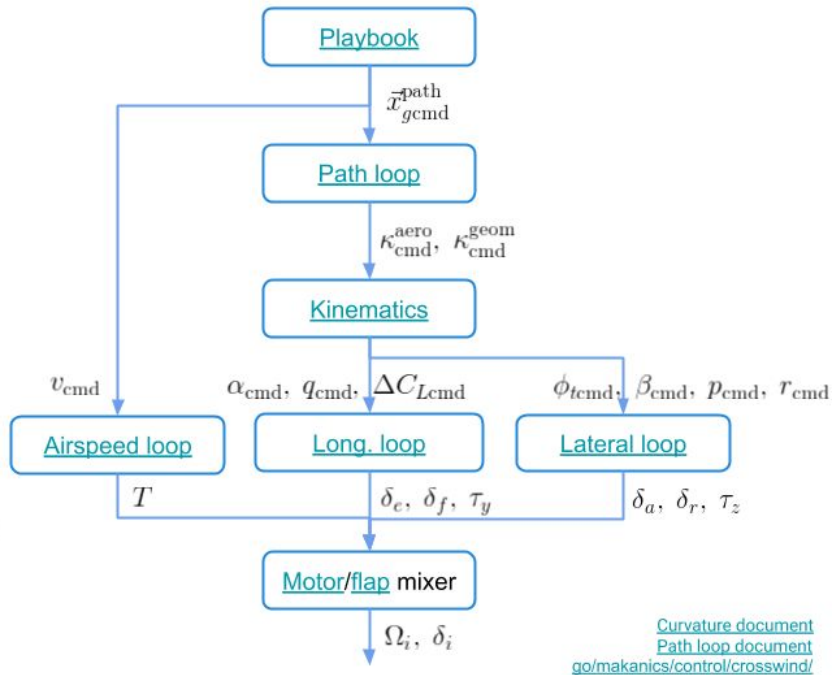


Figure 2: Overview of the crosswind controller.

## 4.2 Path controller

The responsibility of the path controller is to fly the trajectory specified by the playbook given the current environmental conditions. The path controller takes as inputs the desired loop center and radius, and the kite's position and velocity, and commands a centripetal acceleration. We express this centripetal acceleration in terms of "curvature" by dividing out the square of the speed. The curvature command is turned into a tether roll command via the "curvature mixer."<sup>7</sup> This command is passed to the inner loops, described later.

The kite produces centripetal acceleration by banking, rotating its lift. This bank angle is measured with respect to the tether, which, in a simple model, can be approximated as a straight line back to the base station. Gravity provides additional centripetal acceleration over the top of the loop, and a negative contribution around the bottom of the loop. The controller breaks down the required "geometric curvature" into "gravity curvature" (that acceleration provided by gravity) and "aero curvature" (that provided aerodynamically).

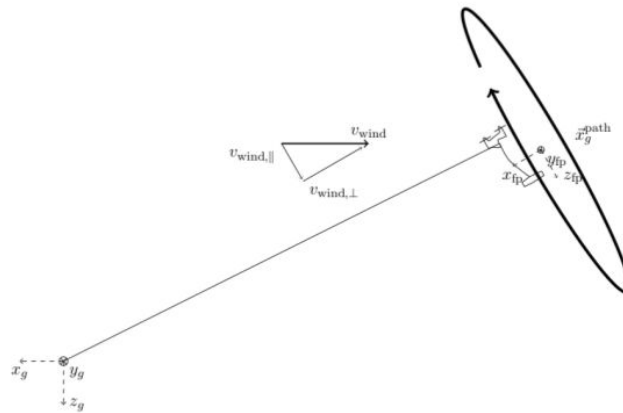
Our path controller can be considered a simple form of model predictive control (MPC). It uses a simple kinematic model of the kite's flight path, which assumes that the kite, starting from its current position and velocity, follows its current curvature for a period of time and then follows a new commanded curvature for a different period of time. The separation of the path into current and commanded curvatures is motivated by the fact that the kite cannot instantly change its

<sup>7</sup> We use the word "mixer" to describe several components of the controller that are simply *calculations* not involving any feedback.

curvature. Multiple potential commanded curvatures are projected forward and the one that minimizes a specific cost function is chosen. The cost function is the dot product of the predicted velocity vector with a vector field of ideal velocities (or ideal headings) at the predicted position. These ideal velocities are tangent to the path on the path, while away from the path they steer the kite back toward the path assuming some minimum turning radius.

### PLAYBOOK

- Responsible for positioning the [center of the flight path](#) and [commanding an airspeed](#) and angle-of-attack.
- Calculated using offline global optimization.
- Sets instantaneous airspeed command based on angle in loop and [expected variation](#) from optimization runs.

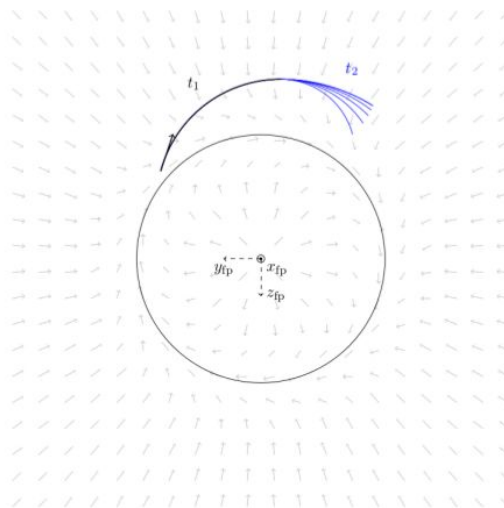


[go/makanics/control/crosswind/crosswind\\_power.c](http://go/makanics/control/crosswind/crosswind_power.c)

Figure 3: Overview of the top level "playbook."

### PATH LOOP

- [Predicts wing position finite time](#) in future to determine curvature command (see [linear analysis](#)).
- Project wing position and heading onto "flight plane".
- Define a vector field of the optimal heading as a function of position.
- [Integrate position and heading](#) forward assuming [current curvature](#) for time  $t_1$ .
- [Integrate future position and heading](#) forward assuming a [new curvature](#) for time  $t_2$ .
- Use [dot product](#) with [optimal heading](#) as the cost function to select the new curvature command.



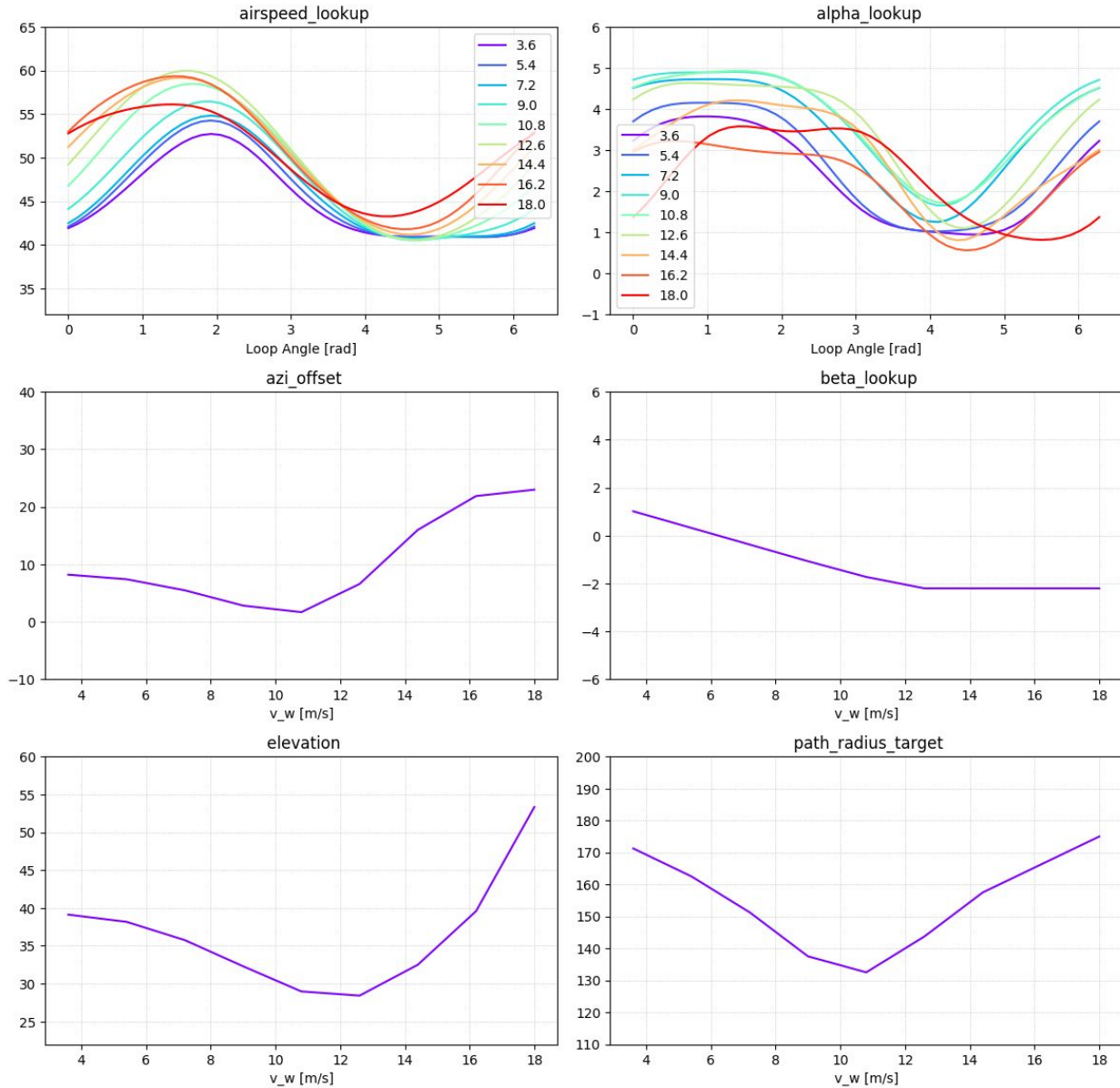
[Path loop document](#)  
[go/makanics/control/crosswind/crosswind\\_path.c](http://go/makanics/control/crosswind/crosswind_path.c)

Figure 4: Overview of the path controller.

When linearized, this controller is equivalent to a linear crosstrack error controller. For details see the technical note "Linear Analysis of the Path Controller" [7], in the Makani controls documentation on github.

One disadvantage of this system is that it does not provide perfect tracking in the presence of modeling errors: for example, if the realized tether roll (bank angle) does not provide the required centripetal acceleration. We addressed this by applying additional integral control on crosstrack error, augmented by adding an *ad hoc* sinusoidal feedforward component to the tether roll command. A more integrated solution seems desirable; we would like the path controller to be able to achieve perfect tracking of any path. One step in this direction might be to provide closed-loop (integral) curvature or centripetal acceleration control.

The instantaneous airspeed, angle of attack, and angle of sideslip commands are functions of the kite's present position along the path (via the playbook) and are not handled by the path controller.



**Figure 5: Example "playbook."** The upper two plots give airspeed (in m/s) and alpha (degrees) commands as functions of loop angle. Loop angle is given in radians and is always *decreasing* in flight. The lower four plots give the azimuth (in degrees), elevation (in degrees), and radius (in meters) of the circular flight path, and the sideslip (in radians) command, as functions of wind speed.

### 4.3 Kinematics: The Required Motion

Pilots are familiar with the maneuver of "turns around a point," the object of which is to fly a circular flight path in a horizontal plane around a fixed point on the ground. In the absence of wind, this is quite easy to do: a fixed bank angle will do it. But in the presence of wind, the pilot must steepen and reduce the angle of bank around the loop as the airplane points downwind and upwind, respectively, while also taking care to keep the turn coordinated.

The M600 experiences a similar phenomenon.<sup>8</sup> Because our loop is in an inclined plane, we now have to compensate for the varying influences of not just wind but also gravity. A particular "head wag" of the aircraft is required to fly the prescribed path while holding aerodynamic angles at their prescribed values.

From the prescribed path and airspeed, angle of attack, and angle of sideslip commands (all functions of loop angle), and an estimate of the wind vector, we can calculate the required kite attitude up to a rotation around the apparent wind vector. This final degree of freedom is used to steer the kite. In the current implementation we approximate this roll angle around the apparent wind vector as being equal to the tether roll angle. This gives us the expected kite attitude, which we express as a direction cosine matrix (DCM).

By performing a central-difference calculation between the attitudes required at loop angles  $\theta + \delta\theta$  and  $\theta - \delta\theta$  we obtain the angular velocity vector required, which becomes a command for the controller inner loops. By taking another derivative, we obtain the angular acceleration, which can be used to produce feedforward moment<sup>9</sup> commands. In these calculations we assume that the kite is on its intended path.

As near-term improvements, we planned to flesh this out a bit further, incorporate an analytical model providing a rate of change of tether roll angle (a significant effect that is currently omitted), and to work out analytical expressions for everything rather than relying on central-difference calculations. One can imagine a "kinematics" box in the control system, taking as an input the centripetal acceleration commanded by the path controller and the aerodynamic angles and their derivatives specified by the playbook, and outputting the required rates and accelerations. An old sketch of these plans is depicted in figure 6.

As a general principle, we have found it advantageous to apply feedforward wherever possible, to reduce the feedback effort required. Unlike feedback, feedforward action is instantly available without first requiring the appearance of an error. The concept of a "feasible trajectory" is useful. A feasible trajectory is the complete specification of control inputs as a function of time that will exactly achieve the desired state trajectory in the absence of disturbances or modeling errors. Computation and execution of a feasible trajectory is the gold standard of feedforward.

---

<sup>8</sup> See "Crosswind Kinematics" [1], in this collection.

<sup>9</sup> Moment is used as a synonym for torque.

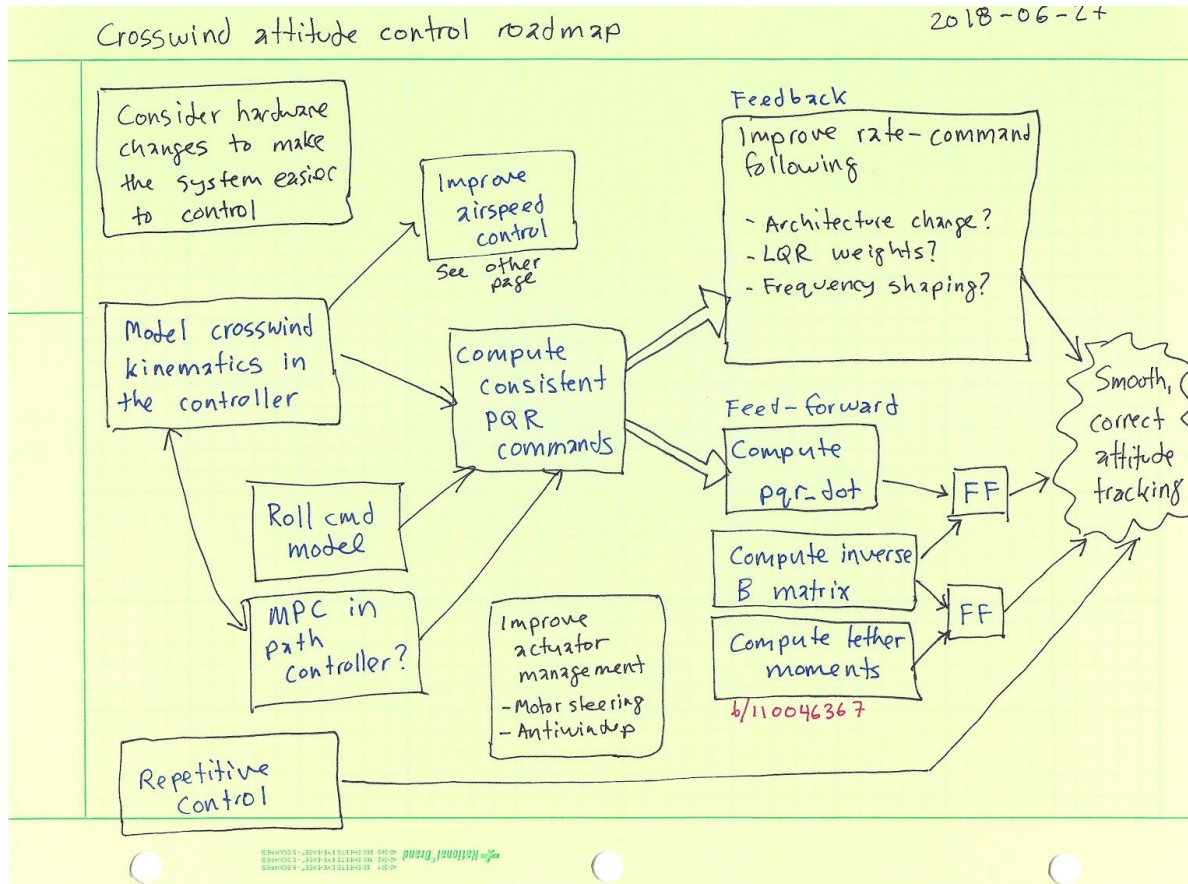


**Figure 6: Road map to improvements to crosswind attitude control, as envisioned mid-2018.<sup>10</sup> The emphasis was on computing the motion required and enough derivatives to have smooth and correct rate and acceleration commands, and full feedforward of these commands to the actuators. Some mechanism (such as some form of model predictive control) allowing the path controller to "plan ahead" (avoiding actuator saturation) was also desired.**

<sup>10</sup> The video "Tech Topic - 20180208 - Michael and Tobin Describe Efforts to Resolve Sideslip Excursions in the Flight Path of the Makani M600" [17] is a good complement to this figure.

## 4.4 Inner loops

The crosswind controller inner loop commands are angle of attack ( $\alpha$ ), angle of sideslip ( $\beta$ ), airspeed, tether roll angle, and angular velocity expressed in body coordinates. Here we simply apply a linear gains matrix to convert error signals (and their integrals) into displacements of the actuators from their trim values. The gains are generated using LQR, which is a standard method that takes a linear model of a system and a quadratic cost function, and computes the optimal linear gains given that model and cost function. The inner loops are block-diagonalized into lateral control, longitudinal control, and airspeed control. This basic linear structure is augmented with a system to suppress periodic errors, and with features to improve the effect of integrator windup or actuator saturation.

### 4.4.1 Trim and Linearization

As the first step of model linearization, we first try to find a trim state: a state of equilibrium of the full (nonlinear) system in an idealized flight scenario. The trim scenario has the kite flying a circular loop in a horizontal plane, with the wind blowing upward, and with no gravity. This approximates crosswind flight with the assumption that the effect of gravity—which requires modulation of the kite's bank angle—is a small perturbation. This equilibrium state is found using a Python program<sup>11</sup> that sets up a nonlinear model of the kite system and solves for a state at which the state derivative is zero, i.e. the system is at equilibrium.

Each trim scenario is defined by a fixed wind speed, kite speed, angle of attack, and loop radius. We trim, linearize, and generate gains for three scenarios, to facilitate gain scheduling: 5 m/s wind with 30 m/s kite speed ("low wind"), 10 m/s wind with 60 m/s kite speed ("nominal wind"), and 15 m/s wind with 90 m/s kite speed ("high wind"), all at an angle of attack of about 8 degrees and a loop radius of 150 meters. We apply linear interpolation to the gains resulting from these three scenarios.

Before attempting to solve the global trim problem, we first solve several smaller problems, in order to give the global optimizer a good starting guess:

1. Trim the vertical position to produce zero vertical acceleration.
2. Trim the thrust to produce zero forward acceleration.
3. Trim the roll angle to produce zero radial acceleration.
4. Trim the pitch attitude to produce the commanded angle of attack.
5. Finally, solve the global trim problem: trim the wing to have zero acceleration and zero angular acceleration using thrust, flap deflections, vertical position, and roll.

---

<sup>11</sup> The crosswind trim, linearization, and gains generation program may be found in the Makani software repository as `analysis/control/crosswind.py`.

### CURVATURE MIXER

- Curvature control mostly independent of wind speed (everything scales as  $v^2$ ).
- Loadcells give direct, robust measurement of turning force.
- Curvature approximately [linearly proportional to tether roll angle](#).
- Approximations:
  - Inertial velocity close to airspeed.
  - Small roll angle.
  - No gravity.
  - **These approximations are subsequently corrected.**
- Trade  $C_t$  for tether roll angle to manage tension.
- Outputs angle-of-attack, sideslip, and tether roll commands.

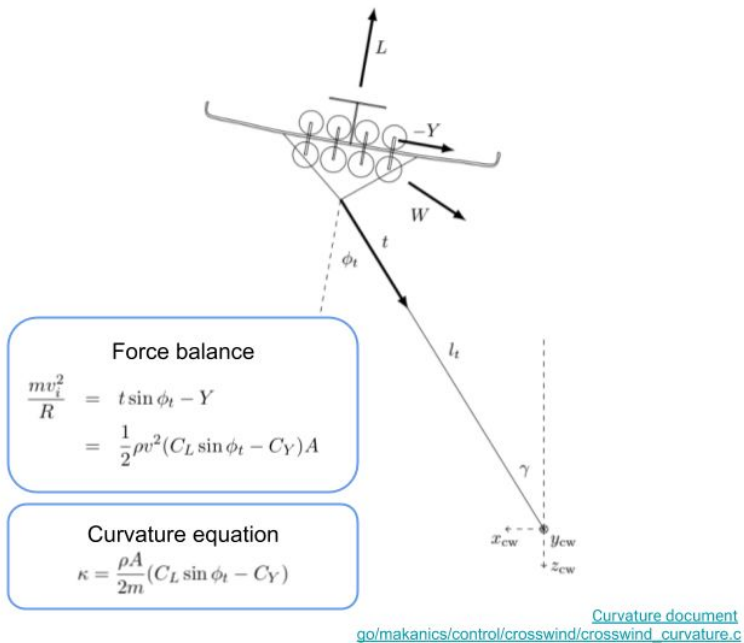


Figure 7: Overview of the curvature mixer.

### LATERAL LOOP

- Not typical lateral plant due to tether force and bridle.
- Use directly measured tether roll, sideslip, roll rate, and yaw rate.
- Acts on **error states** rather than states themselves.
- Augment state vector with [integrated tether roll and sideslip states](#).
- LQR gains with Q and R matrices chosen according to [Bryson's rule](#).
- Integrator saturations are chosen to not exceed the [maximum rudder and aileron deflections](#).
- Improvement desired: Still needs fully-developed feedforward via approximate inverse plant.

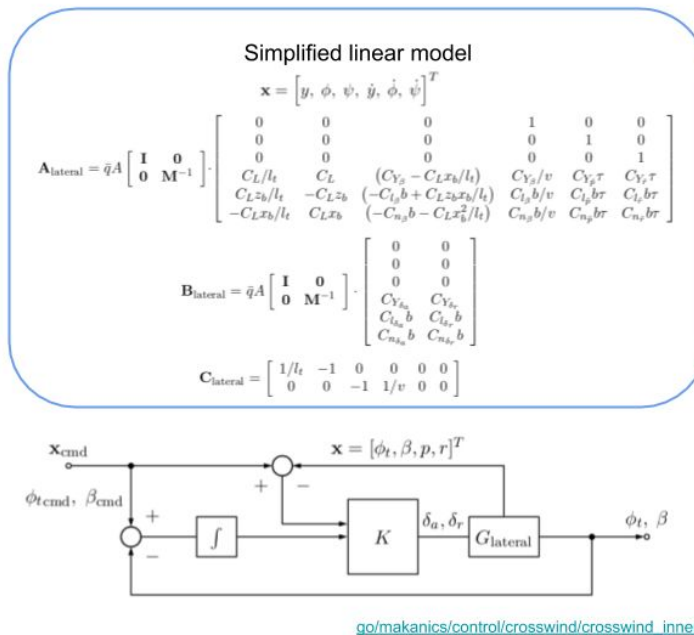


Figure 8: Overview of the crosswind lateral controller.

#### 4.4.2 The Linearized Plant

We employ the standard state space formalism, in which the system is written down as a system of linear first-order differential equations. The linear model is encapsulated by four matrices (A, B, C, and D):

$$\begin{aligned}\dot{x} &= A x + B u \\ y &= C x + D u\end{aligned}$$

where  $x$  is the current state,  $u$  is the current control input (actuation),  $y$  is the current system output (sensor measurements), and  $\dot{x}$  is the time derivative of the state ( $\dot{x} = (d/dt) x$ ).

The matrix A describes the system dynamics, and the matrix B, the control matrix, tells us how we can influence the state via our actuators. In controller development, we generally assume that the state vector  $x$  is directly available to us (it's provided by a dedicated estimator subsystem). Thus, we assume that the matrix C is the identity matrix, and matrix D, which simply passes inputs through to outputs, is typically zero.

We block-diagonalize the system into lateral and longitudinal parts, ignoring the cross-terms that connect these two blocks. Table 1 and table 2 show the elements of the state vector ( $x$ ) and control input ( $u$ ) for the lateral and longitudinal crosswind inner loop plants.

Inspecting the resulting matrices, we find (as expected) that the ailerons control roll rate, the rudder controls yaw rate, and the motor yaw moment also causes yaw rate. The other matrix elements are negligible. The numbers in the "motor yaw" column are small compared to the aileron and rudder columns due to the difference in units (N · m versus radians).

Two elements of the A matrix can be pointed out here: the strong couplings from tether roll angle to roll acceleration, and from roll rate to yaw acceleration. The former is a manifestation of the bridle stiffness; the former, the aerodynamic derivative  $CN_p$ . Both of these terms were sources of trouble.

A much deeper dive into the desirable, undesirable, or otherwise notable properties of the plant is warranted. However, because it is not the author's area of expertise, such a discussion is omitted. The reader is referred to "Kite Stability in Crosswind Flight" [12] in this collection for some relevant discussion.

#	States	Inputs
1	tether roll error [rad]	aileron delta [rad]
2	sideslip error [rad]	rudder delta [rad]
3	roll rate error [rad/s]	motor yaw cmd [N · m]
4	yaw rate error [rad/s]	
5	integrated tether roll error [rad · s]	
6	integrated sideslip error [rad · s]	

**Table 1: Lateral controller states and inputs.**

#	States	Inputs
1	position ground Z [m] ( <i>not used!</i> )	elevator delta [rad]
2	velocity ground Z [m/s] ( <i>not used!</i> )	motor pitch command [N · m]
3	angle of attack error [rad]	
4	pitch rate error [rad/s]	
5	integrated angle of attack err [rad · s]	

**Table 2: Longitudinal controller states and inputs.**

teth roll	sideslip	roll rate	yaw rate	int teth	int slip	→ d/dt
-0.0315	0.0942	<b>-1.0098</b>	0.0651	0	0	teth roll
-1.6823	-0.8699	0.0384	<b>-0.9540</b>	0	0	sideslip
23.5699	-1.0938	-7.6957	5.9300	0	0	roll rate
-1.3264	0.0051	-2.5671	-0.7220	0	0	yaw rate
<b>-1</b>	0	0	0	0	0	int teth
0	<b>-1</b>	0	0	0	0	int slip

**Matrix 1: Crosswind lateral A matrix.**

aileron [rad]	rudder [rad]	motor yaw [N · m]	
-0.0027	0.0042	0	(d/dt) tether roll
-0.067	0.16	0	(d/dt) sideslip
<b>-20</b>	0.3	0.000002	(d/dt) roll rate
0.44	<b>-3</b>	0.000002	(d/dt) yaw rate
0	0	0	(d/dt) int teth roll
0	0	0	(d/dt) int sideslip

**Matrix 2: Crosswind lateral B matrix.**

teth roll	sideslip	roll rate	yaw rate	int teth roll	int sideslip	
0.97	-1.52	-0.22	0.25	-0.63	0.39	aileron
0.69	1.22	0.039	-0.49	-0.77	-0.32	rudder
-80	-100	-3	50	84	28	motor yaw

**Matrix 3: Gain lateral gain matrix at nominal wind speed.**

pos gnd z	vel gnd z	AoA	pitch rate	int AoA		→ d/dt
0	1	0	0	0		pos gnd z
-16	-0.52	-325	-4.4	0		vel gnd z
-0.27	-0.01	-5.4	0.93	0		AoA
-0.19	-0.001	-20	-2.9	0		pitch rate
0	0	-1	0	0		int AoA

**Matrix 4: Crosswind longitudinal A matrix.**

elevator [deg]		motor pitch [N · m]	
0		0	(d/dt) pos gnd z
-21		$-9.4 \times 10^{-6}$	(d/dt) vel gnd z
-0.35		$-0.35 \times 10^{-6}$	(d/dt) AoA
-26		$-25 \times 10^{-6}$	(d/dt) pitch rate
0		0	(d/dt) int AoA error

**Matrix 5: Crosswind longitudinal B matrix.**

pos z	velocity z	alpha	pitch rate	int alpha	
N/A	N/A	-1.0	-0.26	0.32	elevator
N/A	N/A	2060	925	-610	motor pitch

**Matrix 6: Gains matrix for the longitudinal system at nominal wind speed.**

### 4.4.3 Linear Model to Gain Matrices

Once we have a linear model of the kite, we can easily propose gain matrices and consider the resulting controller performance.

To generate the gains matrices, we use LQR, which takes a state-space description of a linear system (i.e. matrices A, B, C, and D) and quadratic cost functions Q and R, producing a gains matrix K that is optimal under a particular set of assumptions.

The LQR cost function is a quadratic form applied to the state vector ( $x$ ) and the control inputs ( $u$ ), i.e. the time integral of  $x^T Q x + u^T R u + x^T N u$ . We select these matrices Q and R using Bryson's rule, a standard heuristic in which Q and R are diagonal and the diagonal elements represent the (inverse of) the maximum acceptable state values and control inputs. In our system, we do not use N (i.e. it is zero).

When Q or R is diagonal, then the associated quadratic form  $x^T Q x$  or  $x^T R x$  turns into a weighted sum of the mean square values of the individual states and control inputs.

Off-diagonal terms in Q or R could be used to penalize two states or two control inputs becoming large simultaneously ("avoid simultaneous large alpha and beta"); similarly, the N matrix offers the opportunity to penalize simultaneous excursions of a particular state and a particular control input ("don't use a lot of aileron when sideslip is large"). In our system we do not currently use any nonzero off-diagonal weights.

In principle, LQR should provide us with a gains matrix resulting in a stable system for any choice of the weighting matrices Q, R, and N. In practice, this is not guaranteed, as we violate some of the assumptions of LQR, for example by linearizing a nonlinear plant, artificially zeroing out all of the lateral/longitudinal cross terms, etc.

Using LQR changes our problem from that of choosing the linear gain matrix K to choosing the LQR weighting matrices, which may together have more or fewer degrees of freedom than K; but the part of the solution space yielding unstable systems is removed. We experimented with using an offline optimizer to further modify these weighting matrices (from the simple starting point given by Bryson's rule) to improve system performance but this did not yield any big wins.

For illustration, matrix 3 is the gain matrix for the lateral system at nominal wind speed. The columns correspond to the states (given in table 1 above), and the rows correspond to actuators. The matrix elements have a variety of different units, so comparing the magnitudes of matrix elements needs to be done with caution.

Inspecting this matrix we see that, for example, a tether roll error results in aileron and rudder commands of similar magnitude and the same sign, while sideslip error results in aileron and rudder commands that are equal(ish) and opposite.

### 4.4.4 Validation

The kite model and LQR gains-computation stage does not consider the linear response function of the actuators. We model the kite and design the controller without considering the actuator response. After the controllers are designed, only then do we apply the linear models of actuators and check that the resulting controller is still stable.

Table 3 below shows the output of the stability verification. The lateral and longitudinal open-loop systems are individually stable, but the full system, and the full closed-loop system, appear unstable as the path controller is not included here; these modes could be stabilized in this model by adding a linear crosstrack controller.

Open-loop poles			Closed-loop poles		
longitudinal	lateral	full	longitudinal	lateral	full
0.00 + 0.00i	0.00 + 0.00i	-2.63 + 8.89i	-26.65 + 26.66i	-26.63 + 26.64i	-26.65 + 26.66i
-2.73 + 7.91i	0.00 + 0.00i	-2.63 + -8.89i	-26.65 + -26.66i	-26.63 + -26.64i	-26.65 + -26.66i
-2.73 + -7.91i	-3.96 + 5.05i	-3.87 + 4.73i	-16.29 + 9.90i	-19.38 + 14.13i	-26.63 + 26.64i
-0.92 + 1.74i	-3.96 + -5.05i	-3.87 + -4.73i	-16.29 + -9.90i	-19.38 + -14.13i	-26.63 + -26.64i
-0.92 + -1.74i	-1.19 + 0.00i	-1.20 + 1.82i	-2.57 + 7.63i	-15.98 + 10.05i	-19.38 + 14.13i
	-0.20 + 0.00i	-1.20 + -1.82i	-2.57 + -7.63i	-15.98 + -10.05i	-19.38 + -14.13i
		-1.24 + 0.00i	-4.74 + 4.35i	-5.32 + 6.07i	-16.26 + 10.17i
		-0.13 + 0.72i	-4.74 + -4.35i	-5.32 + -6.07i	-16.26 + -10.17i
		-0.13 + -0.72i	-0.30 + 0.00i	-6.75 + 0.00i	-15.98 + 9.64i
		0.42 + 0.00i		-0.75 + 0.38i	-15.98 + -9.64i
		-0.13 + 0.04i		-0.75 + -0.38i	-2.61 + 8.55i
		-0.13 + -0.04i		-0.20 + 0.00i	-2.61 + -8.55i
					-5.57 + 5.37i
					-5.57 + -5.37i
					-4.94 + 5.11i
					-4.94 + -5.11i
					-5.77 + 0.00i
					-0.79 + 0.47i
					-0.79 + -0.47i
					-0.03 + 0.64i
					-0.03 + -0.64i
					-0.15 + 0.18i
					-0.15 + -0.18i
					-0.27 + 0.00i
					0.00 + 0.00i
Stable	Stable	Unstable	Stable	Stable	Unstable

**Table 3: Open loop and closed loop poles of the M600 plant with the LQR inner loop controller.**

#### 4.4.5 Discussion

The development above assumes the existence of a "trim" state that can stand in for a "feasible trajectory," with any deviations from that assumption handled by feedback. After all, the promise of a linear quadratic *regulator* is to drive a system to a single equilibrium point, not to track a trajectory. When supplemented with a feasible trajectory, LQR can indeed stabilize to the trajectory (See Tedrake [10]).

Despite abusing LQR in this manner, the method was nonetheless adequate to produce a *stable* control system that was sufficient to explore the mechanics of crosswind flight. Nonetheless we found ourselves in pursuit of a more developed feedforward system that would be guaranteed to produce a feasible trajectory exactly tracking the references (in the absence of modeling errors or disturbances). One might say we found ourselves stumbling towards the formalism known as explicit model reference control, in which a kinematics model provides all the desired derivatives of the commanded path and the implied vehicle motion, and an approximate inverse plant provides a hefty dose of feedforward.

Although the system accepts pitch, roll, and yaw rate commands, rate-command following is very weak. Indeed, earlier versions of the controller fixed the rate commands at the values one arrives at considering only the once-per-loop rotation of the kite. One might consider developing an additional layer in the controller presenting a more assertive rate-command interface. Without an additional feedforward path (not yet implemented), the lateral inner loops consider only sideslip and tether roll angle *errors*, not the absolute value. Due to roll bridling, a constant aerodynamic moment is required to hold a roll attitude; currently no feedforward path is present to provide this.

#### 4.4.6 Airspeed Controller

The airspeed controller operates independently from the lateral and longitudinal inner loops; it's a simple PID controller on airspeed error, greatly aided by feedforward, producing a thrust command that ultimately determines the rotor speeds. Because the D term is currently set to zero, one might refer to the controller simply as a PI controller.

The two included feedforward terms are: (1) the force of gravity, estimated as the projection of the gravity vector onto the kite's heading; (2) the force required to provide the required inertial acceleration implied by the varying airspeed command. Because we command *airspeed* and not simply *speed*, computation of the latter requires knowledge of the path and the environmental wind. The major feedforward term missing from the current formulation is the estimated or expected propulsive lift.<sup>12</sup>

The development of the airspeed controller proceeds in a manner that will become familiar: we develop a simple model and then find a PID controller meeting various stability requirements in conjunction with that model. It is a highly simplified model; the adage "all models are wrong, some are useful" applies here. Here we used the idealized model described in Section 3, A Very Brief Introduction To Crosswind Kite Power. We spell it out here in detail not because it is particularly ingenious but because it illustrates the approach taken also in the hover controller, where for each loop we develop a simple analytic model and then fit a PID controller to it.

Recall that the kite experiences propulsive lift until it reaches a terminal velocity where the components of lift and drag perpendicular to the tether are equal and opposite. If the kite is moving faster or slower than this terminal velocity, then it will experience a net force tending to return it to that velocity. In the idealized scenario, that terminal velocity is  $(C_L/C_D)v_w$ , where we are including rotor drag in  $C_D$ .

To derive the value of the restoring force, we start with the basic force-balance equation for crosswind flight:

$$F_x = \frac{1}{2} \rho A v_a^2 (C_L \sin \theta - C_D \cos \theta) \quad [1]$$

or

$$F_x = \frac{1}{2} \rho A v_a (C_L v_w - C_D v_k) \quad [2]$$

where  $F_x$  is the force perpendicular to the tether,  $\rho$  is the air density,  $A$  is the wing area,  $v_a = \sqrt{v_k^2 + v_w^2}$  is the airspeed seen by the kite,  $v_k$  is the kite speed,  $v_w$  is the wind speed,  $\theta$  is

---

<sup>12</sup> Online estimation of propulsive lift was prototyped, but never enabled on a real flight, as it did not demonstrate a significant improvement in flight performance in simulation.

the angle opposite  $v_w$  in the wind triangle formed by  $v_k$  and  $v_w$ , and  $v_k$  and  $v_w$  are assumed to be perpendicular.

Next, take the derivative with respect to kite speed:

$$\frac{dF_x}{dv_k} = \frac{1}{2} \rho A \left( 2 \frac{v_k}{v_a} (C_L v_w - C_D v_k) - C_D v_a \right) \quad [3]$$

Substitute the steady-state kite speed  $v_k = (C_L/C_D)v_w$  at which  $F_x = 0$  to find the restoring force about the steady state condition:

$$\frac{dF_x}{dv_k} = \frac{1}{2} \rho A v_a C_D \quad [4]$$

$$\text{at } v_k = (C_L/C_D) v_w \quad [5]$$

$$v_a = v_w \sqrt{1 + (C_L/C_D)^2} \quad [6]$$

Taking the approximation  $(C_L/C_D)^2 \gg 1$ , which implies  $v_a \approx v_k = (C_L/C_D)v_w$ , we find the effective spring constant (with units of N per m/s) of the "velocity spring" that tends to hold the kite at its terminal velocity in the idealized scenario:

$$k_{eff} = \frac{dF_x}{dv_k} = \frac{1}{2} \rho A C_L v_w \quad [7]$$

We can now write down the transfer function from thrust to airspeed, linearized around the steady-state airspeed:

$$\left[ \frac{\text{airspeed}}{\text{thrust}} \right] (s) = 1 / (m_{eff}s + k_{eff}) \quad [8]$$

where the effective mass  $m_{eff}$  is taken to be the kite mass plus a third of the tether mass (as the tether tends to sweep out a cone).

This system is further multiplied by the transfer function that takes commanded thrust to realized thrust (or motor speed command to motor speed), which is taken as a single pole at 6 Hz.

Finally, now with a model of the plant in hand, we can calculate gains for the airspeed PI controller. We employ MATLAB's `pidtune` function,<sup>13</sup> asking it to design a PID controller for this plant with a bandwidth of 0.3 Hz and phase margin of 80 degrees. The resulting gains are  $k_p = 3440 \text{ N/m/s}$ ,  $k_i = 2090 \text{ N/m}$ , and  $k_d = 148 \text{ N/m/s}^2$ .

The derivative gain is not used in the actual implementation because there is no direct measurement of the derivative of airspeed and we generally avoid the use of numerical derivatives due to worry of phase loss and numerical noise. If desired, an estimate of the derivative of airspeed could be developed using inertial sensors (similar to the way in which we apply a complementary filter to the pitot data, described in a later section). However, there is likely little benefit in making the airspeed controller more assertive. We would prefer a smooth application of thrust/power.

In addition to this linear controller, several nonlinearities are applied: the airspeed error is saturated at  $\pm 5.0 \text{ m/s}$ , and the integrand is saturated at  $\pm 5000 \text{ N}$ . These nonlinearities had a significant effect on the behavior of the controller, with the integrator chattering between its rails on a once-per-loop basis in many flight conditions. Finally, the thrust command was saturated and slew-rate-limited to obey limits on total power and rate of change of power.

#### 4.4.6.1 Discussion

The main deficiency of airspeed control was in its ability to cope with saturations of the motor thrust (with either sign), which were a normal part of operations. Because the PID controller has absolutely no ability to *plan ahead*, it is absolutely crucial that the controller be presented with a *feasible command* if we are to expect decent tracking. Furthermore, because a PID controller can only attain perfect tracking in the presence of a constant disturbance, and the disturbances here are anything but constant, it is crucial that adequate feedforward be provided to take care of the systematic effects.

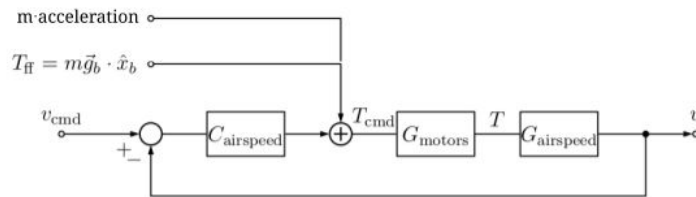
This design of the airspeed controller was found to be generally acceptable but not abundantly satisfying; a revamp here was seen to be growing in priority. The idea of integrating the airspeed controller with the other degrees of freedom (in particular the longitudinal inner loops) was a mainstay of our roadmap for future development, although this idea was never turned into a concrete proposal for how to do so or what improvement could be expected. The numerous nonlinearities (saturations and rate limits) imposed and the chattering integrator should also be seen as signs of marginal health in this controller and interpreted as motivation to explore controller schemes with some ability to *plan ahead* and thus abide by system limits in a more natural way.

---

<sup>13</sup> Gains for the crosswind airspeed controller are generated by the MATLAB script `analysis/control/generate_crosswind_gains.m` in the Makani software repository [18].

## AIRPEED LOOP

- Separate [airspeed](#) and [angle-of-attack](#) loops (just a legacy issue, should combine into single longitudinal loop)
- [Feed-forward thrust](#) term
- Feed-forward of inertial acceleration implied by the airspeed schedule and the loop geometry.
- Propulsive lift is main missing feedforward term.
- Potentially good candidate for repetitive control or some form of MPC. In current form, integrator often goes rail-to-rail.



[go/makanics/control/crosswind/crosswind\\_inner.c](http://go/makanics/control/crosswind/crosswind_inner.c)

**Figure 9: Crosswind airspeed controller overview.**

### 4.4.7 Handling Actuator Saturation

When actuators reach their limits, we have to make the best of our limited control authority. Each actuator has individual, physical limits—but actuators are typically used in concert to achieve a result, such as a coordinated turn. Integrator values are converted to flap displacements via the gains matrix mentioned above. To mitigate integrator wind-up we use a technique called "back-solving." After final actuator saturations are applied, we multiply the final actuator commands by the inverse (or pseudoinverse) of the control matrix and repopulate the integrator values.

### 4.4.8 Handling Periodic Errors

When we first flew the M600, the crosswind flight controller relied almost exclusively on linear feedback on the error states and their integrals. At that time we were happy enough to achieve stable controlled flight at all, but focus quickly shifted to flying *well*, bringing the residual errors to zero. After all, precision flying is directly connected to our bottom line—any power lost to drag is power that we can't sell.

We immediately observed that the error residuals were strongly periodic due to the periodic nature of both the commanded flight path and the resulting disturbances. To put it more bluntly, we flew each loop badly in pretty much the same way as the previous one. To remove these periodic errors, we first experimented with estimating the Fourier components of the errors, and then applying integral control on these Fourier components. This was effective but very slow to correct.

We rediscovered an area of control known as "repetitive control." According to the internal model principle, a control system can only fully suppress a particular disturbance if it can also generate that disturbance internally. The textbook by Franklin, et al. has a great example of this for a single-input, single-output system, shown below in figure 10 [4]. These techniques were originally developed for use in computer tape and disk drives, which involve the need to precisely position a read/write head over rapidly spinning magnetic media. It doesn't take too much imagination to go from a spinning disk to a kite flying loops.

In our system the disturbance does not necessarily occur at a fixed frequency but as a function of the kite's position around the flight loop. We use the sine and cosine of the loop angle as the reference for the repetitive control system, shown in figure 11. The required phase of the feedback is determined empirically, and we only attempt to correct the fundamental Fourier component, although generalization to multiple Fourier components is obvious. This simple repetitive control scheme effectively eliminated the once-per-loop sideslip errors. The residual higher-harmonic errors were deemed to be acceptable.

Although this particular problem was solved using feedback, a feedforward solution would be more satisfying, as the "disturbances" involved here are entirely predictable. We would much rather understand and implement the correct physics to prevent these periodic errors from occurring in the first place.

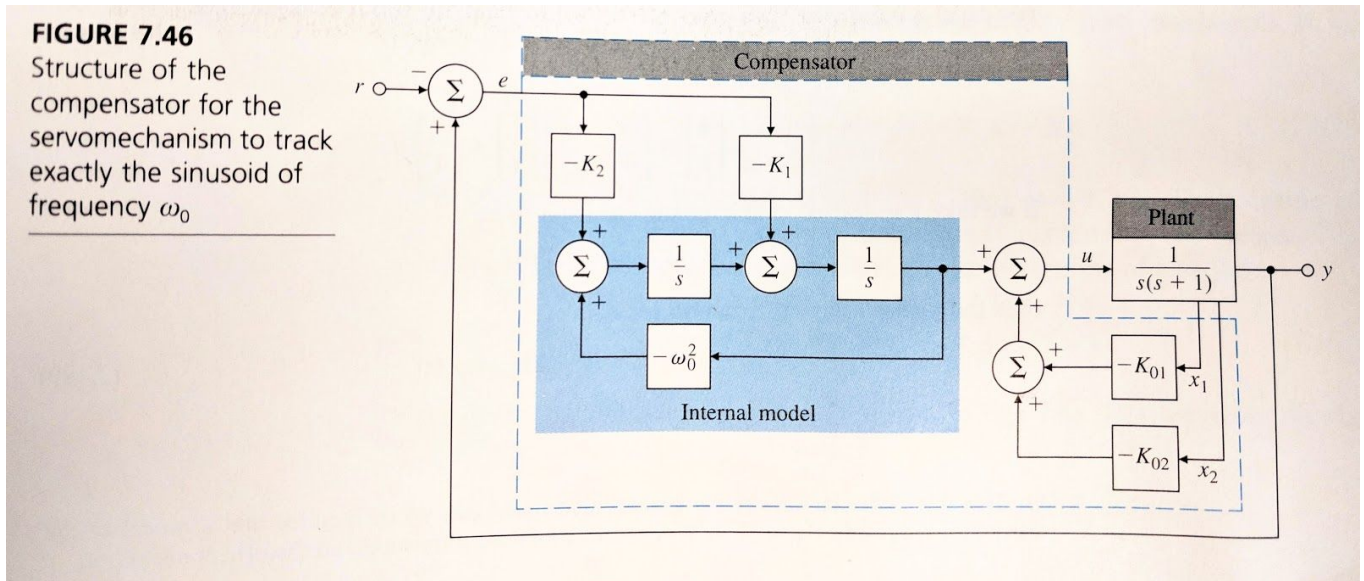


Figure 10. Textbook example of repetitive control [4].

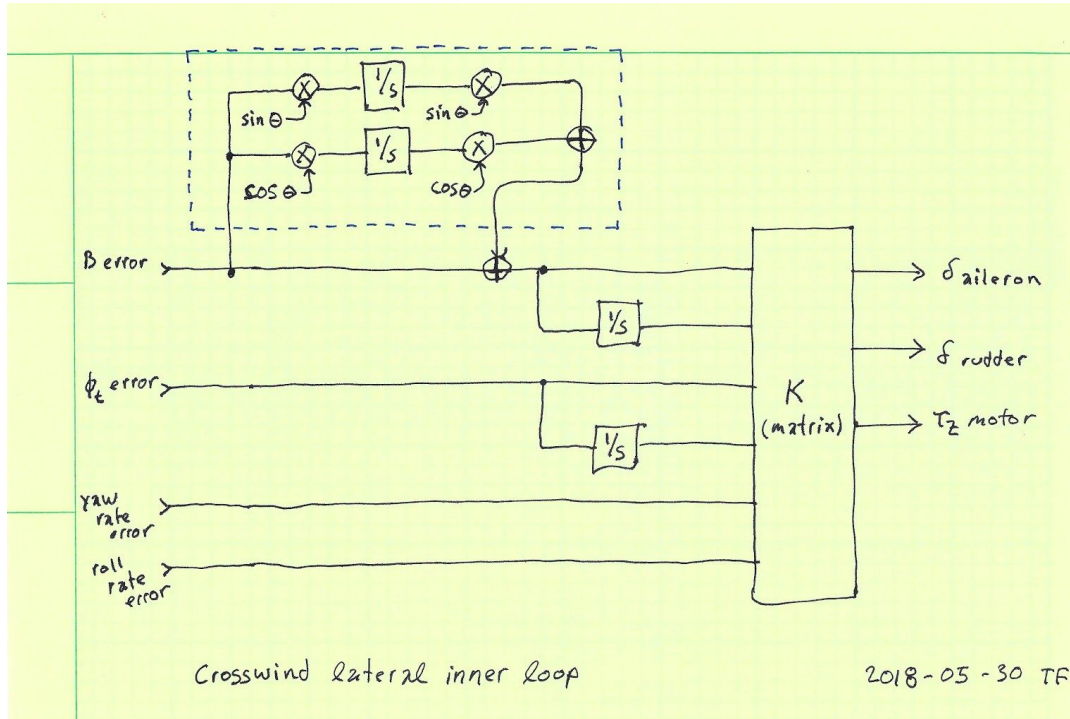


Figure 11: A sketch showing our implementation of repetitive control.

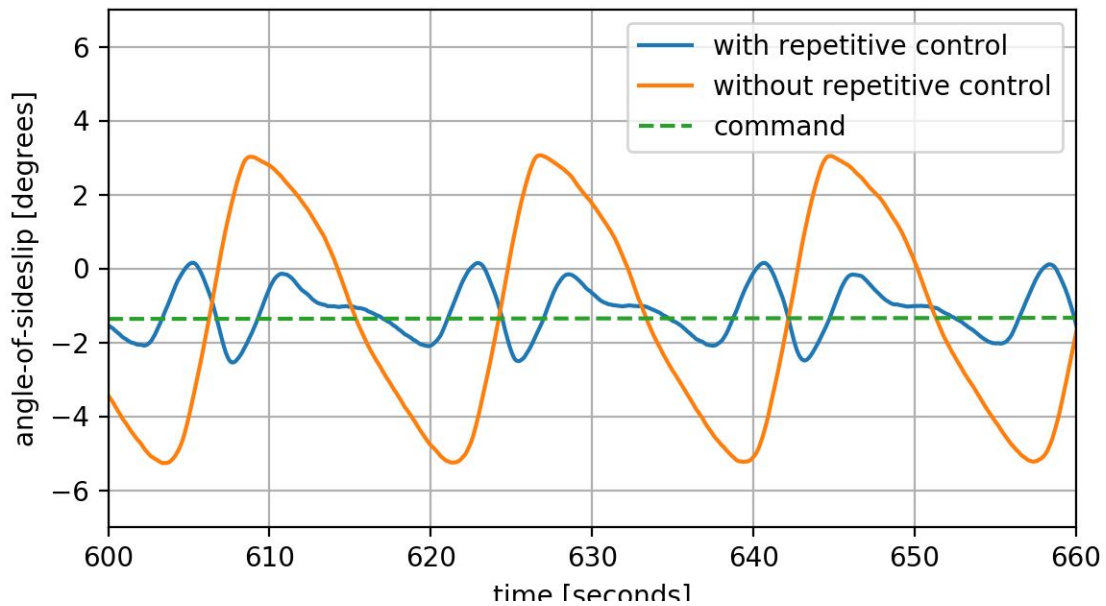


Figure 12: Sideslip command-following with and without the repetitive controller, in simulation with no turbulence.

#### 4.4.9 Tension Control

Tether tension is not actively controlled, and yet is a vitally important quantity: both the tether itself and the airframe must carry the loads. Indeed, in higher wind speeds, optimal operation of the kite is limited by the maximum permissible tension. In this tension-limited regime, airspeed or angle of attack must be lowered to keep the tether tension at or below the maximum allowed value.

Without closed-loop control of tension, we rely entirely on offline modeling to address the tension limit: the schedules of airspeed and angle of attack specified by the playbook are chosen to comply with these limits. This sort of open-loop design is vulnerable to both modeling errors and physical disturbances. To accommodate these possibilities, the resulting playbook may be more conservative than we would like. To address this restriction, some kind of closed-loop control is needed.

While high-bandwidth control of tether tension in crosswind flight seems infeasible without exciting mechanical modes of the tether, low-bandwidth tension regulation seems entirely possible. In one formulation, the expected tension would be added to the playbook. The difference between observed and expected tension would lead to feedback applied to some other aspect of the playbook; for example, perhaps a consistently high tension reading would lead to the airspeed schedule being adjusted downward. Some functionality of this nature will be necessary to operate in the tension-limited regime.

## 4.5 Conclusion

The M600 crosswind flight controller was an evolution of the crosswind flight controller developed for the M600's predecessor, Wing 7, described in Vander Lind [15]. Developed with the experience gained flying several generations of kites, and validated using the in-house simulator, the M600 crosswind flight controller flew successfully during its first crosswind test flight (RPX-02) on December 14, 2016. A controller that works the first time on a new vehicle can be regarded as a tremendous success. The controller was further developed over the course of M600 flight testing, culminating in the offshore flight test in the summer of 2019.

During these three years of M600 flight testing, we came to appreciate more strongly the need to understand the required motion, and to supply the autopilot with the plumbing necessary to fly this motion smoothly and correctly. We came to appreciate the need to handle actuator saturations more gracefully; flying with saturated actuators is a normal flight condition of the M600. We utilized global optimization to choose flight paths offline but came to desire some kind of online planning, perhaps some form of model-predictive-control. Could more general path shapes open up additional freedom to capture more energy while avoiding system limitations? We began pursuing non-circular path shapes. The importance of understanding the plant and designing it to be well matched for the mission was illuminated. And the vital essence of systems engineering was underscored: no amount of control can make a machine perform outside the performance envelope given by physics. Finally, in the field we experienced the realities of flying in turbulent wind fields, with a moving base station floating in the sea, with all of the complexities of the real world.

## 5 Hover

While the main (power-generating) operation of the M600 is in crosswind flight, the vehicle must hover during deployment and landing. In deployment, the kite begins perched on a landing platform, hovers as the tether is payed out to its full length, then transitions from hover to crosswind flight. Similarly, to end the flight, the kite must transition out of crosswind flight and hover for a few minutes as the tether is reeled in, before landing on the perch. This section describes the hover controller.

The M600's hover mode of flight differs from that of typical multi-rotor hovering devices by the presence of the tether, which influences the system design in two major ways: (1) The rotors provide negligible control authority around the roll axis (rotation around the vertical). Instead, roll stability is provided by the bridled tether, and hover is naturally regarded in cylindrical or spherical polar coordinates with the base station at the origin. (2) The radial position of the kite (with respect to the base station) is not controlled directly; instead a loop is closed around tension. These two aspects are at the nexus of the hover controller's greatest weakness, with roll divergence resulting in one severe crash and several near-misses. These challenges are described further in section 7.1.7, The Roll Control Problem and the Bridle.

To the extent that the M600 resembles other hovering multi-rotors, its control system does too and is composed of cascaded PID loops; like the crosswind controller, the hover controller is divided into layers: path, position, and attitude among them.

The PID gains are generated automatically using highly simplified models of the plant and MATLAB's `pidtune` function.<sup>14</sup> For the linear models used in developing these controllers, see "Very Rough Hover Notes" [8], in the Makani controls documentation on github. The overall controller bandwidth is limited by the actuator (motor and servo) bandwidths and slew rate limits, as well as the need to avoid exciting tether dynamics. The weak effective spring of the tether at long pay out also limits the bandwidth of some loops.

### 5.1 Hover Flight Modes

The hover controller utilizes numerous individual flight modes, listed in table 4, to orchestrate the journey of the kite from the perch to the transition-in start position and back again.

---

<sup>14</sup> The MATLAB script generating hover controller gains (and containing all of the simplified models used to do so) is `analysis/control/generate_hover_controllers.m` in the Makani software repository. The use of `pidtune` turned out to be a mixed blessing. Automatic (mechanized) gains calculation was hugely successful. But because the `pidtune` algorithm is not well specified, and changes from one version of MATLAB to the next, we were locked into using a single version of MATLAB (2014a) to avoid unwanted changes in the gains (which would need to be validated somehow before unconstrained flight).

<b>Perched</b>	The kite is on the perch, with motors at idle.
<b>Ascend</b>	The kite is commanded to rise above the perch.
<b>Pay out</b>	The kite is commanded as a function of the payed out tether length and environmental conditions.
<b>Base station transform up</b>	The kite position is commanded to obtain the required departure angle of the tether out of the base station, to allow the base station to transform from “reel” mode to “high tension” mode. (See “Base Station Team Final Documentation” [19])
<b>Full length</b>	The kite is commanded to go to the location required for accel.
<b>Accel</b>	The kite is commanded to accelerate upwards for hand-off to the trans-in controller.
<b>Transition-out</b>	The hover controller takes control of the kite at the end of a crosswind loop and stabilizes the kite at an acceptable altitude and zero velocity.
<b>Base station transform down</b>	The reverse of base station transform up.
<b>Reel-in</b>	The reverse of pay out.
<b>Descend</b>	The reverse of ascend.

**Table 4:** Overview of hover flight modes.

## 5.2 Hover Tension

We do not regulate the radial component of the hover position. Instead, a loop is closed around tension at the kite, measured directly via the bridle-point loadcells. The intention is to regulate the horizontal component of tension only. A horizontal tension command is computed, and converted to a total tension, which is then used as a control variable. Directly controlling horizontal tension may or may not be preferable.

### 5.2.1 Tension Command

A minimum horizontal tension is required to maintain roll stability via the bridle and to keep the tether wrapped on the drum. Tension is provided both by the kite's rotor thrust and by the wind acting on the kite via flat-plate drag. In general, the thinking was that horizontal tension provided by the wind is "free" and generally desirable: it would make little sense to pitch the kite forward to actively fight the wind.<sup>15</sup> Thus, to form the horizontal tension command, we take the greater of (1) an estimate of the horizontal flat-plate drag on the kite from the wind, or (2) a minimum horizontal tension command (initially 3 kN, but ultimately raised to 8 kN).

Experience in flight testing almost always showed a better experience from more horizontal tension (resulting in a stronger restoring action on the otherwise uncontrolled roll axis), provided that motor saturation was avoided. At worst, attempting to achieve an unachievable horizontal tension will also pull the kite out of the sky.

Horizontal tension in the tether is also seen at the base station and can drive mechanical requirements there. In practice this was not a concern with GS02, the base station used at Parker Ranch and offshore in Norway.

### 5.2.2 Tension Plant

The plant seen by the tension loop is essentially a spring, as described below in section 7.1.3.3, The Catenary Spring. The effective spring constant varies by three orders of magnitude over the course of pay-out. We use gain scheduling to cope with this.

The tension controller acts by commanding an offset to the kite's trim pitch attitude. For small offsets from trim, the horizontal force can be approximated as the additional pitch-back angle multiplied by the weight of the kite. Large pitch-back angles require significant additional thrust to maintain hover and are therefore to be avoided.

### 5.2.3 Tension Controller

In addition to an integral controller around tension, we do implement a radial damping term, acting on the radial velocity. This can be viewed as a "D" term of the tension PID loop but does not require taking a derivative.

## 5.3 Hover Path

The hover path controller produces a position command; its main function is to guide the kite during pay out and reel-in and to bring the kite into position for special maneuvers such as

---

<sup>15</sup> In high winds it might be useful or necessary to pitch the kite forward in hover to achieve some flat-plate *lift*. This was much discussed but never attempted.

landing. We also require the kite to arrive at a particular starting position before initiating the acceleration and transition to crosswind.

This is done by generating a series of waypoints and then producing position and velocity commands that constitute a smooth trajectory to get from one waypoint to the next. During pay out and reel-in the waypoints are generated continuously based on a calculation of the tether's catenary geometry.

### 5.3.1 Cat Facts

During pay out and reel-in, the desired hover position is a function of the wind speed and direction, and the length of tether that has been payed out. In hand analysis, we typically modeled the tether as a catenary, neglecting aerodynamic drag on the tether as well as its dynamics. The basic *ab initio* requirements are something like:

1. The tether shall not drag on the ground.
2. Make economical use of thrust.

The base station presented an additional requirement:

3. The elevation angle of the tether departing the base station must be held within a particular range.

In any analysis of the M600's hover modes, one soon becomes well acquainted with some basic properties of catenaries and their governing equations. An ideal catenary carries no moment; at every point the slope of the catenary is equal to the ratio of the vertical and horizontal tensions at that point. The catenary shape is fully specified by its horizontal tension, which is the same everywhere, and its linear density, also assumed to be uniform.

Given requirements 1 and 2, maintaining a hover altitude equal to the height of the tether termination at the base station is motivated. In this situation the catenary is symmetric with its vertex halfway between the base station and kite. Half of the weight of the tether is supported by the base station and half by the kite. Whatever horizontal tension is required to keep the tether vertex from intersecting the ground is maintained.

When the tether departs the base station at an angle above vertical, it must exert an upward force on the base station; this upward force ultimately must be provided by the kite's rotors, and hence one might say it constitutes wasted thrust (manifested in the eating away of margins and operating envelope, etc). Requirement 3 and the desire to have a short tower necessitate a slight upwards tether elevation angle.

### 5.3.2 Tether Elevation Control

The base station must be able to pay the tether out and reel it in again during hover and also support the enormous tension seen in crosswind flight. If the kite is flying in circles, somehow the twisting of the tether must be accommodated. The interface requirements are fierce: twenty tons, a megawatt, and two revolutions per minute during crosswind. And a large panel for the kite to launch from and land on. The engineering solution was to "transform" the base station at the end of pay out, rotating the perch panel out of the way and supporting the force of the tether on the ground-side gimbal (GSG) in high-tension mode for crosswind flight. The GSG allowed angular motion on two axes, and "detwist" rotation around the tether axis, also incorporating the slip rings transmitting electrical power.

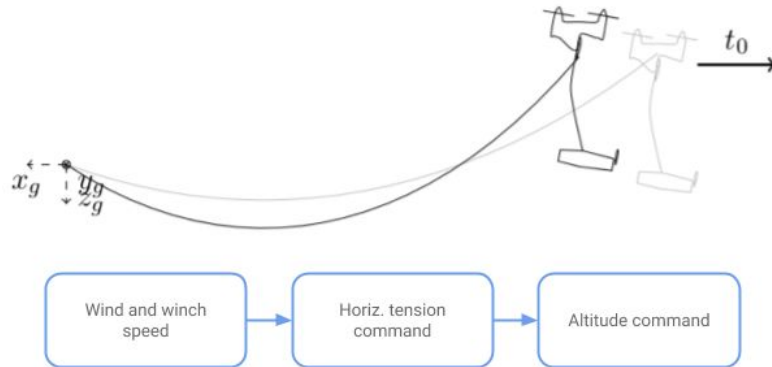
From a controls standpoint, the base station transformation required that the departure angle of the tether be held within a window of about 0-12 degrees above horizontal, which was difficult to do without exciting mechanical modes of the tether and while enduring significant disturbances in gusty wind conditions. Given the tether's linear density (1 kg/m), the horizontal tension, the length that has been payed out, and the desired tether elevation angle ( $6^\circ$ ) we compute the expected location of the kite; it turns out that there's a nice closed-form expression for this. The

### 5.3.3 The Catenary Spring

Modeling the tether as a catenary and the kite as a point mass, the kite sees the catenary as a nonlinear spring. If the kite were to reach the "tether sphere," with the tether extended in a straight line, it would see the tensile elasticity of the tether itself. The tether, its force-carrying members being made of carbon fiber, is extremely stiff. Inside the tether sphere, the compliance of the catenary dominates, and the kite sees a much weaker effective spring constant. This floppy compliance ends up limiting the bandwidth of many of the hover control loops; their gains are scheduled with pay out to allow for higher bandwidth control when nearing the perch.

### HOVER PATH

- Fundamental constraints are to fly downwind and keep the tether off the ground.
- Multiple (tension, altitude) solutions keep tether off ground, but it's always most power efficient to maintain minimum tension and control altitude.
- [Horizontal tension command](#) (rather than measurement) is used to [set elevation command](#) to avoid unwanted feedback.
- Path command is [rate limited](#) to enforce continuity and ensure a feasible path.

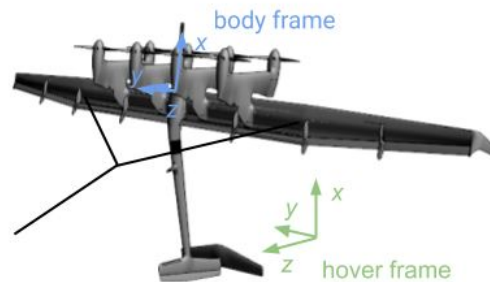


[go/makanics/control/hover/hover\\_path.c](http://go/makanics/control/hover/hover_path.c)

Figure 13: Hover path controller.

### HOVER ATTITUDE

- Slightly modified multi-rotor dynamics linearized about hover state. Uses quasi-static "hover" frame (x up, z towards GS). Mostly ignores airframe aerodynamics.
- [Euler vector representation of attitude error](#).
- Gains limited by [motor bandwidth](#). Chosen with [SISO tools](#) to limit overshoot and meet [phase/gain](#) margins.
- Bridle provides passive roll stability. Also, adds [small coupling](#) between roll and yaw.
- Careful handling of [constrained degrees-of-freedom](#) and [integrators](#) during perching.



**Multi-rotor dynamics**

$$\begin{bmatrix} \mathbf{m} & \mathbf{0} \\ \mathbf{0} & \mathbf{I} \end{bmatrix} \begin{bmatrix} \ddot{\mathbf{x}}_h \\ \ddot{\boldsymbol{\omega}} \end{bmatrix} + \begin{bmatrix} \mathbf{0} \\ \boldsymbol{\omega} \times \mathbf{I} \boldsymbol{\omega} \end{bmatrix} = \begin{bmatrix} TC_b^h \hat{\mathbf{x}}_b + m\hat{\mathbf{g}}_h + \hat{\mathbf{f}}_b^{\text{bridle}} \\ \hat{\boldsymbol{\tau}}_b^{\text{motor}} + \hat{\boldsymbol{\tau}}_b^{\text{bridle}} \end{bmatrix}$$

Motor dynamics:  $T = H_{\text{motor}}(s)T_{\text{cmd}}$

Attitude error:  $q_{b'/b} = q_{b'/h}^{-1} \star q_{b'/h} \Rightarrow \vec{\theta}$

[go/makanics/control/hover/hover\\_angles.c](http://go/makanics/control/hover/hover_angles.c)

Figure 14: Hover attitude controller.

## 5.4 PID in Practice

Before discussing the hover controller's PID controllers, let's briefly compare the idealized PID loop to its more practical implementation. When PID loops are analyzed in a formal setting, they are often literally composed of proportional, integral, and derivative terms, as shown in figure 15. A problem occurs with the derivative term: outside of the formal setting, the exact derivative of an incoming signal is not available. At best, we can compute a first-order difference, which comes with an unavoidable delay of at least one sample, and a magnification of any sensor noise. In a practical implementation, we choose to take the "derivative" signal from a separate sensor, and also take in a separate derivative command, as shown in figure 16. This can cause some confusion when comparing the results of the ideal model from the implemented model. If the velocity command is not the derivative of the position command, the step response of the system will not be as good as in the idealized case. This provides additional motivation for an integrated trajectory generator producing kinematically consistent position and velocity commands (and potentially higher derivatives as needed).

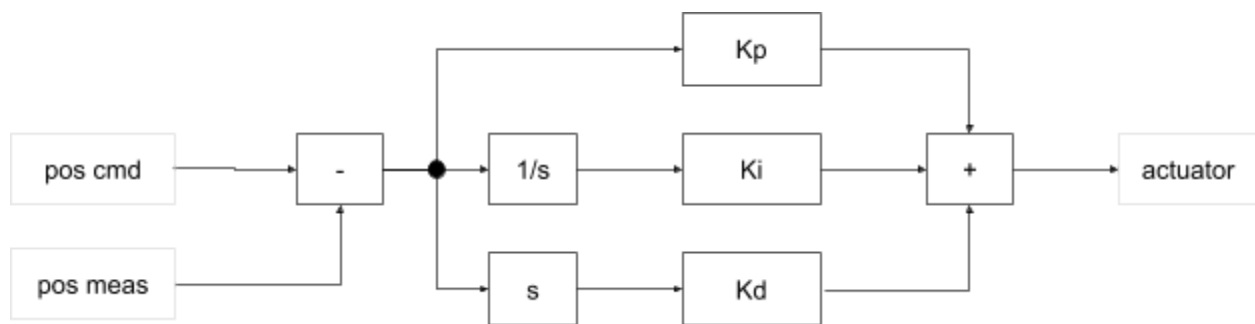


**Figure 15: Idealized PID position controller with explicit derivative.**

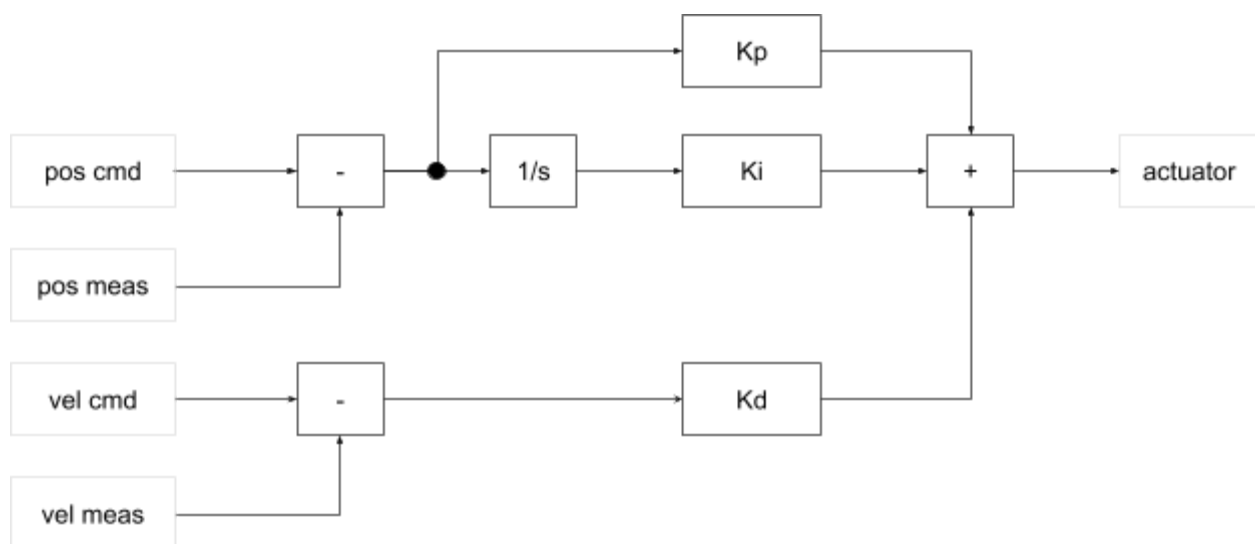


**Figure 16: Practical PID controller with separate position and velocity inputs.**

## 5.5 Hover Position

The hover position controller consists of two PID controllers, one taking the position and velocity error on the kite's y axis (towards the starboard wingtip) and producing a yaw attitude command, and the other taking the position and velocity errors projected onto the z axis (towards the belly) and producing a pitch attitude command. Only the tangential component of the position error relative to the base station is controlled here; altitude is controlled by a separate PID loop, and the radial position error is zeroed. As the radial and tangential dynamics of the system change considerably as a function of pay out (because of the change in the catenary spring constant and the introduction of tether transverse swinging modes), gains are scheduled with altitude and pay out.

Radial position is not directly controlled; rather, there is a pay out command and a tension setpoint. Together these automatically set a radial position. However, at low apparent wind speeds and long tether lengths, the radial position is typically very underdamped, which can cause large overshoots and long settling times if the wing is started from a position far from equilibrium (e.g. after a switch from a piloted mode). To address this, a damping term is added to the radial position loop based on the radial velocity.

## 5.6 Hover Altitude

The hover altitude controller is a simple single-input, single-output (SISO) loop, consisting of a PID controller (with altitude error driving the proportional and integral terms and vertical velocity error driving the D term), ultimately producing a thrust command. In addition to this feedback term, a feedforward term is included that adds the weight of the kite and the weight of the payed out tether.<sup>16</sup> The PID gains of the altitude controller are scheduled with altitude, with significantly lower gain at high altitude.

Anti-windup protection is used in case the motor thrust command is not achieved (and the integrator would otherwise wind up despite the saturated actuator). We use the scheme described by Åstrom and Murray [2]. The difference between the commanded actuation (thrust in this case) and that which is achieved is added into the PID's integrand after applying a tracking gain.

In addition to the standard PID, a double integrator ("boost" term) is switched on during the initial launch, to help achieve the required thrust for liftoff quickly. The "boosted" PID has the form  $(1 + \omega_c \frac{1}{s})(k_p + k_i \frac{1}{s} + k_d s)$  where  $\omega_c$  is the boost's crossover frequency. When the boost

---

<sup>16</sup> This assumes that the tether elevation angle is zero, i.e. the tether departs the base station horizontally, with the catenary vertex at the attachment point. In this case the base station carries no vertical load from the tether. With a positive tether elevation angle, the kite must exert, via the tether, an upwards force on the base station. This effect is ignored for the purpose of computing the feedforward thrust; the integrator is happy to take care of it.

integrator is switched off, its state is added into the integrator in the PID to avoid any transients in the output.

## 5.7 Hover Attitude

The commanded and actual attitudes are subtracted as rotations (in a quaternion representation) and the difference is converted to an axis-angle representation. The angular velocity command and measurement are subtracted as vectors. A PID loop for each axis converts the angle and angular velocity errors around that axis into a moment command around the same axis. The gains corresponding to the roll axis are zero, as we have negligible active control authority around that axis.

## 5.8 The Roll Control Problem and the Bridle

A fundamental aspect of the Makani kite design was the decision to passively stabilize kite roll attitude in hover using a bridled tether rather than any active actuators. The bridle exerts a moment on the kite given by the tension in the tether, the arm from the bridle knot to the kite mass center, and angle of the kite with respect to the tether.

The simplicity of this approach is attractive, but it has been a source of challenge. In several test flights this scheme came near to disaster, and in several others it did fail catastrophically. Either a loss of tension, or too steep an angle between the kite and the tether, would result in a loss of restoring moment—and a corresponding roll excursion. Even when tension was maintained, the roll mode was poorly damped. In these emergencies, we would generally flip to manual pilot control and command a steep pitch-back angle, to restore tension, with varying degrees of success. One problem with this approach from a control perspective is that improving the tether pitch angle by commanding pitch-back is a non-minimum-phase system: it gets worse before it gets better.

These problems might be surmountable via improvements to the control system, but the bridle also turned out to be an annoyance in crosswind, where the roll angle is used to steer the kite. Significantly more bank angle is required at the bottom of the loop—where we need to provide both centripetal acceleration and fight gravity—than at the top of the loop—where gravity helps us turn. This modulated bank angle is always fighting the restoring moment from the bridle, and in crosswind flight the only way to obtain a roll moment is through the use of ailerons. In flight testing we often found ourselves at the limits of aileron authority. This in turn placed a limit on loop radius.

How did we get into this situation? Earlier designs projected a lighter kite mass and thus less bank modulation required to fight gravity; indeed, it was originally explained to me that the bridle would help maintain the trim roll angle in crosswind flight. This turned out to be a fiction.

### 5.8.1 Other Mechanisms for Roll Stabilization

Many alternatives to yaw bridling as a means to stabilize roll in hover were discussed as part of the MX2 project but no convincing alternative was found. With the M600, we tried exploiting the blown lift / thrust vectoring of ailerons<sup>17</sup> A4 and A5 to stabilize roll and using the flat-plate drag of the outer ailerons A1 and A8 to exert a roll moment. Neither method had a detectable effect. Other ideas included using the reaction torque of the rotors as a roll actuator (insufficient authority), canting the rotors slightly, or adding wingtip thrusters (reluctantly due to the increase in complexity, mass, and parts-count).

### 5.8.2 Where It Stands

Roll stabilization of the M600-style kite in hover remains an unsolved problem. Roll bridling does seem like the simplest solution, but in practice it was difficult to maintain the required geometrical discipline for it to be effective. Even in the best of circumstances, with the kite near the ground and at full tether extension,<sup>18</sup> the roll mode was poorly damped and large amplitude, slow frequency oscillations were the norm, potentially excited by the "phantom moments" mentioned below. Perhaps the worst aspect of the roll bridling is its effect in crosswind, where the kite must use full deflection of the ailerons to fight the restoring moment of the bridle in order to roll enough to make the commanded turns. Thus the roll bridling restricted the flyable trajectories in crosswind, contributing to the M600's poor power curve.

## 5.9 Blown Lift and Phantom Moments

The lowest level of the hover controller ultimately commands motor thrust and moments. As we shall see in the next section, moment commands are translated into individual motor thrusts assuming that motors act as ideal thrusters and that the moment imparted is a simple result of the arm from the body origin to the rotor.

Significant departures from this model were observed. Most of these discrepancies could be accommodated by the control system or by adjusting the hard-coded trim attitude, with one exception with catastrophic effects. The observed discrepancies include:

1. The horizontal tension seen in hover is significantly greater than would be explained by the pitch attitude of the kite. Stated the other way around, the pitch attitude required for a given horizontal tension was much further pitch-forward than expected. The integrator in the tension controller is able to compensate for this; and after a flight test we adjusted the trim pitch attitude used as a starting point using the experimentally observed attitude required to attain the desired tension. We hypothesize this may be due to a "blown lift" interaction of propwash being redirected by the main wing.

---

<sup>17</sup> The wingspan was divided evenly into eight "ailerons" labeled A1 through A8 from port to starboard.

<sup>18</sup> For example, when flying from the remote perch (RPX) at China Lake. See "Makani's Flight Testing Approach" [20] for details.

2. A significant "phantom" pitch-back moment of up to about 6000 N·m is observed, inferred by the controller's need to command an equal and opposite pitch-forward moment in hover (again taken care of by an integrator). This manifests as a need to spin the rotors on the top row faster than the rotors on the bottom row. This difference in speeds required for hover could be explained by either one or both of the following effects:
  - a. There is a net positive aerodynamic pitching moment on the kite which the rotors must balance.
  - b. The rotors on the top row are operating in a different local aerodynamic freestream than the bottom row due to the details of the flow around the wing. The top rotors incur a performance penalty as a result.

This asymmetry in the power demand of the top and bottom rows of motors necessary to maintain attitude significantly eats into the total thrust available to hover: if the top rotors are already at maximum, then any margin in the lower motors is unusable without upsetting the moment balance.

Finally:

3. In some cases a large phantom *roll* moment was observed. Here we can rely only on the bridle to resolve the moment. If tether tension or geometry is such that the bridle provides inadequate restoring moment, the roll attitude can diverge. This may have contributed to the crash following the offshore flight. This unintended roll moment may be caused by differential thrust intended to produce a yaw moment creating a roll moment through blown lift. The environmental wind may also play a role here, with a sidewind causing the propwash to create more blown lift on one side of the airframe than the other.

Interaction between propwash and the tail (elevator and rudder) was also a subject of much investigation. The effects tend to be difficult to model (and the models difficult to verify) due to the many possible flight conditions.

In addition to these blown lift effects, another deviation from the idealized model is the effect of edgewise flow on the rotors. The component of the wind in the plane of the rotor discs, which is significant in hover, creates additional forces and moments that are not modeled by the motor solver.

The residual unexplained pitch moment observed in hover is depicted in figure 17.

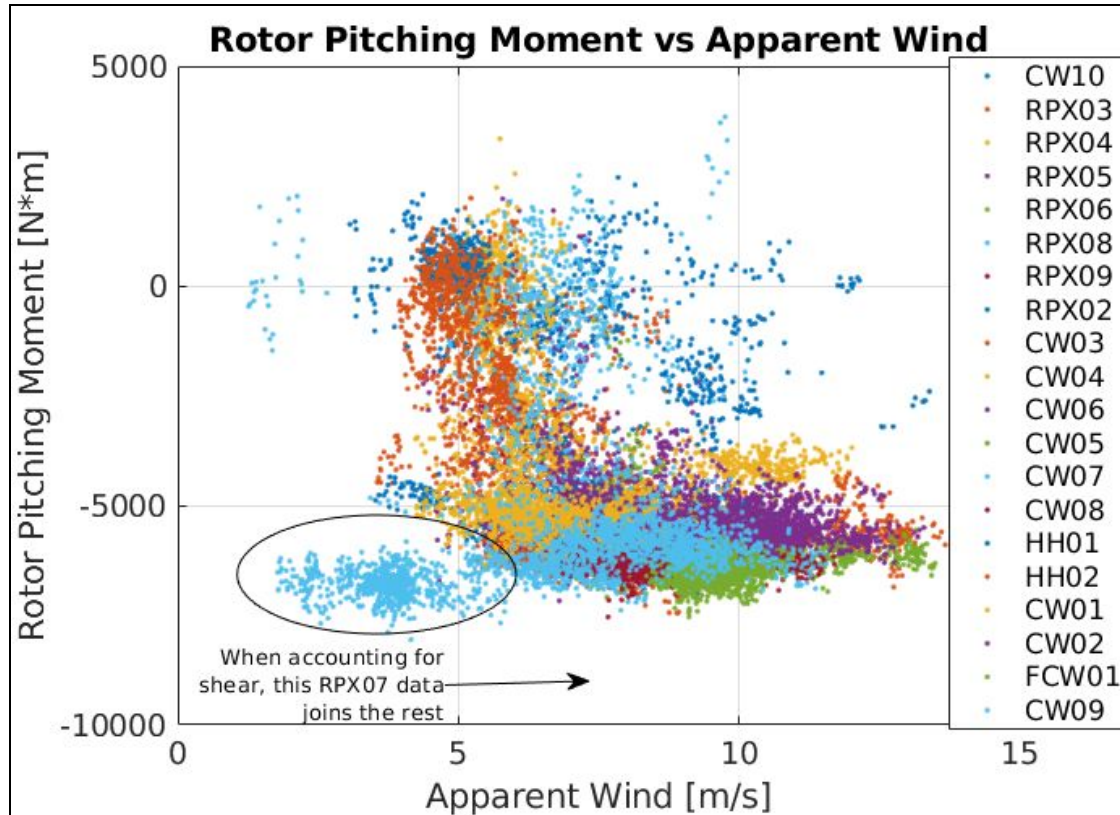


Figure 17: Unexplained moment seen during hover, as a function of wind speed.

## 5.10 Future Improvements and Other Notes

**Improved trajectory generator.** The current trajectory generator is very primitive. To generate a smooth trajectory from one waypoint to another, we simply rate-limit the change in the position command, take the derivative to get a raw velocity command, and then rate limit the velocity command to achieve an acceleration limit. A simple improvement to the hover controller would be to implement a real jerk-limited trajectory generator that would simultaneously produce consistent position, velocity, and acceleration commands, taking the kite from one boundary condition to the next. This has become a theme of this account: commands should be feasible, smooth, and consistent, with as many derivatives provided as needed.

**A more passive approach?** The hover controller described above goes to great effort to achieve through active means the behavior of a passive system, for example calculating the altitude at which the kite should fly to achieve a particular tension in a particular wind condition, etc. Instead, we could embrace a passive approach to position control during pay out and reel-in, simply commanding a feedforward thrust and pitch attitude rather than full closed-loop position control. A helium balloon in the wind does not need an active controller to know at what altitude to fly.

**Closed-loop velocity control.** The current controller closes a loop around a position error signal, commanding acceleration (via kite attitude). Alternatively it may be advantageous to instead, or additionally, close a loop around kite velocity, perhaps in some flight regimes but not others.

**Roll control.** The current system was designed to achieve roll stability during hover via the use of a horizontal bridle. This in turn requires that the system maintain adequate horizontal tension at all times and a suitable bridle geometry. This has proved difficult and divergence of roll attitude has led to loss of vehicle on at least one occasion. It is not obvious how to improve this situation.

**Dedicated transition-out controller.** Currently transition-out is divided into a “prep-trans-out” mode of the crosswind controller and a “trans-out” mode in the hover controller. At some point the trans-out mode of the hover controller simply turns on and attempts to exert position and attitude control of the kite, while the kite may have significant upward velocity and rotation rates. Here we encounter two conflicting engineering constraints: we wish to stop the kite's motion quickly, before the kite climbs to an unacceptably high altitude, but decelerating too aggressively throws the bridle forward, potentially impacting the pylons. Instead of this hacked-together approach, we envision using optimal control techniques to solve for a transition-out trajectory taking the kite from its initial condition in crosswind to a hover state.

**Limit cycles.** We impose numerous rate-limits and saturations. These nonlinearities can lead to limit cycle oscillations, which, without a detailed mathematical model of the controller, are difficult to predict. A test suite consisting of an ensemble of disturbances across the phase space of each controller might be an effective way to automatically discover limit cycles lurking in the system behavior. In practice we have discovered these phenomena in simulation and mitigated them by removing nonlinearities or adjusting saturation thresholds. We learned this lesson: resist the temptation to litter the system with nonlinearities, as it is typically better for a system to briefly exceed a soft limit than to hit a hard one.

## 6 Actuation Allocation: The Motor Mixer

The crosswind, hover, and transition-in flight controllers all ultimately produce motor commands in the form of a total thrust command (generally positive in hover and negative in crosswind), and commanded moments (torques) around the body axes. Together we will call this the "thrust-moment" command and designate it  $u_{hover}$  (although it is applicable in all flight modes):

$$u_{hover} = [T, \tau_x, \tau_y, \tau_z] \quad [9]$$

The "motor solver" (or motor mixer, see figure 18) converts the thrust-moment command into individual thrust commands for each of the eight rotors.

We begin by writing a linear relationship between the vector of individual motor thrusts  $u_{thrusts}$  and the thrust-moment command  $u_{hover}$ :

$$u_{hover} = A_{hover}^{thrusts} u_{thrusts} \quad [10]$$

where the matrix  $A_{hover}^{thrusts}$  is easy to write down based on the placement of the motors and their directions of thrust. In general,  $A_{hover}^{thrusts}$  is not square and not invertible. For our application, this equation is under-determined; there is a subspace of solutions  $u_{thrusts}$  that produce the wanted  $u_{hover}$ . To solve the equation in an unconstrained least-squares sense, one could use the pseudoinverse. Because we have important constraints, we use a constraint least-squares solver. This is closely related to quadratic programming, for which fast solvers exist.

Not every element of the thrust-moment command is of equal importance. Generally we wish to prioritize meeting the moment commands over meeting the thrust command. We can turn this into a weighted least-squares problem by applying a diagonal weighting matrix  $W$ :

$$W(u_{hover} - A_{hover}^{thrusts} u_{thrusts}) = 0 \quad [11]$$

*to be solved in the least-squares sense*

To guide the solver towards a unique solution, we further apply regularization conditions: we wish, all else being equal, to find the solution that minimizes the sum of the squares of the individual thrusts. To do this, we augment the matrix  $A_{hover}^{thrusts}$  with an 8x8 identity matrix, such that, when acting on a column vector of motor thrusts, it will produce a 12-element column vector containing the resulting thrust and moment, in addition to passing-through the individual motor thrusts. We then also augment  $u_{hover}$  with a zero for each individual motor thrust that is

passed through. Finally, we apply a very small weight in  $W$  to these pass-through elements, typically 1/1000 the weight of the thrust command.

Through this regularization condition we avoid chattering in the solution. Furthermore, we can use the pass-through elements to apply constraints on the individual motor thrusts.

We can also add rows to the matrix to penalize other combinations of actuation. We use this to penalize a particular actuation pattern that interacts with a symmetric torsional mode of the airframe.

## 6.1 Stacking

For reasons of power transmission (minimizing the mass for a given resistive loss) and aerodynamics (reducing tether drag by minimizing its diameter), a high operating voltage is preferred for the tether, yet the motors require a lower voltage. The solution we developed is a "stacked" topology, in which the eight motors are grouped into four parallel pairs. These four pairs are wired in series, so that each motor sees only a quarter of the full tether voltage (assuming voltages are balanced across the stack).

From the point of view of the flight controller, the consequence of stacking is that we cannot command each motor thrust individually. The degrees of freedom in the stacked system are the common-mode (total) thrust, and four differential thrusts. This can be readily accommodated in the scheme described above by multiplying  $A_{hover}^{thrusts}$  by another matrix  $A_{thrusts}^{stacking}$  to solve the problem in the stacked basis.

If an individual motor fails, the system responds by shorting out that entire "layer" of the stack, which removes both the failed motor and its diagonally opposite partner from the system. The software system can automatically accommodate this "short stack" situation by using the matrices appropriate to the new configuration.

## 6.2 Roll Actuation

In addition to producing thrust, each rotor also produces a reaction torque. With a suitable choice of rotor spin directions, independent control of roll moment can be achieved. This was indeed supported by the motor solver, but we never successfully made use of the feature. It was generally believed that the available roll moment authority was too small to be useful.

## 6.3 Combining Flaps and Rotors

In crosswind flight, where both the motors and the control surfaces (ailerons, elevator, and rudder) can be used to generate pitch, roll, and yaw moments, they should be used in concert to achieve the desired effect. For example, if the ailerons are reaching saturation, motor turning

should be employed. In the existing crosswind controller, the fraction of control authority demanded of the rotors, as compared to the flaps, is fixed. As a future improvement, it was planned to integrate the flaps-solver with the motor-solver to attain the best usage of all actuators in concert. For example, if more thrust or generation (as needed) could be obtained from the motors at the cost of some adverse moment that could be compensated for by the control surfaces, this could be a win that would be realized by such a combined motors-and-flaps solver. As-is, the system may not be pareto-optimal.

### MOTOR SOLVER

Hover command:	$\mathbf{u}_{\text{hover}} = [T, m_x, m_y, m_z]^T$
Naive eight degrees of freedom:	$\mathbf{u}_{\text{thrusters}} = [T_1, T_2, T_3, T_4, T_5, T_6, T_7, T_8]^T$
Stacked power topology imposes:	$\mathbf{u}_{\text{stacking}} = [T_c, \Delta T_{15}, \Delta T_{26}, \Delta T_{37}, \Delta T_{48}]^T$
Motors have <a href="#">torque constraints</a> *:	$0 \leq T_i \leq T_{\text{max}}^{(\text{static})}$
System has overall <a href="#">power constraint</a> *:	$\sum_i k_P \left(\frac{T_i}{k_T}\right)^{3/2} \leq P_{\text{max}}$
<a href="#">Constrained least squares problem</a> :	$\min_{\mathbf{u}_{\text{stacking}}} \ \mathbf{W}(\mathbf{A}\mathbf{u}_{\text{stacking}} - \mathbf{b})\ ^2$ $\mathbf{l} \leq \mathbf{C}\mathbf{u}_{\text{stacking}} \leq \mathbf{u}$

\* Torque and power constraints are expressed as thrust constraints about an operating point.

[motor solver document](#)  
[go/makanics/control/actuator\\_util.c](#)  
[go/makanics/common/c\\_math/optim.h](#)

**Figure 18: Elements of the “motor solver” algorithm that converts the thrust-moment command into individual thrust commands for each of the eight rotors.**

## 6.4 Simplified Rotor Model

A simplified rotor aerodynamic model is used to convert the various torque, power, and speed constraints into thrust constraints that can be used in the constrained least squares solver. It is also used to convert the output thrust commands of the solver to motor speed commands.

This aerodynamic model is initially based on XROTOR, which is used to generate a lookup table of rotor thrusts and torques as a function of rotor speed  $\Omega$  and inflow velocity,  $V_\infty$ . However, this lookup table is not used directly in the autopilot because it has a large number of parameters and would be difficult to invert, i.e. determine the rotor speed that corresponds to a given thrust or torque at a given inflow velocity. Instead, a simplified rotor model is created by fitting a third order polynomial to thrust and torque coefficients as a function of advance ratio,  $J = 2\pi V_\infty / (\Omega D)$ . The simplified models are:

$$k_T(J) \approx a_1 \Delta J + a_2 \Delta J^2 + a_3 \Delta J^3 \quad [12]$$

$$\text{and } k_\tau(J) \approx b_1 \Delta J + b_2 \Delta J^2 + b_3 \Delta J^3 \quad [13]$$

$$\text{with } \Delta J = J - J_{neutral} \quad [14]$$

where the motor thrust and torque coefficients are defined by:

$$T = \rho \left( \frac{\Omega}{2\pi} \right)^2 D^4 k_T(J) \quad [15]$$

$$\text{and } \tau = \rho \left( \frac{\Omega}{2\pi} \right)^2 D^5 k_\tau(J) \quad [16]$$

The equations for thrust and torque using the polynomial fits can now be inverted using a Newton-Raphson method<sup>19</sup>. This iteratively finds the zero of the following equation:

$$f(\Omega) = T - \rho \frac{D^4}{(2\pi)^2} k_T(J) \Omega^2 \quad [17]$$

---

<sup>19</sup> See `master/control/simple_aero.c` [18] for the implementation. Amusingly, during an audit of the controller's runtime in September 2017 it was found that repeatedly computing `pow(D, 4.0)` was one of the single highest uses of CPU time; the `pow` function should be avoided for fixed exponents, in favor of forms like `D*D*D*D` or repeated squaring. The code was changed to use a precalculated fourth power of rotor diameter.

where the iteration step is

$$\Omega_{n+1} = \Omega_n - f(\Omega_n) / f'(\Omega_n) \quad [18]$$

and

$$f'(\Omega) = \varrho \frac{D^4}{(2\pi)^2} ((3a_3 \Delta J^2 + 2a_2 \Delta J + a_1) J - 2 k_T(J)) \Omega \quad [19]$$

## 7 Other Flight Modes

### 7.1 Transition-In

After the tether is fully payed out, the system transitions from hover to crosswind flight by accelerating upwards and pitching forward slightly (as necessary) to achieve attached flow over the wing and begin flying like an airplane rather than an octocopter. We call this "transition-in," or simply trans-in. The opposite maneuver, transition-out, is dealt with separately.

During trans-in the tether is slack, and the vehicle is in airplane-like flight. MIMO state-feedback is used to control the vehicle to a straight-line trajectory along a chord in the tether sphere until tension returns and the crosswind controller takes over.

Before the first flight, transition-in and transition-out were seen as the riskiest flight regimes, due to the uncertain aerodynamics, with perhaps a bit more attention dedicated to the former, its success being a prerequisite to the sought-after crosswind flight data. Despite (or perhaps because of) this concern, trans-in turned out to be the single most robust flight mode. It worked every time. The engineer responsible for this flight controller left the company before the first test flight, but it turned out that we never needed to make a single change to his code.

The development of the trans-in gains proceeds in the same way as the crosswind and off-tether controllers: a Python program (`analysis/control/trans_in.py`) constructs a nonlinear model of the system, uses a solver to find a trim state, linearizes around that state, and generates gains. As in crosswind, the system is partitioned into lateral and longitudinal parts. For the longitudinal part, LQR is used to calculate gains. For the lateral part, an optimal linear controller is found while enforcing sparsity constraints on the gain matrix.

## TRANSITION OVERVIEW

- Hover controller begins transition by **accelerating vertically**.
- Wing pitches into the wind and briefly flies with the tether slack.
- Pitch forward sooner in high winds, later in low winds (min. speed and altitude required).
- Follow a fixed climb angle trajectory until sufficient speed builds up.
- As speed increases, lift exceeds weight and the tether tension returns.
- Transition frame defined around fixed climb angle trajectory.

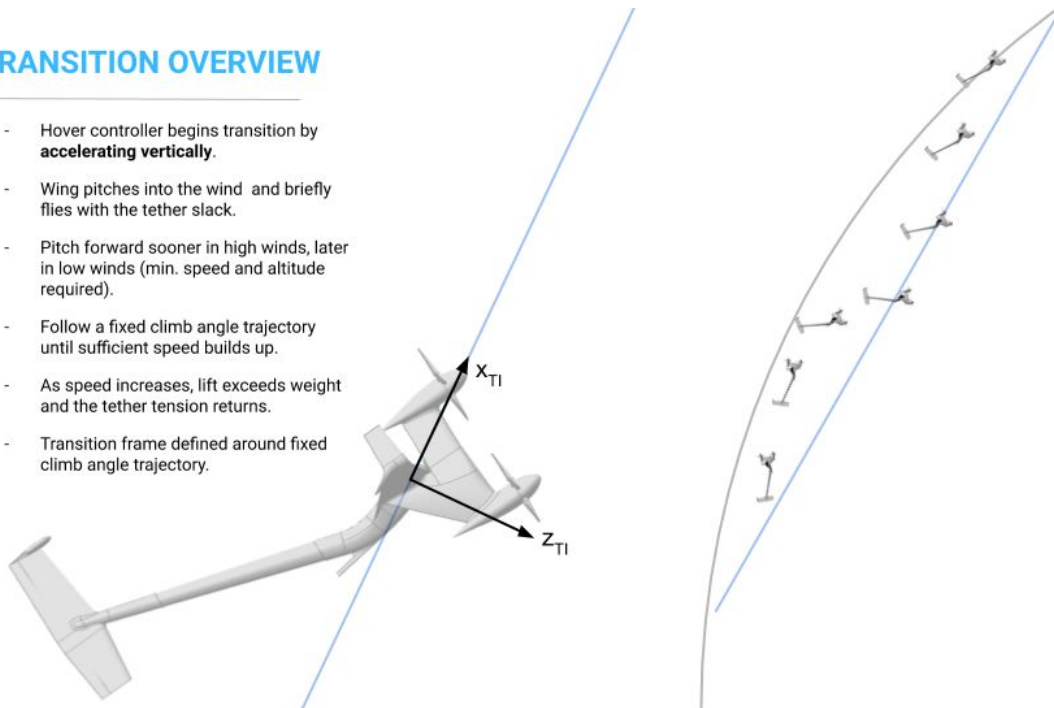


**Figure 19: The kite transitions out of hover flight by accelerating vertically, pitching forward, and briefly flying with the tether slack. As speed builds, the tether tension returns and the kite enters crosswind flight.**

## 7.3 Transition-Out

While a dedicated controller was utilized for transition-in, transition-out was accomplished by using special sub-modes of the crosswind and hover controllers. First, the crosswind controller would switch to a mode called "crosswind-prep-trans-out." When conditions were met, the hover controller was suddenly switched on, in a special mode called "hover-trans-out," in which it would try to arrest the vertical velocity of the kite and stabilize the attitude.

Primary goals for transition-out include:

- Stop the kite's forward motion.
- Bring the kite's attitude to the hover orientation.

With the following restrictions:

- Avoid an excessive power transient at the transition from "braking" to hover.
- Avoid gaining excessive altitude (in order to preserve roll stability via the bridle).
- Avoid losing tension (ditto).
- Avoid exciting tether dynamics.
- Avoid decelerating so fast that the bridle gets ahead of the kite and strikes the pylons.

One is tempted to apply aggressive deceleration at the bottom of the loop; however, aerodynamic lift is required to make the final quarter loop. After the last round of hand-optimizing trans-out to lower the final altitude, we found that the continued inertial motion of the tether could cause it to strike the pylons. A trans-out that results in poor kite placement (too high or too far in) can result in divergence of the roll attitude, as demonstrated catastrophically at the end of the offshore flight.

Because transition-out is subject to (1) well defined boundary conditions and (2) many competing design trade-offs, it might be well-suited to numerical trajectory optimization. Were Makani to continue operations, development of a dedicated trans-out controller would likely be a high priority.

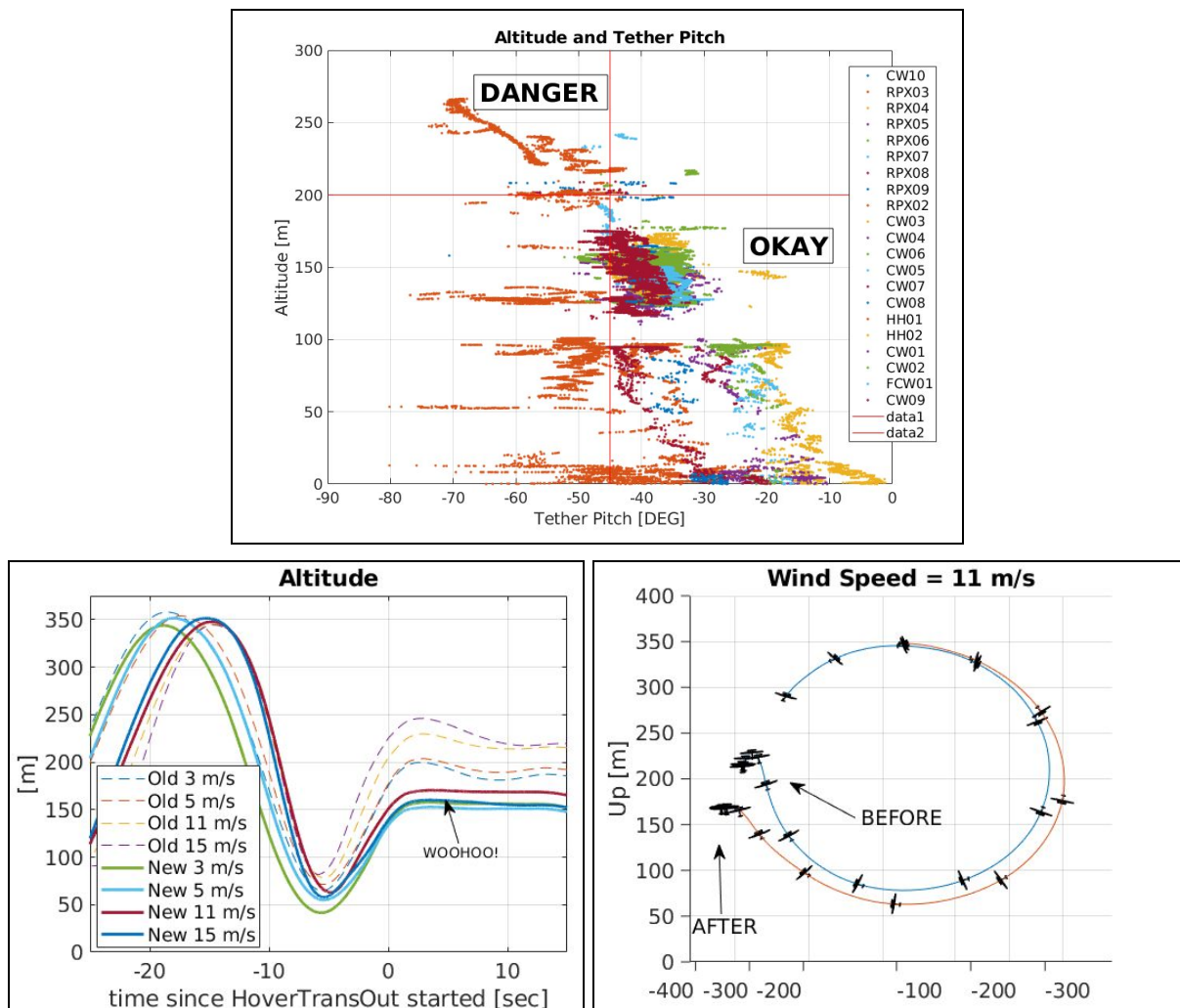


**Figure 20: (Above) Trans-out geometries across the M600 flight test campaign. High altitude, high tether pitch conditions yield poor roll stability. (Below) Modifications to the trans-out trajectories made after the summer 2019 offshore flights, to attain lower trans-out altitude.**

## 7.4 Off-Tether

As an installed product, the M600 was intended to operate autonomously, launching and landing as necessary. For flight testing, however, the kite was outfitted with the ability to release the tether and fly like a glider as a way of rescuing the airframe after abnormal flight termination from crosswind. The flight controller contained a manual "off tether" flight mode to accommodate this, with conventional joystick controls, augmented by a simple attitude controller colloquially called "wing save." Because this flight mode would only be invoked after failure of the primary autopilot, required sensors were kept to a minimum; in particular, the off-tether flight controller made no use of the pitot-static system, although airspeed and angle of attack were displayed to the human pilot to be used if the values were deemed reliable.

While the earlier prototype, Wing 7, could be—and often was—landed nondestructively in this manner, for the M600 an off-tether glide landing typically involved sacrifice of the wing pylons and lower row of motors and rotors, due to the lack of all but *pro forma* landing gear.

The motors are configured to let the rotors windmill freely, a minimum-drag configuration. There was also a concern about presenting a high voltage on the tether, which may be dragging on the ground, creating a potential fire hazard.

### 7.4.1 Pilot Inputs

In off-tether flight, the kite is flown by a human pilot using a joystick. Several aides are available to the pilot to help them land the kite successfully:

- The pilot can see the kite through the window in the command center.
- A video camera mounted to the nose of the M600 provides "first person view" (FPV). This camera is only activated after tether release, as its RF link was found to interfere with the GPS receivers on the kite.
- Other flight testing engineers in the command center can read data to the pilot as necessary, including altitude, angle of attack, angle of sideslip, and speed. The pilot can also glance at a computer monitor to see these values.

The flight controls are standard, with one stick axis directly controlling the elevator, another the rudder, and another the ailerons.

### 7.4.2 Wing Save

The "wing save" stability augmentation was very effective and useful in rapidly attaining a flight attitude suitable for glide, which was especially useful as crosswind flight typically leaves the kite in what all but aerobatic pilots would regard as an "unusual attitude." Wing save controlled for a trim pitch attitude intended to correspond to minimum sink in no wind.

The wing save controller is very simple. First, the kite attitude is converted from its standard representation as a DCM matrix into Euler angles:<sup>20</sup> roll, pitch, and heading. Next, pitch and roll commands (which are fixed, constant values) are subtracted, producing pitch error and roll error. The heading is not used. PID loops are applied to pitch error and roll error, with the body frame pitch-rate and roll-rates, as measured by gyros, used as the derivative term, and the outputs are fed to the elevator and aileron, respectively. The integral gains are zero. There is also a gain on yaw rate with the output fed to the rudder. These aileron, elevator, and rudder control signals are summed with those commanded by the pilot via the joystick when wing save is active.

---

<sup>20</sup> This is one of the few uses of Euler angles in the flight controller.

## 8 Estimator

The M600 flight controllers take as inputs estimates of various state variables: standard ones like the position of the kite, its velocity and the apparent wind, its attitude and rotation rates, and also more application-specific variables such as the force vector of the tether acting on the kite and the angle of the tether departing the base station. In the offshore scenario we also estimate the position, attitude, and rates of the ocean buoy.

In the do-it-yourself spirit of Makani, the estimator was developed in-house, rather than using any off-the-shelf aircraft AHRS system, as part of the same C-language codebase as the controller itself. One motivation for this was that our estimator would take as inputs many additional sensors beyond the standard complement. Additionally, off-the-shelf AHRS systems typically assume that flight is on average unaccelerated, using the accelerometer to measure gravity to get a sense of "down," which would not work in a system whose primary flight trajectory is a continuous aerobatic loop. Finally—what GNC engineer could resist implementing their own state estimator from scratch?

The output of the estimator, the "state estimate," with all quantities in SI units, provided the primary interface to the flight controllers. The estimator was planned to support many redundant means of estimation to allow for robustness in the presence of sensor failure, for example using the direction the tether departs the base station to estimate the position of the kite in the event of loss of GPS.

### 8.1 Kite Rigid Body State

The attitude and position estimators are separate, with the position estimator dependent on the results of the attitude estimator. (A tightly-bound estimator, estimating position and attitude simultaneously, was envisioned—even prototyped—but never flight tested, in part due to being gun-shy about flight testing a radical change to a system that worked well enough. We believe this would provide better observability of attitude without requiring wingtip GPS antennas.)

The M600 includes three identical redundant "flight computers," each with its own inertial measurement unit containing an accelerometer, gyro, and magnetometer. An independent attitude estimate is produced for each flight computer, and the resulting independent attitude estimates are combined by taking the median of the resulting quaternion components.

The attitude estimator consumes as an input a vector estimated simultaneously in both the body frame of the kite and the ambient inertial coordinate system. In the hover flight mode, where acceleration was small, the accelerometer is used to provide a plumb-bob gravity measurement. The gravity vector and the magnetic field vector together fully determine the attitude. (The World Magnetic Model is used to calculate the expected magnetic field vector in earth-fixed coordinates.) Some attitude error was observed when perching, which was attributed

Sensors on Board the M600	
GPS	4× NovAtel OEM617D (2 nose + 2 wingtips)
Accelerometer	3× Analog Devices ADIS16488
Gyro	
Magnetometer	
Air data probe	Aeroprobe 5-port pitot probe, with each channel plumbed in parallel to two differential pressure transducers (one low-range, one high-range).
Loadcells (to measure tether tension vector)	2× two-axis loadcells, located at the bridle hardpoints.
Sensors on the Base Station	
GPS	1× NovAtel OEM617D with dual antennas. Used as a GPS compass and RTK base station.
Accelerometer	1× Analog Devices ADIS16488
Gyro	
Wind sensor	Gill Instruments WindMaster 3-axis ultrasonic anemometer
Weather station	

**Table 5: Selected sensors in the M600 system.**

to the influence of ferrous materials in the base station or remote perch. The influence of magnetic fields from tether and motor currents was also seen in the magnetometers, although this was never seen to pose a real problem, perhaps because of relatively low gain on the magnetometer corrections in the Kalman filter. (A long-standing to-do item was to identify this influence and build in a feedforward path to remove it.) The attitude estimate was stored as a quaternion and communicated to the flight controller as a direction cosine matrix (DCM).

GPS antennas were installed on the wingtips to provide both position and attitude corrections. The wingtip antennas are installed on the top surface of the wing, looking in the dorsal direction, and thus were able to maintain continuous sky view during crosswind loops. (By comparison the two antennas mounted on the nose would often lose signal for part of every loop.) In addition to providing position solutions, these widely-spaced antennas allowed for attitude

corrections. Each of three baselines (nose to each wingtip, and wingtip to wingtip) provided a known vector in the body frame and a measured vector in the ECEF frame. The overall effect over a complete crosswind loop was to provide complete observability of the kite attitude through these corrections.

GPS was operated in RTK (real-time kinematics) mode, which is a form of differential GPS that also takes into account the carrier phase, allowing for centimeter-precision relative positioning between a base-station and "rovers." A GPS receiver on the base station was used as a base station and RTK corrections were transmitted to the kite over the avionics network. On land, the GPS base station could be treated as a fixed point; offshore, the GPS base station was run in "moving base station" mode. Differential GPS can use a cascading sequence of reference stations. After the flight in Norway, we considered adding an additional, remote GPS base station on land to provide an absolute reference.

### 8.1.1 GPS woes

GPS is miraculous. With a local base station for differential corrections, position can routinely be measured to within a few centimeters. With multiple antennas mounted to a rigid body, attitude can be measured too; a "GPS compass" consisting of two antennas, mounted about 2.5 meters apart, was used to measure the heading of the base station. That using a constellation of orbiting satellites to measure the heading of the base station turned out to be competitive in reliability, simplicity, and cost with using a mechanical encoder is astounding. Such is the miracle of GPS.

The miracle of GPS came with many headaches, some existential. In particular, we learned repeatedly that GPS receivers tend to behave badly when the antenna is given a compromised sky view. This was worst when the kite was on the perch, as the kite's slightly pitched-back perch orientation angled the primary GPS receivers slightly below the horizon. Sky-view during crosswind flight was also a concern, as the antennae on the nose would lose sight of the sky for about half of each crosswind loop. Inertial sensors would be relied upon to provide updates to the Kalman filter during GPS outages. To avoid having to freely integrate for more than a few seconds, the wingtip GPS receivers were added, providing continuous GPS availability during most flights.

The experience with GPS<sup>21</sup> is that it works spectacularly well most of the time, but fails often enough or badly enough to require augmentation. It was a regular feature of nearly every flight test to find that the two co-located nose GPS receivers (with antennas pointing in slightly different directions) would disagree by a few meters, leading to a concern that the kite would be navigated into a collision with the base station were the system to switch from using one receiver to the other. This situation usually resolved itself once the kite was a few meters away from the perch panels. Presumably some issue of signal reflection or carrier phase ambiguity was at play here.

---

<sup>21</sup> Our receivers were configured to use not just GPS but also GLONASS signals. It made little difference.

GPS Problem	Symptom
Carrier phase ambiguity	Independent GPS receivers would disagree by a few meters while reporting solution covariance of a few centimeters. Especially prevalent when GPS receivers have limited sky view or a nearby obstacle.
Jumps in solution	The solution from a GPS receiver would suddenly change by several meters, presumably due to some change in sky view or other factor suddenly preferring a new solution.
Multipath	Large errors while operating over the glassy surface of the saltwater fjord at Gismarvik, Norway. Fortunately this effect was no longer observed after towing out to the North Sea, perhaps due to the water surface no longer being a near-perfect plane.
Divergent solution	In at least one incidence (with the kite on the ground and the associated GPS antenna being pointed slightly below the horizon) a GPS receiver solution diverged by many kilometers without reporting an error.

**Table 6: Overview of GPS issues observed during flight testing.**

#### 8.1.1.1 GPS Alternatives

Given our experience of troubles using GPS for position estimation near the perch, and the desire to have a redundant estimation scheme immune to radio frequency jamming, several other position measurement schemes were under development.

##### Ground Line-Angle Sensing (GLAS)

The direction at which the tether departs its termination at the base station is measured at the ground-side gimbal (GSG). By employing a suitable model, the kite's position can be estimated. For a crude estimate, the tether is assumed to be a straight line at its reference length, an approximation which may be adequate in high-tension crosswind flight. In practice, corrections for the tether catenary, aerodynamic drag, and tether dynamics (transverse waves) must be considered. While Wing 7 flew a demonstration flight using GLAS for position estimation, maintenance of the GLAS estimator was deprioritized during the M600 program. As GLAS uses only sensors that are already present, abundant data for training or validation is in-hand.

##### Ultrawideband Ranging (UWB)

As of the time of writing, several small and inexpensive radio devices have come onto the market that permit the measurement of the distance between pairs of devices using radio ranging. Some even permit measurement of angles using MIMO antennas. Sprinkling a

collection of these transceivers onto the kite and onto the base station, and using the collection of measured ranges (potentially  $M \times N$  of them) to estimate the kite position and attitude relative to the perch, could be an option for kite position sensing. An appealing property of this scenario is that accuracy is best when and where it is needed most: when the kite is near the perch.

### Light Sequence Decoding (LSD)

Another proposed position sensing scheme utilizes computer vision. The two wingtip and two tail strobe lights (both visible and infrared) on the kite were programmed to emit distinct high-speed sequences, allowing each light to be individually identified. The strobes can then be observed by a camera mounted on the base station and fed into a kite position and attitude estimator. One concern is whether this scheme would remain effective in the presence of low clouds or fog.

## 8.2 Other Estimated Quantities

### 8.2.1 Apparent Wind

#### 8.2.1.1 Five-Port Pitot Probe

The primary sensor for the apparent wind vector in crosswind flight is a five-port pitot tube from AeroProbe. This probe has five ports on its tip: one in the center, a pair displaced vertically, and a pair displaced to either side horizontally. The horizontal pair is sensitive to angle of sideslip, and the vertical pair is sensitive to angle of attack. There is also a static port.

One complication of the air data probe is that its measurement is affected by the wing and rotors aft of the probe. This was corrected using an empirical fudge factor.

#### Alternatives to the Five-Port Pitot Probe

While the 5-port pitot probe served us well during flight testing of the M600, there was concern that such a probe would be insufficiently robust for an unattended installation. Prior to every test flight, each port of the probe was carefully tested through manual application of pressure using a syringe and manometer. At sea in Norway and in the mists of the Big Island of Hawaii, water ingress was a significant concern, and the probe was kept covered until just before flight.

As an alternative to the 5-port probe, we planned to install a conventional single-port pitot probe accompanied by vanes (which were seen as more robust) to measure the angles of attack and of sideslip. These aerodynamic angles could also be estimated using estimates of the kite attitude and velocity and the wind speed and direction, although it is unclear whether this would be sufficiently accurate to fly robustly. The kite is often flown close to stall, making angle of attack a particularly important quantity.

### 8.2.1.2 Complementary Filter

When flying in gusty conditions, the measured angles of attack and sideslip can change very quickly. It is undesirable (probably impossible) to track these fast changes via feedback control. To attempt to do so would require large, fast control surface deflections and result in erratic motion of the kite. One way to avoid this would be simply to detune the airspeed, angle of attack, and angle of slideslip control loops. However, because our machine requires constantly changing control inputs to track these control variables even in non-turbulent conditions, we chose instead to implement a complementary filter that produces an estimate of the apparent wind vector by combining both measurements from the air data probe (at low frequencies) and measurements of inertial motion (at high frequencies).

A complementary filter typically begins with two estimates of the same quantity, derived from different sources. A low-pass filter  $L(s)$  is applied to one estimate, and a high-pass filter  $H(s)$  is applied to the other, where these filters sum to unity:  $L(s) + H(s) = 1$ .

A first-order complementary filter has  $L(s) = \omega_c / (s + \omega_c)$  and  $H(s) = s / (s + \omega_c)$ , where  $\omega_c$  is the crossover frequency.<sup>22</sup> In our case, it's easy to compute the derivative of the apparent wind vector directly, which takes care of the  $s$  in the numerator of  $H(s)$ . Our complementary filter takes the form:

$$\mathbf{v}_{k/a} = L(s) \mathbf{v}_{k/a}^{(1)} + H(s) \mathbf{v}_{k/a}^{(2)} \quad [20]$$

where  $\mathbf{v}_{k/a}^{(1)}$  and  $\mathbf{v}_{k/a}^{(2)}$  are estimates of velocity of the kite body (b) with respect to the air (a), i.e. the apparent wind vector. The first is derived from the pitot probe in the usual way. For the second, it will turn out that we need only its derivative, obtained from inertial sensors:

$$\mathbf{v}_{k/a} = \frac{\omega_c}{s + \omega_c} \mathbf{v}_{k/a}^{(1)} + \frac{1}{s + \omega_c} \frac{b d}{dt} \mathbf{v}_{k/a}^{(2)} \quad [21]$$

To find  $\frac{b d}{dt} \mathbf{v}_{k/a}^{(2)}$ , we start with a statement that the velocity vector of the kite with respect to the air  $\mathbf{v}_{k/a}$  is the difference between the velocity of the kite with respect to the ground  $\mathbf{v}_{k/g}$  and the velocity of the air with respect to the ground  $\mathbf{v}_{a/g}$  and then take a derivative with respect to the body frame:

$$\mathbf{v}_{k/a} = \mathbf{v}_{k/g} - \mathbf{v}_{a/g} \quad [22]$$

---

<sup>22</sup> Not to be confused with the angular velocity vector!

$${}^b \frac{d}{dt} \mathbf{v}_{k/a} = {}^b \frac{d}{dt} \mathbf{v}_{k/g} - {}^b \frac{d}{dt} \mathbf{v}_{a/g} \quad [23]$$

Use the transport theorem<sup>23</sup> to re-write the derivatives on the right side in the ground frame:

$${}^b \frac{d}{dt} \mathbf{v}_{k/a} = {}^g \frac{d}{dt} \mathbf{v}_{k/g} + \boldsymbol{\omega}_{g/b} \times \mathbf{v}_{k/g} - {}^g \frac{d}{dt} \mathbf{v}_{a/g} - \boldsymbol{\omega}_{g/b} \times \mathbf{v}_{a/g} \quad [24]$$

$${}^b \frac{d}{dt} \mathbf{v}_{k/a} = \mathbf{a}_{k/g} + \boldsymbol{\omega}_{g/b} \times (\mathbf{v}_{k/g} - \mathbf{v}_{a/g}) - {}^g \frac{d}{dt} \mathbf{v}_{a/g} \quad [25]$$

Here the acceleration  $\mathbf{a}_{k/g}$  and angular velocity  $\boldsymbol{\omega}_{k/g}$  of the kite with respect to the ground frame are provided by the estimator using inertial sensors and GPS. For the term  $(\mathbf{v}_{k/g} - \mathbf{v}_{a/g})$  we could use the kite velocity as provided by the estimator, subtracting some estimate of the wind velocity. Or we could use the low-pass-filtered apparent wind vector derived from the pitot probe.

After implementing the complementary filter, there is one parameter to tune: the crossover frequency. Above this frequency, inertial measurements are used instead of direct measurements from the air data probe. Although there seemed to be universal demand for such a filter, opinions on the cutoff frequency spanned at least an order of magnitude. We chose 0.5 Hz. The filter worked as intended and caused no problems.

### 8.2.1.3 Angle of Attack and Angle of Sideslip

Angle of attack (alpha) and angle of sideslip (beta) are obtained by expressing the apparent wind vector in spherical coordinates.

## 8.2.2 Wind Aloft

An estimate of the wind aloft is required to select the optimal flight trajectory. The simplest estimate of the wind aloft is to simply measure the wind at the base station, which we do using an ultrasonic anemometer.

Once the kite is flying crosswind, we can subtract the apparent wind vector from the kite's velocity vector to obtain an estimate of the wind velocity vector in the obvious way. Care must be taken to account for air density variation to obtain true airspeed. Because this involves subtracting two large measured quantities to get a smaller one, the result must be used with care. Indeed, we observed significant variation of the wind aloft measurement obtained in this way over each loop flown by the kite. The wind speed and direction obtained could only be used after significant low-pass filtering.

---

<sup>23</sup> See Schaub and Junkins [11].

This measurement could potentially be improved by using regression techniques to remove the once-per-loop variation in the estimated wind aloft obtained through this subtraction.

The flight test program also made use of SODAR (at China Lake) and LIDAR (at Parker Ranch) to measure the wind field above the test sites. These instruments provided estimates of wind velocity as a function of height, with an update period of around 1-5 minutes. The data from these instruments was not available to the flight control system, but it was used by the test team to inform launch/land decisions, and to aid in post-flight data analysis.

### 8.3 Validation

The estimator was initially validated through the use of the simulator, which simulates all of the raw sensor signals, including representative noise and other signal corruption. After simulating a flight, the estimated quantities could be compared to their "true" values, available from the simulator. After flight test data had been collected, proposed changes could be evaluated by reprocessing raw sensor data collected during flight through the new revision of the estimator and comparing the old state estimate to the new one. This was sometimes tricky as the sensor complement and data structures did evolve from flight to flight.

### 8.4 Discussion

A theme of M600 development was the conflict between wanting to add sensors (for improved state estimation) and wanting to remove them (for simplicity and cost). A desire to improve reliability and robustness often underscored both the argument to add a sensor and to remove it (a sensor that doesn't exist can't fail).

At one point the M600 was festooned with four expensive GPS receivers and four 5-port air data probes. While an abundance of instrumentation is typical for a prototype, the product vision generally called for the removal of the pitot/static system entirely and perhaps GPS as well. The former is subject to clogging or water ingress, and the latter vulnerable to jamming. The remaining sensors are the encoders measuring the tether departure direction, the loadcells measuring the tension vector, and the IMUs—these sensors were seen to be robust and immune to unwanted influence. Indeed, Makani did demonstrate flight using this reduced sensor complement with the M600's predecessor, Wing 7.

## 9 Simulator

Controls development at Makani was made possible through the use of a time-stepped simulator developed in-house, known sometimes as the "C-sim" in a nod to its implementation language (C++). The purpose of this simulator was to facilitate development of the flight controller, estimate the power performance of the system, test new system configurations, provide tools for linearizing models, support hardware-in-the-loop (HITL) testing, and train the system operators. Using this simulator, we were able to arrive at a flight controller that "worked the first time" flying crosswind flight.

The simulator was built in a modular nature, reflecting in part the structure of an earlier Simulink-based simulator that it replaced. Each model or submodel in the simulator is responsible for calculating its own state derivative; ultimately the top-level model is handed to a variable-step ODE integrator to integrate the state from one timestep to the next. The simulator could generally run in real-time (on a standard laptop circa 2015) or up to 10X faster than real-time (performance desktop 2019), depending on the machine in use.

Any flight simulator is only as useful as the tools available to examine its output. The evolution of the simulator could be watched "live" through a simple visualizer or via the same flight displays used during test flights, but the main output of the simulator was a log file in the Hierarchical Data Format HDF5 containing a transcript of all messages passed around the system during the simulation. Again, these logs use the same telemetry format as a real flight, with the addition of additional telemetry from the simulator itself. Many engineers developed their own personal plotting tools in MATLAB or Python to explore the flight or simulation logs. For automated analysis, a large suite of scoring functions was developed to evaluate flight quality and crash risk.

The general development philosophy at Makani was to use simple analytic models for design and then throw in more complex physics into the simulation used for verification. While many approximations were employed in designing controllers, we tried to put all the physical effects we could think of into the simulator. The hope was that this would lead to a more robust system. In an ideal situation one might imagine a firewall between the controls and the simulation groups to ensure independence, so that the controls design would not be overfitted to the simulation.

One important role of the C-sim was as the "principal source of truth" for simulation physics,<sup>24</sup> and changes to the simulator were subject to formal review. This helped alleviate the need to build one-off models (which would invariably initially contain bugs) for individual analyses. This

---

<sup>24</sup> A notable exception here is that a separate tool, the Force Balance Loop (FBL) was developed to understand system sensitivities and to find optimal flight parameters, such as loop position and size and airspeed schedule as a function of wind speed.

was partially successful; in practice it was more difficult than hoped to extract sub-models from the main simulator for these kinds of projects.

## 9.1 Simulator models

### 9.1.1 Kite

The kite (referred to as the "wing" in the simulator code) itself is modeled as a rigid body, subject to forces and moments from the rotors, aerodynamics, gravity, and the tether. The rotor and tether physics are handled by dedicated submodels. To model the aerodynamic forces, we make use of two different aero databases, depending on the flight regime: one for high-incidence flow (hover and transition-in) and another for attached flow. Nondimensionalized coefficients and derivatives are interpolated from these databases.

For the hover and transition aerodynamic databases, we add airspeed and flap<sup>25</sup> deflection as dimensions of the look-up table. Airspeed is added because the rotor wake is advected with the wind during hover. Flap deflection is added so we can deflect some flaps, specifically the elevator, beyond their linear range. To reduce dimensions, we assume the flaps are weakly interacting and thus only need to perform a look-up on a single flap deflection at a time.

The *direct* forces and moments from the rotors are added in separately. However, the *indirect* effects from the propellers such as the interaction of the propwash with the empennage are included in these coefficients.

### 9.1.2 Rotors

Rotor tables were developed using XROTOR, providing a look-up from rotor speed and inflow velocity to thrust, torque, and power. Later, an additional dimension was added to these tables to include the influence of edgewise flow: ambient wind velocity in the plane of the rotors which would result in additional forces and moments.

### 9.1.3 Environment

To model the wind, the simulator offers three models: (1) no turbulence, (2) Dryden turbulence, and (3) use of a wind field generated with TurbSim from NREL. One feature on the drawing board that was never implemented was the ability to use real-time measured wind, or wind recorded from the wind sensor, in a simulation. That could have been useful in flight rehearsals.

### 9.1.4 Tether

The tether is modeled as a linear assembly of lumped masses separated by springs, subject also to aerodynamic drag (and lift, when considering faired tethers). A particular challenge was

---

<sup>25</sup> We use the term "flap" to refer generically to any of the control surfaces, which include eight ailerons, a rudder, and an elevator.

in attaining a well-behaved simulation during pay out and reel-in with a changing tether length. Each segment of tether except the bottom one always had constant length; new nodes were generated (or deleted) at the origin as needed. At a later stage some effort was also made to model bending stiffness to help address unrealistic behavior during the final deceleration out of crosswind and to damp out unphysical oscillations in the simulated tether.

### 9.1.5 Power System and Motors

The modular nature of the simulator allowed us to choose, at run time, to swap out the complex stacked power system simulation for a simpler one, resulting in a substantial improvement in simulation speed.

During the development of the motor controllers, we often wished for a high fidelity motor simulator that included the complicated interactions of our peculiar stacked topology. The vastly different time scales of the problems (with the flight controller running at 100 Hz but the motor controller running at 15 kHz) suggested separate approaches. The motors were modeled using PLECS and the motor and stacking controllers were tested on the "iron bird," a test jig containing a full eight-motor setup.

### 9.1.6 Base Station

The base station GS02 used at Parker Ranch and offshore in Norway was a complex beast of industrial control. Its implementation, which was outsourced, involved a combination of programmable logic controllers (PLCs) and Simulink StateFlow diagrams that were compiled to firmware. As a consequence, its firmware was outside the Makani master code repository and not interoperable with the simulator. To accommodate this we took a two-pronged approach: (1) In the simulator, we implemented an independent GS02 controller, where, for example, we made up PID controllers governing its various axes of control, to give some reasonable response to commands; and (2) we implemented a GS HITL mode, similar to the motor/servo HITL described in section 9.2.3. In this mode the actual base station would be put into the simulation loop. Differences in behavior between simulation and reality were carefully investigated and put into the simulator models by hand.

### 9.1.7 Buoy

For the offshore scenario, the buoy was modeled as a rigid body, receiving a force from the tether in addition to forces from its mooring lines and from hydrodynamical effects. A sea model using a JONSWAP spectrum and linear wave theory generates planar waves, used to derive the corresponding hydrodynamic forces on the buoy. Thanks to the modular nature of the simulator structure, it was not too difficult to create a new reference frame attached to this moving buoy and to attach the base station model to it. Existing IMU and GPS models were instantiated to provide simulated signals to the vessel state estimator (part of the flight controller used in the offshore scenario).

### 9.1.8 Sensors

When running under simulation, the flight controller's inputs must be populated with simulated signals from a complete complement of sensors. Each model maintains a "true" value of its state; the sensor models corrupt the truth with noise, discretization, uncertainty in location and orientation, and discrete update times. For example, the pitot tube sensor model produces simulated values of the pressures seen at each port of the multi-port air data probe, and the GPS models produce simulated positions and velocities with respect to the earth-centered earth-fixed (ECEF) coordinate system used by GPS. This attention to fidelity in the simulator helps guarantee that the software will work "the first time" when it meets real hardware. In addition to corrupting simulated sensor signals with noise and other effects, a "fault schedule" allowed for programmatic failure in various ways of many of the simulated sensors. Simulating effects like IMU misalignment or placement uncertainty was also crucial in ensuring robustness of the estimator.

## 9.2 Simulator Modes

The simulator is run in many different modes during controls development and validation.

### 9.2.1 Desktop Simulation

In its simplest mode of operation, the simulator can be run directly on a laptop or desktop computer. The simulation progress is depicted graphically in the visualizer and is also recorded to a log file, which is typically investigated using MATLAB or Python.

### 9.2.2 Monte Carlo Batch Simulation

Validation of proposed controller changes and evaluation of the system's flight envelope was done via Monte Carlo batch simulations. Each such batch simulation would run an ensemble of around 1200 simulations in parallel, over a sweep of wind speeds, and with numerous system parameters randomly varied according to a plausible distribution of values.

Of course, such simulation batches are only useful insofar as the results may be evaluated. A large suite of scoring functions was developed allowing simulations to be evaluated for quality of flight, crash risk, and power production.

### 9.2.3 Hardware-in-the-Loop (HITL)

Each flight test was preceded by conducting a dry-run, which involved executing as much as possible of the flight plan on the ground. One aspect of this was HITL testing, where as much kite hardware as feasible would be exercised. In a HITL run, the flight controller would run on the kite (as in nominal operation), but its sensor inputs would be driven by simulator outputs. In a simulated HITL hover flight, the motors and servos could be brought into the loop in the

following manner: the motors and servos would respond to commands from the flight controller, then the measured motor speeds and servo positions would be ingested by the simulator, driving its physics models. Thus the general behavior of the electrical power system and the transfer functions of the motors and servos (and any accompanying nonlinearities) would be captured in the "simulation," and the hardware would be put through the paces of a (simulated) hover flight. This "motor HITL" was done in a test bay with the kite securely strapped to a large trailer. While the aerodynamics in this enclosed environment might differ in some ways from hover in an open environment, it was close enough. More than one engineer compared the HITL test to the kite "dreaming."

For crosswind flight, the behavior of the rotors with significant inflow velocity is not captured by spinning the motors on a static test stand. So, for crosswind HITL, we employed an "8+8 dynamometer," in which eight motors, simulating those installed on the kite, were coupled to eight more motors, which provided reaction torque as dictated by the simulator. This beast (with up to a megawatt of closed-loop power conversion) was housed in a standard shipping container. The 8+8 dynamometer is depicted in figure 21 and the associated Tech Topic video, "Sophie & Jessie Introduce the Short Stack: How to Keep The Makani M600 Energy Kite Flying if a Motor Fails In Flight" [17].

#### 9.2.4 Dynamics Replay

In normal operation, the simulator calculates forces and moments on the kite in order to find its acceleration and integrate its state forward in time. In an alternate mode of operation, we can populate the simulator state from flight test data and then compare the predicted motion to the observed motion. The output is a force or moment residual: what is the gap between the predicted force and moments and those observed? We called this mode "dynamics replay." Of course, its accuracy depends on the ability to reconstruct the pertinent inputs from flight test data. One of the biggest unknowns here is the wind field, which we can only estimate coarsely.

Dynamics replay was particularly useful for reconciling the coefficient of lift during crosswind flight and for quantifying "phantom moments" in hover flight. A key achievement here was leveraging the existing simulator models and thus pre-empting the reimplementing of reduced order models in MATLAB or Python by individual engineers investigating particular effects. The use of the C-sim as a "principal source of truth" ensured that this model contained every known effect and had been thoroughly tested; by comparison, one-off models tend to require significant debugging, potentially producing false conclusions along the way.



**Figure 21: Photograph of the 8+8 dynamometer.**

## 9.3 What Wasn't Simulated?

### 9.3.1 Structural Modes of the Kite

The kite was simulated as a rigid body, subject to forces of gravity, aerodynamics, rotor forces, and tether tension; no flexible body modes were simulated. A separate tool—KiteFAST—was commissioned to study aeroservoelastic interactions and to analyze load cases for future kites. The M600 design relied on offline FEA structural analysis and ASWING for aeroelastics.

This separation of concern seems reasonable, especially considering the computational load of a flexible body simulation. The flexible body physics simulator was at least 100X slower than the C-sim. Integration with the flight controller was never completed.

#### 9.3.1.1 Flight Testing Lesson: Flexible Body Modes

An attempt to use rotor reaction torque to provide some control authority around the roll axis during hover resulted in significant damage to the wing pylons before liftoff in one test. It turned out that the symmetric torsional mode of the airframe resulted in significant phase loss between the inertial sensors and the motors and, hence, a control oscillation. This could have

been avoided with better modeling (including flexible body modes) or with more careful bring-up.

### 9.3.2 Propwash/Airframe Interaction

A source of continuing murkiness was the interaction of the propwash with the airframe and empennage combined with the influence of the wind. Attempts were made to include the interaction of propwash with the tail in the hover aero database, but the longstanding fix was to move the elevator from a high position to a low position where its interaction with the propwash was more consistent. After the 2019 offshore flight, the effect of blown lift on the main wing came into the spotlight as a potential major contributing factor to the crash, in which it was hypothesized that differential thrust intended to create a yaw moment had also created a significant roll moment through the action of differential blown lift. Advection of propwash by a side-wind is also relevant here as the side-wind can create an asymmetry in the effective center of the blown lift effect on each wing. Analysis of these effects with the intent of implementing them in the simulator was underway at the time of Makani's shutdown.

## 9.4 Potential Future Improvements

### 9.4.1 Automatic Model Tuning

We have no automated process to update the simulator based upon the results of flight. Ideally we would be able to run some process after a flight that would tune the simulation parameters to close the dynamics replay gap. This could take the form of using machine learning to update the aero databases post-flight.

### 9.4.2 Differentiability

To support the use of optimal control solvers, we would like to be able to compute not just the state derivative, but also its second derivative  $d^2/dt^2 x(x, \dot{x}, t)$  and the constraint derivatives. This can only be done numerically with the current formulation of the simulator, and retrofitting the simulator to support differentiability would be a significant project. Baking this capability in from the get-go would have been nice.<sup>26</sup>

### 9.4.3 Better Modularity and Linearization

Although the simulator C++ code was structured as independent modules that could in principle be recombined or examined individually, in practice this was difficult and required significant software engineering talent. Ideally each engineering group in the company would be

---

<sup>26</sup> Indeed, one amazingly productive intern re-implemented the simulator models in the functional programming language Haskell and hooked it up to a CasADi-based optimal control solver, producing not only optimal trajectories for the M600 and a hypothetical future multi-kite system but also sensitivity derivatives with respect to system parameters. Unfortunately knowledge of how to use this system was lost. See Horn et al. [6] and Van Alsenoy [14] for reports of earlier work along these lines.

responsible for maintaining and validating its own simulator components. Furthermore, we wished to develop a more convenient mechanism to linearize any given component or assemblage of components around any given operating point, or at every point of a flown trajectory. In practice this was cumbersome.

## 10 Visualizer

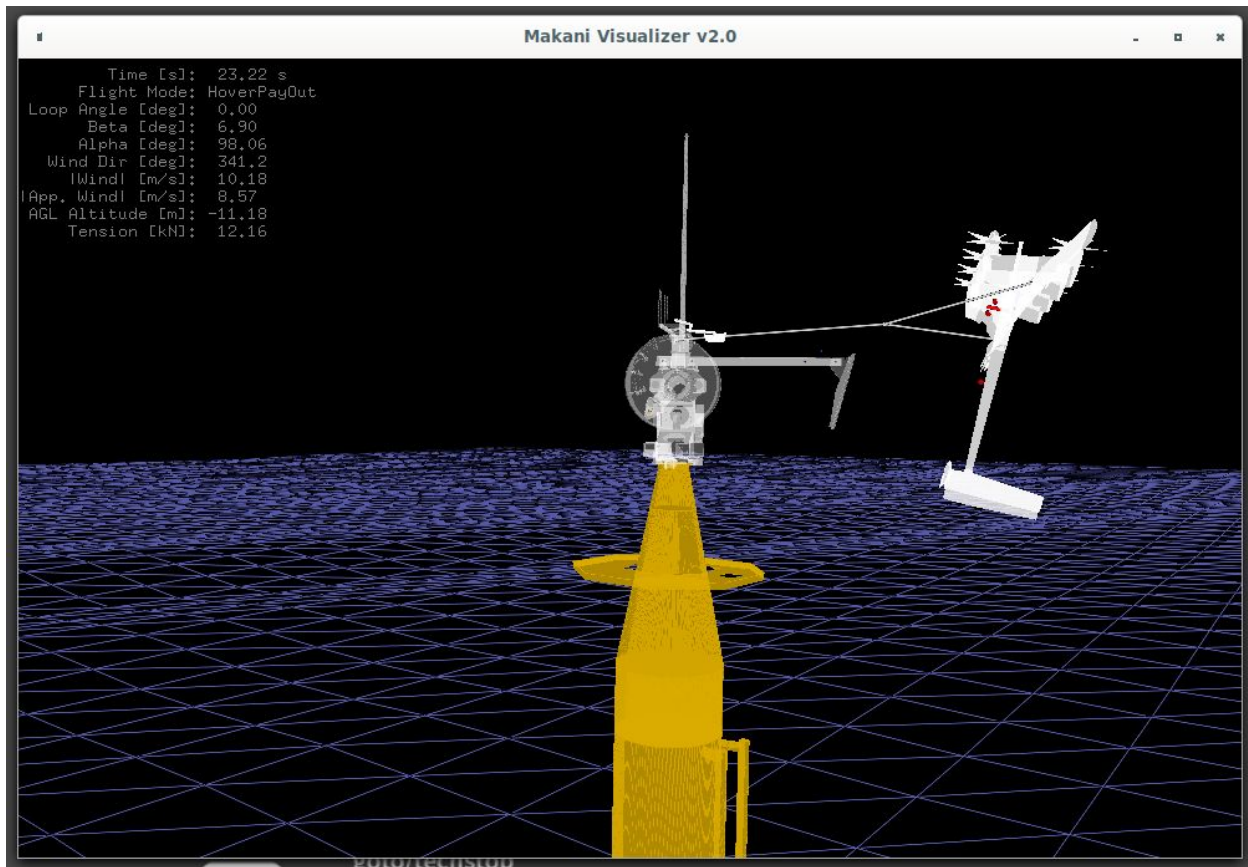


**Figure 22: The Makani visualizer depicting a simulated flight. Here the controller is in pay out mode and the kite has just left the perch, in the offshore scenario.**

The simulator is paired with a visualizer (see screenshot in figure 22) that depicts the state of the system by rendering a graphical representation of it. The visualizer can equally well display a simulation in progress or the estimated state from an actual flight. It can also be used to simultaneously show the "true" and estimated states of the system (kite and buoy) during a simulation. The ability to quickly do a virtual "fit check" during initial bring-up was useful; if the kite is on the perch in reality but not in the visualizer, then something is wrong. Although the visualizer generally employed crude but representative graphics, importing actual CAD models of the kite and base station did prove useful for understanding the state of the system and its various interactions.

Technically speaking, there was little particularly notable about the visualizer's implementation. It was implemented in C and used 1990's era OpenGL immediate mode rendering. The key technical insight was to use the same interface for controller telemetry in simulation and in operation. The visualizer was simple, robust, and very useful.

## 11 Software Development Methodology

Makani employed software development practices familiar to the tech world but perhaps not yet abundantly familiar within the aerospace industry, including code review, continuous integration, and the use of a monolithic git repository for version control. Code quality was held (we liked to think) to very high standards of clarity and style. While newly-onboarded engineers may have initially viewed the code review process as a sort of needlessly pedantic hazing ritual, we felt we benefited tremendously from the codebase's high reliability and minimal technical debt. With the code now published as open source, you may form your own independent opinion of the results.

The use of textual languages like C, C++, and Python resulted in the ability to rigorously compare code revisions and produce clean "diffs." By contrast, with graphical systems like Simulink and LabView, it can be very difficult to compare different revisions of the software and apply version control (`git`). For reasons such as this, Makani abandoned the use of Simulink for the controller and simulator some time before 2014. The use of standard compilers also made the implementation of automated regression testing much easier.

An autoformatter (`clang-format`) was used to automatically format the C and C++ source code according to the style guide, alleviating what can otherwise be a source of disagreement and annoyance.

With a small team of developers, it was always possible to maintain an informal notion of the "owner" of each subsystem. Any code change proposed by one engineer would be reviewed by another engineer (perhaps the subsystem "owner" or someone else known to be familiar with that subsystem) for style, correctness—even spelling and grammar of the comments—and in general for a "fresh set of eyes." Typically several iterations of comments and changes would be exchanged, followed by approval and merging into the master code branch. In addition to this manual review, each proposed code change would automatically be subjected to regression testing including (1) a suite of unit tests, and (2) comparison of the simulation results before and after the code change. After flight testing began, another layer of review and approval was put into place: the Engineering Change Request (ECR), which took the form of a Google Doc containing narrative text illustrated with relevant plots, motivating and justifying the change and its validation.

The practice of code review helped to socialize changes to the code (ensuring that not just one but at least two engineers were familiar with every line) and ensure a consistent style across the system. Ideally, after a piece of code was merged, its authorship could not be determined by inspection without employing a peek at the version control system.

There were very few bugs. Defining "bug" as code that does not operate as intended, we had perhaps five or six bugs in the 5½ years the author was at Makani, and all but one or two were corrected before flight test. One of these (see item 5 below) did contribute significantly to a crash of the M600 and loss of airframe, however.

## 11.1 The Memorable Bugs

The character of the bugs that occurred (briefly) in the code is good fodder for meditation on what software development methodologies might prevent such bugs.

1. (Wing 7 program, before 2014). A bug in a vendor-supplied math library for an embedded microprocessor caused a floating point exception resulting in a crash. Switching to a more common microprocessor platform (ARM) and better tested compiler (gcc) reduced the likelihood of stumbling on latent issues in a niche platform. Adoption of HITL testing rooted out problems in the microprocessor code running on its target platform (as opposed to batch simulations, which are run on commodity computers).
2. A very subtle issue with the low-level firmware affecting the bootloading process. This issue was obvious when it occurred (and thus never threatened flight), but very difficult to debug, as it occurred only infrequently and at a very low level of the firmware, involving a third-party embedded operating system we employed. Ultimately the embedded operating system was removed and our in-house code ran on the bare metal, increasing our ability to understand and reason about the system (consistent with the overall DIY approach of Makani).
3. In a function taking a long list of arguments, two arguments of type double were exchanged in order: `myfunction(..., tension, airspeed, ...)` was called as `myfunction(..., airspeed, tension, ...)`. This was before we had deployed our full suite of automatic regression testing. Situations like this where the code "looks right" can also sneak past manual code review, and unit tests of `myfunction` itself won't catch an issue like this. The bug was found a few days later when manually inspecting simulation results that didn't make sense. Flight was not threatened.

This particular sort of bug can be avoided by using the language's type system. Unfortunately, C's willingness to coerce numeric types is a disadvantage here (C will happily cast even a boolean to a double), and one must use structured types to have such errors be caught by the compiler. A language with a stronger type system might help. Furthermore, one might, as an issue of style, limit the number of arguments that may be passed to a function.

4. Several copy-paste issues, resolved before flight. For example, suppose code for the starboard GPS is copy-pasted to cover also the port GPS; or suppose part of the kite estimator is copy-pasted to form the vessel estimator. Of course, we attempt in all cases

to refactor and remove repeated code (the rule of thumb, DRY ("Don't Repeat Yourself")), but occasional structural repetition or use of boilerplate code is sometimes unavoidable. A common error is to incompletely fix the pasted code, resulting again in code that "looks right" but contains an error.

The solutions here are: (1) when possible, refactor code to avoid repetition (DRY); (2) be particularly careful when "pasting" code, as this is often a source of errors, and (3) the catch-all, employ comprehensive unit and regression tests to automatically catch errors.

5. The infamous "typo" resulting in the crash of RPX-06 on August 7, 2017 also resembles a copy-and-paste error. Code implementing the use of wingtip GPS antennas for attitude determination contained an incorrect calculation for the standard deviation of the length of the baseline. The incorrect code was:

```
// Compute the relative position vector standard deviation.
double a_to_b_sigma = sqrt(wing_a_to_b_sigma * wing_a_to_b_sigma +
                          Vec3NormSquared(&gps_a_data->pos_sigma) +
                          Vec3NormSquared(&gps_a_data->pos_sigma));
```

The second instance of `gps_a_data` should have been `gps_b_data`. This bug contributed to the divergence of the gyro bias estimate which combined with other factors to result in a crash after the transition from crosswind to hover.

This bug represents a failure of our "defense in depth," as it snuck through code review, manual testing, and automatic testing.

## 12 Epilogue

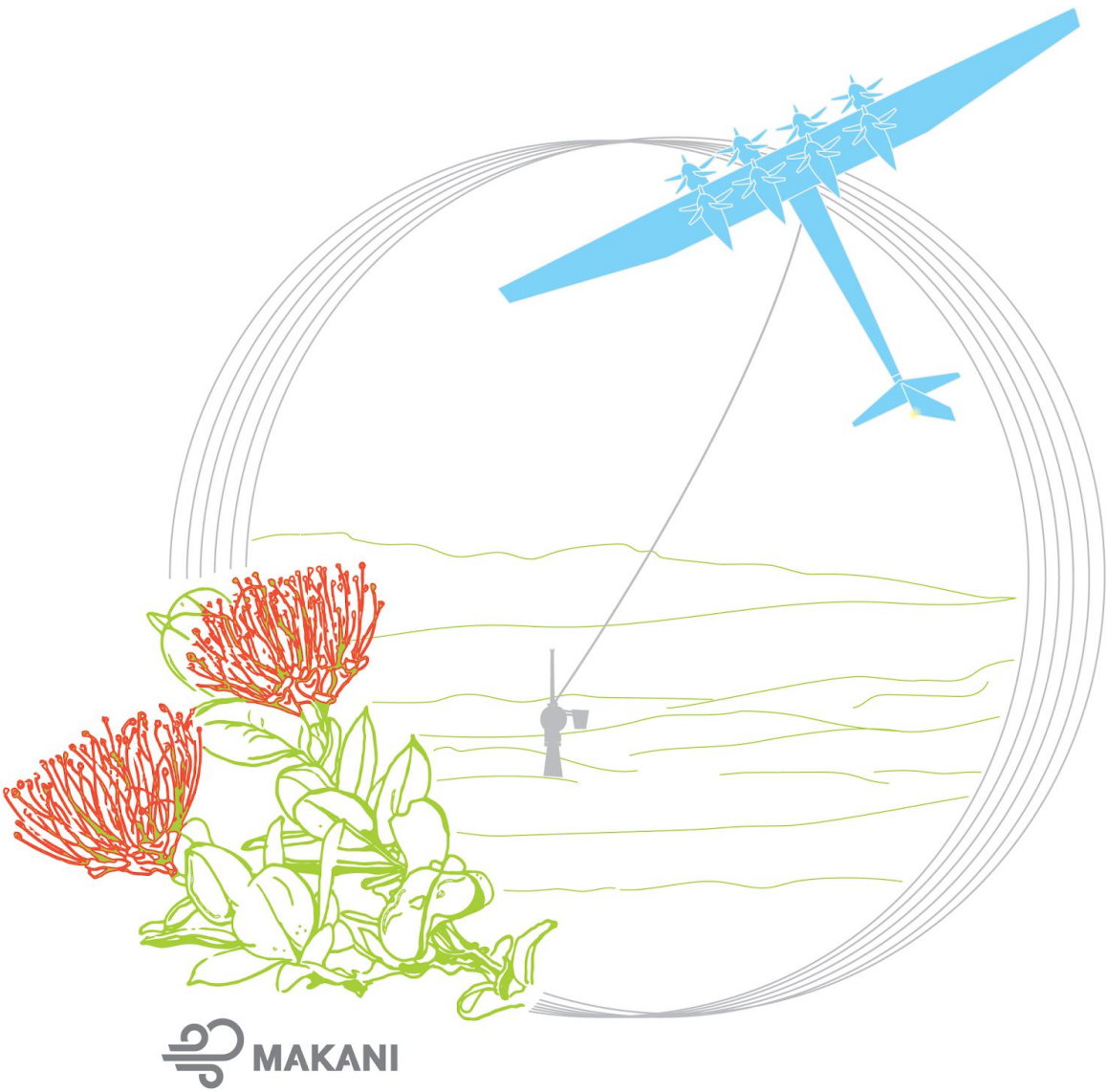
We are proud of the system described here, and we hope that readers are able to take away some of our learnings and apply them to their own systems. A snapshot of the source code of this entire system—autopilot, avionics firmware, motor controllers, flight simulator, visualizer, math library, and other goodies—has been made available on github [18] under a very permissive license in the hope that it might be useful and interesting. The author of this report thanks his teammates for five years of learning and adventure and for the privilege of describing their work.

## 13 References

1. M. Abraham, "Crosswind Kinematics," in *The Energy Kite: Selected Results From the Design, Development and Testing of Makani's Airborne Wind Turbines*, Part II, Makani Technologies, Alameda, CA, USA, 2020. [Online]. Available: <https://x.company/projects/makani>
2. K. J. Åström and R. M. Murray, "PID Control," in *Feedback Systems: An Introduction for Scientists and Engineers*, Princeton, NJ, USA: Princeton University Press, 2008, ch. 10, pp. 293-314.
3. B. Etkin, *Dynamics of Atmospheric Flight* (Dover Books on Aeronautical Engineering), Mineola, NY, USA: Dover Publications, Inc., 2005.
4. G. Franklin, J. D. Powell, and A. Emami-Naeini, "State-Space Design," in *Feedback Control of Dynamic Systems*, 5th ed., Upper Saddle River, NJ, USA: Prentice Hall, 2005, ch. 7.
5. B. Friedland, *Control System Design: An Introduction to State-Space Methods* (Dover Books on Electrical Engineering), Mineola, NY, USA: Dover Publications, Inc., 2005.
6. G. Horn, S. Gros, and M. Diehl, "Numerical Trajectory Optimization for Airborne Wind Energy Systems Described by High Fidelity Aircraft Models," in *Airborne Wind Energy*, (Green Energy and Technology) U. Ahrens, M. Diehl, R. Schmehl, Eds., Berlin and Heidelberg, Germany: Springer, 2013, pp. 205-218, doi: [https://doi.org/10.1007/978-3-642-39965-7\\_11](https://doi.org/10.1007/978-3-642-39965-7_11)
7. K. Jensen, "Linear Analysis of the Path Controller," 2016, in *Makani Code Release*, Makani Technologies, 2020. [Online]. Available: <https://github.com/google/makani/>
8. K. Jensen, "Very Rough Hover Notes," 2016, in *Makani Code Release*, Makani Technologies, 2020. [Online]. Available: <https://github.com/google/makani/>
9. M. L. Loyd, "Crosswind Kite Power," *J. of Energy*, vol. 4, no. 3, May-Jun 1980, Art. no. 80-4075, doi: <https://doi.org/10.2514/3.48021>
10. R. Tedrake, *Underactuated Robotics: Algorithms for Walking, Running, Swimming, Flying, and Manipulation*, Course Notes for MIT 6.832, (2020). Accessed: July 6, 2020. [Online]. Available: <http://underactuated.mit.edu/>
11. H. Schaub and J. L. Junkins, "Particle Kinematics," in *Analytical Mechanics of Space Systems*, 4th ed. Reston, VA, USA: AIAA, 2018, ch. 1, sec. 1.3.3, doi: <https://arc.aiaa.org/doi/book/10.2514/4.105210>
12. J. Sicard, G. Homsy, and M. Abraham, "Kite Stability in Crosswind Flight," in *The Energy Kite: Selected Results From the Design, Development and Testing of Makani's Airborne Wind Turbines*, Part II, Makani Technologies, Alameda, CA, USA, 2020, [Online]. Available: <https://x.company/projects/makani>
13. B. L. Stevens and F. L. Lewis, *Aircraft Simulation and Control*, 2nd ed. Hoboken, NJ, USA: Wiley-Interscience, 2003.
14. T. Van Alsenoy, "Sensitivity Analysis of Airborne Wind Turbine Design Variables: Using trajectory optimization," M.S. thesis, Dept. Wind Energy, Aero. Eng., TU Delft, Delft, Netherlands, 2014.

15. D. Vander Lind, "Analysis and Flight Test Validation of High Performance Airborne Wind Turbines," in *Airborne Wind Energy*, (Green Energy and Technology) U. Ahrens, M. Diehl, R. Schmehl, Eds., Berlin and Heidelberg, Germany: Springer, 2013, pp. 473-490, doi: [https://doi.org/10.1007/978-3-642-39965-7\\_28](https://doi.org/10.1007/978-3-642-39965-7_28)
16. N. Tucker, "Airborne Wind Turbine Performance," in *The Energy Kite: Selected Results From the Design, Development and Testing of Makani's Airborne Wind Turbines*, Part I, Makani Technologies, Alameda, CA, USA, 2020, [Online]. Available: <https://x.company/projects/makani>
17. Makani Technologies, Alameda, CA, USA. *Makani - Energy Kite Technical Videos*. (Aug., 2020). [Online Video]. Available: [https://www.youtube.com/playlist?list=PL7og\\_3Jqea4VRCZmMNK4LDH64sYgkLZzv](https://www.youtube.com/playlist?list=PL7og_3Jqea4VRCZmMNK4LDH64sYgkLZzv)
18. *Makani Code Release*, Makani Technologies LLC, 2020. [Online]. Available: <https://github.com/google/makani/>
19. S. Nolet, D. Levy, and S. Chou, "Base Station Team Final Documentation," in *The Energy Kite: Selected Results From the Design, Development and Testing of Makani's Airborne Wind Turbines*, Part II, Makani Technologies, Alameda, CA, USA, 2020, [Online]. Available: <https://x.company/projects/makani>
20. P. Echeverri, "Makani's Flight Testing Approach," in *The Energy Kite: Selected Results From the Design, Development and Testing of Makani's Airborne Wind Turbines*, Part I, Makani Technologies, Alameda, CA, USA, 2020, [Online]. Available: <https://x.company/projects/makani>

# Makani's Flight Testing Approach



Paula Echeverri



Makani's Flight Testing Approach

Corresponding author: Paula Echeverri, [paulae@alum.mit.edu](mailto:paulae@alum.mit.edu)

The Energy Kite: Selected Results from the Design, Development, and Testing of Makani's Airborne Wind Turbines, Part I of III  
by Paula Echeverri, Tobin Fricke, Geo Homsy, Nicholas Tucker,  
on behalf of the Makani team.

Copyright © 2020 by Makani Technologies LLC

Distributed under the [Creative Commons CC BY 4.0 License](https://creativecommons.org/licenses/by/4.0/). You are free to copy and redistribute this material in any medium or format for any purpose, even commercially.



Intended for electronic publication and distribution. Copies of this volume may be found at <https://archive.org>

Additional information is at: <https://x.company/projects/makani>

Published September 2020

<b>1 Introduction: Philosophy and Circumstance</b>	<b>342</b>
1.1 Safety First	342
1.2 Learn Early	342
1.3 Assessment	344
1.4 About This Article	344
<b>2 Flight Testing Timeline</b>	<b>345</b>
<b>3 M600 Flight Test Program</b>	<b>354</b>
3.1 Constrained Hovers in Alameda	355
3.1.1 Commissioning Full Systems	356
3.1.2 Early Life Issues	358
3.1.3 Containerhenge	358
3.1.4 Relocation and Later Tests	360
3.2 Remote Perch Crosswind (RPX) in China Lake	361
3.2.1 The Range	361
3.2.2 Functional Demonstration of Crosswind	364
3.2.3 Fly Better, Fly More, Make Power	365
3.3 On-shore All-modes Crosswind in Hawaii	369
3.3.1 The Ranch	371
3.3.2 High Hover	371
3.3.3 Hours of Crosswind	373
3.4 Offshore in Norway	376
3.4.1 Deeper Water	378
3.4.2 Floating Crosswind Flight	379
3.4.3 Safety Culture	381
<b>4 Case Studies on Selected Learnings</b>	<b>383</b>
4.1 Hardware Design Evolution: Powertrain Bugs	383
4.1.1 Things Get Hot: Debris in the Cooling Loop	385
4.1.2 Things Rub: Yasa 2 Motor Issues	388
4.1.3 Things Shake Loose: Gin2 Motor Controller Vibration Issues	388
4.1.4 Things Turn Off: Gin3 Motor Controller Assorted Issues	390
4.2 Modeling Physics: Pitot Airspeed Estimate	393
4.3 A Major Lesson: Crosswind Flight Dynamics and the RPX-09 Crash	396
4.4 A Looming One: Loss of Roll Stability in Hover and the FCW-01 Crash	399
<b>5 Conclusion: How Did That Work Out for Us?</b>	<b>402</b>
<b>6 References</b>	<b>408</b>

# 1 Introduction: Philosophy and Circumstance

## 1.1 Safety First

One thing that we learned from flight testing at Makani was to think about safety first. It takes a constant and active effort to maintain a safety mindset, and talking about safety helps us stay mindful. This article does not include an in-depth discussion of our learnings about safety, but in the spirit of showing by doing, we begin by showing how we started every test day and how we planned for every test campaign: by recapping the hazards we would encounter and the behaviors that could prevent or mitigate them.

The hazards in flight testing encompassed the gamut: high electrical potentials, large moving mechanical structures, lifting hazards, working at altitude, harsh environmental conditions (high winds, high temperatures, high seas), remote test sites, and long work days. And the nature of our activities was necessarily uncertain: we were testing a brand new type of flying machine, expanding its envelope, and trying to learn about aspects of its operation that we did not yet understand.

One practice that helped keep people around our operations safe was to keep people away. We established safety perimeters. For example, in the case of our crosswind flights, ensuring that there were no people within several tether-lengths downwind of the flight was the principal consideration in our site selection process. We always cleared and checked the test area before beginning a test.

Another practice that helped keep us safe in the day-to-day was the buddy system. All operations were done with another team member nearby and in direct communication. This person would be there to get us out of trouble if something went wrong, and they also helped keep us out of trouble to begin with. We learned to repeat to our teammates the procedures that we were about to follow, as a way of checking our logic and catching any forgotten critical step. We learned to question each other: if we didn't understand what our buddy was doing, we would ask. That would help her review her logic and check her memory, and would help us get smarter about how our operation worked. We also became better friends.

## 1.2 Learn Early

Makani's flight testing approach is not a novel idea to any successful designer: it's based on the belief that we should test any design early, even before it is complete, in order to guide further development to address the harder or more frequent challenges that it encounters in the real world. Sometimes said challenges are existential and yet unexpected, and testing helps us find them.

Testing before designs are complete, especially for complex systems such as flying robots, makes system integration, interfaces, and configuration management more challenging. The bet, and the tradeoff, is that we get to working systems sooner.

This approach set a fast cadence of flight testing that often overwhelmed all of Makani's engineering activities, in part because the team remained small relative to the breadth of engineering disciplines and tasks. For example, our one computational fluid dynamics engineer would pause analysis to inform future designs when an issue encountered in flight testing had to be addressed before the go-ahead for the next flight. This was sometimes seen as a positive trait that would unblock so-called "analysis paralysis." At other times, it was frustrating, and the team felt that they did not have enough time to run tests in a controlled environment, or to fix known issues that could save time in the long run.

In fact, and despite that constant sense of rush, we never got to as fast a cadence as we would have liked. Besides our motivation to fly often so as to learn early about other aspects of our design, we wanted to fly often because that in itself was a fundamental requirement for our technology: to operate year-round.

The flight testing program was intended to evolve into a demonstration of commercial energy kite operations, and a particular pull was to achieve a measurable (and eventually competitive) system availability. In the wind industry, system availability is the percentage of time that a turbine is ready to operate when the wind is blowing,<sup>1</sup> and it factors directly into a project's annual energy production (AEP). AEP is the denominator of the levelized cost of energy (LCOE) metric, and therefore a direct driver of our commercial bottom line, as described in some detail in the article included in this volume, "Airborne Wind Turbine Performance" [2]. As discussed there, other important pulls to address the bottom line were to scale up the system's rated power (so as to drive down the dominant balance-of-plant costs in LCOE models), and, of course, to achieve a more attractive power curve, reaching rated power at lower wind speeds.

Availability can be achieved in many different ways, which we would capture in our test objectives by aiming for increasingly long periods of continuous, unattended operation. For our engineering design teams, this translated to working on tasks that would improve automation, component reliability, system robustness, and system dispatchability. The number of people required to monitor systems during a test would sometimes limit how soon or how often we could fly. Automation could help us reduce the number of people required. Component reliability could reduce the time the kite was grounded while we were troubleshooting a fault found in preflight checks or in actual flight. Robustness, which in itself could be interpreted in many different ways at different levels of the system, was an important target for the flight controls engineers. More robust flight could reduce the number of unplanned events that often resulted in hardware damage and therefore time grounded before the next flight. Dispatchability was our

---

<sup>1</sup> System availability is one of many ways to define availability, as disambiguated in "Definitions of Availability Terms for the Wind Industry" [1]. Typical values for mature wind turbine designs are around 98%.

ability to quickly get the system checked and ready to go, and it ranged from having spare kites already commissioned, and having an accessible inventory of spare parts, to making it easier to complete assembly and preflight checks at the test site, or to lift the kite onto the perch.

## 1.3 Assessment

The tension around flight testing at Makani was established between the uncomfortable feelings that we were both “moving too fast,” *and* also that we were “moving too slow.” Both assessments were accurate, and it is also true that sometimes we struck the right balance.

For example: we scaled from the 20 kW Wing 7 prototypes to the 600 kW M600 prototypes without having methodically explored flight dynamics and power performance across the wind envelope. Did we move too fast? Perhaps we could have learned some of the expensive lessons of the M600 test program, described in section 4.3 below, if we had kept testing Wing 7 for a longer time. This counterfactual is impossible to assess.

On the other hand, after years of development and testing, we never achieved the continuous, unattended operation that was critical to demonstrate to the wind industry the promise of our technology. Were we moving too slow? The team would argue that we were moving as fast as we could with the resources at hand. We were bold, and often proceeded with high risk, having made a concerted effort to describe and, where possible, quantify that risk.

All that said, the Makani team and Makani's sponsors acknowledge some wonderful accomplishments of the flight testing program. Most visibly, in August 2019 we completed the first offshore flight of the M600 energy kite: a utility-scale airborne wind turbine autonomously taking off, landing, and flying crosswind loops from a floating platform. Most fundamentally, we uncovered challenges of the M600 design that furthered our understanding of airborne wind turbine technology, relating, among other things, to robust crosswind flight dynamics, power performance, and roll stability in hover. The story of flight testing at Makani, with its accomplishments and shortcomings, is shared below.

## 1.4 About This Article

The next two sections are historical accounts of flight testing at Makani. Section 2 is an overview of flight testing each year throughout the 13-year life of the project. Section 3 is a more thorough discussion of the M600 program in particular, centered around the goals and the learnings at each test site.

Section 4 is a selection of case studies on lessons learned during the M600 flight test program:

- A diversity of issues encountered in the early life of the powertrain systems and how these guided our refinement of the design of this subsystem.

- A classic example where identifying a discrepancy between our models and flight test data led us to improve our simulation. In this case, we developed a more accurate estimate of airspeed at the kite.
- A discussion of the causes that led to a mid-air breakup in flight RPX-09, in which we lost our second M600 kite, referred to as serial number 2, or SN2. This event taught us a lot about robust crosswind flight dynamics.
- A discussion of the causes that led to the loss of kite serial number 5 (SN5) in hover after the offshore flight FCW-01. This event highlighted the vulnerability of the M600 design to marginal roll stability in hover.

Any reader who is interested in their own analysis of our flight test data is referred to the collection of flight test logs for the M600 crosswind flights, which have been made publicly available at [3]. The analysis tools included in the Makani code repository [4] can be used to interpret and plot all flight data. (In fact, the simulation in the Makani code repository can be used to generate new, simulated logs in different flight conditions.)

The narrative of the M600 flight test program and the case studies is long, and yet, not comprehensive. We try to give a high level explanation for each hurdle mentioned, but a different writer might have highlighted different events. The intent of this account is not to fully explain the specifics of each event (some other papers in this collection do, and we refer to them for in-depth discussions), but instead to illustrate the nature of the flight testing effort. Flight testing is expensive, laborious, and slow, but from it we learned effectively about how to design and operate our technology, and about the remaining open challenges. We believe that this approach was worthwhile at Makani. It is up to each organization that relies heavily on field testing to inform technology development to navigate the balance between its costs and benefits.

## 2 Flight Testing Timeline

Table 1 is a 13-year timeline of flight testing at Makani that outlines the evolution of Makani systems, from the earliest soft kite prototypes flown in 2007, to the offshore crosswind flight of the utility-scale and fully autonomous M600 in 2019. This history is also being released by Makani in the form of a video documentary, *Pulling Power From the Sky: The Story of Makani* [5] that includes flight footage with different prototypes. We encourage the readers of this article to watch the film as a companion document.

The evolution of the prototypes built and tested could be roughly categorized into four stages:

1. Soft kites built using the fabrication techniques of kite surfing gear. The early Makani team developed ground-based actuation and automated controls, with the signature accomplishment of a 24-hour-long flight in Maui, Hawaii.
2. Rigid demonstrator kites, taking advantage of more effective aerodynamics and on-board actuation, as proof of concept for the crosswind flight-mode described by Loyd [6]. Earlier on, the team experimented with fabrication techniques, building a kite named "Zaftig" out of carbon fiber composite and a kite named "Plank" out of rigid foam, and favoring the latter method to quickly repair or modify prototypes built in the next few years. Wing 4 was the first prototype to incorporate on-board power generation. Wing 6 demonstrated the transitions from hover to crosswind and back. The ground attachment point for these demonstrator kites was a decommissioned fire truck with a bank of lead acid batteries built onto its bed. To launch, Wing 6 was hung from a constraint line that would be retracted remotely once the hover started, and to land, the tether was released and the kite was glide-landed by a pilot with an RC controller.
3. Wing 7 was a carbon fiber composite airframe rated to 20 kW that incorporated onboard power generation with the ability to fly "all-modes": hovering to launch from a perch, to transition in and out of crosswind, and hovering again to land on the perch. We first flew Wing 7 from the firetruck, launching and landing like Wing 6; and eventually we commissioned the first ground station to integrate a perch on the back of a Ford F-650 truck, as part of a set of milestones supported by ARPA-E. Results from Wing 7 flight testing, which accumulated 75 hours of crosswind flight, have been described in a published account by Vander Lind [7].
4. The all-modes M600 kites, rated to 600 kW. The M600 systems are described in "M600 Energy Kite Description" [9], and the M600 flight test program is described in Section 3 of this article.

Year	Major Milestones and Accomplishments
2007	 <p data-bbox="360 995 967 1024">Soft kites on the runway in Alameda, California.</p>
2008	 <p data-bbox="360 1776 1187 1806">Soft kites and the completion of a 24-hour flight in Maui, Hawaii.</p>

2009



Rigid kites Zaftig and Plank (pictured in Sherman Island, California).

2010



Wing 4: On-board power (pictured in Davenport, California).  
Wing 6: Transitions between hover and crosswind (not pictured).

2011



Wing 7: Constrained hovers and first crosswind flights (pictured on the runway in Alameda, California).

2012



Wing 7: Crosswind flight testing (photo taken in Sherman Island, California).

2013



Wing 7: All-modes and long duration crosswind flights at Sherman Island and Pescadero, California.

2014



M600: Design and component fabrication and validation.

2015



M600: Integration and first constrained hovers in Alameda, California.

2016



M600: Move to remote perch configuration at China Lake, California.



<p><b>2019</b></p>	 <p>M600: All-Modes crosswind in Hawaii and first offshore flight in Norway (pictured).</p>
--------------------	-------------------------------------------------------------------------------------------------------------------------------------------------------------------------------

**Table 1: Flight Testing Timeline**

### 3 M600 Flight Test Program

By the end of its test program, the M600 had flown 22 hours and 3630 loops of crosswind flight (more details and flight statistics are presented in figure 1 and table 2). This was two-to-three orders of magnitude less than desired, as per the ultimate goal of the test program to validate a utility-scale commercial product and operation. We would have liked to show thousands of hours on M600 systems, and to test throughout the expected structural lifetime of a single M600 wing. Our expectation was that we were in the inflection point (figure 1) and, at the time Makani shut down, the plan for the next couple of years was to accelerate the pace of testing and to accrue the operational lifetime that would help us develop and validate commercial Makani systems.

The first five years of the M600 development were punctuated by expansions of the operating environment, from hover-only tests under constraints adjacent to the ground-based perch, to a fully autonomous all-modes flight off a platform floating offshore. Those steps are described in this section.

This account frequently refers to other articles in this technical report for more detailed descriptions of the system components mentioned, or for more in-depth discussions of the operation and performance of the M600. The "M600 Energy Kite Description" [9] is a useful reference to keep handy while reading the section that follows.

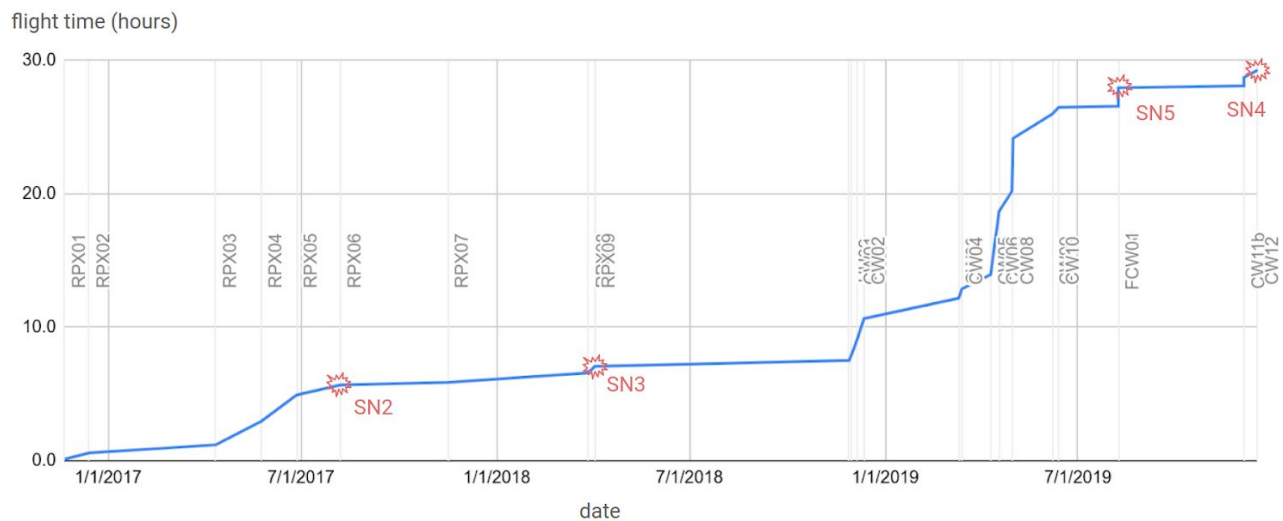


**Figure 1: Cumulative flight time of the M600 system without constraint lines. Each vertical line marks a flight: RPX-01 through RPX-09 in China Lake, CW-01 through CW-12 in Hawaii, and FCW-01 in Norway. The four airframes lost in flight, SN2 through SN5, are marked in red. Extended periods of no flight occurred when we incorporated major learnings (after the first flights in a new configuration or after a crash), and when we moved to a new test site.**

Flight Time (hours)	
Autonomous	28.9
Pilot-in-the-Loop	0.4
Hover	6.4
Crosswind	22.7
Off-tether	0.1

Crosswind Power	
Total Loop Count	3630
Loops with Positive Average Power	696
Best Single Loop Average	290 kW
Worst Single Loop Average	-521 kW
Best Ten-Minute Average	196 kW

Test Days and Unplanned End-of-Flight Events	
Crosswind Test Days	21
Glide Landings	4
Airframes Lost in Hover	3
Airframes Lost in Crosswind	1

**Table 2: M600 Flight Test Program Statistics**

### 3.1 Constrained Hovers in Alameda

We started hover testing the first M600 kite (SN1) in May 2015, before it was complete. That direction was set by the conviction that testing partially integrated systems would highlight critical interface issues as early as possible and would help drive subsystem development. In fact, almost every component in the assembly went through a design iteration before September 2016, when we shipped a full assembly of crosswind-ready SN2 to China Lake—our first crosswind test site.



**Figure 2: The first M600 ground station, GS01, and the first assembled kite, SN1, under constraints at the “E-Lot” hover test site in May 2015. In this photo, the kite is still missing major components, including ailerons and an empennage. Most subsystems (including the main wing structure, the motors and the motor controllers) went through a major design iteration before the crosswind-ready kite left the E-Lot in September 2016.**

The team followed the approach used to test the hovering mode of previous prototypes, Wing 6 and Wing 7—designing a top constraint derrick that could catch the kite and absorb most of the impact in the case of a power-out type of failure during hover. This was set up at a hover test site in the “E-lot,” a parking lot in front of the USS Hornet museum and about a mile away from Makani headquarters in Alameda, California. A similar constraint system was set up in subsequent test sites, China Lake and Parker Ranch (Hawaii), and used the first time we tested a new ground station configuration or a new kite at each site. The Norway campaign was the only time we did not use a constraint system for the first hover flight at a new site.

### 3.1.1 Commissioning Full Systems

The goal of the initial hover test program with SN1 was a functional demonstration of the integrated subsystems: flight controller; on-board and ground power; sensors and actuators on the kite and ground station; mechanical fit and interactions between the kite, tether, and ground station. The ultimate such demonstration possible at the E-Lot was to get the kite to complete launch-hover-land sequences from its perch, and some hover maneuvers such as altitude and

attitude steps with mass added to simulate the weight of a fully-extended tether. The E-Lot served as the site to commission and validate as many of the Makani system components and operation modes as possible before the costly move to the remote test sites where we could fly crosswind.

We built up to these goals in stages. The interactions of the avionics network, the medium voltage (MV) load path, and the flight controller were exercised first by spinning motors with the kite parked on the ground at the foot of the tower, strapped to its trailer, and plugged via an MV umbilical to the ground station. Some other tests involved spinning the motors directly, bypassing the flight controller, to test the power systems and the kite avionics. The mechanical fit of the tether and the kite on the ground station was first done with the power off, carefully lifting the kite onto the perch, guided by the constraints line hoist and a mechanical tether going onto the ground station winch. Since the first tethers were not yet built, we used a length of Spectra rope as the mechanical tether, connecting the bridled kite to the ground station, and we terminated pairs of SO service cord for the electrical connection. Some early tests of the estimator and flight controller state machine were also performed with the motors turned off, or with thrust scaled down to 10%, and using the derrick, guylines, and the ground station to place or move the kite through its poses.

By July 2015 we had built up to characterizing the hover simulation and testing the first version of the hover controller code, which was mostly a version of the Wing 7 hover controller with recalculated gains. These tests uncovered interactions between the rotor wash and the elevator that necessitated a significant design change, whereby we moved the location of the elevator from the top to the bottom of the empennage. That particular design iteration took almost a year to close: the new fuselage with the low tail was first flight-tested in June 2016.

The program moved on to exercise the various hover flight maneuvers involving ground station GS01, shown in figure 2. These sequences can be tricky to visualize, but there are snippets in the Makani video playlist that illustrate the relative motions of the kite and the ground station, and the video "20151128 Hover Flight - Teaching the Makani M600 to Fly Off a Ground Station" [17] summarizes the sequence accomplished with GS01 at the E-Lot.

We first tested the transition from "reel mode," which spans the majority of hover flight, when the tether is reeled on or off the drum as the kite hovers, to "high tension mode" during crosswind, when the tether is directly connected to the load-bearing ground-side gimbal (GSG). The kite was set up to hover about 7 m away from the perch, and as the drum winch turned to unwrap the final wind of a short tether and the tether disengaged from the levelwind, the tension provided by the kite turned the GS01 azimuth bearing until the GSG was pointing at the kite. Then the sequence was reversed, whereby the ground station rotated to first engage the tether in the levelwind, and then to reel it onto the drum.

The next sequence that we tested was launching and landing from the perch. The kite started on the perch with motors idling, then throttled up and ascended into hover, and then the tether was

reeled out a few meters. Then the sequence was reversed, ending with the kite back on the perch. This series of tests was wrapped up by November 2015.

### 3.1.2 Early Life Issues

Over that first year of hovering the first serial M600 (SN1), we found and addressed or circumvented a myriad of early-life issues with hardware subcomponents. A major source of such findings were the powertrains: complex electromechanical subsystems with high voltages, fast data rates, a liquid cooling system, and many moving parts. The powertrain issues are detailed as a case study in section 4.1, Hardware Design Evolution. This period included one iteration of motor controller, two iterations of motors, several improvements to the cooling loop, and issues found and resolved with the stacked power architecture, which is described in [7].

Many of these iterations with hardware components were expected. Hover testing ran in parallel with a comprehensive program of subcomponent validations and ground tests, so the first SN1 assembly used many parts that were not yet validated for crosswind operation. Crosswind would require higher load capability and bidirectional power, and a constantly changing kite attitude. Some components were knowingly not crosswind-capable. (Of course, we verified that components and subassemblies would function well within the scope of the hover demonstrations before incurring the effort of an orchestrated hover test). Some parts were prototypes that never panned out, or alternative functional solutions to allow a hover flight. As an example, the kite and base station were initially outfitted with ethernet-over-power (EoP) modems to send telemetry via the medium-voltage conductors on the tether, as had been previously done with Wing 7. However, the engineering work to use this system had not been completed. As the avionics team triaged priorities for development work, they developed a solution that combined long range and wide band radios to effectively transmit flight-critical and debug telemetry between the kite and the ground station. This solution proved to be sufficient and robust, and a year later the vestigial EoP components were removed from the kite and the ground station.

This also meant that some of the issues or “bugs” encountered during testing were not directly relevant to the eventual crosswind system, but they still needed to be resolved in order to move forward in the test program. We set a regular testing cadence of a week of testing followed by a week or two of integration, which was used to swap components for designs that were more fully vetted, and to troubleshoot or fix parts and systems that had failed during the test period.

### 3.1.3 Containerhenge

By the end of 2015, a significant incompatibility between the ground station (GS) and the first fabricated tether became increasingly apparent. The incompatibility was compound. The levelwind-engage maneuver described above was forceful, and it was prone to the high severity failure of damaging the tether if the levelwind was missed. The ground side gimbal (GSG) was massive, and it would require a bending-strain relief adapter to evenly transfer load to the tether without risking bending failure. The GS geometry around the GSG, with multiple interferences,

made the design of this device challenging. And there was a risk that the tether would break just sitting wound onto the GS drum. The first tether design had a “solid core”: a single pultruded carbon fiber rod as the internal strength member, in contrast to the design described in the “M600 Energy Kite Description” article [9], which had 19 smaller carbon fiber rods stranded in the style of wire rope. Some samples of the solid core tether failed due to creep compression buckling while stored in drums of similar diameter to the drum on the GS. The more flexible, “stranded-fiber core” tether design had been fabricated, but was still undergoing validations.

The team had overwhelming clarity that testing the system in crosswind, its power-generating flight mode, as soon as possible was key to the successful development of the technology. But a redesign and commissioning of a new ground station would be a multi-month and moderate-risk project, whilst everything else—the kite, the controls system, the power system, the avionics network—was ready to be tested in crosswind. We started to brainstorm ways to launch the kite straight up, starting with a fully payed-out tether, as had been done with every previous kite prototype described in table 1.

This led to the design of what came to be known as “Containerhenge,” a comparatively simple structure of two towers built out of flat-rack containers with netted landing pads on top, which is shown in figure 3 below. The kite was modified with mid-span landing pegs on the main wing's trailing edge, which would sit on the landing pads as the tail threaded between the containers. The flight controller was modified with a remote-perch flight plan. A new structure called the “Top Hat” was developed to mount on the ground station tower's azimuth bearing to carry the GSG and the ground sensors suite, doing away with the larger and more complicated structures of the ground station, the winch, and the perch.

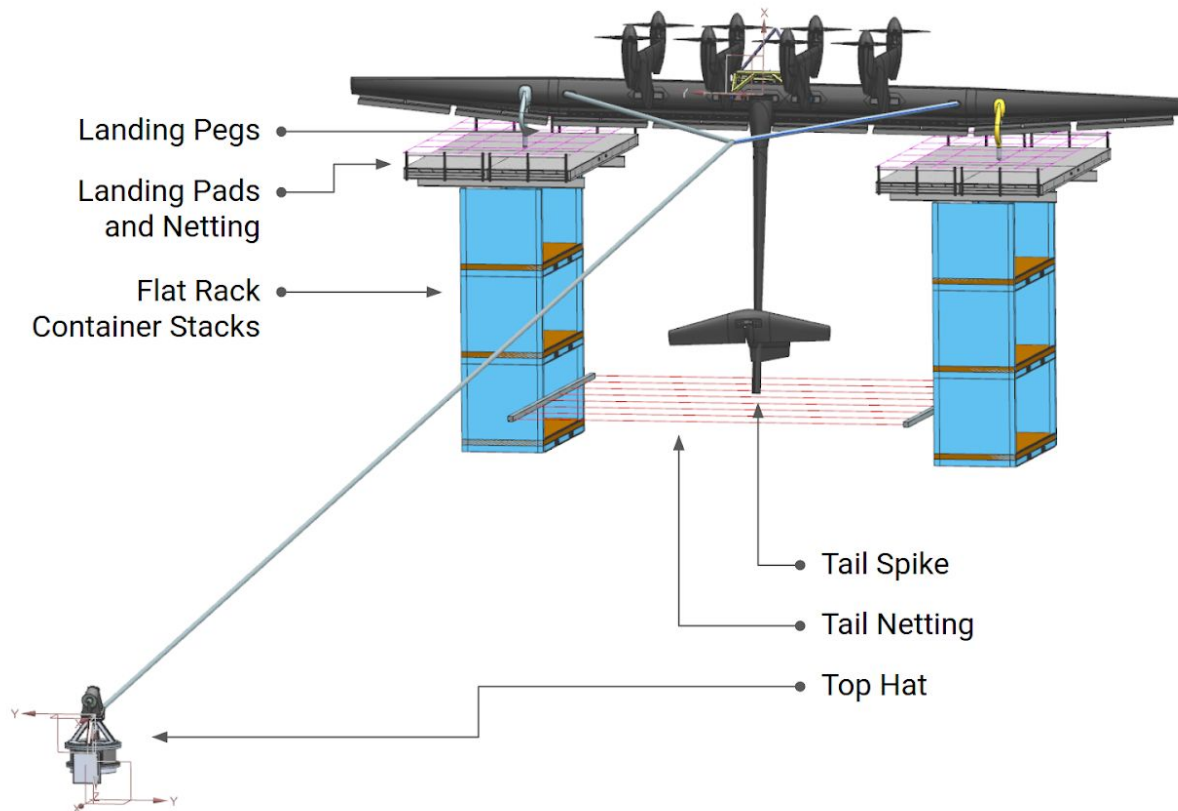


**Figure 3: Rendering of Containerhenge, showing the two stacks of container flatracks, the landing pads on top of the stacks, and the netting to constrain the kite by the landing pegs on the wing trailing edge and the tail spike protruding from the fuselage. The Top Hat frame holding the GSG is also shown.**

Throughout the first half of 2016, Containerhenge and the Top Hat were built, the other necessary system changes were implemented, and the new configuration was validated at the E-Lot. In March 2016 we completed the first fit-check by lifting the kite onto the perch. By late April we completed ascend-descend cycles including 9 m ascends where the tail would clear the containers.

### 3.1.4 Relocation and Later Tests

During the summer of 2016, the design teams continued to slate crosswind-ready sub-components to commission between hover tests. This included the main wing (SN2), a new revision of motors, the tether, tether-release electronics, and ground power distribution containers.

In September 2016 we completed a Relocation Readiness Review, concluding that we were ready to move to the crosswind test site at China Lake, near Ridgecrest, California. We had confidence that every component and interaction was crosswind-capable, and yet we carried

many risks. Notably, we proceeded with the move despite unresolved motor controller issues that could lead to a motor-out and loss-of-kite in an unconstrained hover (potentially before completing the first crosswind milestone!). This is discussed in section 4.1.4.

After moving crosswind-ready systems to China Lake, the E-Lot test site continued to serve Makani. In 2018 it was used to commission a new design of the ground station, GS02, which was later moved to Parker Ranch, the test site in Hawaii, to demonstrate all-modes operation of the M600 system: from perched to crosswind and back. The last test under constraints with SN1 at the E-Lot, in 2018, verified the "short-stack" system, which added the capability to survive a motor-out condition in hover by shorting out one layer of the motor stack and continuing to operate with six motors.

## 3.2 Remote Perch Crosswind (RPX) in China Lake

### 3.2.1 The Range

The first M600 crosswind test site had to meet some unique requirements. Before the Federal Aviation Administration (FAA) developed guidance to effectively mark our operation as an obstruction,<sup>2</sup> we needed to find restricted airspace in which we could test without posing a hazard to aviation. We needed to have control over an area on the ground that was large enough that we could restrict access and control a safety perimeter downwind of our flight. And the wind had to be "good" enough to fly crosswind. These were satisfied within China Lake's restricted airspace near Ridgecrest, California. Makani operated at China Lake from October 2016 until April 2018.

The test site at China Lake is pictured in figure 4. Two 500 m-long radial strips were cleared, starting at the tower and along the two prevailing downwind directions. Containerhenge was re-assembled at the end of the westerly radial, and a constraint system was set atop a 230-ton crane. The tether was laid out from the ground station Top Hat, along the radial, towards the kite on Containerhenge. Since the perch was not collocated with the base station, these crosswind flights were dubbed "Remote Perch Crosswind," or RPX for short.

---

<sup>2</sup> We started collaborating with the FAA on said regulation in 2013, when they visited Sherman Island to observe a Wing 7 crosswind flight. This served to set some marking guidelines we could follow with the M600. But before the FAA observers could return to assess the markings implemented on the M600 in crosswind, we first had to figure out if we could fly crosswind at all! The first crosswind test site was in restricted airspace so that we could develop our confidence in flying. The second crosswind test site, in Hawaii, was the first time we would fly in public airspace. Having reviewed their observations of the scaled Wing 7 system, and our marking scheme for the M600, the FAA issued a temporary, 18-month Determination of No Hazard for our operations in Hawaii [13]. Their follow up visits to assess the conspicuity of M600 operations are described in section 3.3.3.



**Figure 4: China Lake Test Site. The kite is seen in crosswind flight, and the ground equipment visible from the ground includes (from left to right): the tower and Top Hat, three containers with the ground power inverters and switchgear, the SODAR wind profiler, Containerhenge further back along the cleared radial, and the command center on the far right.**

We came to know the idiosyncrasies of the wind at each of our test sites. At China Lake, this was dominated by a common pattern of the western United States: strong afternoon westerlies from the spring to the early fall, as low pressure over the hot desert east of the Sierra Nevada draws the cold air from the Pacific Ocean. Our site was only a few kilometers east of the Sierras, and prone to strong lee effects: lee waves and rotors with sharp features with characteristic scales of about a kilometer, such as described by Smith and Skillingstad [14], and shown in figure 5.

This meant a couple of things that made forecasting particularly challenging and “waiting for wind” particularly exciting. First, the wind speed and wind direction at our test site could be very different from that at nearby weather stations. And second, from one moment to the next, a strong westerly could simply disappear, or fully reverse direction. At our test site, when a westerly “disappeared,” the conditions on site would often be taken over by a milder southwesterly wind—which we perceived on the ground as a shifting wind direction. These two dominant patterns are illustrated well by an instance captured in figure 5. The trends led us to clear the two radials: along headings of 90 degrees and 10 degrees. However, we never fully commissioned the more southerly radial, and so flight testing was always limited to occur

within a long enough window of consistent westerly forecast, such as for the day of RPX-01, which is shown in figure 6.

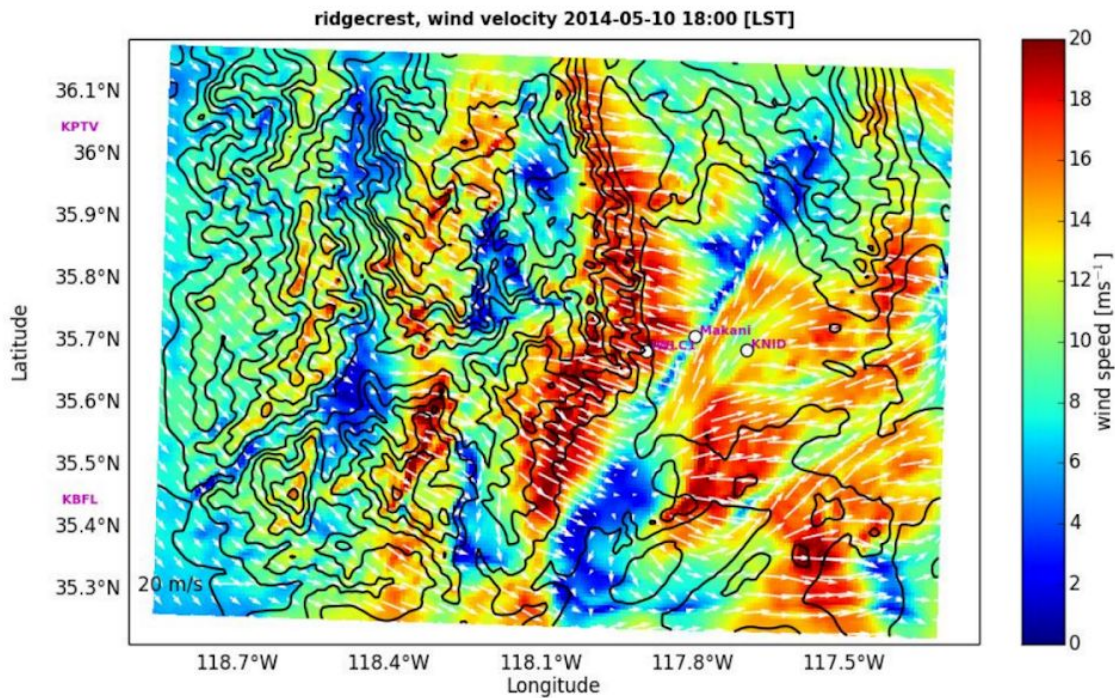


**Figure 5: Map around the Makani test site showing terrain (contours) and wind velocity (colormap and quivers) at 10 m on an afternoon in May. Note that the three neighboring weather stations would show very different wind conditions: strong westerly at IWLC1, calm at Makani, and a moderate southwesterly at KNID. The wind map is derived from the same WRF model used by our contractor at the Desert Research Institute (DRI) to forecast conditions for Makani flight tests.**

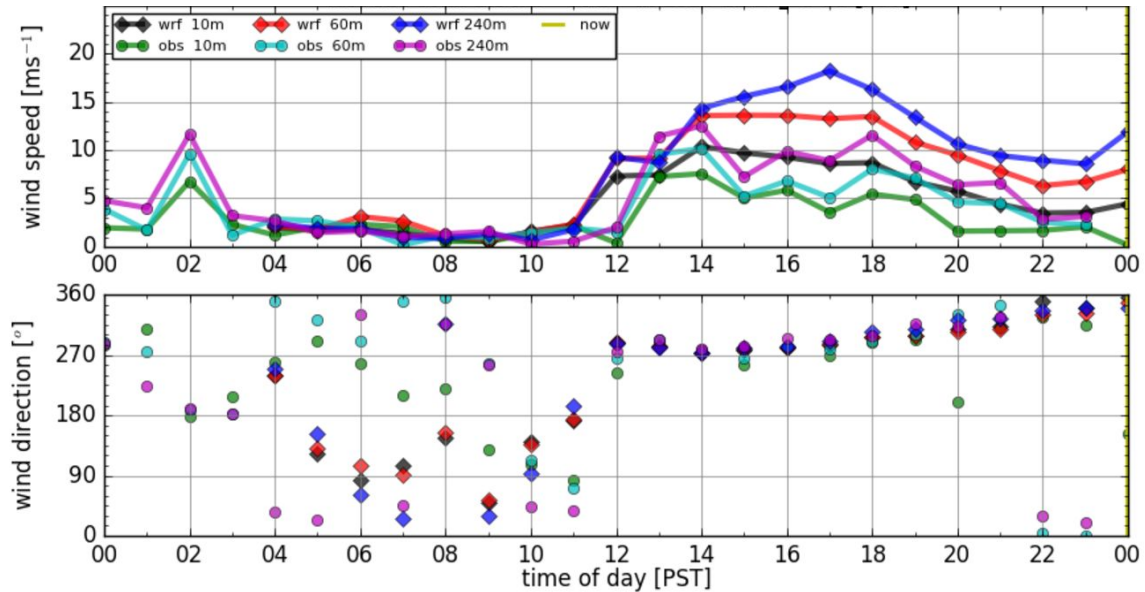


**Figure 6: RPX-01 “day-of” wind forecast (WRF model) and measurements from the ultrasonic sensor on the Top Hat (obs 10 m) and from the SODAR (obs 60 m and obs 240 m). This day was representative of what turned out to be a “good” afternoon for testing, with westerly winds in the 5-10 m/s range, in the wind envelope set for our first crosswind flight. It was common for the forecast to lead or lag the quick westerly onset by about an hour, and to under- or over-estimate wind speeds by a few meters per second.**

### 3.2.2 Functional Demonstration of Crosswind

The first objective of the RPX program was a functional demonstration of the M600 system in crosswind, as well as the transitions from hover and back (“trans-in” and “trans-out,” respectively).

The first attempt, RPX-01 in November 2016, took us as far as the transition into crosswind, and immediately after that the solid core tether snapped at the ground-side termination. The pilot released the kite from the bridles and glide-landed smoothly enough that the main wing and the pylons survived the impact. The tether team traced the cause of the break to the weakening of the core during the period of several weeks when the solid core tether was left hanging from the tower before the first flight attempt. For RPX-02, the team tested with the first stranded-fiber core tether and modified the bending strain relief (BSR) frame to support more bending load.

The first successful crosswind flight, RPX-02, was achieved on December 14, 2016: on the last day, and in fact in the last hour of operations of the range before closing for the year. This first crosswind flight exercised almost every M600 subsystem in almost every flight mode, and it had an action-packed ending. Soon after trans-out, the kite started losing altitude quickly. It recovered, seemingly miraculously, within about 10 m from the ground, but the drama was not over yet. The wind was gusty and had shifted south during the flight, so by the time the kite approached Containerhenge to attempt a landing, it was fighting to maintain a stable azimuth.

At some point, the tail spike hit the top of a landing pad and broke off, hence we could no longer land the kite on Containerhenge without damage. The tail spike is necessary to prevent a "face plant" after throttling down the motors. We elected to re-enter crosswind and from there command a tether release and conduct a glide landing. This episode is featured prominently in the Makani documentary [5].

A few days after the test, all of Makani gathered to share observations about how each subsystem had performed in flight, and posit theories and share early analysis of the events at the end of the flight. The presentation materials from that day are shared in Part III of this report, "Selected Decks from RPX Lessons Learned Reviews" [15]. In reviewing those decks, note that the nature of the review was to share early observations from flight data (telemetry logs, testing team reports, and flight video), rather than complete analyses.

We were especially interested in verifying the loads and structural modes of the M600 airframe during these early flights. SN2 was outfitted with instrumentation (accelerometers, strain gauges and gyros) that was not part of the avionics network, and therefore not in the regular flight telemetry. This data was saved into a stand-alone data acquisition unit and streamed via a separate radio to the team in the command center. During the early flights we expected this to be an important monitor in real time, warning us to back off from maneuvers or flight strategies that were overloading the structure. However, the system was finicky, and often the radio would not be working before take off, so the risk of flying without this monitor was assumed as part of the launch-time decision. The wing design proved out, and we did not overload the wing during controlled crosswind flights.

We did encounter resonant modes in the airframe, especially as the motor speeds ramped up during launch. The pylons would shake and flex, and usually this would damp out as the motor speeds reached the higher values that were typical in hover. On one occasion, this effect was exacerbated by an experimental feature that had just been added to the controller to regulate roll attitude by redistributing the thrust command to rotors with different spin directions. In the first crosswind attempt after RPX-02, the pylon shaking was particularly violent, and the testing team aborted the launch (see video "20170203 Hover Flight - Makani M600 Pylon Shake") [8]. We had done major damage to the pylons, which had to be replaced, grounding the kite for another month. This issue was resolved by reverting the hover controller to the version without the roll control feature.

### 3.2.3 Fly Better, Fly More, Make Power

From April to August of 2017 we established a regular cadence of crosswind flight. RPX-03 through RPX-06 were flown at a rate of about one flight per month. This was a period of rapid learning and improving how the kite flew crosswind.

**Make Power**

After the first successful landing back on the perch in RPX-03, the team's attention turned to power generation. We experimented with increasing the angle of attack to increase performance, lowering the loop altitude to reduce elevation losses, and reducing the loop size to reduce gravity losses and further reduce elevation losses. The article "Airborne Wind Turbine Performance" [2] has an in-depth discussion of the effect of each of these strategies on the kite's power curve. These experiments were first implemented as test cases, with discrete changes to the outer loop commands that were turned on and off during flight. And yet, during RPX-04, with 10 m/s average wind, the maximum loop-average power generated was a mere 65 kW.

The frank observation was that the kite was doing a poor job of following commands; as shown in figure 7: the kite was flying almost 200 m radius loops on a 150 m radius command. The angle of attack excursions were on the order of +/- 3 degrees from command. In order to make more power, it was clear that we had to improve crosswind control. "The Makani Autopilot" [10], also in this volume, includes an in-depth discussion of the crosswind controller architecture and improvements made throughout the test program.

Figure 7 also shows how we modified the trans-out trajectory. In RPX-02 the kite transitioned into hover at a high altitude, which made the hover less controllable because the motors had to use more thrust to carry the weight of the tether, and because the geometry reduced the stabilizing horizontal bridling moments. By RPX-06, we were transitioning more gracefully into a low, stable hover with adequate tether tension.

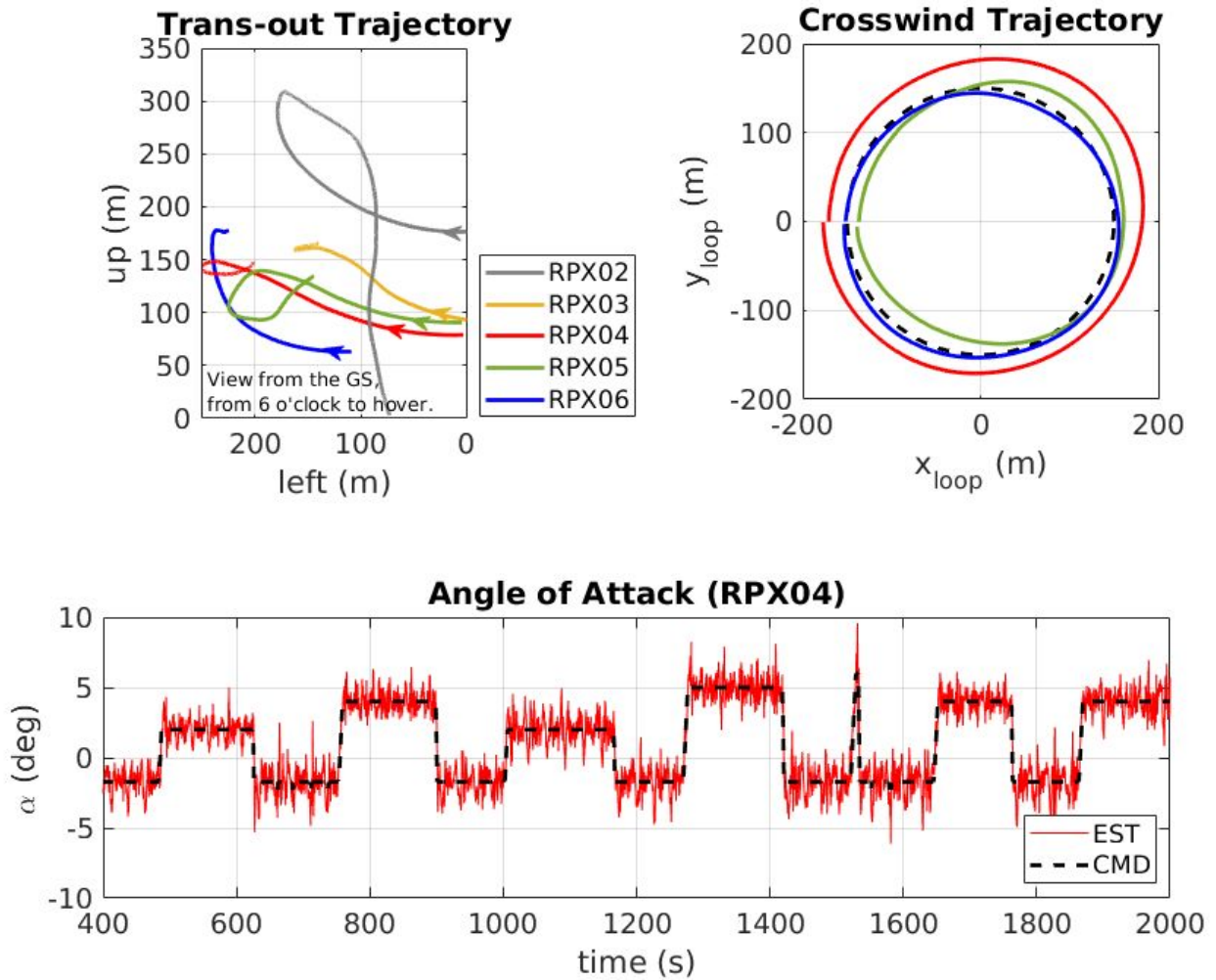


**Figure 7: Selected flight data from early RPX flights. The top left plot shows the trajectory of the kite during the last fraction of the last crosswind loop and the few seconds of hover after trans-out, as viewed from the tower. Note the high trans-out of RPX-02, followed by a dramatic loss of altitude, versus the clean switch where we “stick the hover” after RPX-06, after a number of controls changes. The top right plot shows the commanded crosswind loop (dashed line), and improvements in tracking thanks to controls changes between RPX-04 and RPX-06. The bottom plot shows a series of test cases commanding different angles-of-attack in RPX-06. Note the excursions around each command.**

**Fly Better**

With each subsequent flight, we learned major lessons that led to changes that improved flight controls.

We lost SN2 at the end of RPX-06, due to a bug in the state estimator that manifested after the kite transitioned out of crosswind into hover. A typo<sup>3</sup> in a code change caused a roll rate gyro bias estimate to diverge during crosswind—and this faulty estimate was used to correct the attitude estimate after the mode change to hover. The issue had not been discovered in a thorough preflight validation that, unfortunately, used a processed data structure as the input to the estimator, rather than using the simulated sensor data directly and applying the avionics conversion routines. The kite “thought” that it had rolled 120 degrees after trans-out, and promptly yawed itself out of the sky.

Bringing up SN3 was an opportunity to integrate significant hardware changes to the system. One major change for RPX-07 was to upgrade to new motor controllers, named “Ozones,” which resolved latent and high severity issues, described in detail in section 4.1.4. The second major change was the addition of slats to the leading edge of the main wing. Slats extend the lift profile of an airfoil such that stall is delayed to higher angles of attack, and the team had an interest in commanding an optimal angle of attack to generate power in crosswind, while preventing stall in case of transient excursions from those commands. The target angle of attack for the M600 was around 7 degrees.

In RPX-07 we only ever commanded an angle of attack of 3 degrees. The wind increased and shifted direction, and the whole flight went awry. Among compound flight dynamics issues, the airspeed error saw large oscillations, which in turn commanded steep power rates from the ground power system. At some point, the diesel generator was not able to keep up with the slew rate and shut down, leaving the kite without motor control and unable to hover. The pilot released the tether and glide-landed the kite. In lieu of a full discussion of this flight, from which we learned from many aspects of the operation, the lessons learned decks are included in Part III [15]. These include observations of crosswind flight quality, such as control surface saturations and poor path tracking; a discussion of the glide and of the recovery procedures, since the kite pitched down as it landed and ended up on its nose; and proposed upgrades to the ground power system to make it more robust to fast changes in power demand.

In RPX-08 we commanded an angle of attack of 10 degrees and quickly observed a pitch instability with growing angle of attack oscillations. The team was developing a more comprehensive understanding of the dynamic stability of tethered, crosswind kite flight, and the analysis was starting to shed light on the difficulty of flying the M600 kite in particular. These learnings are captured in a report included in Part II named “Kite Stability in Crosswind Flight” [11], which was developed to inform the MX2 design described in “Oktoberkite and the MX2” [12]. Adding slats changed the center of gravity and the aerodynamic center of the main wing in such a way as to reduce the longitudinal and lateral static stability margins, as well as to reduce the open loop stability of most dynamic modes. The control system was working to close the

---

<sup>3</sup> The specifics of this typo, which snuck in through several layers of review, are described in “The Makani Autopilot” [10].

loop, but, especially in the presence of gusts, control surfaces were often saturated, leading to an open loop, marginally stable plant.

Then, in RPX-09, we lost SN3: the main wing snapped in half in mid-air, after a gust event in which we lost control of the kite, leading to an uncontrolled and jerky return to the taut tether. The spectacular videos showing this event are labeled "20180410 RPX-09 - Mid-Air Break Up" on the *Makani - Energy Kite Technical Videos* playlist on YouTube [8], and section 3.3 covers in more depth the root cause investigation and corrective actions that followed.

We were intent on a step change improvement in our understanding of crosswind dynamics to establish robust flight. But even as we necessarily questioned our ability to fly robustly in crosswind, the time pressure to advance our technology's development also necessitated that we make a bold decision. With RPX-09 analysis in progress and SN4 under construction, we proceeded with the previously-formulated plan to move to the Hawaii test site (described in section 3.3), where we would launch and land from the newly commissioned ground station GS02.

### **Fly More**

The time pressure to advance in the development of our technology was related, through funding milestones, to the urgency of deploying a solution that would truly contribute to global, accessible clean energy. This kept the goal of "flying more" at the top of the list of flight objectives. We learned an immense amount during the RPX program, and yet the learnings were limited to a single-digit number of flight hours, whereas our intent was to develop a machine that could operate for a few thousand hours every year.

Two factors we were only starting to address by the time of RPX-08 were the limited duration of each flight, and what had been so far a preference to do one flight at a time and accommodate planned changes before the following launch. Flight duration had been limited by the capacity of the on-board batteries used to power the 72 VDC bus that served the kite avionics and servos. RPX-05, for example, was ended after 1 hour and 45 minutes of crosswind because the battery level was low. By RPX-08, we integrated a MV-LV converter to step down the 3400 VDC bus to 72 VDC, and flight duration was no longer limited by battery life. Starting with RPX-08, we would set out on test campaigns to complete multiple flights after a given release of hardware and software changes. RPX-09 launched just a few days after RPX-08, and we continued a pattern of two flights in a row, launching CW-02 a few days after CW-01, and so on throughout 2019.

## **3.3 On-shore All-modes Crosswind in Hawaii**

From mid-2017 to mid-2018, the testing team split their effort between crosswind flights in China Lake and hover flights at the E-Lot, commissioning GS02. These two programs merged with the relocation of all testing operations to the first public crosswind test site, on Parker Ranch land near Waimea, on Hawai'i Island, shown in figure 8. Makani tested in Hawaii from August 2018 through December 2019.



**Figure 8: Hawaii Test Site in 2019. This drone photograph shows the 5 m tower and kite SN4 sitting on the perch of GS02. In the foreground are the ground power inverters and the switchgear to the HELCO electrical grid.**

The ground station, GS02, was shipped from Alameda and mounted on a shorter, 5 m-tall tower (see figure 8). Flight test experience had demonstrated that the taller tower, originally envisioned to keep the tether clear of the ground during the transition into crosswind, was not necessary. In fact, a lower perch made the kite installation to the perch swifter, and it allowed preflight checks and other troubleshooting and maintenance requiring team members working in aerial lifts to be done more safely and expediently. This argument by the testing team weighed strongly against the argument by the systems team, described in “Airborne Wind Turbine Performance,” [2] that power generation losses would be minimized by reducing the flight elevation angle, and therefore by increasing the tower height. The height reduction would only cause a 3% attenuation in power available. The short tower even allowed the testing team to experiment lifting the kite with a 5-ton telehandler, which would reduce the operation to two people instead of the carefully orchestrated lifts requiring a team of up to 6 people, a 130-ton crane, and several guylines.

### 3.3.1 The Ranch

Makani's main on-shore test site was conceived to allow us to accumulate thousands of hours of operation in regulated airspace and interconnected to the electrical grid. Here we would streamline procedures and maintenance, learn about our impact on the environment and our relationship with the community, and gather power performance data on our path to certification. The permitting process and outreach that started years prior to the testing team's arrival included:

- *Securing a Temporary Determination of No Hazard (DNH) from the FAA*, based on discussions and evaluations that had started during the Wing 7 flight test program at Sherman Island [13]. A condition for this permit was that the first flight be attended by observers from the FAA Obstruction Evaluation Group to assess the desired conspicuity of the system to air traffic. Neal Rickner reported on progress in this process at the 2019 Airborne Wind Energy Conference [18].
- *Applying for a grid interconnection agreement with HELCO*, the electric utility company. As we commissioned the test site, Makani completed the permitting, installation, and inspection of certified switchgear and we went as far as using power from the grid for the ground station operations. However, we did not get to set up the batteries and safety disconnect that would allow us to use the grid for bidirectional power during crosswind. Instead, Makani's crosswind flights always operated with a local microgrid as pictured in figure 8: a 2 MW diesel generator to supply baseload power, the necessary switchgear, six inverters to convert 480 VAC to 3400 VDC, and a load bank.
- *Completing biological surveys of the area*, followed by a bird and bat conservation plan [19] observing the applicable recommendations in the Wind Energy Guidelines published by the US Fish and Wildlife Service [20]. This plan established procedures that we incorporated into the flight testing training and checklists, such that the Makani team could monitor and respond to any impact on the local fauna. The initial survey was also intended to serve as a baseline to later assess the environmental impact of sustained operations.
- *Actively engaging with the community*, in particular by attending Waimea Community Association meetings to brief attendants on the details of our project, answer their questions, and collect feedback and concerns that we could act on. For instance, we camouflaged the field operations tent to make it less visible from the road, and we chose work lights at the pad for night time operations that respected the dark sky in conformance with the outdoor light ordinance in the Hawai'i County Code. Makani volunteers also led wind physics workshops at middle schools on the island. Our active community engagement connected us with a network of local vendors, contractors and suppliers whose knowledge and expertise benefitted us immensely.

### 3.3.2 High Hover

Both SN1 and SN4 were shipped to the island. As part of introducing the project to the community, these kites were given Hawaiian names by local Kahu Danny Akaka in a ceremony

drawing on the tradition of blessing canoes before they went out to sea, as shown in figure 9. SN1 was named *Huapala*, which means “ripe fruit,” an old-fashioned word for a faithful companion like a cowboy’s workhorse. SN4 was named *Kikaha malea apae me ka lanakila*, or Lanakila for short, which means “soars well and lands victoriously.”



**Figure 9: Kahu Danny Akaka blessing SN4, which he named named *Kikaha malea apae me ka lanakila*, or Lanakila for short.**

Huapala, SN1, was used to continue to validate GS02 through the transform maneuver. Could we in fact “thread the needle”? Hovering the kite high and carrying the full length of the tether, we had to control the tether elevation angle departing the GSG within the clearance window between the levelwind and the perch, as the ground station swung around from reel mode to high-load mode. This high hover implied that on the first real transform attempt the flight could not be completed under the safety constraints line, so we decided to use SN1 rather than expose the brand new SN4 to this risk. The tradeoff was to manage the configuration differences between the two kites, which included the previous generation Gin3 motor controllers, with the associated vulnerabilities described in section 4.1.

The first high hovers were executed in rapid succession on November 28 and 30, 2018 (see “20181128 HH-01 - Hover Flight” in the Makani Technical Videos Youtube playlist for a video of the first full flight [8]). Indeed, controlling the tether elevation proved difficult, and high hover would quickly develop into altitude oscillations. This was even more pronounced during reel in.

The marginal stability of this system had to do with the low bandwidth associated with the control strategy: kite altitude was used as an actuator that was coupled via the low stiffness of the tether catenary to tether elevation at the base. The controls analysis of the first high hover test data, and the desired changes before the second high hover, had to be developed, validated, and implemented quickly, before the first all-modes crosswind flight, which was scheduled for the week of December 3rd, 2018. As a trusted workhorse, SN1 survived the trial and we promptly swapped to SN4 to fly crosswind.

### 3.3.3 Hours of Crosswind

The first all-modes crosswind flight in Hawaii, CW-01, felt like a great accomplishment for several reasons:

- We flew in a newly-commissioned site.
- It was the first M600 all-modes flight, from perch launch to successful perch landing by Lanakila (SN4).
- It was a successful return-to-flight, exhibiting good crosswind flight dynamics after many corrective actions and changes addressing the root cause of the RPX-09 crash, which is described in more detail in section 4.3.
- We flew on schedule for the FAA observers to witness the flight. In fact, in order to complete their observation test plan, we flew CW-02 the following week. Makani was then permitted to fly at will during the daytime after simply filing a notice-to-airmen (NOTAM) with Kona airport.

As a good first, this crosswind test campaign in Hawaii started many new threads: issues to resolve and procedures or designs to streamline or revisit, in order to improve the operation. The CW-01/CW-02 lessons learned decks, in Part III [16], give a good sense of the breadth of observations made across Makani teams. The controls team reviewed crosswind flight performance after dozens of controls changes using, among other things, the dynamics replay tool of Makani's flight simulator. Other team's reviews discuss learnings about operations with two active kites on site (SN1 and SN4), and the performance of a lot of new hardware, such as the ground power set-up and the MV-LV converter.

The program progressed while balancing two main goals. On the one hand, there was a focus on increased automation and robustness. We wanted to reduce the chance of requiring pilot intervention so as to fly with confidence at night during the next visit of the FAA observers that was scheduled for the spring. We were also preparing for the first offshore flight in Norway, scheduled for the summer, which demanded the ability to operate hands-off.

On the other hand, there was a focus on flying in higher wind speeds and reaching rated power. The test cases from the RPX campaign had given way to the "playbook," a tabulation of the optimal flight strategy for power generation at each given wind speed, setting the loop size, the

path elevation and azimuth, and the angle of attack and kite speed schedules around the loop.<sup>4</sup> Makani was yet to produce 600 kW with the M600, or to fly robustly in winds above 12 m/s.

The cadence was once again set to one hardware and software configuration release per month, this time leading to a test campaign of two back-to-back flights after each release. Lanakila flew CW-03/04 in March, CW-05/06 in April, CW-07/08 in May, and CW-09/10 in June, and returned to the perch safely each time. The longest flight was CW-06, at almost four hours of crosswind. The most power produced was during CW-07, with a 196 kW 10-minute average in 10-13 m/s wind speed.

The FAA returned to the site to observe CW-07 and CW-08. Each of these flights started in the late afternoon and continued until nighttime, while the observers flew in a small aircraft around the test site, approaching from different headings and in different light conditions. The goal was to assess whether the kite and tower lights were conspicuous to the pilot, effectively indicating the location and nature of the obstruction. The team in the command center was in contact with the observers and could adjust the brightness of the lights and the frequency of the flashes. The preferred pattern, shown in a 30-second exposure captured in figure 10, was a double-flash at a rate of 40 times per minute, synchronized with the wing tip, tail, and tower lights.



**Figure 10: Makani lighting demonstration for the FAA during a night flight at the Hawaii test site in 2019. The long exposure over a crosswind loop shows the wing tip and tail lights, and the base station tower light, flashing synchronously at 40 flashes per minute. The patterns that appear to be double flashes are, in fact, overlapping successive flight loops.**

<sup>4</sup> The elements of this strategy are discussed in "Airborne Wind Turbine Performance" [2].

Overall, we achieved better crosswind flight quality than during the RPX campaign, but it was not without events that indicated we still had important work to do to achieve robust flight dynamics. Notably, on a low-wind day with inverted shear, CW-06 exhibited some of the same bad dynamics we were now sensitized to: frequent path tracking and angle of attack errors, large roll rates, and aileron and rudder saturations. The wing aloft was as low as 5 m/s and exhibited some veering with respect to the 8 m/s wind measured at the ground. The wind direction often swung +/- 20 degrees. For almost two hours we flew in “fallback” mode, a safe flight strategy commanding large, high loops and moderate angles of attack. A discussion of data from this flight, including the effect of the ambient wind on the flight trajectory and on flight quality, are included in the lessons learned decks in Part III [16].

Another troubling crosswind behavior was first noticed during one loop in CW-08, which showed a wing stall event. The tufts recorded by an onboard camera on the main wing got tousled for a long second before the flow reattached and the tufts realigned—and the flight data showed a fast excursion to 10 degrees angle of attack. This video, “20190501 CW-08 - Onboard View,” is included in the Makani technical videos YouTube playlist, and the event occurs about 2:50:30 into the test [8]. A similar event was observed in CW-09: this time, the video captured a pulse travelling down the tether following the fluctuation in wing lift. Then on CW-10, which launched on a misty day, the flight was sketchy from the get go, showing angle of attack oscillations on almost every loop. The flight was aborted once, reattempted, then ended. The analysis of this event was never completed, but a strong argument was made that the root cause was environmental, since there had been no plant or flight controller changes since CW-09. It is likely that the M600 airfoil design was not robust to the surface contamination caused by water droplets, which made it more prone to stall. This was a consideration in Makani's next-generation (MX2) kite airfoil design, described in the article in this volume called “Oktoberkite and the MX2” [12].

Also notable was that we were usually flying right up against the azimuth limits set, for safety considerations, by the location of the command center. One of the playbook strategies was to shift the flight path away from the downwind direction as the wind speed increased. When the azimuth limit was reached and the wind kept increasing or turning towards the flight path, the playbook would resort to flying higher and larger loops. This would then cause high variability in power around the loop and make us more susceptible to airspeed error excursions in the downstroke. Artificially curtailing our optimal flight strategy in this way was one of the contributing factors to the lukewarm power performance of the M600 during those crosswind flights. A discussion of the M600 power curve is included in the article “M600 Energy Kite Description” [9].

As the summer drew near, the team paused testing in Hawaii and moved to the newly commissioned offshore test site in Norway. We took advantage of that reprieve to move the command center at Parker Ranch to a new upwind location that would no longer constrain the playbook azimuth strategy. We also re-thought the network connections to the tower in a way

that would allow us to develop and test a network configuration representative of a remote command center that, in a hopeful future, would be located onshore, and therefore several kilometers away from the offshore base station and the kite. The intended goal for the flight test program once we came back to Hawaii was to make progress towards the continuous, unattended operation that we would need to demonstrate in offshore pilot projects. Once again, the metrics that would measure our progress towards that goal involved flight hours: could the system operate autonomously (e.g. landing if the wind died) for 24 hours in a row? Could the operation tally a thousand hours of crosswind in 2020, after having completed only about twenty so far?

### 3.4 Offshore in Norway

In Norway, Makani set up a shore base to assemble and commission the M600 systems, and an offshore location to complete the first-ever crosswind flight of an energy kite from a floating platform. The shore base, shown in figure 11, was located at GMC Gismarvik, a field office and warehouse with quayside access to 50 m-deep water in a sheltered fjord (the Fosnasund), where we could moor the uprighted spar buoy that would serve as our floating platform. The spar buoy is described in more detail in the "M600 Energy Kite Description" article [9]. We called this shore base the "Sealot," as a nod to our hover "E-Lot" test site in Alameda. The offshore site, shown in figure 12, was in the Marine Energy Test Centre (Metcentre), in 200 m-deep water and 10 km west of Skudeneshavn, on the southwest coast of Norway. Video of the flight, which took place on August 8th, 2019, can be found in the Makani video playlists [8, 17].

The command center and the microgrid were assembled on a barge. A subsurface cable umbilical (SSC) was developed to carry all power (4 kVAC and 4.5 kVDC) and optical fiber network communications between the barge and the base station.



**Figure 11: Norway "Sealot" quayside test site at GMC Gismarvik.**



**Figure 12: Norway offshore test site at the Marine Energy Test Centre (Metcentre), showing the barge with the command center and the microgrid containers, and the tug boat for station-keeping (top left).**

### 3.4.1 Deeper Water

Expanding our operating environment to the ocean was necessary in the path to verify our business proposition: that energy kites could be flown from relatively small floating platforms, which could be affordably deployed over broader areas of the globe where there was power in the wind blowing offshore. Specifically, in this first offshore campaign we intended to verify a spar design, establish operations at sea, and demonstrate all flight modes (launch, land, and crosswind) off a floating platform that would pitch and heave when pulled by the tether as the kite flew crosswind loops.

That said, deciding to go offshore when we did was bold. The decision to fly the M600 kite off a floating buoy offshore was made in November 2017: after just a handful of hours of flight that revealed hundreds of operational issues. In January of 2019 we shipped the second serial of the base station,<sup>5</sup> GS02-02, to Norway after just having completed the first all-modes flight in Hawaii a couple of weeks prior with dozens of unresolved issues. To demonstrate broad operational capabilities we had to distribute our efforts across various aspects of development. And we had to assume that we would be successful along the way because, due to the scale of our technology, we had to start planning operations in new test sites and at new scales years ahead of time. The short period of our funding cycles reinforced the need to be bold, as we had to prove new capabilities every year.

To handle the additional work, while the majority of the team was focused on challenges at China Lake and Parker Ranch, we assigned a small but dedicated team to prepare the site and the changes associated with getting ready to fly offshore. Throughout 2018 a team of two was busy finding and securing the sites and the permits; contracting an Engineering, Procurement, Construction and Installation (EPCI) firm to develop the spar buoy; and figuring out how to export and ship equipment and how to do work in Norway. The system integration team in Alameda assembled and commissioned GS02-02 and a new M600 kite (SN5) with enclosures and connections revised to improve water-proofing. The command center from the E-Lot was modified with remote emergency-stops and marine power supplies and backup systems.

In the first half of 2019 we commissioned all M600 systems at the Sealot. The transition piece was a conical structure analogous to the tower of the onshore ground station: its flanges mated to the spar buoy at the bottom and to the base station at the top. It housed transformers, switches for all network and power connections, the human platforms, and the SSC hangoff. The base station was assembled onto the transition piece sitting on the yard first, to confirm the operation and calibration of all axes' drives and all sensors. The command barge was moored and the command center, ground power, microgrid, transformers and SSC winch were installed on it. The spar buoy arrived and was uprighted and ballasted quayside. The kite was reassembled and commissioned.

---

<sup>5</sup> The preferred term for GS02 became the "base station," instead of the "ground station," since it was destined to float on the water.

Meanwhile, the simulation and controls teams started preparing for the offshore flight. The first step was to simulate the motion of the buoy due to both the sea state and the tether tension. We augmented the estimator to calculate the heave, sway and pitch of the base station. Remarkably, the crosswind controller did not require major modifications. Work on the hover controller focused on improving control of tether elevation, since the already narrow clearance for the transform would now move with the base station; accelerating the launch and the approach, so as to spend the least amount of time hovering close to the bobbing perch; and timing the final landing descent to coincide with a downward base station motion.

Some hardware modifications were also slotted in as the flight season approached. Since the kite would not be accessible for the usual pre-flight steps or frequent troubleshooting tasks, one engineer designed an actuated protective cover for the pitot tube that would slide on and off on command. Others integrated an onboard camera with the kite's low voltage bus and avionics network. We also developed a remotely operated and monitored restraint system to hold the kite onto the perch during the tow to the offshore site and after landing. We added a sloped block to the ground station winch to push the levelwind frame to a higher elevation angle and improve the clearance for the tether during the transform.

Makani contracted Technip / Genesis to complete EPCI for the spar buoy. Their scope of work encompassed the entire process from detailed engineering design, through procurement and fabrication, uprighting the buoy quayside, installing the base station assembly on the top flange of the spar buoy, and finally towing the buoy, with the perched kite strapped securely on, to the offshore test site to moor it to the ocean floor. Our contractors, with decades of global offshore work experience, coordinated marine operations during the flight test campaign: ferrying the testing team to the command barge and coordinating between the Makani team and the tugboats positioning the barge. One of the operations that we developed procedures for was how to salvage the kite debris in case of an uncontrolled landing in the water.

### 3.4.2 Floating Crosswind Flight

All systems were set up at the offshore site and checked off, the wind and waves were within the established envelope, and the team was ready to launch, just eight days after the spar buoy cast off from the quay. It was noon in Norway and 3 am in California, and about a dozen engineers were monitoring the flight from Makani headquarters in Alameda.

The kite launched, but after a few meters, the testing team paused the pay out. It turned out that the levelwind elevation sensor had been miscalibrated, and there was a yellow warning light on the monitors in the command center. The kite reeled back in and landed on the perch. Having quickly confirmed the levelwind miscalibration, the team recalibrated on the fly and launched again. This time, the system stepped smoothly through all flight modes into crosswind flight.

In 10 m/s wind and 1 m-high waves, with virtually no wind shear and low turbulence, and flying a conservative playbook, crosswind was smooth and all flight quality scores were nominal. The spar buoy travelled almost 60 m downwind as the kite pulled it, pitching, as expected, between 2 and 15 degrees over each loop (see figure 13). After an hour and 24 minutes the wave height was starting to approach the limits recommended by the marine operations teams for transferring personnel off the barge, so the team decided to end the flight.

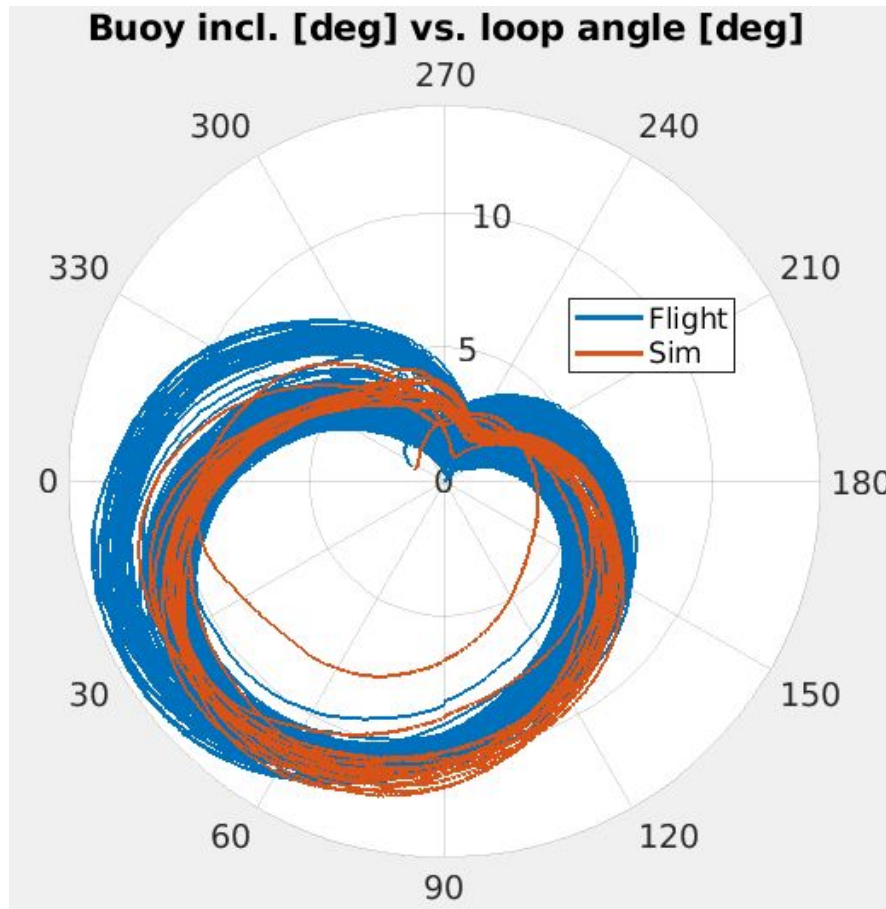


**Figure 13: Buoy inclination during FCW-01, taken from the Controls Lessons Learned Review prepared a few days after the flight. The blue line represents flight data. The red line represents the simulated buoy inclination using the logged tether-tension data. The kite travels clockwise around the loop as depicted here, which is from the point of view of the base station.**

After a successful transition, the kite hovered towards the appropriate downwind position and elevation to attempt the base station transform maneuver. However, at this point, the kite diverged in roll and soon lost attitude control and fell into the sea. The report of the investigation that followed is included in Part III of this volume [23]. We had previously had other close calls due to our inability to maintain a stable roll in hover, as discussed in more detail in section 4.4 and in “The Makani Autopilot” [10].

### 3.4.3 Safety Culture

The testing team was deliberate about safety during on-shore testing, which has its fair number of hazards: high voltages, overhead loads in lifting operations, large moving bodies, and long days outdoors. And the team recognized that offshore operations implied more, and more acute, hazards: colder temperatures, the possibility of getting seasick, slippery decks, and objects sliding or tipping in the rolling vessels. Almost any activity offshore is arduous, requiring significant physical activity and the imperative to stay focused or engaged.

A strong aggravating factor, despite attempts to plan around it, was time pressure. The offshore campaign had to be complete before mid-September, when we would encounter rougher sea states. Marine operations had to be booked 30 days in advance, and we wanted to leave room for a second chance if the first attempt had to be aborted, so our first offshore window was booked for late July/early August. Within that window for which vessels and operators were booked, there was likely a precise day determined by the wind and wave forecast that we would have to target for the flight attempt.

The pressure of the impending deadline was compounded by the fact that the team must travel internationally to work for a few weeks at a time, and away from home. Therefore, everyone was motivated to get as much done as possible during any one trip to Norway. The long summer days provided more hours of possible productivity. And the team in California was on a different schedule, which meant that the team in Norway would often have a second shift after dinner, catching up with colleagues in California.

The offshore campaign became a catalyst for shifting Makani towards a more explicit safety culture. Following the example of partners and contractors with broad offshore experience, and, in particular, investor Shell, the offshore team meetings began with a "safety moment." The team would take turns to remind each other of good principles such as the "buddy system" (always working in pairs, so someone can check your work and can also get help in case of trouble), and everyone's "right to stop work" if they saw something that felt unsafe. As we developed procedures and plans for the summer, again following Shell's lead, we organized a comprehensive hazard identification workshop that brought together Makani, Shell, GMC, Genesis / Technip, and other contractors that would support the campaign. The Makani team followed PPE policies at the GMC site that included wearing high visibility clothing and eye and ear protection whenever working at the warehouse and at the quay.

All this said, after the offshore season was over, we were disappointed with our safety record. There were several incidents during the season: some near misses, some that led to hardware damage and jeopardized the campaign, and one unfortunate incident that led to a contractor injury during the mooring operations. As an example of a near miss, during the kite assembly at the Sealot warehouse, a lifting set-up was incorrectly rigged and the spreader bar slid off and fell on the wing, damaging the wing skin. Among the contributing factors, we identified

ineffective communication of the roles assumed during the procedure between the Makani team, who had arrived recently, and the local site operators, whom they had just met. Both teams had a proactive response to the incident: developing and reviewing safe job procedures together before each significant task that had to be done on site from then on. The Makani team was able to do a wing repair in-place, incurring only a moderate slip in schedule. Among the organizational responses to this assessment, we started setting quarterly safety goals, formed a safety integrated product team (IPT) led by our CEO, and paused work to do a day-long all-hands safety reset workshop.

## 4 Case Studies on Selected Learnings

In our test program, we set out to establish what the M600 could do (functional demonstrations), how well it could do it (performance validations), and, occasionally, to characterize its response (system modeling experiments). However, our major learnings went beyond that: we improved designs, deepened our understanding, and refined our high level requirements. Our flight testing approach was better geared towards discovering unknowns, which, given the nature of our endeavor developing a technology solution that was both novel and complex, we found to be the most valuable results from testing.

The case studies discussed in this section relate to learning about and improving our technology by discovering unknowns:

- *Evolving hardware designs.* Throughout the testing program there was a constant iterative process of hardware and software subsystem design changes to address issues encountered in flight. We describe many issues encountered with the powertrain subsystem in early testing, and how addressing these issues led to better designs.
- *Improving physics models.* We often improved our simulation after noticing flight testing data that did not match our models. The example discussed here relates to correcting the estimate of airspeed derived from the pitot tube measurement.
- *Understanding, rather than validating performance.* The crosswind flight capabilities of the M600 would impact the performance bottom line. We deepened our understanding of these dynamics as we grappled with the mid-air breakup of SN3 during flight RPX-09.
- *Changing requirements.* We lost SN5 in hover after FCW-01 in a manner that highlighted the poor roll stability in hover for our system as-conceived. This aspect of our energy kite design was being re-thought as is discussed in “Oktoberkite and the MX2” [12].

### 4.1 Hardware Design Evolution: Powertrain Bugs

We were weeding out issues in the entire powertrain system since early hovers, and as such it is a good case study of how a continual test program and persistent operation in the field guides the evolution of a system into a mature, reliable block. This section describes more than a dozen critical powertrain issues found over the first 20 months of testing the M600, which had to be addressed by changing or making major revisions to components. In comparison, since late 2017, for the last 15 of 20 hours flown, there wasn't a single powertrain issue that led to a redesign.

Powertrains are complex systems, so the nature of issues that arise is also diverse. In this section, rather than doing a deep dive into a single event, we describe a sampling of bugs that illustrate the diversity of issues dealt with in field testing. The intent of this account is to convey both that dealing with these issues led us to better designs, and that it is effortful—involving

troubleshooting or swapping components in the field, and managing ensuing operational and risk decisions.

For context, before diving into the account, figure 14 shows an early revision of the M600 powertrain components as they were packed into the nacelles at the top and bottom of the pylons. The 130 kW motors were custom-made, and the motor controllers were designed in-house and comprised a main board with a computer, network I/O, and three gate driver boards in a cooled enclosure. The cooling loop consisted of a gearpump magnetically coupled to the motor shaft, a filter/accumulator, a radiator mounted onto a duct, and hoses connecting the pump to the radiator, the radiator to the motor enclosure, and the motor to the motor controller cooling plate. The wiring harnesses carried a 1400 VDC bus for high power, and two twin 72 VDC avionics power buses and twin optical fiber ethernet channels for the communications network.

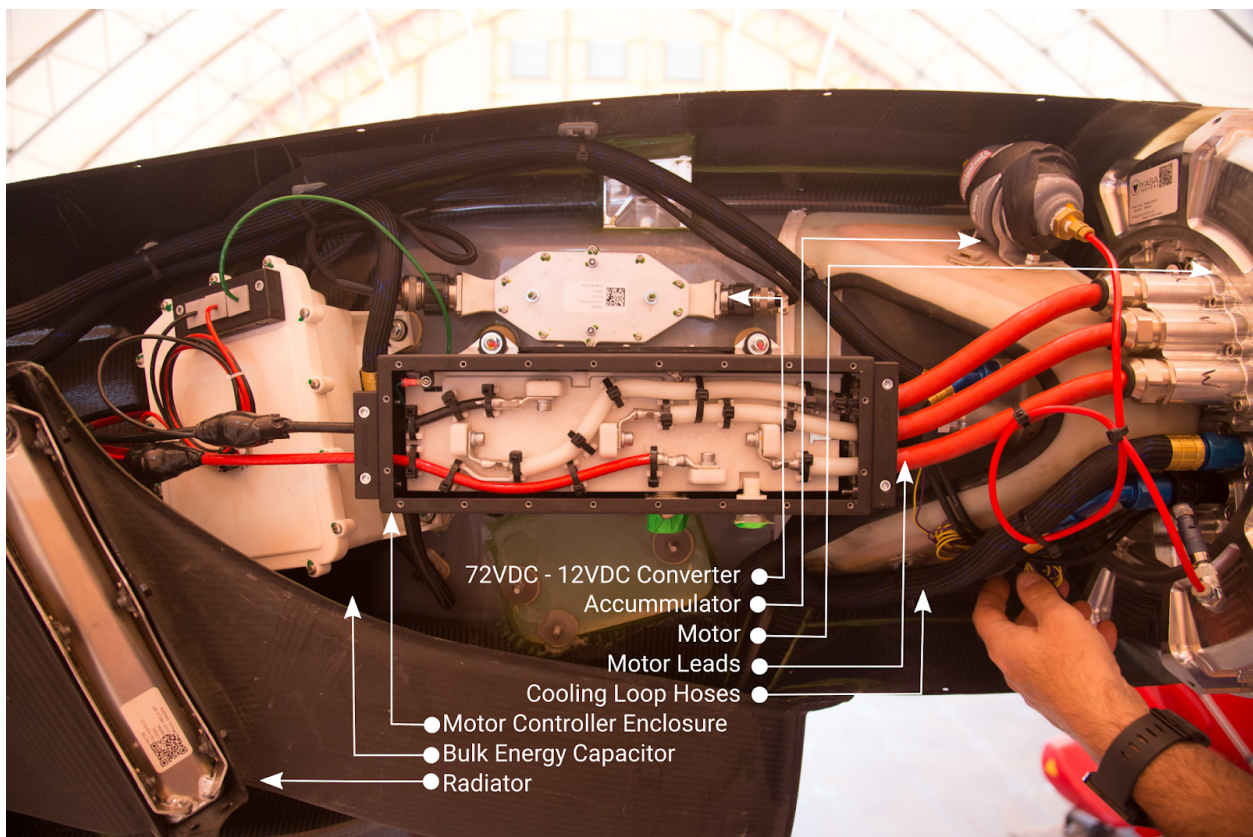


**Figure 14: A powertrain installed onto a top nacelle and photographed from an aerial lift in the tent in China Lake. From left to right, you see the radiator slotted into the exhaust duct, the capacitor bank enclosure, the Gin3 motor controller enclosure, the cooling loop accumulator, and the motor.**

### 4.1.1 Things Get Hot: Debris in the Cooling Loop

We assembled the first M600 powertrains with off-the-shelf motors that did not support the full operating regime but that allowed us to get a head start with testing. We used them in the Iron Bird, a test fixture with a steel structure used to mount eight powertrains and to connect them to the avionics network for system testing in the correct topology before the airframe build was complete. We also used them for the few first hovers of the integrated airframe in the summer of 2015. Specifically, these motors had a dry, potted stator: a possible operational advantage that would allow using water as the coolant, but that also results in poorer thermal performance and therefore lower sustained peak torque and power.

One minute into the very first M600 hover in June 2015, the motor drive temperature for the top port inboard powertrain, shown in the command center monitors, climbed rapidly compared to the others. After the flight, the team methodically took apart and photographed the entire cooling loop, and they found aluminum chips in the line that had jammed the gearpump. Some forensics, including material composition analysis at the X reliability lab, revealed that the debris came from the coolant jacket housing inside the motor. All the powertrains were then disassembled and inspected for debris in the coolant loop. Troubleshooting, developing, and implementing ways to resolve the issue delayed the next hover for a full four weeks.

Even though we were due for a change of motors, and the motors were the source of the issue, encountering this problem was not in vain. We still got several minute-long hover flights that test day, which allowed the controls team and other subsystem owners to begin characterizing their designs and planning the next tests. The mechanical engineering team improved the cooling loop design by adding a filter and an accumulator, changing the pump flow rate, and updating procedures for flushing the loop during installation.

Cooling issues continued to be observed throughout those first months of testing, and the rapid pace of concurrent subsystem changes sometimes led to red herrings. In August 2015, while dry-running for the first hover with the new YASA motors, a different powertrain heated up faster than the others (this time the starboard bottom inboard powertrain). We suspected that either the cooling loop fix hadn't been effective, and perhaps there was still debris floating around, or the change in the pump flow rate was causing the magnetic coupling of the pump to disengage. Eventually, however, the issue was isolated to the poor airflow into the radiator duct in that particular location.

In this case, finding the issue uncovered an interface discrepancy between the aerodynamic design of the pylons and the unforeseen requirement for alternating prop-rotation configurations to manage pitch and yaw coupling in hover. The duct inlets were designed assuming a consistent direction for prop rotation along the bottom of the wing. This issue was quickly addressed on SN1 by installing wickerbill-like sheet metal scoops to modify the shape of the inlet duct and to better guide airflow into the radiator.

Temperature is a loud indicator of hardware issues, flaring up when a system has to work harder to meet its commands, and seeing temperatures rise in the command center monitors was common. It was especially indicative of a malfunction when temperatures rose in a single location within a regular array, such as in the kite's powertrains. However, temperature values were also likely to approach limits evenly as design tried to optimize performance with respect to cost, complexity, or mass—so it was not surprising that we were accustomed to looking for, finding, and addressing hot components.

Before moving to the first crosswind test site in the California desert, which saw regular daily temperatures above 40 C in the summer, we focused on better thermal management across subsystems. For a year before the relocation, every team was reassessing designs for the first extreme real-life operating environment that the M600 would encounter: the hot desert. We would later learn from other harsh environments: China Lake also introduced us to high wind turbulence, hurricane season in Hawaii subjected the kite to heavy rainfall, and Norway brought salt and waves to contend with.

As it pertained to the powertrain, the power and testing teams focused on improving the operational hassle of swapping components in the field as well as developing design changes to the motor controller enclosure. The former involved difficult maneuvers, especially in the top nacelles, with aerial lifts close to light and delicate carbon fiber aerodynamic surfaces, and carrying operators with the tools, pumps, and buckets used to flush the coolant. Instances of this operation are shown in figure 15 and figure 16.



**Figure 15: Swapping a powertrain in the field required pumps to flush and refill the coolant.**

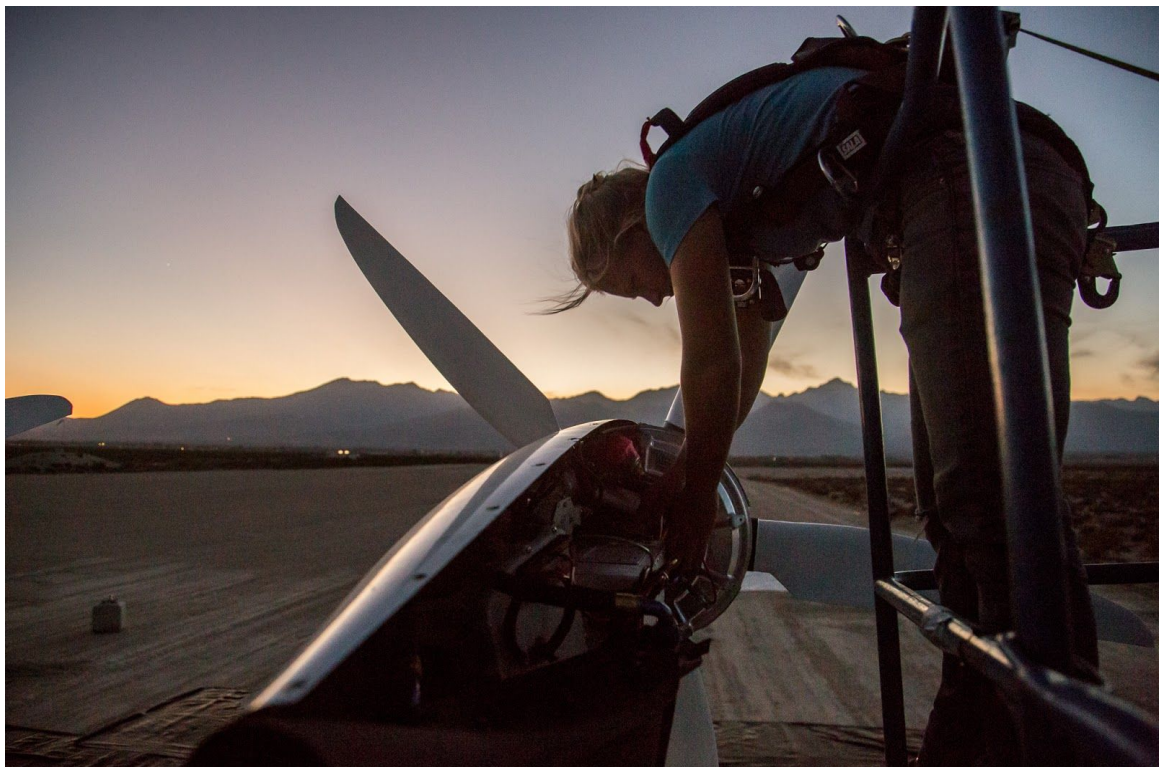


**Figure 16: Aerial lifts were used to access the top nacelles to troubleshoot or swap powertrains.**

### 4.1.2 Things Rub: Yasa 2 Motor Issues

We soon replaced the motors with a bespoke outrunner YASA design, dubbed YASA 2, and were flying the YASA motors by the end of August 2015. The wet stator design is capable of much higher sustained heat flux, leading to higher allowable current density and higher sustained torque, at the expense of requiring pure, clean insulating oil. The off-the-shelf motor was also improved to provide higher torques and better voltage isolation.

The YASA 2 motors were going through validation testing to the initial M600 specifications using ground-based test fixtures, but the testing program was rapidly uncovering aspects of the M600 system that required modification of the specifications. Particularly affecting the motors, we had increased the propeller blade length to better meet growing thrust requirements from missed mass targets, and the built props came in heavier than specified, increasing gyroscopic loads. The pylon torsional vibration modes were more pronounced than expected. All of these led to higher mechanical loads on the motor bearings than were originally planned for.

We uncovered the first issue in November 2015, during vibration reliability tests on a ground fixture: the aluminum stator bulkhead cracked close to the motor mount. This initiated a minor revision, referred to as YASA 2.2, that included a bulkhead reinforcement. Then, in February 2016, the testing team found a coolant leak after a day of testing, which was quickly isolated to the motor housing. The investigation revealed evidence of rubbing between the rotor and stator due to the unexpectedly large loads on the motor bearing. YASA 2.2 was quickly superseded by YASA 2.3, with a larger, sturdier bearing. We first hovered with YASA 2.3 motors in September 2016, with less than a month left to complete integrated system validations before we relocated to the remote crosswind site in China Lake.

Besides a bigger bearing, we also incorporated several opportunistic design changes into the 2.3 motor revision, presuming that performance needs would continue to creep beyond the original M600 requirements as we continued to increase the operating envelope and moved to more strenuous environmental conditions. These changes included: a longer stator capable of achieving more torque, a smaller winding number to fine tune the torque constant, bigger phase leads to reduce heat bleeding back into the controller, and a much higher isolation voltage rating, in anticipation of a higher tether voltage.

### 4.1.3 Things Shake Loose: Gin2 Motor Controller Vibration Issues

The first iteration of the motor controller assembly that flew on SN1 was Gin2, and we hovered with Gin2s from June 2015 to April 2016. As should be expected, ground and field testing revealed issues with the packaging of components into the enclosure that led us to a redesign.

The first event occurred as early as November 2014 during a ground-based vibration endurance test: the lead of a capacitor fatigued and broke. The same type of failure occurred in a flight test

in late September 2015. The data showed small voltage dips that we indeed traced to a capacitor detaching from the bus bar due to a broken solder joint.

Another failure found during vibration endurance testing was traced to a poor connection between the main board and the gate driver boards: the pins were not fully seated, and many had insufficient solder. There were a few unexplained, catastrophic failures on Gin2 motor controllers deployed into powertrain assemblies, and it is possible that some of those traced back to this weak connection. The first such event happened in January 2015, during a motor-run with the integrated kite still in the hangar. The voltage dropped suddenly, and opening the motor controller enclosure revealed the sooty mess shown in figure 17. We never found the precise source of the fault.

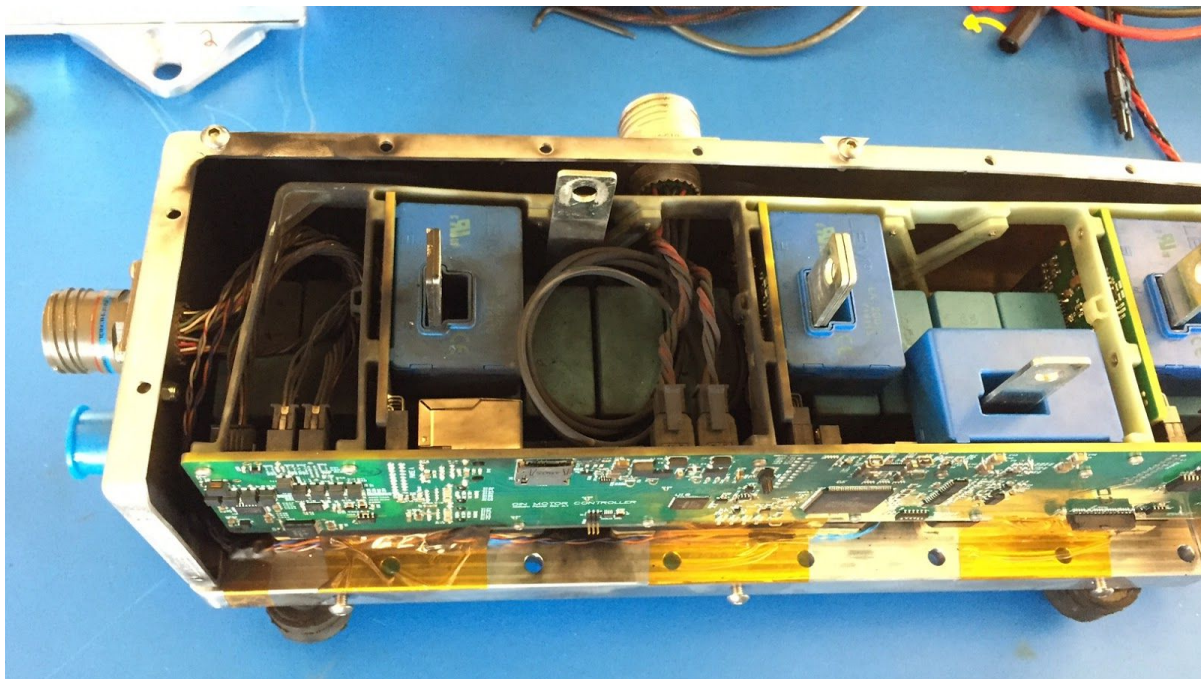


**Figure 17: A unit from the first batch of Gin2 motor controllers after an unexplained catastrophic failure during routine ground tests.**

Some of the unexplained, catastrophic failures of Gin2 motor controllers happened during actual hover flights. In December 2015, a motor controller faulted during hover, the motor turned off, and the kite dropped out of the sky—to be saved by the top constraint line. (A video of a similar event, “20150828 Hover Flight - Makani M600 Drop on Constraints” is included in the Makani technical video playlist [8]). When we opened the motor controller enclosure, we found that a loose screw had backed out and shorted the bus bar to the motor controller housing. Our analysis traced this back to quality control during the enclosure assembly: loose screws in this position were found on several units.

The kite dropped on constraints again in February 2016 because of another motor controller failure. The culprit of the soot inside of the motor controller enclosure this time around was also never found. It turned out that the hover flights of the previous test day had to be cut short because the motor controller drives were heating up quickly, and we had replaced the cover of the motor controller with a perforated lid as a temporary way to improve cooling inside the enclosure. So one hypothesis was that debris or condensation could have snuck in through the 1 mm-wide perforations and caused the short. Another hypothesis, of course, was that another loose part in the assembly had caused the fault and then disintegrated.

The power systems team redesigned the motor controller enclosure in January 2016, officially calling it Gin3, but more often referring to it as the “belt-and-suspenders” design. This incorporated a more robust chassis to secure the gate drives *and* adhesive pads to hold the capacitors in place. It also added thermal gap pads to connect the main board to a new external heatsink on the enclosure.

#### 4.1.4 Things Turn Off: Gin3 Motor Controller Assorted Issues

Just as the powertrain is the most complex subsystem of the kite, the motor controllers are the most complex subsystem of the powertrain: its collocated brain and beating heart. Diverse Gin3 motor controller issues came up often in 2016, during the period leading up to the first crosswind flights. These were usually high severity bugs that caused the power system to shut down—a foreboding prospect once flying without constraints, when shutdown would lead to a loss of kite. The worst case scenario at that stage of the testing program would be to lose the kite during the hover right before the first crosswind flight that we were working so hard to achieve.

- **March 23, 2016:** During a manual motor dry-run before flight, a motor stopped spinning. The motor controller issued a “*Power Good*” error, sensed at the input of the gate driver boards. Eventually, the issue was attributed to electrical noise at the pins of the power quality sensor. We circumvented it by changing the error message to a warning, which alerted the operator in the command center with a yellow light. We also changed the response to motor errors in flight to alert the operator with a red “ABORT” light, rather than shutting off a motor. “Power Good” warnings showed up often with the Gin3 generation of motor controllers.
- **September 12, 2016:** Five hours into a 16-hour endurance hover flight validation, once again a motor shut down and the kite fell onto the constraint line. This was one of the last validations we sought to complete before relocating from the hover test site to the remote crosswind test site. This issue was traced to an *instability in the stacked power controller*, due to a delay in the network messaging between motor controllers, and was promptly corrected with a firmware patch.
- **September 19 and October 10, 2016:** On the last planned test day at the hover test site (September 19), after 17 hours of endurance hover validations, one powertrain did not spin up. We swapped powertrains and decided to relocate to the crosswind test site

anyway: everything else was ready for the move, and despite the criticality of a fresh motor controller issue, we needed to continue making progress across the entire M600 testing program. Alas, during one of the first dry runs at the new test site (October 10) a different powertrain failed to spin up. Both events traced back to the same issue: a *shorted common-mode choke* on the motor controller. The root cause of this failure on the Gin3 motor controllers was never resolved, despite extensive bench testing and forensic analyses. It gave us mild comfort, categorized as a lower severity risk, that the failure seemed to happen only upon bringing up voltage, and not during operation. This issue remained unresolved on our risk register until we changed to a new motor controller design dubbed "Ozone," in the second half of 2017, which used larger and more conservatively rated common mode chokes.

- **October 20, 2016:** On the first day of hovering under constraints at the crosswind test site, a different motor controller failed and turned off, and the kite once again dropped and was caught by the safety line. The issue was traced to the *failure of a 5V regulator* in the motor controller, and remained as a high severity issue in our risk register. This was traced back to a capacitor on the board being exposed to high temperatures, and a failure analysis from the manufacturer reports a manufacturing defect and an observed failure rate of 1 parts-per-million. This issue was also resolved with the Ozone motor controller design, described later in this section, which addressed components overheating.
- **November 2 and November 9, 2016:** A motor warning observed in the command center during a constrained hover on November 2 caused us to end the flight. The warning reoccurred on November 9, the day we had planned to do the last flight under constraints before the first crosswind attempt. The power engineering team analyzed the data from both tests, noticed that one phase had stopped switching, and recommended swapping out the powertrain. Once the hardware was inspected, the team found a *MOSFET gate oxide failure* and the associated discoloration that could be explained by a history of running hot. Indeed, they traced this unit's serial to the powertrain assembly involved in the rotor-stator touchdown incident described in section 4.1.2, Things Rub, when the cooling loop lost its coolant, and yet the powertrain ran for about a minute after touchdown.

Eventually, we completed our first off-constraints flight (RPX-01) in November 2016, and our first crosswind flight (RPX-02) in December 2016, with four unresolved and critical motor controller bugs, listed in table 3.<sup>6</sup> In fact, we completed a total of six unconstrained flights, through RPX-06 in August 2017, without any of these issues being resolved, and without any of them manifesting during unconstrained flight.

---

<sup>6</sup> One of the issues in table 3 is not recounted in the bulleted list because it did not manifest during a test day. On a ground fixture in October 2016, *shoot-through* occurred as a gate driver board lifted off its connecting pins, staying open while the drive switched phases. This motor controller had previously run in a G-load fixture designed to reproduce crosswind forces on the mechanical assembly.

Issue	Likelihood	Severity
Common mode choke short	2	2
5V regulator failure	1	3
Shoot-through	2	3
'Power good' warning	3	1

**Table 3: Unresolved, critical motor controller issues carried as risk during the RPX-01 through RPX-06 launch decisions.**

We made this bold decision because we had to balance the risk of losing the kite during one of its first unconstrained hovers with the urgency to learn about every other part of the system in crosswind. For each of the dozens of subsystems that make up one kite, the engineering teams were waiting for that data from the first crosswind loops to identify their own sets of critical issues. We needed to test the whole M600 system through its range of functions. We could have delayed the crosswind attempt until we resolved the powertrain issues, but that would have necessarily delayed learning in crosswind, whereas the risk we were taking assumed a less than one-in-ten chance that we would lose a kite in hover before getting to that precious first crosswind.

The urgency factoring into this decision also had to do with the need to meet the technical milestones that would drive additional funding. We had scaled up from the 20 kW Wing 7 to a larger, more expensive 600 kW new kite, and we had spent a year and a half hovering it under constraints. We needed to demonstrate that we could fly crosswind.

The issues listed in table 3 were eventually resolved when we swapped to Ozones, a new motor controller design, first installed on SN3 in September 2017. The power systems team wanted to redesign from the ground-up, addressing all the issues a priori, and accommodating for future features, such as continuing to fly on six motors after a single motor failure by shorting out a stack, and lightning protection.

This encompassed better mechanical design, weighing more highly considerations around tolerance stacking, thermal expansion, vibrational flex, and using flexures to mitigate tolerances. We paid more attention to mechanical tolerances on connectors to make sure they didn't vibrate loose and they could withstand high G-loads. We approached thermal design targeting all components, and not just the MOSFETs: we needed to effectively cool the capacitors, the gate drivers, and all internal power supplies.

Another main motivation for the redesign was that higher-rated 1700 V silicon carbide (SiC) MOSFETs had become available since Gin3. Increasing the voltage rating for the powertrains would allow us to short one stack without having to change the ground voltage. We

complemented this component change with mechanical design changes to support higher currents and higher voltage isolation. We used better buswork and larger wires and connections, specifically motor wires, and allowed more space between components at different potentials, shifting away from our previous preference for compact designs. Also, by improving isolation, we could now ground the motors to the wing chassis for better lightning protection. Finally, we updated some of the faulty components, such as the common mode chokes and the voltage regulators, with more conservative choices.

## 4.2 Modeling Physics: Pitot Airspeed Estimate

Any simulation team knows that their models are missing some physics and that the simulator is only an approximation of the real world. The art of it is to accurately capture the aspects of reality that most drive the response of a given design, and a mismatch between simulation and test data is the first indication of the need to improve the fidelity of the model. Makani made a sustained effort to improve the fidelity of the simulation where it mattered the most.

In RPX-07, we noted that the bus power generated at each motor was higher than estimated by using the rotor tables, which map angular speed and inflow velocity to thrust or drag. The top rotors were often generating 80 kW, yet the mechanical power estimate predicted 40 kW. Figure 18, taken from the RPX-07 Lessons Learned presentation [15], shows a time series of the power comparison. The key observation during the ensuing investigation was that the pitot tube was located in the stagnation region ahead of the mass balance tube (MBT), which can be seen in figure 19. The airspeed estimated from pitot tube measurements already accounted for body rates, the wing upwash, and rotor-induced inflow, but not for stagnated flow due to the MBT.

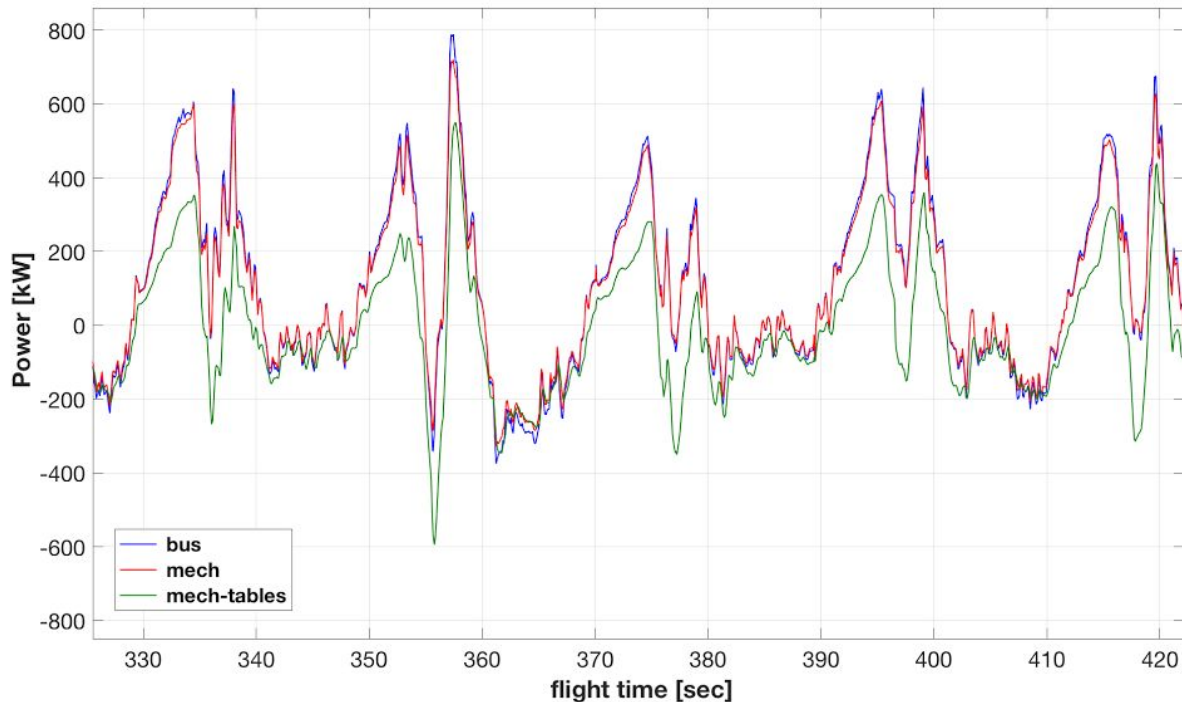


**Figure 18: Time series of power generation by the sum of all eight rotors during a portion of crosswind flight in RPX-07. The blue and red lines show direct electrical bus power and mechanical power calculated using flight telemetry. The green line shows the power estimated using estimated inflow velocity and rotor speed as input to the rotor tables. The discrepancy is as high as 200kW during the peaks in generation.**

The airspeed estimates had been off by 10%: when the team thought the kite was flying at 40 m/s, it was in fact flying at 44 m/s. This was easily corrected by using a coefficient of pressure derived from computational fluid dynamics (CFD) runs. It explained, among a few other things, why estimating the kite's lift and drag coefficients had been elusive over the six previous RPX flights. In calculating coefficients of the form  $C_F = F/qA$  from flight data, the team kept looking for a ~20% error in the force estimates  $\hat{F}$  derived from tether tension measurements, and all along the majority of that error lay in the airspeed estimate  $\hat{v}_a$  used in the dynamic pressure  $q = \frac{1}{2} \rho \hat{v}_a^2$  of the denominator.

Some would justifiably argue that this finding came too late in a flight test program. For instance, we had been carrying pitot tubes on either wing tip for the precise purpose to validate pitot tube measurements since RPX-05, but the team had always dropped analysis of this sensor, which was not directly used for controls. After RPX-07, we in fact confirmed that in previous flights the airspeed estimate from the wing tip pitots (corrected for body rates and wing upwash) was higher than the estimate from the probe ahead of the MBT.



**Figure 19: Profile shot of the mass-balance tube, taken during preflight inspections at China Lake. The pitot tube, covered with a protective orange flag, sticks about 10 cm ahead. The plane of the rotors and the leading edge of the pylons can be seen in this view.**

More significantly, classic system identification was not a major driver of our flight testing program. Early flight testing of more traditional aircraft consists of calibration flights followed by system identification flights to model stability response. This was impractical for our crosswind kites because there is no such thing as a trim state: the kite is constantly turning, accelerating, and seeing a different incoming wind vector. The tether, which is a significant contributor to the dynamic plant, is always changing geometry. Besides, early on, flight opportunities were scarce and we prioritized addressing higher level systems or business objectives: usually a functional demonstration before an investment deadline. And so the aerodynamics and simulation teams had to make do with the short logs of unplanned, but clean, level-wings glide-landings.

We did insert a handful of step response tests during early constrained hover flight, which led to the change in the elevator geometry described briefly in section 3.1.2. But in unconstrained high hover we wondered about phantom pitch-back moments for months (manifested as the top row props working harder in flight than in sim), and we were only just starting to plan the first high hover step response flights in late 2019, as part of the investigation of the FCW-01 crash, which had identified a similarly unmodeled roll-moment effect. These “phantom pitch moments” are discussed in “The Makani Autopilot” [10] and in “Oktoberkite and the MX2” [12].

More often than not, our models were developed analytically, then roughly and opportunistically corrected, trying to fit test data with obfuscating factors such as gusty winds or externally-constrained path locations.

### **Learning in Simulation**

Partly because of the challenge of doing empirical modeling work during flight testing, we recognized incredible value for Makani whenever we could learn about our system's response and performance in the simulator instead of going through the effort and expense of flight testing. We formalized this hard-earned wisdom from the RPX campaign in January of 2018 by constituting a Simulation Integrated Product Team (Sim IPT).

The goals of the Sim IPT were to identify and tackle missing physics in the simulation, and also to make the simulator more accessible to the broader team. Regarding missing physics, one of the most impactful decisions, and somewhat obvious in hindsight, was to use TurbSim windfields, developed at NREL based on statistical models of true, turbulent and variable winds experienced by wind turbines [21], instead of a simpler Dryden turbulence model that we had been using before, which is a parameterized stochastic model with spatial but no temporal variability. Regarding usability, just training the people outside of the controls team's office on how to run the simulator and access the data accelerated the number of insights about how the kites worked and how they didn't. (The flight simulator and the flight test logs have been open-sourced as part of this publication, and we invite any interested reader to dig even deeper! [3, 4]).

Another valuable result from this effort was the much broader use of an existing and powerful Monte Carlo simulation tool. This would run hundreds of simulations with a given configuration of the controller, at different wind speeds with random seeds of turbulence across the wind envelope, while randomly varying dozens of uncertain parameters affecting performance, such as mass properties, coefficients of lift and drag, and so on. The output of these simulations were then run through a list of scoring functions, determining whether the kite had crashed (for instance by violating low altitude or high tension thresholds), or otherwise performed poorly (for instance by exceeding uncomfortable values of sideslip). As part of the Sim IPT effort, the variables were scrubbed to confirm that the range of values used were plausible, and the scores were scrubbed and augmented to represent what was most relevant. The "batch sims" became a crucial tool to validate software changes and set the allowable flight envelope for every new software release.

## **4.3 A Major Lesson: Crosswind Flight Dynamics and the RPX-09 Crash**

The entire RPX campaign led Makani to a deeper understanding of the M600 tethered flight dynamics, discussed broadly in section 3.2.3. The main event that forced us to reckon with these issues was the mid-air break-up of SN3 in RPX-09, which can be seen in three videos with

titles beginning “20180410 RPX-09” on the Makani technical videos YouTube playlist [8]. The ensuing investigation reported root causes as three clauses:

*With a saturated rudder  
we lost control of the kite  
while attempting to reject a gust.*

The rudder was fully deployed to achieve a particularly tight turn into the loop: the test case had been changed such that the commanded path radius was decreasing, and this happened to coincide with a southerly slew of the flight path to follow the shifting wind direction, which also caused the controller to command a tighter turn. Specifically, the kite did not meet the tether roll command during this turn, and the rudder gain from the integrator on the tether roll error was wound up. The rudder was fully deflected to port, and because of the integrator windup, not responsive for a period of time once other contributions to the command started changing. There is a good discussion of the inner loop gains and how we learned to deal with control surface saturations and integrator windup in “The Makani Autopilot” [10].

While the rudder was saturated, a gust that was captured by the pitot tube measurements caused the estimate of the sideslip angle ( $\beta$ ) to drop quickly. The kite tried to compensate using the ailerons to slow the roll rate from -8 deg/s to zero. This effectively removed the balancing yaw moment due to roll rate.<sup>7</sup>

Now unbalanced, the yaw moment from the rudder caused the yaw rate to increase, the kite turned its nose further left into the circle, and tension dropped. Eventually the controller regained authority and guided the kite back to the commanded path, but this jerked on the tether, and neither the tether tension nor the radial location of the crosswind plane are explicitly controlled. Despite the fact that the tension never exceeded design limits, the sudden deceleration created inertial loads that we had not designed for, and the resulting moment distribution in the wing exceeded structural limits.

A long list of corrective actions aimed to address these three root causes. Among them:

- The rudder area was increased, and the slats were removed, both recovering lateral stability margins of the aircraft.
- Motor steering, by which differential thrust is partly used to command yaw, was enabled to complement actuation using the rudder.
- Scoring functions on the control surface saturations were revamped to include the rudder, and to more heavily penalize flying in a way that consistently saturated surfaces at some point or another of the loop.

---

<sup>7</sup> Yaw moment due to roll rate is a force coupling that shows up as the stability derivative coefficient  $C_{N,p}$  in aerodynamic models, particularly well described in Etkin [22]. Rolling induces a varying effective angle of attack along the wing span, rotating the lift vector across the span. This makes the component of lift in the longitudinal direction higher on one side of the wing than the other, thus imparting a yaw moment to the kite.

- The playbook that determined the outer-loop trajectory commands was limited to commanding loop radii higher than 160 m, where RPX test cases had been defined for as low as 100 m; and angles of attack were limited to less than 5 degrees. These changes had a strong detrimental effect on power performance.
- Back-solving was used to prevent integrator windup. Once an actuator was saturated, we calculated the deficit between the actuation request and the saturated values and removed these from the integral term.
- A nifty harmonic-gain controller was used to tackle the large, predictable excursions in sideslip that repeated every loop.
- A complementary filter was added to the airspeed and angle of attack estimates, so as to distinguish true kite motion effects from transient gusts.

Now, the particular sequence of events of RPX-09 was unique to that flight. But the type of vulnerabilities of our plant, and the type of interactions that could lead to uncontrolled crosswind flight, were representative of what made some flights sometimes seem “wobbly,” or what events would lead to a kite crash in the simulator. Those interrelated vulnerabilities included:

- Poor lateral stability of the M600 plant, driven in part due to a relatively small vertical tail area, and worsened by the presence of slats on RPX-07 through RPX-09.
- The asymmetries of the crosswind flight path with respect to gravity and with respect to the wind demand large periodic rotational motions. Gravity helps the kite turn at the top of the loop, but opposes it at the bottom, requiring a larger roll attitude to point the lift vector further into the turn. Wind is perceived as coming from the starboard at the top of the loop, and coming from the port at the bottom of the loop. This changing apparent wind requires the kite to constantly be turning its nose right and left in order to regulate sideslip.
- The large roll rates required to make the turn and balance the asymmetry due to gravity lead to large yaw moments; and the yaw moment due to roll rate ( $C_{N_p}$ ) is particularly strong for the M600 plant. Rolling into the turn tends to make the nose yaw out of the turn and the rudder to deflect to reject this. Note that roll rates increase if we fly faster and tighter loops in an attempt to even out power generation around the loop.
- Large deflections are required of the M600 control surfaces to achieve said roll and yaw rotations, and to balance yaw moments. Even larger deflections are required when the airspeed is low, such as at the top of the loop. This led us to increase the rudder size in order to make it more effective on the M600; and overall, a major design direction of the Oktoberkite effort was to increase the control surface area for both the rudder and the ailerons. Large deflections can be problematic because they move actuation to nonlinear regimes, they more easily lead to flow separation, and they decrease the overall bandwidth of the inner loop.
- The bridle moments on the kite can be large. At the bottom of the loop the kite is flying faster and the tether tension is higher. The bridle knot, where the bridle meets the tether, is due left because we are flying at a large roll angle to counteract gravity. The bridle

knot is also forward, because while the bridle falls with gravity, we are slowing down the kite with rotor drag. The knot forward and left gives the kite's nose a hard tug to the left.

The RPX-09 crash led us to understand that the M600 was not all that good at turning around the crosswind loop, and the simplest change we could make to consistently achieve robust crosswind flight without changing the shape of the kite was to command larger circles for the remainder of the flight test program. This directly affected performance because the higher mean elevation angle reduced the effective wind perceived by the kite; and because the larger potential energy exchange around the loop led to more pumping losses and to suboptimal kite speed commands to prevent overspeeding and overpowering parts of the loop. This is summarized in the discussion of the M600 power curve in the "M600 Energy Kite Description" [9].

We were unable to validate the M600 power curve; instead, we understood why we were not meeting it. This was a disappointing result for the M600 design, and indeed for Makani, but it was a successful result for the test program.

## 4.4 A Looming One: Loss of Roll Stability in Hover and the FCW-01 Crash

Another major challenge of M600 flight was maintaining a stable roll attitude in hover, and Makani was only beginning to tackle this difficulty as the project closed. This issue had the most clear and severe consequences at the end of the offshore flight FCW-01: having achieved an apparently stable hover after the transition out of crosswind, the kite diverged in roll, and we fully lost control of the kite attitude, which then crashed into the North Sea. However, indications of roll stability being an issue for the M600 were numerous and frequent before this event—from the first transition from crosswind to hover in RPX-02, discussed in section 3.2.2, and even during some dramatic moments in the Wing 7 test program. Each of these moments can be found in the *Makani - Energy Kite Technical Videos* playlist [8] (see especially "20190808 FCW-01 - Offshore - End of Flight Wide View," "20161214 RPX-02 - Roll of Makani M600 Following Transition Out of Crosswind," and "Tech Topic - 20130911 - Lack of Roll Control Illustrated in Wing 7 All Modes Flight.").

The "Root Cause Analysis and Corrective Actions for FCW-01" report [23] states the primary root cause of the loss-of-kite as follows:

*The root cause of the crash is the loss of tether tension. The kite lost tether tension after transitioning out of crosswind, while it was moving into position to allow the ground station to transform into the reel-in configuration. This resulted in insufficient roll stability. The system lost attitude control, could not recover, and crashed.*

Many factors contributed to this situation, and it's hard to summarize them here accurately any more concisely than the executive summary of the report. The investigation team identified, among other factors:

- The initial conditions after trans-out: the kite was excessively high (in part because of a large error in the altitude estimate due to poor handling of a GPS error) and pitched forward, and the rocking buoy motion would periodically tend to slacken the tether.
- The contributions of the controller: the feedback and feedforward commands from the tension controller were slow and ineffective, and the path controller damping of the radial velocity counteracted the tension regulator.
- The key dynamics missed by the simulation: the roll moments on the kite leading to the fast divergence in attitude, and the details of the buoy's rocking motion.

Figure 20, with plots taken from the report, shows how the roll excursion grew quickly in FCW-01 in comparison to in CW-05 and CW-02, which were flights that shared some, but not all, of the contributing factors.

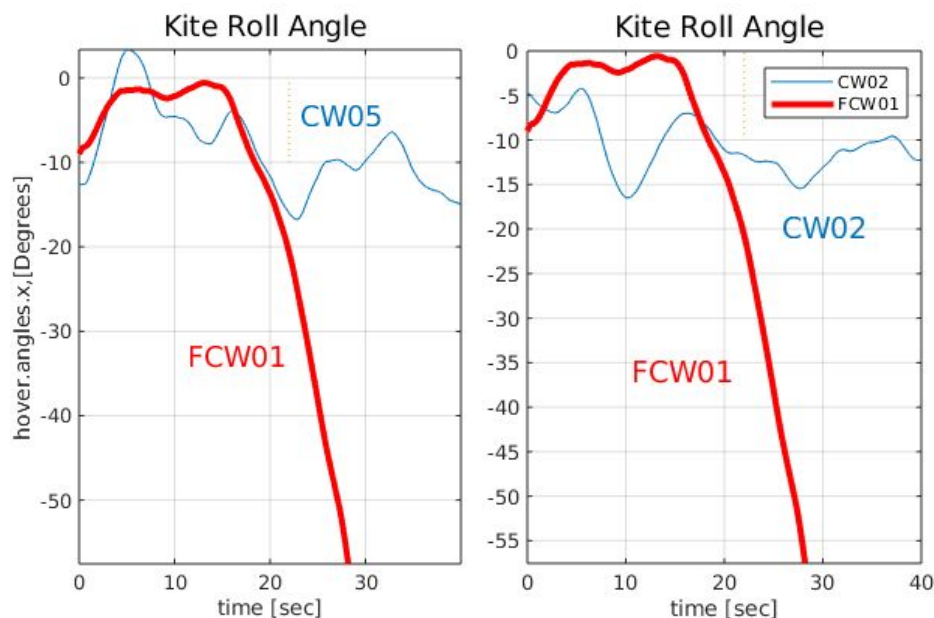


**Figure 20: Comparisons of kite roll in hover after the beginning of the ‘PrepTransformGsDown’ flight mode, during which the kite moved to position before initiating the GS transform. The roll excursion diverged in FCW-01, whereas the kite recovered in roll in both CW-05 and CW-02. In CW-05, the kite altitude at the beginning of the flight mode was 240 m (similar to FCW-01) but tether tension was higher than that in FCW-01, at 10 kN. In CW-02, the tether tension at the beginning of the flight mode was 8 kN (slightly lower than in FCW-01) but kite altitude was also lower, at 215 m. These figures are taken from the “Root Cause Analysis and Corrective Actions for FCW-01” report [23].**

Some preventive actions recommended in the report were implemented immediately, such as modifying the hover trajectory to descend first, thus recovering stability from the bridle geometry; and slowing down the translation in azimuth, thus reducing sideslip that could exacerbate the roll moments. The full corrective actions were more open-ended challenges, including recommendations to effectively model missing hover roll moments in simulation, and to incorporate active roll control mechanisms for the kite in hover.

The roll divergence was not predicted by the simulation, suggesting that there was an unmodeled moment acting on the kite. A leading hypothesis suggested that “blown lift,” the force generated by the main wing as it redirects the prop wash, was unevenly distributed, either because of differential thrust intended to produce a yaw moment, or because the prop wash was skewed by the apparent side wind as the kite translated laterally. Blown lift is discussed in a section of “The Makani Autopilot” [10]. This was not the only known deficiency in our hover models: the “phantom pitch moments” mentioned in section 4.2 were known unknowns. These dynamics could be, but had not yet been, further studied and characterised with system identification experiments in flight tests.

The consideration of incorporating active roll control in hover is mentioned in “The Makani Autopilot” [10] and in “Oktoberkite and the MX2” [12]: both offer a simple list of possible roll actuation mechanisms. We didn't get to the point of developing requirements or a sizing specification for such mechanisms. On the one hand, the team was understandably reluctant to complicate the passive solution of relying on the bridle to provide roll stability, and wanted to first consider control schemes that would keep the tether tension and bridle geometry within safe margins of the stable region. On the other hand, the evidence that we were gathering from flight testing suggested that the kite was often close to the boundary of that stability region, and that many possible contributing factors could nudge the hovering kite out of that region. The analysis in [23] found different combinations of factors present on many previous flights. And, during actual hover flight, it was common for the pilot to manually intervene to pitch back and increase tension to recover from a roll excursion.

Robust autonomous roll stability in hover, required to achieve continuous unattended operations, remains unsolved for Makani-style energy kite designs. What is clear is that roll stability in hover is a critical shortcoming of the M600 design in particular, and possibly of the passive bridled stability concept.

## 5 Conclusion: How Did That Work Out for Us?

Our approach to flight testing was to do it early, often before we felt “ready,” and to bias towards getting to product scales and operational environments. We made such decisions when we scaled the 20 kW Wing 7 to the 600 kW M600, and each time we moved operations to more remote and challenging test sites: first to complete crosswind in China Lake, then to fly all-modes in public in Hawaii, and eventually to fly offshore in Norway. Flight testing set the direction and the cadence for engineering development at Makani, and it was effective at identifying and prioritizing major technical challenges, eventually leading us to design a new airframe to address the shortcomings of the M600 performance. The opportunity costs were incomplete learnings before moving on to the next expensive step, but we believed that promptly reckoning with the learnings from taking said steps held even higher value. We did not get to fulfill a main goal of the program, despite our persistence in flight testing, which was to establish continuous, unattended operations in order to track a trend of increasing system availability.

The noteworthy results from our flight test program can be listed briefly:

- *Functional demonstrations* were approached like building blocks: with the M600, we proved that we could launch and land from a perch at the E-Lot, that we could fly crosswind in China Lake, then that we could bring these together and fly all-modes in Hawaii, and that we could fly all-modes from a floating platform in Norway. As we were building up to full functionality, we also demonstrated operations in diverse environments such as the hot desert and turbulent winds in California, wet seasons in Hawaii and Norway, and at-sea in Norway.
- *Performance validation* objectives led us to attempt good and eventually optimal power strategies during crosswind flights in China Lake and in Hawaii, and to fill out a power curve (shown in “M600 Energy Kite Description” [9]). Unfortunately, the demonstrated M600 power performance fell short of the original design. We demonstrated robust crosswind flight in a wind envelope from 5 to 12 m/s, and this too fell short of the original intent of 5 to 20 m/s to match the operational ranges of the industry’s horizontal-axis wind turbines. We understood the challenge of flying in higher winds, discussed in detail in “Airborne Wind Turbine Performance” [2].
- We completed a few *systems modelling experiments* as part of flight testing. As discussed in section 4.2, classic system identification was challenging in crosswind, where there is no trim state. Early modelling of hover flight led to the elevator redesign, and we were planning a more comprehensive suite of experiments to characterize the hovering plant.
- *Uncovering unknowns* was the most impactful outcome of our flight test program. Most of the narrative in this report reflects on such learnings, from finding vulnerable elements of the initial powertrain designs, to identifying robustness challenges in crosswind and

hover flight. These findings guided development and informed the next generation design.

The tension that came up often in planning and executing flight testing built up between expanding operations—towards different operating environments, higher wind speeds, longer durations, and higher performance—and methodically deepening our understanding. Many examples are described in this article. For instance, the team deprioritized the wingtip pitot data analysis, and eventually found a significant discrepancy with the main flight pitot in an indirect way. And we developed, installed, and flew with slats before understanding the complete stability of our plant, which turned out to be hindered by slats.

However, most of the deliberate decisions to assume risk, although not easy to make at the time, had positive—and often wonderful—outcomes. There is an example of this in the day-of decision to launch before every single flight: for example, the times we decided to fly a relatively new structure even though the airframe loads telemetry was not working, or to launch with a southerly wind in the forecast. Whatever risk factor was assumed, the team was now better prepared to monitor and react to it, and it so happened that none of these assumed risks led to a loss of airframe, and instead each of these decisions led to a flight ripe with new insights.

The decisions to use work-arounds for part of the system in order to test the full operation sooner, such as doing the first hovers without an empennage, or building Containerhenge to launch more directly into crosswind, accelerated our learnings. Some decisions plainly assumed risk that we had quantified, such as moving to China Lake and removing the top constraints to get to crosswind with unresolved and critical motor controller issues. We moved to Hawaii after a major flight dynamics failure in RPX-09. We decided to go offshore before the first flight off an onshore platform was complete, and we even shipped the second serial of the base station overseas before we had the opportunity to incorporate any changes based on that first flight. If we had not made such decisions, we would have missed the opportunity to tally the accomplishments we had at each of the new test sites within a short window of funding, which we were able to renew several times.

Our parting assessment is that managing these tensions, and the boldness of the overall approach, was appropriate for the magnitude and the urgency of the challenge. Broadening access to clean renewable energy with a brand-new technology would require operating reliably in some harsh environments at large scale and low cost, soon. There was not much time to expand the operating regime of our budding technology because the climate crisis was already underway, and because the funding cycles to support development are short. We didn't get there, but we believe that we were following an apt approach.

## 6 References

1. "Definitions of Availability Terms for the Wind Industry," DNV GL, Høvik, Norway, white paper, 2017. [Online]. Available: <https://www.ourenergypolicy.org/wp-content/uploads/2017/08/Definitions-of-availability-terms-for-the-wind-industry-white-paper-09-08-2017.pdf>
2. N. Tucker, "Airborne Wind Turbine Performance," in *The Energy Kite: Selected Results From the Design, Development and Testing of Makani's Airborne Wind Turbines, Part I*, Makani Technologies, Alameda, CA, USA, 2020, [Online]. [x.company/projects/makani](https://x.company/projects/makani)
3. *Makani Flight Logs*, Makani Technologies LLC, 2020. [Online]. Available: <https://console.cloud.google.com/marketplace/product/bigquery-public-datasets/makani-logs>
4. *Makani Code Release*, Makani Technologies LLC, 2020. [Online]. Available: <https://github.com/google/makani/>
5. A. Dunlap (Dir. of Photography, Ed., Narrator) and K. Stirr (Writer, Director), *Pulling Power from the Sky: The Story of Makani*, Makani Technologies, Alameda, CA, USA, 2020, included in *Makani*. (Aug., 2020). [Online Video]. Available: [https://www.youtube.com/playlist?list=PL7og\\_3Jqea4UFajQX-wwc702tUJcBMFMU](https://www.youtube.com/playlist?list=PL7og_3Jqea4UFajQX-wwc702tUJcBMFMU)
6. M. L. Loyd, "Crosswind Kite Power," *J. of Energy*, vol. 4, no. 3, May-Jun 1980, Art. no. 80-4075, doi: <https://doi.org/10.2514/3.48021>
7. D. Vander Lind, "Analysis and Flight Test Validation of High Performance Airborne Wind Turbines," in *Airborne Wind Energy*, (Green Energy and Technology) U. Ahrens, M. Diehl, R. Schmehl, Eds., Berlin and Heidelberg, Germany: Springer, 2013, pp. 473-490, doi: [https://doi.org/10.1007/978-3-642-39965-7\\_28](https://doi.org/10.1007/978-3-642-39965-7_28)
8. Makani Technologies, Alameda, CA, USA. *Makani - Energy Kite Technical Videos*. (Aug., 2020). [Online Video]. Available: [https://www.youtube.com/playlist?list=PL7og\\_3Jqea4VRCZmMKNK4LDH64sYgkLZzv](https://www.youtube.com/playlist?list=PL7og_3Jqea4VRCZmMKNK4LDH64sYgkLZzv)
9. P. Echeverri, T. Fricke, G. Homsy, and N. Tucker, "M600 Energy Kite Description," in *The Energy Kite: Selected Results From the Design, Development and Testing of Makani's Airborne Wind Turbines, Part I*, Makani Technologies, Alameda, CA, USA, 2020, [Online]. Available: <https://x.company/projects/makani>
10. T. Fricke, "The Makani Autopilot," in *The Energy Kite: Selected Results From the Design, Development and Testing of Makani's Airborne Wind Turbines, Part I*, Makani Technologies, Alameda, CA, USA, 2020, [Online]. Available: <https://x.company/projects/makani>
11. "Kite Stability in Crosswind Flight," in *The Energy Kite: Selected Results From the Design, Development and Testing of Makani's Airborne Wind Turbines, Part II*, Makani Technologies, Alameda, CA, USA, 2020, [Online]. Available: <https://x.company/projects/makani>
12. G. Homsy, "Oktoberkite and the MX2," in *The Energy Kite: Selected Results From the Design, Development and Testing of Makani's Airborne Wind Turbines, Part I*, Makani

- Technologies, Alameda, CA, USA, 2020, [Online]. Available: <https://x.company/projects/makani>
13. "FAA Determination of No Hazard to Air Navigation for Temporary Structure," Federal Aviation Administration, in *The Energy Kite: Selected Results From the Design, Development and Testing of Makani's Airborne Wind Turbines*, Part III, Makani Technologies, Alameda, CA, USA, 2020, [Online]. Available: <https://x.company/projects/makani>
  14. C.M. Smith and E. D. Skillingstad, "Investigation of Upstream Boundary Layer Influence on Mountain Wave Breaking and Lee Wave Rotors Using a Large-Eddy Simulation," *J. of the Atmos. Sci.*, vol. 66, no. 10, pp. 3147–3164, Oct. 2009, doi: <https://doi.org/10.1175/2009JAS2949.1>
  15. "Selected Decks from RPX Lessons Learned Reviews," in *The Energy Kite: Selected Results From the Design, Development and Testing of Makani's Airborne Wind Turbines*, Part III, Makani Technologies, Alameda, CA, USA, 2020, [Online]. Available: <https://x.company/projects/makani>
  16. "Selected Decks from All-Modes Lessons Learned Reviews," in *The Energy Kite: Selected Results From the Design, Development and Testing of Makani's Airborne Wind Turbines*, Part III, Makani Technologies, Alameda, CA, USA, 2020, [Online]. Available: <https://x.company/projects/makani>
  17. Makani Technologies, Alameda, CA, USA. *Makani*. (Aug., 2020). [Online Video]. Available: [https://www.youtube.com/playlist?list=PL7og\\_3Jqea4UFajQX-wwc702tUJcBMFMU](https://www.youtube.com/playlist?list=PL7og_3Jqea4UFajQX-wwc702tUJcBMFMU)
  18. N. Rickner, "Airborne Wind Energy Systems as an Obstruction: Makani's Journey with the US Federal Aviation Administration," presented at the Airborne Wind Energy Conf., Glasgow, United Kingdom, October 15-17, 2019, DOI: <http://resolver.tudelft.nl/uuid:ea8256a2-2c52-402e-a72f-fd60b0794c6b>
  19. Makani Technologies, Akinaka & Associates, Ltd., and Rana Biological Consulting, "Bird and Bat Conservation Plan: Makani Energy Kite Project, South Kohala District, Island of Hawai'i, Hawai'i," in *The Energy Kite: Selected Results From the Design, Development and Testing of Makani's Airborne Wind Turbines*, Part III, Makani Technologies, Alameda, CA, USA, 2020, [Online]. Available: <https://x.company/projects/makani>
  20. U.S. Fish and Wildlife Service, Arlington, VA, USA. *Land-Based Wind Energy Guidelines* (2012). [Online]. Available: [https://www.fws.gov/ecological-services/es-library/pdfs/WEG\\_final.pdf](https://www.fws.gov/ecological-services/es-library/pdfs/WEG_final.pdf)
  21. B.J. Jonkman, "TurbSim User's Guide," NREL, Golden, CO, USA, Version 1.50, Aug. 26, 2009. [Online]. Available: <https://www.nrel.gov/docs/fy09osti/46198.pdf>
  22. B. Etkin, *Dynamics of Atmospheric Flight* (Dover Books on Aeronautical Engineering), Mineola, NY, USA: Dover Publications, Inc., 2005.
  23. K. Hallamasek, "Root Cause Analysis and Corrective Actions for FCW-01," in *The Energy Kite: Selected Results From the Design, Development and Testing of Makani's Airborne Wind Turbines*, Part II, Makani Technologies, Alameda, CA, USA, 2020, [Online]. Available: <https://x.company/projects/makani>